Experimental Study of the Geotechnical Properties of UK Mudrocks

Ramtin Hosseini Kamal

Department of Civil & Environmental Engineering

Imperial College London

February 2012

A thesis submitted to Imperial College London

in partial fulfillment for the degree of

Doctor of Philosophy

To Baba, Arvin & Barbara.

بنگر ز جهان چه طرح بربستم؟ هیچ!
وز حاصل عمر چیست در دستم؟ هیچ!
شمع طربم ، ولی چو بنشستم ، هیچ!
من جام جمم ، ولی چو بشکستم ، هیچ!

عمر خیام
۴۲۷-۵۱۰

Look, of the world what an image I have created? Naught!
And of life's fruit what have remained in my hands? Naught!
I am a candle of joy, but once I sit, Naught!
I am the Jamshid's Chalice, but once I break, Naught!

Omar Khayyam
1048-1131

Abstract

Quantifying soil characteristics using state of the art equipments is a necessary step in introducing comprehensive constitutive models which can be used in engineering design. Large areas of the Southern UK are covered by Triassic to Eocene mudrocks that were deposited in dissimilar geological environments, and have experienced diverse post depositional histories leading to a range of current natural structures. The aim of this study was to investigate different aspects of the mudrock's structure and their implication on the mechanical behaviour of these soils.

Three mudrocks were chosen and sampled; Oxford, Kimmeridge and Gault Clays. These were to be compared with London Clay which was previously studied at Imperial College by Gasparre (2005), Nishimura (2006) and Minh (2007). High quality block and rotary core samples obtained for these soils were used in two experimental studies carried out by the author and Brosse (2011) as well as for a micro-structure analysis performed by Wilkinson (2011). The author carried out series of tests using triaxial apparatus equipped with bender elements and high resolution displacement transducers. These tests provided the strength envelopes of each soil, undrained stiffness and drained elastic parameters. Oedometer cells were also used to investigate the 1-D compression of each material. These were complimented by ring shear tests and index tests performed on all four mudrocks.

Findings of this study highlighted the highly anisotropic behaviour of these soils. No clear correlation was found to relate the anisotropy or any other characteristics of these materials to their geological age or their depth of burial. For Gault Clay, the effects of weathering and root action were investigated and the importance of highly fissured macro-structure of the soils was noted. The results from this study are in good agreement with those from tests carried out by Brosse (2011) using a hollow cylinder apparatus and the micro-analysis carried out by Wilkinson (2011).

Acknowledgments

I would like to express gratitude to my first supervisor Prof. Matthew Coop for his intelligent and friendly support during my PhD. I would also like to thank my second supervisor Prof. Richard Jardine for his rich and useful advices throughout the work. The contributions made by Dr. Clark Fenton are also appreciated.

Special thanks go to Miss Amandine Brosse and Dr. Steve Wilkinson who worked with me on this project. Amandine's intelligence was a blessing in solving difficult issues during the work and also her help in the laboratory will never be forgotten. Steve's hard work in finding right and accessible sites for sampling as well as his effort in obtaining samples, which were mainly used by the author and Amandine, were of great value. Also his insight into the geology and the micro-structure of the soils were of great importance to this study.

Anyone who has worked in a soil's laboratory knows the great role technicians are playing in helping students in performing their experiments; Mr Alain Bolsher was more than a help, he is a great character whose positive support and advice was always generously available. Working with him on site was one of the most memorable moments of the last four years. Mr Steve Ackerly also was kind and patient in helping me out of the most complex experimental problems. Here I would also want to thank those who taught me how to work in the laboratory or gave me technical advices on different grounds: Dr. Appolonia Gasparre, Dr. Alessandra Carrera, Dr. Gregor Vilhar and Mr Miguel Carrion Carmona.

I am also grateful to MSc students who worked on this project and their help was of great value; Miss Yue Gao, Mr Patrick Moran, Mr Manjesh Narayana and Mr David Cunliffe. Mr Darren Ward is also to be thanked for as he kindly carried out three CPT investigations at our sites.

The company of great comrades Nima Bahramalian, Marco Ottolini and Ali Shayegan during the last four years was a great contentment and I am most grateful to them.

Finally I want to show my respect and to thank those who this thesis, the symbolic outcome of the last four years, is dedicated to them; ***Baba, Arvin*** and ***Barbara***. I find it very hard to find words which can express my high feelings for them and I shall leave it in silence …

Contents

Abstract 4

Acknowledgments 5

Contents 7

List of Figures 11

Nomenclature 24

1 **Introduction** 28
1.1 Background and objectives of the project 28
1.2 Thesis layout 29
2 **Literature review** 30
2.1 Introduction 30
2.2 Structure 30
2.3 Sensitivity framework 32
2.3.1 Sedimentation and post-sedimentation structure 32
2.3.2 Sensitivity 33
2.3.3 Post-yield behaviour 34
2.4 Yielding behaviour 36
2.5 Small strain parameters 38
2.6 Influence of recent stress history 42
2.7 Time dependent behaviour of the soil 44
2.8 Effects of weathering 48
2.8.1 Effect of vegetation on the soil profile 51
3 **Sampling, Apparatus and Procedures** 71
3.1 Introduction 71
3.2 Sampling 71
3.2.1 Site selection 71
3.2.2 Block sampling 72
3.2.3 Rotary coring 73

3.3 Apparatus 74
3.3.1 Introduction 74
3.3.2 Oedometer apparatus 74
3.3.3 Triaxial apparatus 75
3.4 Testing procedures 81
3.4.1 Sample preparation 81
3.4.2 Testing procedures 84
3.5 Analysis of the data 90
3.5.1 Introduction 90
3.5.2 Specific volume 90
3.5.3 Area correction 91
3.5.4 Volumetric and shear strains 92
3.5.5 Shear plane analysis 95
3.5.6 Bender element analysis 95
4 **Oxford Clay** 119
4.1 Introduction 119
4.2 Background 119
4.2.1 Geology and the site 119
4.2.2 Previous studies 120
4.2.3 Evaluation of the in-situ stresses 122
4.3 Intrinsic properties 123
4.3.1 Compression behaviour 123
4.3.2 Shearing behaviour 124
4.4 Natural properties 125
4.4.1 Compression behaviour 125
4.4.2 Shearing behaviour 127
4.5 Summary 135
5 **Gault Clay** 171
5.1 Introduction 171
5.2 Background 171
5.2.1 Geology and the site 171
5.2.2 Previous studies 173
5.2.3 Evaluation of the in-situ stresses 174
5.3 Intrinsic properties 175

5.3.1 Compression behaviour....175
5.3.2 Shearing behaviour....175
5.4 Natural properties....177
5.4.1 Compression behaviour....177
5.4.2 Shearing behaviour....178
5.5 Summary....184
6 **Kimmeridge Clay**....221
6.1 Introduction....221
6.2 Background....221
6.2.1 Geology and the site....221
6.2.2 Previous studies....222
6.2.3 Evaluation of the in-situ stresses....223
6.3 Intrinsic properties....223
6.3.1 Compression behaviour....223
6.3.2 Undrained shearing behaviour....224
6.4 Natural properties....225
6.4.1 Compression behaviour....225
6.4.2 Shearing behaviour....226
6.5 Summary....231
7 **Discussion**....261
7.1 Introduction....261
7.2 Geological history of UK mudrocks....262
7.2.1 General background....262
7.2.2 Oxford Clay....263
7.2.3 Kimmeridge Clay....264
7.2.4 Gault Clay....264
7.2.5 London Clay....265
7.3 Micro-structure and macro-structure....266
7.3.1 Oxford Clay....266
7.3.2 Kimmeridge Clay....266
7.3.3 Gault Clay....267
7.3.4 London Clay....267
7.3.5 Analysis of particle orientation....268
7.4 Behaviour in 1-D compression....269

7.5 Behaviour in shear 272
7.5.1 Strength of the mudrocks 272
7.5.2 Stiffness of the mudrocks 277
7.6 Summary 278
8 **Conclusions** 307
8.1 Current study 307
8.2 Future work 309
References 311

List of Figures

Figure 2-1: The effect of structure on the relative location of compression curves of natural and reconstituted soil..... 53
Figure 2-2: Sedimentation compression curves for normally consolidated argillaceous sediments (Skempton, 1969)……..53
Figure 2-3: Sedimentation compression curves normalised in the I_v space (Burland, 1990)…….. 54
Figure 2-4: Classification of fabric (Sides & Barden, 1970) 54
Figure 2-5: The response of clays to one-dimensional compression; natural clay with a) sedimentation and b) post-sedimentation structure (Cotecchia & Chandler, 2000) 55
Figure 2-6: Idealized behaviour of natural and reconstituted clays (Cotecchia & Chandler, 2000)..... 55
Figure 2-7: Sedimentation compression curves in the sensitivity framework (Cotecchia & Chandler, 2000) 56
Figure 2-8: Normalised stress paths for Bothkennar clay (Smith et al., 1992)..... 56
Figure 2-9: Stable and meta-stable structure in : a) compression; b) shearing (Baudet & Stallebrass, 2004)..... 57
Figure 2-10: Pappadai clay behaviour normalised for both volume and structure (Cotecchia & Chandler, 2000) 58
Figure 2-11: Effects of clay fraction on the post-peak shear behaviour of soils (Lupini et al., 1981)..... 59
Figure 2-12: Behaviour of overconsolidated clays in undrained shear; a) low plasticity clay, b) stiff plastic clay (Jardine et al., 2004) 59
Figure 2-13: Conceptual multiple surface kinematic model with three zones (Jardine, 1992)..... 60
Figure 2-14: Comparison of secant stiffness curves for three materials in the small strain region (Clayton & Heymann, 2001)..... 61
Figure 2-15: Relationship between permanent and total strains for Magnus till (1992) 62

Figure 2-16: Planes and lines representing special types of material (Pickering, 1970) 63
Figure 2-17: Stiffness response of reconstituted London clay with different stress histories (Atkinson et al., 1990) 64
Figure 2-18: Secant stiffness degradation curves for Bothkennar clay with different stress paths (Clayton & Heymann, 2001)..... 65
Figure 2-19: Tangent stiffness degradation curves for different probe lengths and creep periods (Gasparre et al., 2007)..... 66
Figure 2-20: Stress-strain curves for step-changed strain rates and relaxation procedures; a) triaxial compression, b) triaxial extension and simple shear tests (Graham et al., 1983)..... 67
Figure 2-21: Change in undrained shearing resistance with log (strain rate), (Graham et al., 1983)..... 67
Figure 2-22: Effect of stepwise changes in strain rate on the undrained stress-strain behaviour of intact and reconstituted London clay after isotropic compression (Sorensen et al., 2007)..... 67
Figure 2-23: Effect of stepwise change in strain rate on small to large strain stiffness of NC reconstituted London clay (Sorensen et al., 2007) 69
Figure 2-24: Normalised state boundary surfaces of both the natural (weathered yellow and unweathered grey) and reconstituted clays (Cafaro & Cotecchia, 2001) . 69
Figure 2-25: Variation of soil properties with depth as affected by trees; a) cone end bearing, b) undrained shear strength, c) water content, d) suction (Crilly & Driscoll, 2000)..... 70
Figure 3-1: Sampling sites (Wilkinson, 2008) 99
Figure 3-2: Image of the pond and the sampling location for Oxford clay at Elstow looking north east 100
Figure 3-3: Oxford clay block sampling; a) the trench, b) trimming the block of soil, c) sample covered with cling film and wax to stop changes in water content, d) closing the box and filling it with expanding foam..... 101
Figure 3-4: A block sampling column that failed on a weak horizontal layer 101
Figure 3-5: Excavated trench for sampling Gault clay at High cross, Cambridge.... 102
Figure 3-6: Presence of tree roots in Gault clay block sample (depth= 3 m)..... 102
Figure 3-7: Oedometer cells used for the current project..... 103
Figure 3-8: Details of a typical oedometer consolidation cell (BS1377:1990)..... 103

Figure 3-9: Schematic diagram of the hydraulic triaxial apparatus (Gasparre, 2005) 104
Figure 3-10: Old radial belt 105
Figure 3-11: Mid-height pore water pressure probe (Hight, 1983) 105
Figure 3-12: Orientation of bender elements in the triaxial samples (Pennington et al., 1997) 106
Figure 3-13: Lateral bender elements (Pennington et al., 1997) 106
Figure 3-14: Schematic sketch of new radial displacement set-up 107
Figure 3-15: 38 mm sample with the new radial displacement set-up 107
Figure 3-16: Radial strains in a load-unload radial probe using radial belt and the new set-up 108
Figure 3-17: High pressure triaxial cell (7 MPa) 108
Figure 3-18: a) cutting the sample box, b) trimming the sample with a band saw to a cylindrical shape 109
Figure 3-19: a) final trimming on a soil lathe, b) trimming the ends 109
Figure 3-20: 100 mm triaxial sample with local transducers 110
Figure 3-21: a) 38 mm diameter consolidometer, b) 230 mm diameter consolidometer 110
Figure 3-22: Testing programme types: A) reconsolidation to the 'in-situ' state and shearing to failure in compression and extension, B) isotropic compression or unloading followed by shearing in compression or extension to failure, C) axial, radial, constant p’ or constant q probing from the 'in-situ' state 111
Figure 3-23: Evidence of incomplete drainage of pore water pressure during an intended drained axial probe, applying a rate of 0.3 kPa/hr to a 100 mm diameter sample of Oxford clay 111
Figure 3-24: The effect of an exceptional temperature change on a 38 mm sample of Gault clay; a) the change in temperature, b) change in mean of local axial strain gauges, c) change in volumetric strain measured by volume gauge 113
Figure 3-25: Drained axial probes in compression and extension on 38 mm diameter samples of Oxford clay; a) deviatoric stress vs axial strain, b) radial strain vs axial strain 114
Figure 3-26: Complex strain localisation on 50 mm in diameter sample of Gault clay 115

Figure 3-27: Shear plane analysis for peak and post-rupture strength of Oxford clay 115
Figure 3-28: Typical S-wave signal; a) first deflection, b) first bump maximum, c) zero after first bump, and d)major first peak (Lee & Santamarina, 2005) 116
Figure 3-29: Frequency domain analysis to obtain G_{hv} for Gault clay at p'=200 kPa; a) arrival times derived from the slope of stacked phase vs. frequency, b) projection of arrival times calculated from frequency domain 117
Figure 3-30: Frequency domain analysis to obtain G_{hh} for Gault clay at p'=200 kPa; a) arrival times derived from the slope of stacked phase vs. frequency, b) projection of arrival times calculated from frequency domain 118
Figure 4-1: Sampling site for Oxford clay; a) map of Bedford and the site location at Elstow, b) field map of the Pond 1 and site investigations (after Wilkinson, 2011). 141
Figure 4-2: Vertical section of Oxford clay: dominance of horizontal lamination in structure 142
Figure 4-3: Soil profile at Elstow (Brosse, 2011) 143
Figure 4-4: Soil profile at Elstow (Brosse, 2011, CPT data provided by In-situ SI) 143
Figure 4-5: Particle size distribution of Oxford clay 144
Figure 4-6: Multi-stage procedure to obtain stiffness parameters of Oxford clay at the in-situ stress state (Hird & Pierpoint, 1997) 144
Figure 4-7: Suction measurment on a block sample of Oxford clay 145
Figure 4-8: One-dimensional compression of reconstituted Oxford clay 145
Figure 4-9: Isotropic compression of reconstituted Oxford clay 146
Figure 4-10: Stress-strain behaviour of reconstituted Oxford clay 146
Figure 4-11: Pore water pressure change during the shearing of reconstituted Oxford clay 147
Figure 4-12: Normalised stress-strain behaviour of reconstituted Oxford clay 147
Figure 4-13: Effective stress paths for reconstituted isotropically consolidated Oxford clay 148
Figure 4-14: Normal Compression and Critical State Lines for reconstituted Oxford clay 148
Figure 4-15: Normalised effective stress paths of reconstituted Oxford clay 149
Figure 4-16: Compression curves of intact Oxford clay 149
Figure 4-17: Compression lines for intact and reconstituted Oxford clay 150
Figure 4-18: Normalised one-dimensional compression curves 150

Figure 4-19: Compression curves of horizontally cut intact Oxford clay 151
Figure 4-20: Comparison between compression curves of horizontally and vertically cut samples of Oxford clay 151
Figure 4-21: Effective stress paths for intact Oxford clay in compression 152
Figure 4-22: Effect of sample size on the strength of Oxford clay in compression .. 152
Figure 4-23: Effective stress paths for intact Oxford clay in compression and extension 153
Figure 4-24: Stress-strain behaviour of intact Oxford clay 153
Figure 4-25: Pore water pressure change during the shearing of intact Oxford clay 154
Figure 4-26: Normalised stress-strain behaviour of intact Oxford clay 154
Figure 4-27: Pore water pressure change at the base and mid-height of a sample of intact Oxford clay sheared in compression 155
Figure 4-28: Peak and post-rupture strength envelope for intact Oxford clay 156
Figure 4-29: Effective stress paths of horizontally and vertically cut samples of intact Oxford clay 157
Figure 4-30: Stress-strain behaviour of intact and remoulded Oxford clay at small displacements in ring shear apparatus 157
Figure 4-31: Stress-strain behaviour of intact and remoulded Oxford clay at large displacements in a ring shear apparatus 158
Figure 4-32: Normalised stress-strain behaviour for the intact and reconstituted Oxford clay 158
Figure 4-33: Effective stress paths for the intact and reconstituted Oxford clay 159
Figure 4-34: Normalised effective stress paths for the intact and reconstituted Oxford clay 159
Figure 4-35: Stiffness degradation curves for the undrained compression tests on intact Oxford clay at different stress levels 160
Figure 4-36: Stiffness variation with stress level at different strain levels for the intact Oxford clay 160
Figure 4-37: Stiffness variation with stress level for vertically and horizontally cut intact samples of Oxford clay 161
Figure 4-38: Typical bender element signals to obtain G_{hv} values for the intact Oxford clay 162
Figure 4-39: Typical bender element signals to obtain G_{hh} values for the intact Oxford clay 163

Figure 4-40: Typical bender element signals to obtain G_{vh} values for the intact Oxford clay 164
Figure 4-41: Stiffness of the intact and reconstituted samples of Oxford clay in different directions 165
Figure 4-42: Stiffness of the intact and reconstituted samples of Oxford clay normalised for the void ratio 165
Figure 4-43: Axial probe in compression and extension; axial stress against axial strain 166
Figure 4-44: Axial probe in compression and extension; radial strain against axial strain 166
Figure 4-45: Radial probe in compression and extension; radial stress against radial strain 167
Figure 4-46: Radial probe in compression; axial strain against radial strain 167
Figure 4-47: p' constant probe in compression; deviatoric stress against shear strain 168
Figure 4-48: p' constant probe in compression; deviatoric stress against volumetric strain 168
Figure 4-49: q constant probe in compression; mean effective stress against volumetric strain 169
Figure 4-50: q constant probe in compression; mean effective stress against shear strain 169
Figure 5-1: Sampling site for Gault clay;a) map of Cambridge and the site location, High Cross (Ordnance Survey, 2008), b) field map and Google Earth image of the sampling locations (after Wilkinson, 2011) 190
Figure 5-2: Soil profile at High Cross 191
Figure 5-3: Soil profile at High Cross (CPT data provided by In-situ SI) 192
Figure 5-4: Macro-structure of rotary core sample of Gault clay from 10m depth, natural discontinuities are outlined with dotted line (produced with Brosse, 2012) 193
Figure 5-5: Particle size distribution of samples from 3.5m depth 193
Figure 5-6: Gault clay CPT profile; a) close to trees, b) away from trees 194
Figure 5-7: Suction measurments on rotary core samples of Gault clay at shallow (3.5m) and deep (9.6m) depths 195
Figure 5-8: One-dimensional compression of reconstituted Gault clay 195
Figure 5-9: Isotropic compression of reconstituted Gault clay 196

Figure 5-10: Undrained triaxial stress-strain behaviour of isotropically compressed reconstituted Gault clay....196
Figure 5-11: Pore water pressure change during the shearing of reconstituted Gault clay....197
Figure 5-12: Normalised stress-strain behaviour of reconstituted Gault clay....197
Figure 5-13: Effective stress paths for reconstituted isotropically consolidated Gault clay....198
Figure 5-14: Normal Compression and Critical State Lines for reconstituted isotropically consolidated Gault clay....198
Figure 5-15: Normalised effective stress paths of reconstituted Gault clay....199
Figure 5-16: Oedometer compression curves for intact Gault clay from rotary core samples....199
Figure 5-17: Oedometer compression curves for ntact Gault clay from rotary core and block samples at 3.5m depth....200
Figure 5-18: Oedometer compression lines for intact (full symbols) and reconstituted (empty symbol) Gault clay....200
Figure 5-19: Normalised one-dimensional compression curves....201
Figure 5-20: Stress paths for intact Gault clay in compression....201
Figure 5-21: Stress paths for intact Gault clay in compression and extension....202
Figure 5-22: Effect of sample size on the strength of Gault clay....202
Figure 5-23: Stress-strain behaviour of intact Gault clay....203
Figure 5-24: Pore water pressure change during the shearing of intact Gault clay....203
Figure 5-25: Normalised stress-strain behaviour of intact Gault clay....204
Figure 5-26: Peak and post-rupture strength envelope for intact Gault clay....205
Figure 5-27: Stress paths of horizontally and vertically cut samples of intact Gault clay....206
Figure 5-28: Stress-strain behaviour of intact and remoulded Gault clay at small displacements in the ring shear apparatus (d = shear displacement, h = sample height)....206
Figure 5-29: Stress-strain behaviour of intact and remoulded Gault clay at large displacements in a ring shear apparatus (d = shear displacement, h = sample height)....207
Figure 5-30: Normalised stress-strain behaviour for the intact and reconstituted (Normally consolidated & Overconsolidated) Gault clay....207

Figure 5-31: Stress paths for the intact and reconstituted Gault clay.....208
Figure 5-32: Normalised stress paths for the intact and reconstituted Gault clay.....208
Figure 5-33: Stiffness degradation curves for the undrained compression tests on intact block samples of Gault clay at different consolidation effective stress levels.209
Figure 5-34: Stiffness degradation curves for the undrained compression tests on intact rotary core samples of Gault clay at different consolidation effective stress levels.....209
Figure 5-35: Stiffness degradation curves for the undrained compression tests on intact rotary core and block samples of Gault clay from the same depth at similar stress levels.....210
Figure 5-36: Stiffnesses at different strain levels for the intact rotary core and block samples of Gault clay 210
Figure 5-37: Undrained stiffness variation with stress level at different strain levels for the intact Gault clay; a) strain levels 0.001% and 0.1%, b) strain levels 0.01% and 1%.....211
Figure 5-38: Typical bender element signals to obtain V_{hv} and G_{hv} values for the intact Gault clay 212
Figure 5-39: Typical bender element signals to obtain V_{hh} and G_{hh} values for the intact Gault clay 213
Figure 5-40: BE stiffness of the intact and reconstituted samples of Gault clay in different directions 214
Figure 5-41: BE stiffness of the intact and reconstituted samples of Gault clay normalised for the void ratio 214
Figure 5-42: Normalised bender element shear moduli for reconstituted and intact samples of Gault clay following isotropic and anisotropic stress paths (Pennington et al., 1997).....215
Figure 5-43: BE shear moduli for reconstituted samples of Gault clay following isotropic loading and unloading (Pennington et al., 1997) 215
Figure 5-44: Normalised BE shear moduli for reconstituted samples of Gault clay during isotropic loading 216
Figure 5-45: Normalised BE shear moduli for reconstituted samples of Gault clay during isotropic loading and unloading.....216
Figure 5-46: Axial probe in compression and extension; axial effective stress and strain increments 217

Figure 5-47: Axial probe in compression and extension; radial strain plotted against axial strain 217
Figure 5-48: Radial probe in compression and extension; radial effective stress and strain increments 218
Figure 5-49: Radial probe in compression and extension; axial strain plotted against radial strain....218
Figure 5-50: p' constant probe in compression; deviatoric stress plotted against shear strain....219
Figure 5-51: p' constant probe in compression; deviatoric stress plotted against volumetric strain....219
Figure 5-52: q constant probe in compression; mean effective stress plotted against volumetric strain....220
Figure 5-53: q constant probe in compression; mean effective stress plotted against shear strain....220
Figure 6-1: Sampling site for Kimmeridge clay; a) map of Steventon and the site location, Willow Brook Farm (Ordnance Survey, 2009b), b) field map of the sampling locations (after Wilkinson, 2011).... 236
Figure 6-2: Soil profile at Willow Brook Farm.... 237
Figure 6-3: Soil profile at Willow Brook Farm (CPT data provided by In-situ SI).. 238
Figure 6-4: Macro-structure of rotary core sample of Kimmeridge clay from 10m depth, natural discontinuities are outlined with dotted line (produced with Brosse, 2012)……...239
Figure 6-5: Particle size distribution of sample from 10m depth.... 239
Figure 6-6: Suction probe measurment on a sample of Kimmeridge clay.... 240
Figure 6-7: One-dimensional compression of reconstituted Kimmeridge clay 240
Figure 6-8: Isotropic compression of reconstituted Kimmeridge clay.... 241
Figure 6-9: Undrained triaxial stress-strain behaviour of isotropically compressed reconstituted Kimmeridge clay 241
Figure 6-10: Pore water pressure change during the shearing of reconstituted Kimmeridge clay 242
Figure 6-11: Normalised stress-strain behaviour of reconstituted Kimmeridge clay 242
Figure 6-12: Effective stress paths for reconstituted isotropically consolidated Kimmeridge clay 243
Figure 6-13: Normal Compression and Critical State Lines for reconstituted isotropically consolidated Kimmeridge clay.... 243

Figure 6-14: Normalised effective stress paths of reconstituted Kimmeridge clay .. 244
Figure 6-15: Oedometer compression curves for intact Kimmeridge clay 244
Figure 6-16: Oedometer compression lines for intact and reconstituted Kimmeridge clay 245
Figure 6-17: Normalised one-dimensional compression curves 245
Figure 6-18: Effective stress paths for intact Kimmeridge clay..... 246
Figure 6-19: Effect of sample size on the strength of Kimmeridge clay 246
Figure 6-20: Stress-strain behaviour of intact Kimmeridge clay 247
Figure 6-21: Pore water pressure change during the shearing of intact Kimmeridge clay 247
Figure 6-22: Normalised stress-strain behaviour of intact Kimmeridge clay 248
Figure 6-23: Peak and post-rupture strength envelope for intact Kimmeridge clay . 249
Figure 6-24: Stress-strain behaviour of intact and remoulded Kimmeridge clay at small displacements in ring shear apparatus (d = shear displacement, h = sample height)..... 250
Figure 6-25: Stress-strain behaviour of intact and remoulded Kimmeridge clay at large displacements in a ring shear apparatus (d = shear displacement, h = sample height)..... 250
Figure 6-26: Normalised stress-strain behaviour for the intact and reconstituted (Normally consolidated & Overconsolidated) Kimmeridge clay 251
Figure 6-27: Effective stress paths for the intact and reconstituted Kimmeridge clay 251
Figure 6-28: Normalised effective stress paths for the intact and reconstituted Kimmeridge clay 252
Figure 6-29: Stiffness degradation curves from the undrained compression tests on Kimmeridge clay at different consolidation effective stress levels..... 252
Figure 6-30: Undrained stiffness variation with stress level at different strain levels for the intact Kimmeridge clay..... 253
Figure 6-31: Typical bender element signals to obtain V_{hv} and G_{hv} values for the intact Kimmeridge clay (KIMCL-NT-8 at isotropic p'=220 kPa) 254
Figure 6-32: Typical bender element signals to obtain V_{hh} and G_{hh} values for the intact Kimmeridge clay (KIMCL-NT-8 at isotropic p'=220 kPa) 255
Figure 6-33: BE stiffness of the intact and reconstituted samples of Kimmeridge clay in different directions 256

Figure 6-34: BE stiffness of the intact and reconstituted samples of Kimmeridge clay normalised for the void ratio 256
Figure 6-35: Normalised bender element shear moduli for reconstituted samples of Kimmeridge clay under isotropic loading 257
Figure 6-36: Normalised bender element shear moduli for reconstituted samples of Kimmeridge clay following isotropic loading and unloading 257
Figure 6-37: Axial probe in compression and extension; axial effective stress and strain increments 258
Figure 6-38: Axial probe in compression and extension; radial strain plotted against axial strain 258
Figure 6-39: Radial probe in compression and extension; radial effective stress and strain increments 259
Figure 6-40: Radial probe in compression and extension; axial strain plotted against radial strain 259
Figure 6-41: p' constant probe in compression; deviatoric stress plotted against shear strain 260
Figure 6-42: p' constant probe in compression; deviatoric stress plotted against volumetric strain 260
Figure 7-1: Montage of 16 SEM images taken of the surface of the Oxford clay 10m below ground level. S1, S2 and S3 are shells. Scale: 1.2mm across image (Wilkinson, 2011) 284
Figure 7-2: SEM images of Kimmeridge clay; a) 12.71m below ground level, b) 8.54m below ground level (Wilkinson, 2011) 285
Figure 7-3: Montage of 16 SEM images of a vertical broken surface taken from a block sample of Gault clay, 3.5m below ground level. Scale: 1.2mm across image (Wilkinson, 2011) 286
Figure 7-4: Montage of 16 SEM images of a vertical broken surface of London clay from 7.9 -9.4m below ground level (Wilkinson, 2011) 286
Figure 7-5: Rose diagrams of the summation of particle long axis orientations 287
Figure 7-6: Rose diagrams of the summation of particle long axis orientations 288
Figure 7-7: Vectors V_{max} and V_{min} (Wilkinson, 2011) 288
Figure 7-8: Examples of where rose diagrams of different shapes plot on the Vmax-Vmin graph (Wilkinson, 2011) 289

Figure 7-9: Plot of preferred particle orientation δV plotted against percentage of clay minerals (redrawn from Wilkinson, 2011) 290
Figure 7-10: Particle size distributions of four UK mudrocks sampled at around 10m depth (London clay curve re-plotted from Gasparre, 2005) 290
Figure 7-11: Changes in the in-situ void ratio with previous depth of burial (London clay data from Gasparre, 2005) 291
Figure 7-12: Estimated in-situ void ratio and effective stresses of four mudrocks in comparison with normally consolidated soils studied by Skempton (1969) 291
Figure 7-13: Compression and swelling curves of intact UK mudrocks (London clay curve re-plotted from Gasparre, 2005) 292
Figure 7-14: Compression and swelling curves of reconstituted UK mudrocks (London clay curve re-plotted from Gasparre, 2005) 292
Figure 7-15: Normalised compression curves of intact UK mudrocks and the *ICL** (London clay curve re-plotted from Gasparre, 2005) 293
Figure 7-16: 1-D compression of natural and reconstituted clays (data from Burland, 1990; Smith, 1992; Coop et al., 1995; Burland et al., 1996; Cotecchia, 1996; Gasparre, 2005) 293
Figure 7-17: State Boundary Surfaces of reconstituted UK mudrocks (London clay curve re-plotted from Gasparre, 2005) 294
Figure 7-18: State Boundary Surfaces of reconstituted UK mudrocks normalised based on P'^{*}_{e} and M (London clay curve re-plotted from Gasparre, 2005) 294
Figure 7-19: Changes in the residual angle of shearing resistance with the clay fraction (Lupini et al., 1981) 295
Figure 7-20: Changes in the residual angle of shearing resistance with the plasticity index (Lupini et al., 1981) 295
Figure 7-21: Plasticity chart for a wide range of soil types (Wesley, 2003) 296
Figure 7-22: Residual angle of shearing resistance plotted against distance above or below the A-line (Wesley, 2003) 296
Figure 7-23: State Boundary Surfaces of reconstituted and intact UK mudrocks; a) Oxford clay, b) Kimmeridge clay, c) Gault clay, d) London clay (from Gasparre, 2005) 297
Figure 7-24: Framework of shearing behaviour of natural and reconstituted clays (Vitone et al., 2009) 298

Figure 7-25: State Boundary Surfaces of intact UK mudrocks (London clay curve re-plotted from Gasparre, 2005) 298
Figure 7-26: State Boundary Surfaces of intact UK mudrocks normalised based on P'^{*}_{e} and M (London clay curve re-plotted from Gasparre, 2005) 299
Figure 7-27: Post-rupture strength envelope for different overconsolidated clays (data from Burland, 1990; Burland et al., 1996) 300
Figure 7-28: Anisotropy of peak shear strength of UK mudrocks (Brosse, 2011) ... 301
Figure 7-29: Shear strength of UK mudrocks in extension (London clay curve re-plotted from Gasparre, 2005) 301
Figure 7-30: Stiffness variation with stress level at 0.001% strain level for intact soil 302
Figure 7-31: Variation of the mean effective stress level exponent, n, of stiffness (E^{u}_{v}) with strain level for intact soil..... 302
Figure 7-32: Variation of the normalised stiffness with stress level for the reconstituted samples of mudrocks (London clay data re-plotted from Gasparre et al., 2007)..... 303
Figure 7-33: Variation of the normalised stiffness (G_{hv}) with stress level for the reconstituted and intact samples of mudrocks (London clay unit B_2 data re-plotted from Gasparre et al., 2007)..... 303
Figure 7-34: Variation of the normalised stiffness with stress level for the intact samples of mudrocks (London clay unit B_2 data re-plotted from Gasparre et al., 2007) 304
Figure 7-35: Shear moduli G_{vh} and G_{hv} measured in-situ, empty symbols, and in the laboratory, filled symbols (London clay data re-plotted from Gasparre et al., 2007)304
Figure 7-36: Effect of preferred particle orientation on the degree of anisotropy calculated based on G, empty symbols, and E, filled symbols (London clay data re-plotted from Gasparre et al., 2007) 305
Figure 7-37: Effect of preferred particle orientation on the degree of anisotropy calculated based on G (London clay data re-plotted from Gasparre et al., 2007)..... 305
Figure 7-38: Profiles of the four UK mudrocks (some of the Atterberg limits for Oxford clay re-plotted from Hird & Pierpoint 1997; some of the Atterberg limits for Gault clay re-plotted from Butcher & Lord 1993; Gmax for Gault clay re-plotted from Butcher & Powell; 1993; London clay data re-plotted from Hight et al., 2007, CPT data provided by In-situ SI)..... 306

Nomenclature

$*$	Effective stress parameters applying to reconstituted clay
α	Anisotropy factor, $\sqrt{E_h/E_v}$
ϵ_a	Axial strain
ϵ_{crit}	Critical strain of the Y_2 surface
ϵ_{max}	Maximum plastic strain
ϵ_p	Plastic strain
γ	Bulk unit weight
ν'_{hh}	Poisson's ratio for horizontal strains due to horizontal strains
ν'_{hv}	Poisson's ratio for horizontal strains due to vertical strains
ν'_{vh}	Poisson's ratio for vertical strains due to horizontal strains
ϕ'	Effective angle of shearing resistance
ρ	Total mass density of the soil
σ'^{*}_{ey}	Equivalent pressure, taken on the ICL for the void ratio of the natural clay at gross yield
σ'_p	Preconsolidation pressure
σ'_v	Vertical effective stress
σ'_y	Gross yield stress
τ_{peak}	Peak shear stress
τ_r	Residual shear stress
B	Coefficient of saturation, $\Delta u/\Delta\sigma_r$
c'	Effective cohesion intercept
C^*_s	Intrinsic swelling index

C_s Intact swelling index

CD Consolidated Drained triaxial test

CF Clay Fraction

CSL Critical State Line

CU Consolidated Undrained triaxial test

DE Drained Extension triaxial test

e Void ratio

e^*_{1000} Void ratio on the ICL for 1000kPa vertical pressure

e^*_{100} Void ratio on the ICL for 100kPa vertical pressure

E_h Young's modulus in the horizontal direction

E_v Young's modulus in the vertical direction

G Shear modulus

G_{HH} Shear modulus in horizontal plane

G_{HV}, G_{VH} Shear modulus in vertical plane

G_{max} Elastic shear modulus

H Horizontally cut sample

I_b Brittleness index

I_v Void index

ICL Intrinsic Compression Line

J Coupling modulus

K Bulk modulus

K_0 Stress ratio σ'_h/σ'_v for zero lateral strain

LBS Local Boundary Surface

LL Liquid Limit

OCR Overconsolidation Ratio

p' Mean effective stress

p'^{*}_{e} Equivalent pressure; p' on the isotropic intrinsic compression line at the same v

p'_{iy},$p'_{K_0 y}$ Mean effective stress at gross yield. Subscripts i and K_0 refer to isotropic and K_0 states, respectively

p^{*}_{iy},$p^{*}_{K_0 y}$ Mean effective stress on the reconstituted normal compression line at the same specific volume. Subscripts i and K_0 refer to isotropic and K_0 states, respectively

PL Plastic Limit

q Deviatoric stress

q_{peak} Peak deviatoric stress and vertical size of the SBS at its apex

S_s Swell sensitivity

S_t Strength sensitivity

S_u Undrained strength

S_σ Stress sensitivity

SBS State Boundary Surface

SBS^* Intrinsic State Boundary Surface

SCC Sedimentation Compression Curve

TC Triaxial Compression test

TE Triaxial Extension test

u_b Pore water pressure at the base of the sample

u_m Pore water pressure at the mid-height of the sample

UU	Unconsolidated Undrained triaxial test
V	Vertically cut sample
v	Specific Volume
v_s	Shear wave velocity
Y_1, Y_2, Y_3	Kinematic yield points
YSR	Yield Stress Ratio

1 Introduction

1.1 Background and objectives of the project

Large areas in the Southern UK are covered by Triassic to Eocene mudrocks that were deposited in dissimilar geological environments, and have experienced diverse post depositional histories leading to a range of current natural structures. Accurate constitutive modelling of these soils' strength and stiffness characteristics is required to enable more secure and economic civil engineering design. Recent studies (e.g. Cotecchia & Chandler, 2000; Lings et al., 2000; Gasparre et al., 2007) have emphasised the importance of quantifying the effects of mechanical properties of structure, defined here as the combination of fabric (the geometrical arrangement of particles) and bonding (inter-particle forces). Establishing the intrinsic properties of reconstituted material, and comparing these with natural material properties has proved helpful in such investigations (Burland, 1990).

A recent project at Imperial College, determining the mechanical properties of London Clay through advanced laboratory testing accompanied by micro analysis of the soil and geological study, was a valuable starting point in the investigation of geologically older clays and mudrocks (Gasparre, 2005; Nishimura, 2006; Minh, 2007). The Author has taken part in an extensive investigation of three UK mudrocks: Oxford Clay, Kimmeridge Clay and Gault Clay. A fellow PhD candidate, Dr Stephen Wilkinson reviewed the background geology and undertook micro-structural analysis. The Author and Miss Amandine Brosse (another PhD candidate) undertook intensive mechanical testing on high quality block and rotary core samples, focussing principally on the uppermost 10 metres of the mudrocks. Seismic CPT profiling was also conducted at each site to track lithology and stiffness. The Author focussed on the triaxial shear strength, compressibility and stiffness characterisation of the mudrocks, carrying out tests on natural and reconstituted samples in advanced stress path and high pressure cells, as well as oedometers. These were accompanied by Brosses's advanced hollow cylinder tests as well as ring shear, index and other tests by MSc colleagues.

1.2 Thesis layout

This Thesis starts with an overview of the relevant literature (Chapter 2) and an explanation of the techniques and apparatuses employed (Chapter 3). The following chapters (Chapters 4 to 6) set out the suites of experiments performed on each deposit, focusing particularly on the strength and stiffness behaviour of natural and reconstituted samples. A synthesis (Chapter 7) is then provided that also embraces the earlier London clay study (Gasparre, 2005; Nishimura, 2006; Minh, 2007) and the available field measurements. Finally conclusions are drawn and recommendations made for further work in Chapter 8.

2 Literature review

2.1 Introduction

The geotechnical properties of stiff clays are largely related to their structure which has been formed during the sedimentation and post-sedimentation processes. The geological age of these clays can result in deeper burial, more diagenesis and higher erosion. In this chapter some aspects of the structure of stiff clays and their behaviour will be covered and the overview of the studies on each of the soils tested in this study will be presented in Chapters 4 to 6.

2.2 Structure

The term structure is defined as the combination of fabric (particle arrangement) and inter-particle bonding (Mitchell & Soga, 2005). Structure is created both during the deposition and after the deposition of the soil. Factors such as mineralogy, water chemistry during deposition, pressure, temperature, organic content and mechanical factors such as consolidation rate and unloading can affect the structure (Cotecchia & Chandler, 1997). It is usually understood that structure enables the natural soil to have more strength and a larger void ratio compared to the reconstituted soil at a given stress level (e.g. Burland, 1990), as illustrated in Figure 2-1. However this is not always the case and some natural soils can have lower void ratios compared to their reconstituted soil and show signs of "negative structure" (e.g. Fearon & Coop, 2002). It is believed that bonding is typically a meta-stable component of the structure while fabric is generally a stable component (Coop et al., 1995).

The common practice to define the effects of structure on the behaviour of a soil is to compare the natural soil with the same soil after reconstitution. The term intrinsic is used for properties of the soil after being mixed to a slurry at a water content of 1 to 1.5 times liquid limit and without prior drying (Burland, 1990). However, Fearon & Coop (2000) have shown that although this process may result in destructuration at

the macro-level, it may not degrade the micro-structure fully. Void index, I_v, was introduced by Burland (1990) as a normalising parameter to compare the compression and swelling behaviour of the intrinsic and the natural soil:

$$I_v = \frac{e - e^*_{100}}{e^*_{100} - e^*_{1000}} \qquad \text{(Equation 2-1)}$$

The void ratios e^*_{100} and e^*_{1000} are those of the reconstituted clay compressed to vertical effective stresses of 100 and 1000kPa respectively. The effects of structure and its degradation on the behaviour of the soil have been taken to account in various constitutive models (e.g. Kavvadas & Amorosi, 2000; Baudet & Stallebrass, 2004).

A classical study on the relation of the effective stress, in-situ void ratio and mineralogy was carried out by Skempton (1969) on various normally consolidated argillaceous deposits. Sedimentation compression curves for different deposits are shown in Figure 2-2. As can be seen, the in-situ void ratio of each soil at a given overburden pressure depends on the nature and amount of the clay minerals in the soil; soils with higher Liquid Limit placing at higher range of these curves. Burland (1990) showed, in Figure 2-3, that when these curves are normalised for the void ratio, a unique Sedimentation Compression Line for natural normally consolidated soils is reached which is located above the Intrinsic Compression Line.

Fabric

The fabric of the soil may be initially formed during deposition but can also be created or altered after the initial deposition. The inherent anisotropy of the soil may also be formed during the depositional processes but can again be altered by post-depositional processes. The depositional environment therefore affects the formation of the fabric. The two main parameters affecting structure are the rate of deposition and the stillness of the water. The soil fabric is more open and sensitive after slow deposition in still water compared to denser fabrics formed by rapid deposition with significant currents (Burland, 1990). Figure 2-4 shows the fabric classification given by Sides & Barden (1970).

Bonding

Bonding refers to all inter-particle forces that are not of a purely frictional nature. These can be of electrostatic, electromagnetic or any other forces acting to connect particles together during the geological age of the soil (Cotecchia & Chandler, 1997). Inter-particle bonding can be formed with different geological processes such as percolation of calcium carbonate or weak lithification (e.g. Amorosi & Rampello, 2007).

2.3 Sensitivity framework

2.3.1 Sedimentation and post-sedimentation structure

Cotecchia & Chandler (2000) divided different clay structures into two main categories; sedimentation structure and post-sedimentation structure. Sedimentation structure includes all the structures that develop during and after deposition only as a consequence of one-dimensional compression. Normally consolidated or lightly overconsolidated natural clays and normally consolidated reconstituted clays have this type of the structure. Post-sedimentation structure is that which has been created or altered by some other geological processes after deposition and compression. Processes such as unloading, creep, and post-depositional bonding can alter the sedimentation structure of the clay. Clays with sedimentation structure follow the Sedimentation Compression Curve when they are subjected to one-dimensional compression (Figure 2-5a). Therefore for this type of the structure the in-situ vertical stress, σ'_v, the preconsolidation pressure σ'_p and the gross yield stress σ'_y are all equal. However it should be noticed that creep and ageing can always alter these. Gross yield is a state in effective stress space at which the soil stiffness falls rapidly and plastic strain increments become larger due to degradation of the soil structure (Hight et al., 1992). The preconsolidation pressure corresponds to the actual geological overburden stress on the soil before unloading. As a result, the term overconsolidation ratio ($OCR = \sigma'_p / \sigma'_v$) is used based on a known geological history of the soil, while the term yield stress ratio ($YSR = \sigma'_y / \sigma'_v$) corresponds to degradation of the natural structure due to compression. In Figure 2-5b the

compression curve of clays with post-sedimentation structure yields at higher stresses compared to SCC and therefore: $\sigma'_y > \sigma'_p > \sigma'_v$ and $YSR > OCR$ for these soils.

2.3.2 Sensitivity

Sensitivity is a parameter representing the micro-structure differences between natural and reconstituted soil (Cotecchia & Chandler, 2000). Terzaghi (1944) defined sensitivity S_t as the ratio of the undrained strength of the undisturbed soil to the undrained strength of the remoulded soil at the same water content. Swell sensitivity, S_s, introduced by Schmertmann (1969), is another parameter to define structure; it is the ratio of intrinsic to the natural swelling indices (C_s^* / C_s). Cotecchia & Chandler (2000) defined the strength sensitivity S_t, for both sedimentation and post-sedimentation structures, as the ratio of the undrained strength after consolidation to gross yield to that of the reconstituted clay normally consolidated to the same water content as the natural clay at gross yield ($S_t = q_{peak} / q^*_{peak}$). They also defined stress sensitivity ($S_\sigma = \sigma'_{vy} / \sigma^*_{ey}$) as the distance between the yield stress of the natural material and the vertical stress on the *ICL* at the same void ratio. Figure 2-6 shows the construction of the sensitivity parameters in (p'- q - v) space. In their study, Cotecchia & Chandler (2000) have noticed that for most of the clays with both types of structure S_t is approximately equal to S_σ so that:

$$\sigma'_{vy} / \sigma^*_{ey} = p'_{K0y} / p^*_{K0y} = p'_{iy} / p^*_{iy} = q_{peak} / q^*_{peak} \qquad \text{(Equation 2-2)}$$

where p'_{K0y} and p'_{iy} are mean effective stresses at gross yield in K_0 and isotropic compression respectively, and p^*_{K0y} and p^*_{iy} are the mean effective stresses on the reconstituted Normal Compression Line at the same specific volume as at gross yield for the natural clay. This implies that there are geometric similarities between the intact clay State Boundary Surface, *SBS*, and the reconstituted *SBS**, and the ratio between the sizes of these boundary surfaces is similar for clays of equal sensitivity. Sedimentation compression curves with different strength sensitivities are illustrated in Figure 2-7; it should be noticed that for reconstituted clays, by definition, S_t is equal to unity.

Smith (1992) compared three clays (Berthierville, Bothkennar and Queenborough clays) each with different geological histories. Berthierville clay is a glacio-lacustrine deposit formed under very still conditions, Bothkennar clay is a lightly cemented shallow marine clay and Queenborough clay is an organic estuarine (highly tidal) clay derived from weathered mudrocks. Smith (1992) showed, Figure 2-8, that as a result of different depositional environments sensitivity of the soils varied from 50 for the Berthierville clay to unity for the Queenborough clay with the Bothkennar clay being in between.

2.3.3 Post-yield behaviour

After the gross yield, the compression curve of many natural soils tends to bend down toward the *ICL* (Burland, 1990). The structural degradation after gross yield, in compression, is a gradual process which may result in a continuous convergence between the natural and reconstituted compression curves, as a sign of degradation of meta-stable structure, or result in parallel compression curves for the natural and reconstituted as a sign of stable structure (Coop et al., 1995). The same trend can be seen in the shearing behaviour of a soil; soil with meta-stable structure bends down toward the SBS^* after reaching its natural *SBS* (e.g. Bothkennar clay studied by Smith et al., 1992), while soil with stable structure stays on its natural *SBS* (Figures 2-8 and 2-9). Cotecchia & Chandler (2000) normalised the *SBS* of Pappadai clay for the effects of volume using an equivalent pressure p'^*_e, which corresponds to the mean effective stress on the isotropic intrinsic compression curve at the same specific volume as the soil (Hvorslev, 1937), and also structure using the strength sensitivity S_t. This normalisation results in a unique *SBS* for natural and reconstituted Pappadai clay and captures the similarities between the natural and reconstituted soil (Figure 2-10). However, in this normalisation the sensitivity value stays constant after gross yield, while in reality this value may fall because of the accumulation of the plastic strains. In some constitutive models (e.g. Baudet and Stallebrass, 2004) the reduction in sensitivity is captured by taking to account the degradation of the structure as a result of plastic volumetric and shear strains, and both stable and meta-stable components of the structure are included in the model.

The soil strength mobilised post-peak varies with the proportion of the clay minerals in the soil. Once shear strain localisation occurs, plastic soils with a high clay mineral

content show sliding shear behaviour, also known as a residual shear strength (Skempton, 1964), while soils with a lower clay mineral content show turbulent shear behaviour between particles (Figure 2-11). Jardine et al. (2004) highlighted the importance of ductile (strain hardening) or brittle (strain softening) behaviour of the soil in engineering practice. Stress history, formative history, micro-structure, rate effects, composition and fabric are all factors that they proposed to affect the soil behaviour after peak. Figure 2-12a shows the ductile behaviour of low plasticity clay, the undrained shear strength of which is a function of water content. However, for stiff plastic clays that undergo brittle strain localisation, the undrained shear strength varies with effective stress level rather than water content (Figure 2-12b). Atkinson (2007) reported the results of triaxial tests on stiff clays at small effective stresses and large overconsolidation ratios. He observed that the Mohr-Coulomb criterion does not capture the curvature in the strength envelope at low pressure and suggested the use of non-linear power law criterion.

Burland (1990) noticed that the strength of natural stiff clays can fall rapidly from peak to a well defined albeit temporary plateau which he called the post-rupture strength. The post-rupture strength envelope appears to fall very close to the intrinsic strength line (ie. Critical State Line) and is not very sensitive to stress history or rotation of principle stresses (Georgiannou & Burland, 2001). Although the authors observed that at low and high pressures the post-rupture strength envelope and the intrinsic strength line are different, they anticipated that the fabric on the rupture plane could be similar to that of the reconstituted material. The fall from the peak strength to the post-rupture strength is attributed to the breakage of the inter-particle bonding and is followed by rearrangement of particles resulting ultimately in a residual strength. This brittleness can be quantified with Bishop's Brittleness Index (1967):

$$I_b = \frac{(\tau_{peak} - \tau_r)}{\tau_r} \qquad \text{(Equation 2-3)}$$

Atkinson & Richardson (1987) showed that in undrained tests non uniform pore water pressure distribution in the sample can lead to local drainage and local volume change even if very fast rates are employed in the loading stage. As a consequence of local drainage at the rupture zone, the soil at this zone dilates and becomes less stiff and weaker than the surrounding soil; therefore the measured strength does not perfectly

correspond to the overall strength of the material but the strength of the soil at the rupture zone. The authors suggested that among other factors affecting the undrained shear strength of the soil (e.g. sample size, loading conditions and previous stress history) the degree of drainage in the rupture zone should also be considered.

2.4 Yielding behaviour

The classical yield point for a solid is defined as the stress at which it begins to deform plastically. Plastic straining commences at very small strains in soils and yielding has been identified historically at far later stages, such as the 'gross' yield point in oedometer tests. More generally yielding can be defined at points where the stress-strain behaviour of the soil shows a significant change. Soil structure degrades in a continuous process and hence yielding can be gradual. There have been several constitutive models aimed at capturing the yielding of the soil considering multiple kinematic surfaces for each stage of yielding (Al-Tabbaa & Muir Wood, 1989; Jardine, 1992; Stallebrass & Taylor, 1997). In the kinematic model proposed by Jardine (1992), the soil stress-strain response is divided to three main zones. Two kinematic surfaces Y_1 and Y_2, describe behaviour at relatively small strains and can move with the current stress point within a larger surface Y_3 which is relatively immobile. Destructuration and change in volume affect the size of the Y_3 surface. Figure 2-13 shows the schematic soil behaviour with three yielding surfaces.

Zone-I

This is the zone of perfectly linear elastic behaviour. Up to this limit the soil stress-strain curve is linear and completely recoverable. The size of *zone-I* is dependent on the material tested but in general the strains are very small. Without high resolution displacement transducers it is very difficult to characterise this zone under static conditions for many soils. However with improvements in local displacement transducers (e.g. Cuccovillo & Coop, 1997) this region can be resolved and has been reported to be of the order of 10^{-3} % axial strain for stiff clays. In the study carried out by Clayton & Heymann (2001), three soils were tested using high resolution LVDTs. They tested chalk (very stiff), London clay (stiff) and Bothkennar clay (soft) to compare their small strain behaviour. Figure 2-14 shows the stiffness response of

these three soils in the small strain region. The plateau in the beginning of each curve corresponds to the linear region and the limit of this plateau is similar for all three materials, and is approximately between 0.002-0.003% axial strain. This is in contrast with the idea that for relatively strongly cemented soils this zone is larger (Jardine, 1992).

To demonstrate that behaviour in *zone-I* is elastic load-unload tests are required to check if the strains are recoverable or not. The soil behaviour in this zone is not significantly altered by strain rate changes and can be modelled as an assembly of particles with elastic contacts (Jardine, 1992).

Zone-II

This is the region of non-linear stress-strain behaviour where behaviour may be in-elastic, but where the strain increment vectors retain the same orientation as in the elastic zone (Jardine, 1992). The load-unload paths are hysteretic and the strains may be partially irrecoverable (Kuwano, 1999). The energy dissipated within such hysteresis stress-strain loop was attributed to small-scale local yielding and fretting at the inter-particle contacts, which are subjected to normal and shear loading (Jardine, 1992). When the strains pass the Y_2 limit and develop beyond zone-*II*, at ε_{crit}, the ratio of the plastic strains to maximum total strains increase significantly and a rapid change in stiffness can occur at this limit, this is shown in Figure 2-15 (Jardine, 1992). Initially, Jardine (1992) proposed cyclic loading to investigate the limit of *zone-II* as the point in which the strains are not recoverable. Following Kuwano (1999), Gasparre (2005) determined the Y_2 limit as the point at which the direction of the strain increment vectors changed during drained probing tests, or from the change of gradient of the pore pressure-deviatoric stress curve for undrained tests. However there is no information in the literature on the compatibility of the cyclic and the monotonic loading methods for defining the Y_2 limit. One shortcoming of the monotonic definition is its inability to capture a Y_2 limit under isotropic monotonic loading of a soil with isotropic properties. The latter would show no change in strain increment direction, as would constant p' loading probing test. The value of ε_{crit} can vary between 0.005% for some reconstituted soils to around 0.07% for some

cemented materials (Gasparre, 2005). Stress-strain behaviour becomes notably rate dependent and subject to creep after undergoing Y_2 yielding (Jardine et al., 2004).

Zone-III

Continued loading within zone-*III* out towards the State Boundary Surface leads to ratios of plastic strain increments to maximum permanent strains, $d\varepsilon_p / d\varepsilon_{\max}$, (Figure 2.15) tend to unity. The points at which 'gross' yielding occur, involving large plastic strains, contraction, dilation or failure, correspond to the conventional geotechnical definition of yielding and are termed Y_3 yield points (Jardine, 1992; Jardine et al., 2004). In undrained tests, the effective stress paths have to remain within the Local Boundary Surface (*LBS*) defined by their prior stress history. However drained tests that can develop volumetric strains, can cross this limit towards the outer *SBS* (Jardine et al., 2004). The Y_3 yield points define a surface whose size is affected by the consolidation path prior to shearing (Gens, 1982). As mentioned earlier the *SBS* can be normalised by an equivalent pressure p'^{*}_{e} and sensitivity. Smith et al. (1992) showed that the Y_3 surfaces of natural soft clays are strongly anisotropic and sensitive to damage caused by shear or volume strains, for example, they can be affected by sampling method.

2.5 Small strain parameters

Many simple constitutive models consider soil behaviour as linear elastic up to the point of failure. However, as mentioned earlier only soil behaviour at very small strains can be considered linear elastic (*zone –I*). However, the non-linear stiffness characteristics applying from very small to moderate strains dominates the ground movements developed in most practical geotechnical engineering problems (Jardine et al., 1986; Simpson et al., 1996; Puzrin & Burland, 1998; Atkinson, 2000; Clayton, 2011).

An isotropic elastic material is one for which the elastic properties are independent of the direction in which that property is referred to; when the properties are dependent on the orientation of the sample, the material is called anisotropic (Graham &

Houlsby, 1983). Most soils have been deposited vertically over large areas and many have experienced equal horizontal deformations and stresses resulting in different vertical and horizontal properties. Tectonic activity or mass deformation processes can result in different characteristics in the horizontal plane, although this is not addressed in the current study. The most common type of anisotropy to be considered is cross-anisotropy, or transverse isotropy, in which the vertical axis is an axis of symmetry (Love, 1927; Graham & Houlsby, 1983; Lings et al., 2000).

The derivation of cross-anisotropic elastic parameters has been carried out by several authors, and the equations presented here are from Lings et al. (2000). The relationship between stress increments and strain increments for a cross-anisotropic material is achieved through the compliance matrix shown in Equation 2-4:

$$\begin{pmatrix} \delta\varepsilon_{xx} \\ \delta\varepsilon_{yy} \\ \delta\varepsilon_{zz} \\ \delta\gamma_{yz} \\ \delta\gamma_{zx} \\ \delta\gamma_{xy} \end{pmatrix} = \begin{pmatrix} \frac{1}{E_h} & \frac{-\nu_{hh}}{E_h} & \frac{-\nu_{vh}}{E_v} & 0 & 0 & 0 \\ \frac{-\nu_{hh}}{E_h} & \frac{1}{E_h} & \frac{-\nu_{vh}}{E_v} & 0 & 0 & 0 \\ \frac{-\nu_{hv}}{E_h} & \frac{-\nu_{hv}}{E_h} & \frac{1}{E_v} & 0 & 0 & 0 \\ 0 & 0 & 0 & \frac{1}{G_{hv}} & 0 & 0 \\ 0 & 0 & 0 & 0 & \frac{1}{G_{vh}} & 0 \\ 0 & 0 & 0 & 0 & 0 & \frac{1}{G_{hh}} \end{pmatrix} \times \begin{pmatrix} \delta\sigma'_{xx} \\ \delta\sigma'_{yy} \\ \delta\sigma'_{zz} \\ \delta\tau_{yz} \\ \delta\tau_{zx} \\ \delta\tau_{xy} \end{pmatrix} \qquad \text{(Equation 2-4)}$$

where the z axis is vertical. The seven elastic parameters in Equation 2-4 are related to the increments of strains and effective stresses and are:

- E_v, Young's modulus in the vertical direction
- E_h, Young's modulus in the horizontal direction
- ν_{vh}, Poisson's ratio for horizontal strain due to vertical strain
- ν_{hv}, Poisson's ratio for vertical strain due to horizontal strain
- ν_{hh}, Poisson's ratio for horizontal strain due to orthogonal horizontal strain

- G_{hv}, shear modulus in the vertical plane, equal to G_{vh} for homogenous material
- G_{hh}, shear modulus in the horizontal plane

These parameters are not all independent. Because the horizontal plane is the plane of isotropy, the term G_{hh} is related to E_h and ν_{hh} through Equation 2-5:

$$G_{hh} = \frac{E_h}{2(1+\nu_{hh})} \qquad \text{(Equation 2-5)}$$

For an elastic material, thermodynamic rules require the compliance matrix to be symmetric (Love, 1927) and therefore:

$$\frac{\nu_{hv}}{E_h} = \frac{\nu_{vh}}{E_v} \qquad \text{(Equation 2-6)}$$

Considering Equations 2-5 and 2-6, the compliance matrix in Equation 2-4 can be simplified using five parameters E_v, E_h, ν_{vh}, ν_{hh} and G_{hv}:

$$\begin{pmatrix} \delta\varepsilon_{xx} \\ \delta\varepsilon_{yy} \\ \delta\varepsilon_{zz} \\ \delta\gamma_{yz} \\ \delta\gamma_{zx} \\ \delta\gamma_{xy} \end{pmatrix} = \begin{pmatrix} \frac{1}{E_h} & \frac{-\nu_{hh}}{E_h} & \frac{-\nu_{vh}}{E_v} & 0 & 0 & 0 \\ \frac{-\nu_{hh}}{E_h} & \frac{1}{E_h} & \frac{-\nu_{vh}}{E_v} & 0 & 0 & 0 \\ \frac{-\nu_{vh}}{E_v} & \frac{-\nu_{vh}}{E_v} & \frac{1}{E_v} & 0 & 0 & 0 \\ 0 & 0 & 0 & \frac{1}{G_{hv}} & 0 & 0 \\ 0 & 0 & 0 & 0 & \frac{1}{G_{vh}} & 0 \\ 0 & 0 & 0 & 0 & 0 & \frac{2\times(1+\nu_{hh})}{E_h} \end{pmatrix} \times \begin{pmatrix} \delta\sigma'_{xx} \\ \delta\sigma'_{yy} \\ \delta\sigma'_{zz} \\ \delta\tau_{yz} \\ \delta\tau_{zx} \\ \delta\tau_{xy} \end{pmatrix} \qquad \text{(Equation 2-7)}$$

Due to thermodynamic requirements there are some bounds on the values of these five parameters. In an elastic material strain energy should be positive and as a result

E_v, E_h and G_{hv} should all be positive and -1 < ν_{hh}< 1. Also the two inequalities shown below should be satisfied:

$$\frac{E_v}{E_h}(1-\nu_{hh})-2\nu_{vh}^2 \geq 0 \qquad \text{(Equation 2-8)}$$

$$G_{hv} \leq \frac{E_v}{2\nu_{vh}(1+\nu_{hh})+2\times\sqrt{\frac{E_v}{E_h}(1-\nu_{hh}^2)\left[1-(\frac{E_h}{E_v})\nu_{vh}^2\right]}} \qquad \text{(Equation 2-9)}$$

Pickering (1970) presented these bounds on elastic parameters in a 3-D graphical form (Figure 2-16). The vertical axis in the graph represents the ratio of the horizontal to the vertical Young's moduli, E_h/E_v, and the horizontal axis are Poisson's ratios μ_{hv} and μ_{hh}. All possible combinations of drained elastic parameters should lie inside the "ship's bow" shape with some special cases. Plane *ABC* in Figure 2-16 is the plane of an uncoupled material, which undergoes no distortional strain with isotropic loading, nor volumetric strain with deviatoric loading. Line *CD* within this plane represents an isotropic material and line *AB* represents all incompressible materials. All combinations of undrained elastic parameters should lie on the line *AB*. Lings (2001) noted that all drained points within this space can be mapped onto the line *AB*, but undrained points on line AB can be reached from infinite number of drained points. As a consequence the mapping is only one-way, from drained to undrained and he presented all the equations relating drained to undrained parameters.

Horizontal or vertical shear stresses can not be applied in triaxial tests where $\delta\varepsilon_{xx}=\delta\varepsilon_{yy}=\delta\varepsilon_h$ and $\delta\sigma'_{xx}=\delta\sigma'_{yy}=\delta\sigma'_h$. Hence Equation 2-7 can be simplified to:

$$\begin{pmatrix}\delta\varepsilon_v\\ \delta\varepsilon_h\end{pmatrix}=\begin{pmatrix}\frac{1}{E_v} & \frac{-2\nu_{vh}}{E_h}\\ \frac{-\nu_{vh}}{E_v} & \frac{1-\nu_{hh}}{E_h}\end{pmatrix}\times\begin{pmatrix}\delta\sigma'_v\\ \delta\sigma'_h\end{pmatrix} \qquad \text{(Equation 2-10)}$$

These parameters can be obtained using static probes accompanied by bender element readings; the equations can be found in Lings et al. (2000) and are presented in Section 3.5.5. Another representations of elastic cross-anisotropy involving the parameters E^*, ν^*, α was set out by Graham & Houlsby (1983), where α is an anisotropy factor, or $G', K', J', (G^*, K^*, J)$ (Atkinson et al., 1990), where G is a shear modulus, K is a bulk modulus and J is a coupling modulus. The equations relating all these parameters to those presented in this section can also be found in Kuwano & Jardine (1998), Lings et al. (2000) or Lings (2001).

2.6 Influence of recent stress history

It has been observed that the recent stress history and current state of the soil can affect the small strain stiffness response of the soil, and this effect can be considered in kinematic constitutive models (Atkinson et al., 1990; Stallebrass & Taylor, 1997; Baudet & Stallebrass, 2004). The history surface used in these models substitutes the Y_2 surface, being larger in size and often more clear to define compared to Y_2 surface. Atkinson et al. (1990) carried out several stress probes on reconstituted London clay, with each probe being about 90 kPa long. The probes were at constant p' and constant q, but with different angles in q-p' space compared to their common approach stress path (Figure 2-17a). Before each probe a three hour pause was allowed that led to some limited creep hardening. The stiffness degradation curves are shown in Figure 2-17b. The response clearly shows that the stiffness degradation curve is dependent on the angle of rotation between the approach stress path and the probe, with higher stiffnesses for larger rotations. The dependence on stress history disappeared after about 0.5% axial strain after which the tangent stiffness curves tend to coincide.

Clayton & Heymann (2001) carried out sets of probing tests on Bothkennar clay and London clay to study the effects of recent stress history. The stress paths and their corresponding stiffness degradation curves are shown in Figure 2-18. Each probe was around 10 kPa long and creep was allowed until no increments of axial and volumetric strains could be measured. These results are in contrast with those from Atkinson et al. (1990); they argued that the recent stress history does not affect the soil stiffness if creep is allowed. They noted that when creep has decayed, the

degradation curve is regained by some "healing" process that is associated with ageing and creep strains (Clayton & Heymann, 2001). They found out that while recent stress history does not affect the soil stiffness, if creep is allowed the direction of the outgoing stress path is an important factor for the soil stiffness degradation. Those stress paths that take the soil states towards the isotropic state give stiffer behaviour compared to those taking the soil towards failure. Gasparre (2005) argued that the reason for these results may be due to the size of the approach paths which may have not passed the Y_2 surface found by Smith et al. (1992). However, Clayton & Heymann (2001) reported 0.06% axial strain in the 9 kPa long probe which is in excess of the Y_2 yield strain level of about 0.02% reported by Smith et al. (1992). However, the strains engaged in these probes were still very small, in order to minimize the destructuration of the soil, and this may be why stronger effects of the recent stress history are not observed.

In order to investigate further the effects of recent stress history, Gasparre et al. (2007) carried out three sets of undrained probes in extension and compression. The tangent stiffness degradation curves for these tests are illustrated in Figure 2-19. In the first case (Figure 2.19a), the probes remained within the Y_2 region and a creep period of seven days was allowed before each probe. The two results are in agreement with the findings of Clayton & Heymann (2001), showing no effects of recent stress history. For the second case (Figure 2.19b), only a three hour pause was allowed for the creep while the probes stayed within Y_2, similarly to case one. The recent stress history effect on stiffness is evident for these probes. Finally the probes in case one were repeated, this time passing the Y_2 region with $\Delta q = 100$ kPa and allowing a 10 day creep pause period. In this case recent stress history again affected the stiffness (Figure 2.19c). Gasparre et al. (2007) concluded that when the test paths did not engage the Y_2 surface, creep could erase the effects of recent stress history. However, when stress paths engage and relocate the Y_2 surface, recent stress history affects the stiffness of the soil even after a long creep period.

2.7 Time dependent behaviour of the soil

Different aspects of time dependent behaviour of soils have been acknowledged for many years. Effects of ageing both in geological time scales, and its digenetic effects, or in a laboratory time scale, creep (plastic strains that occur under constant effective stress) and rate dependency of soils parameters have been studied extensively and different constitutive models have been proposed to capture these effects. Some of this research will be summarised in this section.

Casagrande & Wilson (1951) carried out creep-strength tests and long-term compression tests on nine different soils (including sandy clay, soft clay, clay-shales, silty clays and clayey sand) both in their undisturbed state and in their remoulded and compacted form. They realised that the water content should stay constant during all these tests as any change in water content could have changed the effective stresses and consequently the stiffness and strength of the soils. They observed that sustained loads at constant water content reduced the strength of fully saturated brittle clays and clay-shales. However they noticed an increase in strength of some undisturbed samples and compacted soils, which were partially saturated, with time. They also highlighted the effects on the design of embankments and slopes. This rate dependency of undrained shear strength, S_u, has been confirmed by many authors (eg. Graham et al., 1983; Atkinson & Richardson, 1987).

Graham et al. (1983) carried out undrained triaxial compression, triaxial extension and simple shear tests on few lightly overconsolidated clays. They used two methods to study the rate dependency of the soils, using constant strain rate and step-changed strain rates. The results for Belfast clay, Winnipeg clay and Mastemyr clay are shown in Figure 2-20. The change in undrained shear strength is around 12-14% for a ten fold change in the strain rate and the two methods of testing were in good agreement. They suggested that there was no significant pore water pressure change due to changes in the strain rates and therefore the differences in the strength values resulted from rate dependency of the soil. The changes in undrained shear strength with the logarithm of strain rate are shown for different soils in Figure 2-21, in which the strength values decrease with decreasing strain rate. They have also observed no correlation between plasticity index, overconsolidation, consolidation path (isotropic

and anisotropic) and test type with the strain rate dependency of the strength. As the consequence of this rate dependency they concluded that the yield envelope contracts as strain rate decreases. Finally they observed that the strain rate effects decrease with increasing strain.

Tatsuoka (2006) classified the time dependent behaviour of the soil to three major categories. The *positive isotach viscosity* is when changes in the strain rate result in repositioning of the stress-strain curve to a new curve corresponding to that particular strain rate with higher strengths for the higher strain rates. The second type of behaviour is '*TESRA*' Temporary Effects of Strain Rate and strain Acceleration, in which changes in strain rate only make the stress-strain curve to change position temporally before coming back to the initial curve corresponding to the previous strain rate. Finally by testing some granular materials (Albany silica sand, corundum A and Hime gravel) he found out that some materials show decrease in strength with increase in the strain rate, opposite to most common isotach behaviour, and he termed this as *negative isotach viscosity*. The author suggested that soils can have a combination of these behaviours depending on their particle size, particle shape, grading characteristics, inter-particle bonding, inter-particle contact point and the strain level.

An extensive study to investigate the rate dependency of soil behaviour was carried out by Sorensen at al. (2007) on reconstituted and natural London clay as well as artificially cemented kaolin. The research was aimed to study the influences of structure caused by diagenesis, mechanical unloading and ageing on the rate dependency of London clay. They changed the consolidation rates from 1 kPa/hr to 3 kPa/hr during the isotropic consolidation of reconstituted samples and then employed stepwise changes in strain rates, from 0.007%/hr to 0.9%/hr, during shearing for all the tests. The excess pore water pressure was believed to be insignificant during the consolidation independent of the employed rates. They observed different but parallel NCLs for the two rates with higher rate plotting above the other one. This was in agreement with Kutter & Sathialingam (1992) who showed the position of virgin compression line in e-log (p') is not unique and is time dependent. The stress-strain response for the normally consolidated sample of London clay during shearing to failure is shown in Figure 2-22a. The behaviour at lower strains was rate dependent

(isotach) with a unique stress-strain curves for each specific strain rate. Higher strain rates resulted in higher curves and consequently changed the position of the Local Boundary Surface (LBS). However the isotach behaviour gradually faded away as strains became larger and stresses reached the peak strength.

The influence of these strain rate changes on the stiffness of the soil is shown in Figure 2-23. At the moment of the change in the rates there was an abrupt change in the stiffness due to the acceleration of the strains and then the value stabilised on a unique degradation curve for each strain rate. They observed that higher strain rates resulted in a lower stiffness value. This observation for stiffness is in contrast with the study carried out on soft Bangkok clay by Teachavorasinskun et al. (2002). A combination of undrained triaxial compression, extension and cyclic tests on Bangkok clay showed higher stiffness for higher strain rates. This rate dependency decreased at larger strains. Sorensen at al. (2007) also observed no significant change in the stiffness degradation of the natural London clay with changes in the strain rate.

The influence of post-sedimentation structure, due only to unloading, on the rate dependency was investigated by comparing the Normally Consolidated, NC, and Over Consolidated, OC, samples of reconstituted London clay (Sorensen et al., 2007). A similar behaviour was observed for the overconsolidated samples with isotach behaviour at small strains and more temporary behaviour after peak (Figure 2-22b). The only difference between the two tests, which could have been caused by the unloading process, was the stress dependency of the jumps (at the moment of strain rate change) for the OC samples, while the magnitude of this jump stayed constant for the NC sample. The influence of post-sedimentation structure, due to diagenetic processes other than unloading only, was studied by comparing the natural and reconstituted samples of London clay. The natural sample showed isotach behaviour both at smaller strains and after peak. This is similar to what was observed for the clays studied by Graham et al. (1983) in which different curves for different rates were present after peak (Figure 2-20 and 2-22c). In all cases in this research, the pore water pressure was measured and showed no significant and permanent change with changes in the strain rates which made the authors conclude that rate sensitivity is associated with the soil matrix behaviour and is independent of drainage.

To investigate if the rate dependency of natural London clay was due to the bonding between the particles rather than the fabric of the soil, cemented kaolin was tested. The stress-strain response showed rate dependency up to peak but more temporary behaviour at larger strains, suggesting that bonding can not be the only factor influencing the rate dependency of this soil. The authors divided the time dependency of the soils into two categories: particulate and continuum materials. They proposed that in the particulate material deformations are more concentrated at contacts of each particle while for the continuum material this is based on deformation of the entire volume of soil. Based on this division and the studies suggesting a fabric dominated structure of London clay (Gasparre et al., 2007), they have considered London clay (among other clays) to be of the continuum material type with higher creep deformations and significant isotach behaviour.

A similar study was carried out by Krizek et al. (1977) to investigate the directional creep of anisotropic mixtures of kaolin consolidated both isotropically and anisotropically from flocculated and dispersed slurries. They noticed that the greater number of bonds formed in the samples made from the flocculated slurry resisted the creep deformation more than the samples made from the dispersed slurry. They also suggested that a more randomly oriented fabric (as a result of isotropic consolidation), which allowed more bonds to form, could resist the creep deformation more than the highly orientated samples. Although highlighting the effects of bonding they also observed a strong directional dependence of creep relative to particle orientation with higher values of creep in the vertical direction compared to the horizontal direction.

Following Mitchell (1964), different authors used rate process theory to model creep of soils. Andersland & Douglas (1970) explained the fundamental aspects of the model based on the movements of atomic sized particles from one equilibrium position to another by overcoming an energy barrier. The magnitude of this barrier is the free energy of activation which controls the rearrangement of those particles. This process however, is a thermally activated mechanism and is not completely applicable for soil as there are significant mechanical forces involved in the displacement of soil particles. These mechanical forces should be accounted for if using this model and are particularly important for sands. This model considers the bonding between the particles as a major factor in the controlling mechanism of soil creep. Feda (1989)

highlighted some of the problems involved in this model. The inelastic nature of the soil, multi-axial deformations and coupling phenomena (deformation in one direction induced by a stress change in the perpendicular direction) are some of the factors that the model is unable to capture. After carrying out tests with a ring shear apparatus on four different soils, the author also emphasized the effects of bonding on the creep deformation of the soils.

Mesri et al. (1981) tested kaolin and Cucaracha shale and based on their results proposed a model correlating the creep parameter (which controls strain rate) to the ratio of undrained Young's modulus to undrained shear strength, E_u/S_u, and strain at failure, ε_f. More recent constitutive models consider the plastic strain of the soil as the combination of the elastic and viscoplastic elements (eg. Kutter & Sathialingam, 1992; Tatsuoka et al., 2002).

2.8 Effects of weathering

Weathering is normally attributed to the changes that occur to the soil mass at its surface in contact with air and water. The weathering processes are mainly divided into mechanical and chemical categories (Chandler, 1972). Disturbance caused due to seasonal water content variations (desiccation and swelling), frost action and mass movements (land sliding, bulging and subsidence) are the mechanical factors involved in weathering (Chandler, 1972; Vaughan & Kwan, 1984). Chemical weathering is comprised of spontaneous affects of dissolution and re-precipitation (Zhang et al., 2004). Dissolution is a process in which cations from the parent material are removed by the acidic solutions in the soil resulting in a higher porosity in the weathered material. In general this process results in mass loss, reduction in strength and stiffness and can be considered as the weakening element of weathering. On the other hand, re-precipitation is the process of recrystallisation of clay minerals and other material from the pore solution. These new materials can act as a cement between the existing particles forming larger aggregates resulting in a lower porosity, and higher strength and stiffness for the weathered soil (Vaughan & Kwan, 1984; Zhang et al., 2004). It is very important to consider both the weakening and bonding affects of weathering.

Mechanical and chemical weathering may interact with each other. One example is the account of Fuller's Earth formation (overconsolidated calcareous mudstone) given by Hawkins et al. (1988). Initially stress relief from erosion opens fissures allows surface water to percolate into this low permeability material. Weak acids in the rainwater interact with the material resulting in decalcification of the soil. This is followed by the decomposition of pyrite by oxygenised water and the production of sulphuric acid which in turn interacts with the calcite to form gypsum. The acidic ground water reacts with the clay minerals and transforms them; in this case illite is transformed into interstratified illite-smectite. A similar change in mineralogy was reported in the work on an old alluvium in Puerto Rico for which weathering produced a combination of kaolinite and smectite (Zhang et al., 2004). In contrast with the above studies, Chandler & Apted (1988) did not observe a significant change in mineralogy for London clay due to weathering. Cafaro & Cotecchia (2001) also reported no change in mineralogy in the Pappadai clay as a result of weathering. This contrast shows that change in mineralogy is dependent on the parent material as well as the weathering processes and can not be similar in every case.

One major chemical change during weathering is the oxidation which results in a colour change in the weathered material. During this process ferrous ions (FeO) are converted to ferric oxide (Fe_2O_3) and the degree of oxidation can be represented by the ratio of Fe_2O_3 / FeO (Chandler, 1972). This process can be very slow as was shown for Lias clay by Chandler (1972). Different authors reported the change in colour for various soils including London clay from blue-grey to brown (Chandler, 2000), Pappadai clay from grey to yellow (Cafaro & Cotecchia, 2001), the Fuller's Earth formation from grey to brown (Hawkins et al., 1988) and old alluvium in Puerto Rico from brown to red in the upper clay and to light brown or yellowish in the middle zone (Zhang et al., 2004). It should be noted that presence of Fe oxides also changes the microstructure of the soil as well. Zhang et al. (2004) reported two functions for these oxides; the formation of an impermeable coating around the clay particles suppressing the activity of these minerals and also the creation of cementation between the particles resulting in larger aggregates of clay particles.

The depth of weathered material is dependent on various factors including previous erosion, climatic conditions and the overlying materials. For instance, the depth of weathered material is smaller in London clay profiles that were covered by terrace gravels in a humid environment than in Pappadai clay outcrops which were exposed at the surface and experienced a drier environment (Chandler, 2000).

Weathering affects the mechanical behaviour of the soil in different manners. The change in structure altering both fabric and bonding is the main cause of this. Chandler (1969) reported that weathering increased the clay fraction of Keuper Marl (ie. Mercia Mudstone, a heavily overconsolidated Triassic deposit) due to the breakage of silt-sized aggregates of clays. Hawkins et al. (1988) also observed a decrease in the calcite content and removal of coarser particles in the Fuller's Earth formation which resulted in a higher clay content. The higher clay content in these examples resulted in lower permeability, higher plasticity and lower shear strength for the weathered material in comparison with the unweathered soil. However, Cafaro & Cotecchia (2001) noticed that the clay fraction was smaller for the weathered Papppadai clay due to aggregation of clay particles caused by drying processes. They also found that the permeability was lower for the weathered material due to rearrangements of these aggregates. It should also be noted that index testing involves breakage of the material causing disturbance far more significant than partial weathering and therefore masking the differences in index properties of weathered and partially weathered materials (Chandler, 1969).

Cafaro & Cotecchia (2001) investigated the compression and shear behaviour of weathered Pappadai clay. They observed a lower compression index (C_c) for the weathered material showing less degradation of structure for the weathered soil. They also noticed a higher swell sensitivity (C_s^* / C_s) for the unweathered soil showing higher bonding in the unweathered soil in comparison with weathered material. Various authors reported higher strength parameters for unweathered soils in comparison with weathered soils (Chandler, 1969; Chandler, 1972; Cafaro & Cotecchia, 2001). Taking the effects of volume into account, Cafaro & Cotecchia (2001) showed that state boundary surface for the unweathered soil envelopes that of the weathered SBS which in turn envelopes the intrinsic SBS* (Figure 2-24). By introducing the sensitivity parameter (S_σ) into the equation relating stress level and

shear modulus at small strains, they concluded that small strain stiffness is higher for the unweathered soil due to its 'stronger' structure. This is not in agreement with Gasparre et al. (2007) who showed that small strain stiffness, G_0, is similar for reconstituted, weathered and unweathered London clay when measured at similar states.

The most common effect of weathering on mechanical behaviour is the reduction in the residual angle of shearing resistance due to the presence of a higher proportion of clay particles (Chandler, 1969; Chandler, 1972; Hawkins et al., 1988; Moore, 1991).

2.8.1 Effect of vegetation on the soil profile

As will be discussed later in Chapter 5, the initial block sampling of Gault clay was complicated by the presence of tree roots. The sampling location was near to trees and bushes and the effect of their roots was observed both in the CPT profiles established at the site and in the suction measurements. Understanding the effects of vegetation on the soil profile was therefore necessary. Most of the relevant research is concerned with the desiccation of swelling/expansive clays due to vegetation and the relative settlements or heaves caused by this, and the potential damage it may cause to shallow foundations and road pavements (Bozozuk & Burn, 1960; Driscoll, 1983; Biddle, 1983; Richards et al., 1983; Crilly & Driscoll, 2000). There is also some research dealing with the stabilising benefits of the presence of roots in the soil, mainly in slope stability design, in particular the higher shear strength generated by high suction values (Wu & Watson, 1998; Indraratna et al., 2006). The relevance of these studies to the current project is limited to the patterns in which vegetation affects the soil profile.

Crilly & Driscoll (2000) studied the effects of vegetation on piles in London clay in the vicinity of 20-25 m high Lombardy Poplar trees. Figure 2-25 shows the changes in water content, undrained shear strength and suction in the soil profile. As can be seen from the figure the depth to which soil is affected by the presence of trees is around 5 m below ground level, with suction values close to the trees almost six times those far from the trees. The same pattern was reported by Cameron (2001) for a more extreme case in Adelaide, South Australia. In the latter case, the suction close to the trees

reached a wilting point and stayed constant. The suction in the roots needs to be higher than that in the ground to promote water uptake; the wilting point is the limit at which the suction in the roots can not increase due to the limit in the osmotic pressure in the leaf cells (Blight, 2005). This limit is dependent on tree species, but is believed to generally be above 1.5 MPa (Richards et al. 1983).

Driscoll (1983) and Biddle (1983) studied the effects of the tree vicinity (with different species) on the variation of water content of some UK soils including Gault clay, Oxford clay and Kimmeridge clay. Based on their index properties and clay content, these three stiff clays were considered to posses high to very high shrinkage potential. Biddle (1983) concluded that the pattern of soil water deficit was not affected by the soil type with the exception of permeability which affected the depth of water deficit. However, the significance of various species was highlighted with high water demand species like poplar, willow, oak and elm trees causing the more extensive water loss in the soil surrounding them. It should also be noted that even grass and bushes can in some cases result in a water deficit over significant depths (Blight, 2005). In general the magnitude of the effect of vegetation is dependent on the soil type, the species of the tree and hydrology (Richards et al., 1983).

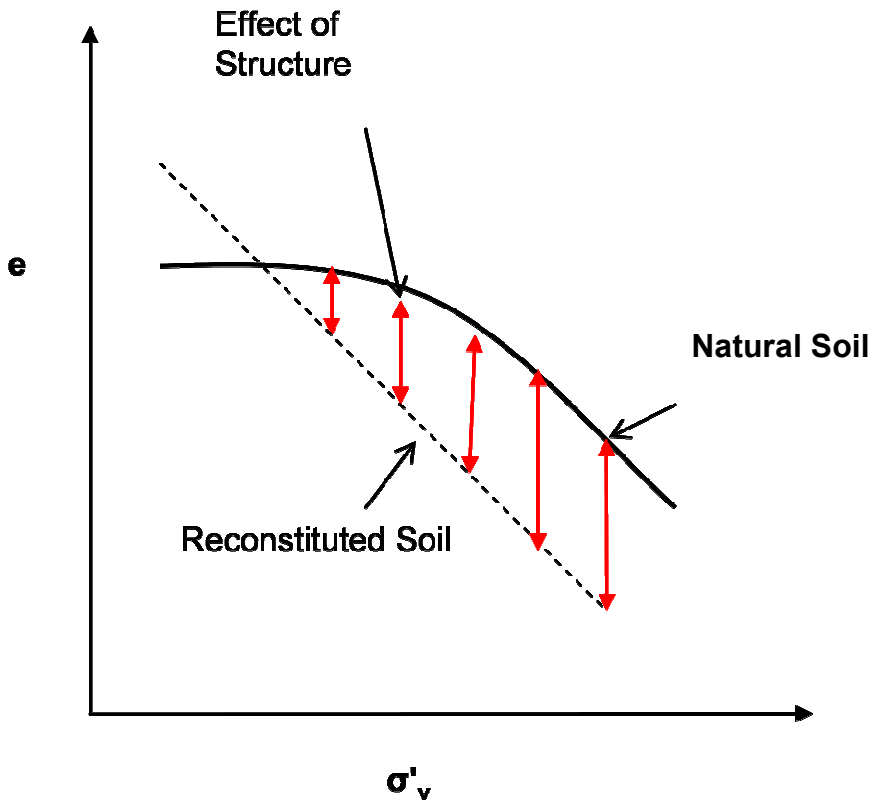


Figure 2-1: The effect of structure on the relative location of compression curves of natural and reconstituted soil

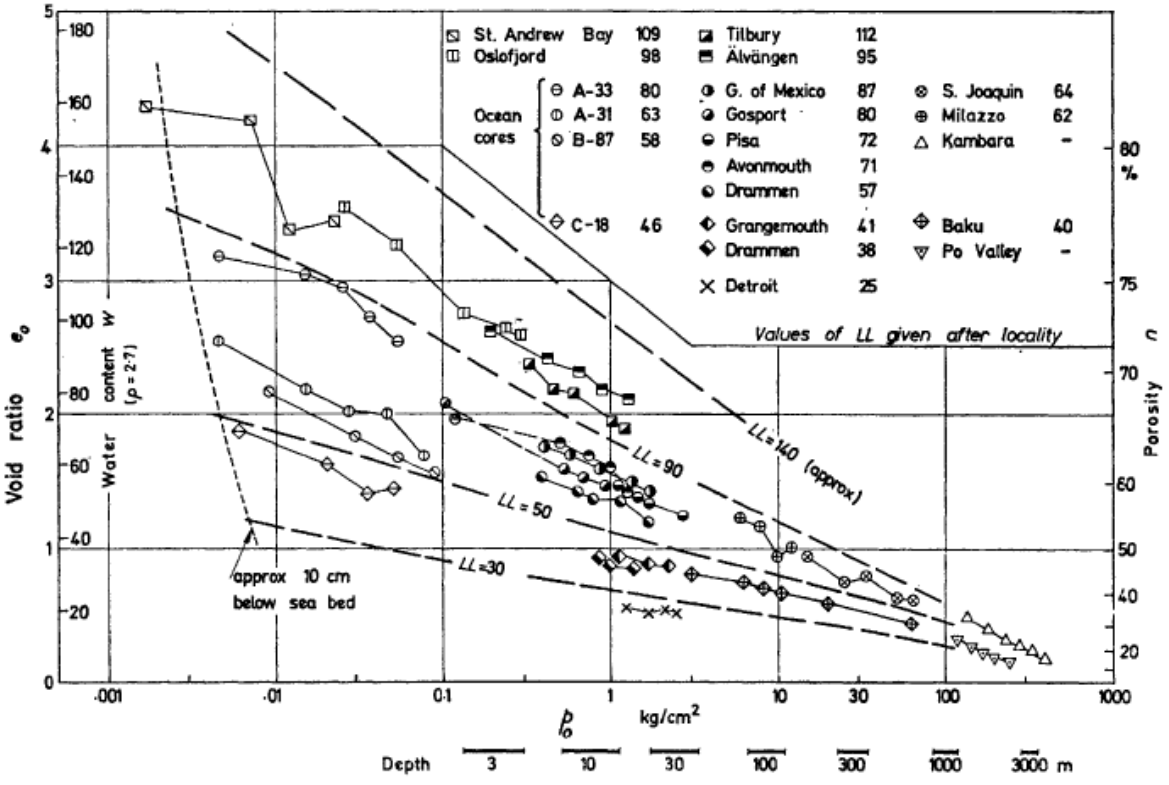


Figure 2-2: Sedimentation compression curves for normally consolidated argillaceous sediments (Skempton, 1969)

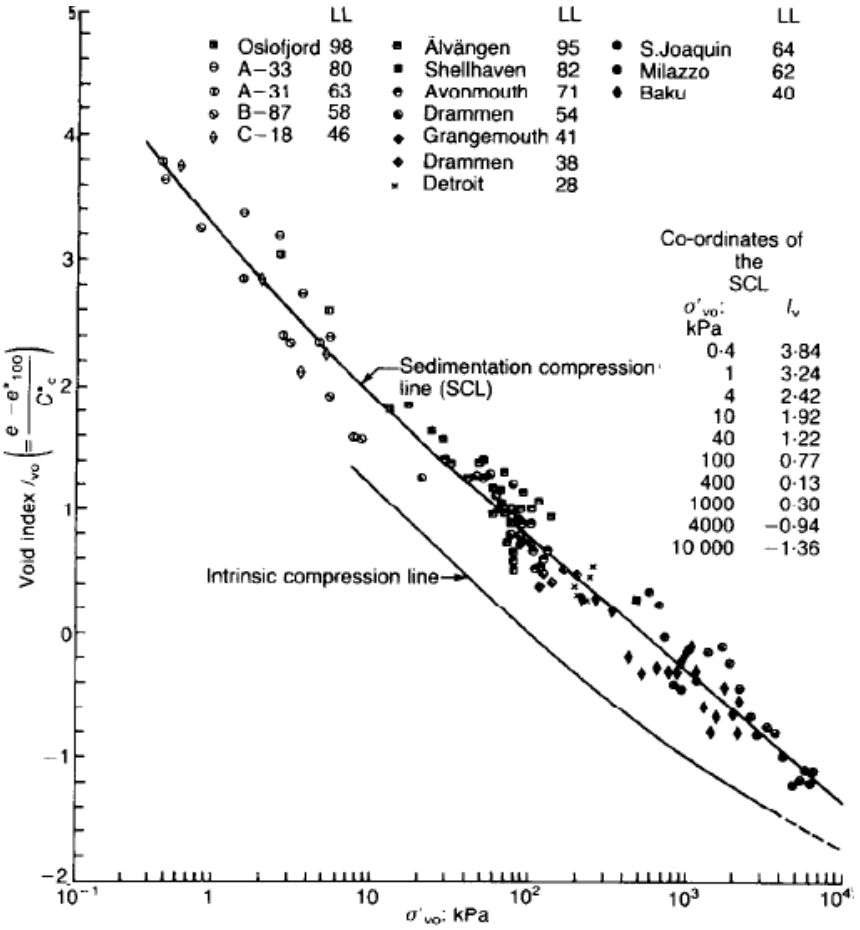


Figure 2-3: Sedimentation compression curves normalised in the I_v space (Burland, 1990)

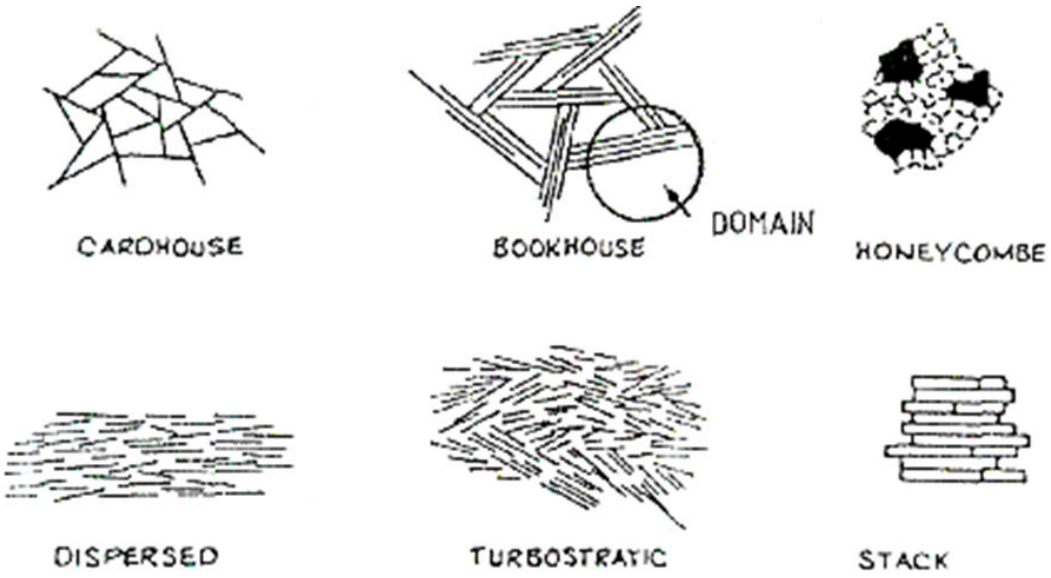


Figure 2-4: Classification of fabric (Sides & Barden, 1970)

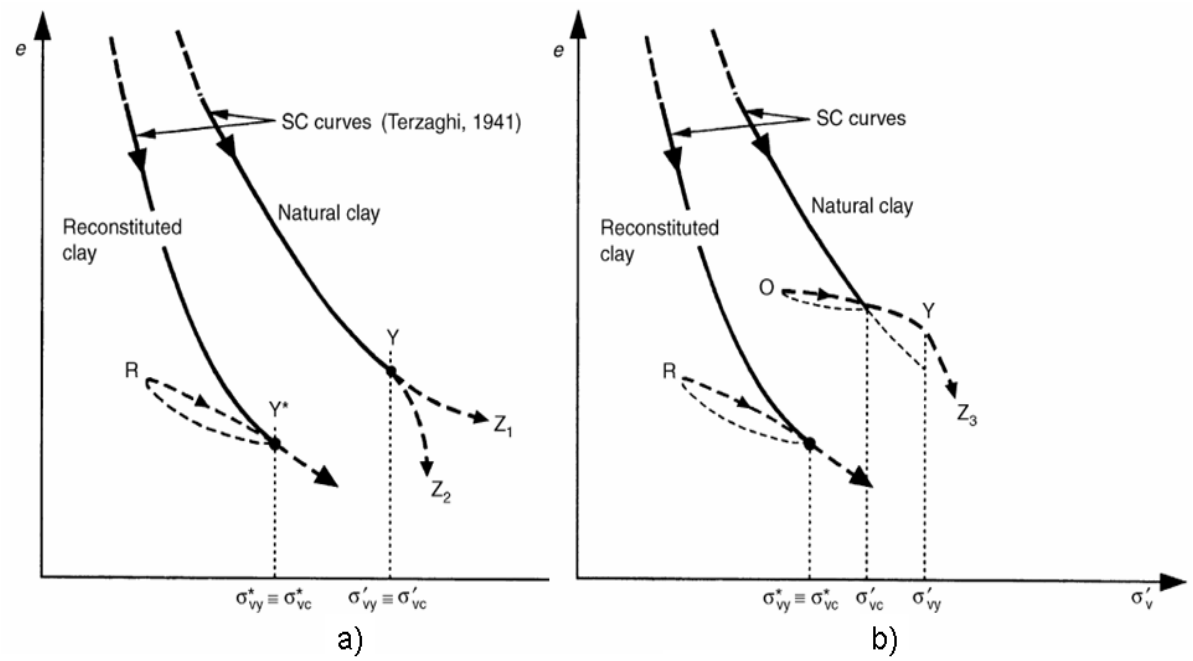


Figure 2-5: The response of clays to one-dimensional compression; natural clay with a) sedimentation and b) post-sedimentation structure (Cotecchia & Chandler, 2000)

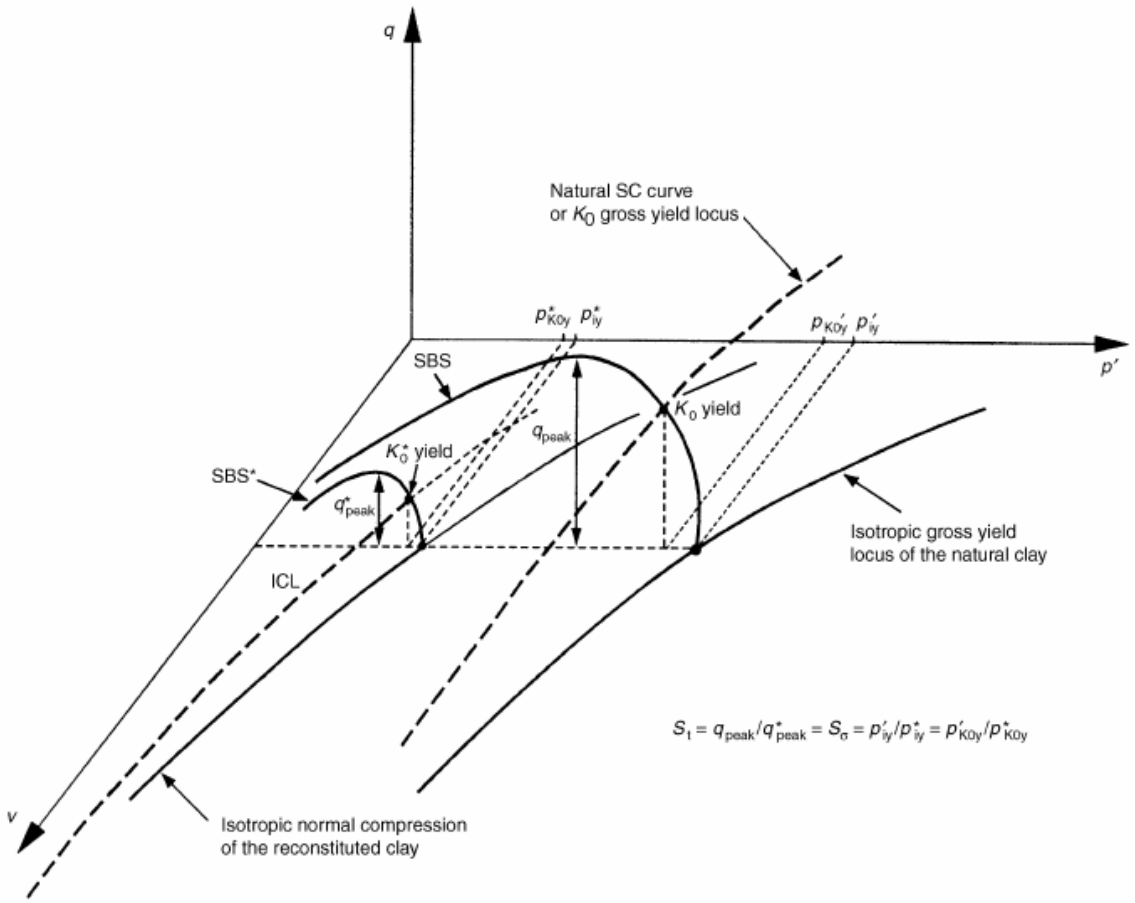


Figure 2-6: Idealized behaviour of natural and reconstituted clays (Cotecchia & Chandler, 2000)

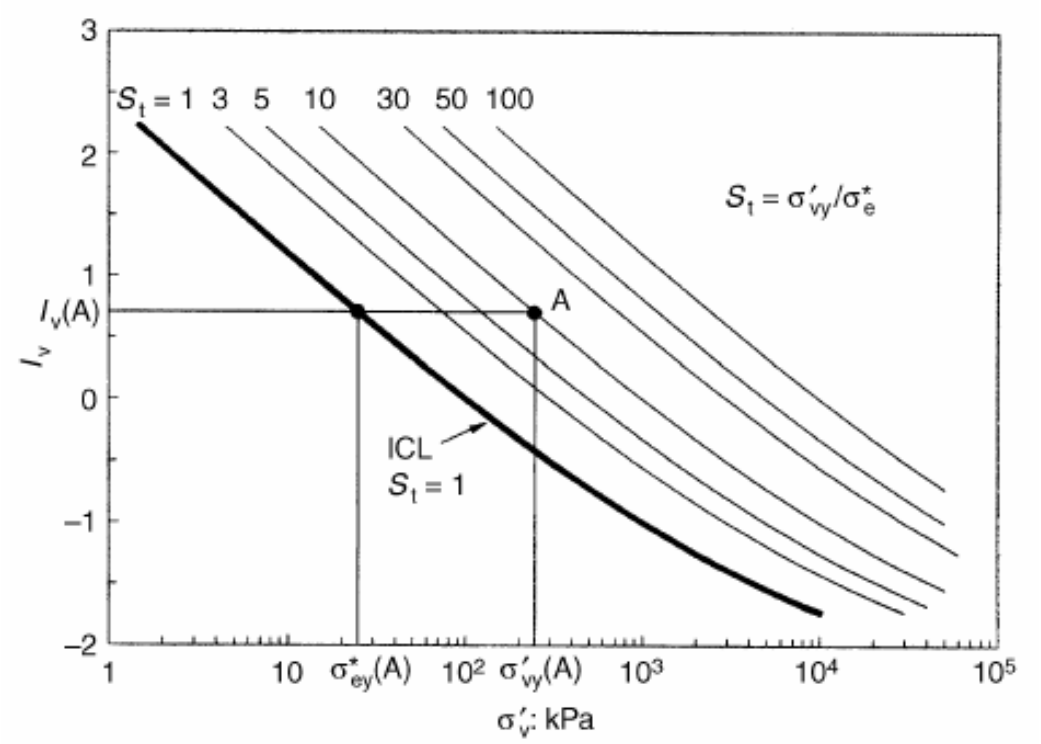


Figure 2-7: Sedimentation compression curves in the sensitivity framework (Cotecchia & Chandler, 2000)

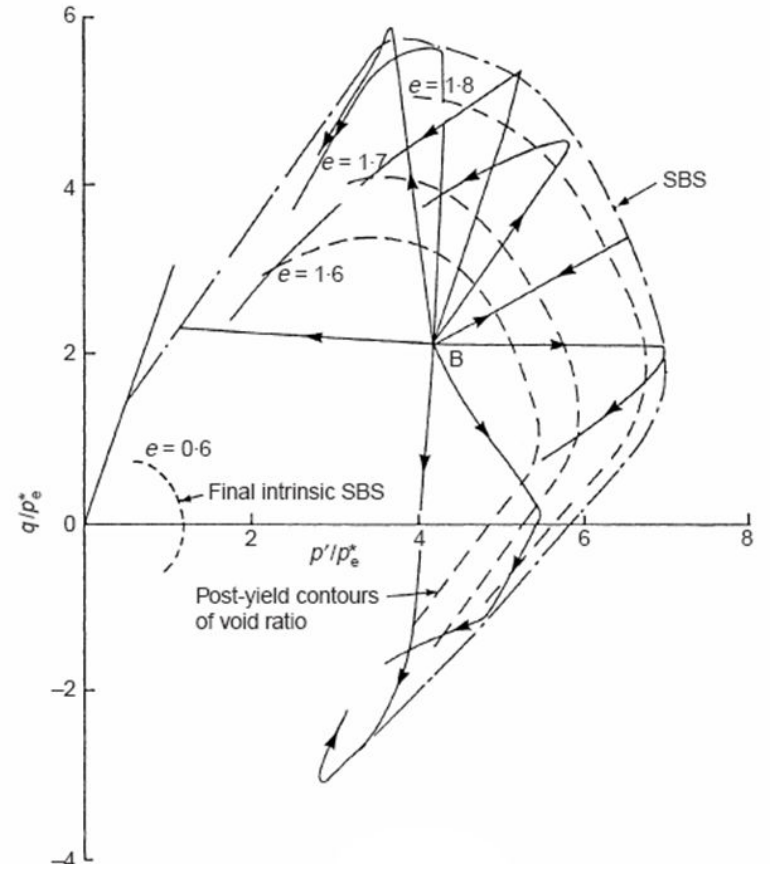
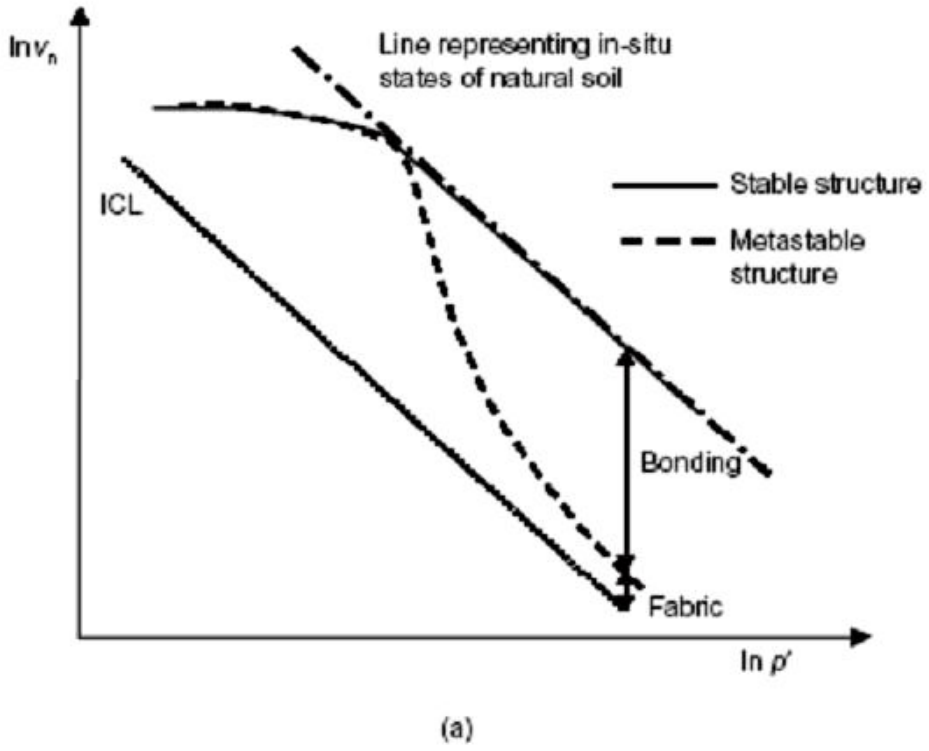
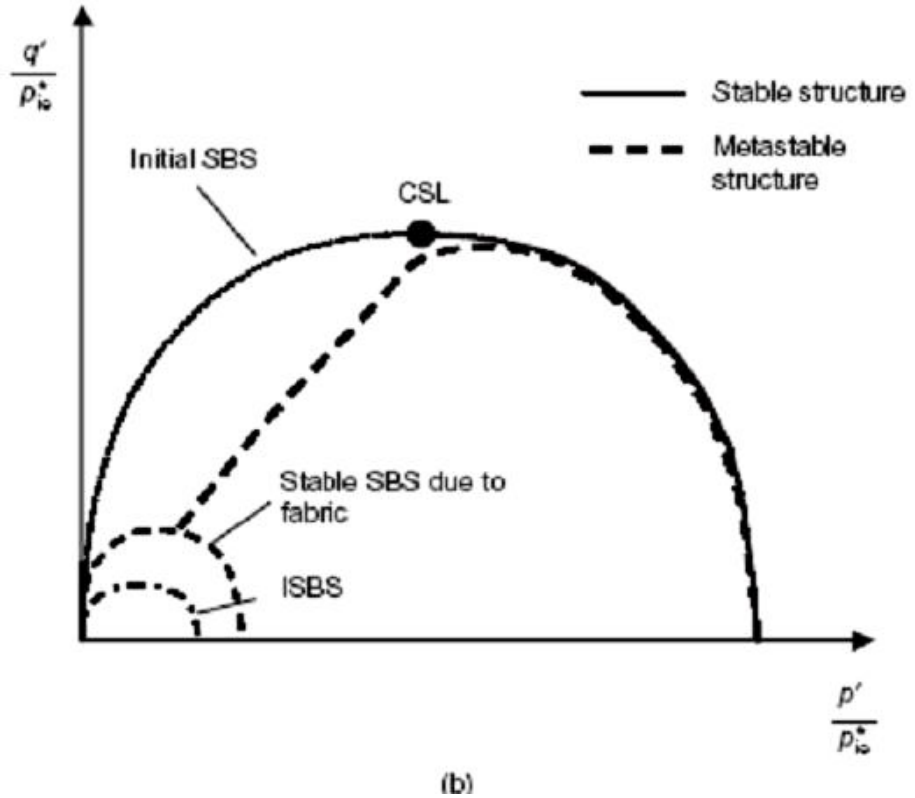


Figure 2-8: Normalised stress paths for Bothkennar clay (Smith et al., 1992)



(a)



(b)

Figure 2-9: Stable and meta-stable structure in : a) compression; b) shearing (Baudet & Stallebrass, 2004)

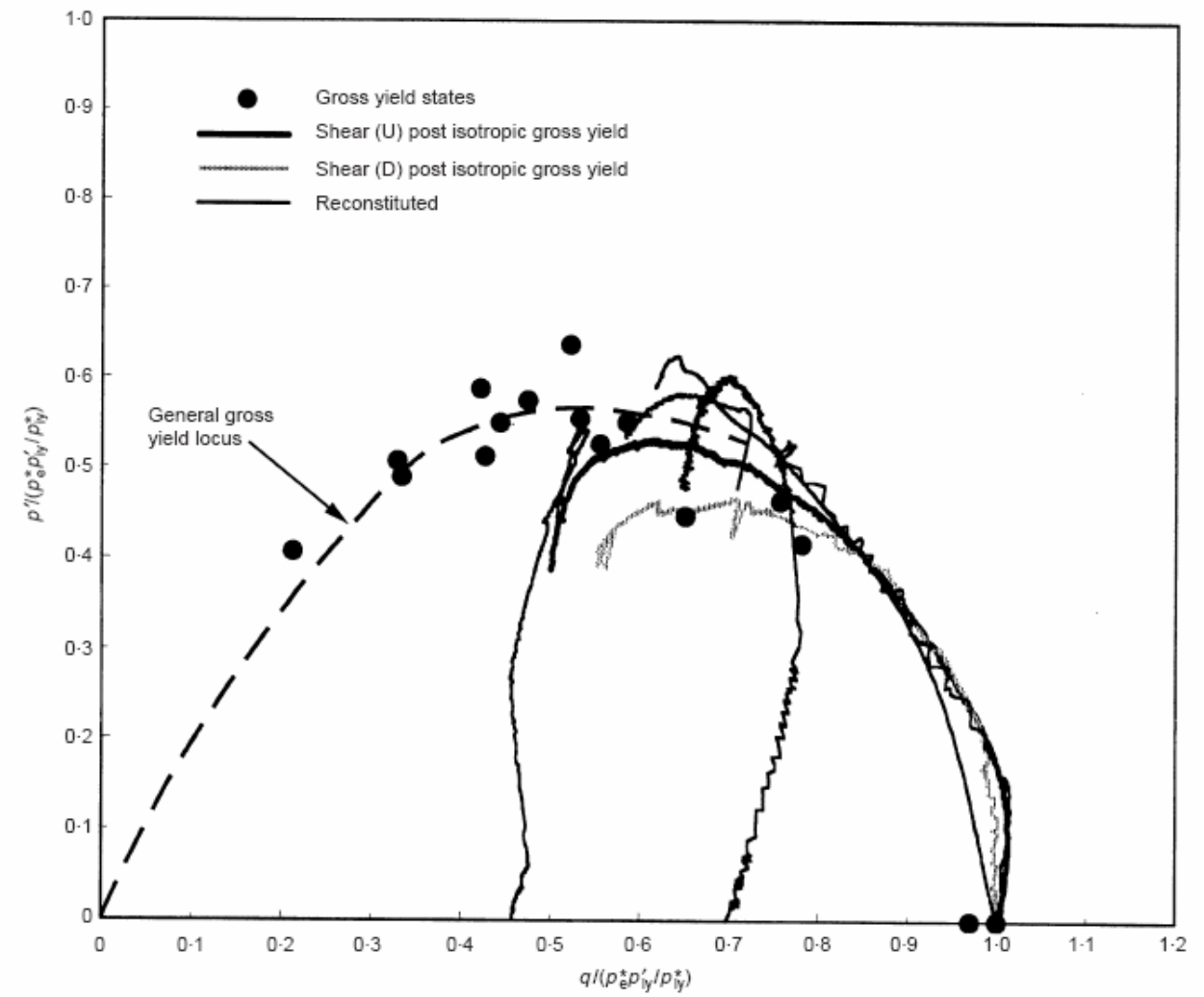


Figure 2-10: Pappadai clay behaviour normalised for both volume and structure (Cotecchia & Chandler, 2000)

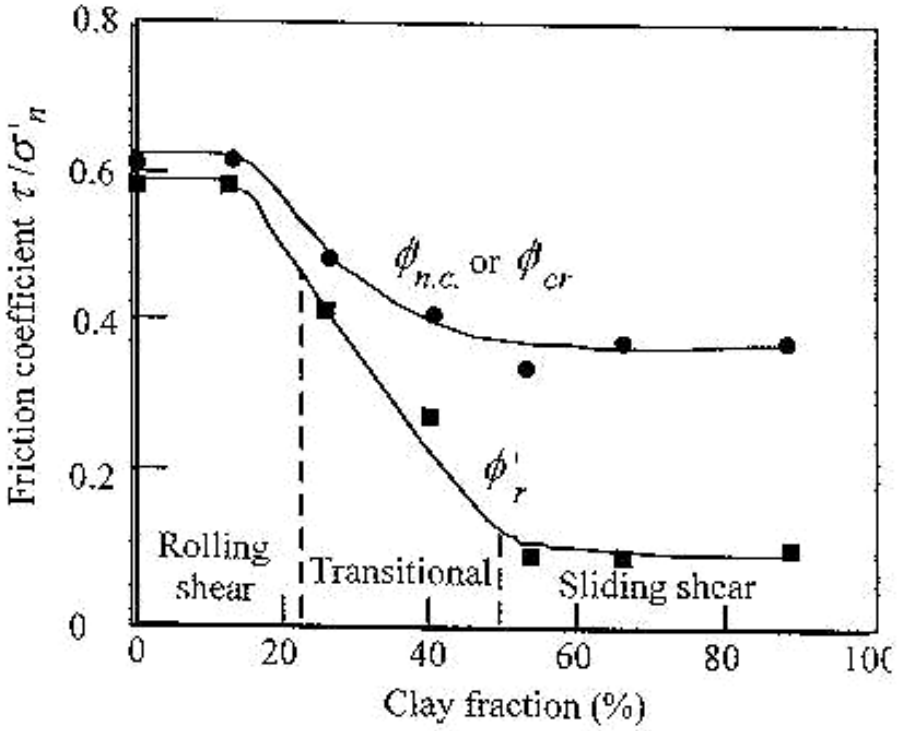


Figure 2-11: Effects of clay fraction on the post-peak shear behaviour of soils (Lupini et al., 1981)

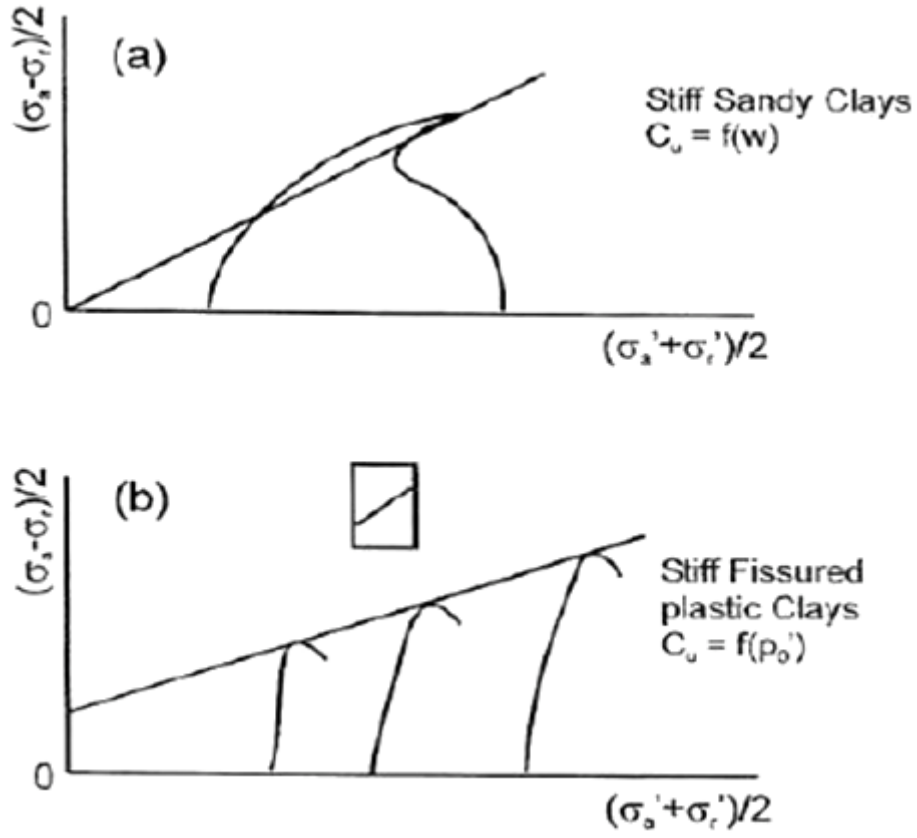


Figure 2-12: Behaviour of overconsolidated clays in undrained shear; a) low plasticity clay, b) stiff plastic clay (Jardine et al., 2004)

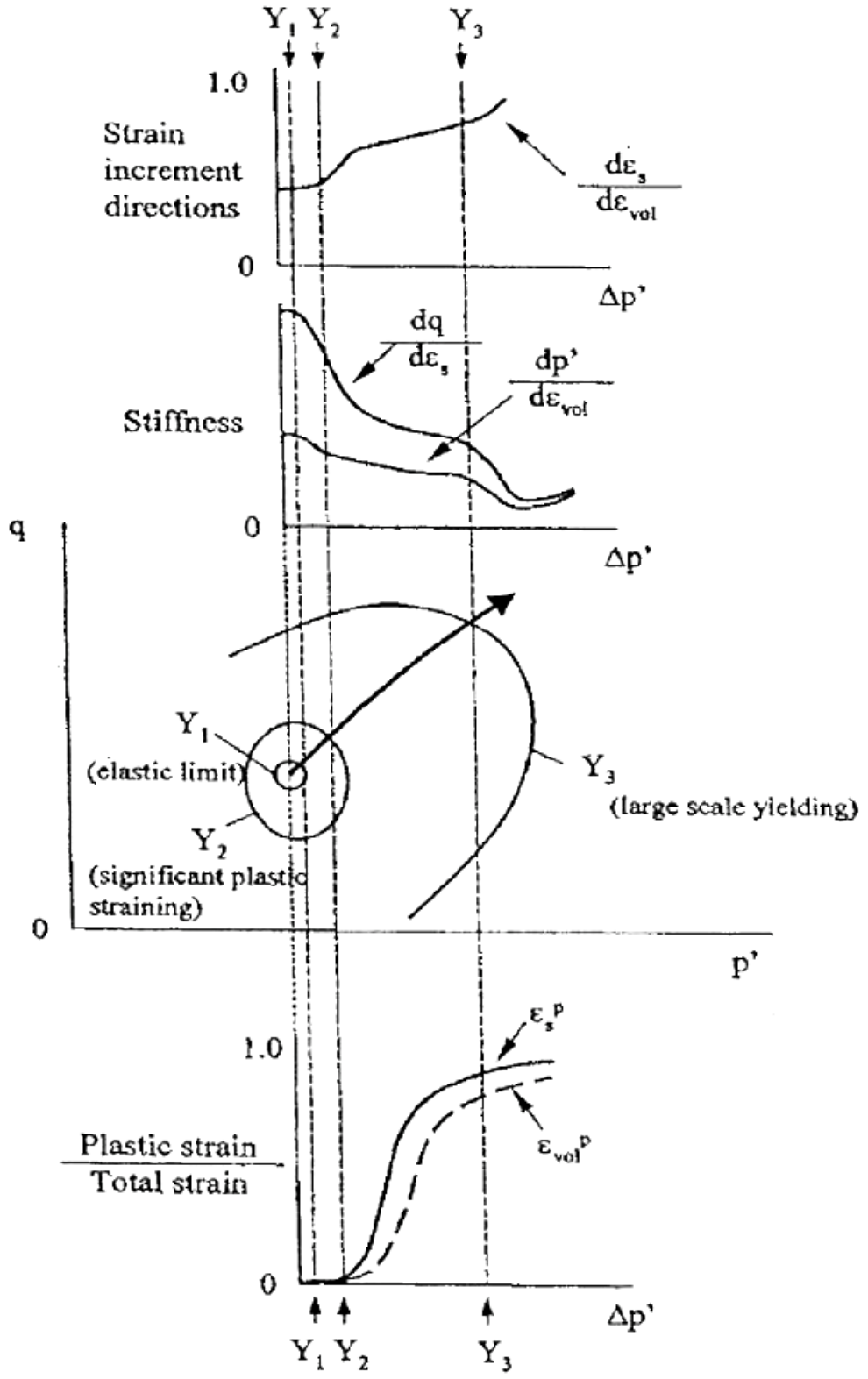


Figure 2-13: Conceptual multiple surface kinematic model with three zones (Jardine, 1992)

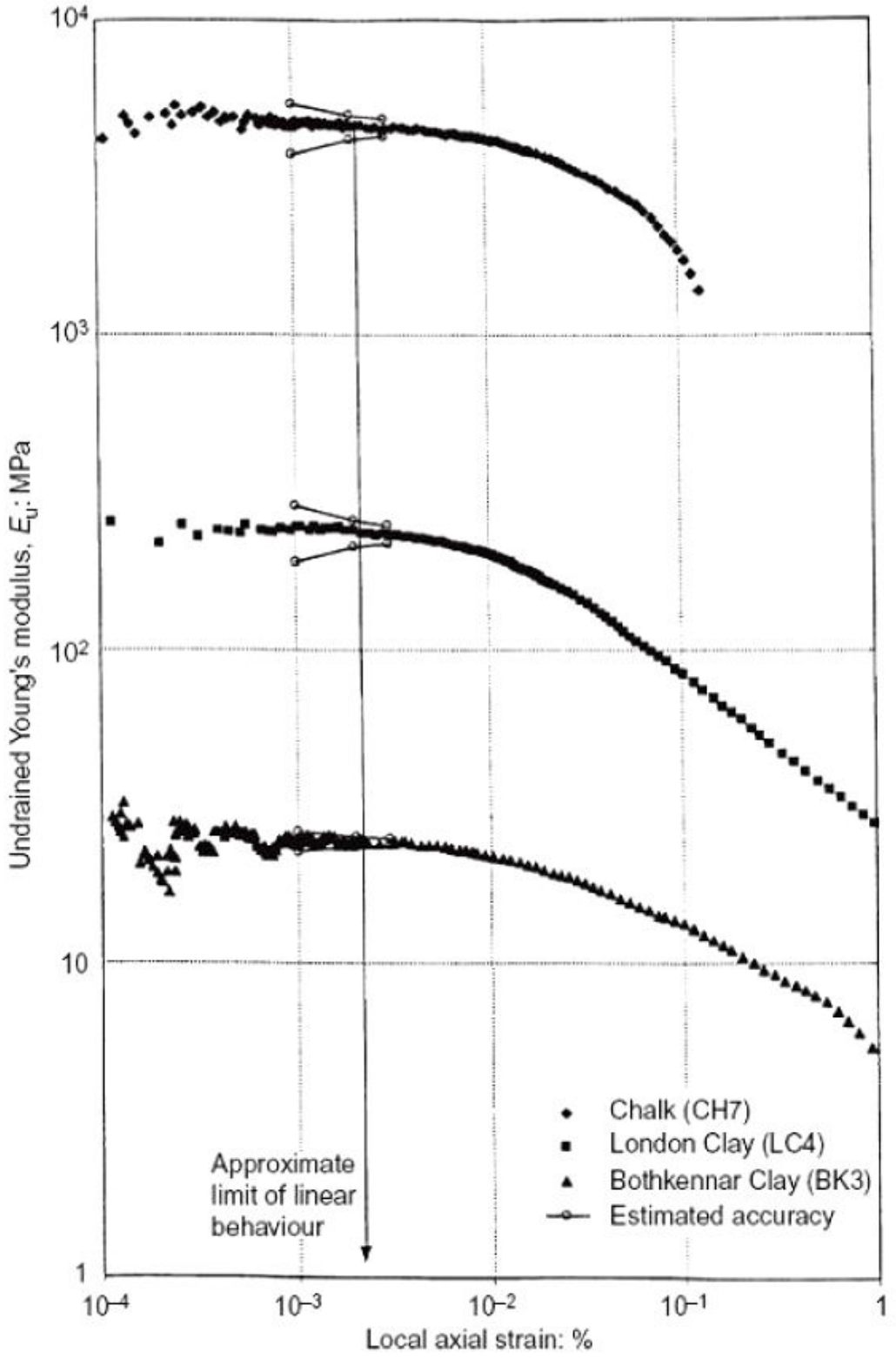


Figure 2-14: Comparison of secant stiffness curves for three materials in the small strain region (Clayton & Heymann, 2001)

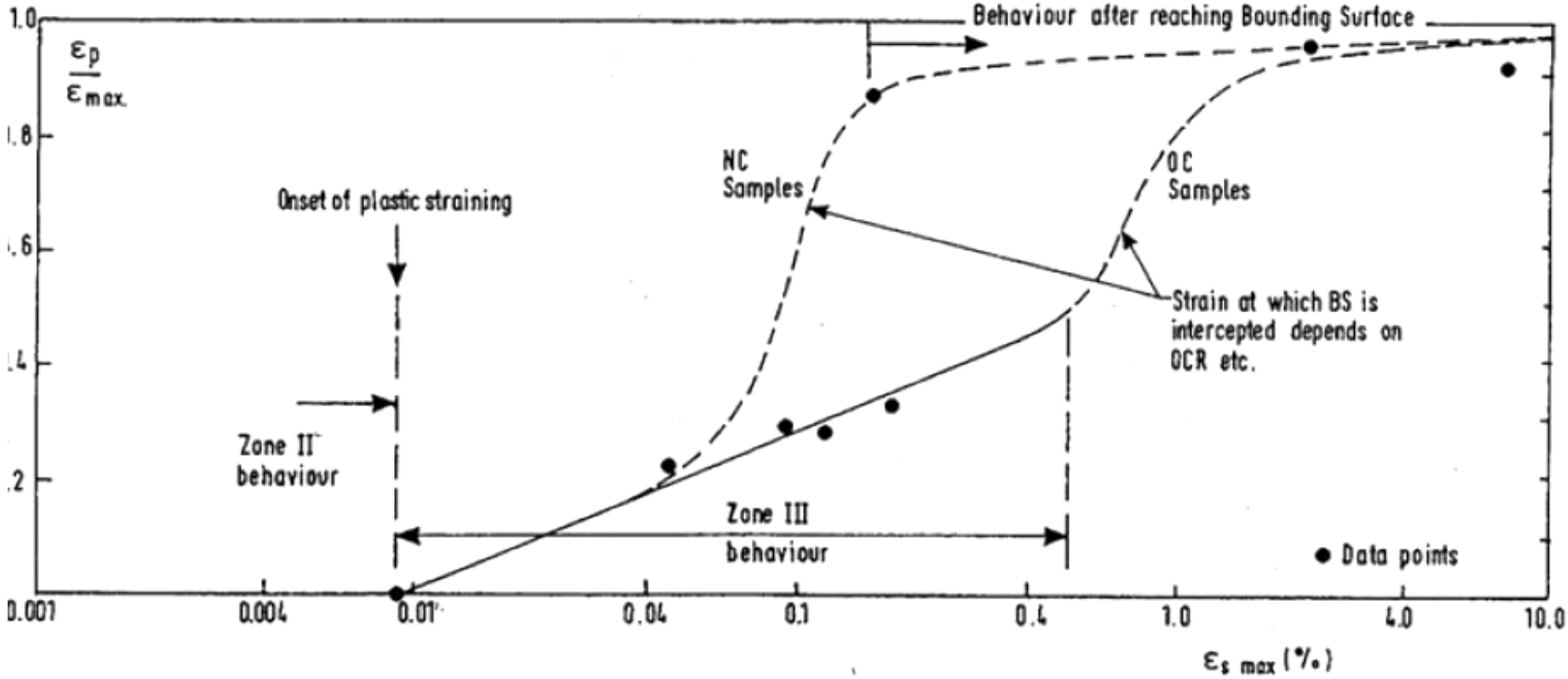


Figure 2-15: Relationship between permanent and total strains for Magnus till (Jardine, 1992)

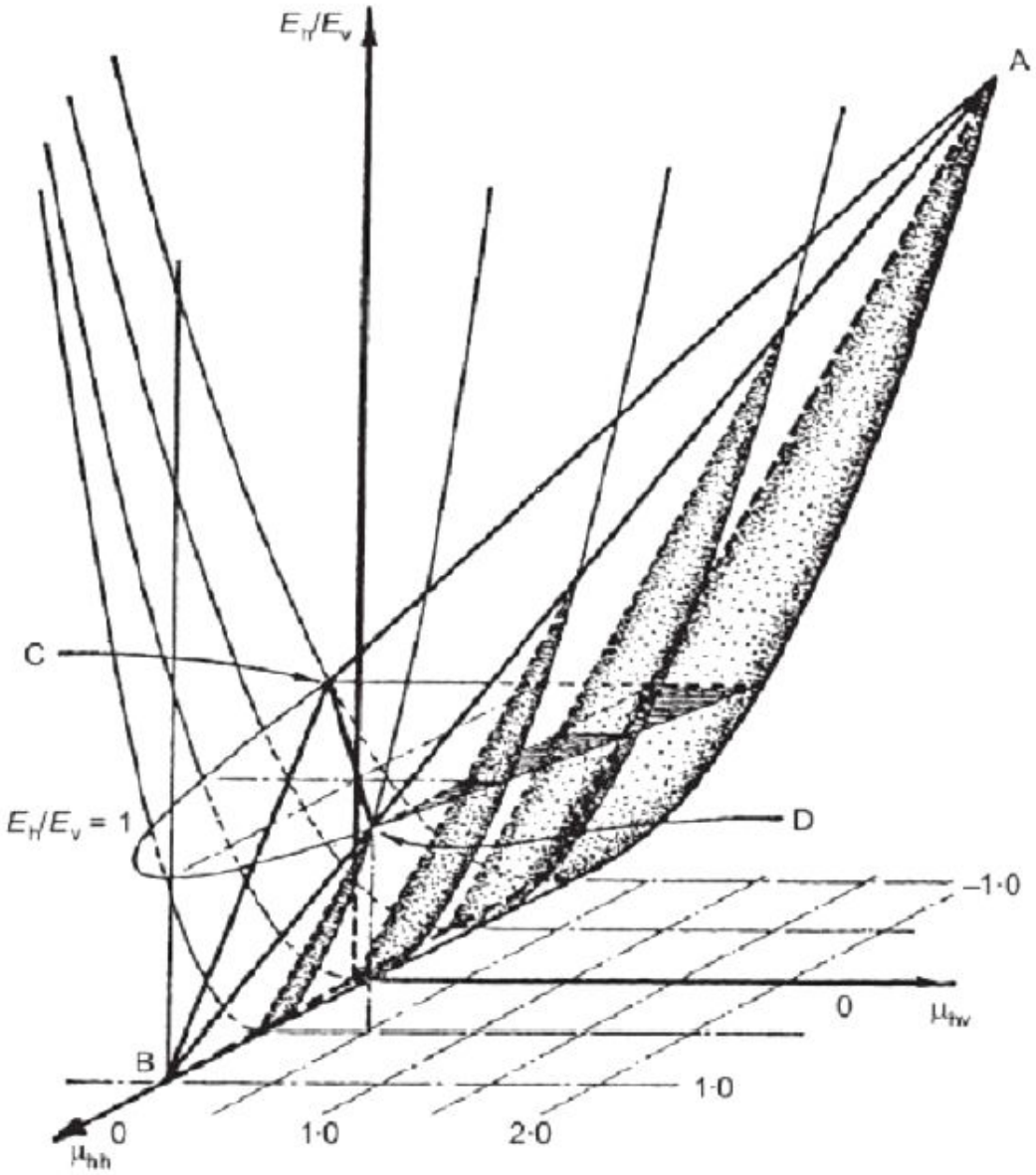


Figure 2-16: Planes and lines representing special types of material (Pickering, 1970)

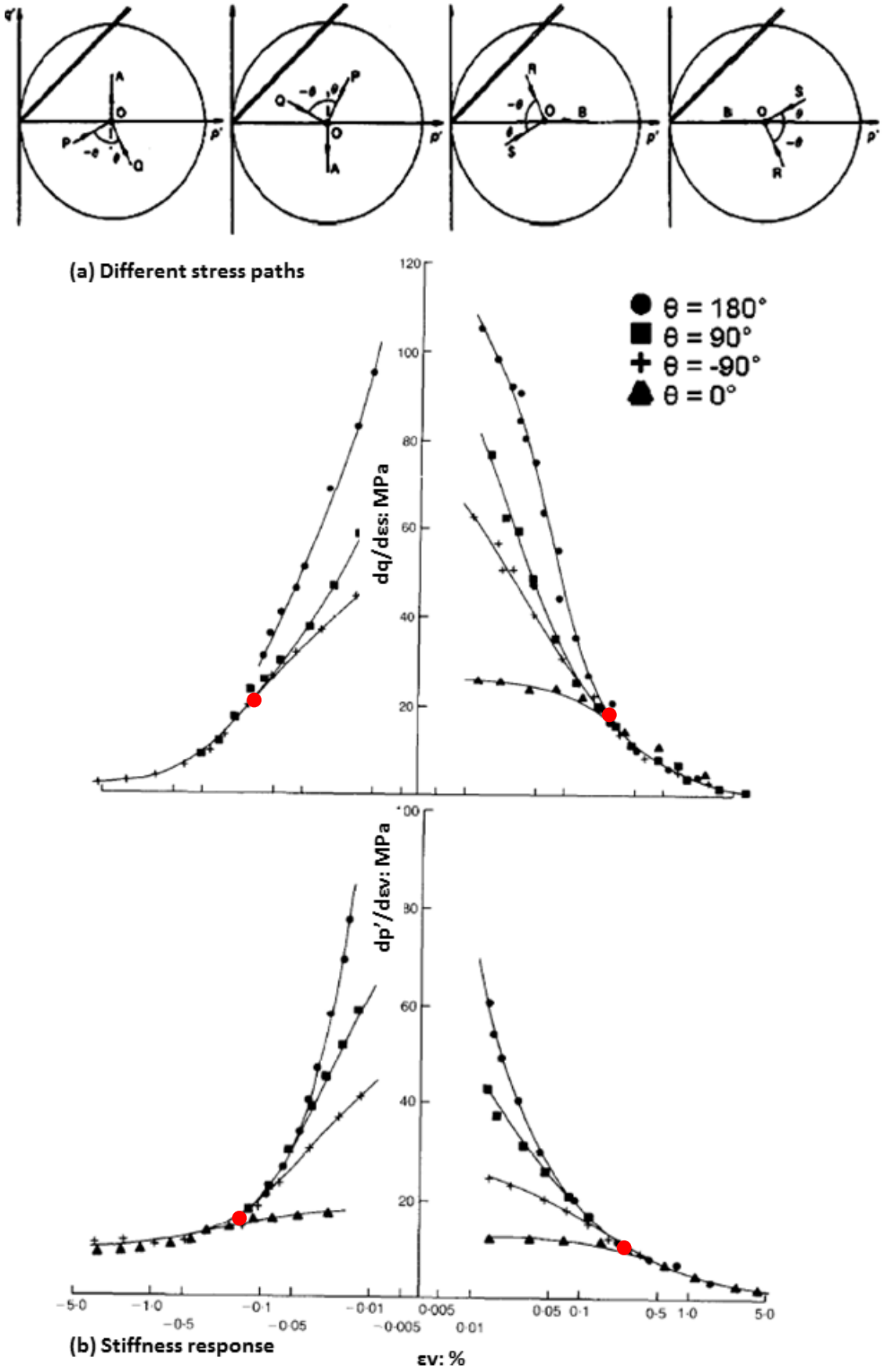
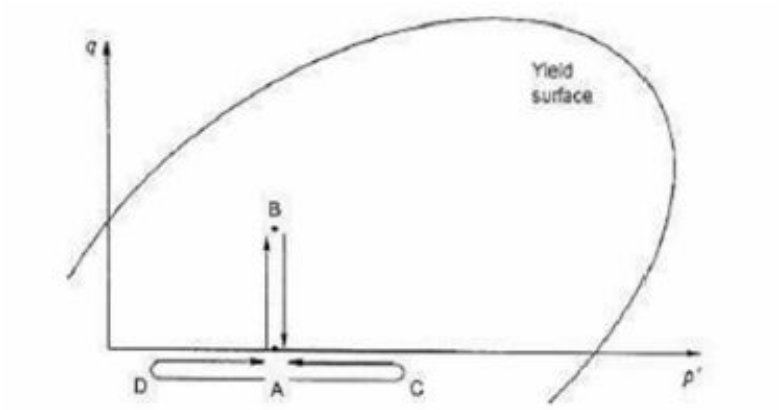
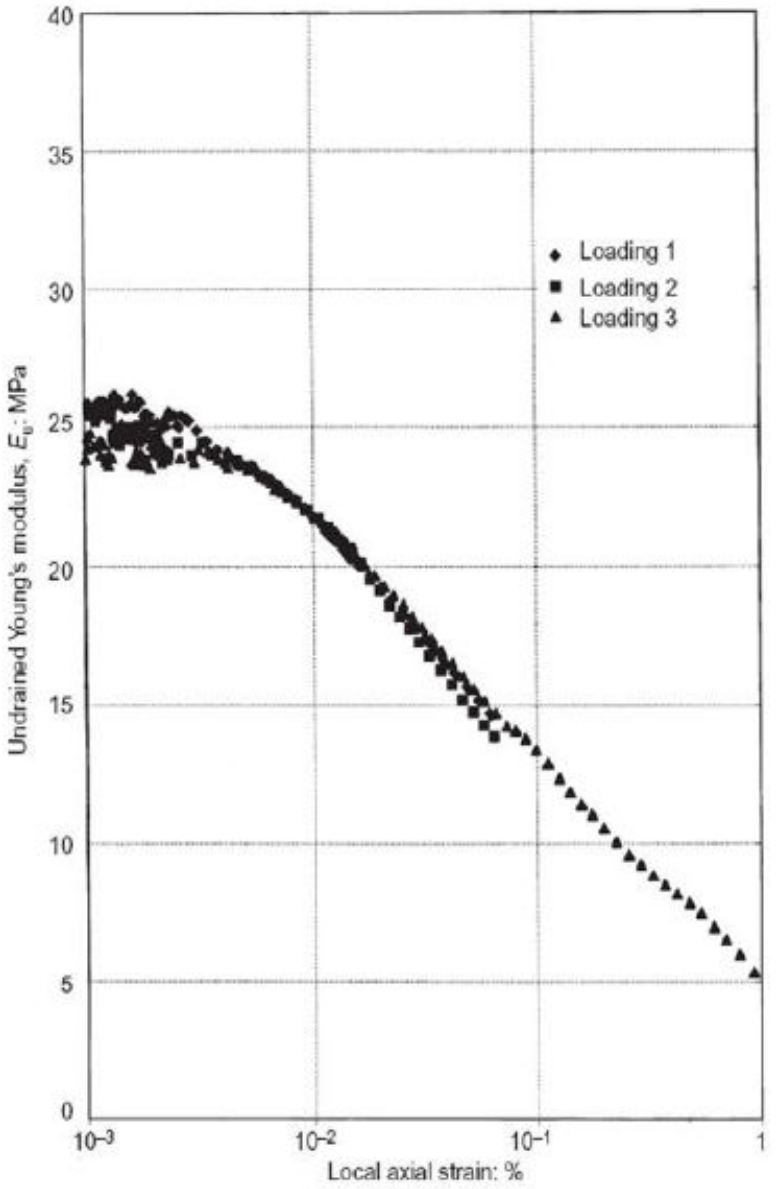


Figure 2-17: Stiffness response of reconstituted London clay with different stress histories (Atkinson et al., 1990)

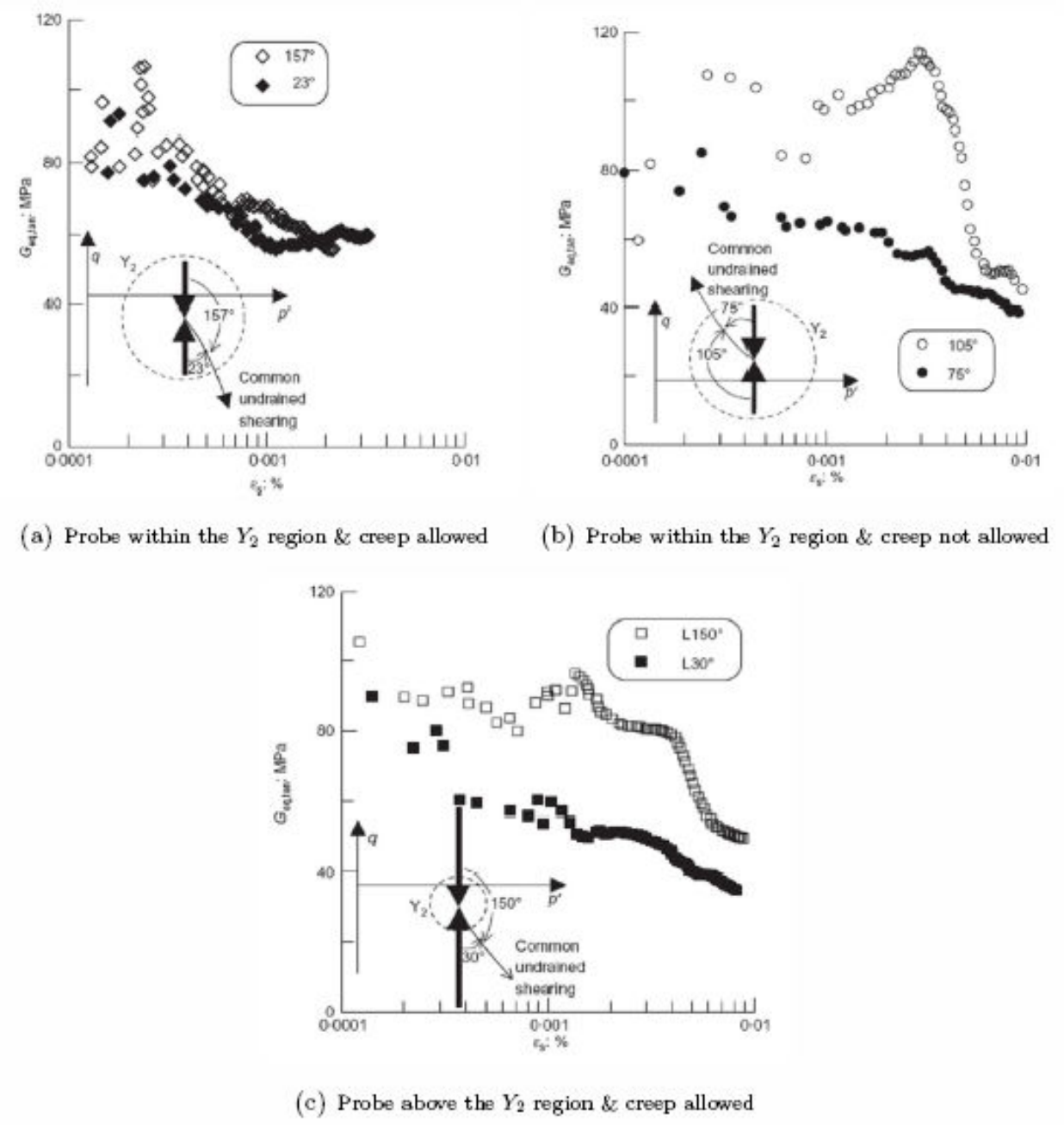


(a) Different stress paths



(b) Stiffness response

Figure 2-18: Secant stiffness degradation curves for Bothkennar clay with different stress paths (Clayton & Heymann, 2001)



(a) Probe within the Y_2 region & creep allowed

(b) Probe within the Y_2 region & creep not allowed

(c) Probe above the Y_2 region & creep allowed

Figure 2-19: Tangent stiffness degradation curves for different probe lengths and creep periods (Gasparre et al., 2007)

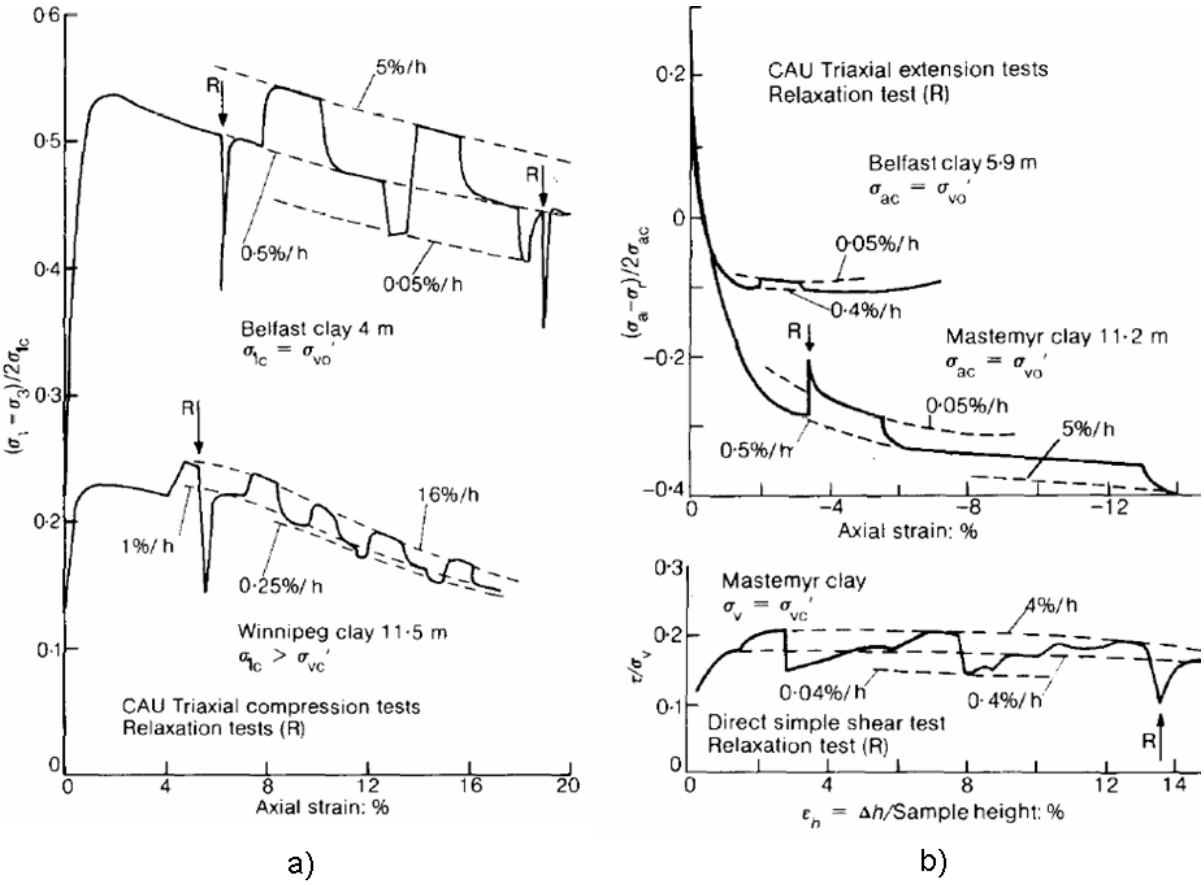


Figure 2-20: Stress-strain curves for step-changed strain rates and relaxation procedures; a) triaxial compression, b) triaxial extension and simple shear tests (Graham et al., 1983)

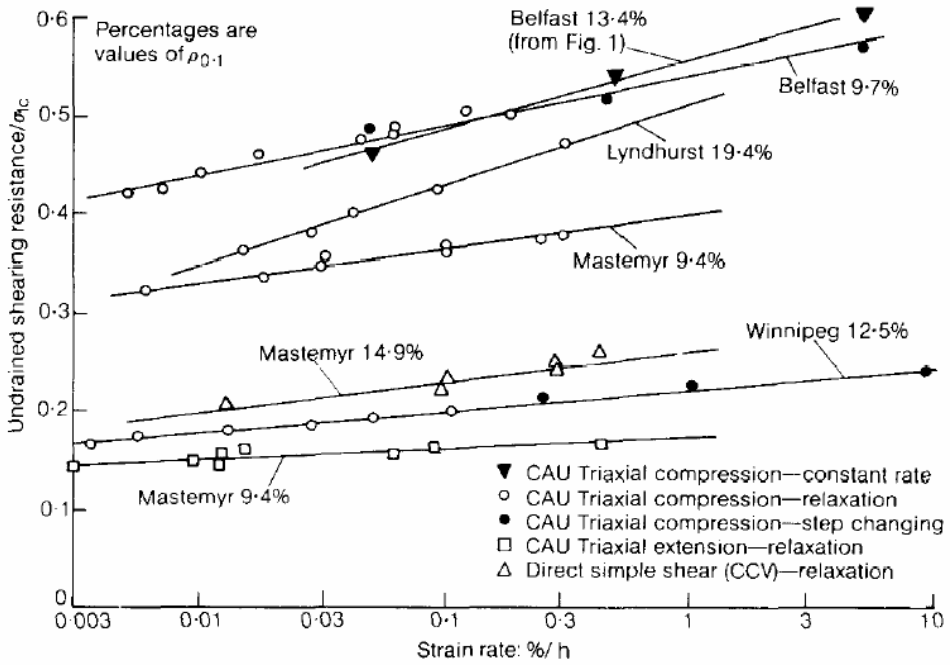
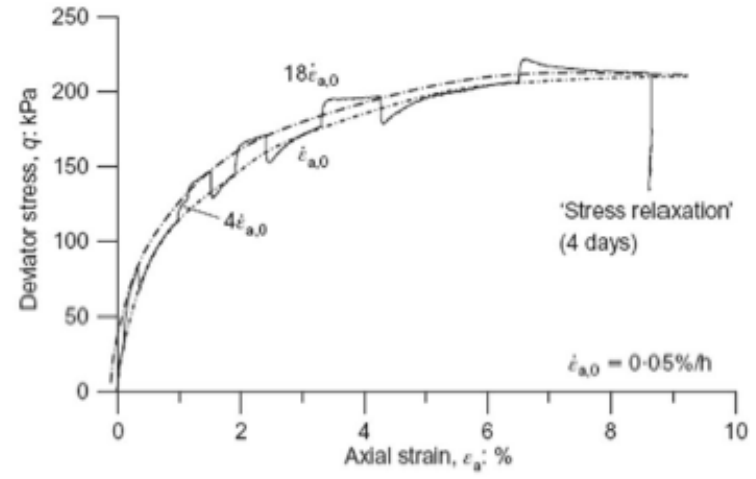
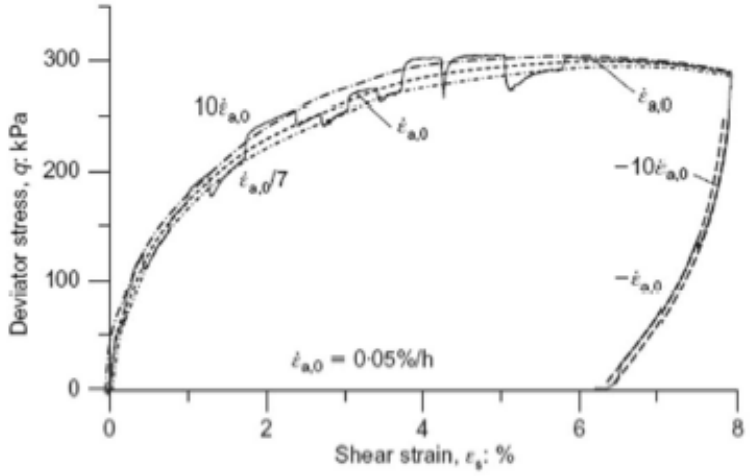


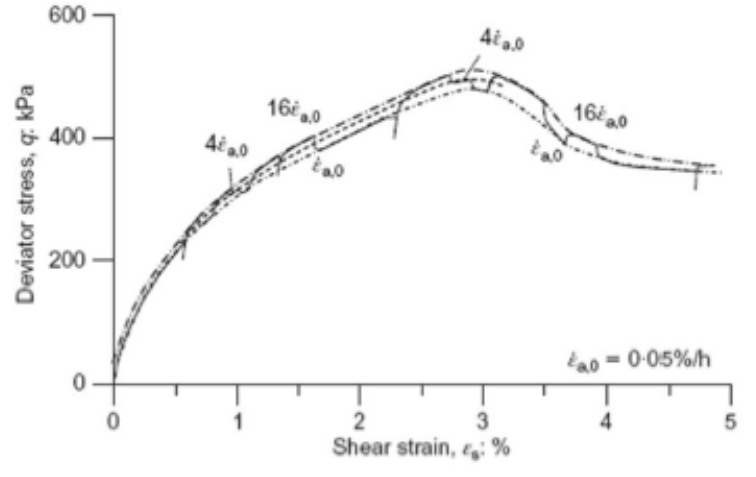
Figure 2-21: Change in undrained shearing resistance with log (strain rate), (Graham et al., 1983)



(a) NC reconstituted London clay



(b) OC reconstituted London clay



(c) OC intact London clay

Figure 2-22: Effect of stepwise changes in strain rate on the undrained stress-strain behaviour of natural and reconstituted London clay after isotropic compression (Sorensen et al., 2007)

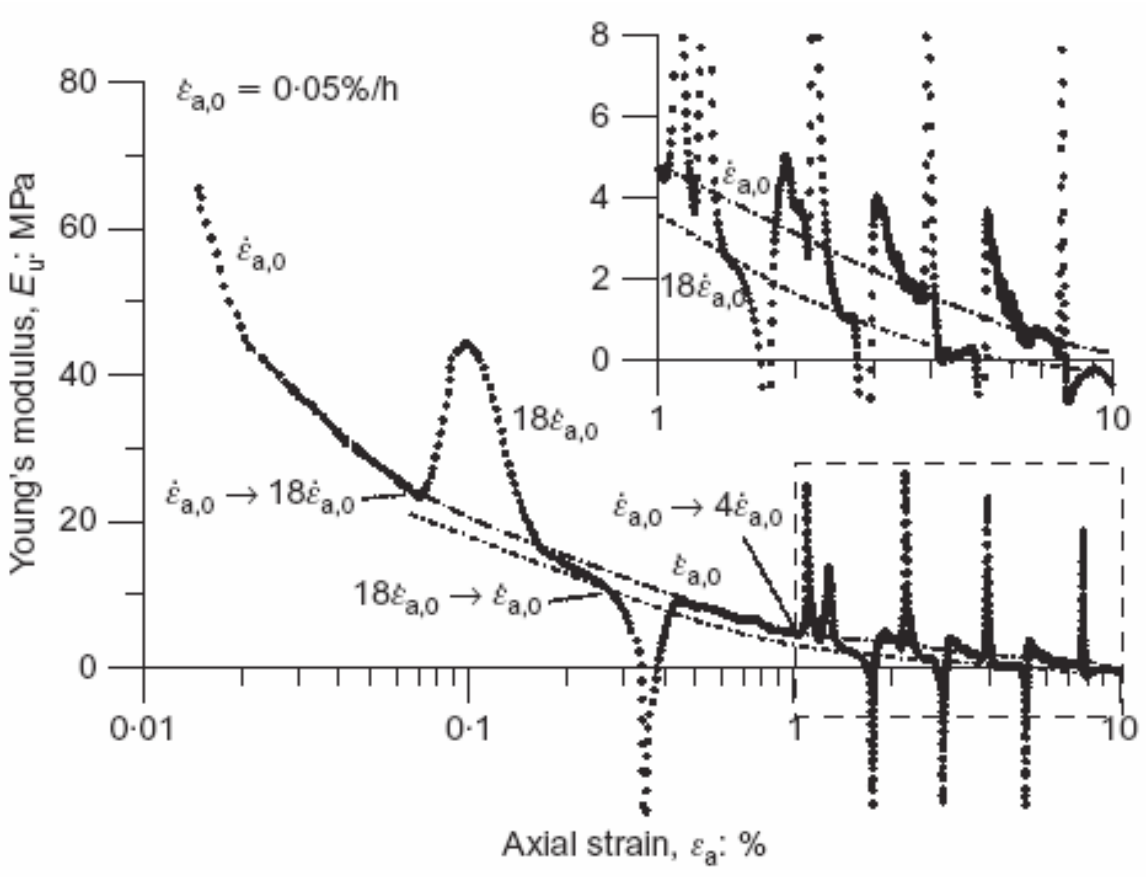


Figure 2-23: Effect of stepwise change in strain rate on small to large strain stiffness of NC reconstituted London clay (Sorensen et al., 2007)

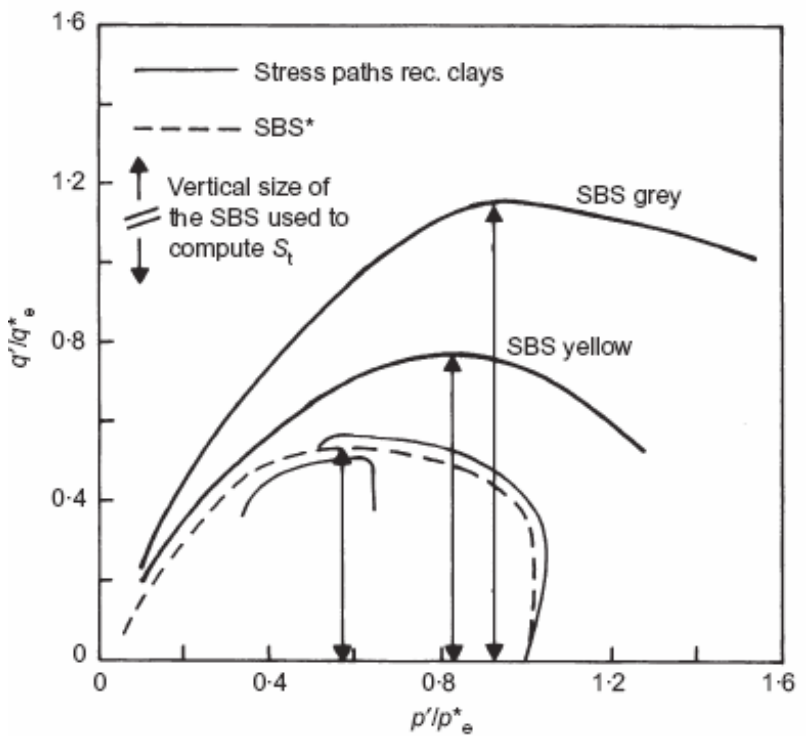


Figure 2-24: Normalised state boundary surfaces of both the natural (weathered yellow and unweathered grey) and reconstituted clays (Cafaro & Cotecchia, 2001)

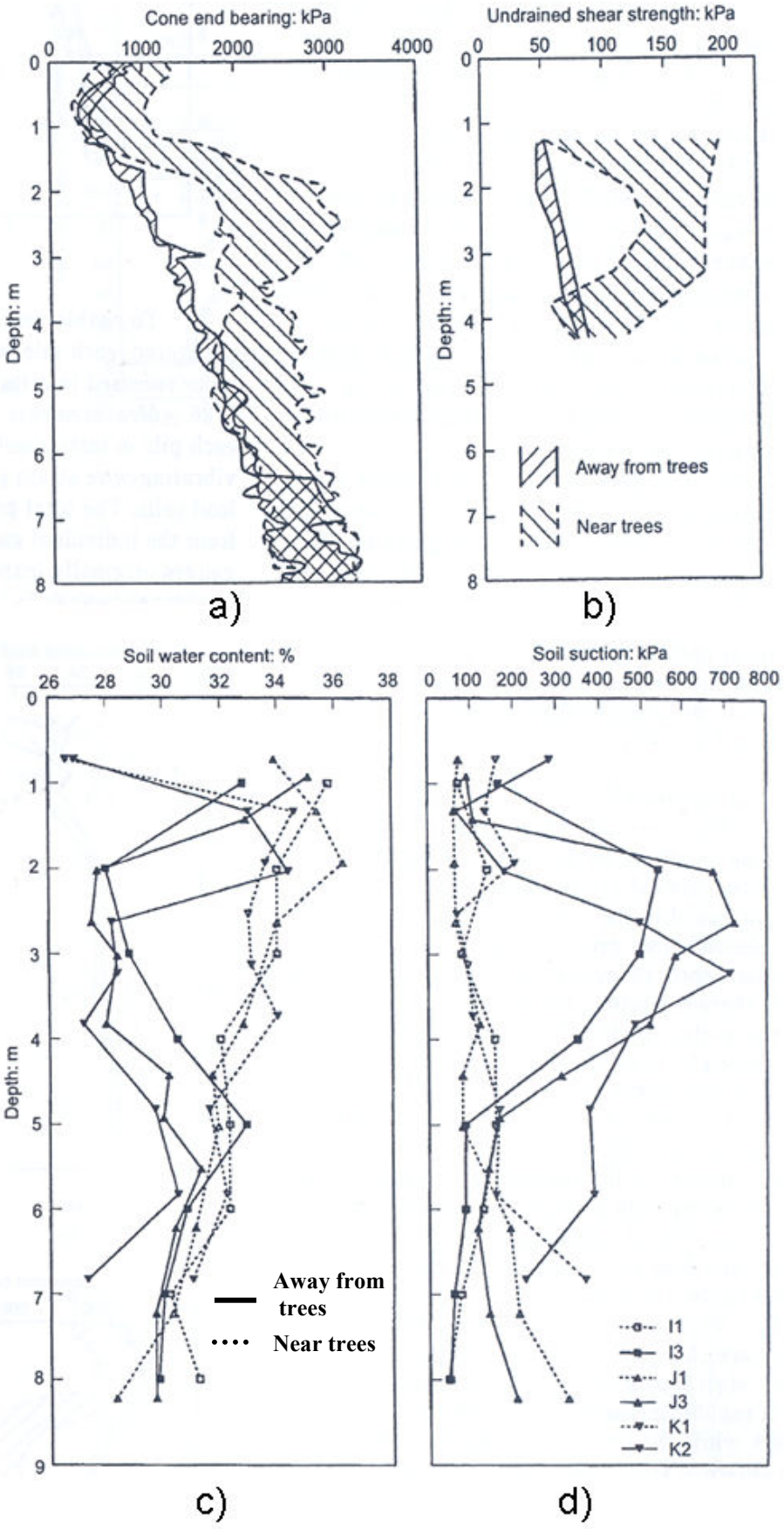


Figure 2-25: Variation of soil properties with depth as affected by trees; a) cone end bearing, b) undrained shear strength, c) water content, d) suction (Crilly & Driscoll, 2000)

3 Sampling, Apparatus and Procedures

3.1 Introduction

For the current project high quality block and rotary core samples were retrieved from three different sites for tests using oedometer and triaxial apparatuses on natural and reconstituted samples. In this chapter the sampling methods will be explained, the apparatus introduced and the testing procedures described.

3.2 Sampling

Different methods of sampling were carried out at the various sites and on different soils. Block samples were retrieved for Oxford clay and Gault clay and rotary core samples for Kimmeridge clay and Gault clay (the two types of sampling for the Gault clay were at the same site).

3.2.1 Site selection

The sampling sites for the three soils are shown in Figure 3-1. The main criterion for the site selection was if the site was representative of the material for that formation. This would allow the research to be comparable with other works studying the same material but at different locations. The Midlands Platform and the East Midlands Shelf were the main focus for sampling as they were least affected by tectonic activity.

It was also important to find sites which had been studied previously for research or where commercial site investigation data was available. Finally the availability of the sites played an important role. Oxford clay samples were taken from an excavation in Elstow, south of Bedford, Gault clay samples from High Cross, west of Cambridge and Kimmeridge clay samples were taken from Willow Brook Farm, south west of Abingdon. A CPT truck was also brought to each site to provide in-situ testing information for the research. Each of these sites is described individually in the chapter concerning each soil (Chapters 4 to 6).

3.2.2 Block sampling

The project started with block sampling of Oxford clay in September 2007. Seven blocks were retrieved from the base of a pond excavation at Elstow. The pond was approximately 120 m wide, 210 m long and 10 m deep (Figure 3-2). The excavation for the pond had been carried out six months prior to sampling. The excavation was carried out in three stages with flooding after the first stage, followed finally by drainage of the water. A simplified 1-D consolidation analysis of the sampling location indicated that conditions at the sampling depth had remained essentially undrained over the excavation period (Brosse, 2008).

The sampling procedure is illustrated in Figure 3-3. A mechanical digger was used to excavate a 70 cm deep trench and a mechanical clay spade was employed to cut columns of soil from the sides of the trench (Figure 3-3a). Each of these columns was 50 x 50 cm in size. From this point a sharp spade was used to hand trim the sample down to the required 30 x 30 cm size (Figure 3-3b). The block of soil was then covered with three layers of cling film and wax to prevent the sample drying from its in-situ water content (Figure 3-3c). The blocks were covered with wooden boxes open at two ends and the space between the soil and the box was filled with expanding polyurethane foam. The top side of the sample was also covered with expanding foam before being closed with the wooden box top (Figure 3-3d). The samples were then left overnight to allow the foam to harden. The day after, the underside of the samples were detached from the ground using a clay spade. The box was turned over and the open surface was closed after it was trimmed, and covered with the layers of cling film, wax and the expanding foam. The final dimensions of the samples were 30 x 30 x 30 cm. All of the samples were labelled accurately. During the site operation, some attempts to cut block samples failed due to the weakness of the material along fissures and bedding planes (Figure 3-4).

The block sampling for Gault clay was carried out in July 2008 at High Cross, Cambridge. A three metre deep trench was excavated by a mechanical excavator (Figure 3-5) and block samples were retrieved from the sides of the trench. The same procedure of sampling described above for Oxford clay was carried out for the Gault clay.

3.2.3 Rotary coring

After testing had started in the laboratory on the block samples of Gault clay two observations were made; firstly, the clay's dry and desiccated nature which was believed to be related to the frequent presence of tree roots (Figure 3-6) and secondly the weathered nature of the samples. To avoid these two issues and also to provide a comparable sample depth to the Oxford clay samples (10 m below ground level), rotary core sampling was carried out in July 2009 on the same site. Two boreholes were drilled to 13 m below ground level using a Geobore 'S' wireline system with a natural polymer based drilling fluid. Nominally 100 mm diameter samples were brought up to the surface and the outer layer of softened soil of approximately 2 mm was removed to avoid excessive swelling. This outer layer of the soil was highly swelled as it was in contact with the drilling fluid. After the logging was completed, samples of approximately 25 cm in length were cut and preserved with three layers of cling film and wax. As noted by Butcher & Powell (1995) the fissure spacing reduces with depth in Gault clay. The highly fissured nature of the soil noted in samples at about 10 m depth led to a significant effect of the sampling method. This was due to the opening of the fissures and some loss of the drilling fluid. Therefore samples retrieved using this method of sampling swelled to some extent and lost some of their in-situ structure. Further details of the soil behaviour and a comparison of the two types of sampling will be covered in the subsequent chapter on Gault clay (Chapter 5).

In July 2009 Geobore rotary coring was also carried out for the Kimmeridge clay at Willow Brook Farm, south west of Abingdon. This was done to avoid a weathered zone close to the surface (that have been observed from the CPT profile) and also to retrieve samples again from depths of around 10 m. The same procedures of drilling and preservation described above for the Gault clay were carried out on samples retrieved from two 14 m deep boreholes. In comparison with the Gault clay the samples were of better quality at all depths due to a lower frequency of fissuring in the Kimmeridge clay.

3.3 Apparatus

3.3.1 Introduction

Five stress path triaxial cells and three oedometer cells were used for the laboratory testing. These apparatuses will be introduced in the next two sections.

3.3.2 Oedometer apparatus

The oedometer apparatus was used to study the one-dimensional compression and swelling behaviour of the soils. The rigid boundary at the sides of the specimen restricts the lateral movements and hence the strains are only in the vertical direction. Drainage can be from the bottom or the top of the sample only or from both ends at the same time. After each loading increment full consolidation should have been reached; this is ensured by monitoring the displacement.

The oedometer apparatuses available in the Imperial College soil laboratory are shown in Figures 3.7 and 3.8. The soil specimen is placed in a rigid stainless steel ring and then fitted in a lateral restraint frame which is tightened to the base of the apparatus. Porous stones and filter papers were placed on the bottom and top of the specimen. This configuration is enclosed in a cylindrical perspex water bath which is filled with water to avoid drying of the soil during the tests. The load from the weights on the lever arm is transmitted to the sample top platen through a loading yoke. The lever arm ratio of the apparatus available was 1: 11.04. The possible sample sizes for these apparatuses were 38 mm or 50 mm in diameter and 18 mm in height. The lower the ratio of height to diameter the smaller the effects of friction. A maximum vertical stress of about 30 MPa could be reached using a 38 mm sample in the highest pressure apparatus. The only difference between this apparatus and other apparatuses was in the loading capacity which enabled more loads to be applied in the former case. A displacement transducer was used to measure the settlement and a computer logging system was used to scan and record data. The volumetric stain (ε_v) was calculated directly from the vertical displacement (δ) considering zero lateral movement:

$$\varepsilon_v = \varepsilon_a = \frac{\delta}{H_0} \qquad \text{(Equation 3-1)}$$

where ε_a is the axial strain and H_0 is the initial height of the sample.

3.3.3 Triaxial apparatus

The triaxial apparatus is used extensively in soil mechanics research, providing a good control and measurement of stresses and strains. However there are limitations to the stress regimes this apparatus can reach; the rotation of the principal stress axes and control over the intermediate principal stress, σ_2, are two elements which cannot be studied. In the current project two 100 mm and two 38 mm diameter sample size cells were used at conventional engineering stress levels (<800 kPa) as well as one 50 mm diameter sample size high pressure triaxial cell. Each will be introduced in the following pages with an emphasis on their respective special features. A summary of all the instrumentation is presented in Table 3-1.

100 mm diameter sample size triaxial cell

The typical configuration for the 38 mm diameter sample hydraulic triaxial cell (designed by Bishop & Wesley 1975) is shown in Figure 3-9. The principal elements of the 100 mm diameter sample cells are the same. A cylindrical sample 100 mm diameter and 200 mm in height is placed on the pedestal in the centre of the cell. The height to diameter ratio of two is used to ensure the strain and stress uniformity in the centre of the sample. The cell is filled with water which is put under pressure to control the radial stress, σ_r. The base of the sample is connected to an Imperial College volume gauge that monitored the drainage of the sample under an applied back pressure to the sample.

The top of the sample was connected to an Applied Measurements load cell that measured the deviatoric load, F_a, which was applied to the sample by the moving base piston. A suction cap was used for the load cell connection to align the sample. This also enabled extension stress paths to be carried out. A rubber cap and a half ball on the sample were used in addition to a conical extension on the load cell.

An air pressure supply of up to 800 kPa was provided by a central compressor that powered hydraulic pressures in the cell pressure, the ram pressure and the back pressure through air-water or air-oil interfaces. The pressures were managed using three stepper motors with air pressure valves controlled by the computer. The base piston was connected to an air-oil interface instead of an air-water interface to gain a better control of the stress changes. For the axial strain controlled tests, a constant rate of strain pump (CRSP) was used. This pump was connected to the ram pressure interface and transferred to the base ram the volume of fluid generated by a definite displacement of the pump.

The cell and back pressures were measured with Druck semiconductor pressure transducers, the volumetric strain by a linear displacement gauge connected to the volume gauge and the axial displacement by similar device connected to the base piston. The load cell and pressure transducers were calibrated against a Budenberg dead-weight tester. The volume gauge was calibrated by measuring the volume of water entering the gauge using a Bishop ram under 200 kPa of constant pressure. The Bishop ram had a calibrated volume change of 0.8 cc per revolution. This method was preferred to empting the volume gauge and measuring the volume of water, as this was done with an atmospheric pressure and not at the normal pressures which would be used during the testing. The linear displacement gauge was calibrated using a micrometer. The cells were also equipped with a thermometer to check the internal temperature of the cell.

The output signals of all the transducers were automatically data logged using a data acquisition system connected to a PC. The software used to monitor and control the applied pressures was Triax-Version 5.1.7, developed originally at Imperial College and upgraded subsequently at Durham University. The software allows the experiments to be controlled with different stages, minimising the interference of the operator.

In addition to the above, there were some transducers locally mounted on the sample; axial and radial LVDTs, a mid-height pore pressure probe and bender elements.

a) Axial and radial LVDTs

Following the system proposed Cuccovillo & Coop (1997), two axial and one radial LVDT were placed directly on the sample to resolve very small strains within a linear range of 10mm. The movement of the armature within the transducer's body generates an electrical voltage which is recorded by the data logger. The best resolution could be reached when the LVDTs were at their electrical zero, which was about 2 x 10^{-5} mm. An LVDT was also placed in a radial belt which was mounted on the sample to resolve the radial displacements (Figure 3-10). During this research, different designs of the radial belt were used to check the efficiency of the measurements. However, none of the designs seemed to be satisfactory as in all cases the armature could become stuck under its own weight in the transducer. This was crucial when measurements of very small strains were required. A new set-up to measure the radial displacements was engineered and will be introduced in the section later in this chapter concerning the 38 mm sample size triaxial cell. All these LVDTs were calibrated using a micrometer.

b) Mid-height probe

Use was made of the piezometer probe described by Hight (1982), and shown in Figure 3-11. The mid-height probe was placed in a hole made in the membrane and was sealed by O-rings and liquid latex which was left to harden. A layer of soft kaolin was placed between the soil and the probe to reduce the risk of cavitation due to high suction within the sample. This probe was used to measure pore water pressure at the mid-height of the sample, and was checked against the pore pressure at the base of the sample, measured by the pore/back pressure transducer, as a measure of consolidation. The mid-height probe responded faster to stress changes than to the base pore pressure transducer. Gasparre (2005) suggested that a difference between the base and the mid-height pore water pressure of less than 5% of the current p' is an acceptable condition during drained tests. The mid-height probe was calibrated in the filled cell against the base pore pressure transducer under varying cell pressures.

c) Bender elements

Bender elements are piezoceramic plates that are sensitive to strains normal to their plane and are capable of measuring a shear wave velocity through the soil and consequently measuring G_{max}. Although it is difficult to define the exact strains they produce, the maximum shear strain involved in bender element testing is believed to be very small and within the elastic linear range of the soil (Dyvik & Madshus, 1985; Kuwano & Jardine, 2002). There is a transmitter element and a receiver element. Each element is comprised of two electrodes that can have the same polarity (parallel type) or opposite polarity (series type). The parallel type generates twice the displacement for the same voltage and therefore it is recommended they are used as a transmitter element, while the series type is used as a more sensitive receiver (Lee & Santamarina, 2005; Leong et al., 2009).

Different types of electrical pulse can be sent to the transmitter using a function generator. Jovicic et al. (1996) argued that using a square pulse complicates the interpretation of the signals as it is composed of a spectrum of different frequencies. In this research a single sine pulse was used with frequencies between 3 to 15 kHz. These frequencies were believed to be appropriate for the interpretation of the signals received in stiff clays. The sine pulse triggers the transmitter element to vibrate perpendicularly to its face generating a shear wave. When the wave reaches the receiver element it makes it vibrates creating an electrical pulse which is captured by a digital oscilloscope. The distance which the wave travels is defined by that between the element tips, L (Viggiani & Atkinson 1995). By knowing the travel time of the wave, t_{arr}, its velocity, v_s, can be calculated. The shear modulus of the soil, G_{max}, is related to shear wave velocity and the density of the soil, ρ, through Equations 3-2 and 3-3:

$$v_s = \frac{L}{t_{arr}} \qquad \text{(Equation 3-2)}$$

$$G_{\max} = \rho . v_s^{\,2} \qquad \text{(Equation 3-3)}$$

The major concern regarding bender elements is how to estimate a reliable travel time, t_{arr} . The issues related to the interpretation of the signals to achieve t_{arr} will be explained in Section 3.5.6. Figure 3-12 shows different arrangements that are possible for bender elements on triaxial samples. The lateral bender elements available in the current research can be seen in Figure 3-13. In the 100mm cells two bender elements installed to measure the v_{hv} shear wave velocities (wave propagation in the horizontal plane and a wave polarisation in the vertical plane) and the v_{hh} velocities (wave propagation and polarisation both in the horizontal plane) were used. These elements were placed within holes made in the membrane at the mid-height of the sample and sealed with O-rings and liquid latex.

38 mm sample size triaxial cell

These two cells were initially intended only for use with reconstituted samples, but because of the issues regarding drainage (Section 3.4.2) they were equipped with high resolution transducers and applied to test natural samples. The two 38 mm sample size apparatuses were also Bishop & Wesley (1975) hydraulic triaxial cells. They differed with the 100 mm sample size cells in their ram interface which was a air-water interface and in the new radial displacement set-up.

The new radial displacement set-up is shown in Figures 3-14 and 3-15. The design was carried out by Mr Ackerley, research technician at Imperial College, and was tested by the author under a variety of conditions. The main principle behind the design was to make sure that the LVDTs could stand vertically, avoiding the friction between the armature and inner walls of the transducer stopping smallest movements. For this purpose at least two transducers were required to measure the displacements in diametrically opposite positions on the sample and the total displacement was calculated using the sum of each individual displacement.

An adjusting rod connected to the base pedestal comprised of three pieces and was utilised to hold the LVDTs vertically by the sample. To allow the horizontal displacement to be transformed into a vertical one an ‘L’ shaped rotating arm with equal arm lengths was used. A very low friction pin at the hinge facilitated the

rotation with no significant restraint. To maintain contact small dead weights were connected to the bottoms of the armatures and placed on the rotating arm. An example of the radial strains recovered during a probe, using the radial belt and the new set-up is shown in Figure 3-16. As discussed earlier the main drawback of using the radial belt was the sticking of the armature within the LVDT. This can be seen in Figure 3-16 in the loading stage and more significantly in the unloading stage with no movements being resolved. It can be seen using the new set-up enabled the displacements to be resolved both in loading and unloading.

High pressure triaxial cell

The high pressure apparatus with a cell pressure capacity of 5 MPa and sample size of 50 mm was used for a number of tests on each of the soils (Figure 3-17). The apparatus was designed at City University and an earlier version is described in Cuccovillo & Coop (1997). The outer cell was made of a 12.5 mm thick steel tube in order to sustain the high pressures. To allow standard non-immersible LVDTs to be used, the cell liquid had to be non-conductive and therefore silicone oil was used instead of water for this purpose. Cell and ram air-oil interfaces were used for pressures up to 800 kPa. A Constant Rate of Strain Pump (CRSP) was connected to the cell interface and was used to reach higher cell pressures. To reach higher ram pressures a pressure multiplier was used. The multiplier was connected to the ram interface from the bottom and with different ratios of the Bellofram it was able to multiply the pressure by 2.25 times. An Imperial College volume gauge was also connected to the base of the sample and could reach a maximum of 800 kPa.

The cell was equipped with internal axial and radial LVDTs and top and bottom mounted bender elements. This bender element arrangement enabled the measurement of shear wave velocity v_{vh} (wave propagation in the vertical plane and a wave polarisation in the horizontal plane). The original control program was written by Professor Coop at City University but half way through the research it was substituted with Triax-Version 5.1.7.

3.4 Testing procedures

3.4.1 Sample preparation

Natural oedometer samples

The oedometer samples were cut manually with a knife while pushing a rigid ring into the soil block minimising sample disturbance by cutting very slightly ahead of the approaching cutting edge of the ring. They were either 38mm or 50mm in diameter and 18mm in height. Filter papers were placed on both ends to prevent the porous stones being clogged by soil particles. The base and top porous stones were de-aired by placing them in water under a vacuum. Six water content measurements were taken during the trimming to find out the initial void ratio of the soil.

Reconstituted oedometer samples

Most of the reconstituted oedometer tests were carried out by MSc students under the author's supervision (Gao, 2009; Moran, 2010). The samples were remoulded at water contents 1.25 times their Liquid Limit following Burland (1990). In some cases the samples were remoulded to a water content varying between one times the liquid limit and one and a half times the liquid limit. This exercise was to study the effects of initial water content on the position and slope of the intrinsic Normal Compression Line, and generally examining the potential transitional behaviour of these clays.

Natural triaxial samples

Trimming the soil samples, from a block, to the required cylindrical shape and size was a tedious procedure due to the stiff nature of these materials. Ideally trimming should have been rapid to stop the sample from drying while causing minimum disturbance. Drying of the sample allowed fissures to open up potentially resulting in the sample falling apart. However the fissures re-closed under the initial pressure in the cell and so did not alter the specimen strength. Drying also changes the moisture content of the specimen, and its suction. The suction in the soil was measured under an initial isotropic total stress as a means of determining the in-situ stress conditions; drying would have changed this value.

Prior to testing, each block sample was cut into quarters using an electric saw for the wooden part of the box and a band saw for the soil. The three quarters which were not going to be tested immediately were waxed and preserved. The quarter which was going to be used was cut into a cylindrical shape with a diameter of about 110 mm and a height of about 220 mm, using the band saw. The band saw accelerated this procedure and did not noticeably disturb the sample (Figure 3-18). The cylinder was then trimmed using a blade in a soil lathe to the final size of 98mm in diameter and the ends were trimmed using a cradle to reach a 180mm in height. The soil lathe and trimming equipment are shown in Figure 3-19. Damp towels were placed around the lathe to keep the environment moist and keep drying to a minimum level. Six water content measurements were taken from the sides and ends of the specimen and during different stages of trimming. With experience the time for the trimming was reduced from couple of hours to 30 minutes.

Trimming procedure for the smaller 50mm and 38mm samples was essentially the same, although a longer time was needed. Noting the smaller volume to surface area ratio of the smaller samples, these were more prone to drying and suction change than the larger specimens.

Trimming was easier and faster for the rotary core samples as they were already formed into approximate cylinder of around 100 mm in diameter. Only a thin layer of around 1mm needed to be trimmed off to leave a uniform specimen diameter from the top to the bottom. The ends were trimmed easily and samples could be prepared within 10 minutes.

After trimming was finished the soil specimen was weighed and its dimensions were measured. Because the suction in the sample was high, if it came to a direct contact with the base pedestal of the cell would probably have cavitated the back pressure system. Samples were kept on the bench while being covered with filter papers and membrane. Filter papers were placed on the sides and the ends of the specimen to accelerate drainage. A top cap was then placed on the sample and the whole specimen was covered with a latex membrane. Three nozzles were prepared on the membrane for the mid-height probe and the bender elements. Bender elements, mid-height probe and radial belt were attached to the sample at this stage. For the bender elements it

was necessary to cut cross-shaped slots in the soil with a small screwdriver and to fill them with reconstituted soil before pushing the bender elements into the soil. This allowed the bender elements to be placed natural in the soil without being broken. The mid-height probe was also placed in a nozzle. To avoid cavitation of the probe a layer of wet kaolin was placed on its face so that it did not make a direct contact with the soil. These three nozzles were closed with O-rings and layers of liquid latex.

When the sample was ready it was placed on a solder wire spacing system that made a gap between the soil and the porous stone. The base porous stone was de-aired by immersing it in water and applying a vacuum with a pump. The mount for the axial LVDTs were then attached to the side of the sample with a few drops of super glue. Finally the membrane was sealed with O-rings at the top and the bottom. A soil specimen with all the transducers attached is shown in Figure 3-20.

Reconstituted triaxial samples

As with the oedometer tests, the triaxial tests on the reconstituted material were mainly carried out by MSc students under the author's supervision. Two methods were used for the sample preparation; compressing slurry in a single 38 mm or 50 mm consolidometer and making a 'cake' in a 230 mm diameter consolidometer (Figures 3-21a and Figure 3-21b).

For the Oxford clay and Gault clay 230 mm of diameter cakes were made as there was ample material from trimming the block samples to make slurry samples for the big consolidometer. Soil was broken down by hand and knife into small pieces and then soaked in water for two days to make it softer. A mechanical mixer was then used to reach a smooth and consistent paste.

When the slurry was ready it was placed carefully in the consolidometer trying to avoid any air trapped in the sample. The sample was left for a day to consolidate under its own weight. After this point, the top cap was placed on the sample which was then loaded in stages to a maximum vertical effective stress of 50 kPa. After the sample was consolidated it was taken out of the consolidometer and was cut into smaller blocks of around 50 x 50 x 100 mm. Each of these blocks was then waxed and preserved for further testing. Prior to testing these blocks were trimmed easily to the

required 38 mm or 50 mm diameter triaxial samples again using the soil lathe and cradle.

In the case of the Kimmeridge clay, there was not enough material left from the rotary core samples to make a 230 mm of diameter 'cake'. Therefore small consolidometers (38 mm and 50 mm in diameter) were used. The slurry was made by adding water to the soil and manually mixing it, the slurry was placed in the consolidometer trying to avoid any air trapped in the sample. The disadvantage of using these small consolidometers is the non-uniformity of the water content within the sample which is caused by the side friction within the tube. In most cases the 50 mm consolidometer was used to minimise the disturbance caused by the friction. The side friction was also reduced by the floating ring design. After the sample was consolidated to a vertical effective stress of 50 kPa it was extruded carefully and its sides were trimmed to provide a 38 mm diameter sample. The sample was placed within the cell and internal instruments were attached to it in a similar manner as for the natural samples.

3.4.2 Testing procedures

Natural oedometer samples

Some of the tests described herein were carried out by MSc student (Moran, 2010) under the author's supervision. Compliance test was carried out on the oedometer cells used in this research and the results were taken into consideration when analysing the tests carried out on the soil samples.

Natural samples from different depths were tested to investigate each site's geotechnical profile. After placement in the oedometer the samples were loaded to an estimate of its in-situ vertical effective stress after which the water bath was filled with water. It is important not to fill the bath before loading as it would cause unwanted swelling. The samples were compressed to maximum stress levels of between 8 MPa and 28 MPa. Then they were swelled back to their initial stress, and in some cases they were unloaded to lower stresses or swelled and compressed more than once. During the test the vertical displacement was measured either with a conventional dial gauge or with a displacement transducer.

At the end of each loading test, the water bath was emptied (with the sample still under load) and area surrounding the sample was dried to avoid any unwanted swelling during sample retrieval. The sample was then unloaded and removed from the apparatus as quickly as possible and the final water content was measured.

Reconstituted oedometer samples

The procedure for the reconstituted samples was the same as for the natural samples, the only difference being their initial and final loading levels. The tests were started with small vertical effective stresses (around 10 kPa) and the compression stages did not exceed 10 MPa vertical effective stress.

Natural triaxial samples

Before starting any test the cell was filled with water and kept under 700 kPa pressure and the volume gauge under 200 kPa for at least 24 hours. The cell was emptied just before the test; this was done to ensure any air in the drainage system was dissolved. After the sample was located on the pedestal, the cell was closed and filled with deaired water. While the back pressure system was kept closed (undrained), a cell pressure of around 400kPa was applied to the sample. Assuming perfect sampling with zero change of p' (applicable for isotropic material only) the in-situ effective stress in the sample should be equal to the suction in the sample and consequently equal to the initial effective stress within the triaxial cell. The initial cell pressure (total stress) was chosen to be sufficient to generate a positive pore water pressure within the sample. The sample was then left for 24 hours to stabilize; this stabilisation was checked by convergence between the pore pressure response at the base and the mid-height of the sample. As mentioned earlier, the samples tended to dry to some extent during preparation and consequently their initial p' values could be higher than those estimated in-situ. This problem was counteracted in the rotary cored samples by potential swelling due to contact with drilling fluid. A number of suction measurements have also been made using a suction probe on samples before being tested.

At this stage, sample saturation was checked by increasing the cell pressure by 50 kPa and measuring the change in the pore pressure at the mid-height of the sample. The *B* value then was calculated from Equation 3-4:

$$B = \frac{\Delta u}{\Delta \sigma_r} \qquad \text{(Equation 3-4)}$$

A *B* value of 95% or more was considered to be sufficient to start the test. If the *B* value was lower then the degree of saturation was reached by opening the drainage to the volume gauge and applying back pressure. Such saturation stages were only required for the Gault clay block samples, the reason for which will be discussed in Chapter 5. After saturation the suction cap was used to connect the top platen to the axial loading system. To connect the sample and suction cap to the load cell the sample was brought in the vicinity of the load cell by increasing the ram pressure until the rubber cap covered the conical extension and closed the space between the two. The water within this space was removed using a Bishop ram while the sample was moved further upwards towards the load cell. This was done with great care so as to not generate any significant deviatoric loading on the sample. When the suction cap space was fully emptied of water the pressure inside the rubber was reduced to atmospheric pressure while the outer cell pressure was maintained. This difference in pressures ensures the connection remained firm. The suction cap connection was always carried out after the saturation stage and before the consolidation stage.

Three main testing exercises carried out in this research are shown schematically in Figure 3-22 and explained further below:

A) Undrained compression and extension from the in-situ stress state

The in-situ stress state was estimated for each soil by calculating the K_0 value based on the average initial p' in the triaxial cell or based on the suction measurements. A detailed explanation for each soil is covered in Chapters 4 to 6. The stress path which was chosen to reach the in-situ state involved isotropic consolidation or swelling to the in-situ p' (in case the initial p' for that particular test was away from the expected in-situ value). From that point the path progressed to an anisotropic in-situ state under

constant p'. Gasparre (2005) suggested limiting volumetric strain (ε_v) and axial (ε_a) strains to 1% and 0.5% respectively on the approach stress paths as a means to limit sample disturbance. These limits were applied over the anisotropic stress paths in this research; the isotropic path in some cases resulted in unavoidably larger strains (Chapter 5).

The stress change rates used for the consolidation stages on 100 mm diameter samples were 1 kPa/hr for Oxford clay and Gault clay and 0.5 kPa/hr for the Kimmeridge clay. The criterion applied to gauge whether consolidation was fully drained was to ensure that the difference between the mid-height pore water pressure and base pore water pressure was less than 5 % of the current p'. These consolidation rates were doubled for the 38 mm samples. Because no mid-height probe was used on the 38 mm samples, drainage checks for these tests involved stopping the consolidation after each 100 kPa of change and checking any remaining excess pore water pressure by closing the drainage valve or alternatively by letting the volumetric change stabilise and observing the degree of volumetric straining developed under constant stresses.

During the isotropic stress path stages bender element readings were taken at several effective stress levels. In some tests small strain probes were also carried out before starting the anisotropic stress path. After reaching the 'in-situ' state the sample was left under constant effective stresses until the axial strain creep rate was smaller than 5 x 10^{-5} (%/hr). In most tests small strain probes were carried out from this point and the sample was finally sheared to failure either in compression or in extension. The samples were taken to failure under strain control, at a rate of 0.02 %/hr for both 100 mm and 38 mm diameter samples.

B) Drained and undrained compression and extension from an isotropic state

To study the effects of stress level on the strength and stiffness of the soil, samples were consolidated isotropically to different stress levels. Bender element readings were again taken during the consolidation path.

In some cases the high pressure apparatus was used to reach greater stresses (up to 3 MPa). The rates of consolidation and shearing were similar to those of the stress paths

used to reach the in-situ stress state. In the only drained test carried out to failure the rate used for shearing was 0.002 %/hr; checks made using the mid-height probe showed that this ensured full drainage.

C) Drained and undrained probing

Static small strain probing tests were performed to obtain the drained elastic parameters combined with dynamic bender element measurements. These probes were performed under stress control in compression and in extension. Initially the 100 mm cells were assigned for the probing programme; however the degree of drainage could not be obtained satisfactorily within a time scale. Excess pore water pressures amounting to one tenth of the applied total stress change were considered as the limit to acceptable drainage. An example of the pore pressure change at the mid-height and base of a 100 mm diameter sample is shown in Figure 3-23. The slowest rate used for these probes was 0.3 kPa/ hr. Tests at slower rates were not practical as the effects of even small cell water temperature changes and sample creep became large and could overwhelm the results. As discussed earlier in Chapter 2, the undrained parameters cannot be converted to drained parameters and therefore undrained probes are not sufficient to define a full set of cross-anisotropic elastic parameters.

To overcome this problem, 38 mm diameter samples were tested with shorter drainage paths that facilitated the drainage. The main challenge in conducting these probes was measuring the radial displacements in order to calculate the Poisson's ratios and horizontal stiffness. As discussed earlier the conventional radial belt did not function well for very small displacements and a new set-up was required. With the new set-up drained probes were conducted on each soil at the in-situ stress state and the results are presented in Chapters 4 to 6.

One of the important issues affecting the small strain probes was the effect of temperature on the internal LVDT measurements and on the pore water pressure. Gasparre (2005) examined the effects of temperature on the transducers and concluded that the cyclic change of strains and pore water pressure was related to the soil behaviour rather than sensitivity of the transducers. She recommended the isolation of the cell by bubble wrap and aluminium foil to reduce the range of

temperature change. The laboratory in which all these tests were conducted was temperature controlled and the normal variation in temperature was about ±0.4 °C. For the 100 mm sample size cells, by isolating the cell this variation was reduced to about 0.1 °C for duration of the probing test. Sometimes due to technical problems the temperature control in the laboratory exceeded its usual limits and larger changes in temperature occurred. Figure 3-24 shows changes of strains due to changes in the temperature. The increase in temperature results in positive excess pore water pressure (Gasparre, 2005), and the contraction of the sample, although the transducers are also highly sensitive to the temperature and it is difficult to separate the effects. The temperature was monitored carefully and the probing tests were performed during the periods of minimal temperature change were chosen for probing.

The problems with temperature change were more severe with the 38 mm samples. The effects were amplified and made faster by their smaller volume. While these cells were isolated with even more layers of insulating wrap, it was still difficult to avoid the effects of temperature. Long waits and monitoring periods were required for these cells to find suitably stable periods of minimum temperature change. A typical example for a small strain axial probe on Oxford clay is shown in Figure 3-25.

Reconstituted triaxial samples

Tests performed on reconstituted samples were to study the effects of natural clay structure. All but two triaxial tests were carried out by MSc students (Gao, 2009; Moran, 2010) as part of their dissertation projects, all fully supervised by the author. Three tests for each soil were designed at OCR values of 1, 3 and 5. The samples were isotropically compressed at a rate of 5 kPa/hr with hold periods after each 100 kPa to assure full consolidation. The samples were sheared with similar rates to those of the natural samples. Bender elements were used for one test on each soil to obtain the G_0 parameters for the reconstituted material.

3.5 Analysis of the data

3.5.1 Introduction

The software used to control the tests, Triax, has in-built calculations for many of the variables required. However not all of the desirable corrections are considered in the equations it applies. Therefore the final calculations and data corrections were carried out separately and based on the raw data. The most important aspects of these will be presented below. It should be mentioned that no membrane correction was required because of the relatively high stress levels and the samples high stiffness.

3.5.2 Specific volume

Water content measurements were taken before and after each test and the dimensions and weights were also measured before each test. The initial specific volume, v_i, was calculated from the independent measurements as represented by the following four equations (assuming full saturation) and the average was used for the analysis:

$$v_i = G_s \frac{\gamma_w}{\gamma_d} \quad \text{(Equation 3-5)}$$

$$v_i = G_s w_i + 1 \quad \text{(Equation 3-6)}$$

$$v_i = \frac{G_s - 1}{\frac{\gamma}{\gamma_w} - 1} \quad \text{(Equation 3-7)}$$

$$v_i = \frac{G_s w_f + 1}{1 - \varepsilon_v} \quad \text{(Equation 3-8)}$$

where symbols in the above equations are:

γ, bulk unit weight

γ_w, unit weight of water

γ_d, dry unit weight

w_i and w_f, initial and final water content respectively

G_s, specific gravity

ε_v, the volumetric strain during the test including the saturation, the consolidation and the shearing stage.

It should be noted that the first three equations are only applicable for fully saturated samples. Shipton (2010) considered a difference of less than ± 0.01 to ± 0.02 between different methods to be satisfactory and proposed an alternative approach where larger differences were suspected to result from lack of saturation. Apart from the Gault clay block samples, all of the samples were well saturated and the above equations were suitable. In some oedometer tests, mainly on reconstituted material, the final water content was not very accurate and therefore the last equation did not match with the other three methods. This was probably caused by not retrieving the sample quickly enough and letting it swell in contact with residual water left in the cell despite drying. In these cases the anomalous value was not considered in the calculations.

At different stages of the test the current specific volume, $v_{current}$, was calculated using the volumetric strain, ε_v, and the initial specific volume, v_i :

$$v_{current} = v_i\left(1-\varepsilon_v\right) \qquad \text{(Equation 3-9)}$$

3.5.3 Area correction

Considering a right cylinder Bishop & Henkel (1957) proposed the following equation to achieve the current cross sectional area of the sample, A :

$$A = A_0 \frac{\left(1-\varepsilon_v\right)}{\left(1-\varepsilon_a\right)} \qquad \text{(Equation 3-10)}$$

where A_0 is the initial cross-sectional area of the sample and ε_v and ε_a are the volumetric (from volume gauge) and axial strains. This correction is applied to calculate representative deviatoric stress values.

For those samples which developed planar strain localisation, the post-localisation (reducing) areas were corrected applying Equation 3-11 (Chandler, 1966), based on two wedges sliding on a single shear plane. When more complicated localisation systems developed no further area correction was carried out, since it was considered more accurate to assume a constant area rather than reducing one (shear plane) or increasing one (right cylinder). An example of these complex shear plane formations is shown in Figure 3-26.

$$A = \frac{D_f^2}{2}\left[\frac{\pi}{2} - a\sin\left(\left(\frac{\Delta h - \Delta h_f}{D_f}\right)\cot\alpha\right)\right] - \left(\Delta h - \Delta h_f\right)\cot\alpha\sqrt{\frac{D_f^2}{4} - \frac{\left(\Delta h - \Delta h_f\right)^2\left(\cot\alpha\right)^2}{4}}$$

(Equation 3-11)

where D_f is the diameter of the sample at the time of shear plane formation, h_f is the sample height at the time of the shear plane formation, Δh is the axial displacement and α is the angle of the shear plane to the horizontal, which was measured after each test.

3.5.4 Volumetric and shear strains

The volumetric and shear strains were used to calculate the shear modulus, G, and effective stress bulk modulus, K'. The volumetric strain was calculated directly from water entering or leaving the volume gauge, ΔV, using the following equation:

$$\varepsilon_v = \frac{\Delta V}{V_0} \qquad \text{(Equation 3-12)}$$

in which V_0 is the initial volume. The volumetric strain could also be calculated indirectly using the local instrumentation, from:

$$\varepsilon_v = \varepsilon_a + 2\varepsilon_r - \varepsilon_r{}^2(1 - \varepsilon_a + 2\frac{\varepsilon_a}{\varepsilon_r}) \qquad \text{(Equation 3-13)}$$

where ε_a and ε_r are the axial and radial strains respectively. There was always very good agreement between the values obtained from the two equations at smaller to

intermediate strains. However for the small strains the second approach was used, resulting in a higher accuracy.

The shear strain invariant, ε_s, was calculated from:

$$\varepsilon_s = \frac{2}{3}(\varepsilon_a - \varepsilon_r) \qquad \text{(Equation 3-14)}$$

3.5.5 Small strain drained elastic parameters

As discussed earlier the compliance matrix can be simplified to (Equation 2-10) with only five parameters. Axial probe (constant radial stress) allows two of these parameters to be directly measured using the following equations:

$$E_v = \left(\frac{\delta\sigma'_v}{\delta\varepsilon_v}\right)_{\delta\sigma_r=0} \qquad \text{(Equation 3-15)}$$

$$\nu_{vh} = -\left(\frac{\delta\varepsilon_h}{\delta\varepsilon_v}\right)_{\delta\sigma_r=0} \qquad \text{(Equation 3-16)}$$

The radial probe (constant axial stress) results in the following equations:

$$\frac{E_h}{(1-\nu_{hh})} = \left(\frac{\delta\sigma'_h}{\delta\varepsilon_h}\right)_{\delta\sigma_a=0} \qquad \text{(Equation 3-17)}$$

$$\frac{2\upsilon_{hv}}{(1-\nu_{hh})} = -\left(\frac{\delta\varepsilon_v}{\delta\varepsilon_h}\right)_{\delta\sigma_a=0} \qquad \text{(Equation 3-18)}$$

By using a simplifying parameter F_h where:

$$F_h = \frac{E_h}{(1-\nu_{hh})} \qquad \text{(Equation 3-19)}$$

and considering (Equation 2-5) for G_{hh}; E_h and ν_{hh} can be obtained from the following equations:

$$E_h = \frac{4F_h G_{hh}}{F_h + 2G_{hh}} \quad \text{(Equation 3-20)}$$

$$\nu_{hh} = \frac{F_h - 2G_{hh}}{F_h + 2G_{hh}} \quad \text{(Equation 3-21)}$$

As mentioned in Section 2.4, the elastic parameters can also be presented in terms of G', K', J'. These parameters can be measured directly by carrying out constant p' and constant q probes. In the constant p' probe, G' (shear modulus) and J'_{qp} (coupling modulus linking changes in deviator stress and changes in volumetric strain) can be evaluated from:

$$G' = \frac{1}{3}\left(\frac{\delta q}{\delta \varepsilon_s}\right)_{\delta p'=0} \quad \text{(Equation 3-22)}$$

$$J'_{qp} = \left(\frac{\delta q}{\delta \varepsilon_v}\right)_{\delta p'=0} \quad \text{(Equation 3-23)}$$

And constant q probe results in K' (bulk modulus) and J'_{pq} (coupling modulus linking changes in mean effective stress and changes in shear strain) through:

$$K' = \frac{1}{3}\left(\frac{\delta p'}{\delta \varepsilon_v}\right)_{\delta q=0} \quad \text{(Equation 3-24)}$$

$$J'_{pq} = \left(\frac{\delta p'}{\delta \varepsilon_s}\right)_{\delta q=0} \quad \text{(Equation 3-25)}$$

The values for G', K', J' can also be evaluated using the parameters obtained from the axial and radial probes using the following equations:

$$G' = \frac{3E_v F_h}{4F_h + 8\nu_{vh} F_h + 2E_v} \quad \text{(Equation 3-26)}$$

$$K' = \frac{E_v F_h}{F_h - 4\nu_{vh} F_h + 2E_v} \quad \text{(Equation 3-27)}$$

$$J' = \frac{3E_v F_h}{2F_h - 2\nu_{vh} F_h - 2E_v} \quad \text{(Equation 3-28)}$$

And equations to map the drained parameters to the undrained ones are:

$$E_v^u = \frac{E_v^{'}\left[2(1-\nu'_{hh})E_v^{'} + (1-4\nu'_{vh})E_h^{'}\right]}{2(1-\nu'_{hh})E_v^{'} - 4\nu'^{\,2}_{vh}\,E_h^{'}} \quad \text{(Equation 3-29)}$$

$$E_h^u = \frac{E_h^{'}\left[2(1-\nu'_{hh})E_v^{'\,2} + (1-4\nu'_{vh})E_v^{'}E_h^{'}\right]}{\left(1-\nu'^{\,2}_{hh}\right)E_v^{'\,2} + (1-2\nu'_{vh}-2\nu'_{vh}\nu'_{hh})E_v^{'}E_h^{'} - \nu'^{\,2}_{vh}\,E_h^{'\,2}} \quad \text{(Equation 3-30)}$$

3.5.6 Shear plane analysis

To obtain the post-rupture angle of shearing resistance applying to a planar shear surface the stresses on the shear plane should be known. Mohr's circle analyses were carried out to calculate these stresses. The Mohr's circle was drawn from the principal effective stresses for the average plane orientation obtained at post-rupture state. Post-rupture points are shown on stress-strain curves of natural samples. A line with the angle of the shear plane was drawn from the pole and its intersection with the circle represents the stresses on the shear plane. A line joining this point and the origin of the Cartesian system gives the post-rupture envelope (Figure 3-27).

3.5.7 Bender element analysis

As mentioned earlier in Section 3.3.3 the main issue regarding bender element analysis is to obtain a reliable travel time for the shear wave. The difficulty in picking this quantity arises from the highly dispersed nature of the received signal. Dispersion

in the received signal results from the complex interactions between the bender elements and the soil specimen. Greening & Nash (2004) mentioned some of the factors which cause the dispersion: the presence of the specimen boundary, the frequency dependence of the material constitutive parameters, wave scattering due to material inhomogeneity and the dissipation of wave energy into heat. Arulnathan et al. (1998) highlighted the effects of refracted and reflected waves from the rigid boundaries on the received signal. They also noted that there can be a significant error in the interpretation due to a phase lag between the input electrical signal and the physical wave generated from the transmitter. Other researchers emphasised the frequency dependency of the system and the presence of multiple modes of vibration (Blewett et al., 2000; Alvarado & Coop, 2011).

One of the main dispersive effects that obscure the arrival of the shear wave is the near field effect (Sanchez-Salinero et al., 1986). The near field effect is usually thought to be the cause of the initial drop in the received signal due to a wave with an opposite polarity to the input signal. The arrival of a shear wave component with the velocity of the compression wave, and the arrival of refracted compression waves or interaction of pulse components close to the source can be considered as possible causes (Blewett et al., 2000; Alvarado & Coop, 2011). The near field effect can be minimised by optimising the wavelength over bender element length ratio and the travel distance to the wave length ratio (Arulnathan et al., 1998; Jovicic et al., 1996). Jovicic et al. (1996) noted that the effect of shear wave velocity on the near field dispersion varies depending on the soil stiffness. They suggested that a distorted input signal or forced oscillation can help to overcome the problem caused by the near field effect in estimating the travel time.

Two major interpretation strategies have been applied to bender element testing: time domain and frequency domain. Both methods were considered in this research and the results compared. The time domain approach simply required the visual determination of the arrival time. Different geometrical features in the received signal have been considered in finding the arrival time: the first rise of the received signal, the first change of curvature on the received signal, the first peak of the received signal and the time difference between the peaks on the transmitted and received signals (Figure 3-28). Some authors considered multiple wave reflections and the time difference

between the first arriving and the second arriving signals (Arulnathan et al., 1998; Lee & Santamarina, 2005). If considering an ideal received signal with no dispersion the first rise of the output corresponds to the arrival time, and this point was used in this research. As mentioned earlier, sine signals with frequencies between 3 and 15 kHz were adopted. The input signal frequency which results in the strongest response is that which results in resonance of the bender-soil system (Alvarado, 2007; Jovicic & Vilhar, 2009). Performing tests with a range of frequencies enables the sharpest response to be chosen for the analysis. In most cases the strongest response was observed with an input frequency of around 6 kHz.

In the second approach the input and output signals are transformed and manipulated from the time domain to the frequency domain. The transformation is normally carried out using a fast Fourier transform (FFT) algorithm. The phase shift between the input and output waves is calculated and the arrival time was obtained using the slope of this phase shift against frequency from the following equation:

$$t_{arr} = \frac{1}{2\pi}\frac{d\phi}{df} \qquad \text{(Equation 3-31)}$$

where ϕ is the phase shift and f is the frequency (Figures 3-29 and 3-30). Blewett et al. (2000) showed that due to dispersion in the output signal the relationship between the phase and frequency is non-linear. Therefore the arrival time calculated from the linear plotting method can induce some error.

In the current research the two methods were in good agreement for most cases. Typical signals are shown in Figure 3-29 and 3-30 where the arrival time from frequency domain and the first rise in the output signal are almost identical. However when the values were different (in which cases the frequency domain always resulted in longer times) the time domain values were selected to keep consistency with the other signals. Typical signals for each soil will be presented in later chapters (Chapters 4 to 6).

Transducer	Capacity	Resolution	Accuracy
Pressure transducer	1700 kPa	0.03 kPa	± 0.3 kPa
Mid-height probe	1000 kPa	0.01 kPa	± 0.2 kPa
Load cell	4 kN	0.2 N	± 0.25 N
Imperial College volume gauge	50 and 100 cc	0.001 cc	± 0.4 cc
External LVDT	25 mm	2×10^{-4} mm	± 0.06 mm
Internal LVDT	± 5 mm	2×10^{-5} mm	± 0.035 mm

Table 3-1: summary of transducers used in this project

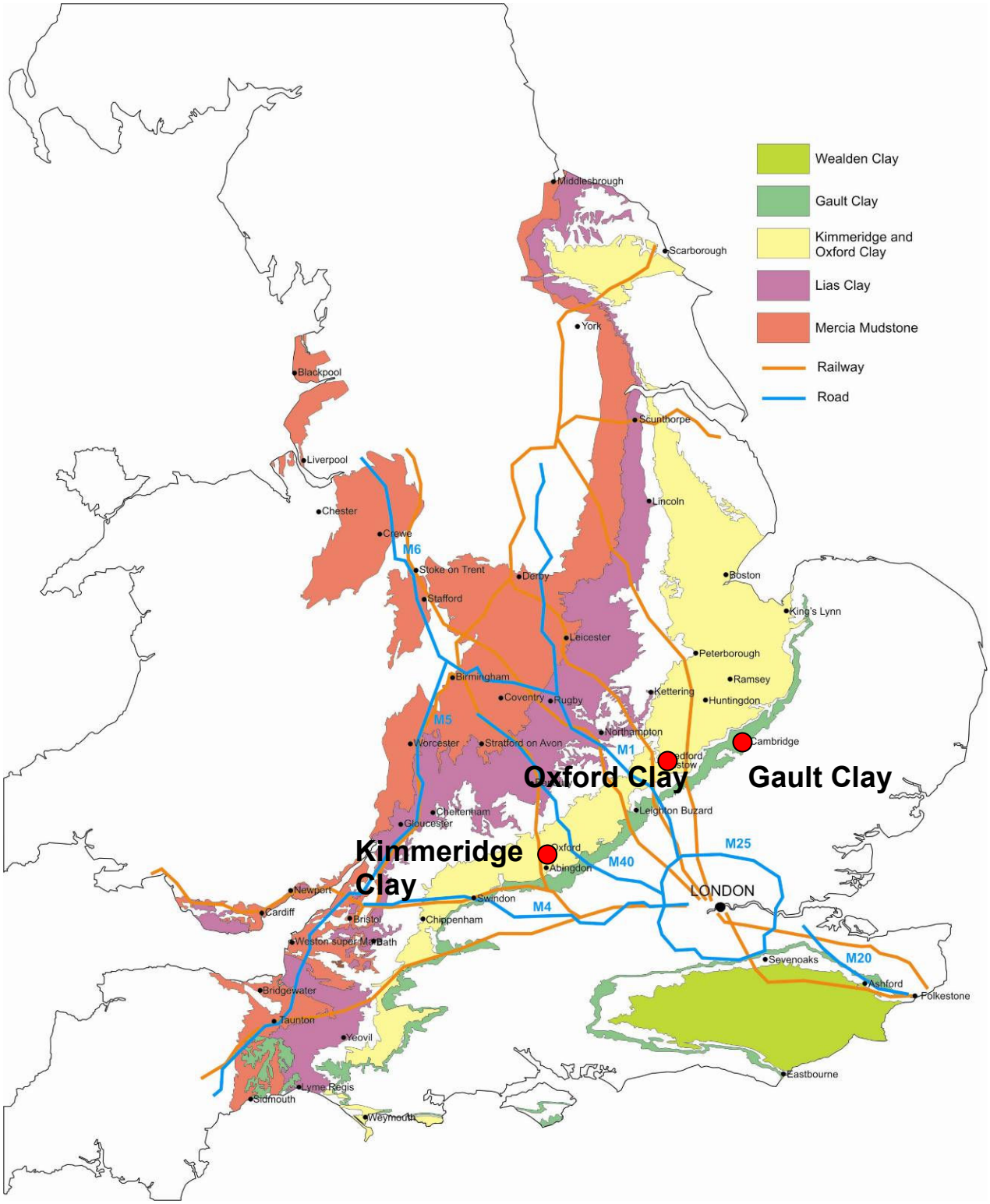


Figure 3-1: Sampling sites (Wilkinson, 2008)



Figure 3-2: Image of the pond and the sampling location for Oxford clay at Elstow looking north east



Figure 3-3: Oxford clay block sampling; a) the trench, b) trimming the block of soil, c) sample covered with cling film and wax to stop changes in water content, d) closing the box and filling it with expanding foam



Figure 3-4: A block sampling column that failed on a weak horizontal layer



Figure 3-5: Excavated trench for sampling Gault clay at High cross, Cambridge



Figure 3-6: Presence of tree roots in Gault clay block sample (depth= 3 m)

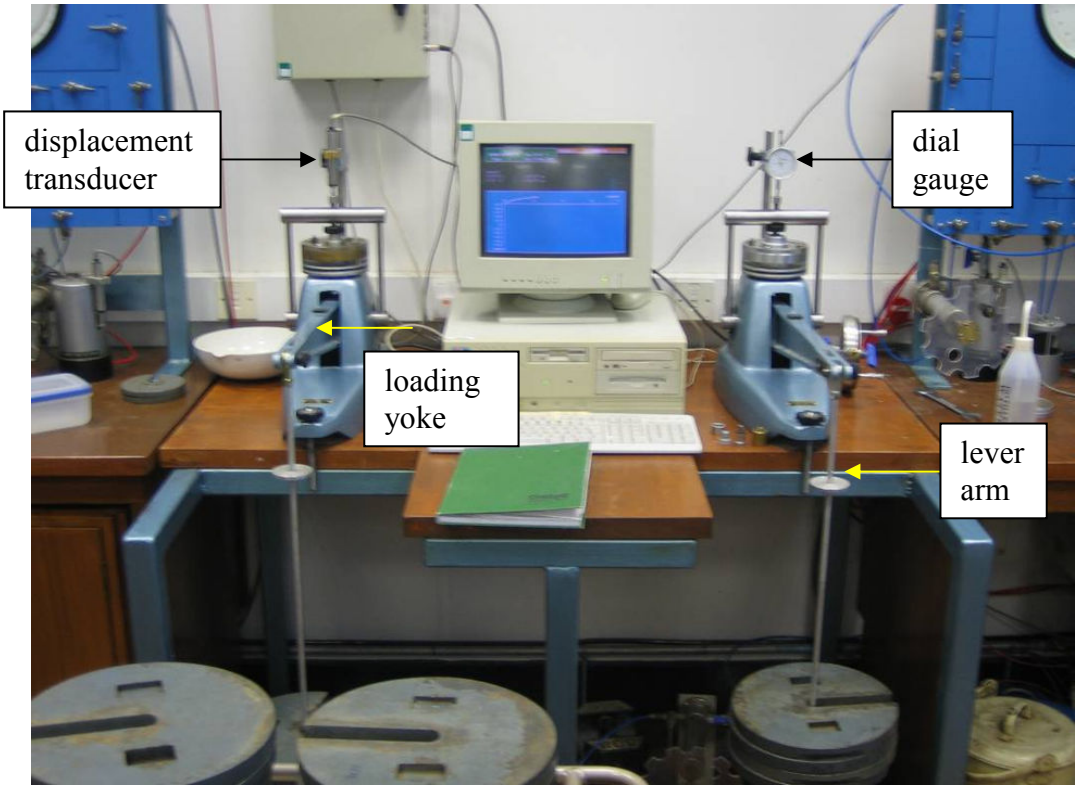


Figure 3-7: Oedometer cells used for the current project

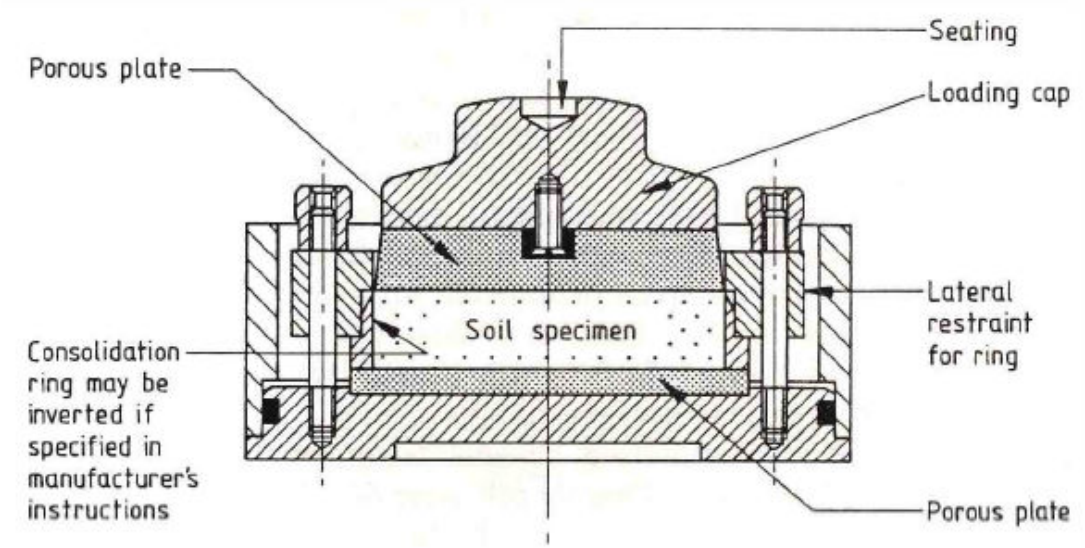


Figure 3-8: Details of a typical oedometer consolidation cell (BS1377:1990)

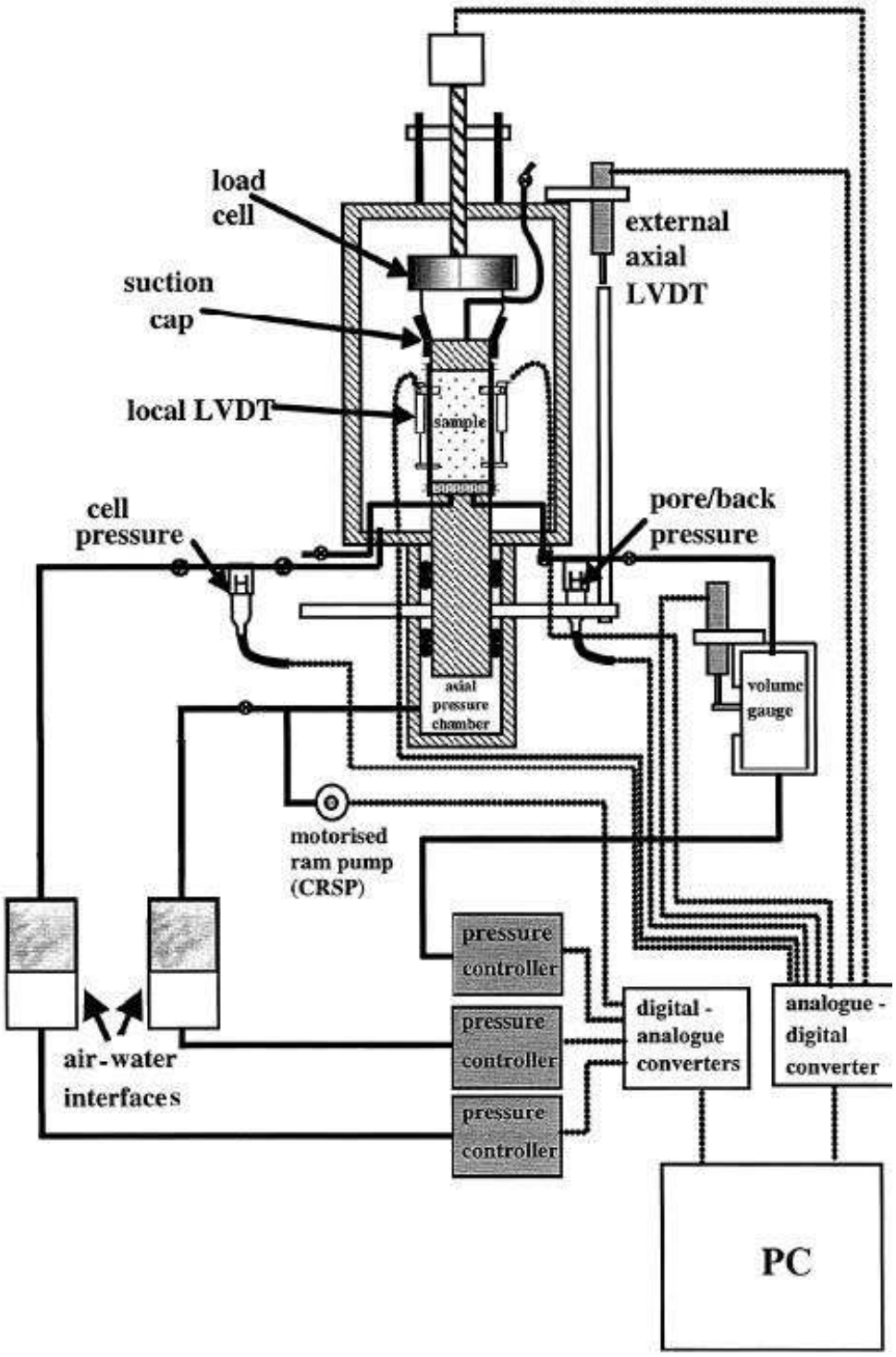


Figure 3-9: Schematic diagram of the hydraulic triaxial apparatus (Gasparre, 2005)

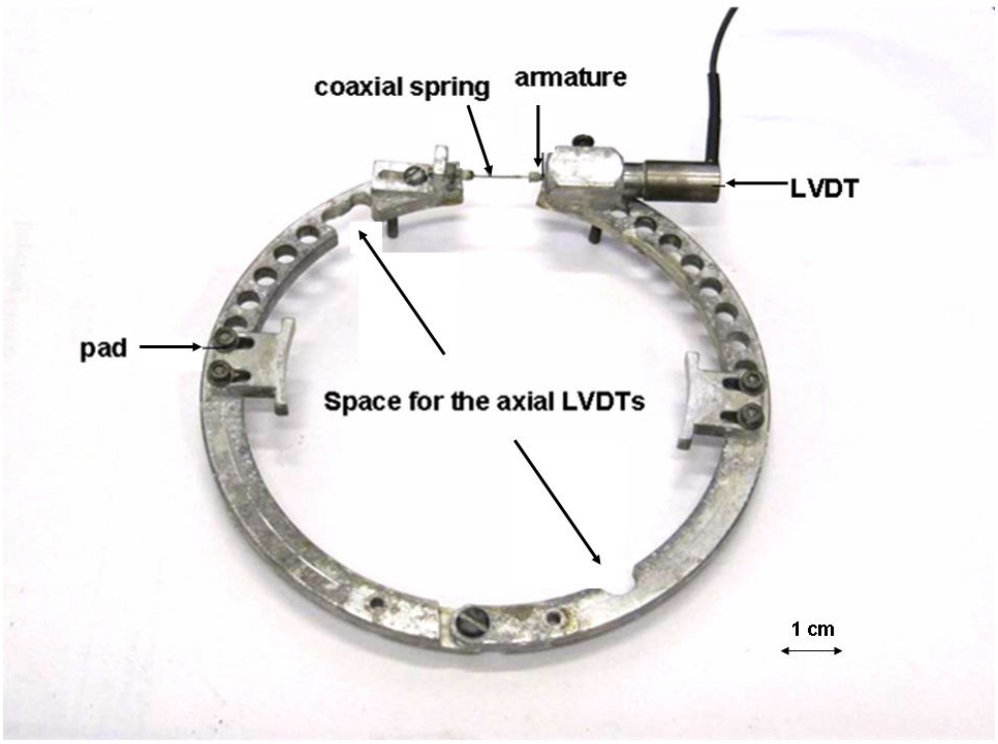


Figure 3-10: Old radial belt

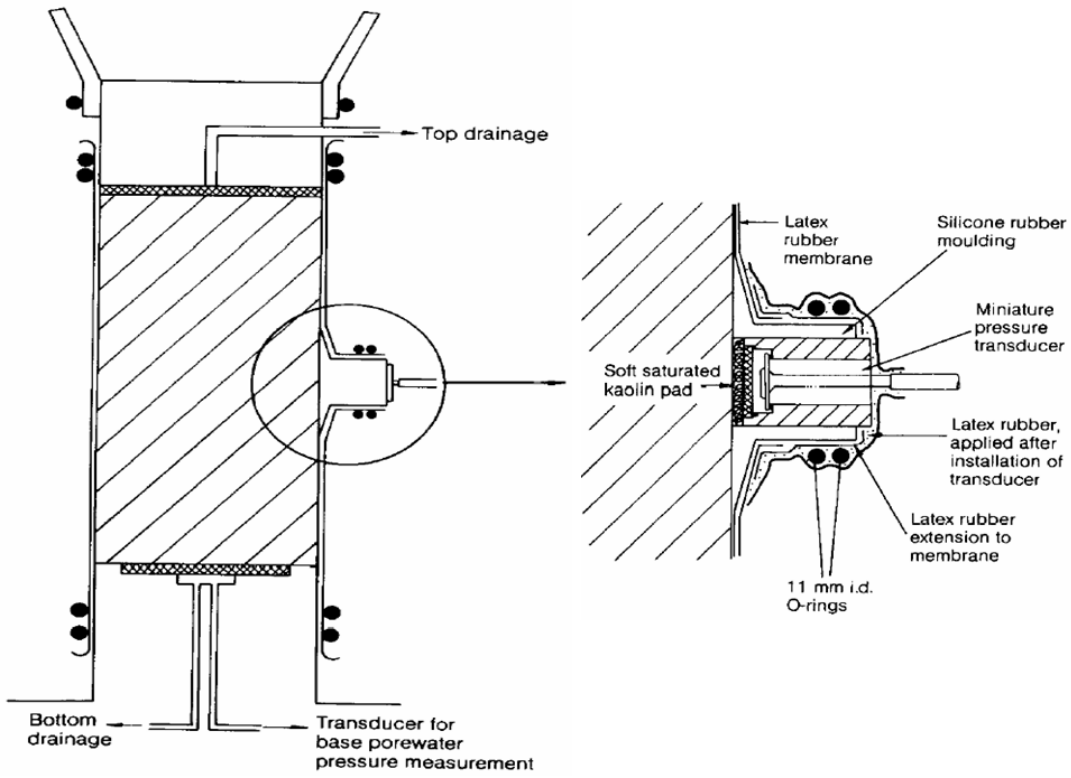


Figure 3-11: Mid-height pore water pressure probe (Hight, 1983)

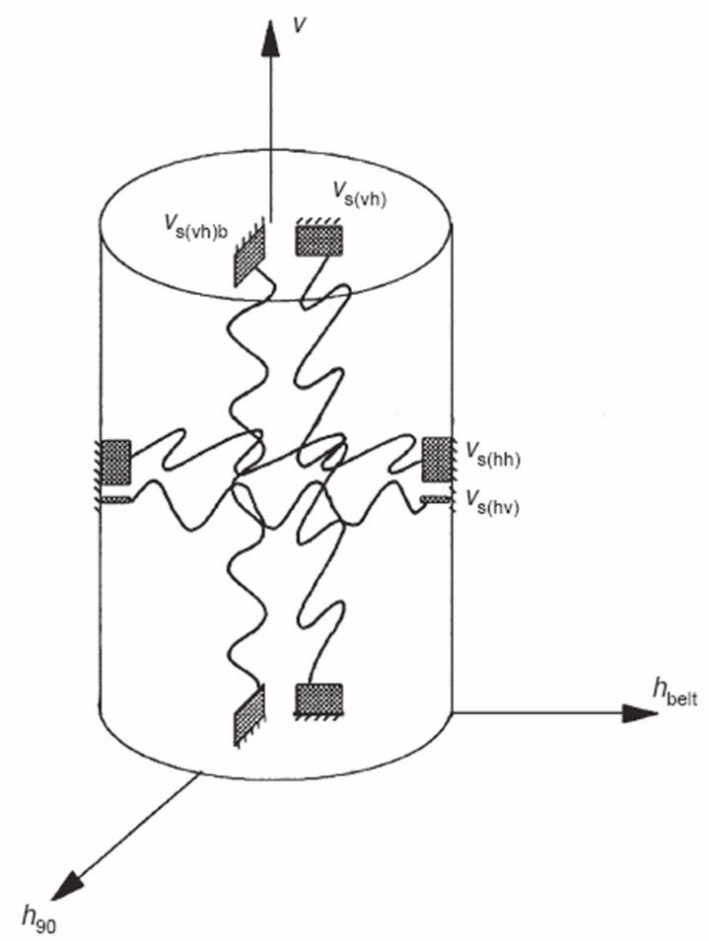


Figure 3-12: Orientation of bender elements in the triaxial samples (Pennington et al., 1997)

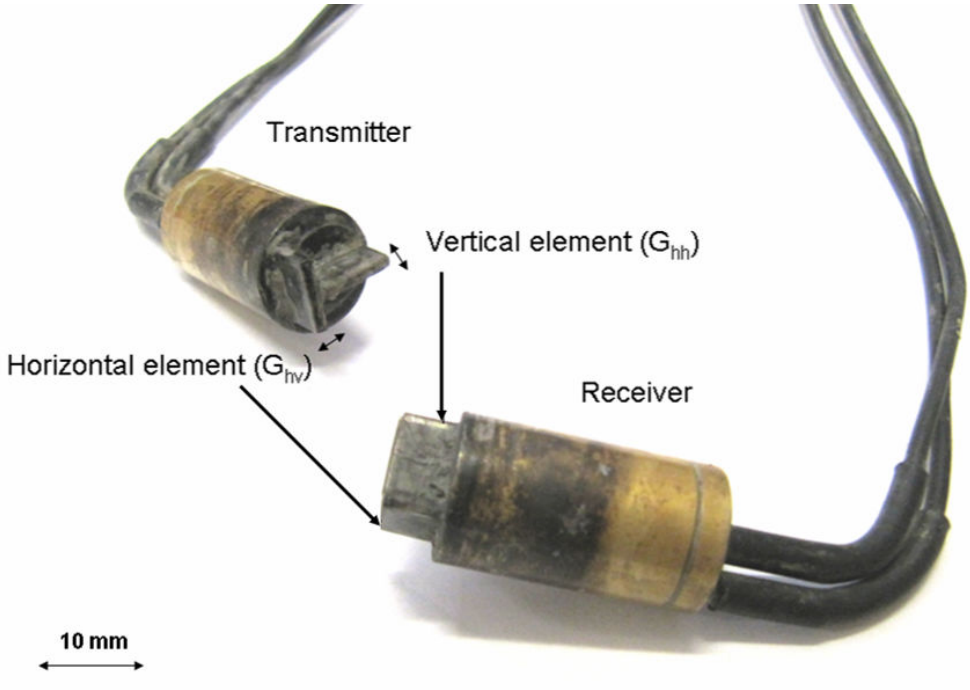


Figure 3-13: Lateral bender elements (Pennington et al., 1997)

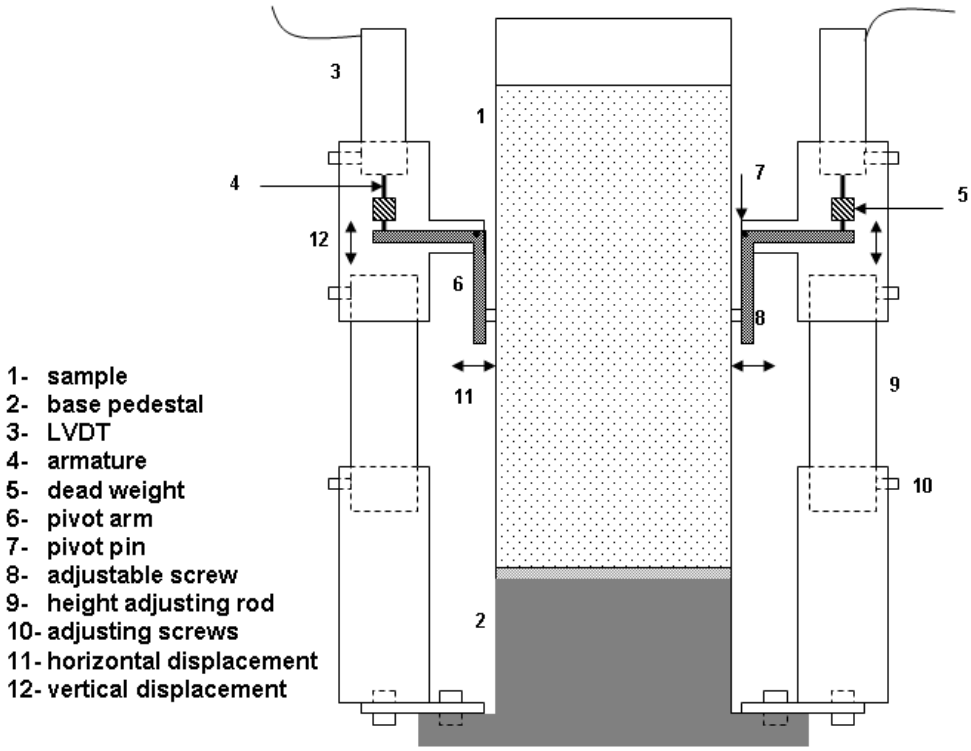


Figure 3-14: Schematic sketch of new radial displacement set-up

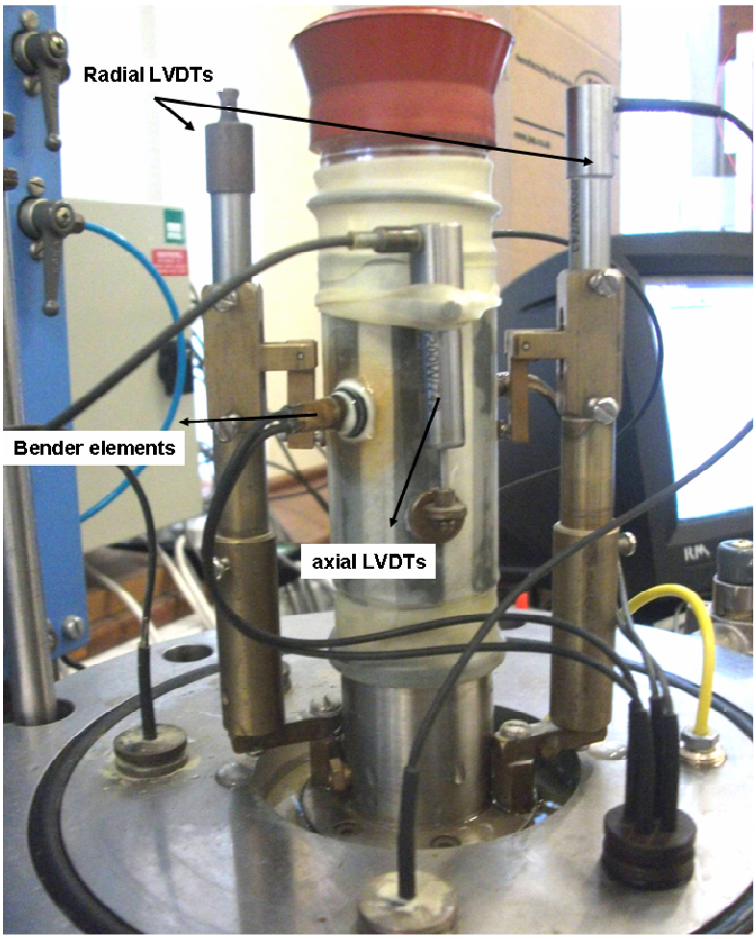


Figure 3-15: 38 mm sample with the new radial displacement set-up

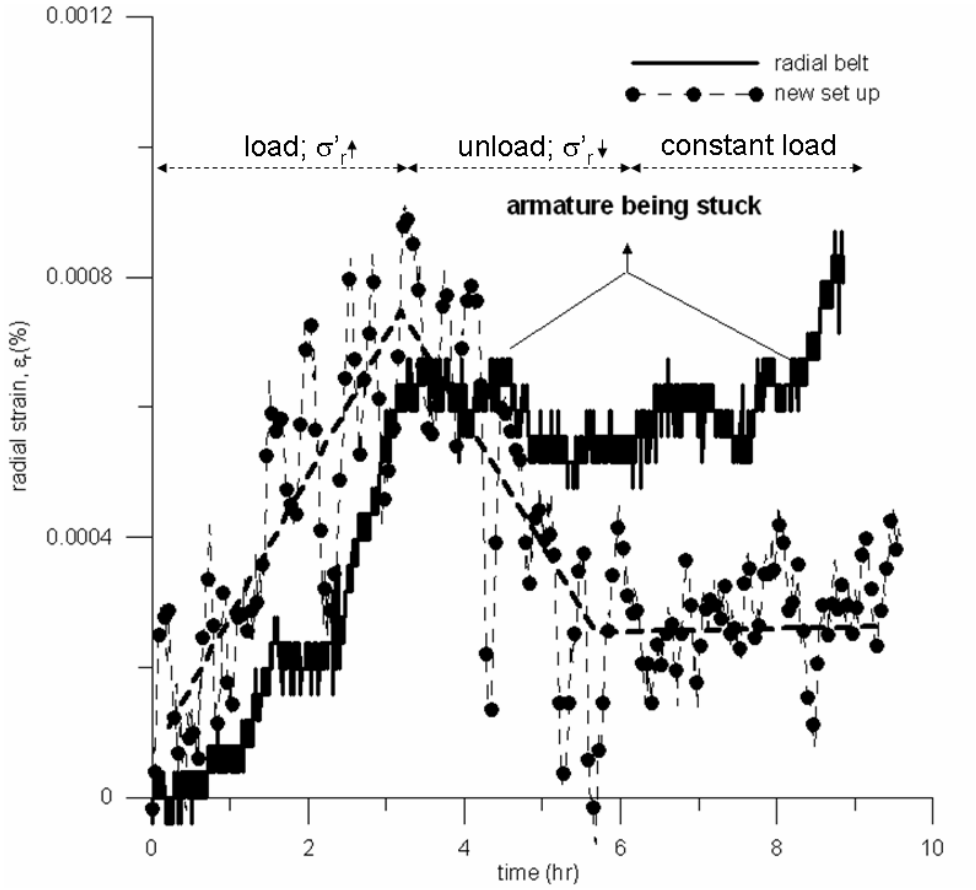


Figure 3-16: Radial strains in a load-unload radial probe using radial belt and the new set-up

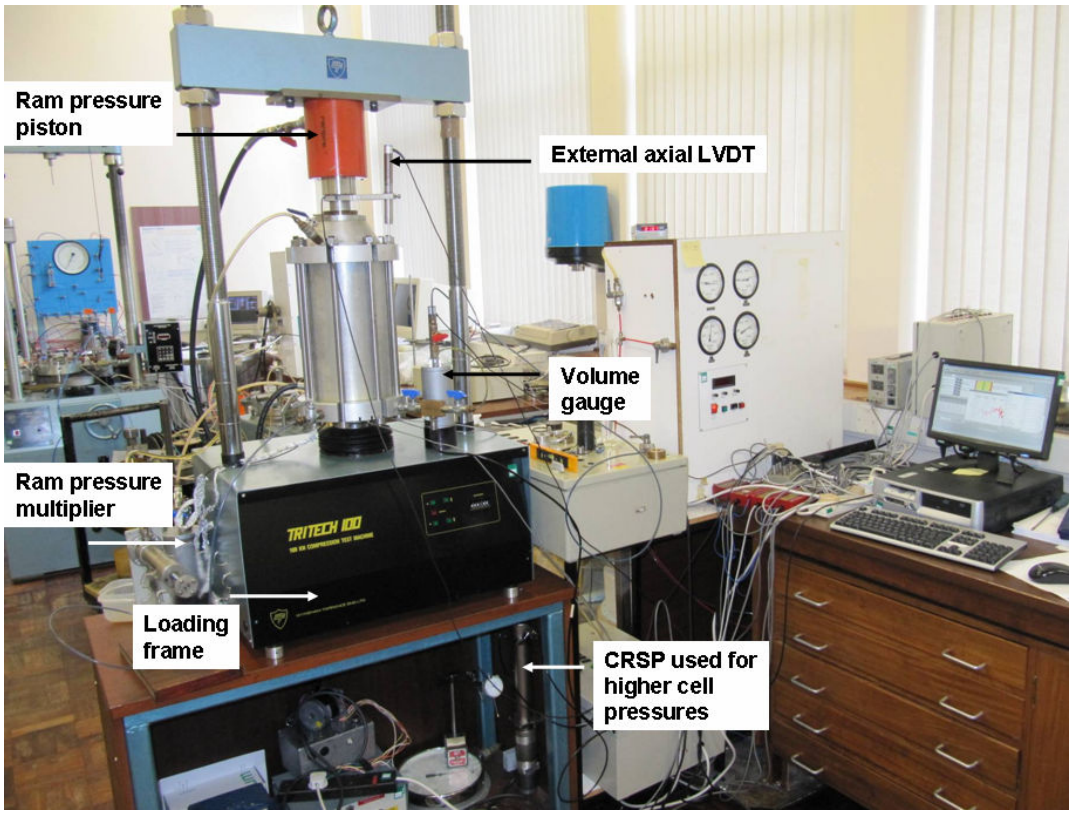


Figure 3-17: High pressure triaxial cell (7 MPa)

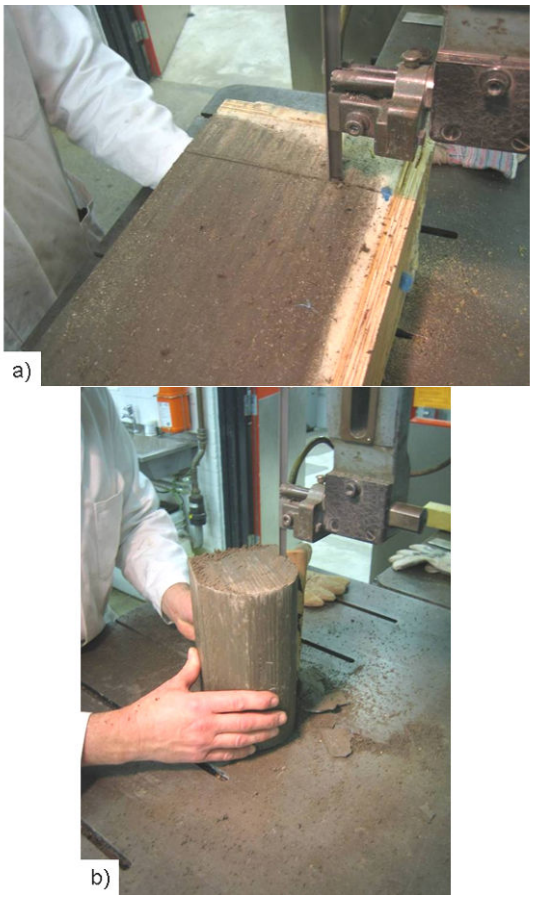


Figure 3-18: a) cutting the sample box, b) trimming the sample with a band saw to a cylindrical shape



Figure 3-19: a) final trimming on a soil lathe, b) trimming the ends

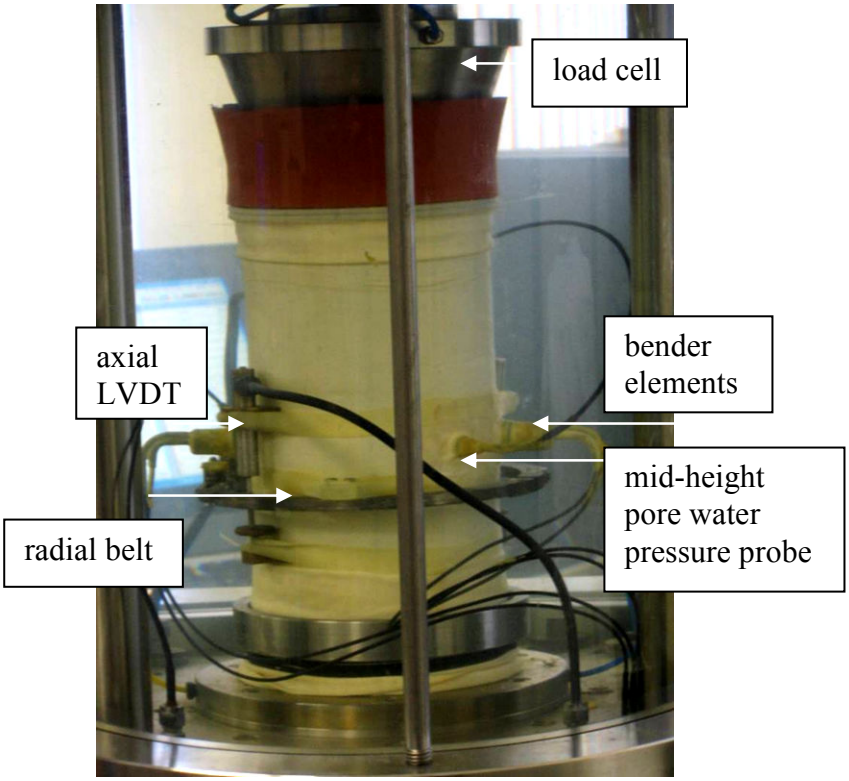


Figure 3-20: 100 mm triaxial sample with local transducers

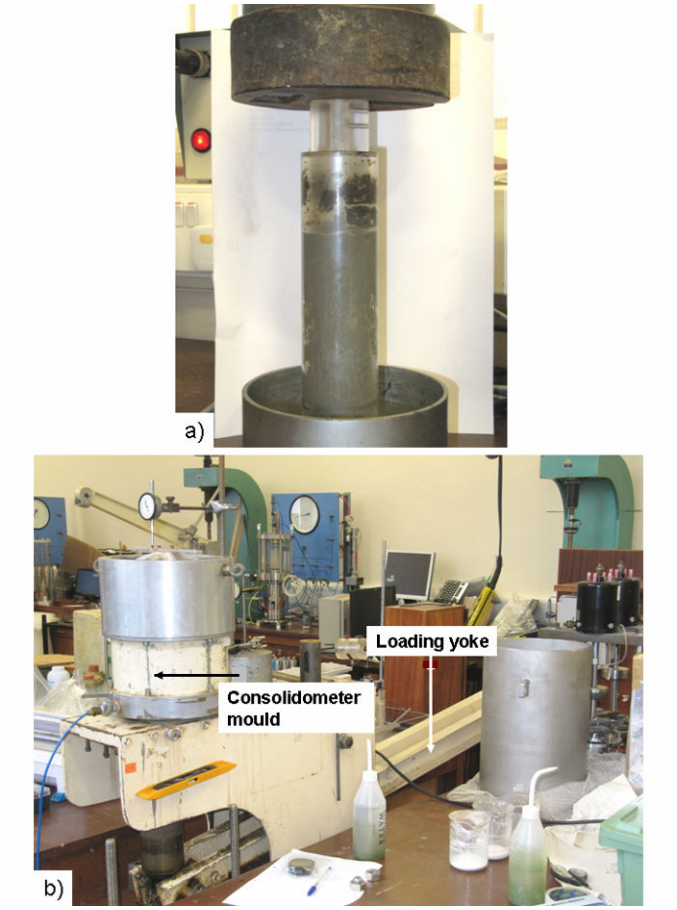


Figure 3-21: a) 38 mm diameter consolidometer, b) 230 mm diameter consolidometer

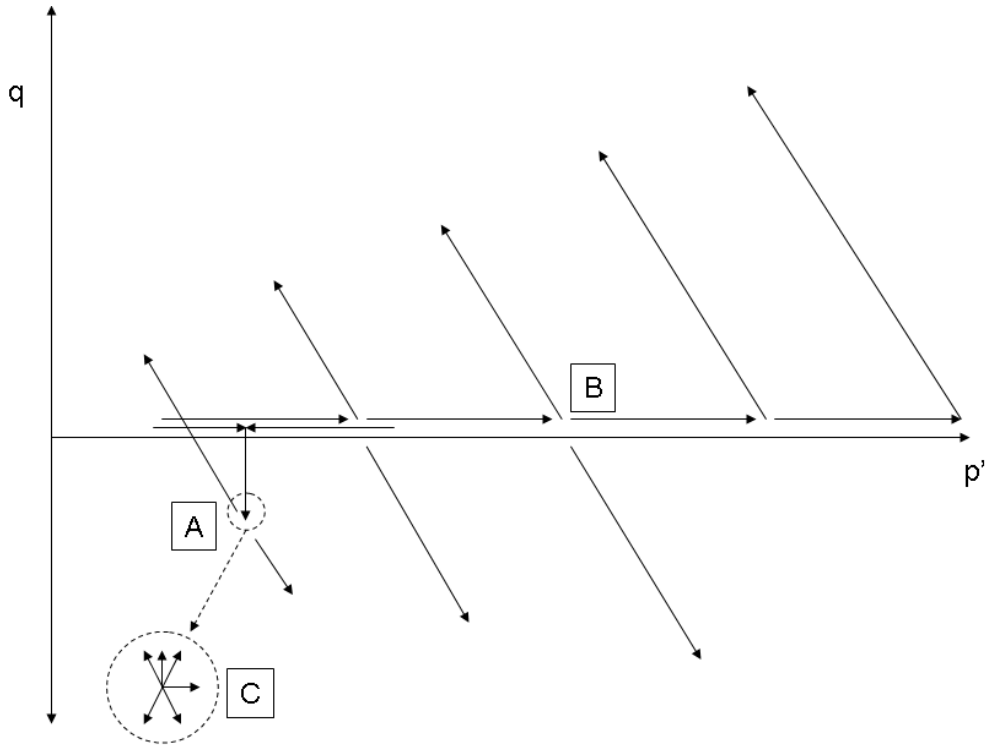


Figure 3-22: Testing programme types: A) reconsolidation to the 'in-situ' state and shearing to failure in compression and extension, B) isotropic compression or unloading followed by shearing in compression or extension to failure, C) axial, radial, constant p' or constant q probing from the 'in-situ' state

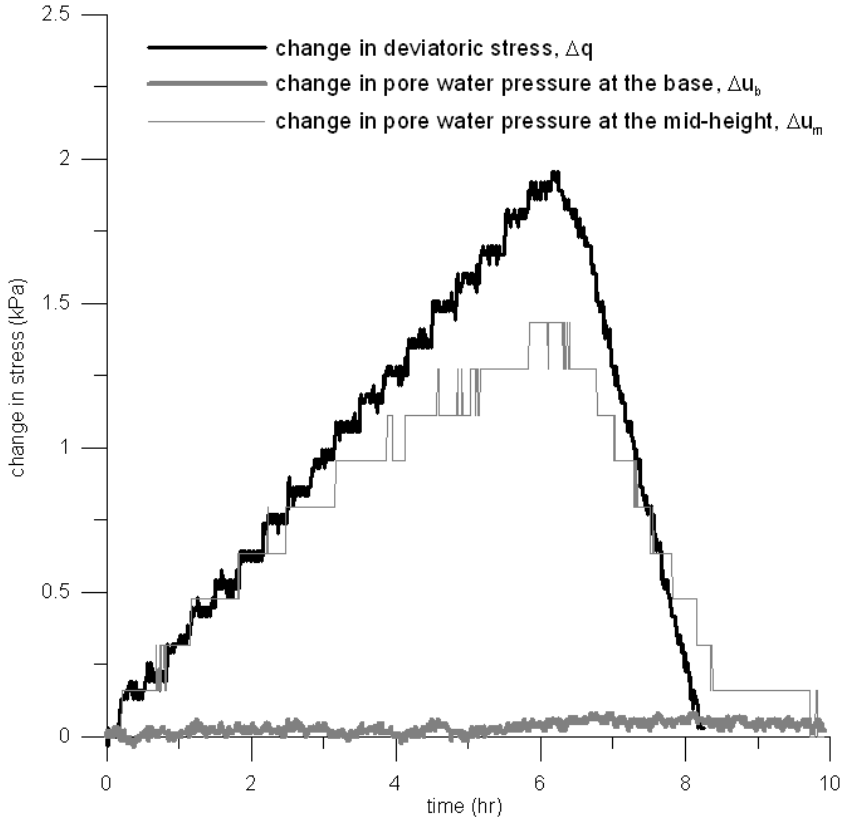
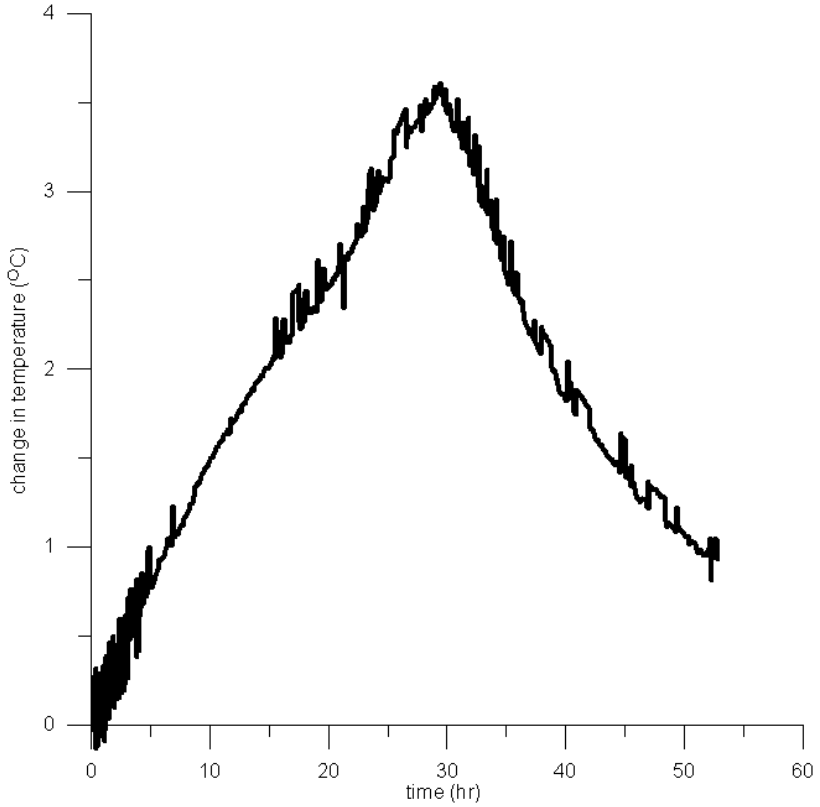
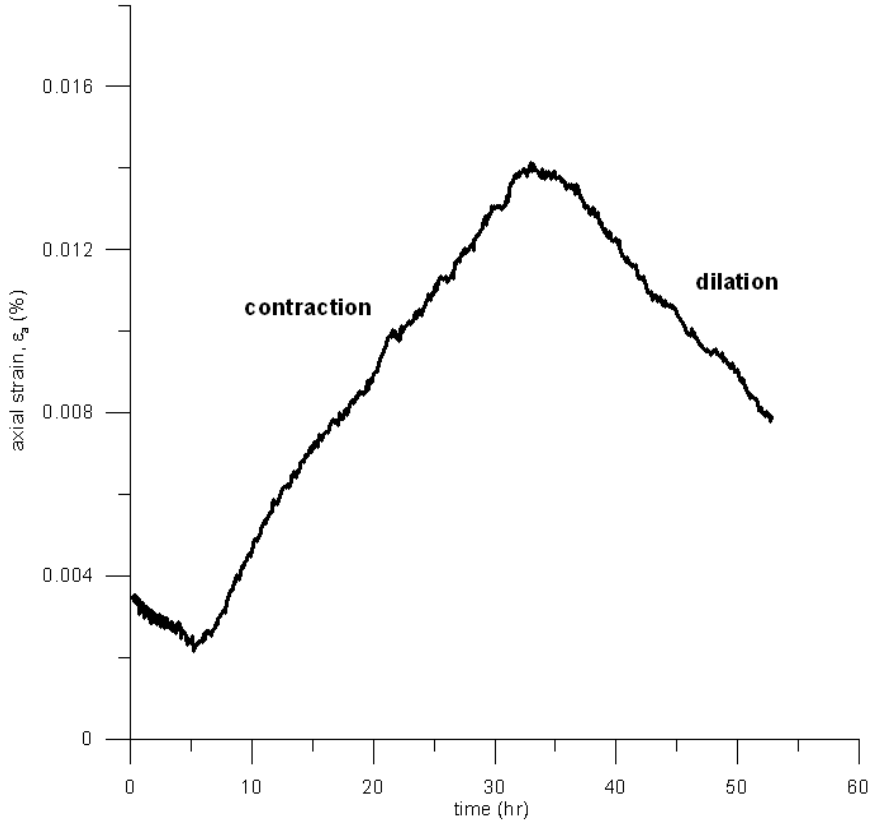


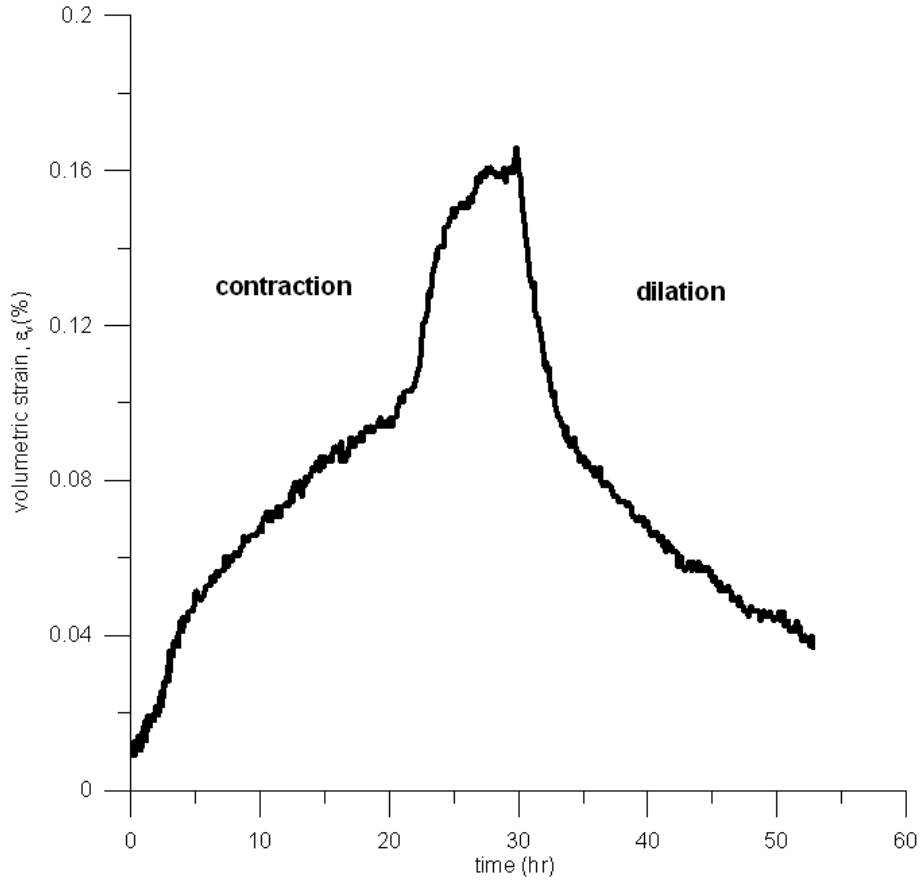
Figure 3-23: Evidence of incomplete drainage of pore water pressure during an intended drained axial probe, applying a rate of 0.3 kPa/hr to a 100 mm diameter sample of Oxford clay


change in temperature (°C)
time (hr)
0
1
2
3
4
0
10
20
30
40
50
60

a)


axial strain, ε_a (%)
time (hr)
contraction
dilation
0
0.004
0.008
0.012
0.016
0
10
20
30
40
50
60

b)



c)

Figure 3-24: The effect of an exceptional temperature change on a 38 mm sample of Gault clay; a) the change in temperature, b) change in mean of local axial strain gauges, c) change in volumetric strain measured by volume gauge

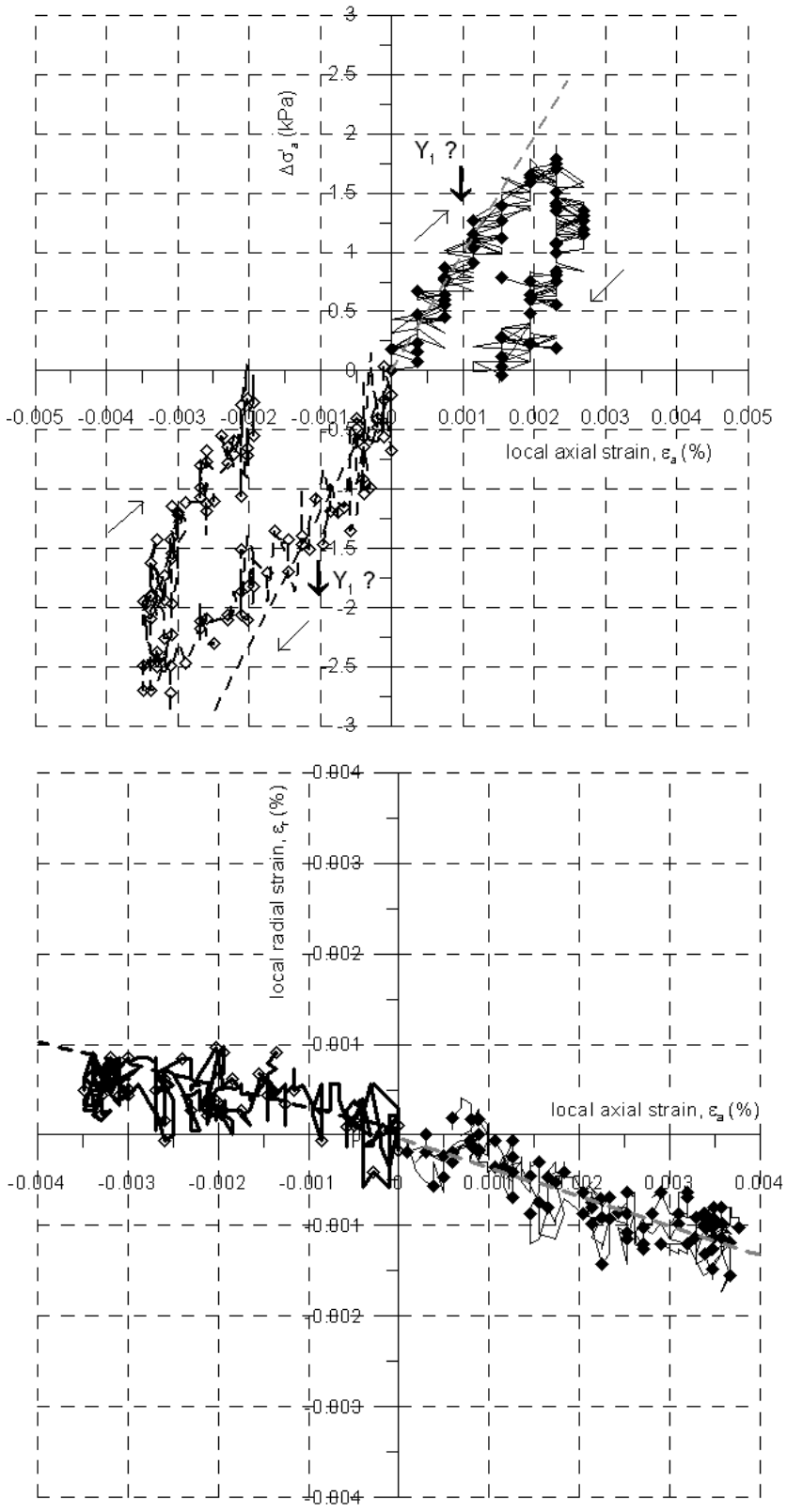


Figure 3-25: Drained axial probes in compression and extension on 38 mm diameter samples of Oxford clay; a) deviatoric stress vs axial strain, b) radial strain vs axial strain



Figure 3-26: Complex strain localisation on 50 mm in diameter sample of Gault clay

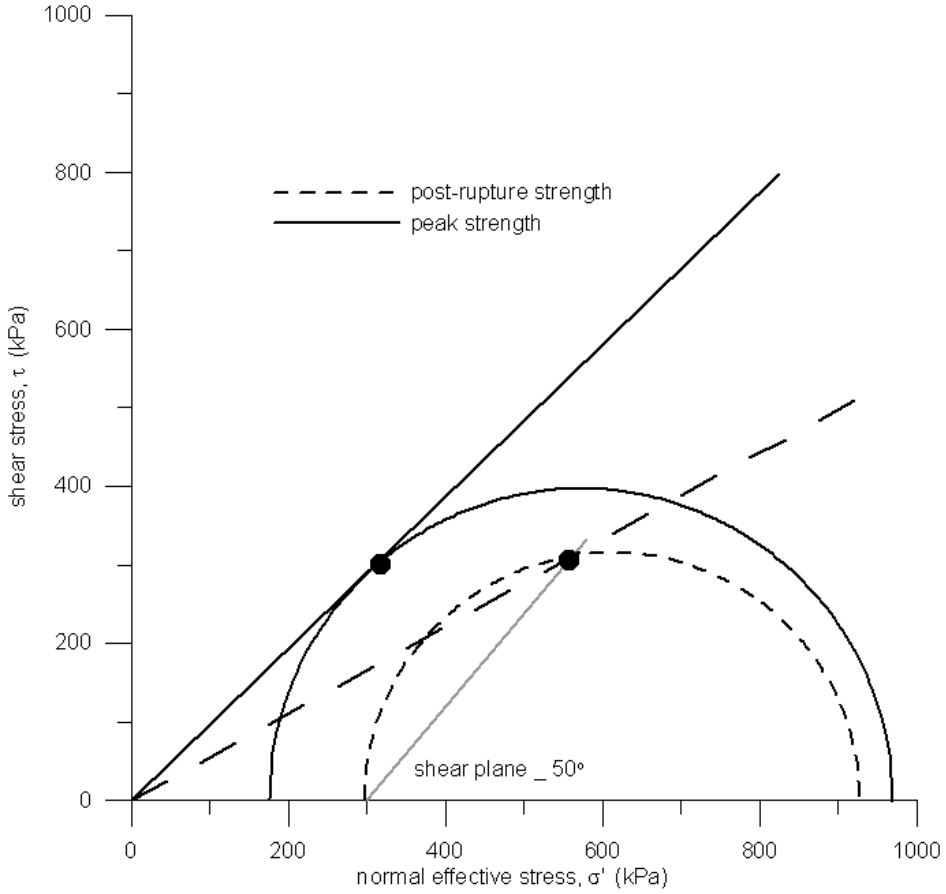


Figure 3-27: Shear plane analysis for peak and post-rupture strength of Oxford clay

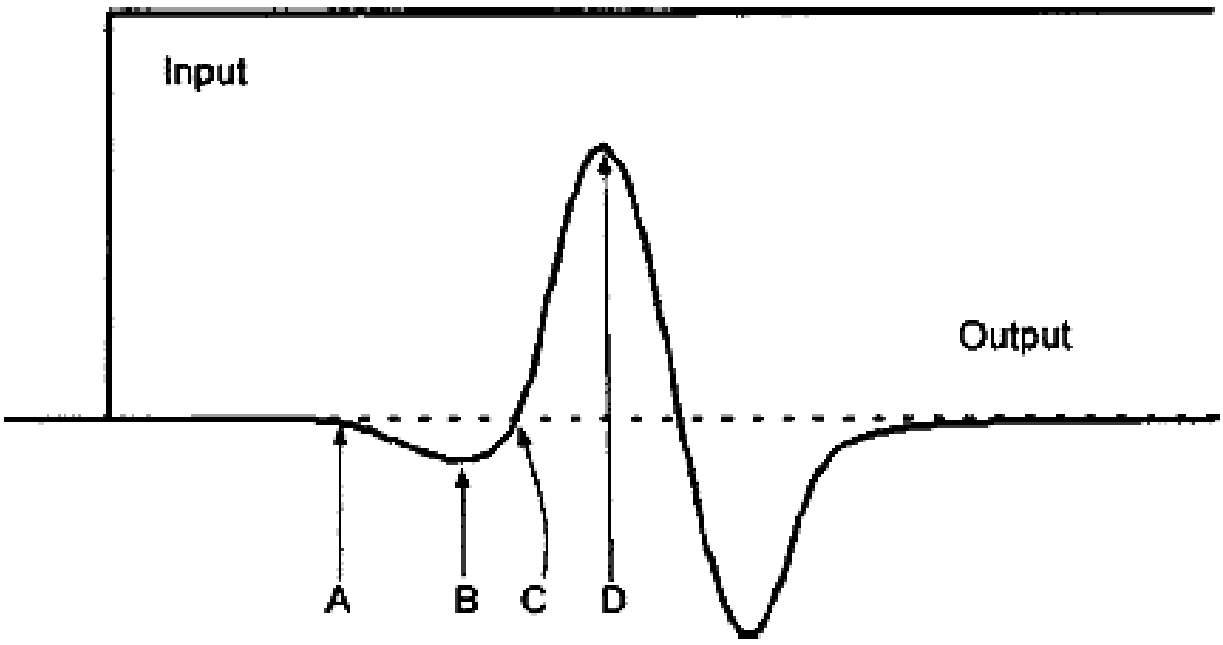


Figure 3-28: Typical S-wave signal; a) first deflection, b) first bump maximum, c) zero after first bump, and d)major first peak (Lee & Santamarina, 2005)

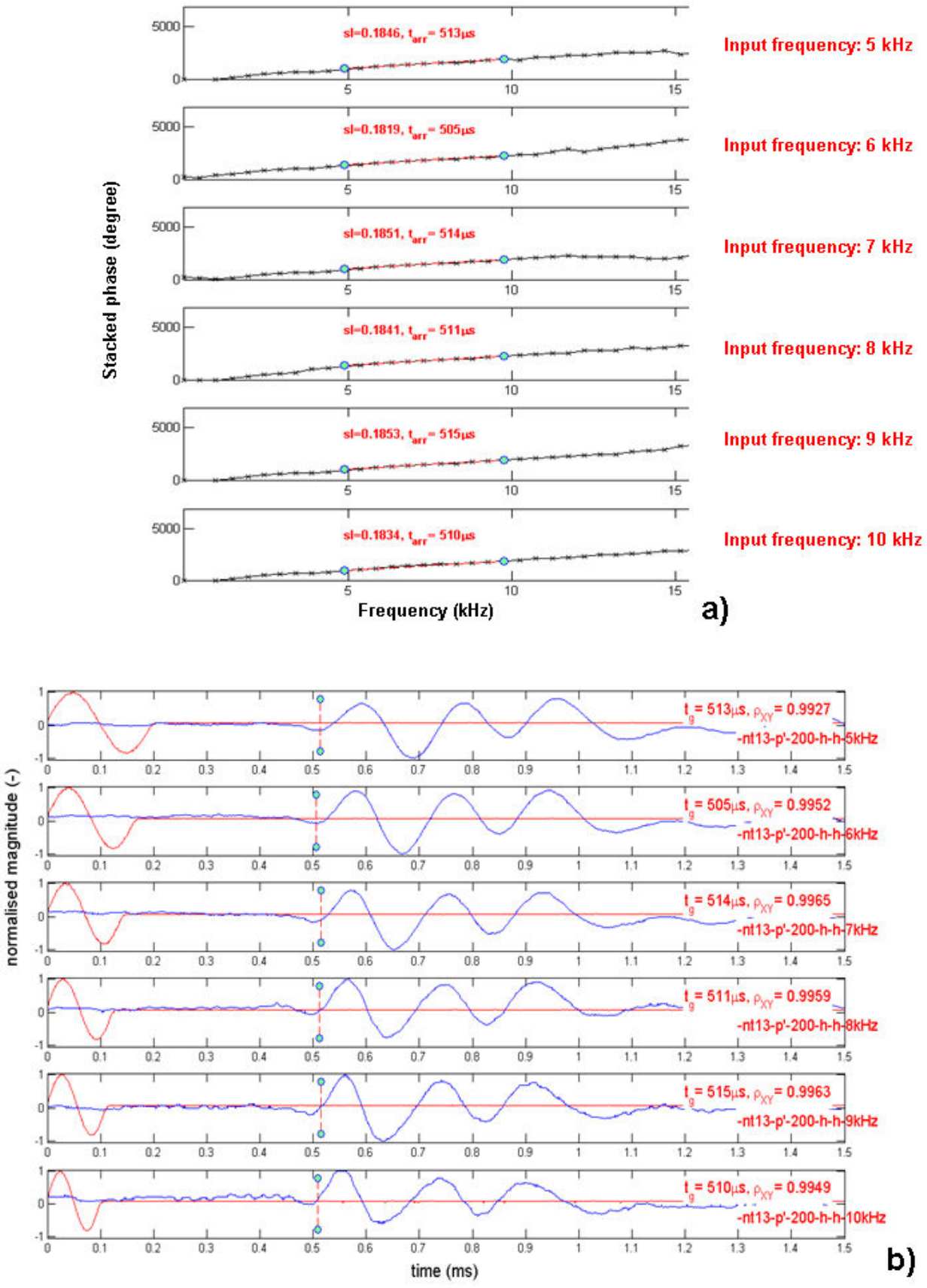


Figure 3-29: Frequency domain analysis to obtain G_{hv} for Gault clay at p'=200 kPa; a) arrival times derived from the slope of stacked phase vs. frequency, b) projection of arrival times calculated from frequency domain

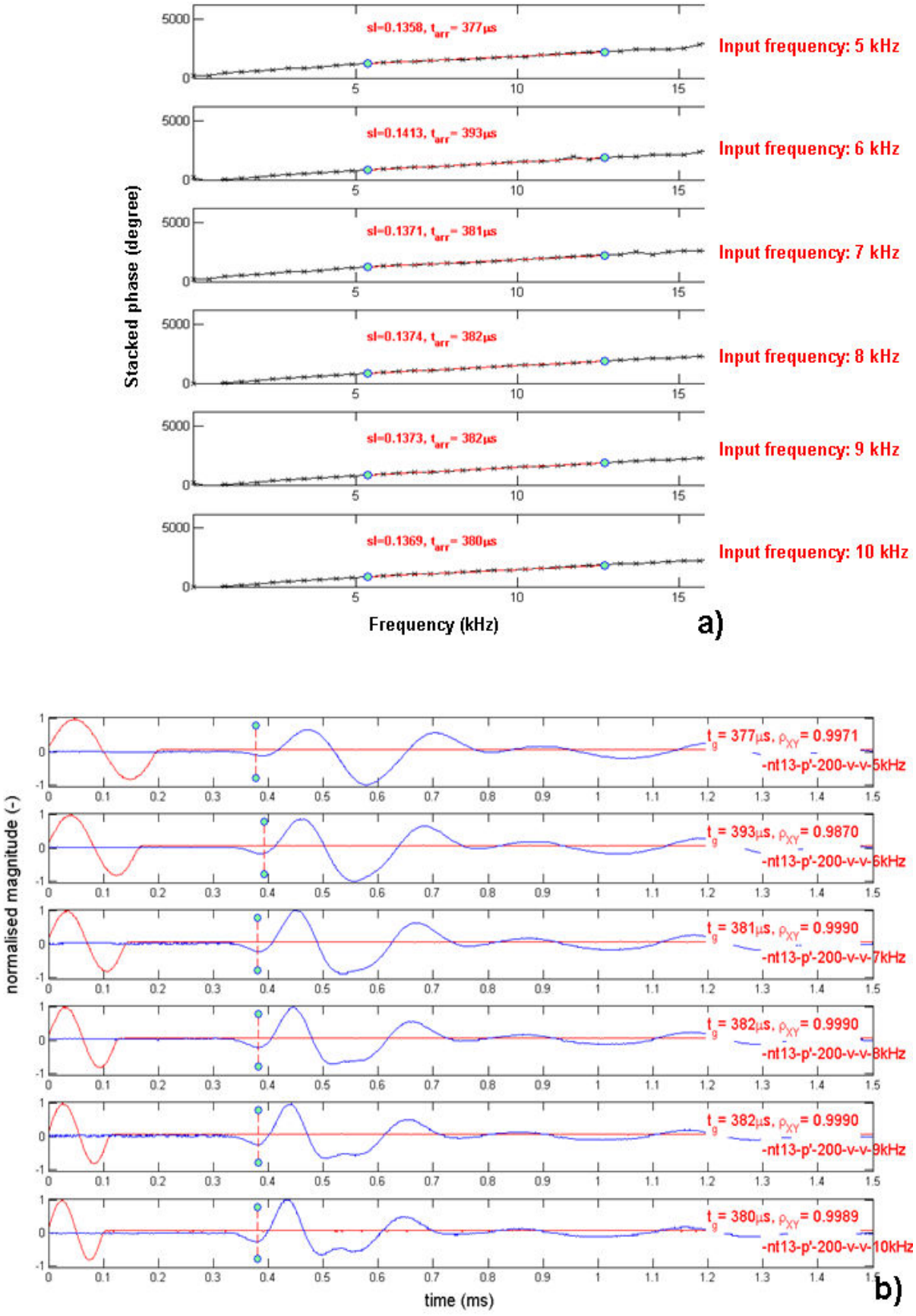


Figure 3-30: Frequency domain analysis to obtain G_{hh} for Gault clay at p'=200 kPa; a) arrival times derived from the slope of stacked phase vs. frequency, b) projection of arrival times calculated from frequency domain

4 Oxford Clay

4.1 Introduction

The author's research into UK mudrocks started with sampling of and laboratory testing on Oxford Clay. This chapter first outlines a brief summary of earlier works on this stratum, which has been studied less extensively than, for example, the London Clay. The main part of the chapter is concerned with describing the author's new experimental research on Oxford Clay. Chapter 7 presents a synthesis of the research on the three mudrocks investigated in this project.

4.2 Background

4.2.1 Geology and the site

Oxford Clay is a highly bedded, stiff overconsolidated clay deposited during the upper Jurassic (around 160 million years before present) in quiet water in a relatively shallow sea (Hallam, 1975). The top, weathered part of currently exposed section are reported to be around 3m thick (Hird & Pierpoint, 1997). The unweathered Oxford clay is green-grey in colour and is highly laminated. There are numerous shells present in the soil, some of which have been transformed to pyrite. The specific gravity, G_s, of Oxford clay is 2.46. The clay's organic content as measured in the current study was the highest of mudrocks at 10.06%. This high organic content encouraged the extensive use of the clay in brick making.

Parry (1972) and Burland et al. (1977) studied the effects of the joints and fissures found in Oxford clay on its mechanical behaviour, concluding that the main feature of the soil is its horizontal lamination rather than the fissures or joints. Based on stratigraphic evidence, Jackson & Fookes (1974) suggested the maximum depth of burial for the Oxford Clay to be between 460m and 661m. A more recent study using apatite fission track analysis (Green, 1989) gave a higher depth of burial of up to 1500m. All of the previous studies on Oxford clay considered the former in their analysis to obtain K_0 values.

The author's soil samples were taken from a site near Elstow, south of Bedford, shown in Figure 4-1. The laminated and bedded nature of Oxford clay can be seen in Figure 4-2 with some shell fragments in the soil. The geotechnical profile at the site is shown in Figures 4-3 and 4-4. Brosse (2012) developed these summary plots by synthesising data from the recent Imperial College study with soil properties from other research and site investigations. The profile also includes data from the seismic CPT carried out as a part of the current project. As can be seen, the water content and plasticity index is relatively uniform with depth, while there is more scatter in the bulk unit weight. The values of bulk unit weight measured in the current study, both by the author and by Brosse (2012), match best the upper range of the values from the other studies. The typical particle size distribution curves shown in Figure 4-5 are in good agreement with the other site investigation results. The CPT cone resistance and sleeve friction data provide indicators of the depth of the weathered zone and the presence of several cemented bands. The elastic G_{vh} values obtained from the seismic CPT increase with depth. As discussed later the values measured at 10 metres depth are in generally good agreement with the authors, bender element data and the resonant column measurements by Brosse (2012). However, as discussed later, G_{hh} values measured using a pressuremeter (Pierpoint, 1996) appear to be lower than the elastic maxima recorded by bender elements.

4.2.2 Previous studies

Research on Oxford clay over the last four decades has concentrated on lower Oxford clay samples obtained from sites around Bedford, which is near Elstow. Table 4.1 summarizes the Oxford clay properties from previous studies. They all noted the clay's highly anisotropic nature. Higher strength and stiffness was recognised in the horizontal direction compared to the vertical.

The most comprehensive study of Oxford clay to date was carried out by Hird & Pierpoint (1997). The objective of their research was to model and predict the ground movements around a trial excavation using a numerical method, and to compare predictions with field measurements. To obtain the correct parameters for their analysis they carried out laboratory tests including multi-stage triaxial tests to obtain

stiffness parameters for Oxford clay. After reaching the estimated in-situ state (considering K_0 = 2.5), they carried out constant p' or q probes in compression followed by shearing to failure in undrained extension (Figure 4-6). By comparing two identical probes at different stages of the test, they concluded that this multi-stage procedure did not disturb the sample and so was appropriate. These effective stress paths were approximately 100kPa long which, in terms of the framework discussed in Chapter 2, engaged the Y_1 and Y_2 kinematic yield surfaces and resulted in plastic deformation. However the strain changes that they could have resolved using proximity transducers was not sufficiently small enough to capture possible plastic straining. Another issue related to these probes was the stress rate of 1kPa/hr used on 100 mm in diameter samples. Hird & Pierpoint (1997) recognised that this rate was too fast for excess pore water pressure to dissipate fully but they had to tolerate this due to time limitations. They observed 10kPa differece between the pore water pressure measured at the mid-height and the base of the sample for a 100kPa change in stress. As was shown in Section 3.4.2, significant excess pore water pressure can develop even when slower rate of 0.3 kPa/hr was used causing problems in measuring drained parameters. Although the authors highlighted the effects of creep rates on stiffness measurements, their hold periods of 2-3 days appeared insufficient to eliminate creep.

Hird & Pierpoint (1997) argued that Oxford clay stiffness did not show a significant dependency on recent stress history but was mainly affected by the recent strain history. This conclusion can not be examined critically as the creep rate criteria led to interactions that probably obscured the effects of changes in the direction of probing at small strains. The range of stress levels involved in the study carried out by Hird & Pierpoint (1997) was between p' = 100kPa to 300kPa which was not large enough to study the effects of stress level on the stiffness of the soil. The other shortcoming of their study was a lack of any comparison between tests on natural and reconstituted samples to study the effects of structure on the behaviour of the soil. In the current research all these aspects have been tried to be addressed.

4.2.3 Evaluation of the in-situ stresses

To obtain the most representative and realistic stiffness and strength parameters it is better to conduct the tests at their in-situ stress state. Knowing the depth of sampling, the level of water table and the bulk unit weight of the material makes it relatively easy to estimate the vertical effective stress. However for an old soil such as Oxford Clay, which underwent massive erosion followed by load-unload loops due to glaciations, the estimation of the horizontal stresses is not straightforward. Mayne & Kulhawy (1982) suggested sets of empirical equations to calculate the K_0 value for normally and overconsolidated soils. These equations are only valid for simple assumptions such as one stage unloading following *1-D* deposition for overconsolidated soils. They were also derived from data for soft and reconstituted clays and are not necessarily applicable to stiff clays. The *OCR* value is not easily estimated for the Oxford clay due to uncertainties about the previous depth of burial. Considering the possible limits for the value of *OCR* and using the equations suggested by Mayne and Kulhawy (1982), the K_0 value varies between 3 and 5. These high horizontal stresses are very close to passive failure and the upper limit of K_0. A value of 3 to 4, corresponding to a depth of burial of 500m to 700m is more probable.

As mentioned in Section 3.4.2, considering perfect sampling the initial p' obtained in a triaxial test is related to the suction of the sample and therefore the in-situ p'. However, this is only true if the unloading and reduction in q results in no changes in p' (for the isotropic material). The undrained compression and extension tests for the natural Oxford clay will be presented later in this chapter showing inclined effective stress paths ($\delta p'/\delta q$ = -0.32) which are caused by the anisotropy of the soil. Therefore it is expected that values measured in the triaxial apparatus were lower than the in-situ p'. The initial values obtained in the current research varied between 200kPa and 340kPa, with higher values for most of the early tests. Drying and disturbance of the sample could affect these values and by considering the fastest sample preparations for more recent tests, lower values of p' were found. There have been some in-situ tests, such as the self boring pressuremeter (Pierpoint, 1996), which gave a wide range of K_0 values between 3 and 7. Considering all these methods and the fact of being very close to passive failure, an in-situ p'= 250 kPa was adopted and the in-situ stresses were estimated based on K_0 = 3.2 (Table 4-2). Later on, during the project, a

suction probe (Ridley & Burland, 1993) became available and a suction measurement on an Oxford clay block sample was carried out. Figure 4-7 shows the suction plotted against time with the value of 215 KPa at the end of test, which indicates the estimation used was not significantly far from the in-situ stress state. However as discussed in Section 3.4.2 limits were imposed on the axial and volumetric strains during the path taken to reach the in-situ stress state. These limits were reached at q = -100kPa corresponding to K_0 = 1.98 and therefore probing was carried out at this K_0 value.

4.3 Intrinsic properties

The intrinsic properties found by testing reconstituted soil, can be a measure of structure when being compared with the natural properties. In this section these properties will be presented. Both oedometer and triaxial tests have been carried out on the reconstituted samples of Oxford clay to measure all the required parameters. The triaxial tests were carried out by an MSc student (Gao, 2009) under author's supervision. The tests carried out on Oxford clay samples are presented in Tables 4-3 and 4-4 and Table 4-5 summarises all the parameters obtained for the reconstituted samples.

4.3.1 Compression behaviour

K_0 and isotropic compression curves for reconstituted Oxford clay are shown in Figures 4-8 and 4-9. Figure 4-8 shows the 1-D compression in void ratio (e) plotted against logarithm of vertical effective stress (σ'_v). Pairs of tests started at different initial void ratios (different initial water contents) and were compressed to different stress levels. As can be seen, the intrinsic compression line (*ICL**) is unique for these two tests. The isotropic compression curves from triaxial tests are presented in Figure 4-9 in specific volume (v) plotted against logarithm of mean effective stress (p'). All the tests started at similar specific volumes but were compressed to different stress levels, with one test being swelled back after compression. Burland (1990) proposed a curved intrinsic *NCL**, but in the current study a straight line fitted to a short section

of isotropic *NCL** was used to normalise the effective stress paths of both reconstituted and natural samples.

4.3.2 Shearing behaviour

Five triaxial tests were carried out on reconstituted samples cut from a 'cake' consolidated to 50 kPa (see Section 3.4.1). Three of these tests were normally consolidated and two overconsolidated. The first two tests were isotropically consolidated to p'= 600 kPa and then sheared undrained and in compression. The reason for having two identical tests was to check the repeatability of the data for the MSc student who was performing the tests. The third test was overconsolidated with *OCR*=10, while the fourth test was normally consolidated in the high pressure apparatus to p'=1000 kPa. Bender element data are available for this high pressure test. The last test was also overconsolidated with *OCR*=2, however the control program failed during the shearing and the test stopped before reaching a critical state. It should be noticed that here the term *OCR* is used based on the mean effective stress, p', during an isotropic loading and unloading.

Figures 4-10 and 4-11 show the stress-strain and pore water pressure behaviour observed. The overall behaviour for the normally consolidated samples and lightly overconsolidated sample is contractant with samples bulging at the end of the shearing. However the sample which was sheared at higher stresses developed a shear plane after the peak at large strains. The effect of this strain localisation can be seen in the sudden fall in the strength after peak. The *OCR*=10 sample showed a dilative behaviour with strain localisation again at large strains, which was followed by a drop in strength. The rate of pore water pressure change, $du/d\varepsilon_a$, tended to zero at large strains for all tests.

The stress ratios q/p' are shown in Figure 4-12, plotted against axial strain. The stress ratio, M = q/p', at critical state was estimated considering the first three tests, being the most reliable tests, to be 0.98 corresponding to an internal angle of shearing resistance $\phi'_{cs} = 24.9°$. In the normalisation based on p' (stress level), the stiffness is almost the same for all the normally consolidated and the lightly overconsolidated

samples. However the highly overconsolidated sample shows a much stiffer behaviour induced by unloading. The effective stress paths for these tests and the failure envelope corresponding to M = 0.98 are shown in Figure 4-13. An intrinsic Critical State Line, CSL*, is plotted along with isotropic Normal Compression Line, *NCL**, in Figure 4-14. The Critical State Line was constructed using the last point of shearing and its corresponding specific volume; the results show that the *CSL** and *NCL** are parallel.

The effective stress paths, normalised by equivalent pressure (p'^*_e) on the straight isotropic Normal Compression Line are shown in Figure 4-15. The same normalisation is carried out on the natural material to remove the effects of volume on the strength. Gens (1982) showed that for samples compressed along different effective stress paths by varying the ratios of the vertical to the horizontal stresses, the undrained shearing paths form Local Boundary Surfaces (*LBS*) which are within an outer State Boundary Surface (*SBS*). The State Boundary Surface plotted in Figure 4-15 is based on the undrained tests and probably therefore represents a Local Boundary Surface, *LBS**; further drained tests would be required to identify the outer *SBS**.

4.4 Natural properties

4.4.1 Compression behaviour

Five oedometer tests have been carried out on samples of natural Oxford clay and the compression curves for these tests are shown in Figures 4-16 to 4-20. As can be seen, there is no noticeable yield point for any of the three tests regardless of the stresses they were compressed to and in all cases there is a significant swelling. The high swelling capacity of stiff clays often results from the presence of swelling minerals such as smectite or intense fissuring in the soil mass (Cotecchia, 2007). But Oxford clay contains only traces of smectite or other swelling minerals. Oxford clay is also highly laminated by bedding but it is not intensely fissured. Comparing the swelling lines in Figure 4-16 suggests that compressing the soil to high pressures did not cause much destructuration with the unloading lines being almost parallel.

Figures 4-17 and 4-18 compare tests on samples of natural and reconstituted Oxford clay. The natural sample just passes above the *ICL** line at very high effective stresses and does not show significant structure based on the sensitivity framework. The swelling lines for the two tests are almost parallel resulting in a swell sensitivity ($S_s = C_s^*/C_s$) of around unity ($S_s = 1.3$), indicating that either considerable destructuration occurred during the compression or there was little structure in the sample initially. Since the swelling lines for tests compressed to different stress levels are parallel, the latter may be the case. The swelling is normally expected to be much more significant in the reconstituted material due to the absence of strong structure. These tests were normalised for volume using the void index, I_v (Figure 4-18). Similar behaviour is observed in the normalised plot with no significant sign of structure in compression with compression curves heading towards SCL at very high pressures. The alternative method of normalisation proposed by Gasparre & Coop (2008), which takes the swelling lines into account, can not be applied here as the swelling lines are parallel for the natural material regardless of the level of compression. Although these compression tests show no significant structure, as will be shown later in this chapter the effect of structure is evident in the shearing behaviour.

Two oedometer tests were carried out on horizontally cut samples, Figure 4-19. The two tests were started at similar state and were compressed to different stress levels followed by swelling to lower stresses. Yielding occurs at the same stress level for both tests with compression lines that are parallel to each other. However the swelling line for the sample compressed to the higher stress is steeper than the swelling line for the sample compressed to the lower stress. These compression curves also show a clearer yield in comparison with the vertically cut samples (Figure 4-20). Both the clearer yield and the change in the slope of the swelling line indicate the existence of structure in the horizontal direction. As mentioned earlier, the highly bedded nature of Oxford clay is its dominant micro- and macro-structure the effects of which can be seen in the tests capturing this element.

4.4.2 Shearing behaviour

a) Large strain behaviour

Triaxial tests were carried out on natural Oxford clay samples at different stress levels and on different sample sizes. Figures 4-21 to 4-28 show the effective stress paths, stress-strain curves, pore water pressure changes, and failure envelopes developed in these tests. Also as a part of this research two MSc students conducted their projects on the residual strength of stiff clays using the ring shear apparatus (Narayana, 2010; Cunliffe, 2010). A Bishop ring shear apparatus was used on remoulded material and a Bromhead ring shear apparatus was used to test natural samples. The results of these tests will be presented in this section.

The first test carried out on Oxford clay was a drained test in extension. The intention was to establish the passive failure envelope so it could be avoided for the stress paths to reach the in-situ state. Other samples were isotropically consolidated from their initial state, of between p'= 200 kPa and p'= 340 kPa to p'=250 kPa. Then they followed a constant p' path to reach the in-situ state mentioned in Section 4.2.3. To avoid serious disturbance by taking the sample too close to the passive failure there were two limits imposed on the strains developed during this anisotropic path; the volumetric strain $\varepsilon_v \leq 1\%$ and the axial strain $\varepsilon_a \leq 0.5\%$. These limits were reached at q =-100kPa well before the in-situ state. Therefore the samples were held at this stress state before being sheared in compression or extension. The tests which are labelled as 'in-situ' represent tests from this state.

To determine the failure envelope, tests were also carried out at different isotropic stress levels. Medium stresses could be reached using the normal 100 mm or 38 mm sample size cells, with the limit of cell pressure around 800kPa. For the higher stresses the high pressure cell was employed with sample size of 50 mm in diameter. The effective stress paths for all the tests in compression are shown in Figure 4-21. There was no particular reason why one test showed a slightly higher strength. All the samples developed a strain localisation with a single shear plane with angles varying between 50 and 65 degrees to the horizontal. To observe the effects of swelling on the strength of the soil, one sample was swelled back to p'=50kPa and was sheared in

compression. As can be seen, from the graph this effective stress path reaches the tension cut off line and follows this line to failure. Figure 4-22 shows the effective stress paths for various sample sizes with no definite change in strength based on the sample size. This can be caused by lack of prominent joints and fissures within the samples and dominance of the bedding structure. However, more tests on 100 mm in diameter samples are required to further investigate this.

The comparison between tests sheared in compression and extension can be seen in Figure 4-23. The tests in extension (both drained and undrained) failed on a sub horizontal shear plane with 13 degrees inclination to the horizontal. They also reached a slightly lower strength which may indicate the dominant effect of bedding and presence of weak horizontal layers within the soil.

Figures 4-24 and 4-25 show the stress-strain behaviour of all these tests. The high brittleness is an important factor to be considered when any design is to be done on this material (Burland et al., 1977). Figure 4-26 shows the normalised graph of stress ratio plotted against axial strain. The q/p' value at peak, as well as at post rupture, tends to be higher for tests performed at lower stresses. The stress ratios for different tests do not tend to converge to a unique value at this level of strain. It should be noticed that due to the strain localisation the M value can not be calculated for the natural samples.

The pore water pressure distribution in the samples was investigated by comparing the measurements at the base and mid-height of the sample. Figure 4-27 shows an example of change in pore water pressure at the base and mid-height of the sample. The pore water pressure was uniformly distributed, with both measurements being almost identical, until the formation of the shear plane. The shear plane formation was associated with a higher pore water pressure in the mid-height of the sample, which is in agreement with studies carried out by Sandroni (1977) and Gasparre (2005).

Mohr's circles were constructed for each test by taking the stress values at peak and post rupture. By drawing a line from the pole with the shear plane inclination, the shear stress on this plane can be calculated (Section 3.5.5). This analysis has been

done for all tests, and the peak strength and post rupture strength envelopes for Oxford clay can be obtained (Figure 4-28). As was mentioned earlier the stress ratios were lower for tests at higher stresses, this can be seen in the curved failure envelopes presented in the figure. For the tests performed at lower stresses, the internal angle of shearing resistance at post rupture is around $\phi'_{pr} = 26.5°$. The critical state envelope from the reconstituted tests is plotted in this figure. As can be seen, the post-rupture envelope and the Critical State Line (from reconstituted tests) are very close to each other with slightly higher strengths for the post-rupture at lower stress levels and lower strengths at higher stresses. The lower post rupture strength at higher strength can be attributed to rapid loss of structure and rearrangement of particles towards the residual strength.

Three tests have been carried out on horizontally cut samples, two of which were tested by MSc and MEng students under the author's supervision and one by the author. The effective stress paths for these tests are shown in comparison with the vertically cut samples in Figure 4-29. A typical behaviour can be observed for stiff overconsolidated clays with effective stress paths for the vertically cut samples inclined to the left of vertical and the horizontally cut samples to the right of vertical. The stiffness anisotropy affects the slope of the effective stress path in undrained triaxial tests through Equation 4-1 (Lings, 2001):

$$\frac{\delta p'}{\delta q} = \frac{2E'_v / F'_h - 2(1 - \nu'_{vh})}{6E'_v / F'_h + 3(1 - 4\nu'_{vh})} \qquad \text{(Equation 4-1)}$$

where E'_v is the vertical Young's modulus, ν'_{vh} is the Poisson's ratio for horizontal strain due to vertical strain and F'_h is a horizontal modulus ($= E'_h / (1 - \nu'_{hh})$). These parameters were obtained through small strain drained probes and will be presented later in this chapter. Using these parameters the value for $\delta p' / \delta q$ was calculated to be -0.31 for the vertically cut samples which is in very good agreement with the value measured from the slope of effective stress paths (-0.32).

As discussed earlier the highly brittle behaviour of Oxford clay can result in progressive failure with the strength falling rapidly from high peak values to very low residual strengths at large strains. Therefore it is important to measure the residual strength as well as the peak and post rupture strengths. Figures 4-30 and 4-31 show the results of ring shear tests on Oxford clay, carried out by MSc students for their final project (Narayana, 2010; Cunliffe, 2010). The first figure shows the residual angle of shearing resistance, ϕ'_r, plotted against shear displacement divided by sample height for the small range of displacements. The rates used at this stage of shearing were 0.01mm/min for the remoulded sample, 0.024mm/min for the slow test on an natural sample and 0.267mm/min for the fast test on an natural sample. These tests were carried out under 400 kPa normal stress.

The peak strength is slightly higher for the remoulded sample, $\phi'_p = 22.5°$, compared to the peak strength of the natural samples, $\phi'_p = 20°$. The contrary is normally expected as the structure in the natural material should result in a higher peak strength. One reason behind the lower peak strength for the natural samples could be the sample preparation method. The natural samples were cut to only 5 mm thickness which could have resulted in significant destructuration. It should also be noted that due to the strain non-uniformities in the ring shear apparatus the values of the peak shear strength are not very accurate. The shearing rate affects the stiffness of the natural material tested without any alteration in their peak or post peak strength. At large displacements (Figure 4-31) both remoulded and natural tests are in a good agreement, both resulting in a residual angle of shearing resistance, $\phi'_r = 10°$. This value is lower than $\phi'_r = 13°$ which was reported by Burland et al. (1977), who tested their soil in a shear box apparatus which probably did not cause as much particle orientation as in the ring shear test.

b) Effects of structure at large strains

The comparison between natural and reconstituted samples was made to investigate the effects of structure on the strength and stiffness of the Oxford clay. Figure 4-32 shows the stress ratio, q/p', plotted against axial strain for the natural and reconstituted samples. The peak strength is almost double for the natural material

compared to the reconstituted samples, with a much greater brittleness caused by the structure. However, as discussed earlier the stress ratio, q/p', for the natural samples falls rapidly from the peak and reaches a value close to the reconstituted value ($M \approx 1$). Also the behaviour is much stiffer for the natural samples in comparison with the normally consolidated reconstituted samples. The difference is less significant when comparing the overconsolidated reconstituted sample with the natural samples.

The effective stress paths for both natural and reconstituted samples can be seen in Figure 4-33. The natural failure envelope is located well above the reconstituted one. However, it should be noted that these samples had different void ratios at the time of shearing and normalisation for the volume is required. All the effective stress paths were normalised by the equivalent pressure, p'^*_e, on the intrinsic isotropic Normal Compression Line, Figure 4-34. The structure allows the natural samples to pass the intrinsic *SBS** and form a natural *SBS* above it. Only the dry side of the natural *SBS* could be located as none of the samples were tested at high enough pressures to determine the wet side.

c) Pre-failure behaviour

High resolution local instrumentation enabled the investigation of soil behaviour at the small strain levels. In this section the stiffness of Oxford clay at small strains will be covered. Stiffness degradation curves for Oxford clay are shown in Figure 4-35, with undrained vertical Young's modulus, E^u_v, plotted against axial strain, ε_a. E^u_v was preferred to shear modulus, G, as it is a direct measurement with no assumptions or errors involved in calculating the shear strains. Tests sheared at different stress levels were chosen to highlight the effects of stress level on the stiffness. The stress:strain behaviour is highly non-linear with a very small linear range resulting in a plateau in the stiffness curves until roughly 0.005% axial strain. Any elasticity of the material requires load-unload tests to be examined which can not be seen in this graph.

The stiffness is affected by different factors including strain level and stress level. The relationship between the stiffness and the stress level was proposed by Wroth & Houlsby (1985) to be:

$$\frac{G}{p_r} = A\left(\frac{p'}{p_r}\right)^n \qquad \text{(Equation 4-2)}$$

where A and n are dimensionless parameters depending on the nature of the soil and the current strain. p_r is a reference pressure (= 1kPa) so that parameters A and n will be dimensionless. To study these two factors, the logarithm of stiffness values for contours of equal strain level were plotted against their current mean effective stress, (Figure 4-36). It should be noticed that the above equation is derived for the normally consolidated soil and *OCR* and void ratio should also be included in the equation (Ni, 1987). However, for sake of comparison with other works, the 'n' value from Equation 4-2 is used for the stress level exponent of the stiffness. Viggiani & Atkinson (1995) suggested that the 'n' value in Equation 4-2 increases with the strain level, reaching n = 1 at large strains when G is proportional to p'. The same trend was reported by Jardine (1994) when compiling 'n' values for various soils. However, Hird & Pierpoint (1997) found that the 'n' value for the Oxford clay is constant at different strain levels and is 0.67. The results from the current project show a slight reduction in 'n' for the larger strains, which is in contrary to the widely believed behaviour considering the frictional behaviour of the soil.

The stiffness values for horizontally and vertically cut samples are shown in Figure 4-37. As mentioned earlier the stiffness is much higher in the horizontal direction and this can be seen in the direction of the undrained effective stress paths.

Typical bender element signals in different directions are shown in Figures 4-38 to 4-40. Input signals with different frequencies between 6 and 10 kHz and the corresponding output signals are presented using a normalised amplitude. Figures 4-38 and 4-39 show signals used to measure the G_{hv} and G_{hh} values for a 38 mm in diameter sample and Figure 4-40 shows the signals used to obtain G_{vh} values for a 50 mm in diameter sample. The point at which the output signal ascends towards the highest amplitude has been selected as the first arrival time. A frequency domain analysis was also carried out using a code developed by Alvarado (2007). The results from both methods are shown in the figures and as can be seen, there is a difference in the arrival time obtained from two methods. The difference in stiffness calculated

using the two methods is around 20% with values being lower for those obtained using the frequency domain. This difference between the two methods has been reported by other authors (e.g. Alvarado & Coop, 2011) and due to the complexities involved in the frequency domain analysis, the time domain method has widely been preferred (Section 3.5.6). As will be shown in Chapters 5 and 6 this difference between the two methods is insignificant for the Gault and Kimmeridge clays and for the sake of consistency the stiffness values presented here for the Oxford clay are obtained using the time domain approach.

The shear moduli in different directions are plotted against mean effective stress for the natural and reconstituted samples of Oxford clay in Figure 4-41. A significant anisotropy is evident with G_{hh} values higher than G_{vh} and G_{hv} values. It is also important to notice that, as expected, G_{vh} and G_{hv} are the same. The reconstituted sample shows a lower stiffness with larger changes with stress level. This is mainly due to difference in void ratios and the normalisation proposed by Jamiolkowski et al. (1991) based on $F(e) = e^{-1.3}$ removes most of this difference (Figure 4-42). Jovicic & Coop (1998) also used bender elements to investigate the stiffness anisotropy of London clay and found the inherent anisotropy as a more significant factor in comparison with the stress-induced anisotropy. They also observed that the degree of anisotropy is not significantly changed for the range of stresses over which they tested their samples. Similar behaviour can be seen for Oxford clay with no significant change in the degree of anisotropy.

The bender element data show that both G_{hh} and G_{hv} (also G_{vh}) increase with stress level with a similar value of $n = 0.49$. This value is smaller than those obtained for the small strain levels in undrained shearing (presented in Figure 4-36) and is closer to the value corresponding to larger strain levels. Factors which may have caused this variation are the drained and undrained nature of the tests, static and dynamic testing and different shearing rates used but more investigation is needed to support this.

As discussed earlier in Sections 2.4 and 3.4.2, drained elastic parameters can be obtained by carrying out small strain probes; all the parameters measured using different probes are presented in Table 4-6. Changes in the stresses and strains during an axial probe are shown in Figures 4-43 and 4-44. The change in the axial stress

during the compression test was 1.5 kPa and 2.5 kPa in the extension test. As can be seen, the behaviour is not fully elastic with some non-recoverable strains. By considering the initial linear part of the loading curves the Y_1 surface has been identified and is shown on the graphs. This point occurs at approximately 0.001 % axial strain and 1 kPa axial stress change. The behaviour appears slightly stiffer in the extension test with a higher E'_v. The total change in the radial strains was around 0.001 % for both probes and in both cases they were fully recoverable. Results from the radial probes in compression and extension are shown in Figures 4-45 and 4-46. As was expected the behaviour was stiffer in the horizontal direction. The strains in the extension test were fully reversible showing a fully elastic behaviour up to 0.002 % radial strain and 4 kPa change in the radial stress. However the test in compression was not completely elastic, although it showed a slightly stiffer response (Table 4-6). It should be noted that in the elastic region the stiffness should be unique in loading and unloading probes, the difference which was shown here could be due to an experimental error or it could be part of the soil behaviour. The change in the axial strains is only plotted for the test in compression as the axial LVDTs were not functioning well during the extension test.

As mentioned earlier in Section 2.4 the compliance matrix can also be written in terms of G', K', and J. The equations relating these parameters and the five drained elastic parameters are presented in Section 3.4.2, and values based on these equations are presented in Table 4-6. To check the probing programme and validate the measured and calculated parameters, two probes were conducted, one keeping p' constant and one keeping q constant and both in compression. These probes are shown in Figures 4-47 to 4-50 and the moduli measured from them are presented in Table 4-6. The values measured and calculated for the G' and K' are close and there is a good agreement between the two measured coupling moduli (J_{qp} and J_{pq}), but the calculated J values based on the elastic parameters is much higher than the measured ones. With the exception of the latter case, the other results were reassuring for the probing programme.

4.5 Summary

Some geotechnical aspects of Oxford clay have been investigated in the current chapter. A short summary of the previous studies on this material was presented with highlighting shortcomings related to the significant excess pore water pressure developing during drained stress probes and the effect of creep rate on the stiffness measurements.

Oxford clay is highly laminated by bedding but it is not intensely fissured. Samples compressed to different stress levels did not show a significant yield point with their swelling lines being parallel regardless of the stresses they were compressed to. Comparisons between compression and swelling lines for the natural and reconstituted samples were made, resulting in a swell sensitivity of around unity, indicating that either considerable destructuration occurred during the compression or there was little structure in the sample initially. This confusing behaviour was better understood when horizontally cut samples were compressed to different stress levels; both the clearer yield point and the change in the slope of the swelling lines indicate the existence of structure in the horizontal direction.

The comparison between triaxial tests carried out on the natural and the reconstituted samples was made to investigate the effects of structure on the strength and stiffness of the Oxford clay. The peak strength was almost double for the natural material compared to the reconstituted samples, with a much greater brittleness caused by the structure. The structure allowed the natural samples to pass the intrinsic *SBS** and form a natural *SBS* above it. All the natural samples tested in compression developed a strain localisation with a single shear plane with angles varying between 50 and 65 degrees to the horizontal. The tests in extension (both drained and undrained) failed on a sub horizontal shear plane with 13 degrees inclination to the horizontal. They also reached a slightly lower strength which may indicate the dominant effect of bedding and presence of weak horizontal layers within the soil. Due to lack of prominent joints and fissures within the samples and dominance of the bedding structure, sample size effect was not clear on the shear strength of Oxford clay.

Bender elements were employed to measure shear moduli of the soil at very small strain level; a significant anisotropy was evident for the natural Oxford clay with G_{hh} values higher than G_{vh} and G_{hv} values and with degree of anisotropy being almost constant regardless of the stress level. The difference between the G_{vh} values measured for the natural and the reconstituted samples were not significant when normalisation based on the volume was carried out, masking the effects of structure at small strain levels. Drained elastic parameters were obtained using small stress probes with good agreement between the parameters calculated based on different approaches.

Source	Site	Sampling Method	Lab tests
Parry (1972)	Stewartby Lake, 8 *km* south of Bedford	U-100 tube sampling	CD-TC (V); D-DSB (V,H)
Jackson & Fookes (1974)	Stewartby	Blocks	Oedo D-DSB (V,H)
Burland et al. (1977)	Wittlesey	BH- core drilling & blocks	CU & CD- TC (V,H); D-DSB (V)
Crabb & Atkinson (1991)	M1, junction 13 14 *km* SW of Bedford	Thin walled tube	TC
Rudrum (1990)	Elstow, 5 *km* South of Bedford	Rotary coring & blocks	UU & CU-TC (V,H); CD-TC (V); Oedo
Peirpoint (1996)	Elstow & Kempston brick pit	Block samples	CD-TC & TE (V); Oedo

* V: Vertically cut sample, H: Horizontally cut sample, TC: Triaxial Compression, TE: Triaxial Extension, CD: Consolidated Drained, UU: Unconsolidated Undrained, DSB: Direct Shear Box, Oedo: Oedometer test

a)

Source	γ (kN/m^3)	*LL* (%)	*PL* (%)	*CF* (%)	Activity
Parry (1972)	16.61-20.6	65-75	20-30	-	-
Jackson & Fookes (1974)	-	62-70	25-35	50-70	0.50-0.75
Burland et al. (1977)	19.9	55	24	≥ 55	-
Crabb & Atkinson (1991)	-	60	32	-	-
Rudrum (1990)	17-18.4	52-70	23-33	30-35	0.69-0.91
Peirpoint (1996)	18-19	-	-	-	-

b)

Source	c'_{peak} (*kPa*)	ϕ'_{peak} (*Deg*)	ϕ'_{r} (*Deg*)	S_u (*kPa*)
Parry (1972)	25	28-29	-	95-165
Jackson & Fookes (1974)	59-89	29-30	15-16	-
Burland et al. (1977)	-	27-28	13	50-1200
Crabb & Atkinson (1991)	-	25	-	-
Rudrum (1990)	6	26	-	20-66
Peirpoint (1996)	-	21-32	-	-

c)

Table 4-1: Summary of other research on Oxford clay; a) site locations, sampling type and testing plans, b) index properties, c) strength parameters

Bulk unit weight, γ	19 (kN/m^3)
Water table below ground level	1 (m)
Sample depth	10 (m)
Estimated in-situ σ'_v	102 (kPa)
K_0	3.2
p'	250 (kPa)
q	-223 (kPa)

Table 4-2: Estimation of the in-situ stress state (after Brosse, 2012)

Sample name	Sample type	Initial void ratio (e)	Maximum stress reached in compression σ_v' (kPa)
OXCL-RO-1	Reconstituted	1.8	6350
OXCL-RO-2	Reconstituted	1.87	1000
OXCL-NO-1	Natural-Block	0.6	27600
OXCL-NO-2	Natural-Block	0.6	13800
OXCL-NO-3	Natural-Block	0.6	3560
OXCL-NO-H1	H-cut-Natural-Block	0.6	8000
OXCL-NO-H2	H-cut-Natural-Block	0.62	27600

Table 4-3: Summary of oedometer tests on natural and reconstituted samples of Oxford clay

Sample name	Sample type	D (mm)	Effective stresses before shearing		Bender elements	Shear	Researcher (if not the author)
			p' (kPa)	q (kPa)			
OXCL-RT-1	Reconstituted	38	600	0		UC	Gao (2009)
OXCL-RT-2	Reconstituted	38	600	0		UC	Gao (2009)
OXCL-RT-3	Reconstituted	38	50	0		UC (OCR=10)	Gao (2009)
OXCL-RT-4	Reconstituted	50	1000	0	●	UC	Gao (2009)
OXCL-RT-5	Reconstituted	38	310	0		UC (OCR=2)	Gao (2009)
OXCL-NT-1	Natural-Block	100	200	0		DE	
OXCL-NT-2	Natural-Block	100	290	0	●	UC	
OXCL-NT-3	Natural-Block	100	250	-100	●	UE	
OXCL-NT-4	Natural-Block	38	360	0	●	UC	
OXCL-NT-5	Natural-Block	50	1000	0	●	UC	
OXCL-NT-6	Natural-Block	50	1300	0	●	UC	
OXCL-NT-7	Natural-Block	50	1800	0	●	UC	
OXCL-NT-8	Natural-Block	50	3000	0	●	UC	
OXCL-NT-9	Natural-Block	38	590	0	●	UC	
OXCL-NT-10	Natural-Block	38	50	0	●	UC	
OXCL-NT-11	Natural-Block	38	500	0		UC	
OXCL-NT-12	Natural-Block	38	650	0		UC	
OXCL-NT-13	Natural-Block	38	400	0		UC	
OXCL-NT-14	Natural-Block	38	270	0		UC	
OXCL-NT-15	Natural-Block	38	250	-100	●	UC	
OXCL-NT-16	H-cut-Natural-Block	100	360	0		UC	
OXCL-NT-17	H-cut-Natural-Block	38	200	0		UC	MSc & MEng lab class (2009)
OXCL-NT-18	H-cut-Natural-Block	38	100	0		UC	

Table 4-4: Summary of triaxial tests on natural and reconstituted samples of Oxford clay

φ'_{cs}	N*	Γ*	λ	κ	C_c^*	C_s^*
24.9 °	2.85	2.77	0.169	0.036	0.390	0.104

Table 4-5: Parameters measured for one-dimensionally and isotopically compressed reconstituted samples of Oxford clay

	Drained															Undrained		
Probe	**G_{hh}**	**G_{hv}**	**E'_v**	**E'_h**	**υ'_{vh}**	**υ'_{hv}**	**υ'_{hv}**	**υ'_{hh}**	**G'**	**G_{eq}**	**K'**	**K'**	**J_{qp}**	**J_{pq}**	**J**	**E^u_v**		**E^u_h**
	MPa	**MPa**	**MPa**	**MPa**		**Eq 2-6**	**Eq 3-18**		**MPa**	**Eq 3-26 MPa**	**MPa**	**Eq 3-27 MPa**	**MPa**	**MPa**	**Eq 3-28 MPa**	**MPa**	**Eq 3-29 MPa**	**Eq 3-30 MPa**
Bender elements	244	105																
axial probe compression			95		0.23													
axial probe extension			105		0.20													
radial probe compression				330		0.80	0.76	-0.32										
radial probe extension				312		0.6	0.78	-0.36										
p'cnst probe									42	43			105		365			
q cnst probe											112	113		112				
UC																200	145	365

Table 4-6: Elastic parameters derived from static probes



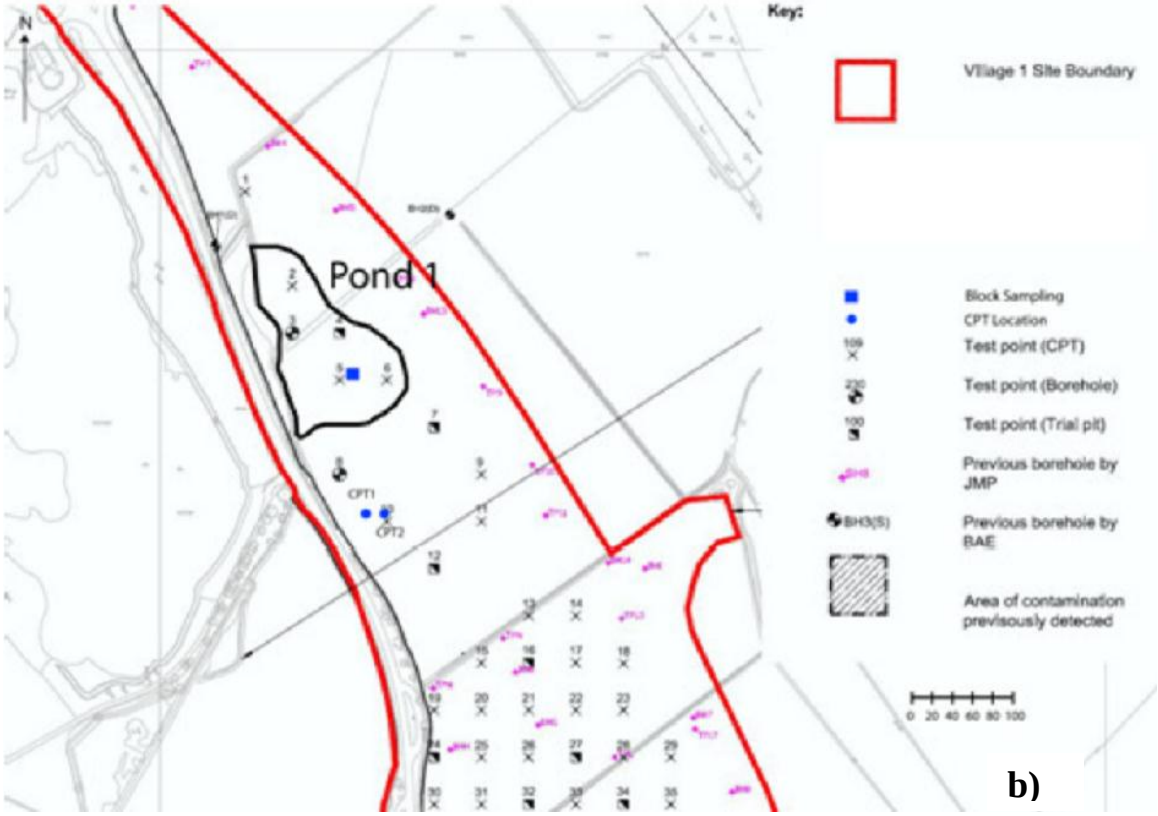


Figure 4-1: Sampling site for Oxford clay; a) map of Bedford and the site location at Elstow, b) field map of the Pond 1 and site investigations (after Wilkinson, 2011)

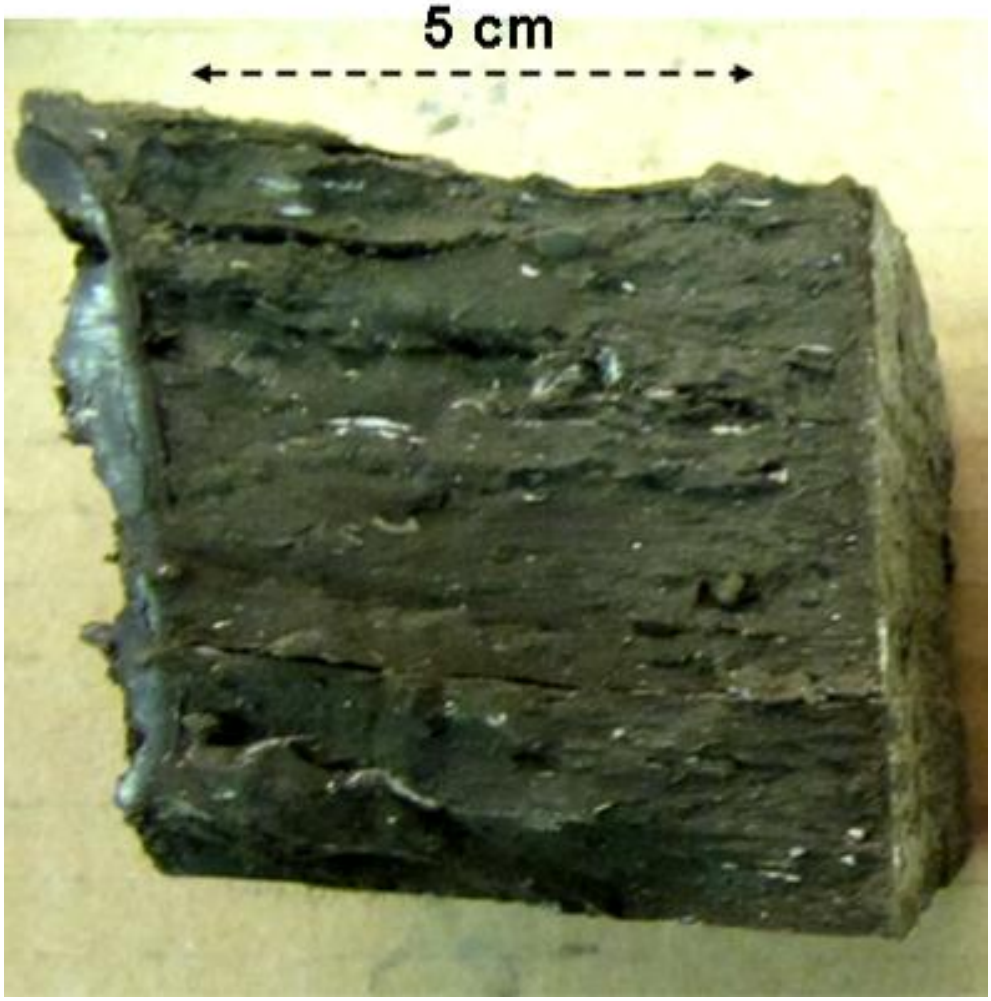


Figure 4-2: Vertical section of Oxford clay: dominance of horizontal lamination in structure

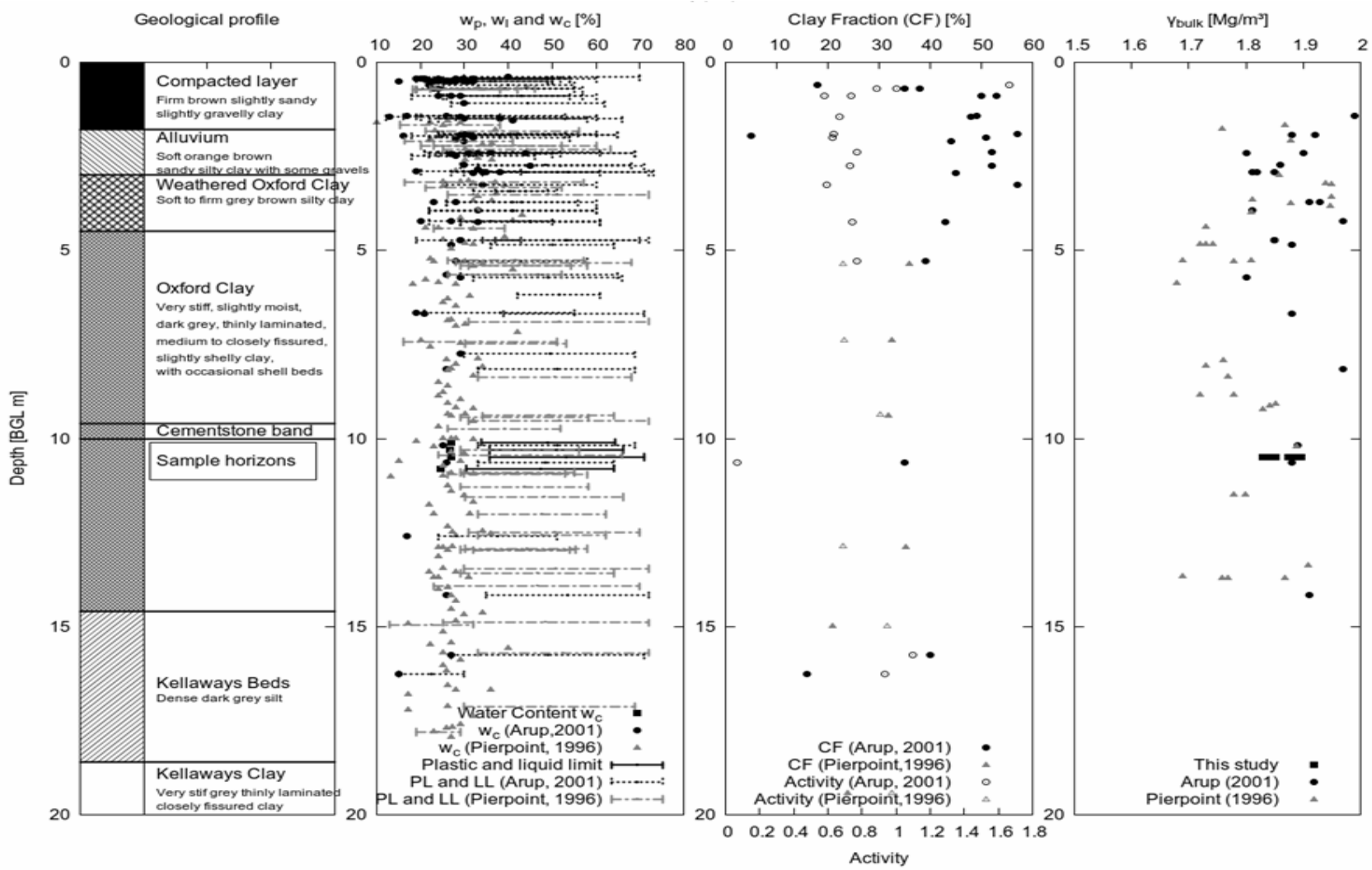


Figure 4-3: Soil profile at Elstow (Brosse, 2012)

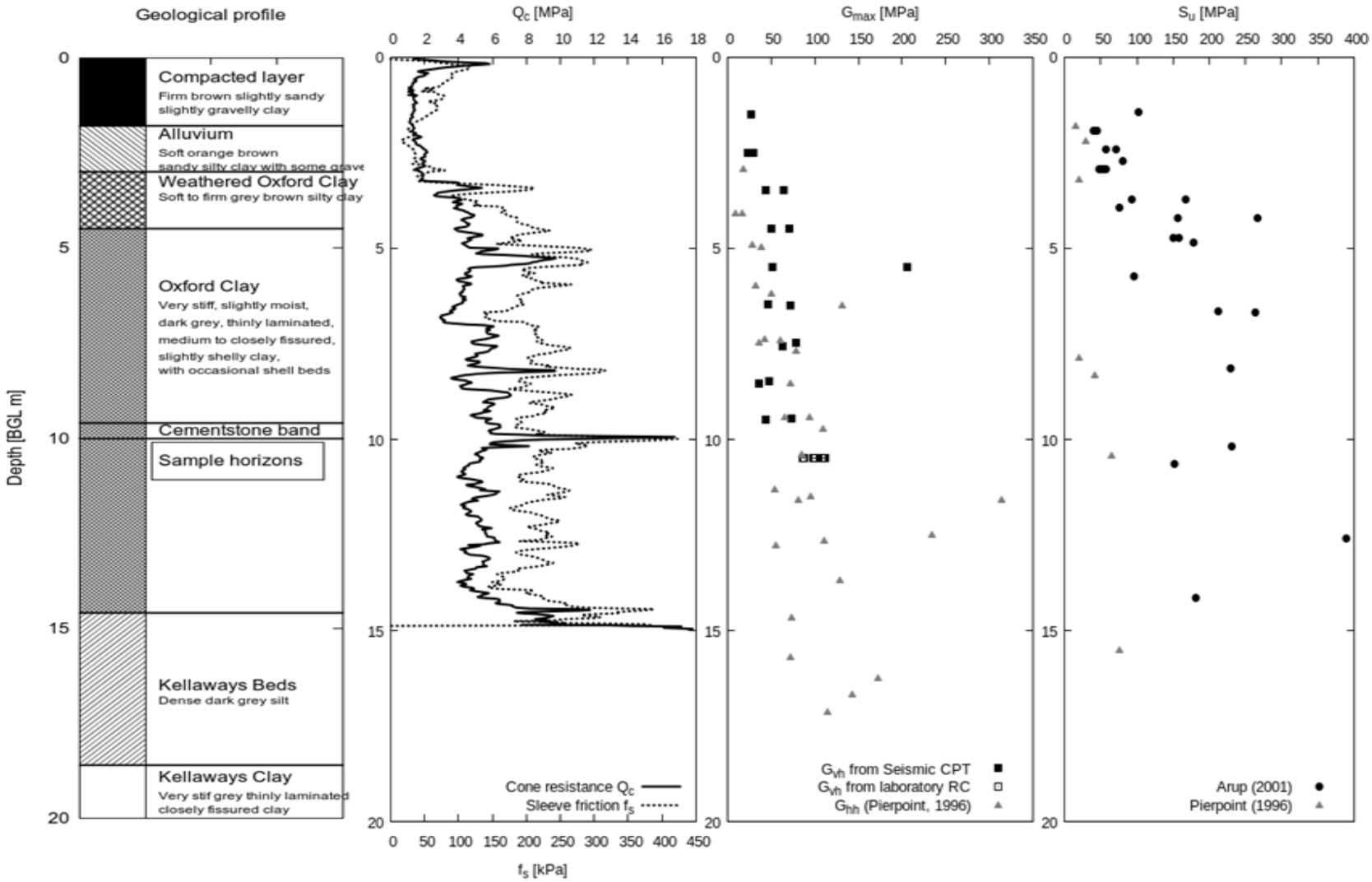


Figure 4-4: Soil profile at Elstow (Brosse, 2012, CPT data provided by In-situ SI)

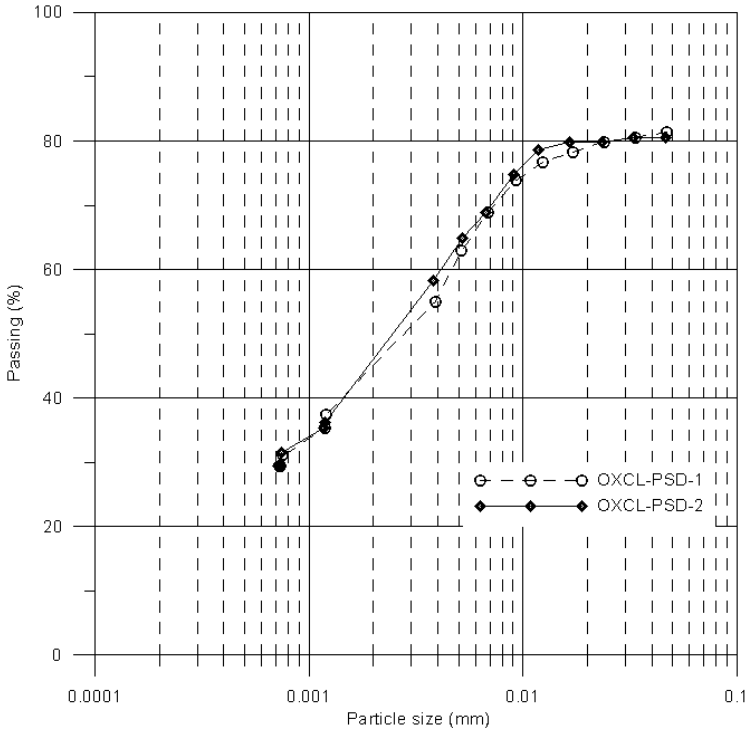


Figure 4-5: Particle size distribution of Oxford clay

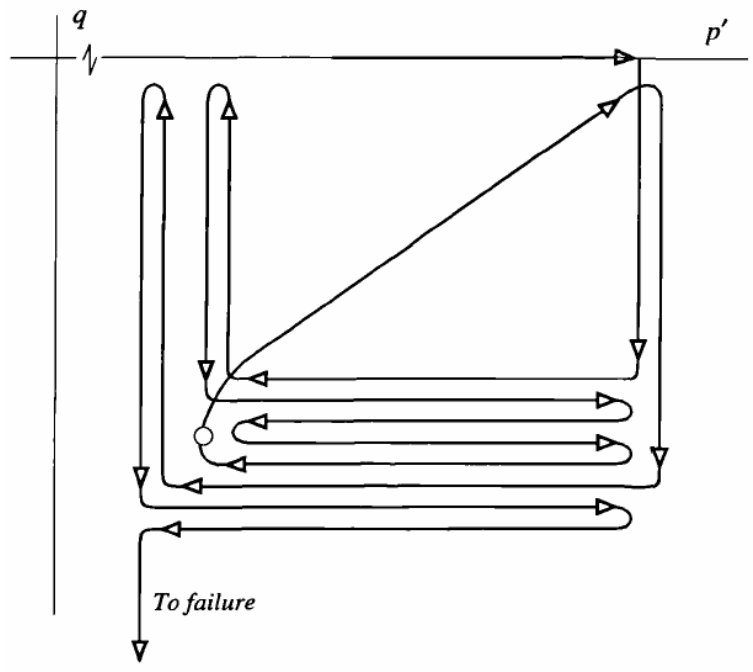


Figure 4-6: Multi-stage procedure to obtain stiffness parameters of Oxford clay at the in-situ stress state (Hird & Pierpoint, 1997)

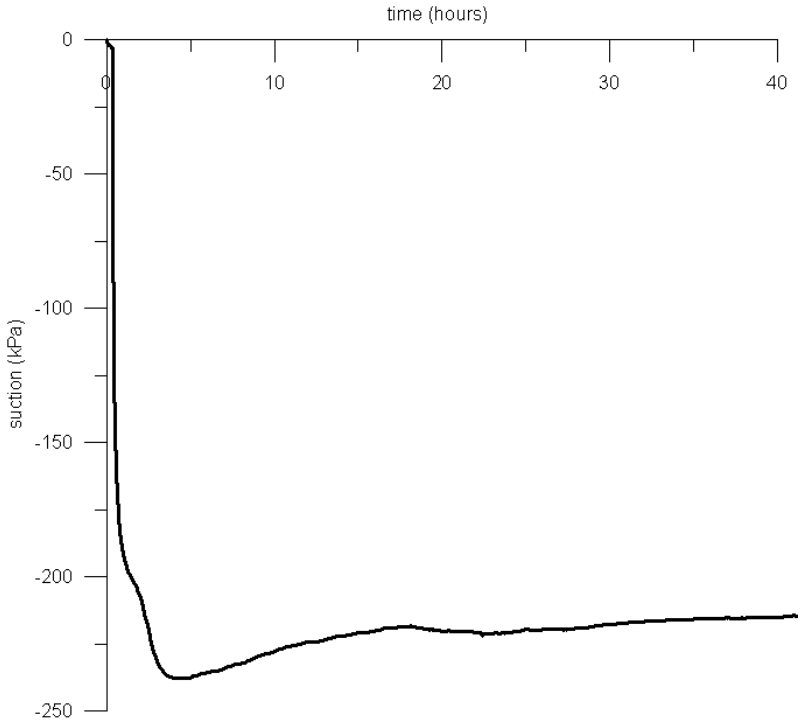


Figure 4-7: Suction measurment on a block sample of Oxford clay

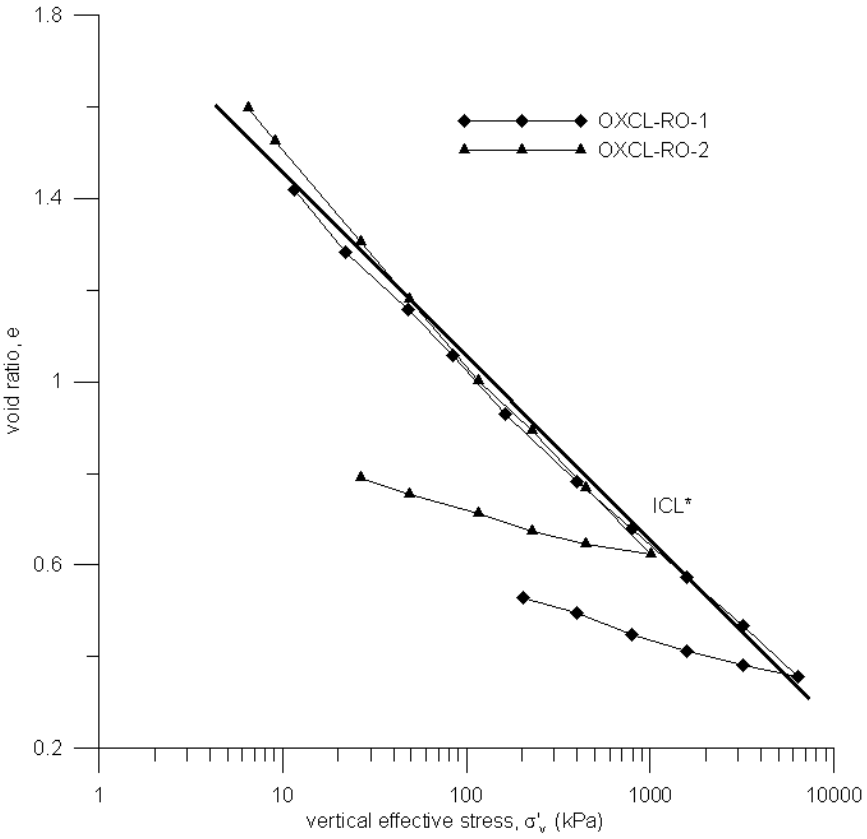


Figure 4-8: One-dimensional compression of reconstituted Oxford clay

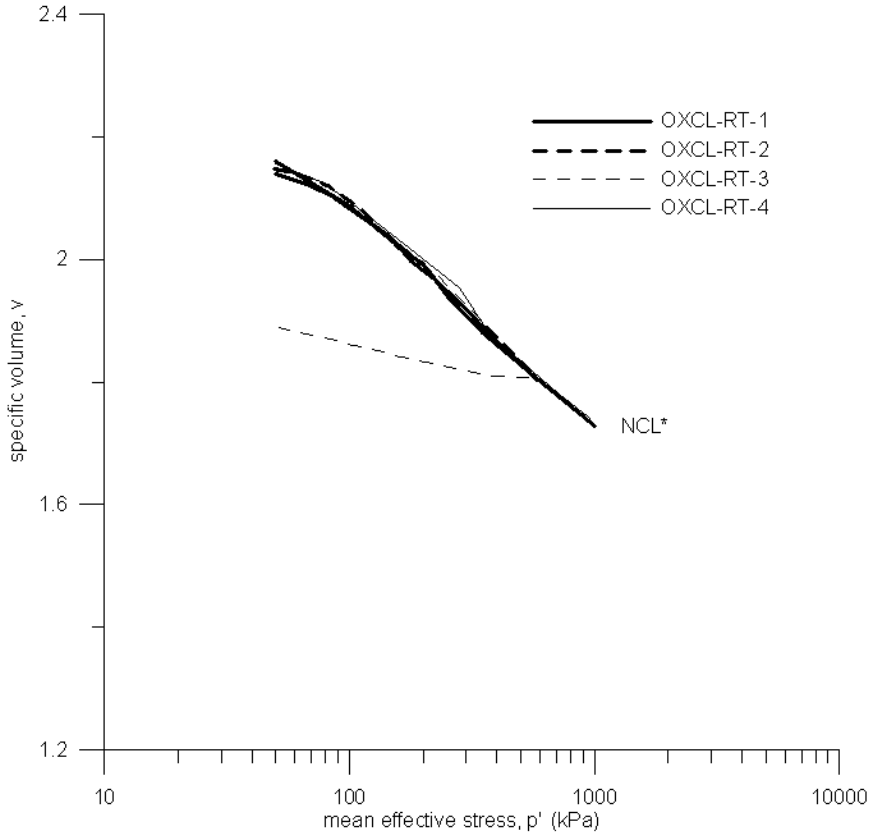


Figure 4-9: Isotropic compression of reconstituted Oxford clay

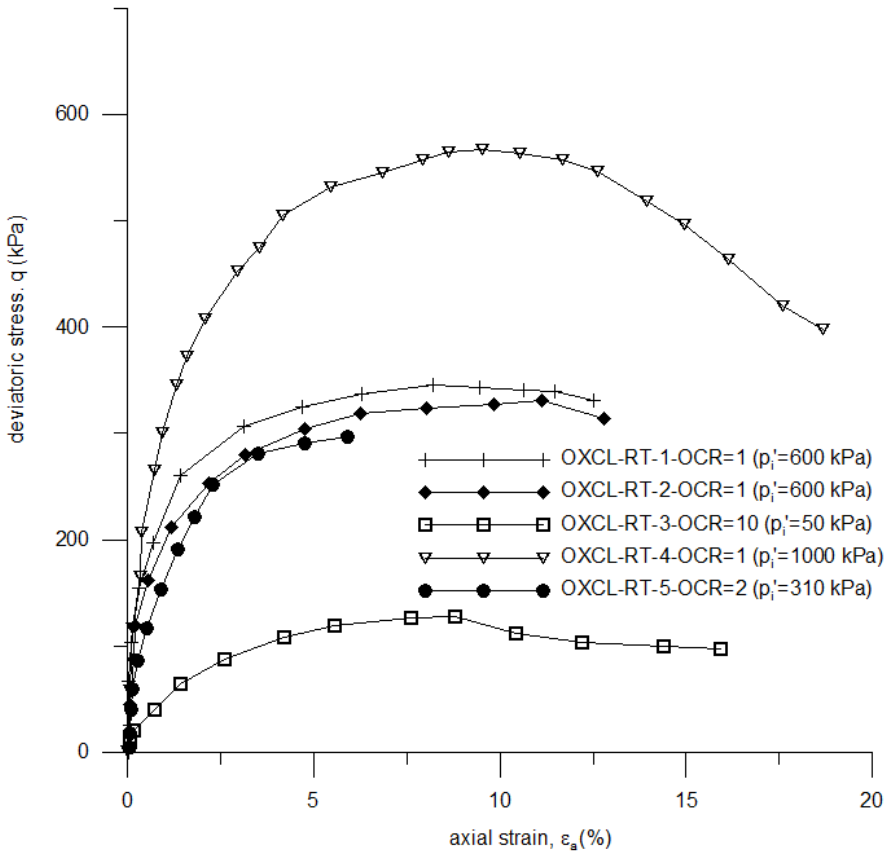


Figure 4-10: Stress-strain behaviour of reconstituted Oxford clay

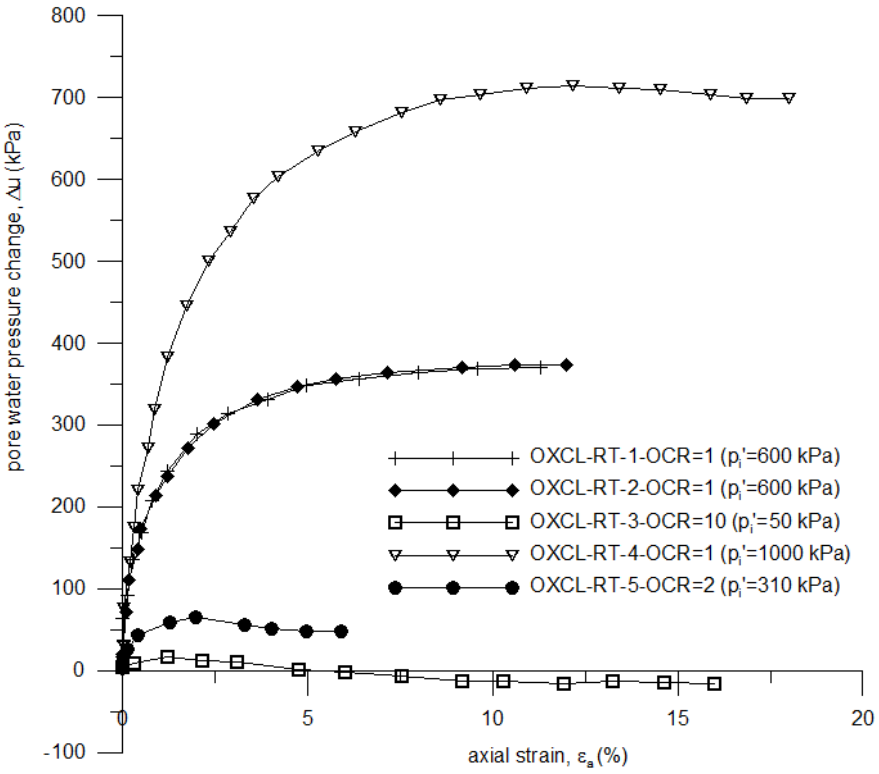


Figure 4-11: Pore water pressure change during the shearing of reconstituted Oxford clay

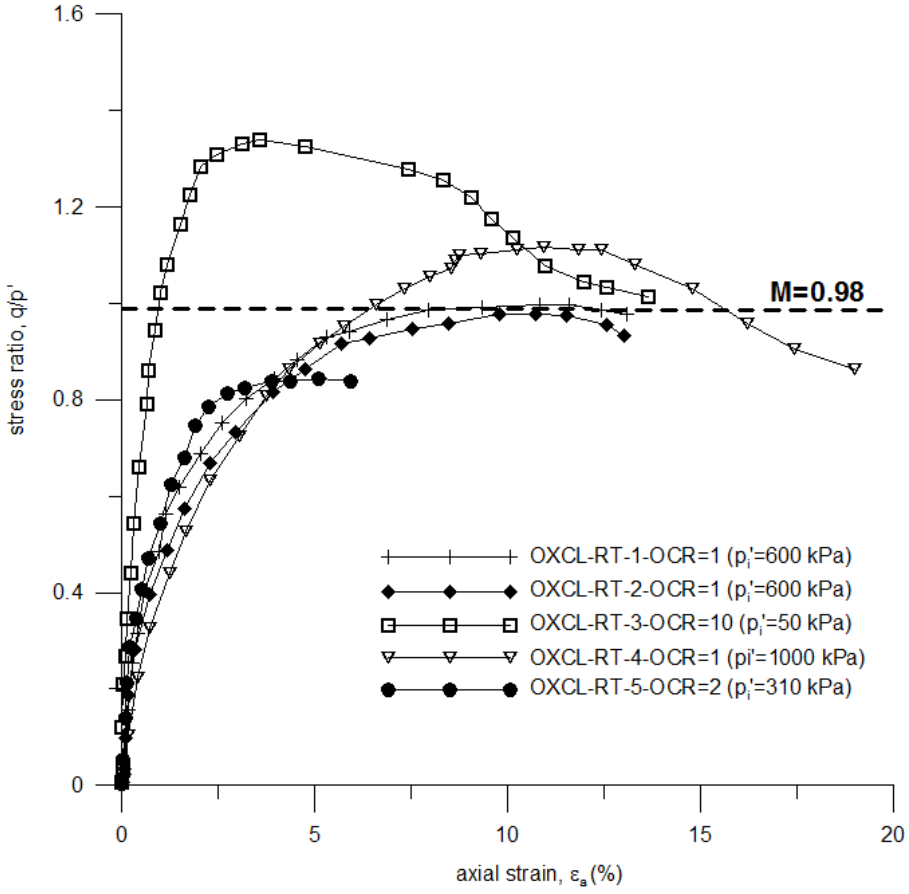


Figure 4-12: Normalised stress-strain behaviour of reconstituted Oxford clay

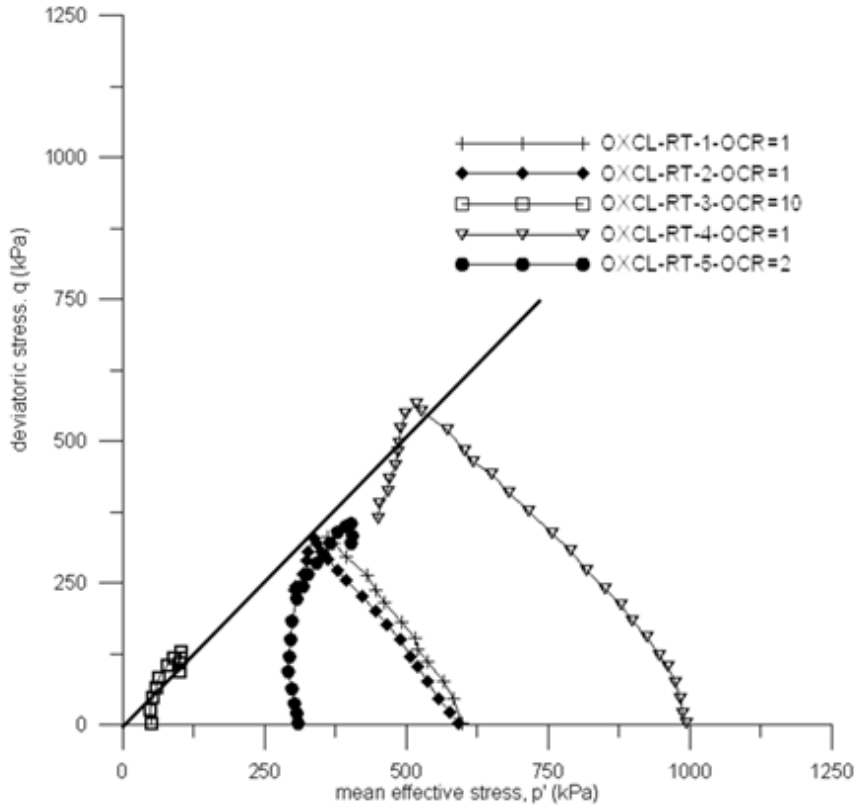


Figure 4-13: Effective stress paths for reconstituted isotropically consolidated Oxford clay

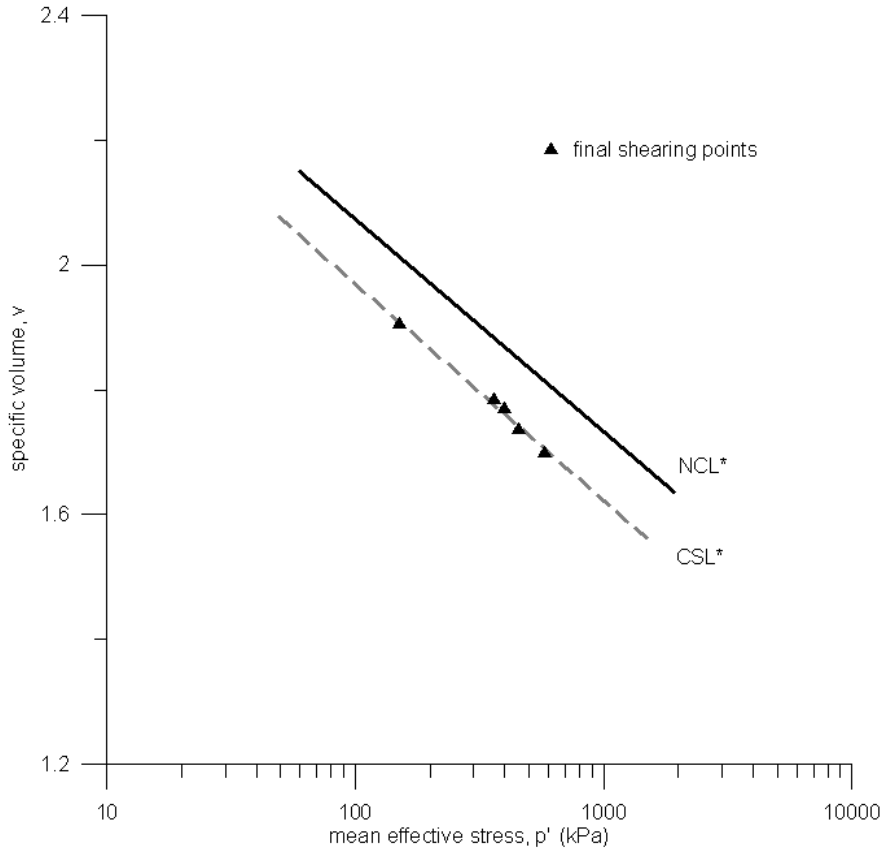


Figure 4-14: Normal Compression and Critical State Lines for reconstituted Oxford clay

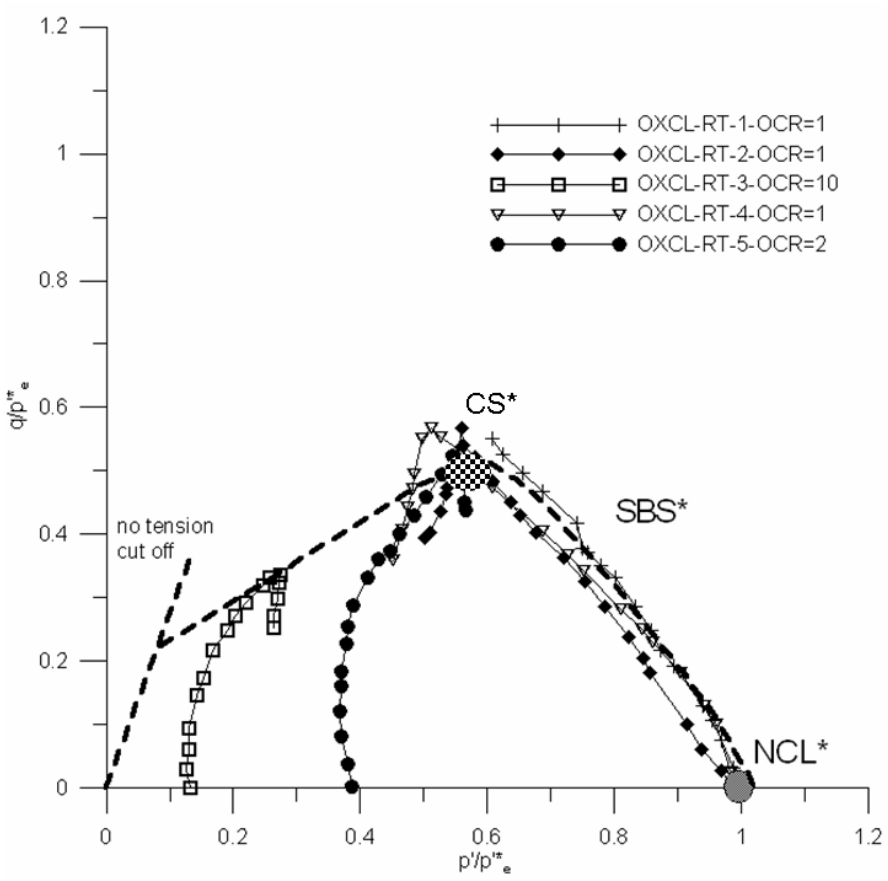


Figure 4-15: Normalised effective stress paths of reconstituted Oxford clay

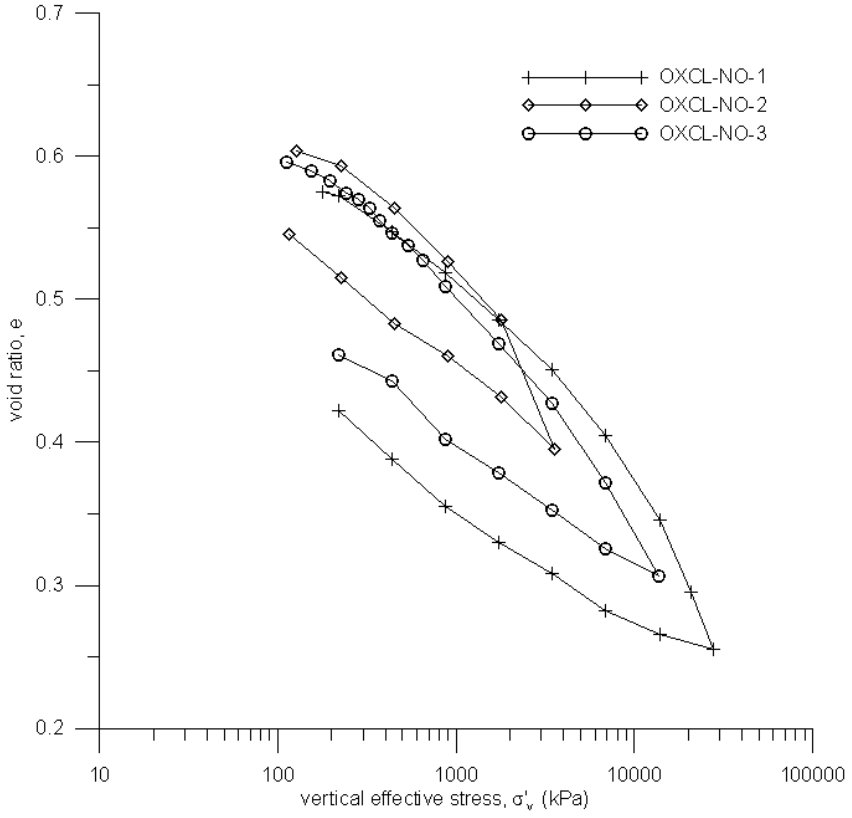


Figure 4-16: Compression curves of natural Oxford clay

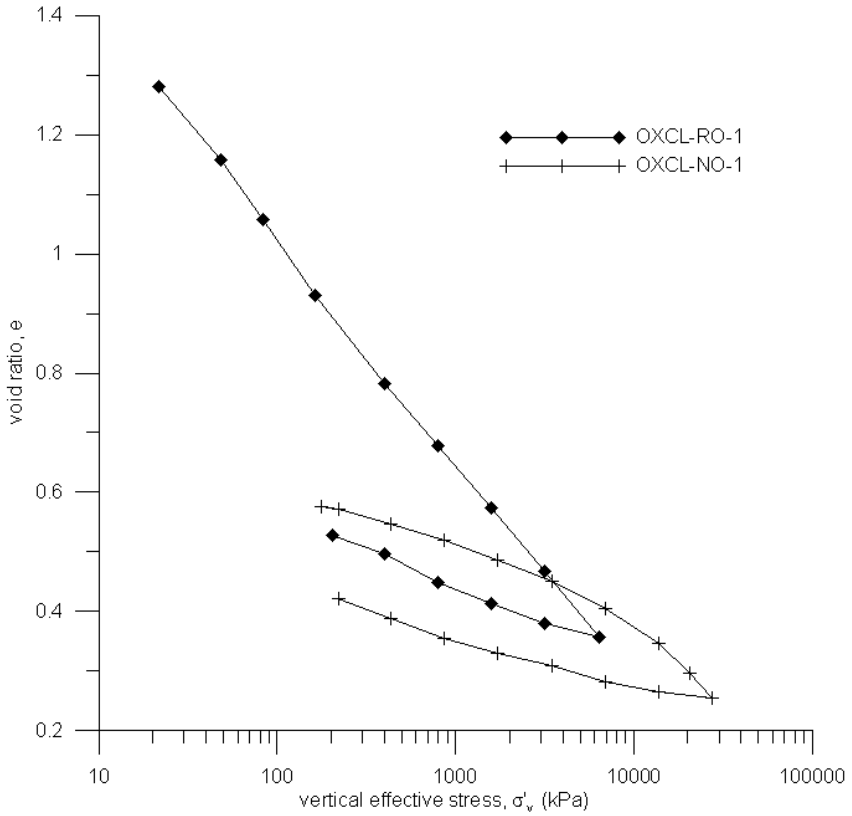


Figure 4-17: Compression lines for natural and reconstituted Oxford clay

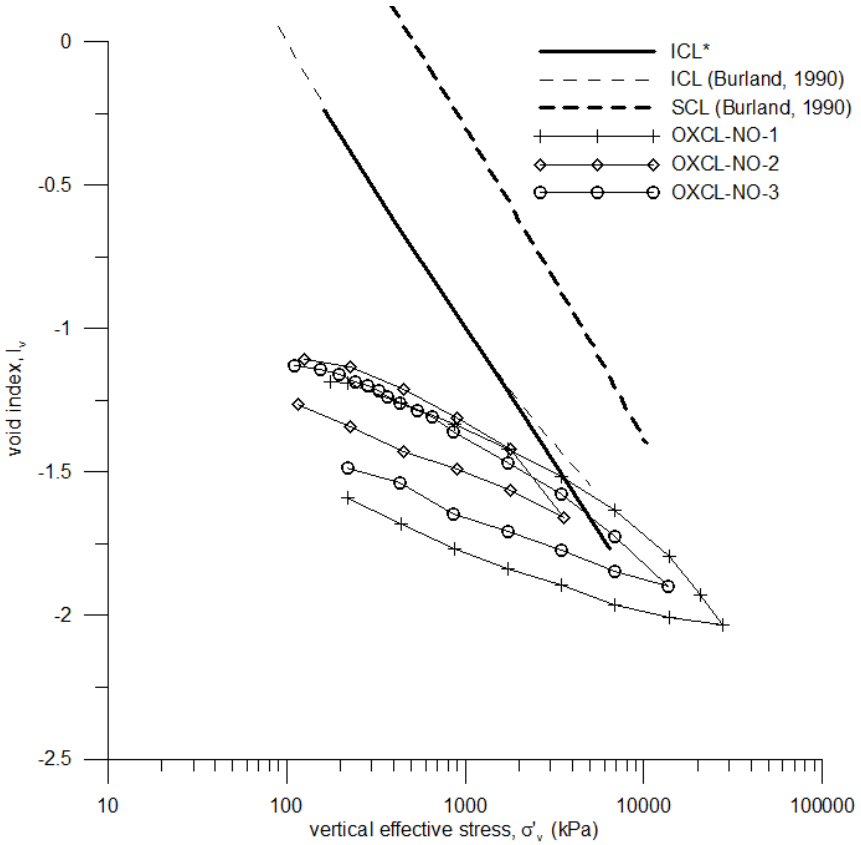


Figure 4-18: Normalised one-dimensional compression curves

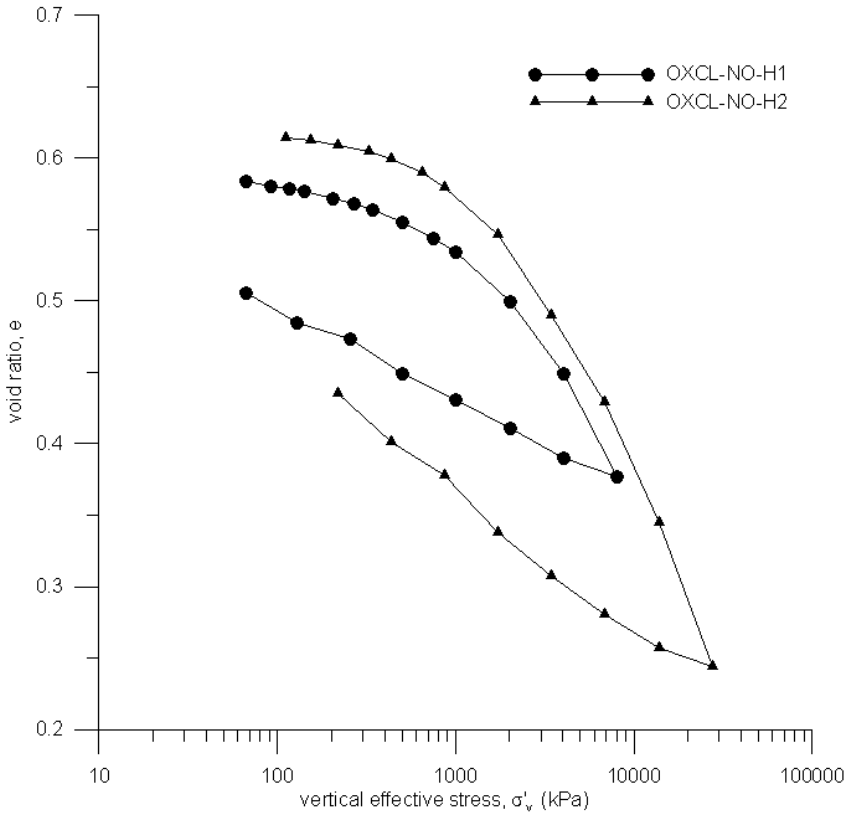


Figure 4-19: Compression curves of horizontally cut natural Oxford clay

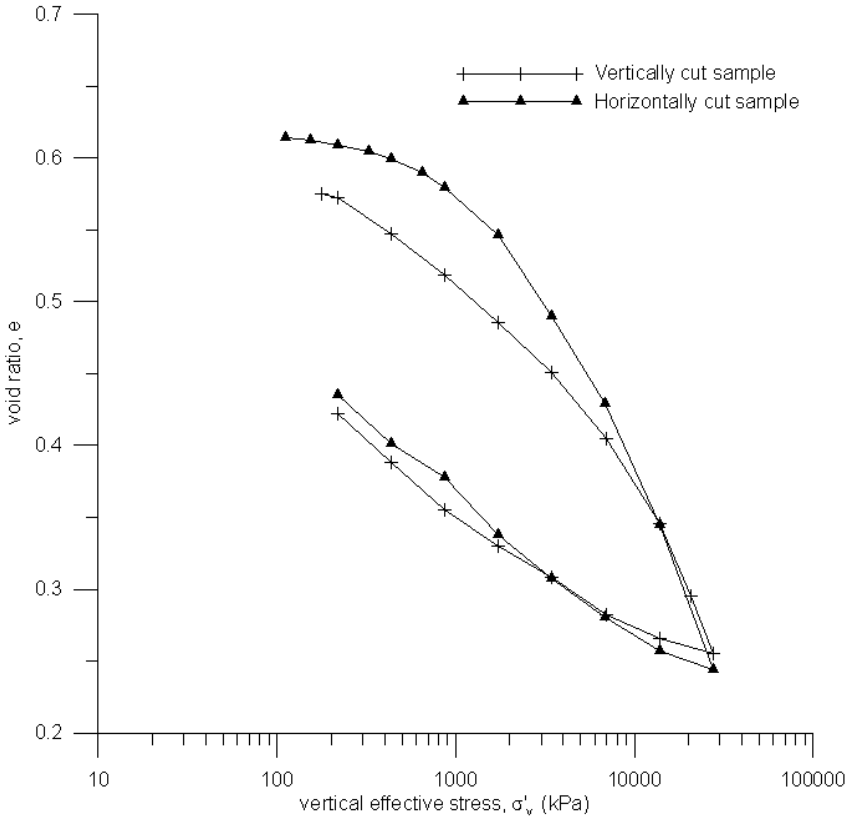


Figure 4-20: Comparison between compression curves of horizontally and vertically cut samples of Oxford clay

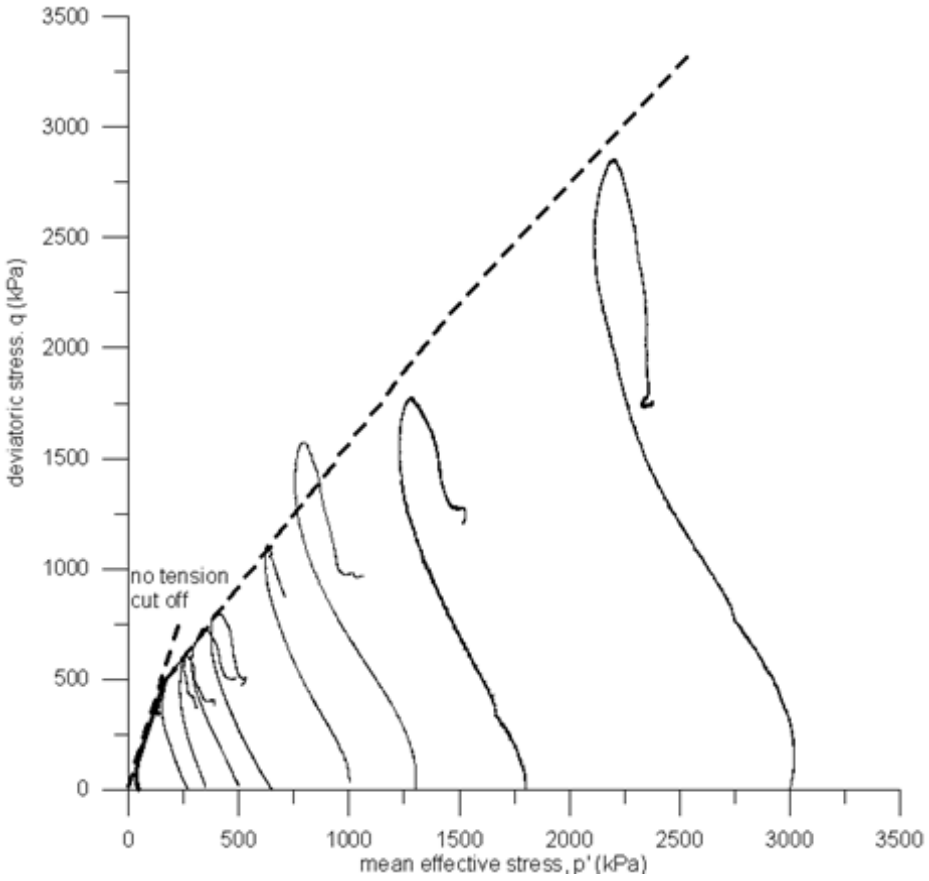


Figure 4-21: Effective stress paths for natural Oxford clay in compression

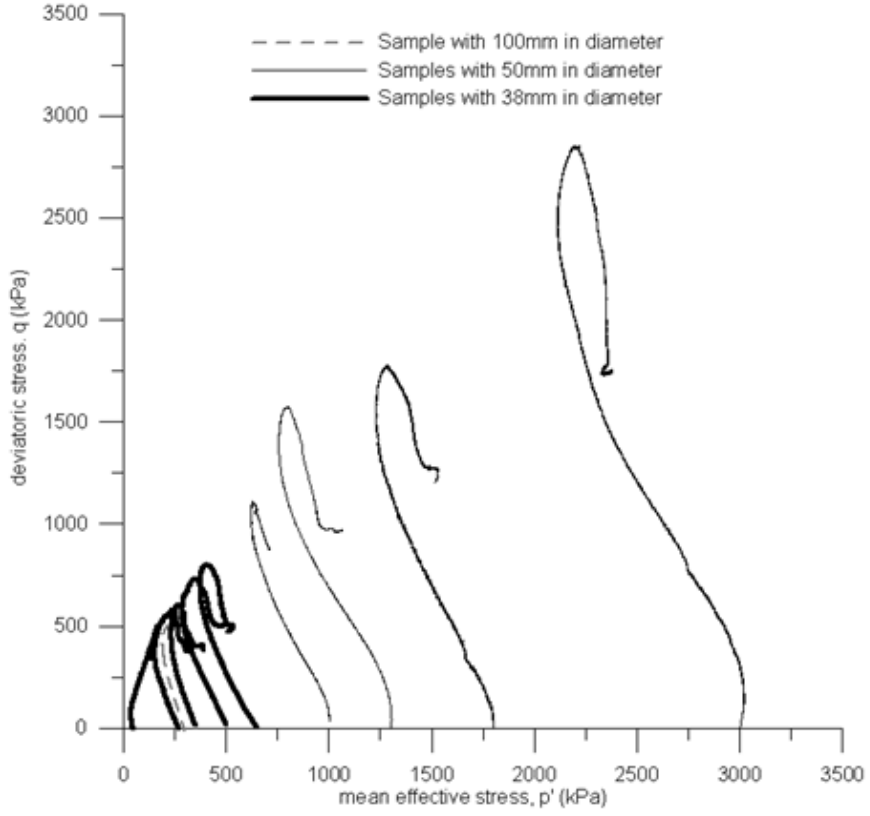


Figure 4-22: Effect of sample size on the strength of Oxford clay in compression

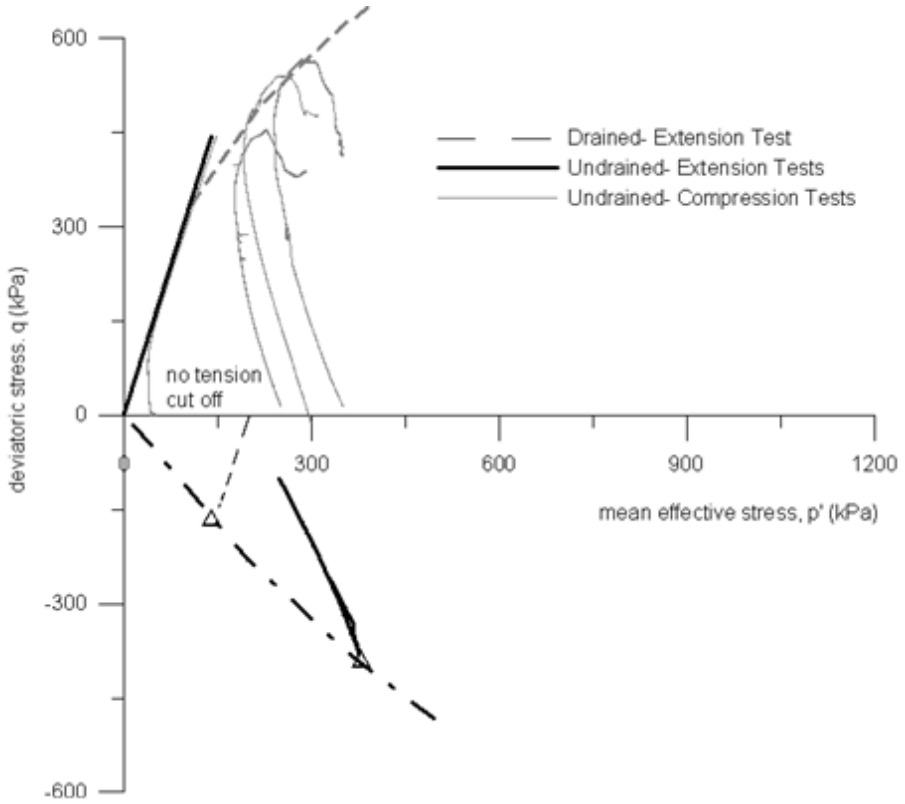


Figure 4-23: Effective stress paths for natural Oxford clay in compression and extension

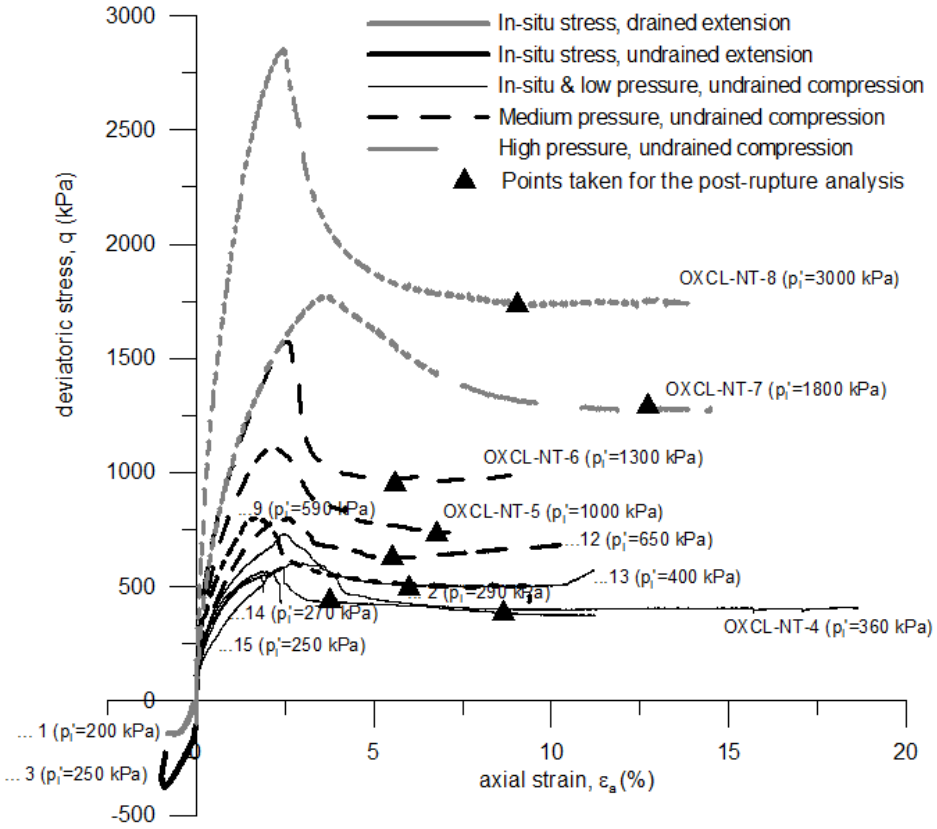


Figure 4-24: Stress-strain behaviour of natural Oxford clay

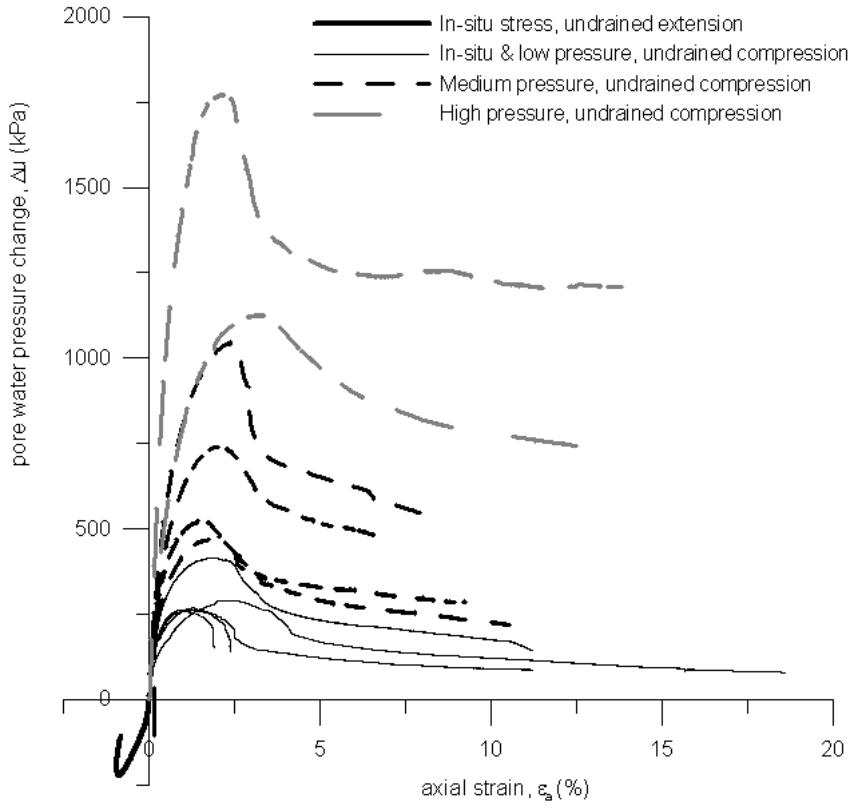


Figure 4-25: Pore water pressure change during the shearing of natural Oxford clay

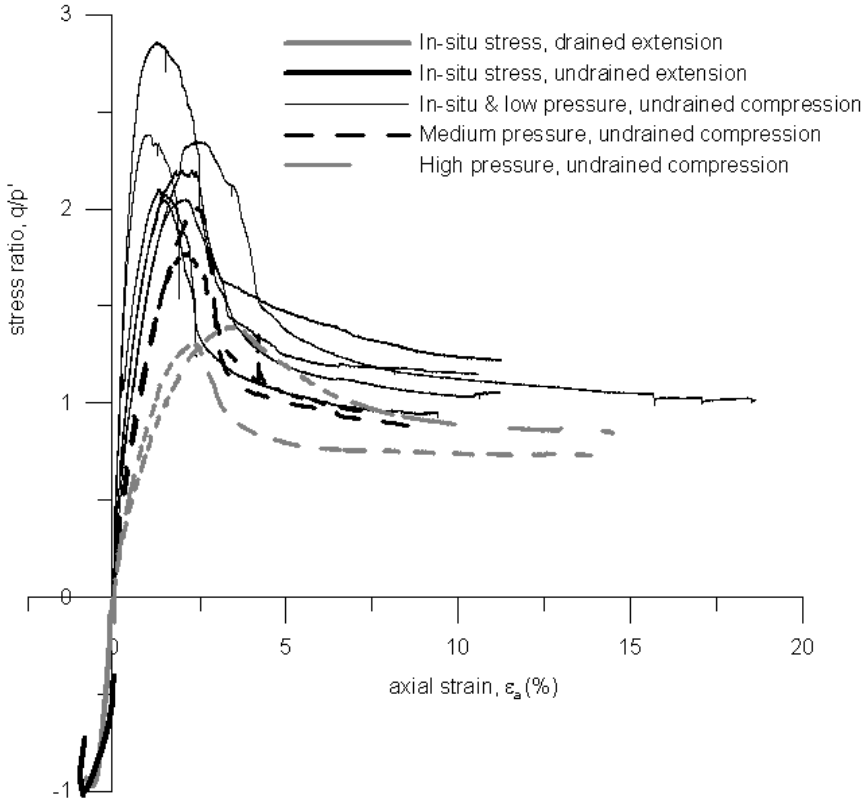


Figure 4-26: Normalised stress-strain behaviour of natural Oxford clay

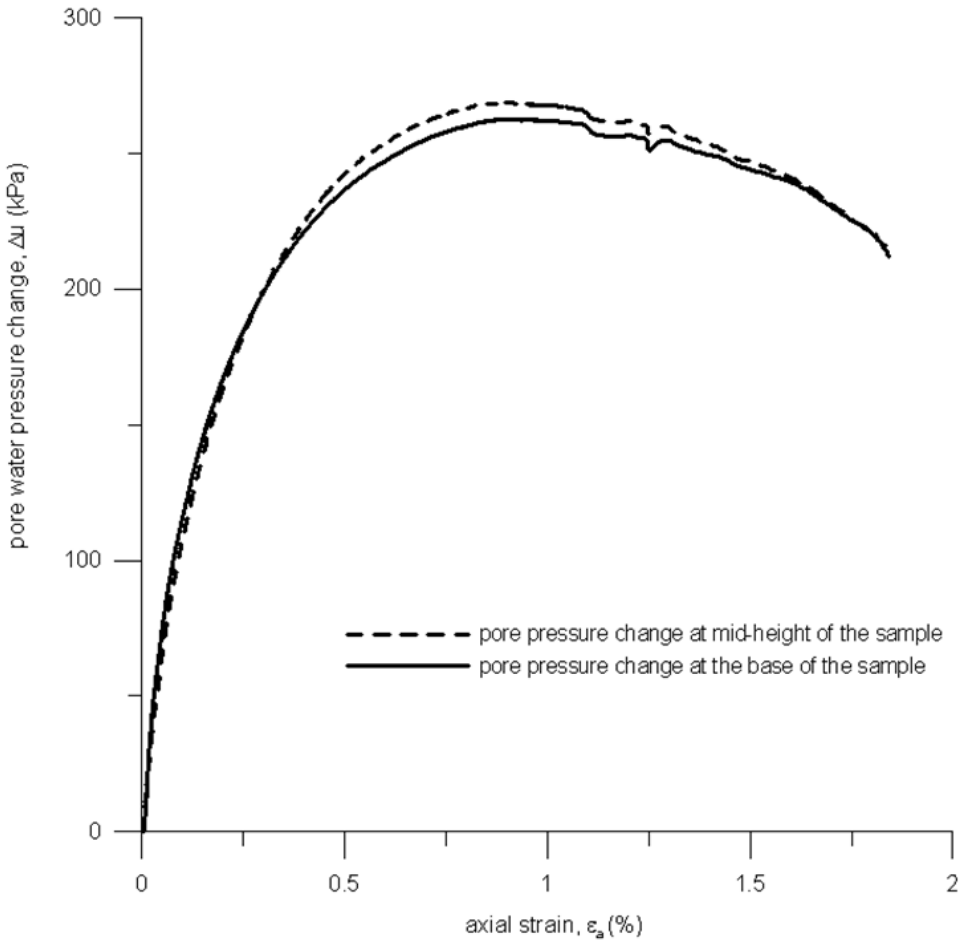


Figure 4-27: Pore water pressure change at the base and mid-height of a sample of natural Oxford clay sheared in compression

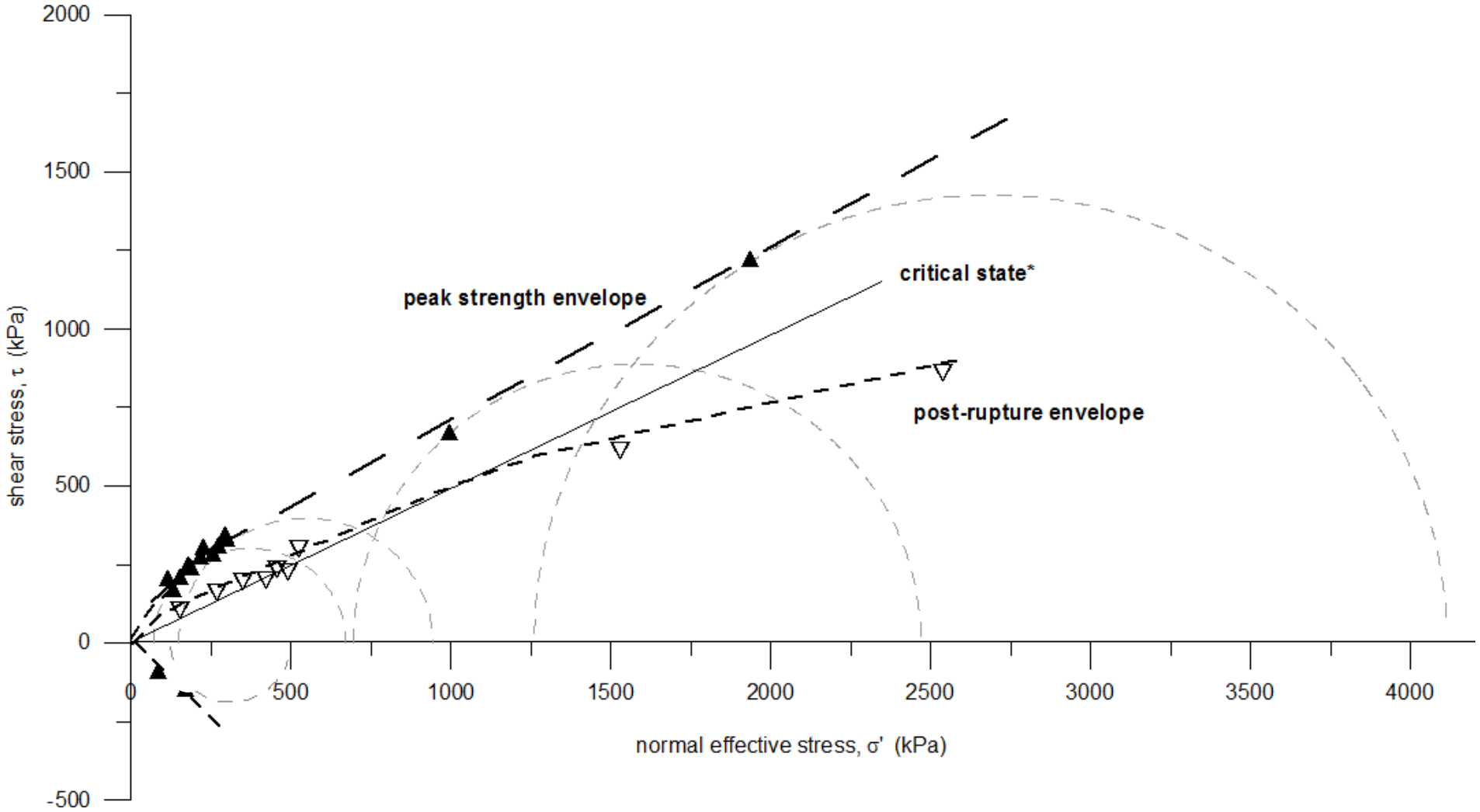


Figure 4-28: Peak and post-rupture strength envelope for natural Oxford clay

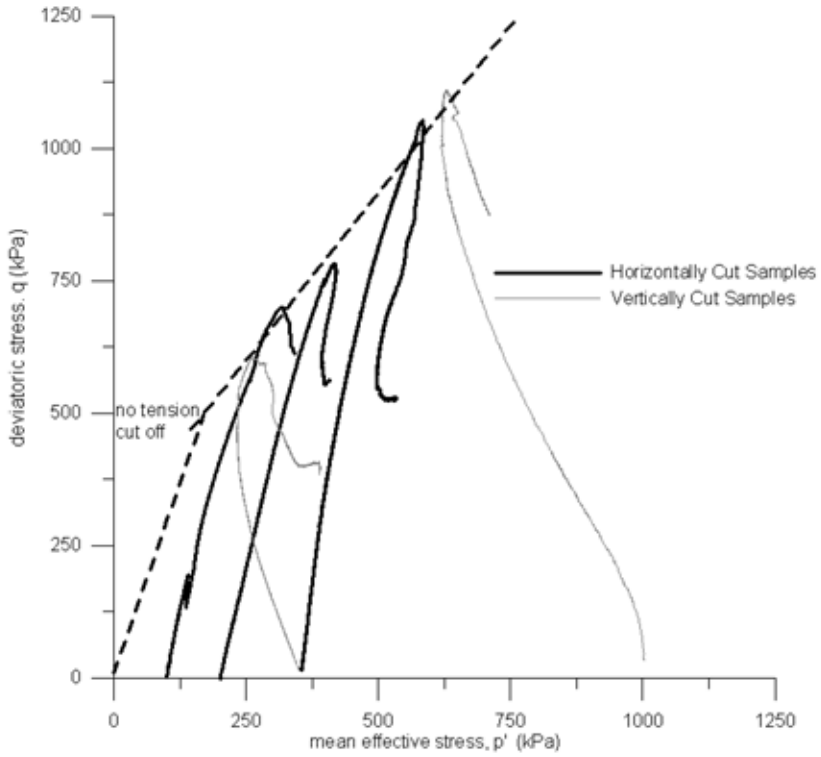


Figure 4-29: Effective stress paths of horizontally and vertically cut samples of natural Oxford clay

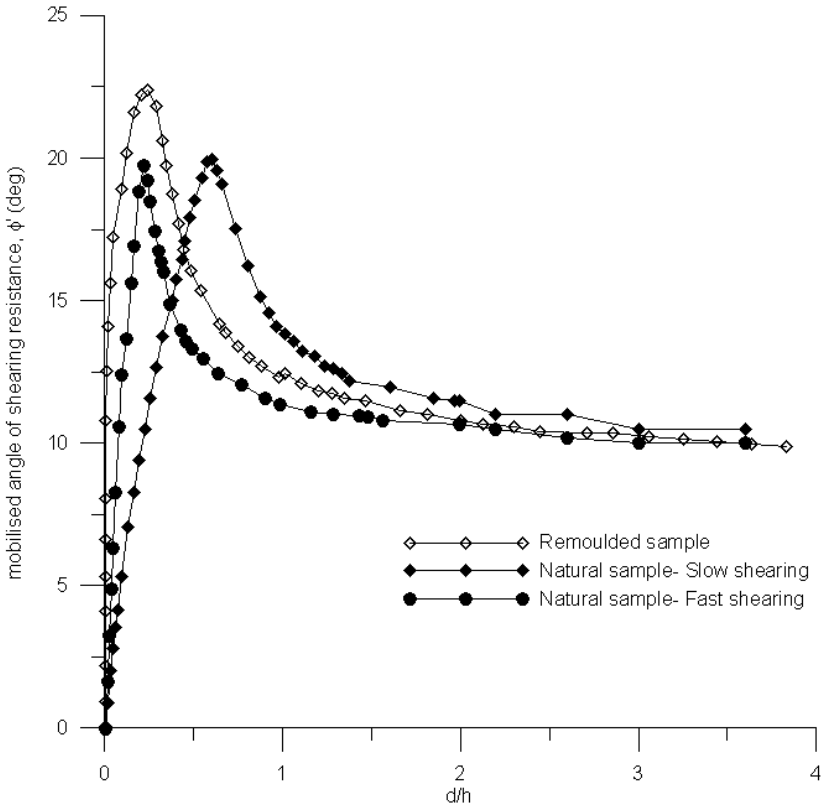


Figure 4-30: Stress-strain behaviour of natural and remoulded Oxford clay at small displacements in ring shear apparatus under 400 kPa normal stress (d = shear displacement, h = sample height)

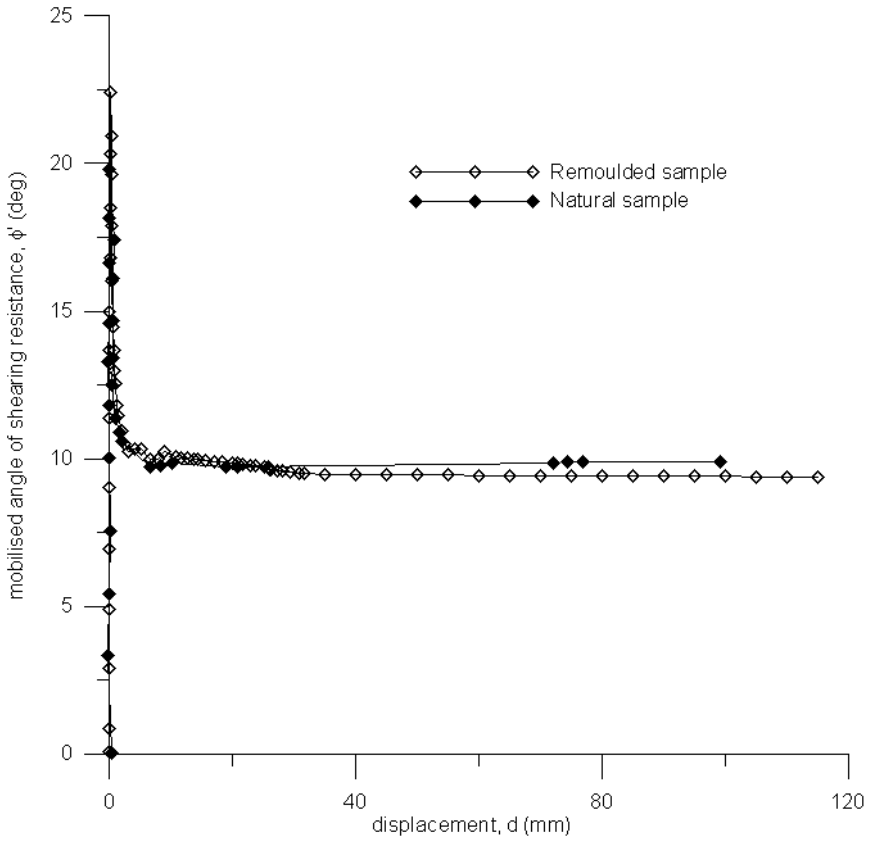


Figure 4-31: Stress-strain behaviour of natural and remoulded Oxford clay at large displacements in a ring shear apparatus under 400 kPa normal stress (d = shear displacement, h = sample height)

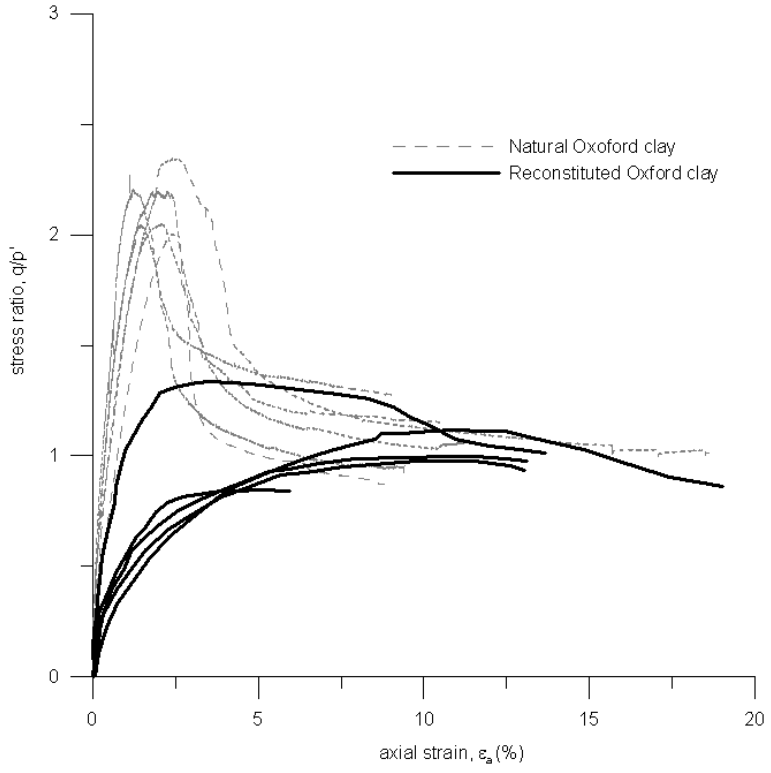


Figure 4-32: Normalised stress-strain behaviour for the natural and reconstituted Oxford clay

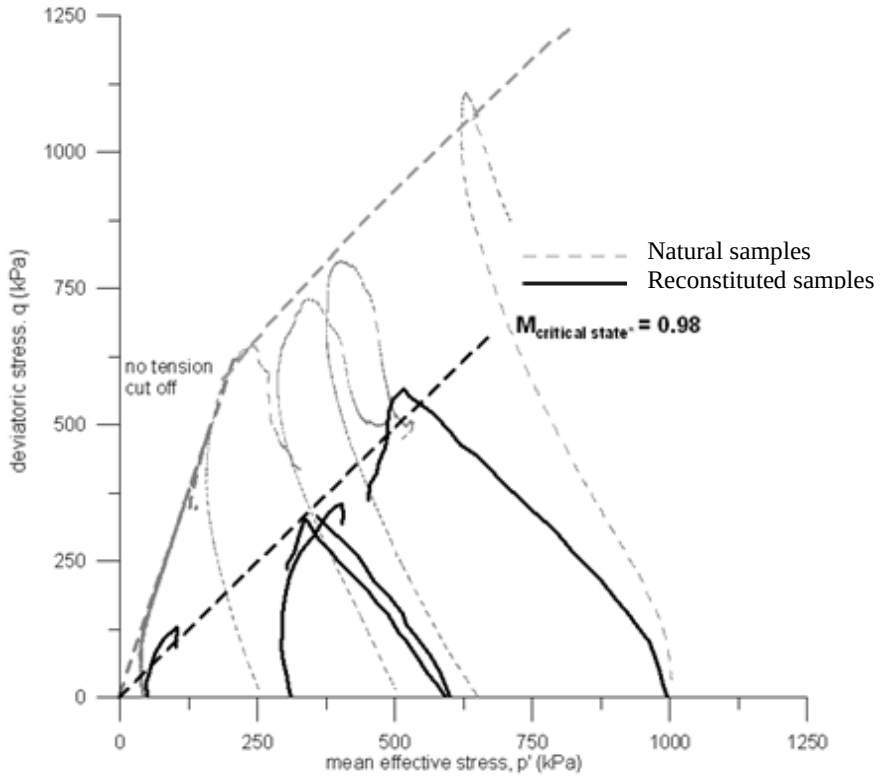


Figure 4-33: Effective stress paths for the natural and reconstituted Oxford clay

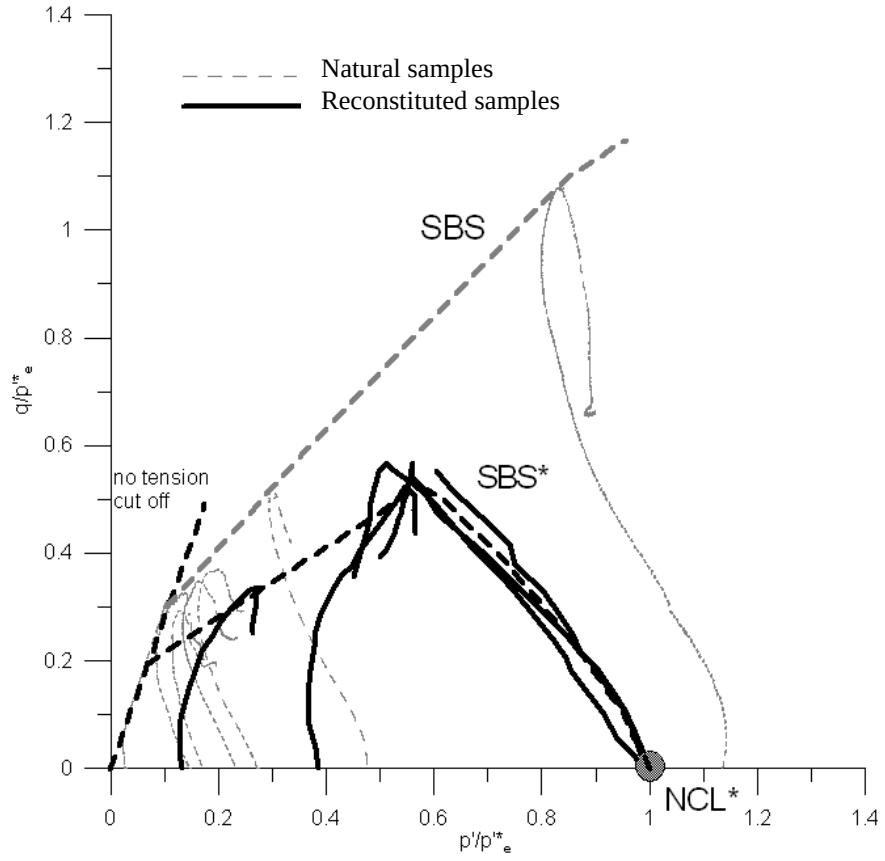


Figure 4-34: Normalised effective stress paths for the natural and reconstituted Oxford clay

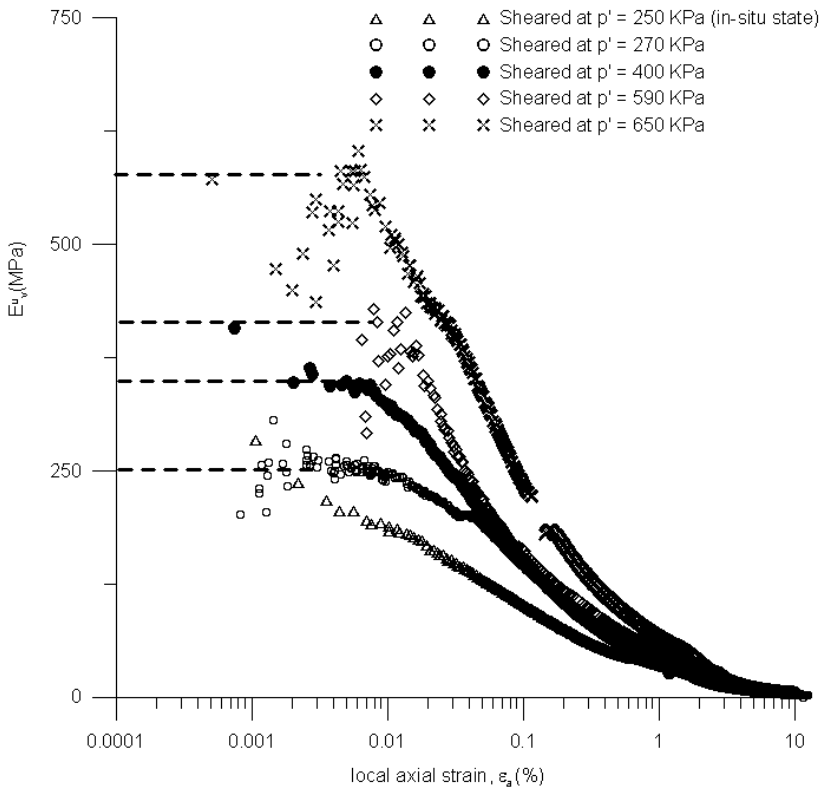


Figure 4-35: Stiffness degradation curves for the undrained compression tests on natural Oxford clay at different stress levels

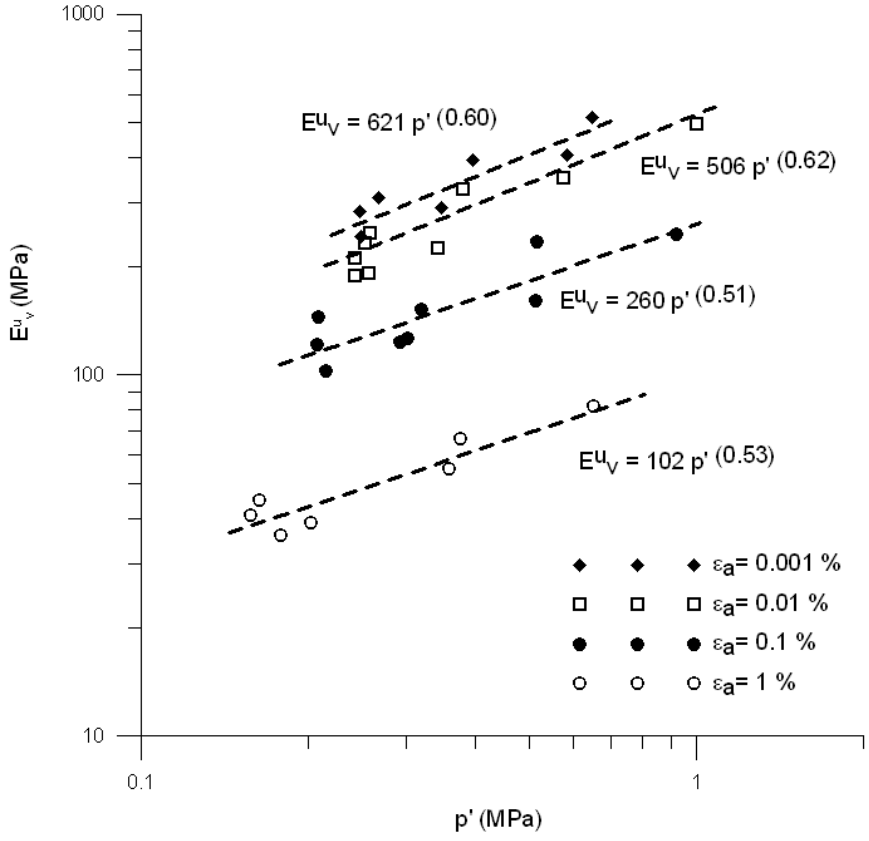


Figure 4-36: Stiffness variation with stress level at different strain levels for the natural Oxford clay

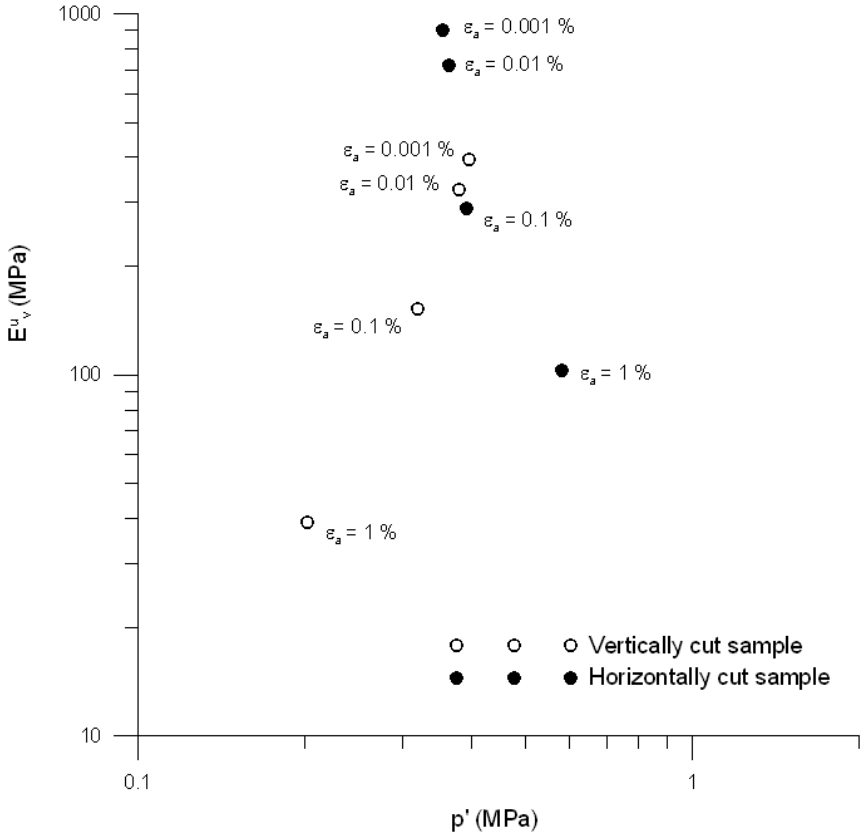


Figure 4-37: Stiffness variation with stress level for vertically and horizontally cut natural samples of Oxford clay

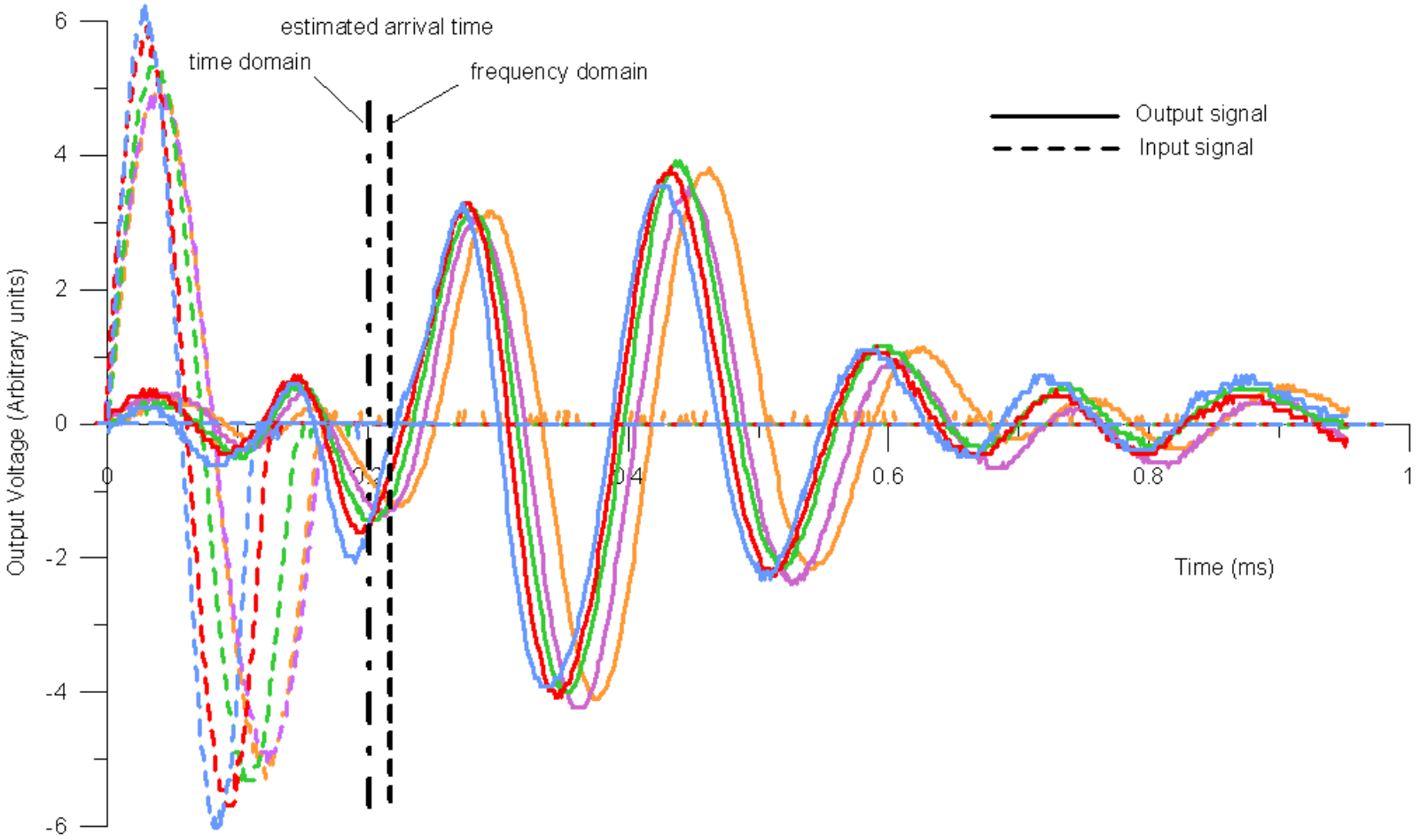


Figure 4-38: Typical bender element signals to obtain G_{hv} values for the natural Oxford clay

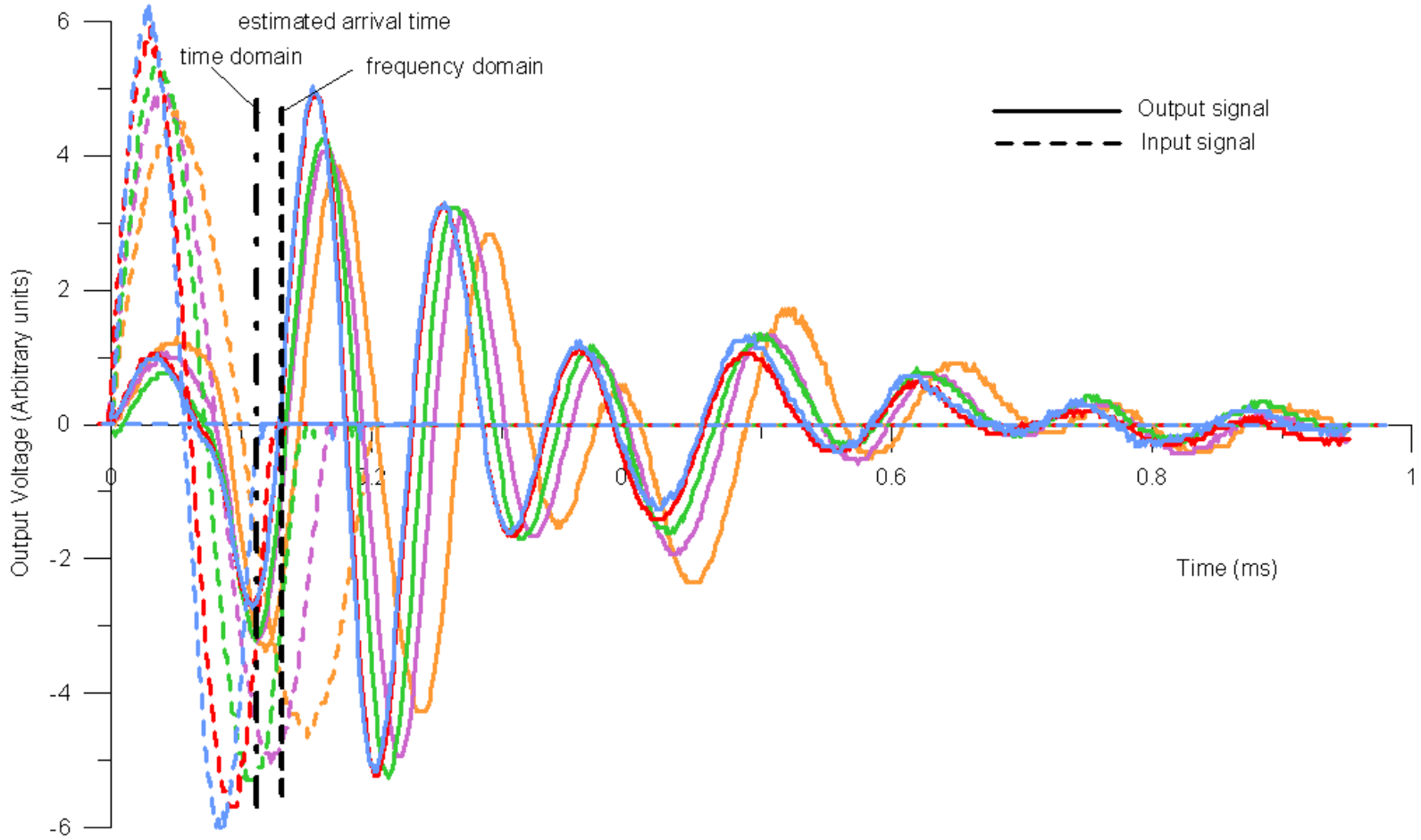


Figure 4-39: Typical bender element signals to obtain G_{hh} values for the natural Oxford clay

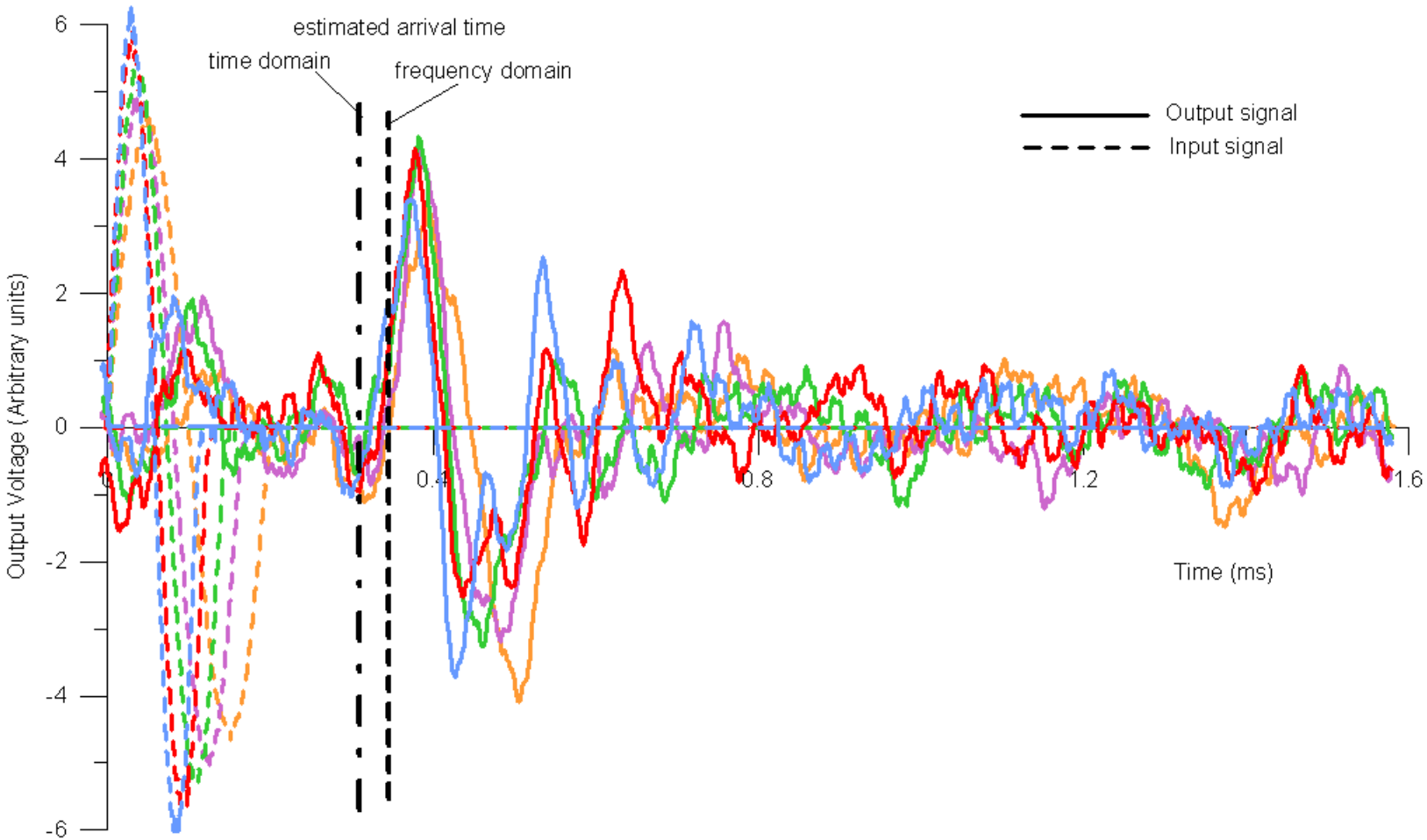


Figure 4-40: Typical bender element signals to obtain G_{vh} values for the natural Oxford clay

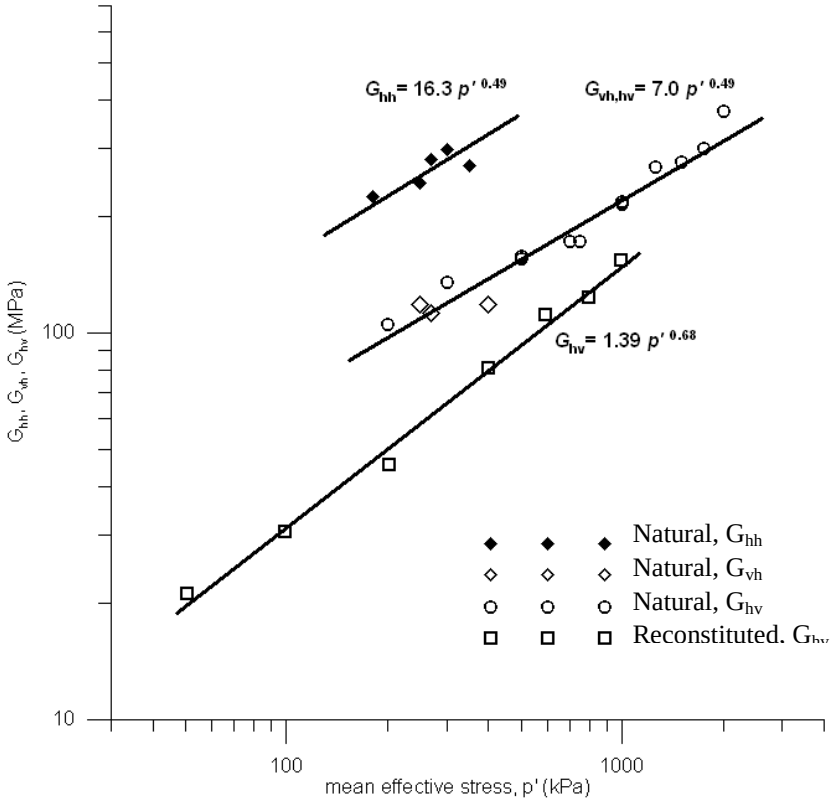


Figure 4-41: Stiffness of the natural and reconstituted samples of Oxford clay in different directions

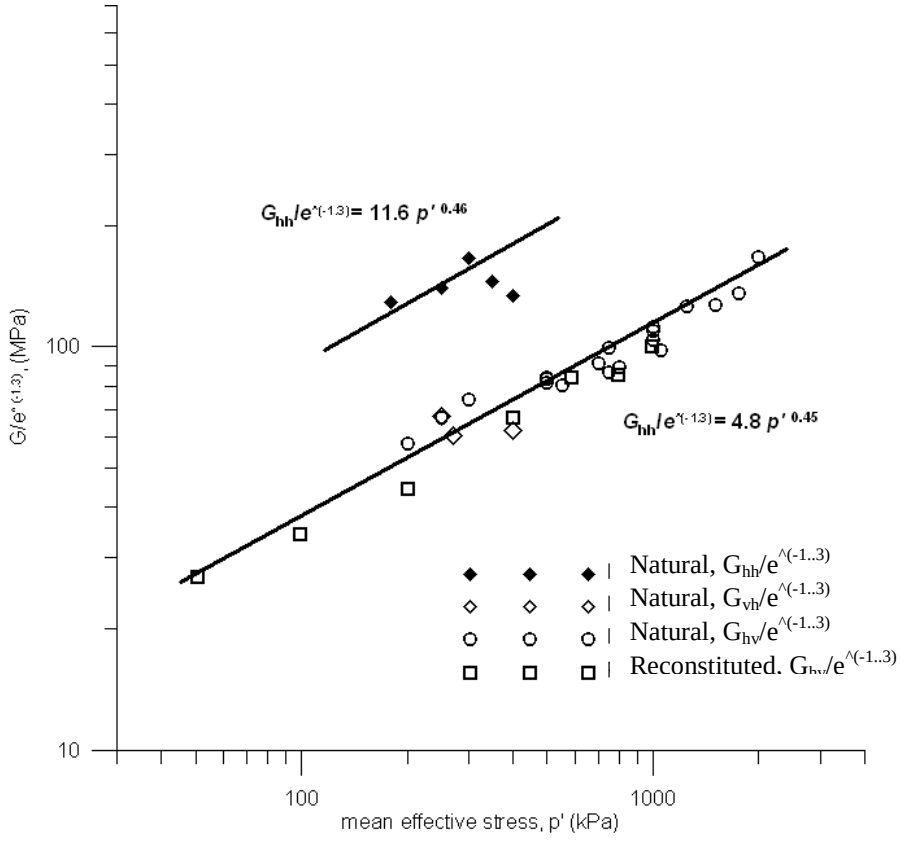


Figure 4-42: Stiffness of the natural and reconstituted samples of Oxford clay normalised for the void ratio

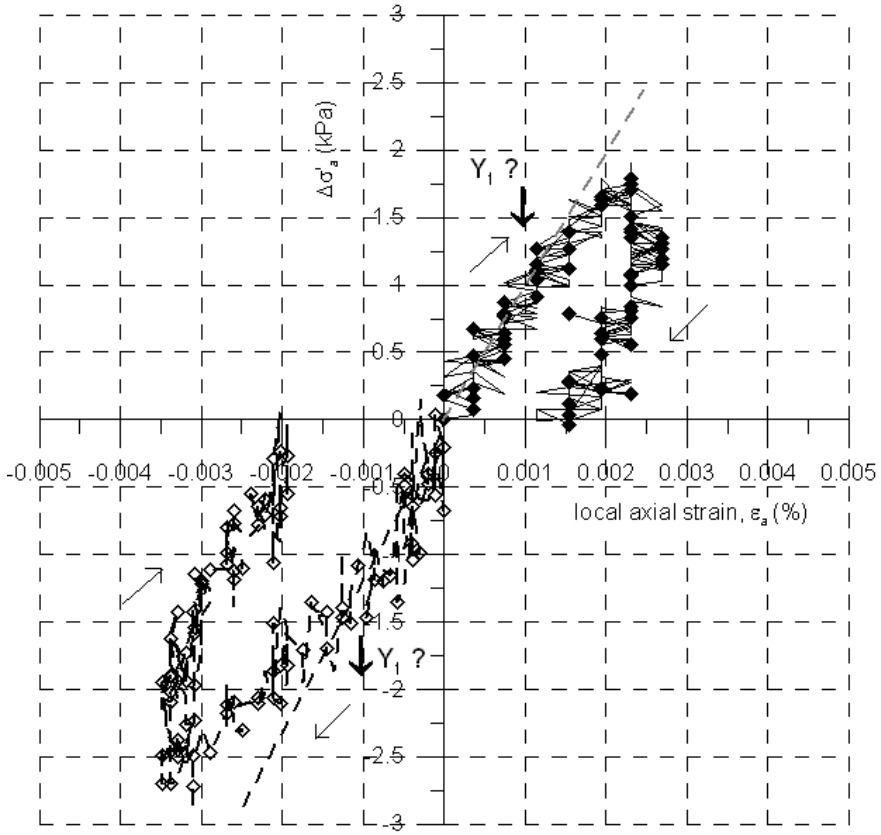


Figure 4-43: Axial probe in compression and extension; axial stress against axial strain

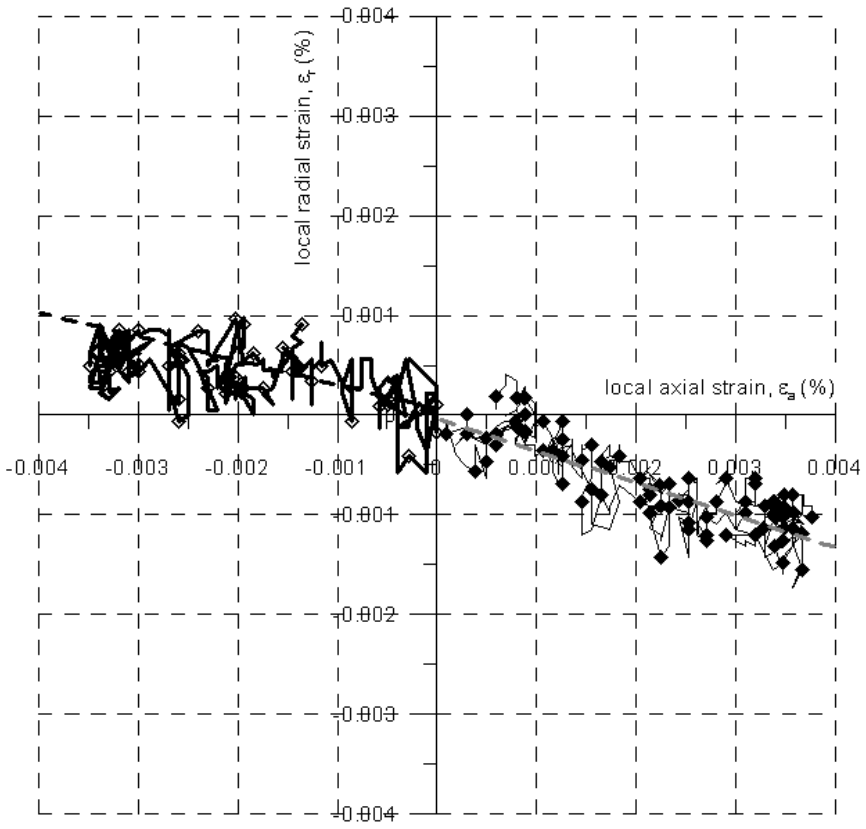


Figure 4-44: Axial probe in compression and extension; radial strain against axial strain

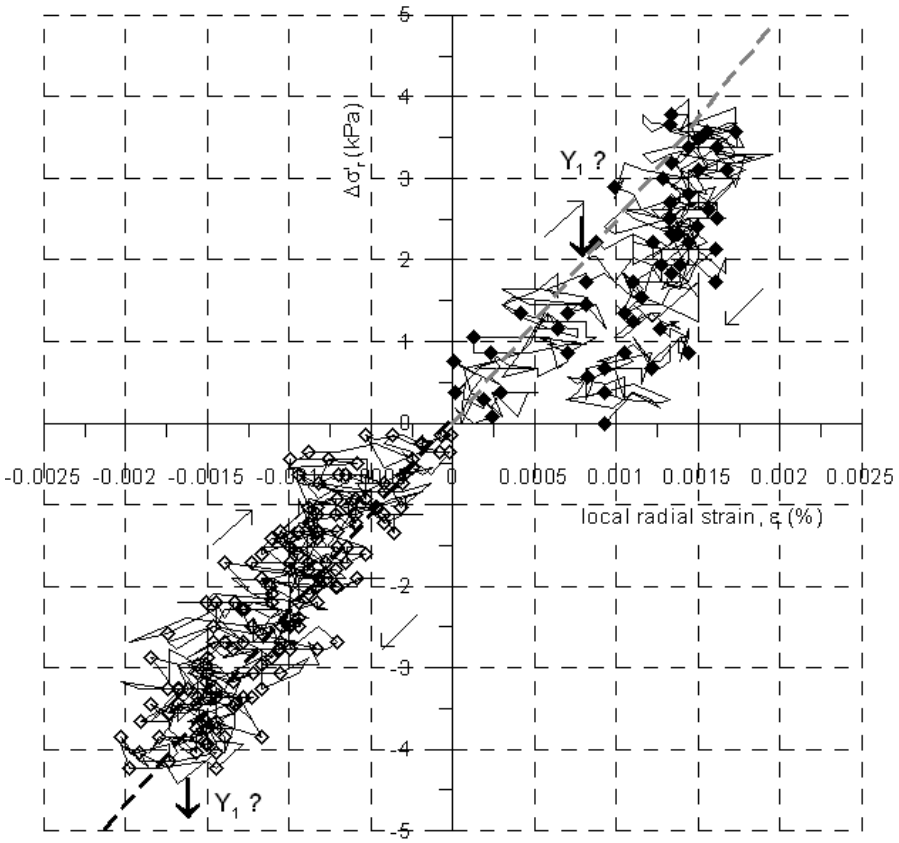


Figure 4-45: Radial probe in compression and extension; radial stress against radial strain

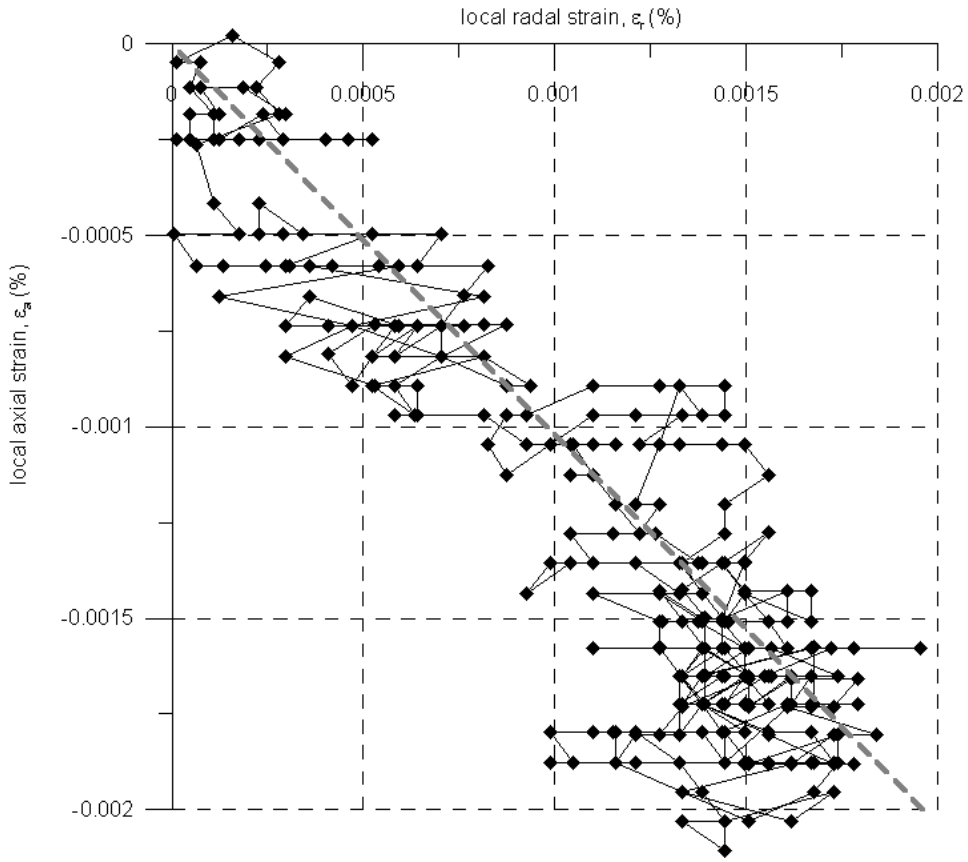


Figure 4-46: Radial probe in compression; axial strain against radial strain

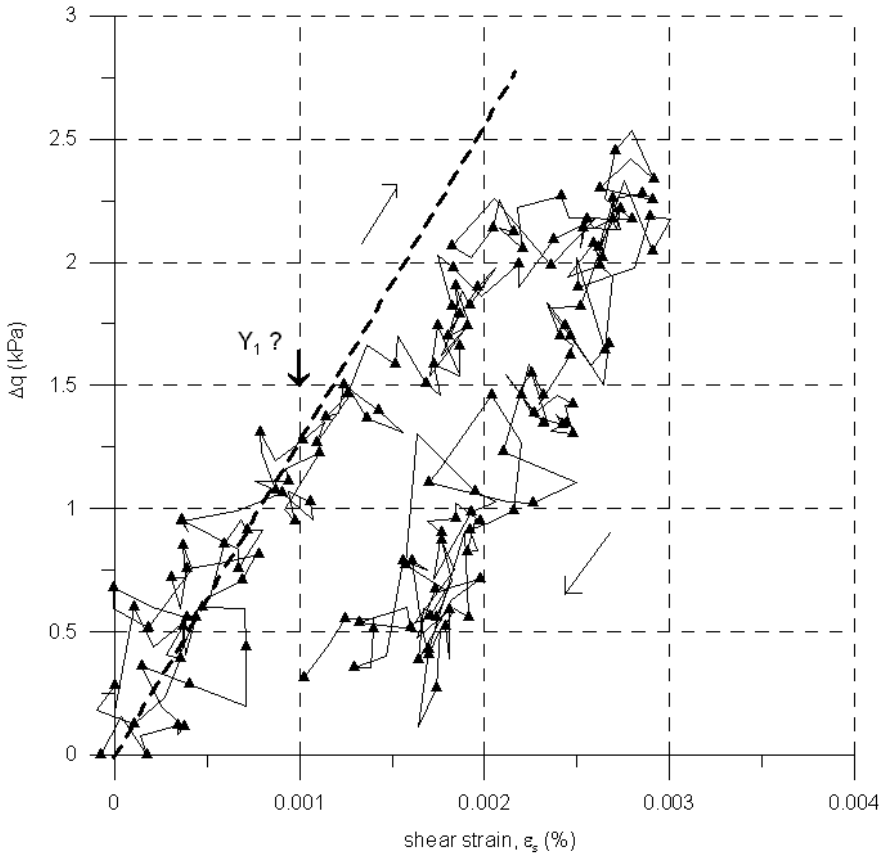


Figure 4-47: p' constant probe in compression; deviatoric stress against shear strain

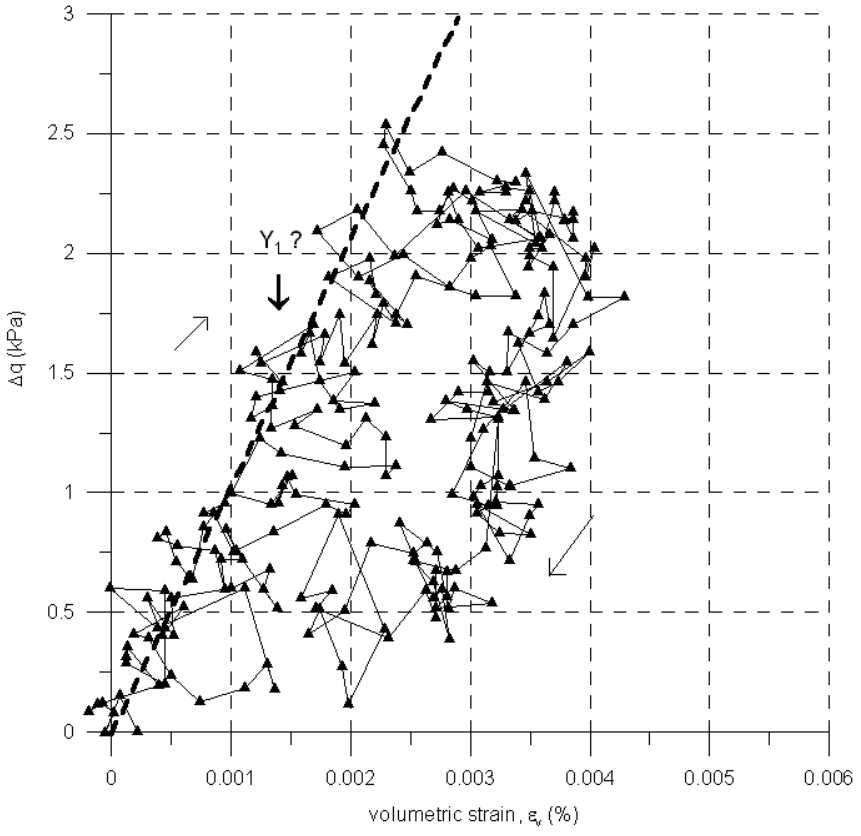


Figure 4-48: p' constant probe in compression; deviatoric stress against volumetric strain

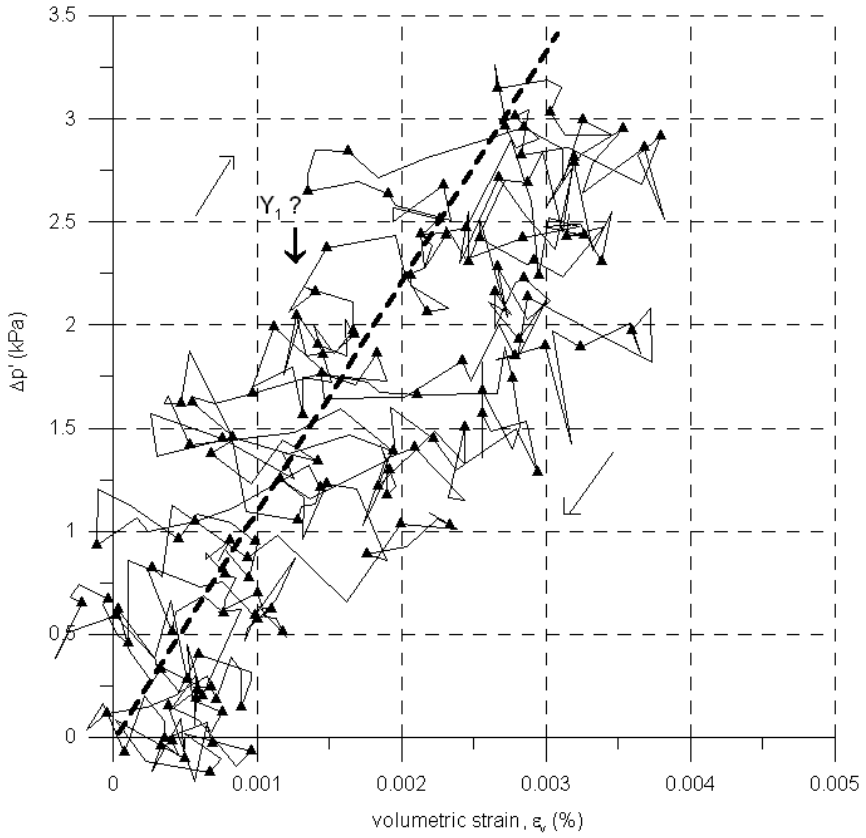


Figure 4-49: q constant probe in compression; mean effective stress against volumetric strain

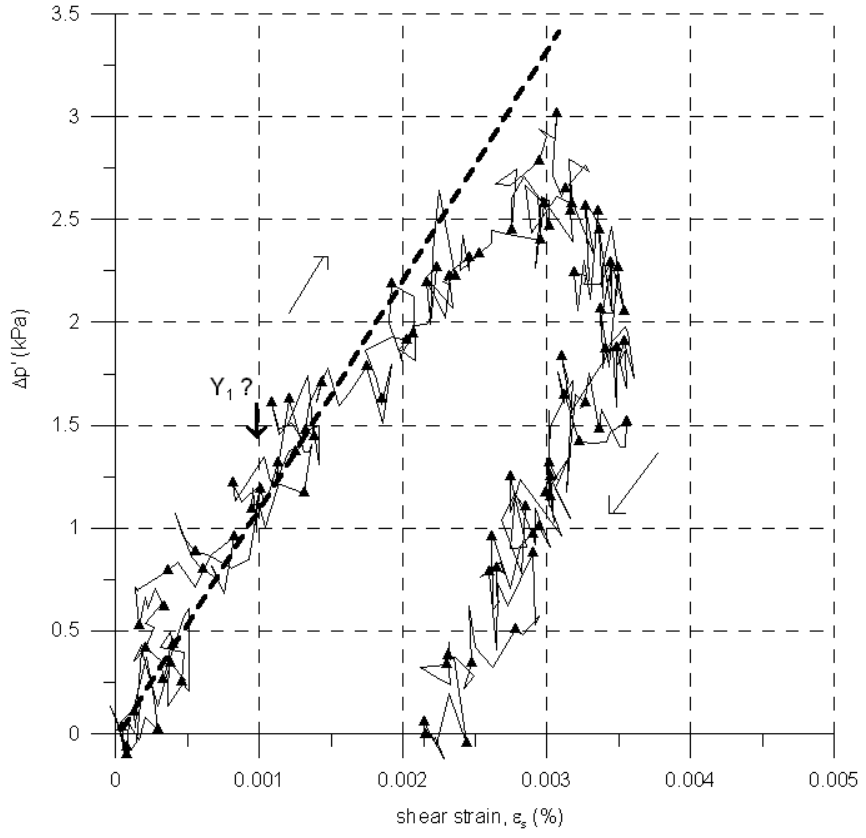


Figure 4-50: q constant probe in compression; mean effective stress against shear strain

5 Gault Clay

5.1 Introduction

Gault clay is the youngest mudrock studied in this research. Both block sampling and rotary coring have been carried out at the High Cross site (also known as Madingley) along with seismic CPT testing to enable a detailed study of the soil profile. In this chapter the various characteristics of Gault clay will be discussed and in Chapter 7 a comparison with the other soils will be made.

5.2 Background

5.2.1 Geology and the site

Gault clay was deposited in a deepening muddy sea during the Lower Cretaceous. The deposition was followed by deposition of chalk when the sea became clearer (Garrett & Barnes, 1984; Butcher & Lord, 1993). Uplift and extensive erosion of the chalk and overlying sediments left the Gault clay highly overconsolidated. The thickness of eroded chalk at Cambridge has been estimate to be around 200 to 400 metres (Lings et al., 1991). The Gault clay would have been covered by trees during interglacial periods and under periglacial conditions the upper layer of Gault clay experienced frost action which resulted in cryoturbation and solifluxion in the upper layers (Garrett & Barnes, 1984). The weathered layer of Gault clay tends to have a thickness of around seven metres with the fissuring becoming more extensive with depth as the soil becomes stiffer and more brittle (Butcher & Powell, 1995). Gault clay was also subjected to mild to moderate levels of tectonic loading including folding and faulting (Marsh & Greenwood, 1995), which might affect the assumption of cross-anisotropy for this material. The unweathered Gault clay is a grey, very stiff to hard, finely fissured soil with a very high swelling/shrinkage capacity. Gault clay is a very calcareous material with around 30% calcium carbonate (Ng, 1998). The thickness of Gault clay at High Cross is 40 metres and it is underlain by Greensands (Pennington et al., 1997).

The locations of the site, as well as the block and rotary core sampling and CPT measurements are shown in Figure 5-1. The Gault clay profile at the site prepared by the author and Brosse (2012), is shown in Figures 5-2 and 5-3. A summary of some other research on Gault clay is also included in these profiles. There is a change in soil profile at around 7.5 metres below ground level which is believed to be caused by the weathering of the upper layer. The water content, plasticity index and bulk unit weight are uniform with depth with small changes in their values at shallow depths of up to 2 metres due to high degrees of weathering. There is a scatter in the clay fraction values reported by Butcher & Lord (1993) with values generally increasing with depth. Rotary core samples were split into half so macro-structure discontinuities can be seen. Fissuring in a sample from the testing horizon of 10m depth can be seen in Figure 5-4. Two major fissuring patterns can be seen; major fissures with sub-horizontal and sub-vertical inclinations and with spacing of around 20 to 50 mm and zone of fragmented soil matrix with small fissures spaced in every few millimetres apart.

Figure 5-5 shows the particle size distribution for Gault clay samples from 10 metres depth; the clay fraction value from this study is slightly lower than those shown from Butcher & Lord (1993). The G_{max} values obtained from downhole seismic measurements show significant difference between G_{hh} and G_{vh} as expected for a highly anisotropic material. However the values of G_{vh} and G_{hv} are also different, as will be discussed further in the next section. There is a considerable scatter in the G_{vh} values measured in this study at depths down to 6 metres below ground level, with all being higher than those measured by Butcher & Powell (1995). This is most probably caused by the presence of vegetation close to the CPT location selected for the seismic testing. After this depth there is a good agreement between the values measured in both studies. As discussed later, the field measurements are also in general agreement with the author's laboratory measurements.

As discussed in Section 3.2.3, the Gault clay block samples retrieved at 3.5m depth were desiccated and showed a frequent presence of tree roots. The effects of vegetation on the soil profile were also discussed in Section 2.7. The trees on this site were about 3 to 4 metres high. Figure 5-6 shows the CPT profile of Gault clay close to and away from trees. As can be seen, the vegetation alters the cone end resistance and

sleeve friction down to 5 metres below ground level with a maximum effect at around 3 metres below ground level (close to the sampling horizon for the block samples that were initially taken). The new CPT profile interpretation and high suctions measured on the block samples prompted rotary core sampling boreholes to 14 metres below ground level to obtain material outside most weathered soil horizon and away from the influence of the vegetation.

5.2.2 Previous studies

Several authors have studied Gault clay at several sites including High Cross and the centre of Cambridge. Table 5-1 and Figures 5-2 and 5-3 summarise some of these studies while we consider below a recent study by the research group at Bristol University (Pennington et al., 1997; Lings et al., 2000). The main objective of their research was to examine the stiffness characteristics of Gault clay and to evaluate the small strain stiffness in terms of cross-anisotropy. For this purpose they developed a novel bender element system with T shaped elements oriented in the vertical and horizontal directions, which were used in combination with bender elements placed at the two ends of sample in perpendicular directions. This arrangement enabled the measurement of shear wave velocity in different directions and with different polarisations without the need to use separate oriented samples like the ones used by Jovicic & Coop (1997) or Kuwano & Jardine (1998).

One of the main findings was the difference between values of the two stiffness parameters G_{vh} and G_{hv}, measured at the ends and the sides of the sample respectively. Butcher & Powell (1995) also found the same trend in their in-situ seismic measurements, but with a bigger difference between the shear velocities V_{vh} and V_{hv}. However, both groups argued that this behaviour was probably due to inhomogeneity and bench top test results on both natural and reconstituted Gault clay showed G_{vh}= G_{hv}. The reason for the different values measured during the triaxial testing was believed to be related to the end effects due to the rigid platens at the two ends of the sample and therefore they suggested that it is more reliable to use G_{hv} instead of G_{vh}.

The static laboratory testing programme Lings et al. (2000) employed was comparable to that used by Hird & Pierpoint (1997) for the Oxford clay with multiple probing

tests carried out at the estimated in-situ state. Each static probe engaged about 0.1% strain which was believed to have an insignificant effect on the measurements as bender element G_0 checks at the beginning and the end of testing gave similar values. The major shortcoming of the testing was the local transducers used to measure the axial and the radial displacements. Hall effect gauges were used to measure the local strains with a resolution of 0.0015%, which may have exceeded the elastic limits. Curves fitted to the stress-strain data indicated no linear stress-strain range and it was not possible to measure the elastic Poisson's ratios accurately. They also imposed relatively short pauses before conducting the probes; 18 to 30 hr waiting periods were allowed that led to final creep rates of about 0.003%/hr. This creep rate is significant when keeping in mind that size of the Y_1 region is around 0.001% as the probing took the sample well out of this linear elastic region.

5.2.3 Evaluation of the in-situ stresses

The same approach as for Oxford clay was used for Gault clay to estimate the in-situ stress state. As mentioned earlier, because of the presence of tree roots, all the initial p' values measured in a triaxial cell on a specimen cut from 3.5m deep block samples were much higher than what was expected considering the equations suggested by Mayne & Kulhawy (1982). These high suctions were also observed when the suction probes were found to cavitate in contact with the block samples of the Gault clay. When the suction was measured using suction probes on the rotary core samples the values were too low as all the samples had swelled due to the presence of drilling fluid during the sampling (Figure 5-7). The measured suctions, were elevated by tree action or reduced by drilling operation compared with the ideal estimation based on undisturbed sampling not affected by trees. By considering K_0 values suggested by other authors (e.g. Butcher & Lord, 1993) and to keep consistency between all three soils tested in this project and following the limits of the axial strain and volumetric strain on the path to the anisotropic state, $K_0 = 1.8$ were chosen for samples of around 10 metres below ground level and the in-situ stress state was calculated as presented in Table 5-2.

5.3 Intrinsic properties

Oedometer tests were performed on the reconstituted Gault clay by two MSc students, Gao (2009) and Moran (2010), under the author's supervision. Two triaxial tests were also carried out by Moran (2010) on reconstituted Gault clay at *OCR*=1 and 5, again under the author's supervision. The data from these studies have been incorporated in the current research. A summary of all these tests is presented in Tables 5-3 and 5-4, while Table 5-5 summarises the intrinsic parameters of the Gault clay.

5.3.1 Compression behaviour

K_0 and isotropic compression curves for the reconstituted Gault clay are shown in Figures 5-8 and 5-9. Figure 5-8 shows the 1-D compression data plotting void ratio (e) against the logarithm of vertical effective stress (σ'_v). These reconstituted samples were made of the material at shallow (3.5 m) and deep (9.2 m) depths with different initial void ratios (different initial water contents). As can be seen, the intrinsic compression lines (*ICL**) were not affected in these cases by the sample depths. The parallel swelling lines also show no significant effect of sample depth. The isotropic compression lines are presented in Figure 5-9 with specific volume (v) plotted against the logarithm of mean effective stress (p'). All the tests started at similar specific volumes; one test was normally consolidated (*OCR*=1) and the other two tests were swelled back to two different *OCR* values (3 and 5). Here the term *OCR* is used in terms of p' in an isotropic loading-unloading. A straight line fitted to a short section of the *NCL** was used to normalise the effective stress paths for both reconstituted and natural samples.

5.3.2 Shearing behaviour

Three undrained triaxial compression tests have been carried out on 38mm diameter samples of reconstituted Gault clay. The samples were cut from a 'cake' which had been consolidated to vertical effective stress of 50 kPa (Section 3.4.1). The first test was isotropically consolidated to p'= 500 kPa and then sheared undrained in compression. The second test was overconsolidated with *OCR*=5 and the third test was overconsolidated with *OCR*=3. Side mounted bender elements were used for the last test.

Figures 5-10 and 5-11 show the stress-strain behaviour of the reconstituted Gault clay. The overall behaviours of the normally consolidated sample and the *OCR*=3 samples were contractant with the samples bulging at the end of the shearing due to the effects of end restraint. The more heavily overconsolidated sample with *OCR*=5 showed a dilative behaviour but still no clear strain localisation up to 17% axial strain. The rate of pore water pressure change, $du/d\varepsilon_a$, tended to zero at large strains in all three tests.

The normalised stresses, q/p', are shown in Figure 5-12 plotted against axial strain. The stress ratio at critical state, M = q/p', was estimated to be 0.97 corresponding to an angle of shearing resistance $\phi'_{cs} = 24.8°$. In the normalisation based on p' (stress level), the two overconsolidated test show a much stiffer behaviour induced by unloading. The effective stress paths for these tests are shown in Figure 5-13. A Critical State Line, *CSL**, is plotted along with the isotropic Normal Compression Line, *NCL**, in Figure 5-14. The Critical State Line was constructed using the last point of shearing and its corresponding specific volume.

The effective stress paths were then normalised using the equivalent pressure, p'^*_e, defined on the isotropic Normal Compression Line. The same normalisation has also been carried out with tests on natural samples to remove the effects of volume on the strength. Similar to the Oxford clay, the boundary surface plotted in Figure 5-15 is based on the undrained tests which probably represents the Local Boundary Surface, *LBS** for isotropically consolidated sample (Jardine et al., 2004). A more extensive programme of drained tests would be required to identify the outer *SBS**. Two overconsolidated tests were used to draw the Hvorslev surface with a considerable degree of uncertainty and as can be seen, tests with higher *OCR* would be required to define fully the Hvorslev surface.

5.4 Natural properties

5.4.1 Compression behaviour

Oedometer tests have been carried out on samples of natural and reconstituted Gault clay taken from different depths by different sampling procedures. Compression curves of natural Gault clay are shown in Figures 5-16 to 5-19. Figure 5-16 shows the compression curves for rotary core samples of Gault clay from three depths; their initial void ratios decreased with depth. The samples from 6.1 m and 9.2 m show similar behaviour both in compression and swelling, with the deeper sample showing marginally lower compressibility, and possibly greater structure. However the 3.5m deep rotary sample shows much higher compressibility and steeper swelling curves which indicate much greater effects of disturbance and weathering. As can be seen, no test shows a clear yield point, and all show significant rebound in swelling.

The effects of sampling procedure and trees on the compression behaviour of shallow Gault clay from 3.0 to 3.5m depth can be seen in Figure 5-17. As mentioned earlier the block samples were highly desiccated due to root action. The block samples, which were taken in the dry, suffered minimal disturbance and the block sample test curve starts at a lower void ratio compared to the rotary core sample which had swelled (despite careful removal of drilling mud immediately after retrieval) due to the drilling fluid ingress. However, the two tests converge from around σ'_v=2 MPa and follow the same paths subsequently in compression and swelling. This indicates that the effects of swelling during sampling were reversible and did not affect the soil structure unduly. Samuels (1975) reported that compressibility was much lower for the soil specimen taken from the block samples in comparison with specimens taken from the borehole of the Gault clay, signifying the sampling disturbance.

Figure 5-18 shows a comparison between both deep and shallow natural samples with a test on reconstituted material from around 10m depth. The natural samples do not pass the k_0 *ICL** line and do not show significant effects of structure based on the sensitivity framework. The swelling curves of the weathered sample and the reconstituted sample are almost parallel, resulting in a swell sensitivity (S_s) of around unity, indicating that considerable destructuration occurred during the compression. The deep sample swelled less than the reconstituted sample showing a greater effect of structure. Noting that minor variation occurred with depth in soil composition,

these tests and another from 6.1m are shown normalised for volume using the void index, I_v in Figure 5-19, with compression curves not reaching the SCL. The normalised plot suggests a slightly more developed structure for the deepest (9.2m) sample.

5.4.2 Shearing behaviour

a) Large strain behaviour

As in the Oxford clay study, undrained compression and extension triaxial tests were carried out on Gault clay samples. Most tests were performed on 100mm diameter specimens, although others were conducted on 38mm diameter samples. Ring shear tests were also carried out by Narayana (2010) and Cunliffe (2010) as part of their MSc projects to investigate the brittle behaviour of the soil.

Figures 5-20 to 5-22 show the effective stress paths for block and rotary core samples of Gault clay. The block samples were all weathered while the rotary core samples from below 6m are considered essentially un-weathered. As can be seen, both sets of samples conform to a single peak shear strength envelope, in contrast to the behaviour observed by Cafaro & Cotecchia (2001) for the Pappadai clay, where a lower strength envelope applied to the more weathered material. The data presented in Figure 5-22 suggest a possible sample size effect as shown, although this impression comes mainly from a single sample tested at high pressure of 1000 kPa.

All compression tests developed a strain localisation with a single shear plane with angles varying between 50 and 60 degrees. The Gault clay samples tested were all highly fissured with close fissure spacing. Wilkinson (2011) measured the fissure spacing at shallow depths to be 60mm to 100mm and as mentioned earlier fissuring at the testing horizon of around 10 metres depth becomes more intense with two types of fissuring observable: major fissures with sub-horizontal and sub-vertical inclinations and with spacing of around 20 to 50 mm and zone of fragmented soil matrix with small fissures spaced in every few millimetres apart. It is very likely that the fissured, macro-fabric of the samples affected the samples test strengths.

Figures 5-23 and 5-24 show the stress-strain behaviour of all these tests. The behaviour is not really brittle, and less markedly so than the Oxford clay. Some of these tests were incomplete as leakage occurred around peak and for those tests the post-rupture strength could therefore not be reached. Figure 5-25 shows the normalised graph of q/p' against axial strain. The q/p' value at peak, as well as at post-rupture, tends to be higher for tests performed at lower stresses. The post-rupture stress ratios do not tend to converge to steady or unique values at the strain levels imposed. The final ratios fall in the broad range of $0.75<M<1.35$.

As with the Oxford clay (see Section 3.5.5) a Mohr's circle construction was carried out to obtain the peak and post-rupture failure envelopes. The peak strength and post-rupture strength envelopes for Gault clay are shown in Figure 5-26. The critical state slope from the reconstituted tests is also plotted in this figure. As can be seen, the post-rupture envelope and the Critical State Line (from reconstituted tests) are close to each other at low stress levels. Unfortunately, unlike for Oxford clay, tests at higher strain levels were not performed to see if the post-rupture strength reduces towards the residual at higher strain levels.

One horizontally cut sample was sheared in compression, and the effective stress path for this test is shown in comparison with those of the vertically cut samples in Figure 5-27. The first point to note is the far higher shear strength. This anisotropy is explored further by Brosse (2012). The second point is that while the effective stress paths for the vertically cut samples all incline to the left of vertical, the stress path for the horizontally cut sample is almost vertical, as is often the case with high OCR clays. Stiffness anisotropy affects the slopes of the effective stress paths in undrained triaxial tests, and as shown later $E'_h > E'_v$ for Gault clay. Using the small strain stiffness parameters discussed later and assuming an elastic response, Equation 4-1 (after Lings, 2001), the value for $\delta p'/\delta q$ was calculated to be -0.55 for the vertically cut samples which compares with the measured slope of -0.40.

As discussed earlier the brittle behaviour of these stiff clays can result in progressive failure with the strength falling rapidly from high peak values to very low residual strengths at large strains. Therefore it is important to measure the residual strength as

well as the peak and post-rupture strengths. Figures 5-28 and 5-29 show the results of ring shear tests on Gault clay samples at around 10 metres depth (Narayana, 2010; Cunliffe, 2010). The first figure shows the mobilised angle of shearing resistance, ϕ'_r, plotted against shear displacement, d, divided by sample height, h, for the small range of displacements. The rates used for this stage of shearing were 0.01mm/min for the 20mm thick remoulded sample tested in the Bishop apparatus and 0.024mm/min for the 5mm thick natural sample tested in the Bromhead cell. These tests were carried out under 400 kPa normal stress. The peak strength is almost the same for the remoulded and natural samples with $\phi'_p = 20°$. It should be kept in mind that the non-uniform strains in the ring shear apparatus will result in progressive failure across the radius and this hinders an accurate measurement of the peak strength. At large displacements (Figure 5-29) both remoulded and natural tests are in a good agreement, both giving a residual angle of shearing resistance, $\phi'_r = 10°$.

b) Effects of structure at large strains

A comparison between the behaviour of natural and reconstituted samples was made to investigate the effects of structure on the strength and stiffness of the Gault Clay. Figure 5-30 shows the stress ratio, q/p', plotted against axial strain for the natural and reconstituted samples. The natural samples show higher peak strengths and a more brittle behaviour compared to the reconstituted samples. It is also clear that the natural and overconsolidated reconstituted samples were stiffer than the normally consolidated reconstituted sample. The differences are less significant between the overconsolidated natural and reconstituted samples.

The effective stress paths of both natural and reconstituted samples are shown in Figure 5-31. Unlike Oxford clay, the failure envelope for the natural samples lies only marginally above the reconstituted one. Noting that the samples had different void ratios at the time of shearing and the paths are shown normalised by the equivalent pressure, p'^*_e, on the isotropic Normal Compression Line in Figure 5-32. As can be seen, the natural state boundary surface passes close to the Critical State strength of the reconstituted tests showing no clear sign of enhancement by structure. This feature is not that expected for an old stiff clay. This feature may be related to the close

fissure spacing in the macro-fabric. It could also be due to a greater degree of disturbance by vegetation, pre-glacial or tectonic activities.

c) Pre-failure behaviour

The pre-failure behaviour of Gault clay will be discussed in this section. Figures 5-33 and 5-33 show stiffness degradation curves for the block and rotary core samples respectively. Tests from different stress levels have been chosen to highlight its effect. As was expected the stress-strain behaviour is highly non-linear with a small region of linear response. The linear plateau at small strains can be identified below an approximate limit of 0.002 to 0.005 % axial strain.
The effects of sampling type on the stiffness of Gault clay can be seen in Figures 5-35 and 5-35. In the first figure the stiffness degradation curves for the rotary core and the block samples, from the same depth, and sheared at similar stress levels are shown. As can be seen, the two curves are almost identical with the block sample being slightly stiffer. Figure 5-36 shows undrained vertical Young's modulus plotted against mean effective stress at different strain levels for the same samples. Only minor differences can be seen between the values. The small differences might be attributed to the swelling of the rotary core samples due to opening of joints and loss of drilling fluid into them during the sampling. Again effect of sampling disturbance on the shear strength is less than what Samuels (1975) reported for block and borehole specimens of Gault clay, with block samples having strength double the borehole ones.

The stiffness data from all the different tests are presented in Figure 5-37. The full dots represent the deep and unweathered samples while the open circles show the more weathered shallow samples. For the sake of clear presentation the strain levels of 0.001% and 0.1% are plotted together in part (a) and those for 0.01% and 1% together in part (b). As can be seen, the weathered and unweathered samples show similar stiffness-pressure relationship at small strains, but the more weathered material shows a softer relationship at larger strains. This contrasts with the findings of Cafaro & Cotecchia (2001) who found lower initial stiffnesses for the weathered Pappadai clay compared to the unweathered material. The stiffness and strength data presented here for Gault clay implies that the degree of weathering was probably not high enough to change fundamentally the mechanical behaviour of the soil. As

mentioned earlier, in Chapter 4, it is widely believed that the stress level exponent of the stiffness increases towards unity with increase in strain level (e.g. Jardine, 1995; Viggiani & Atkinson, 1995). However, as with Oxford clay, the contrary seems to be true for the Gault clay where the 'n' value decreased with strain level.

Typical input and output signals are shown in Figures 5-38 and 5-39 from bender element tests designed to obtain G_{hv} and G_{hh} respectively. Unfortunately platen mounted bender elements were not available for the tests on Gault clay and so no measurements of V_{vh} were made to confirm the findings of Pennington et al. (1997) regarding disparities between V_{vh} and V_{hv}. Input signals with frequencies between 6 and 10 kHz were chosen and are plotted together with the output signals. The Y axis shows voltage amplitude, with both input and the output signals normalised to comparable scales, while the X axis plots time. The point at which the output signals start to ascend was chosen as the time-domain first arrival point. The signals were also sent to Dr Vilhar, a specialist at the Slovenian National Building and Civil Engineering Institute, for an independent check and the same time domain points were chosen by him. A frequency domain analysis was also carried out using the code developed by Alvarado (2007). As shown the arrival time calculated from this method was generally in good agreement with the time domain estimate. Both methods were applied to all signals, but the results presented here reflect only the time domain estimates.

The bender element results are shown in Figure 5-40, plotting the logarithm of shear modulus at very small strain, G_0, against the logarithm of mean effective stress, p'. As expected for a highly overconsolidated stiff clay, the values are higher for the G_{hh} mode than that for G_{hv}. The degree of anisotropy is not degraded by increases in the effective stress level. The G_{hv} (as will be shown below $=G_{hh}$) data from the single isotopically consolidated reconstituted test is also shown in this graph, indicating lower values than the natural samples. However, when normalised for the void ratio (Figure 5-41) this difference is no longer apparent. Although this is in agreement with findings on Oxford clay and London clay (Viggiani & Atkinson, 1995) it is not in agreement with significant differences between the stiffnesses of the reconstituted and the natural Gault clay tested by Pennington et al. (1997), as shown in Figure 5-42.

Another important observation from the stiffness data presented by Pennington et al. (1997) is the difference between G_{hh} and G_{hv} for the reconstituted Gault clay, both in isotropic and anisotropic loading (Figures 5-42 and 5-43). In the current project, the triaxial test on the reconstituted sample with *OCR*=3 was equipped with side bender elements which enabled the measurement of G_{hh} and G_{hv} during compression and swelling. Figure 5-44 shows that the normalised shear moduli are essentially the same during isotropic compression. Figure 5-45 shows the values for the normally consolidated and overconsolidated states during unloading. An effect of overconsolidation is evident, after normalisation for e, with an increase of stiffness with *OCR* in comparison with the normally consolidated trend. The normalised stiffnesses at *OCR*=2 and 3 are 10 and 20% higher than for normally consolidated soil.

Drained elastic parameters were obtained for the natural Gault clay and are presented in Table 5-6. Drained static small strain tests involving axial probes, with constant radial stress, in compression and extension are shown in Figures 5-46 and 5-47. Figure 5-46 shows axial stress and strain increments developed in a load-unload probe. As can be seen, although the size of the probe is less than 1 kPa change in axial stress for the compression test, the behaviour is not fully linear-elastic. This is more evident in the extension probe in which the change in the axial stress is slightly more than 1 kPa. However it is possible to identify a linear part of these probes and calculate the vertical Young's modulus, E'_v. It is also possible to indicate the point in which the behaviour starts to become non-linear as Y_1. The stiffness is slightly higher in extension with Y_1 being reached at a larger strain and stress; this is not expected for an elastic material and it is not clear if the difference is caused by an experimental error or reflects true the soil behaviour.

To evaluate the Poisson's ratio, υ'_{vh}, changes of the radial strain against axial strain were required. Lings et al. (2000) reported the Poisson's ratio to be zero for the Gault clay, but this was probably due to the low resolution transducers they used that were unable to measure very small radial displacements. These small strains could only be measured using the new radial displacement set-up described in Chapter 3. The changes in the radial strains plotted against the axial strains are shown in Figure 5-47 with Poisson's ratios, υ'_{vh}, equal to 0.23 and 0.17 for the compression and extension

tests respectively. Figures 5-48 and 5-49 show the radial probes, with constant axial stress, in compression and extension. The load-unload probes show a linear and fully elastic response over the ±2 kPa applied. The response also seems to be similar in compression and extension. The values of υ'_{hv} calculated based on these radial probes and using Equation 3-18 seem to be more reliable in comparison with those obtained from Equation 2-6 (from both axial and radial probes).

As mentioned earlier in Chapter 4, constant q and p' probes were used to check the parameters from the probing programme. These are reported in Figures 5-50 to 5-53, and the parameters are summarised in Table 5-6. The local axial and radial strains were used to calculate the shear and volumetric strains. Moving away from uniaxial parameters increases the scatter, as data from two scattered sources are required to calculate q, p', ε_s and ε_v, instead of one source per axis in the earlier plots. The applied changes (Δq and $\Delta p'$) were around 2 kPa and appeared to take the sample beyond the recoverable, linear limits. Interpretation of the apparently initial linear parts of these tests was used to obtain the elastic parameters given in Table 5-6. Despite scatter, there is generally good agreement between the parameters obtained with the uniaxial probes.

5.5 Summary

An overview of the geotechnical properties of Gault clay was presented in this chapter. The existing literature was summarised and the shortcomings related to the stiffness measurements were highlighted. Both block sampling at a shallow depth of 3 metres below ground level and rotary coring of up to 13 metres below ground level enabled the study of weathering of Gault clay. The weathered layer of Gault clay tends to have a thickness of around seven metres with the fissuring becoming more extensive with depth (Butcher & Powell, 1995). The effects of vegetation on the soil profile were also discussed by comparing the CPT profile of Gault clay close to and away from trees. The vegetation alters the cone end resistance and sleeve friction up to 5 metres below ground level. This was also confirmed by measuring high suction values on the highly desiccated block samples.

The oedometer tests on samples of Gault clay from different depths showed the effects of weathering on the structure of the material. The deepest sample showed the lowest compressibility, indicating stronger structure, while the shallow sample showed much higher compressibility and swelling which may indicate the effect of weathering. There was no clear Y_3 yield point for any of the tests and in all cases there is significant swelling. The swelling lines for the weathered sample and the reconstituted tests were almost parallel, resulting in a swell sensitivity (S_s) of around unity, indicating that considerable destructuration had occurred during the compression or a lack of strong structure initially.

Triaxial tests on the weathered and unweathered material showed no significant difference in their strength in contrast to the behaviour observed by Cafaro & Cotecchia (2001) for the Pappadai clay where there was a lower shear strength envelope for the weathered material. There was also no significant difference in strengths based on sample size. All the samples developed a strain localisation with a single shear plane with angles varying between 50 and 60 degrees. On the dry side the natural state boundary surface was lower than the reconstituted one showing no sign of structure; this is not normally expected from an old stiff clay. It should be noticed that Gault clay tested in the current research was highly fissured with close spacing, with fissures increasing with depth. None of the shear planes formed at the end of each test could have been attributed to a failure on the pre-existing fissure. It is possible that presence of these fissures, a macro-fabric element of the structure, affected the matrix strength of the soil for the deep samples. This reduction in the strength due to fissures could be similar to the strength reduction caused by the weathering of shallower samples.

The small strain stiffness of Gault clay was studied using bender elements and local transducers. Changes in the stiffness with stress and strain level showed that the stress exponent of the stiffness ‘n’ decreased with strain level in contrast with other studies. The degree of anisotropy did not change with the stress level; with stiffnesses having a higher value in the horizontal plane. The normalisation based on void ratio was carried out on these stiffness values resulting in insignificant variance between the reconstituted and natural samples. Drained elastic parameters were also obtained with good agreement between various methods.

Source	Site	Sampling Method	Lab testing	In-situ testing
Garrett & Barnes (1984)	Dunton Green, 3km north of Sevenoaks	U100	DSB	-
Butcher & Lord (1993)	Centre of Cambridge & Madingley	U100, 75-98mm thin walled tube	UU	plate loading, pressuremeter, static cone and Marchetti dialometer, pile test
Butcher & Powell (1995)	Madingley	-	-	Seismic field measurements
Pennington et al. (1997)	Madingley	250mm thin walled push sampler	TC, TE & Small strain probing	-
Cooper et al. (1998)	Selborne, Hampshire	Rotary cores, 105-600mm thin walled tube & block samples	TU, TD & DSB	-
Dasari & Bolton (1998)	Madingley	38mm pushed in by drop hammer	DC with p' constant	-

* TC: Triaxial Compression, TE: Triaxial Extension, DC: Drained compression, UU: Unconsolidated Undrained, DSB: Direct Shear Box

a)

Source	LL (%)	PL (%)	CF (%)	c'_{peak} (*kPa*)	ϕ'_{peak} (*Deg*)	$*c'_{peak}$ (*kPa*)	$*\phi'_{peak}$ (*Deg*)	ϕ'_{r} (*Deg*)
Garrett & Barnes (1984)	75	28	-	13 (13)$^{+}$	24.5 (24.5) $^{+}$	10	23	-
Parry (1988)	76	30	-	-	-	-	-	-
Cooper et al. (1998)	-	-	-	25(15) $^{+}$	26(25) $^{+}$	-	-	14.1(13.3) $^{+}$
Dasari & Bolton (1998)	-	-	68	-	-	-	-	-

* Reconstituted tests, + Weathered material

b)

Table 5-1: Summary of other research on Gault clay; a) site locations, sampling type and testing plans, b) index properties & strength parameters

Bulk unit weight, γ	19.3 (kN/m^3)
Water table below ground level	1 (m)
Sample depth	10 (m)
Estimated in-situ σ'_v	105 (kPa)
K_0	1.8
p'	160 (kPa)
q	-85 (kPa)

Table 5-2: Estimation of the in-situ stress state

Sample name	Sample type	Sample depth (m)	Initial water content w_c (%)	Maximum stress reached in compression σ_v' (kPa)	Researcher (if not the author)
GACL-RO-1	Reconstituted-Block	3.5	70	15000	Gao (2009)
GACL-RO-2	Reconstituted-Rotary	9.2	90	8000	Moran (2010)
GACL-NO-1	Natural- Rotary	6.1	29.6	13900	Moran (2010)
GACL-NO-2	Natural- Rotary	9.2	27.3	13700	Moran (2010)
GACL-NO-3	Natural- Rotary	3.5	31	28500	
GACL-NO-4	Natural- Block	3.5	24	30000	

Table 5-3: Summary of oedometer tests on natural and reconstituted samples of Gault clay

Sample name	Sample type	Sample depth (m)	D (mm)	State before shearing		Bender elements	Shear	Researcher (if not the author)
				p' (kPa)	q (kPa)			
GACL-RT-1	Reconstituted-Block	3.5	38	500	0		UC	Moran (2010)
GACL-RT-2	Reconstituted-Block	3.5	38	100	0		UC (OCR=5)	Moran (2010)
GACL-RT-3	Reconstituted-Block	3.5	38	167	0	●	UC (OCR=3)	
GACL-NT-1	Natural-Block	3.5	100	200	-20	●	UE	
GACL-NT-2	Natural-Block	3.5	100	200	20	●	UC	
GACL-NT-3	Natural-Block	3.5	100	145	-55	●	UE	
GACL-NT-4	Natural-Block	3.5	100	145	-55	●	UC	
GACL-NT-5	Natural-Block	3.5	100	500	0	●	UC	
GACL-NT-6	Natural-Block	3.5	100	350	0	●	UC	
GACL-NT-7	Natural-Block	3.5	100	400	20	●	UC	
GACL-NT-8	H-cut-Natural-Block	3.5	100	400	20	●	UC	
GACL-NT-9	Natural-Block	3.5	100	600	20	●	UC	
GACL-NT-10	Natural-Rotary	9.8	100	250	20	●	UC	
GACL-NT-11	Natural-Rotary	3.9	100	275	0	●	UC	
GACL-NT-12	Natural-Rotary	12.8	100	500	0	●	UC	
GACL-NT-13	Natural-Rotary	3.5	100	350	0	●	UC	
GACL-NT-14	Natural-Rotary	9.6	100	200	-100		UC	
GACL-NT-15	Natural-Rotary	6.5	100	125	-50		UC	
GACL-NT-16	Natural-Block	3.5	38	70	0		UC	
GACL-NT-17	Natural-Rotary	12.9	38	1000	0		UC	
GACL-NT-18	Natural-Block	3.5	38	50	0			
GACL-NT-19	Natural-Rotary	10.3	38	160	-85	●	UC	

* UC: Undrained Compression, UE: Undrained Extension, H-cut: Horizontally cut sample

Table 5-4: Summary of triaxial tests on natural and reconstituted samples of Gault clay

φ'_{cs}	N*	Γ*	λ	κ	C_c^*	C_s^*
24.8 °	2.99	2.85	0.215	0.040	0.496	0.168

Table 5-5: Parameters measured for one-dimensionally and isotopically compressed reconstituted samples of Gault clay

	Drained															Undrained		
Probe	G_{hh}	G_{hv}	E'_v	E'_h	υ'_{vh}	υ'_{hv}	υ'_{hv}	υ'_{hh}	G'	G_{eq}	K'	K'	J_{qp}	J_{pq}	J	E^u_v	E^u_v	E^u_h
	MPa	**MPa**	**MPa**	**MPa**		**Eq 2-6**	**Eq 3-18**		**MPa**	**Eq 3-26 MPa**	**MPa**	**Eq 3-27 MPa**	**MPa**	**MPa**	**Eq 3-28 MPa**	**MPa**	**Eq 3-29 MPa**	**Eq 3-30 MPa**
Bender elements	110	57																
axial probe compression			67		0.23													
axial probe extension			75		0.17													
radial probe compression				239		0.83	0.92	0.06										
radial probe extension				239		0.54	0.94	0.06										
p'cnst probe									27.5	31			250		200			
q cnst probe											107	112		200				
UC																137	129	240

Table 5- 6: Elastic parameters derived from static probes

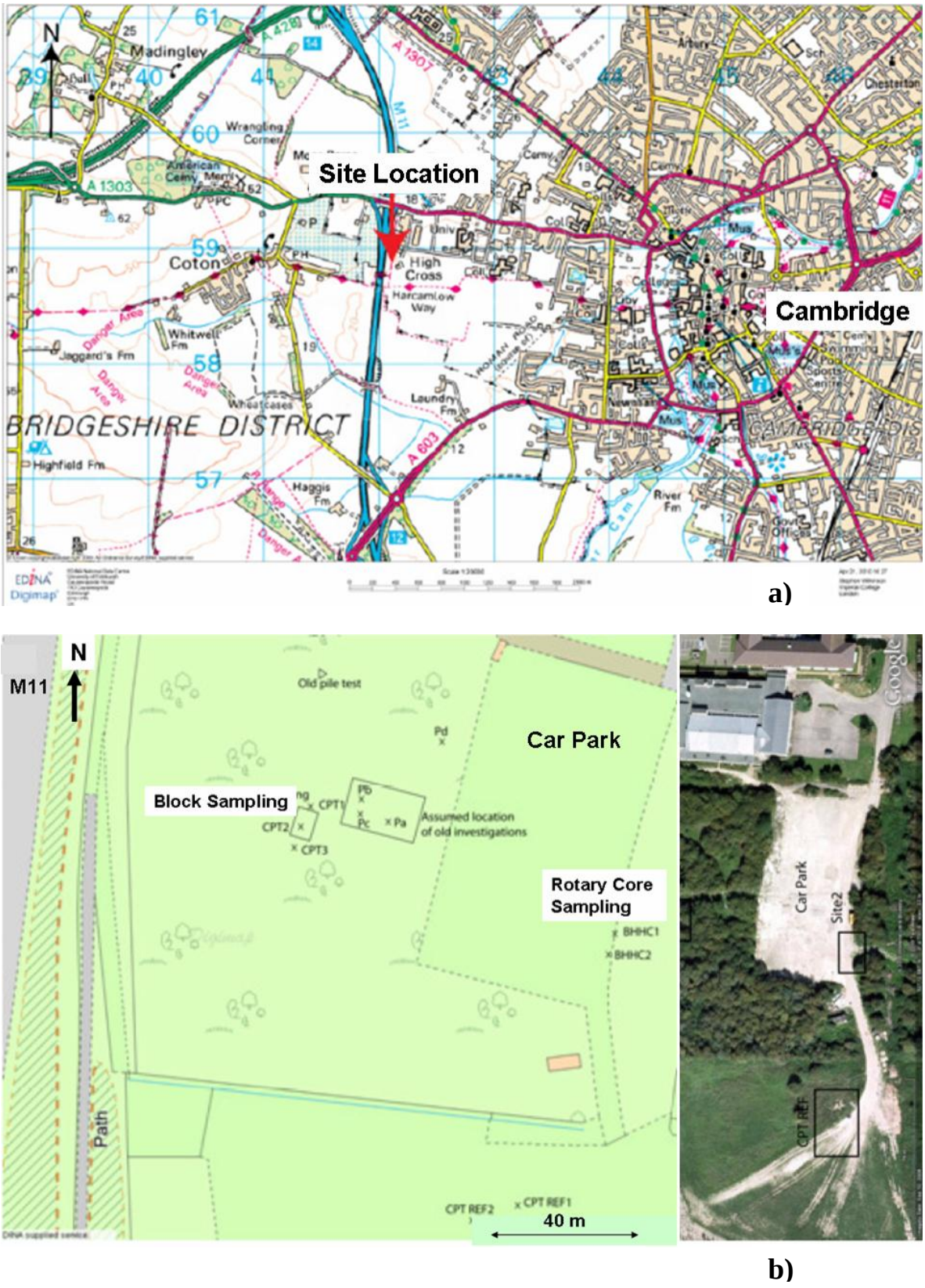
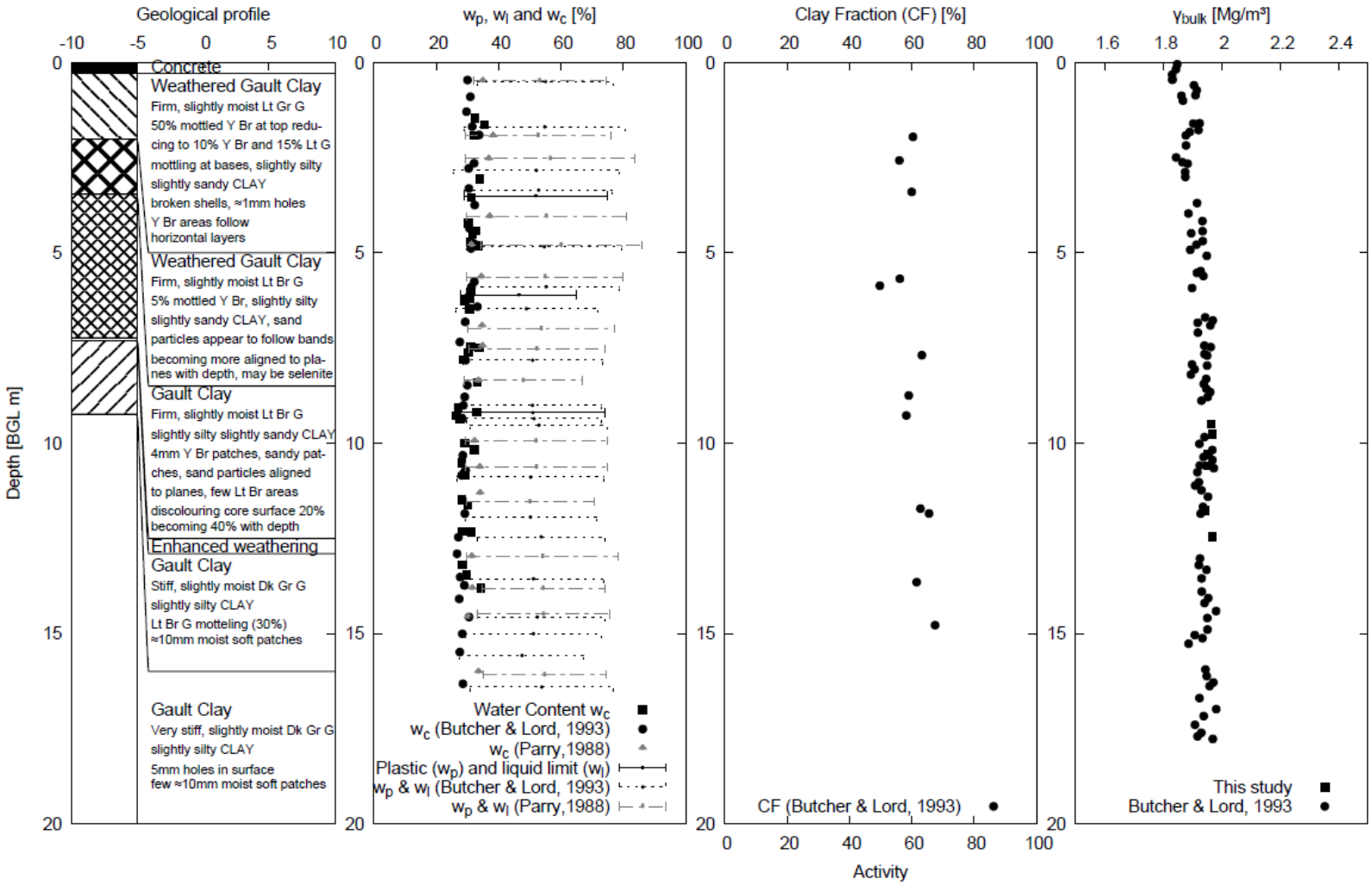


Figure 5-1: Sampling site for Gault clay;a) map of Cambridge and the site location, High Cross (Ordnance Survey, 2008), b) field map and Google Earth image of the sampling locations (after Wilkinson, 2011)



***Lt Gr G: Light Greenish Grey, Y Br: Yellowish Brown, Lt G: Light Grey, Lt Br G: Light Brownish Grey, Lt Br: Light Brown, Dk Gr G: Dark Greenish Grey**

Figure 5-2: Soil profile at High Cross

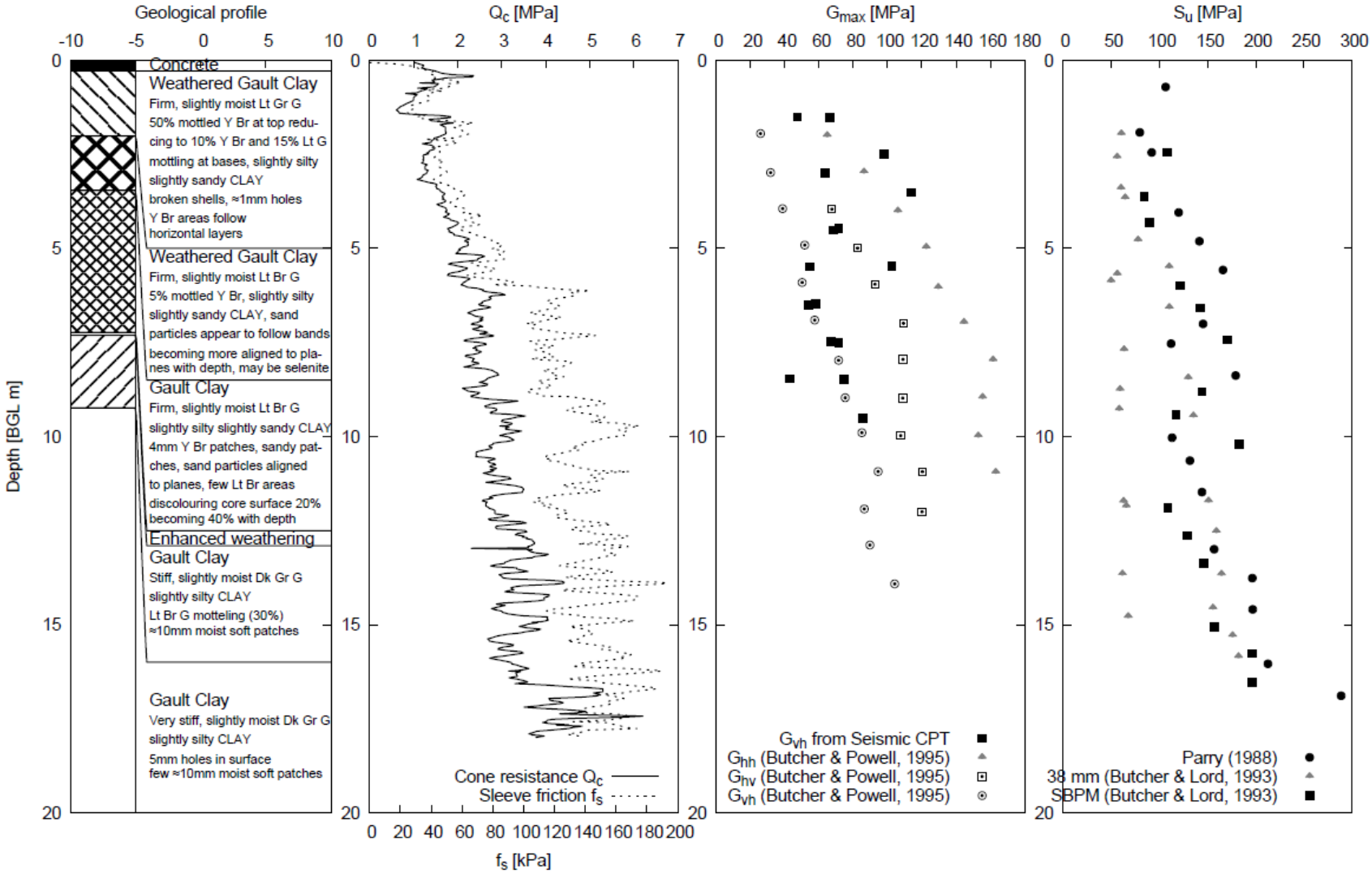


Figure 5-3: Soil profile at High Cross (CPT data provided by In-situ SI)



Figure 5-4: Macro-structure of rotary core sample of Gault clay from 10m depth, natural discontinuities are outlined with dotted line (produced with Brosse, 2012)

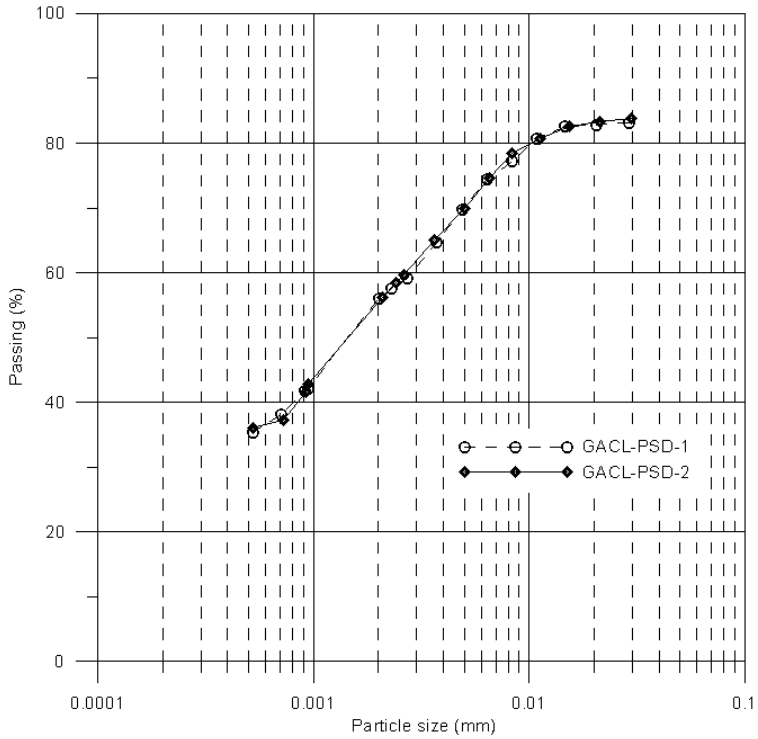


Figure 5-5: Particle size distribution of samples from 3.5m depth

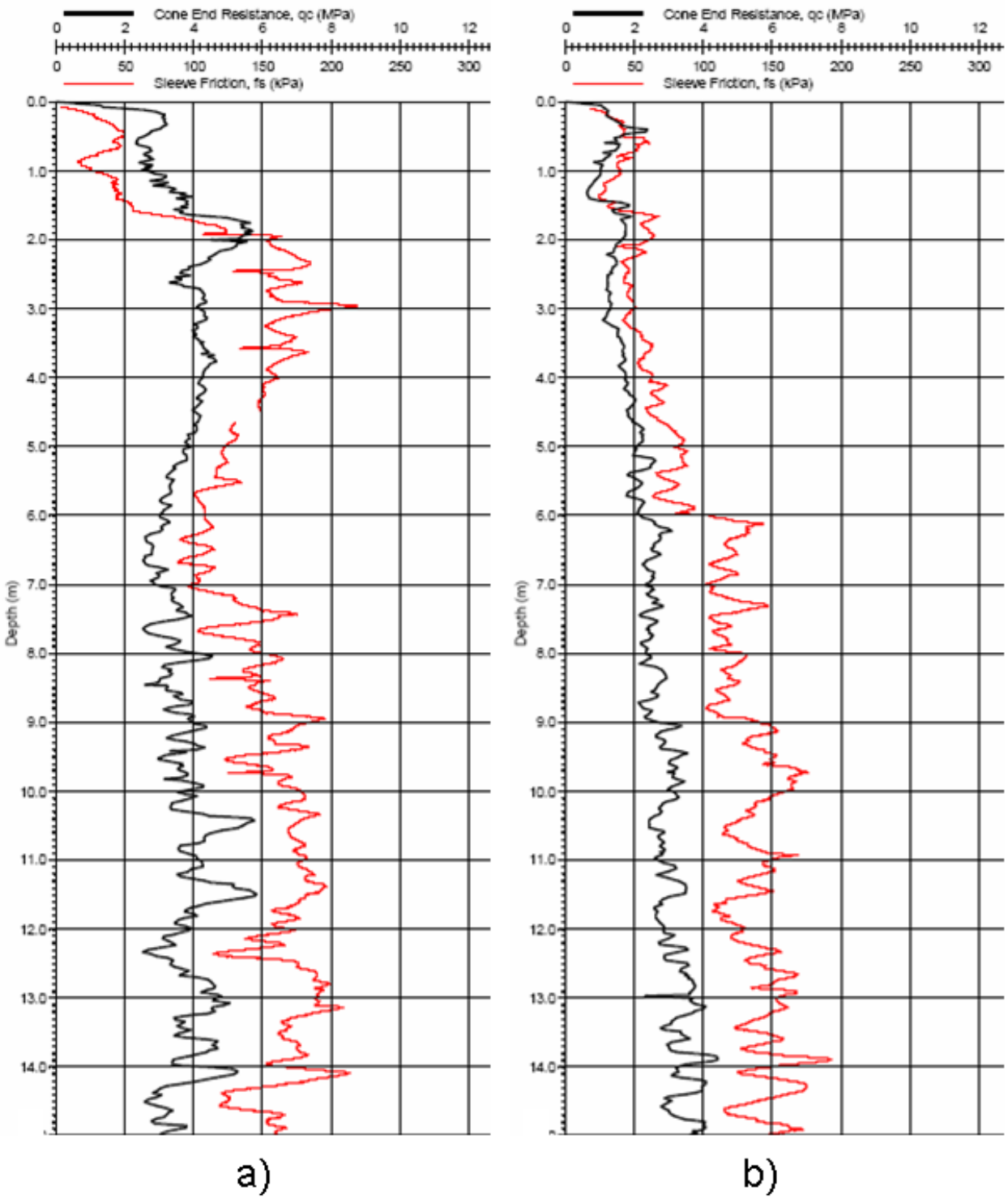


Figure 5-6: Gault clay CPT profile; a) close to trees, b) away from trees (data provided by In-situ SI)

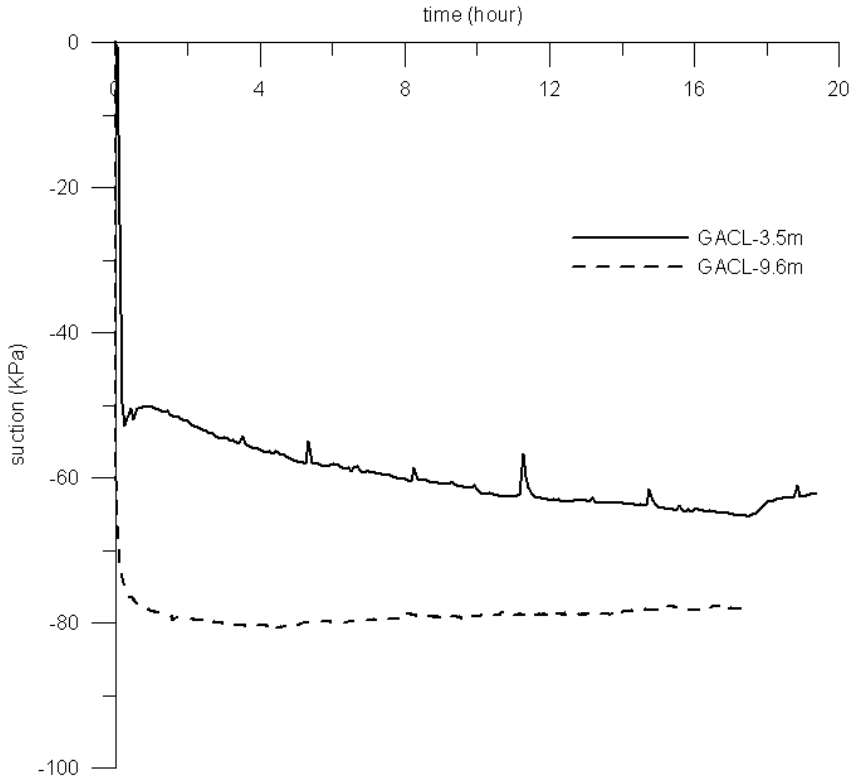


Figure 5-7: Suction measurments on rotary core samples of Gault clay at shallow (3.5m) and deep (9.6m) depths

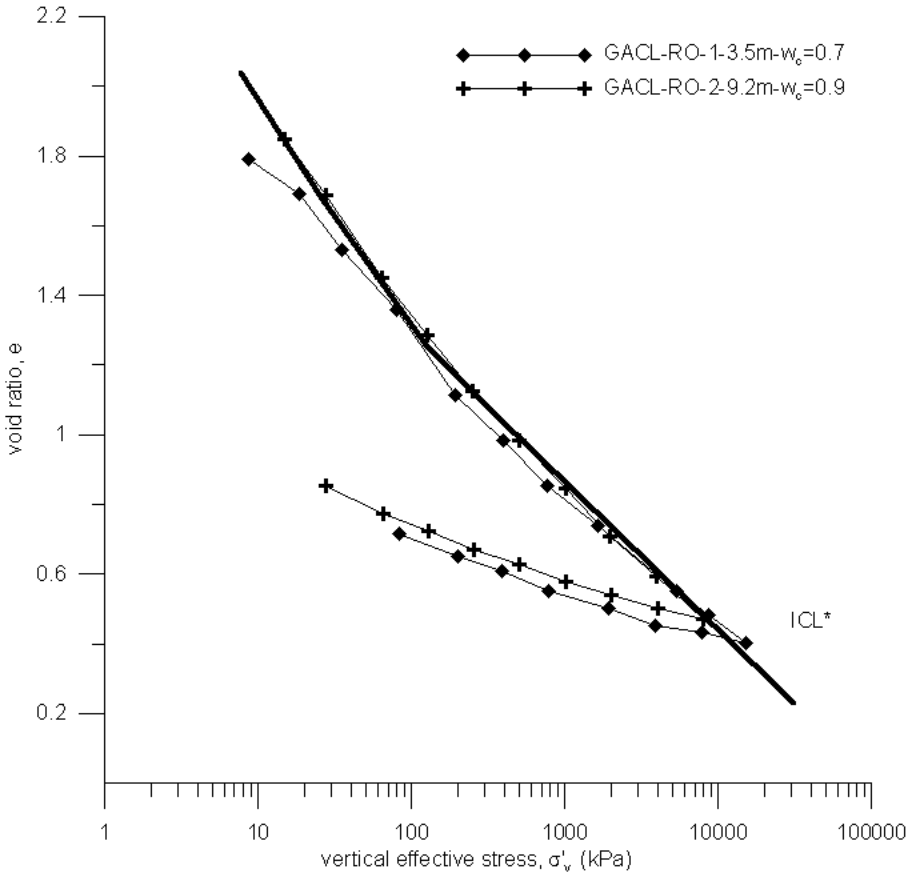


Figure 5-8: One-dimensional compression of reconstituted Gault clay

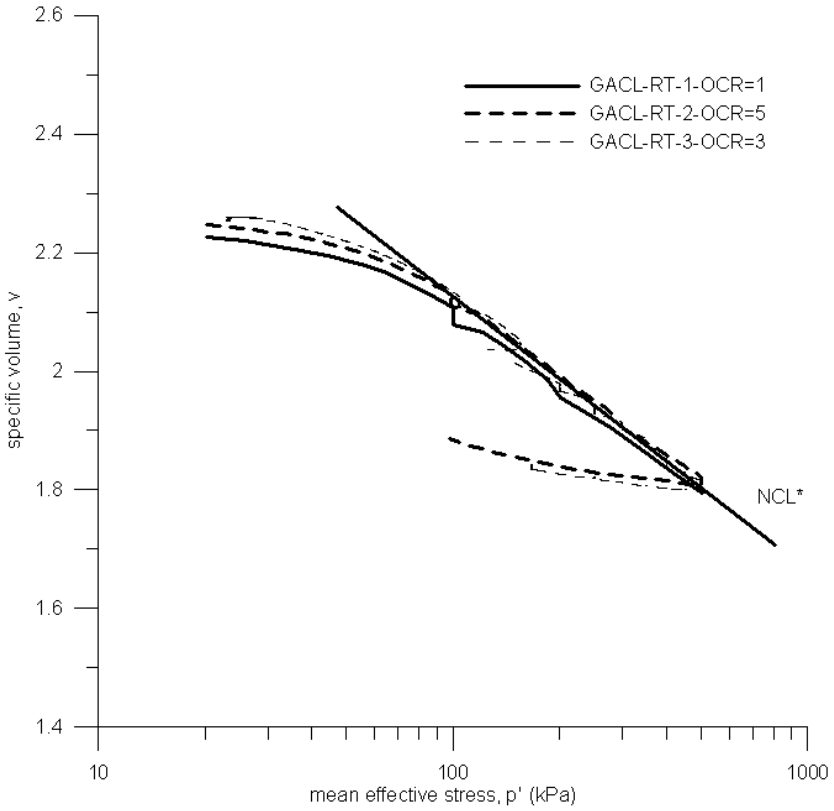


Figure 5-9: Isotropic compression of reconstituted Gault clay

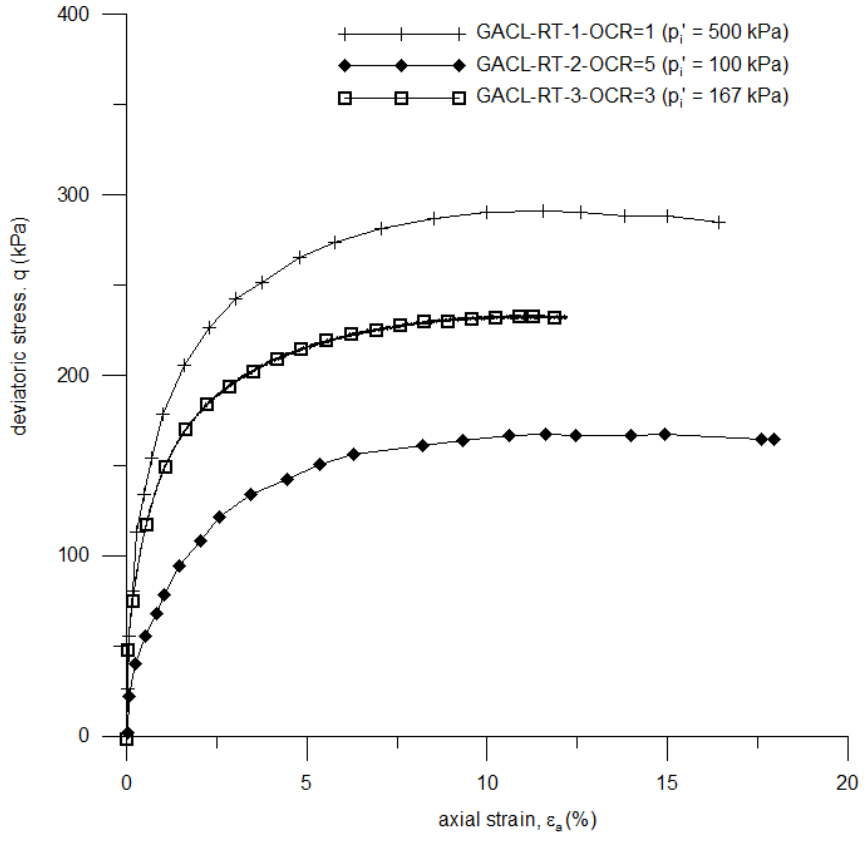


Figure 5-10: Undrained triaxial stress-strain behaviour of isotropically compressed reconstituted Gault clay

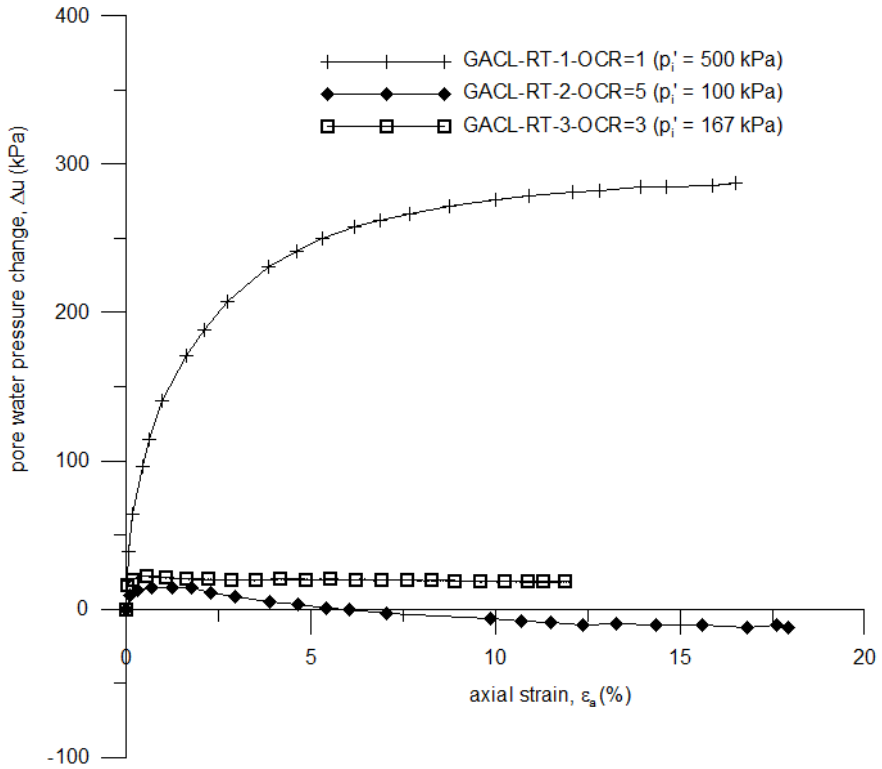


Figure 5-11: Pore water pressure change during the shearing of reconstituted Gault clay

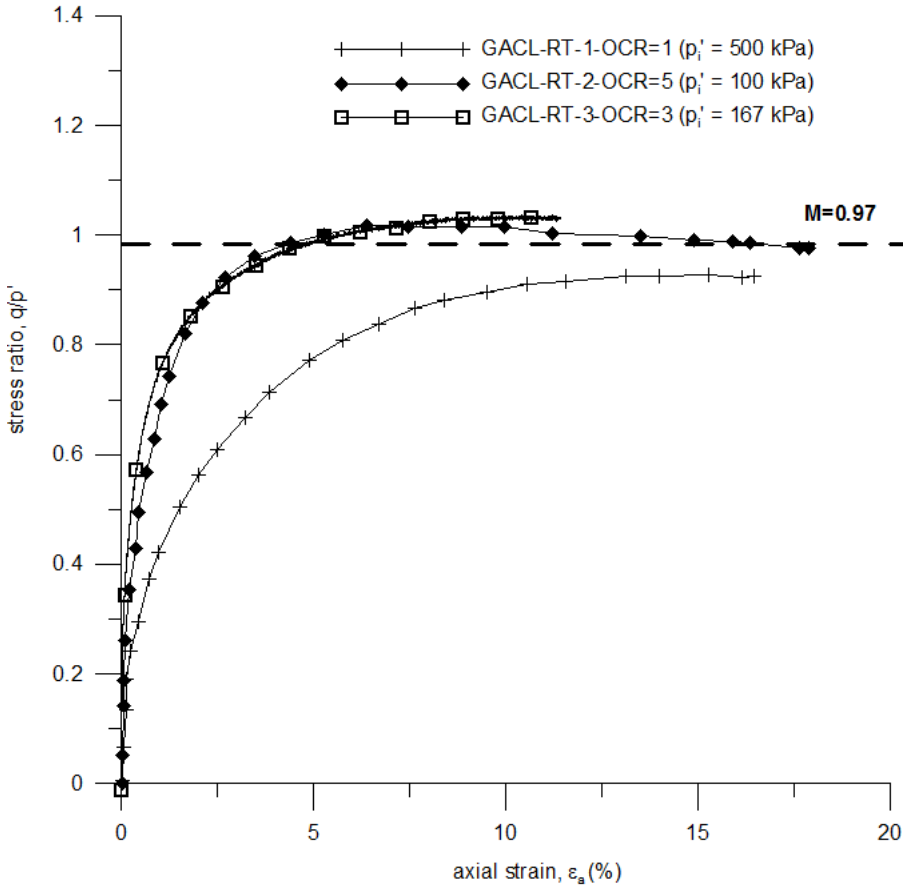


Figure 5-12: Normalised stress-strain behaviour of reconstituted Gault clay

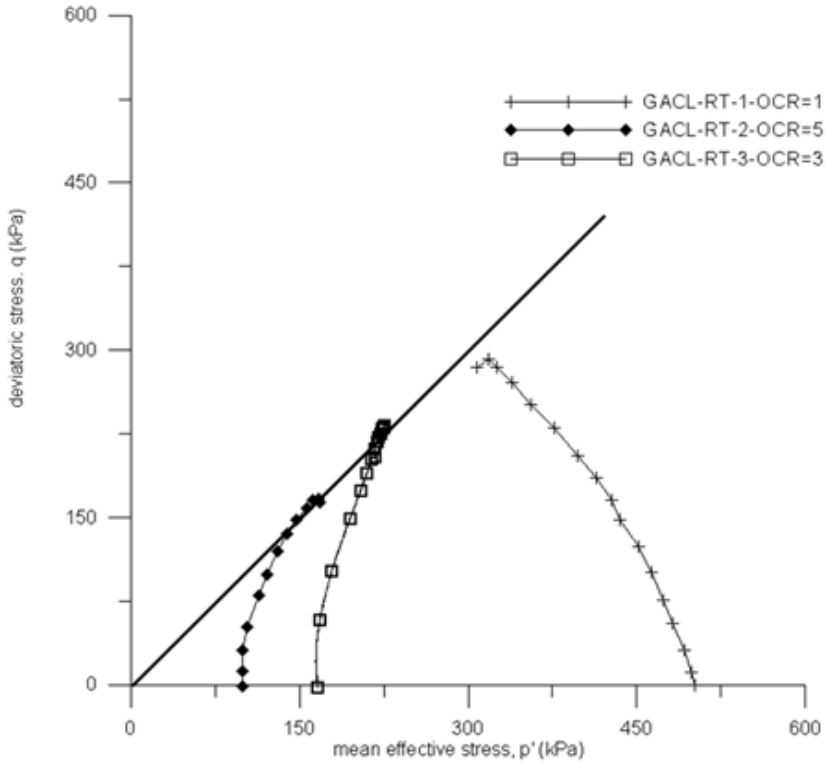


Figure 5-13: Effective stress paths for reconstituted isotropically consolidated Gault clay

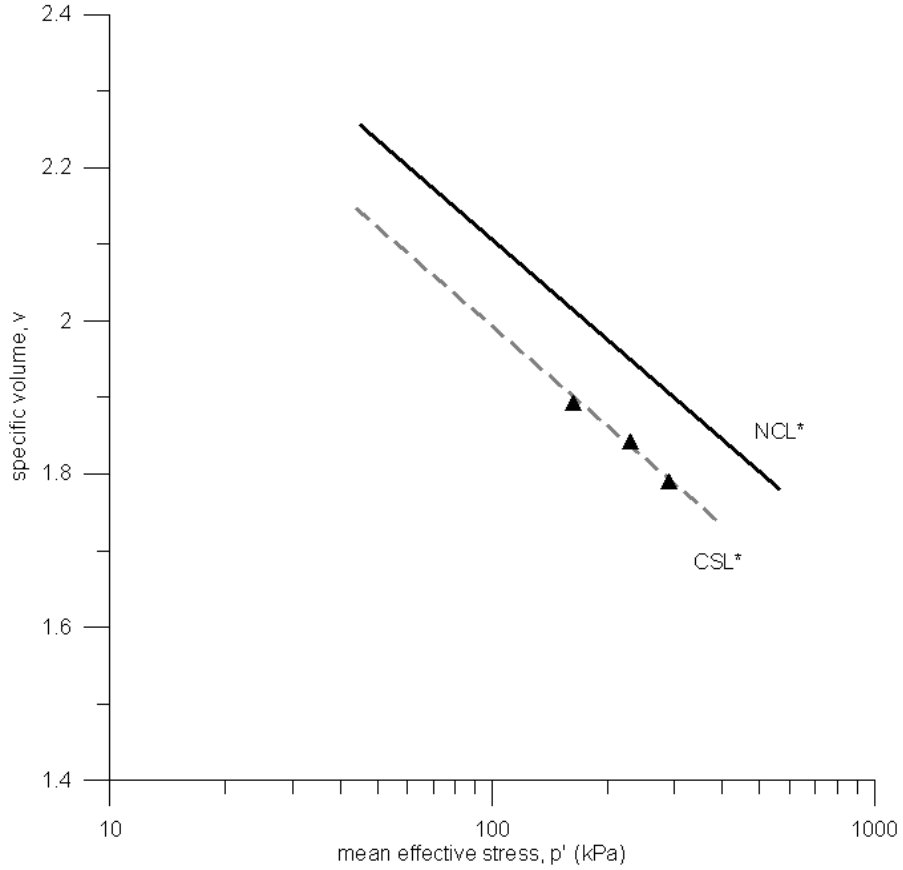


Figure 5-14: Normal Compression and Critical State Lines for reconstituted isotropically consolidated Gault clay

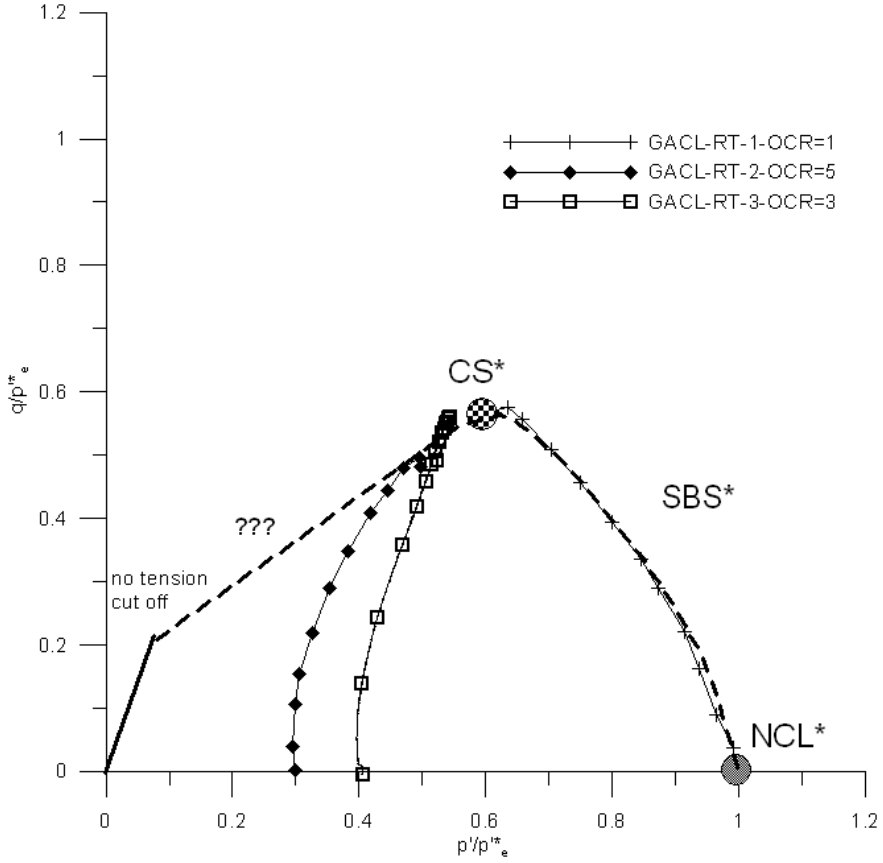


Figure 5-15: Normalised effective stress paths of reconstituted Gault clay

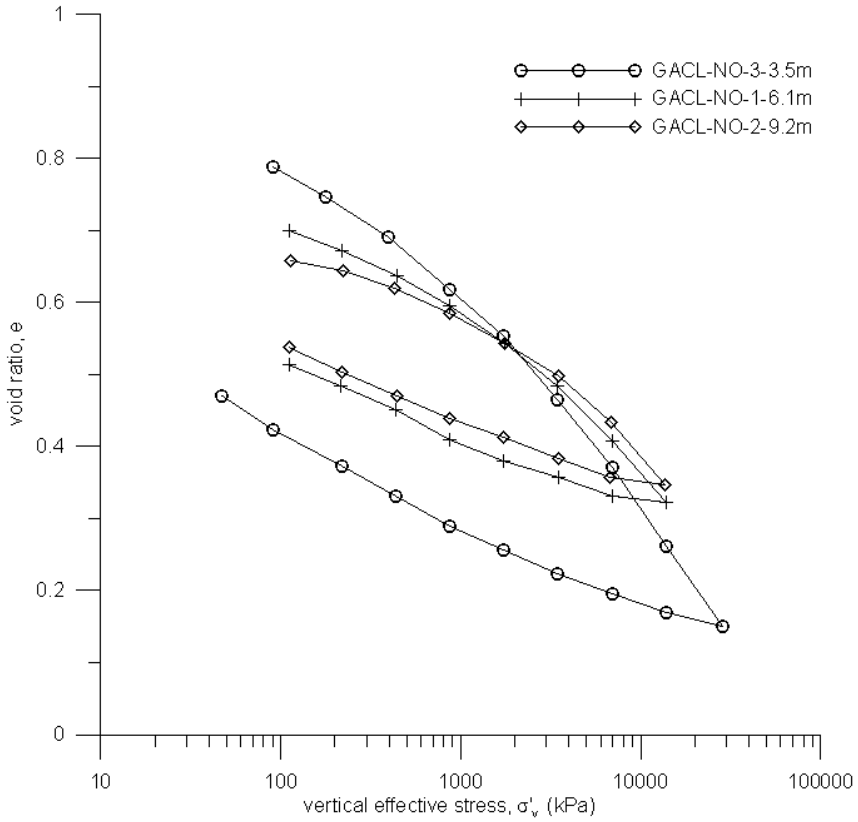


Figure 5-16: Oedometer compression curves for natural Gault clay from rotary core samples

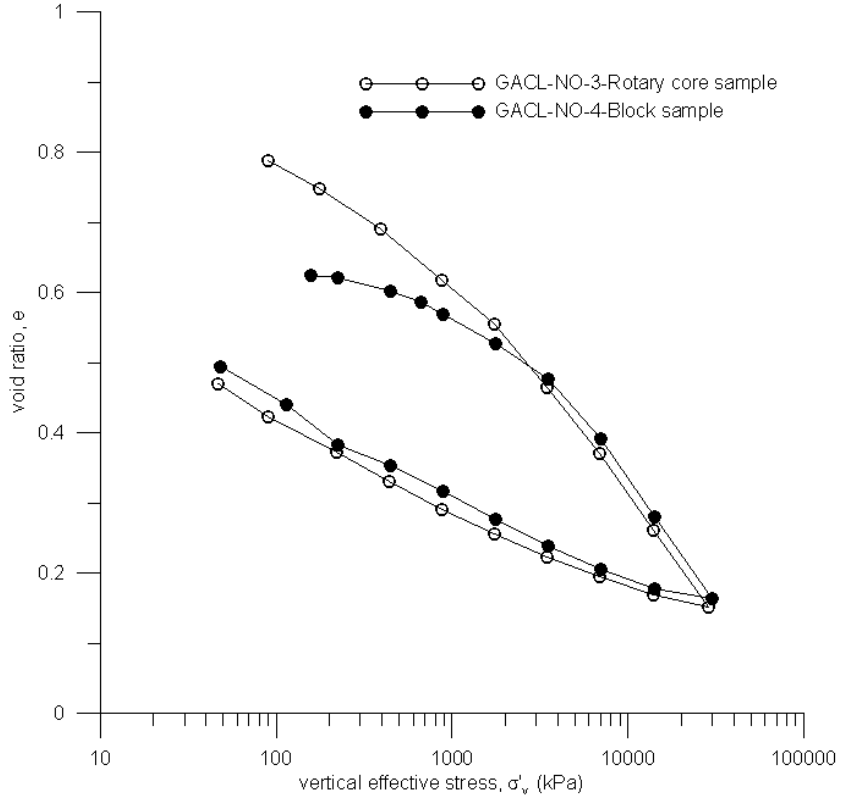


Figure 5-17: Oedometer compression curves for ntact Gault clay from rotary core and block samples at 3.5m depth

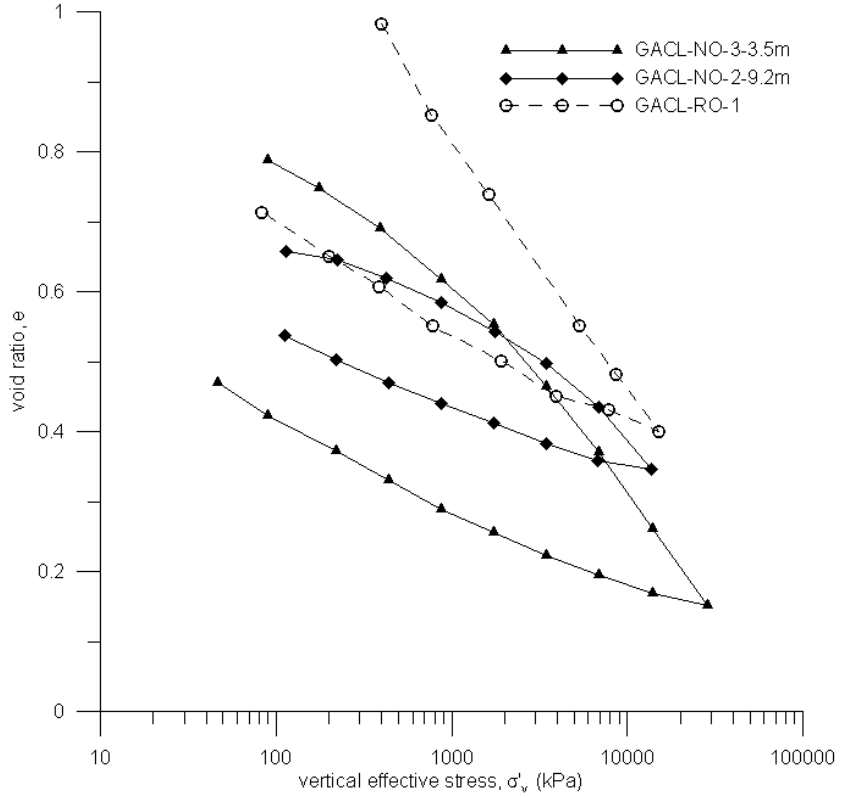


Figure 5-18: Oedometer compression lines for natural (full symbols) and reconstituted (empty symbol) Gault clay

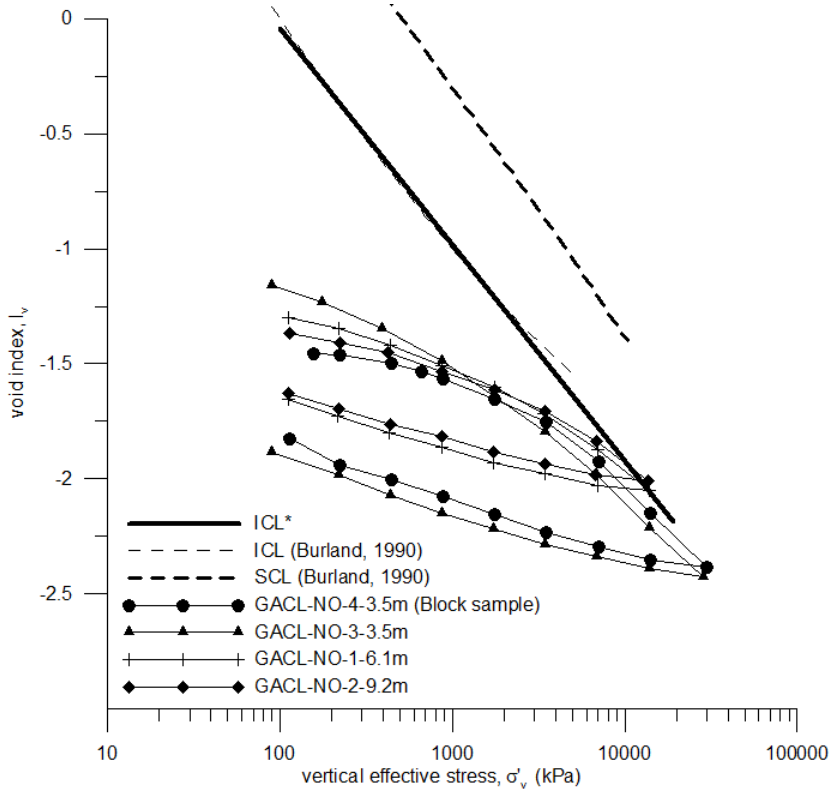


Figure 5-19: Normalised one-dimensional compression curves

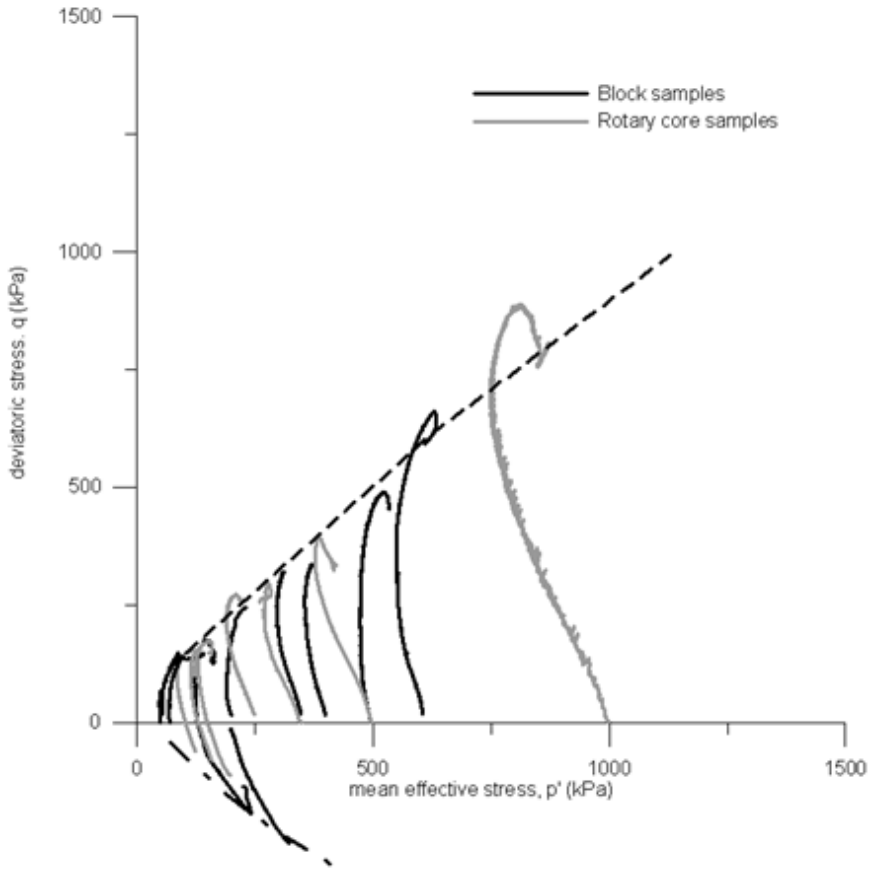


Figure 5-20: Stress paths for natural Gault clay in compression and extension

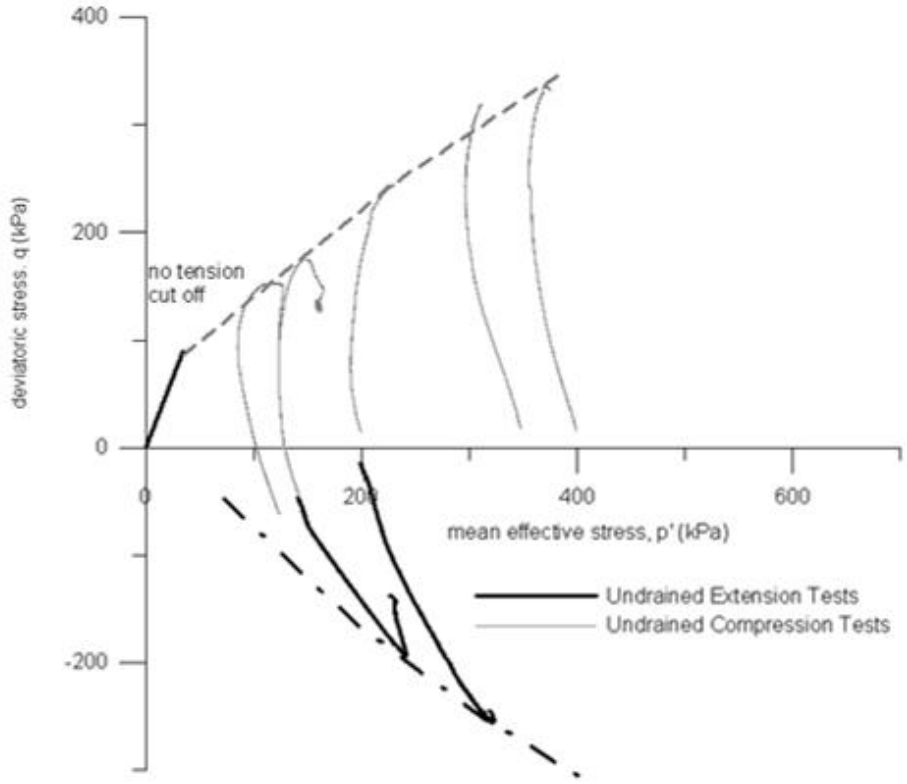


Figure 5-21: Stress paths for natural Gault clay in compression and extension

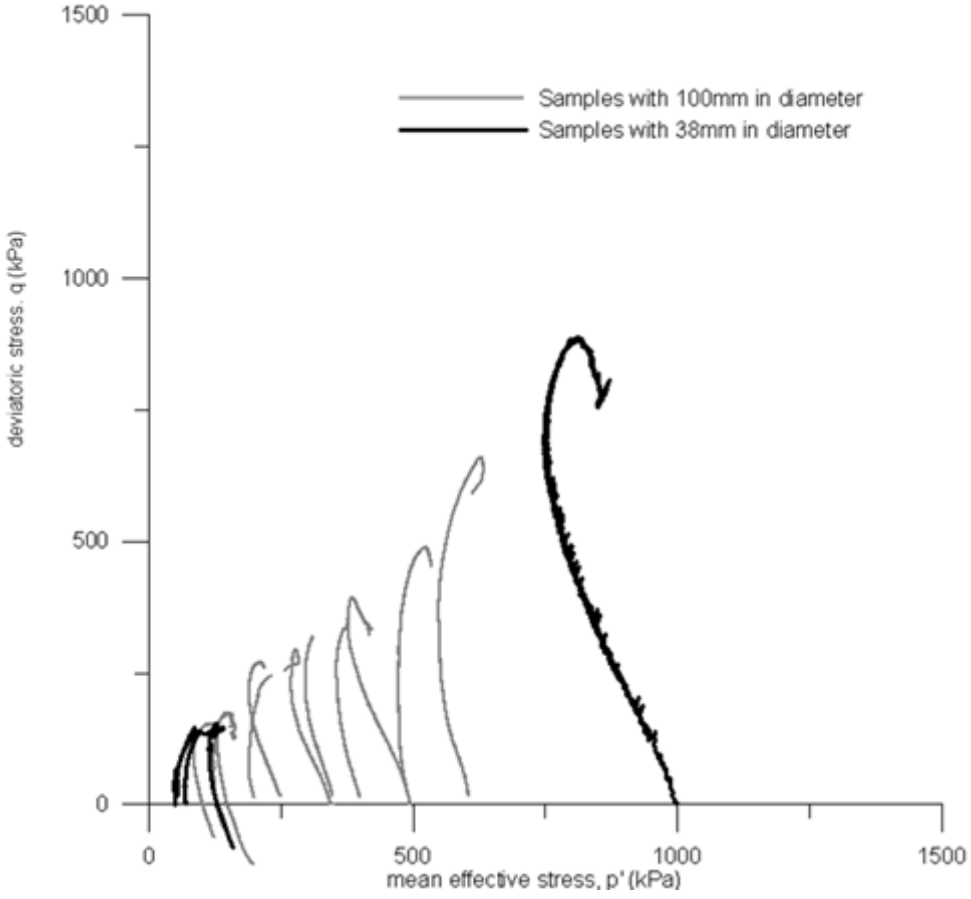


Figure 5-22: Effect of sample size on the strength of Gault clay

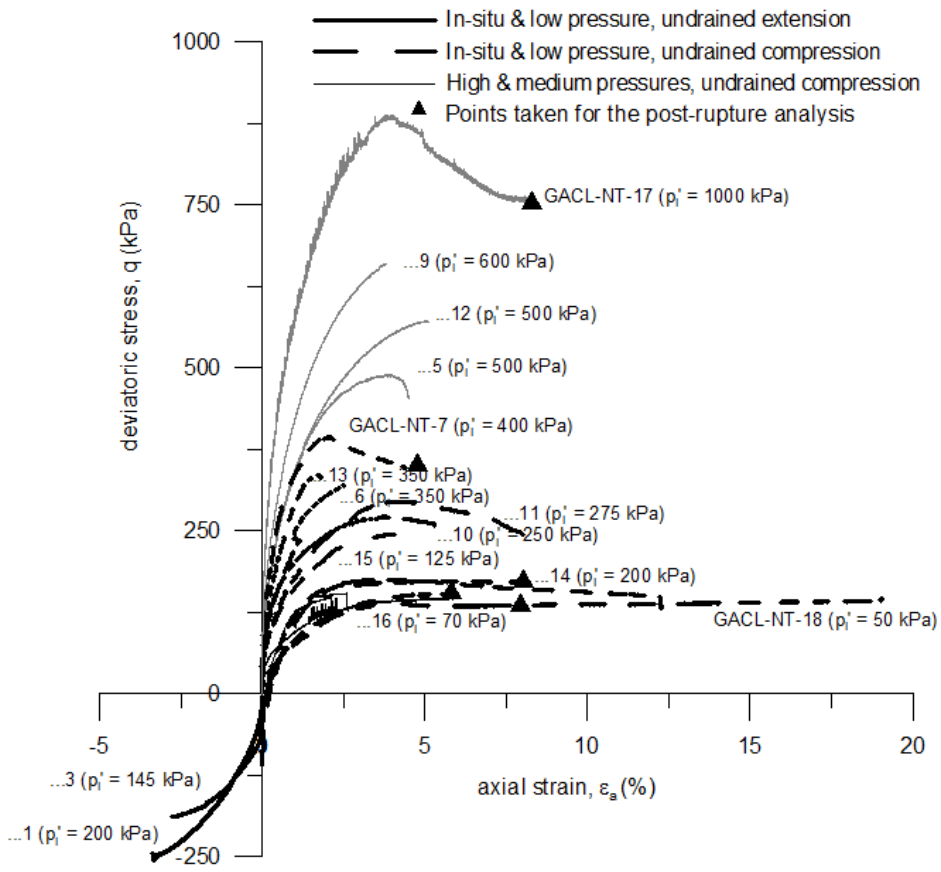


Figure 5-23: Stress-strain behaviour of natural Gault clay

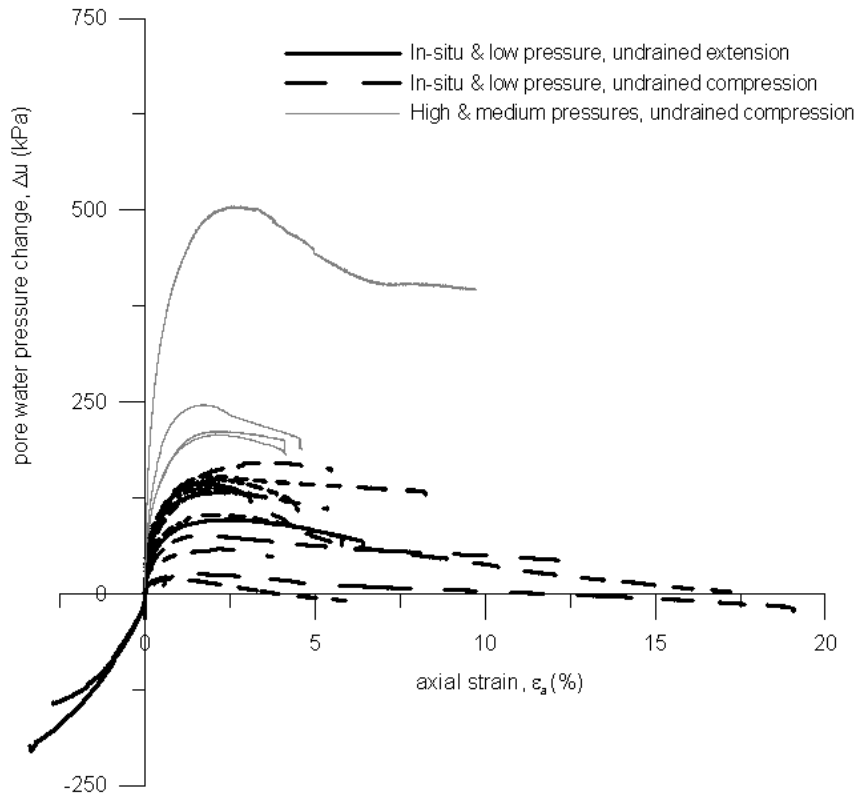


Figure 5-24: Pore water pressure change during the shearing of natural Gault clay

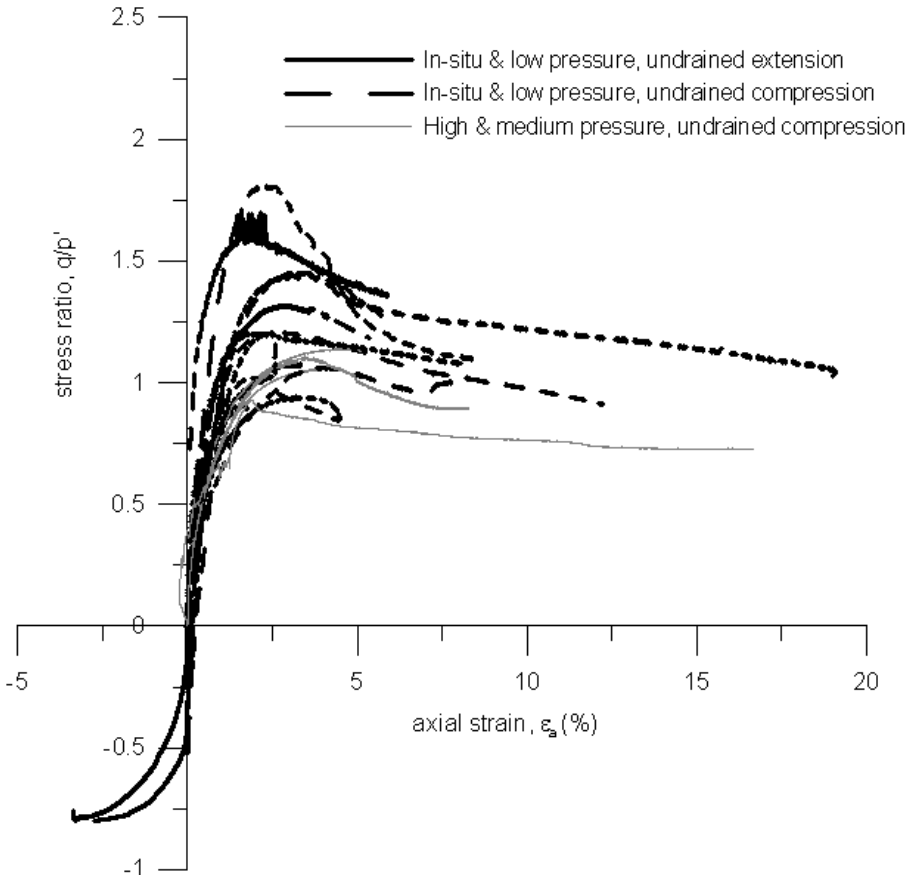


Figure 5-25: Normalised stress-strain behaviour of natural Gault clay

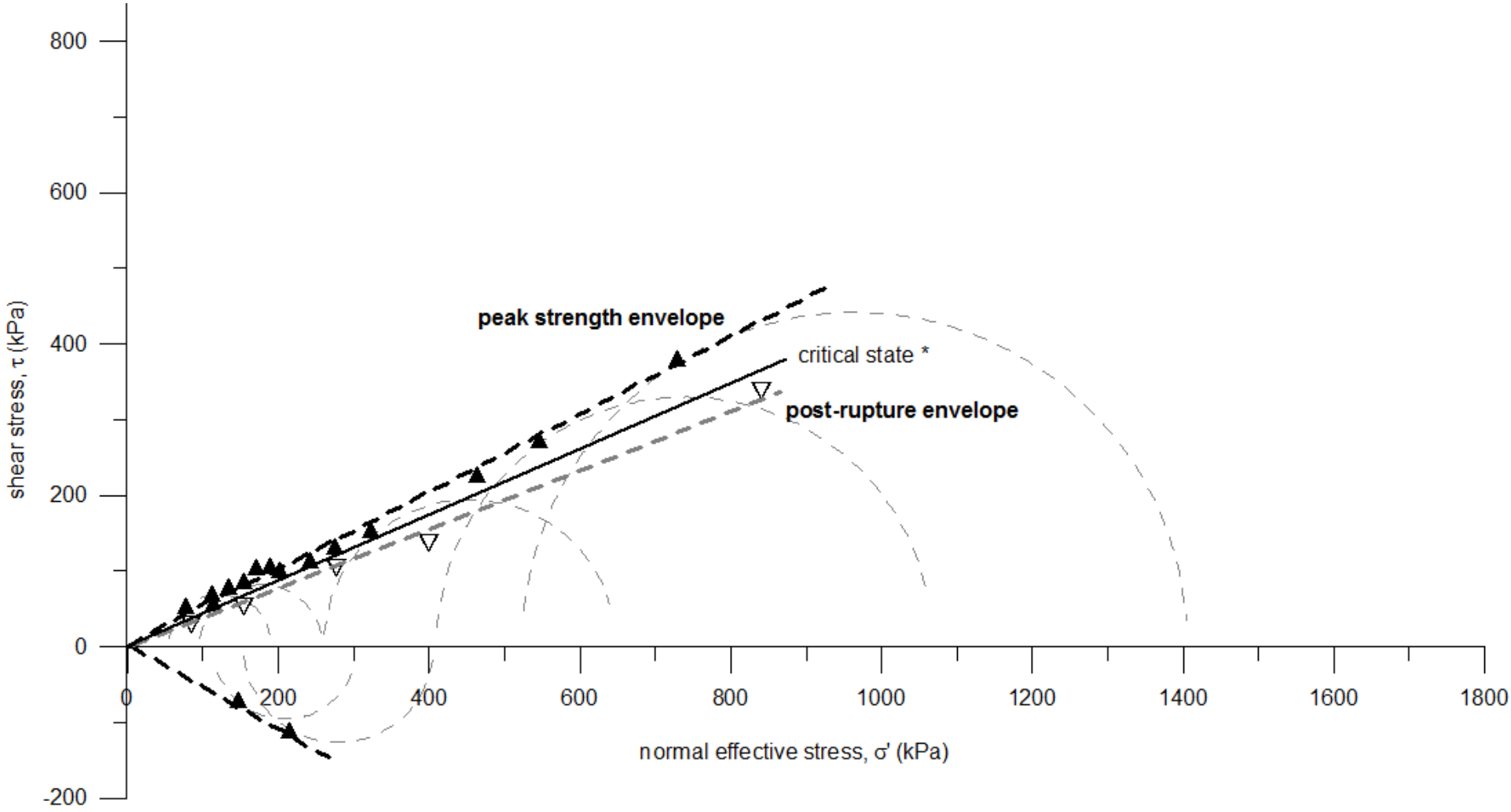


Figure 5-26: Peak and post-rupture strength envelope for natural Gault clay

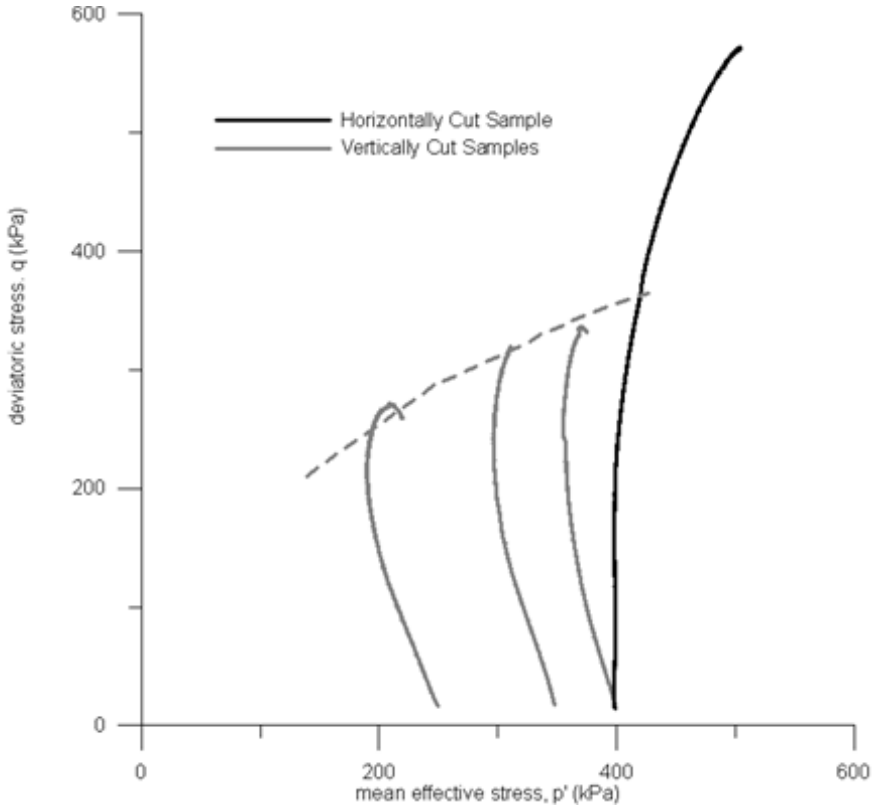


Figure 5-27: Stress paths of horizontally and vertically cut samples of natural Gault clay

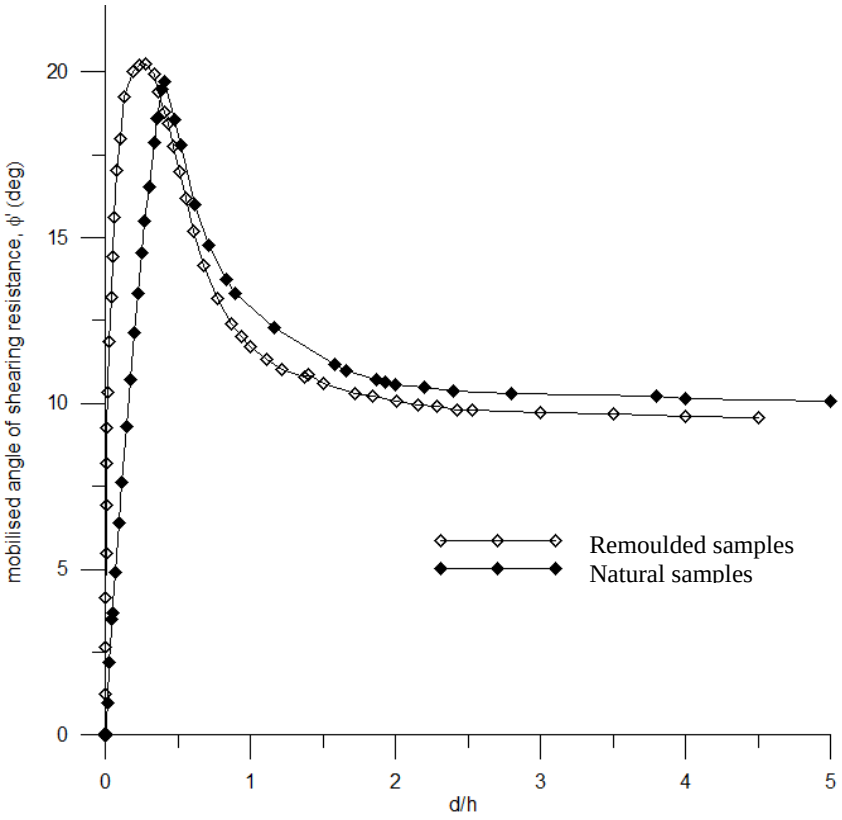


Figure 5-28: Stress-strain behaviour of natural and remoulded Gault clay at small displacements in the ring shear apparatus under 400 kPa normal stress (d = shear displacement, h = sample height)

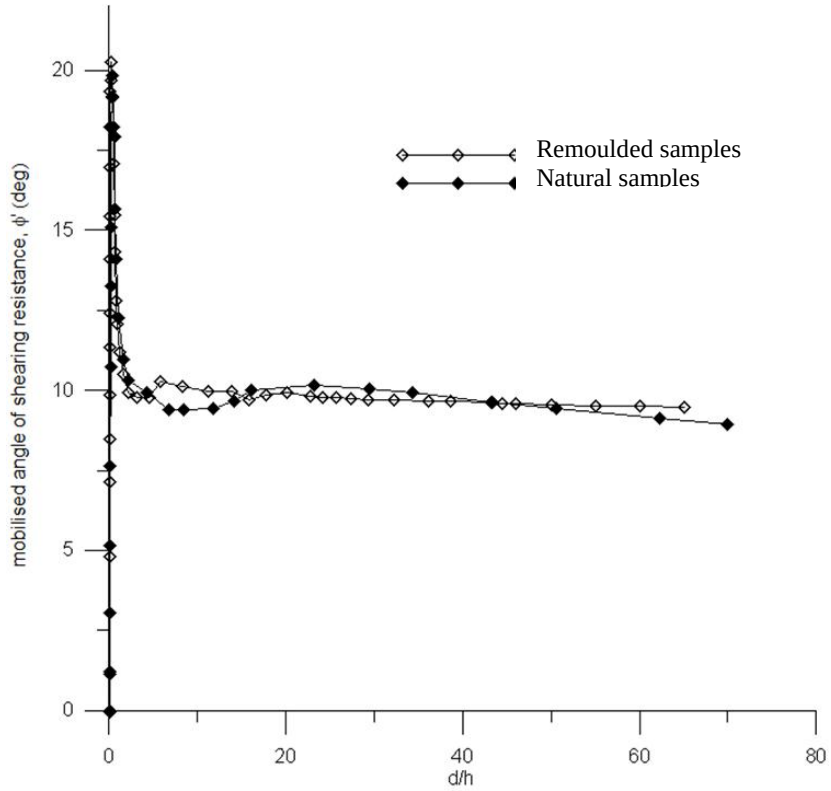


Figure 5-29: Stress-strain behaviour of natural and remoulded Gault clay at large displacements in a ring shear apparatus under 400 kPa normal stress (d = shear displacement, h = sample height)

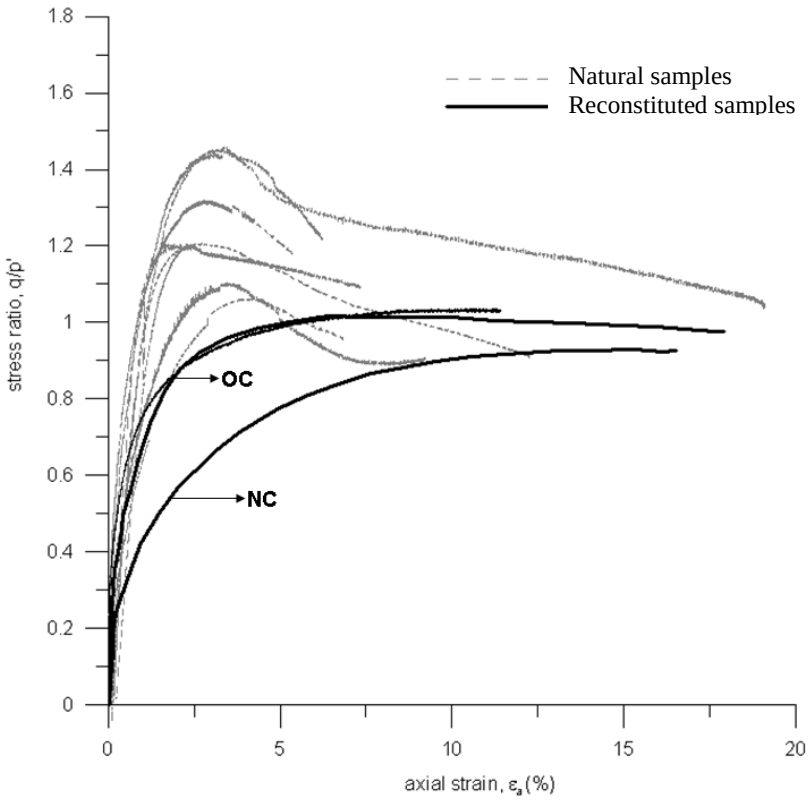


Figure 5-30: Normalised stress-strain behaviour for the natural and reconstituted (Normally consolidated & Overconsolidated) Gault clay

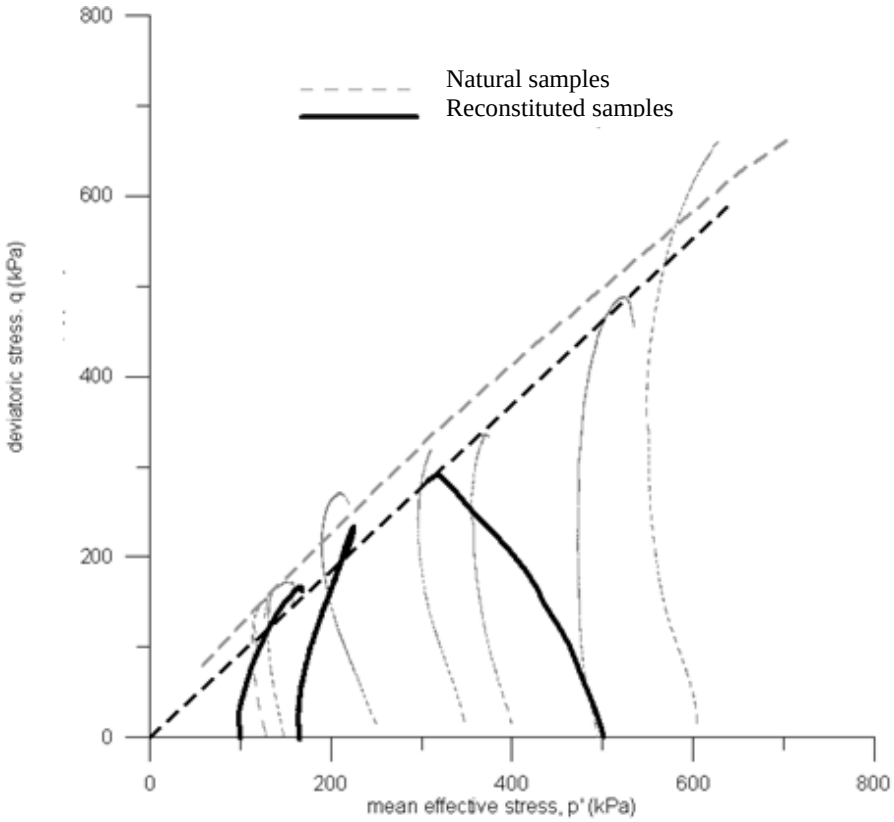


Figure 5-31: Stress paths for the natural and reconstituted Gault clay

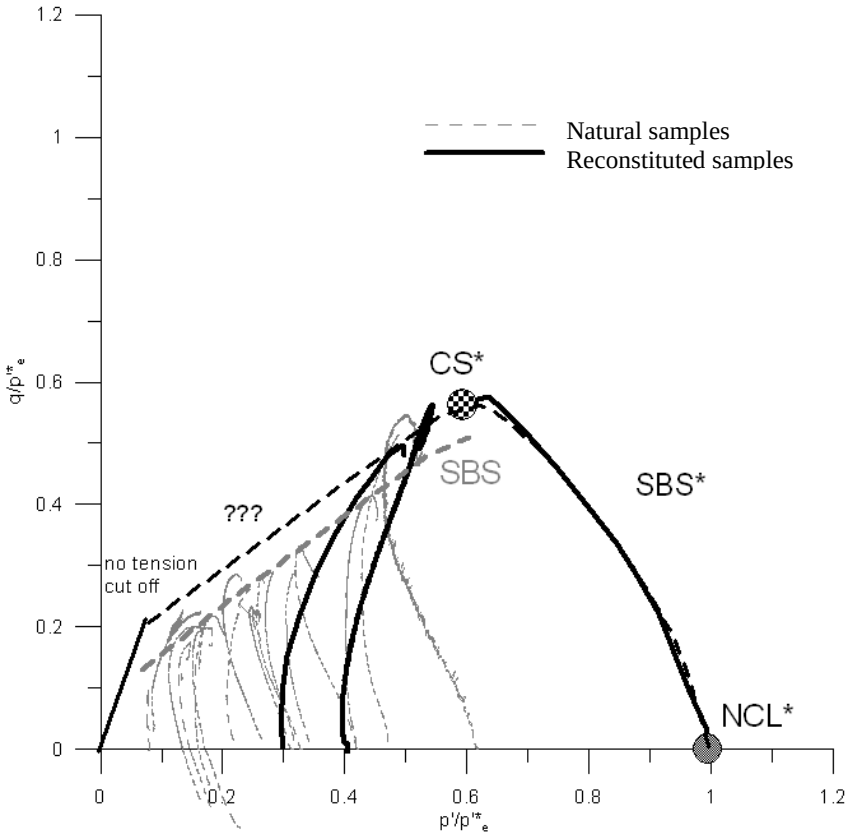


Figure 5-32: Normalised stress paths for the natural and reconstituted Gault clay

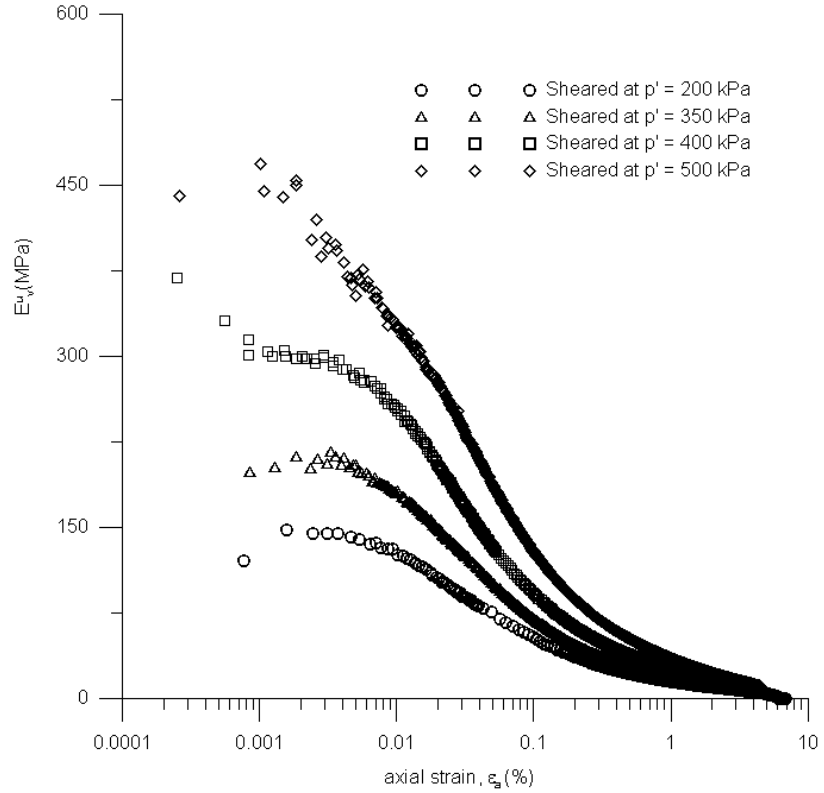


Figure 5-33: Stiffness degradation curves for the undrained compression tests on natural block samples of Gault clay at different consolidation effective stress levels

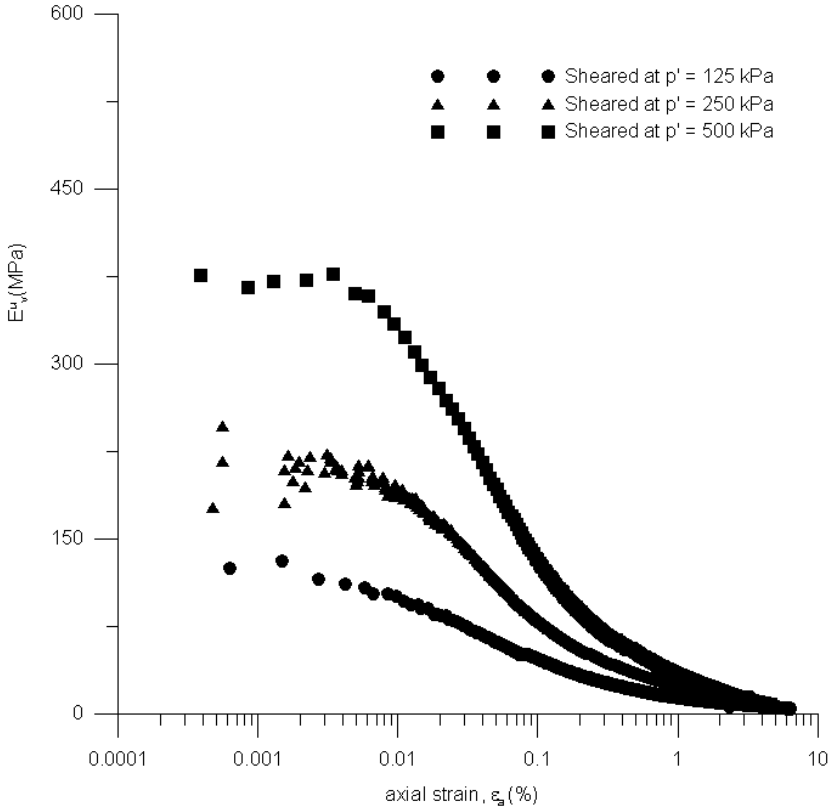


Figure 5-34: Stiffness degradation curves for the undrained compression tests on natural rotary core samples of Gault clay at different consolidation effective stress levels

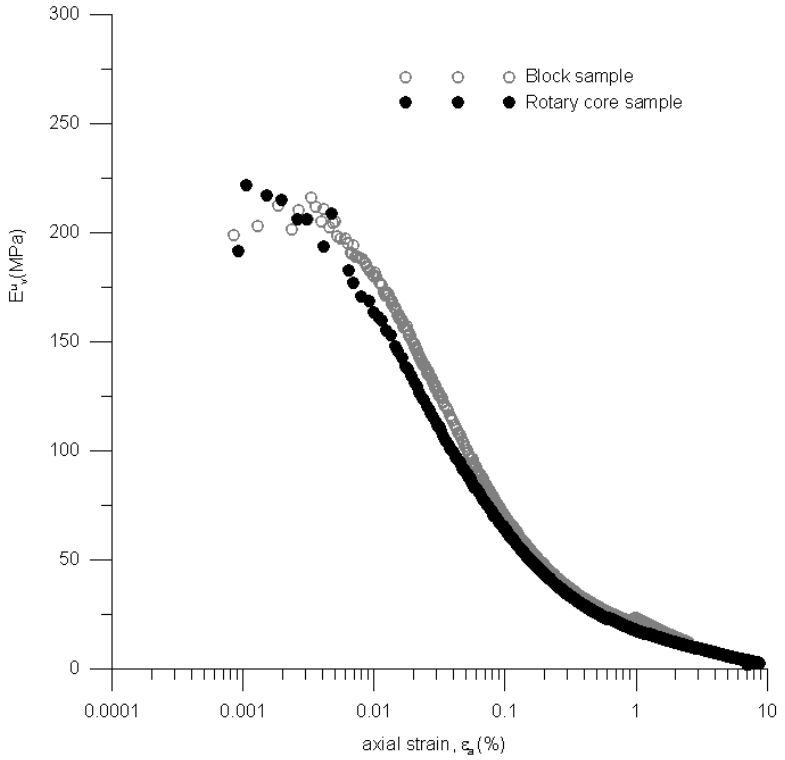


Figure 5-35: Stiffness degradation curves for the undrained compression tests on natural rotary core and block samples of Gault clay from the same depth at similar stress levels

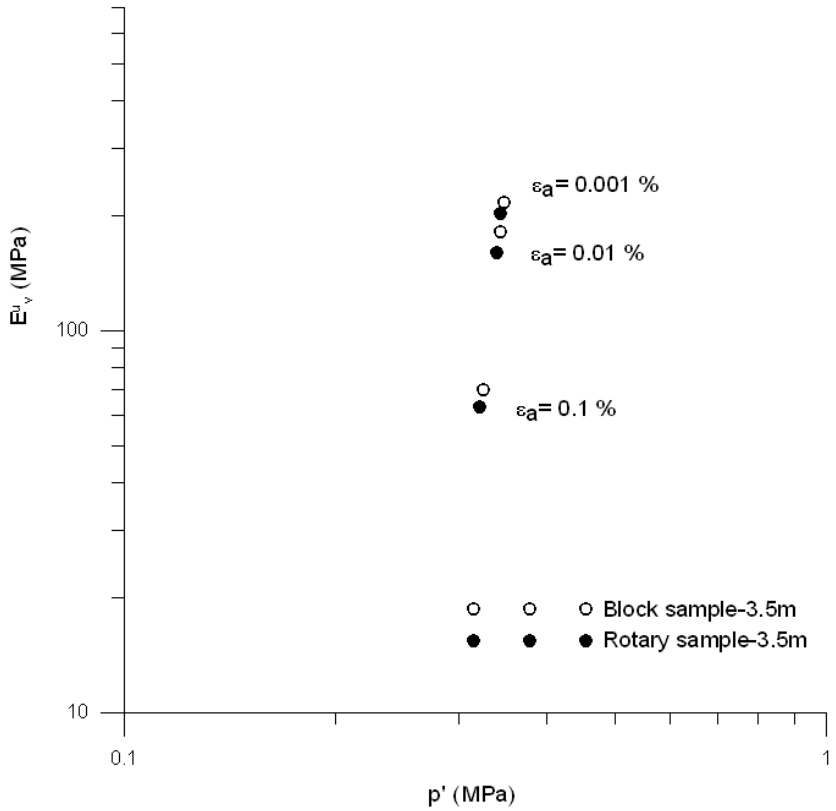


Figure 5-36: Stiffnesses at different strain levels for the natural rotary core and block samples of Gault clay

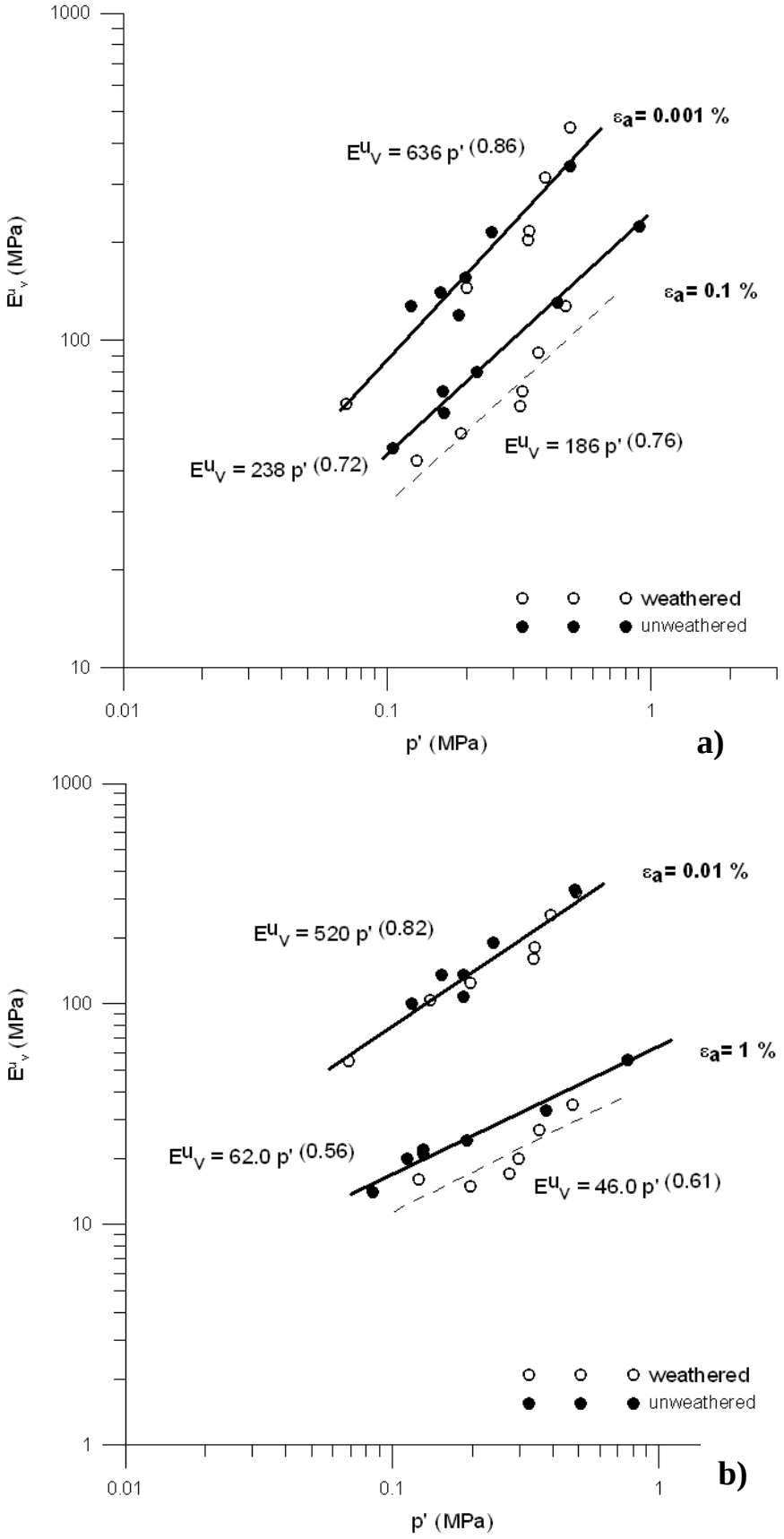


Figure 5-37: Undrained stiffness variation with stress level at different strain levels for the natural Gault clay; a) strain levels 0.001% and 0.1%, b) strain levels 0.01% and 1%

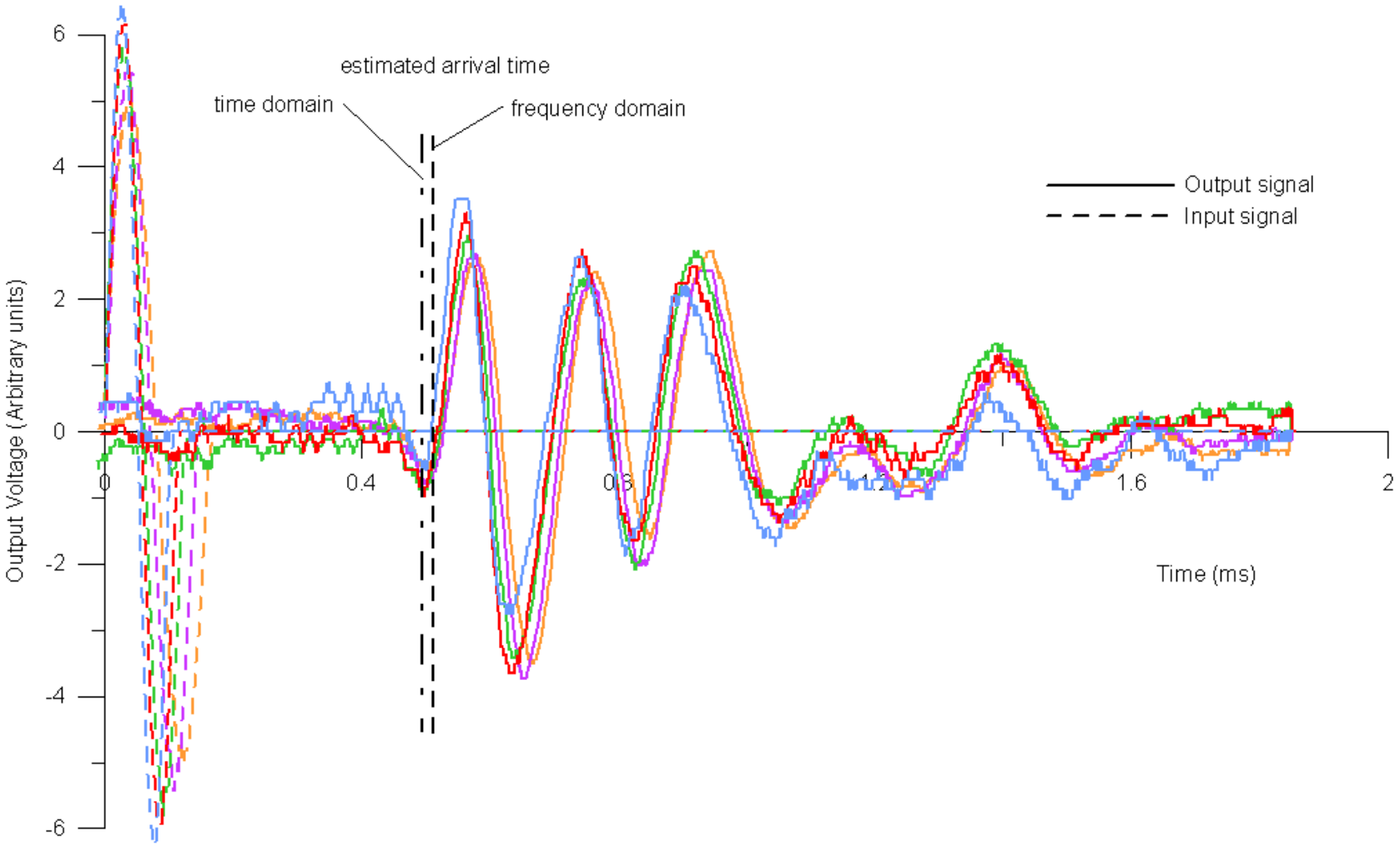


Figure 5-38: Typical bender element signals to obtain V_{hv} and G_{hv} values for the natural Gault clay

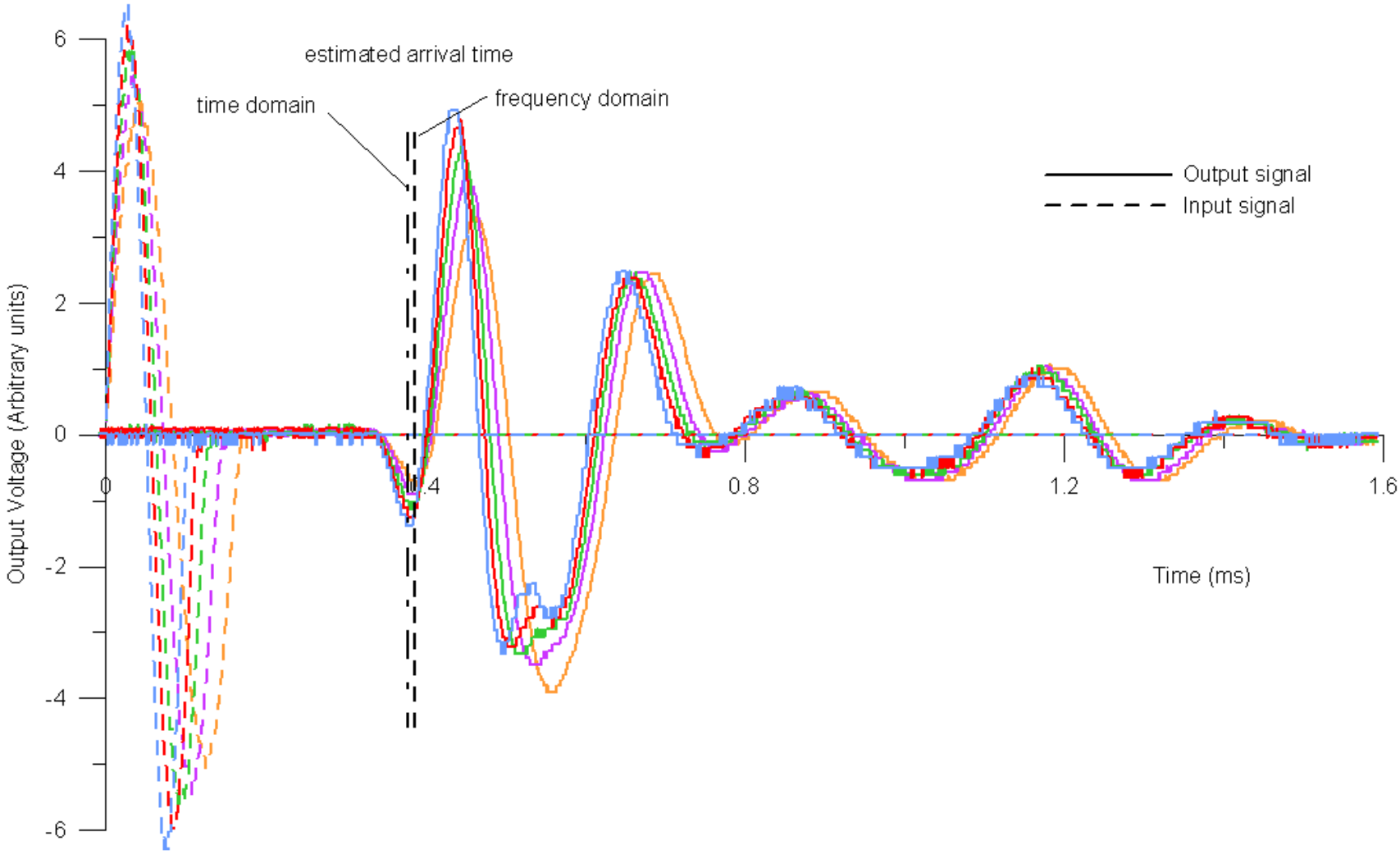


Figure 5-39: Typical bender element signals to obtain V_{hh} and G_{hh} values for the natural Gault clay

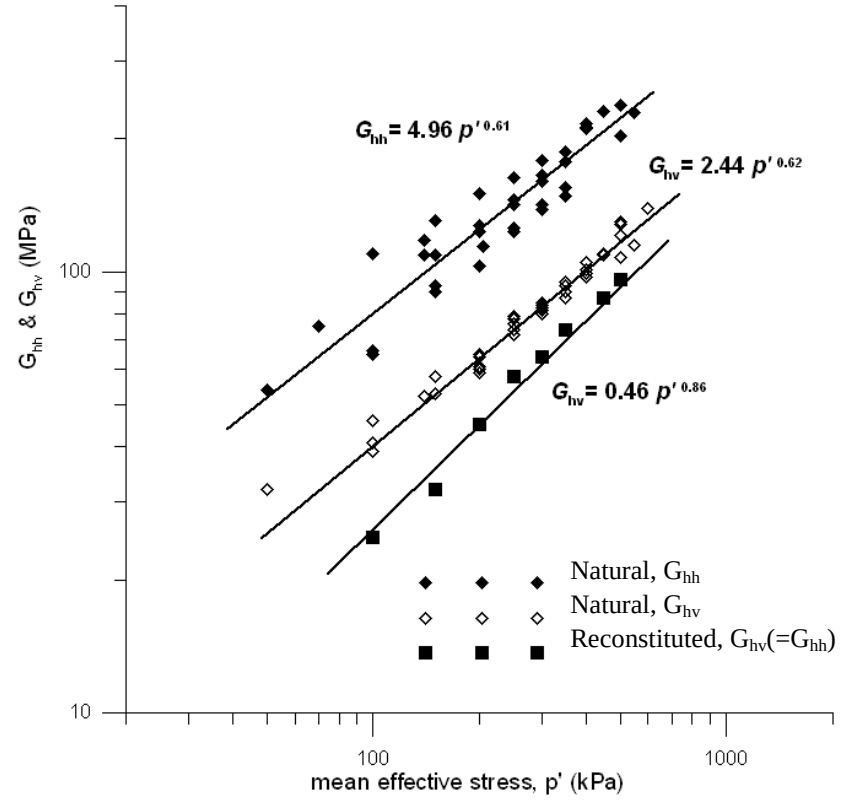


Figure 5-40: BE stiffness of the natural and reconstituted samples of Gault clay in different directions

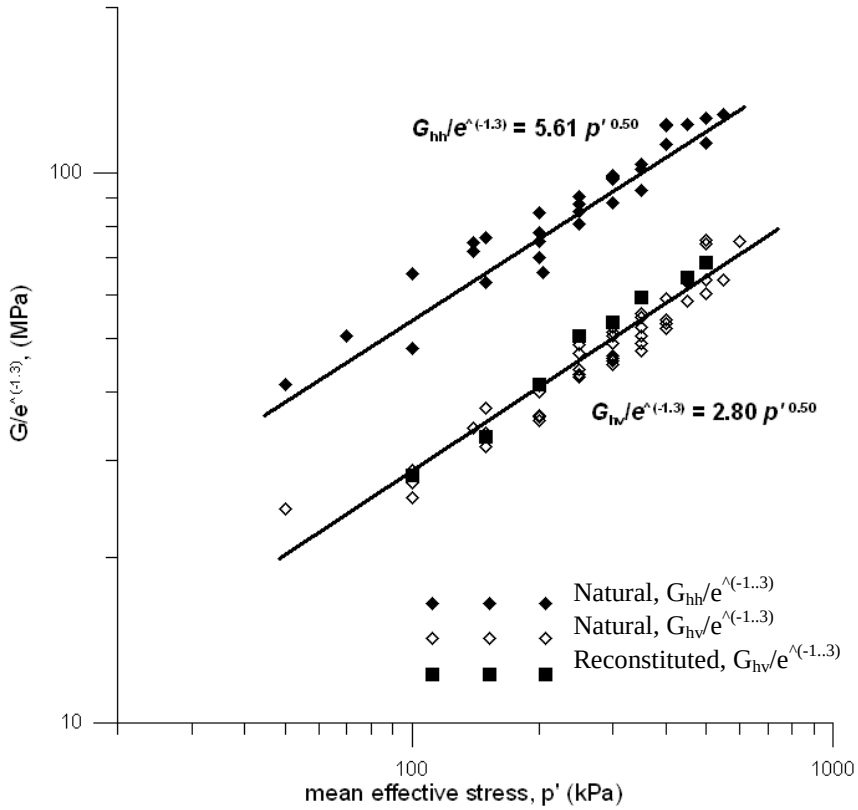


Figure 5-41: BE stiffness of the natural and reconstituted samples of Gault clay normalised for the void ratio

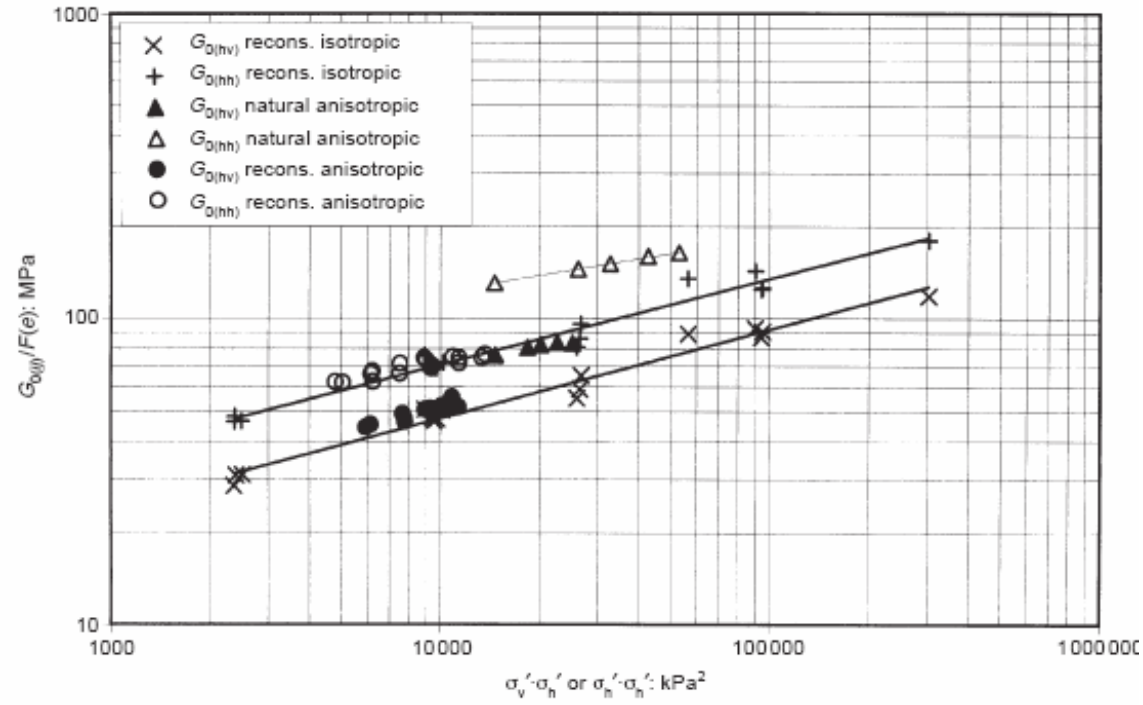


Figure 5-42: Normalised bender element shear moduli for reconstituted and natural samples of Gault clay following isotropic and anisotropic stress paths (Pennington et al., 1997)

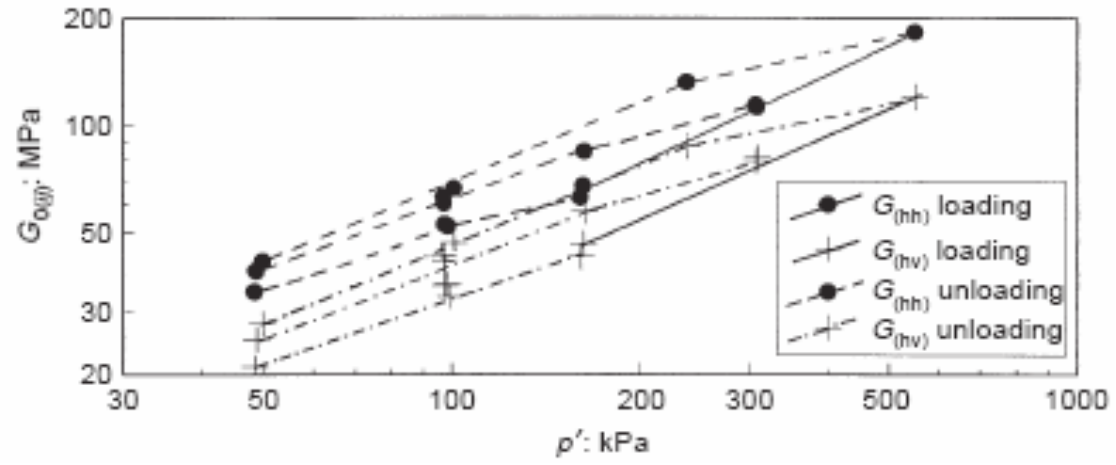


Figure 5-43: BE shear moduli for reconstituted samples of Gault clay following isotropic loading and unloading (Pennington et al., 1997)

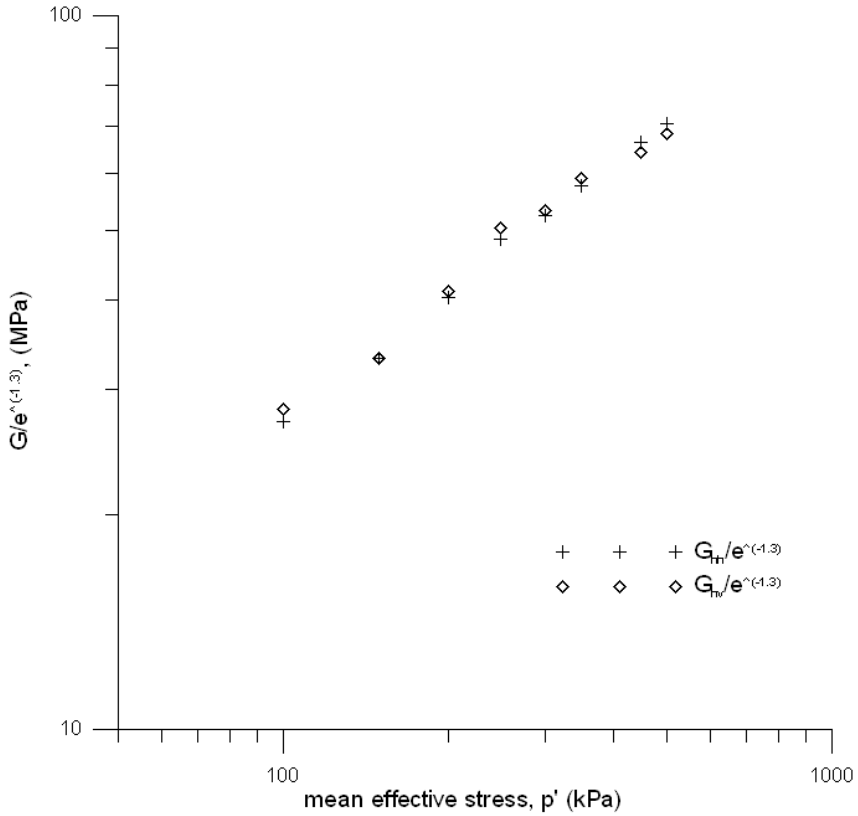


Figure 5-44: Normalised BE shear moduli for reconstituted samples of Gault clay during isotropic loading

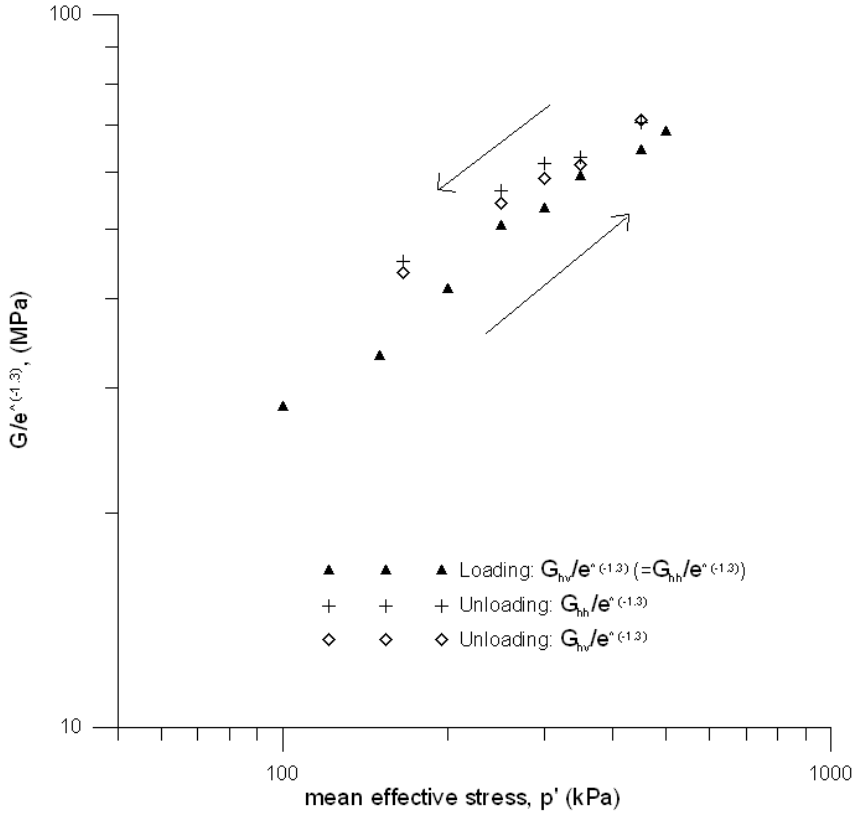


Figure 5-45: Normalised BE shear moduli for reconstituted samples of Gault clay during isotropic loading and unloading

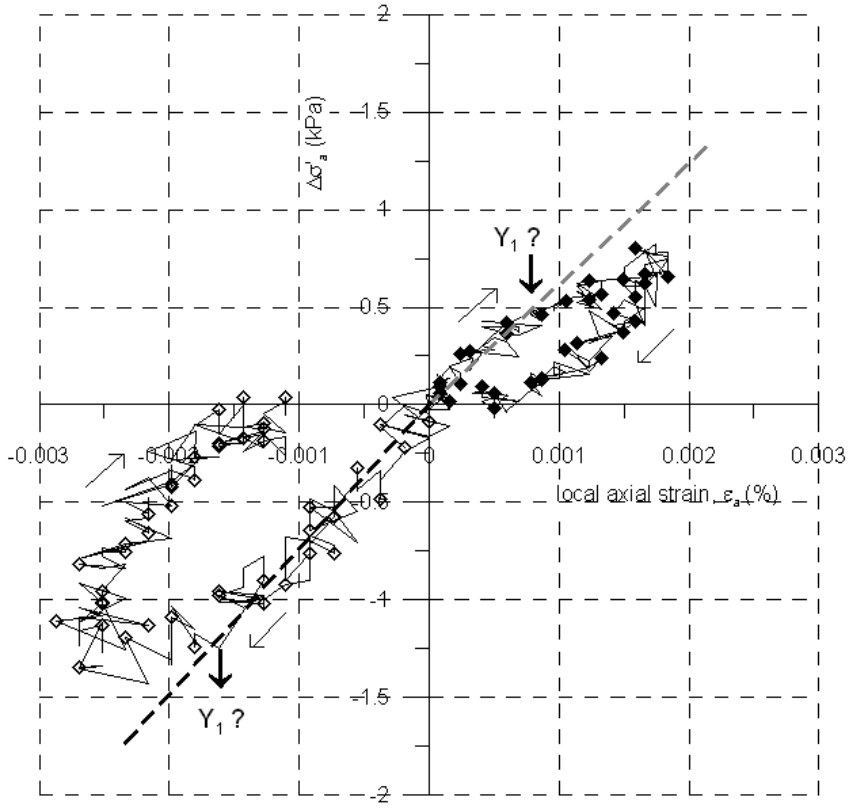


Figure 5-46: Axial probe in compression and extension; axial effective stress and strain increments

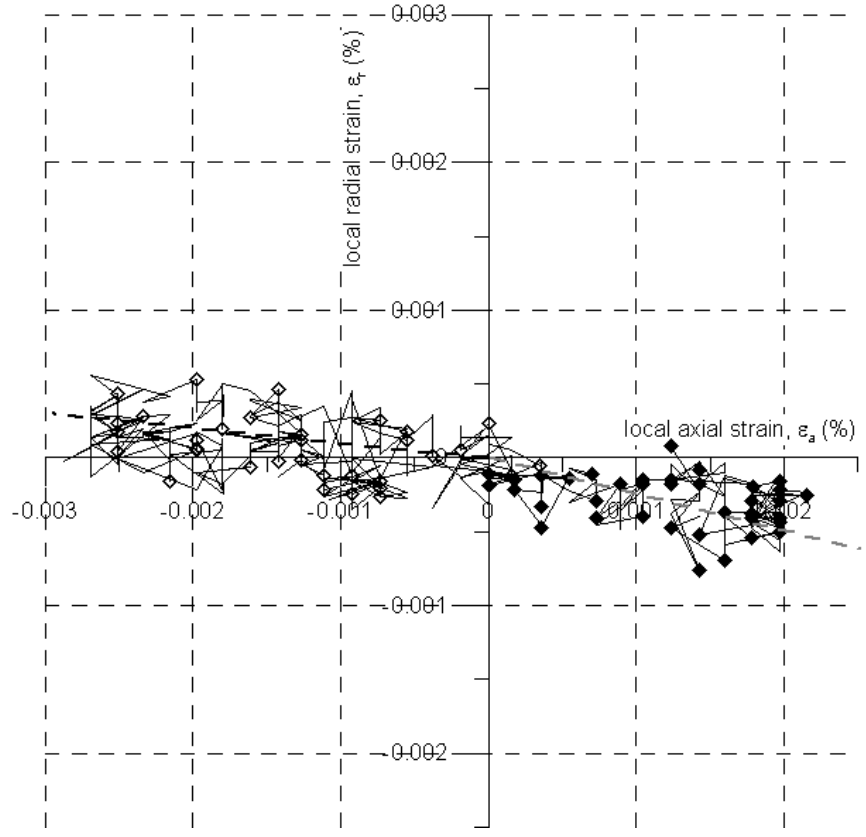


Figure 5-47: Axial probe in compression and extension; radial strain plotted against axial strain

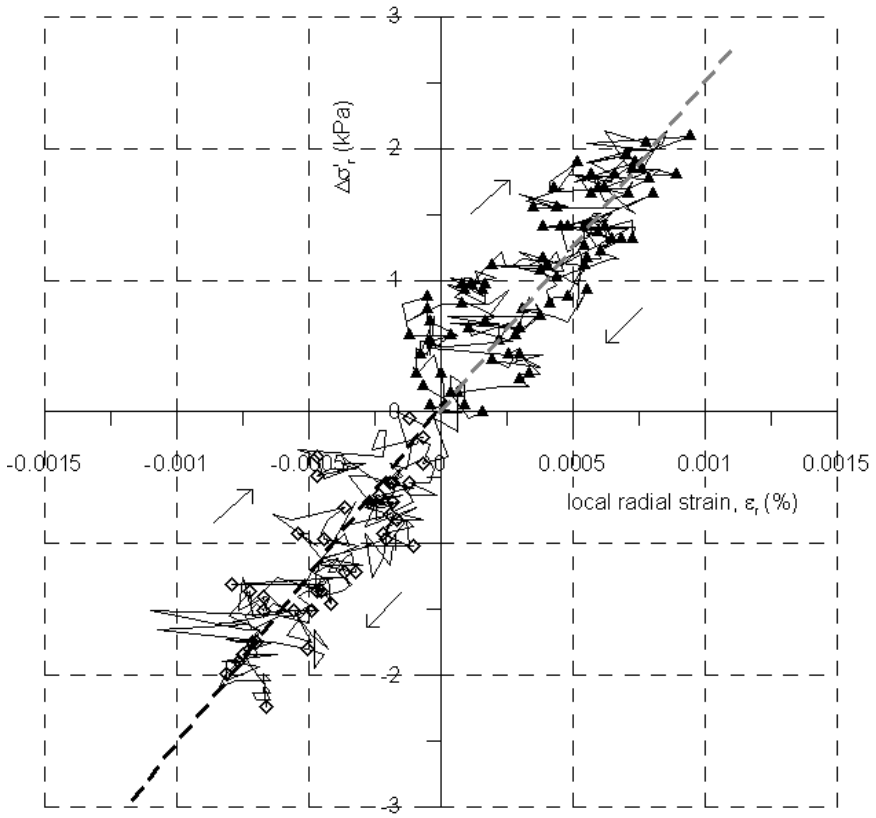


Figure 5-48: Radial probe in compression and extension; radial effective stress and strain increments

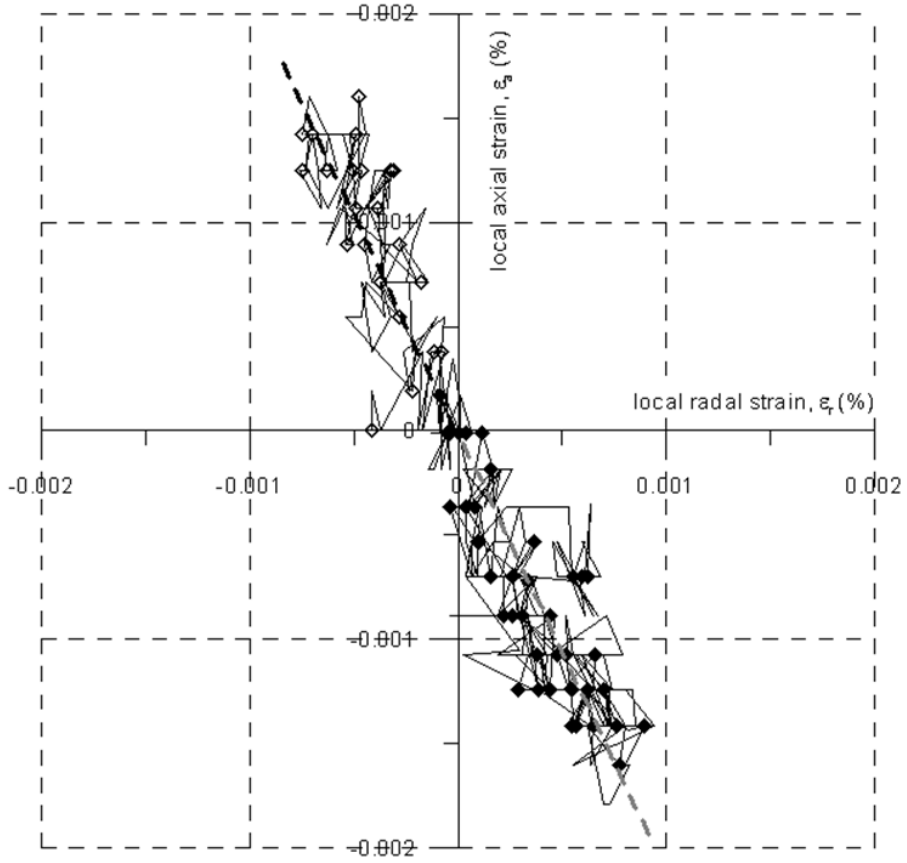


Figure 5-49: Radial probe in compression and extension; axial strain plotted against radial strain

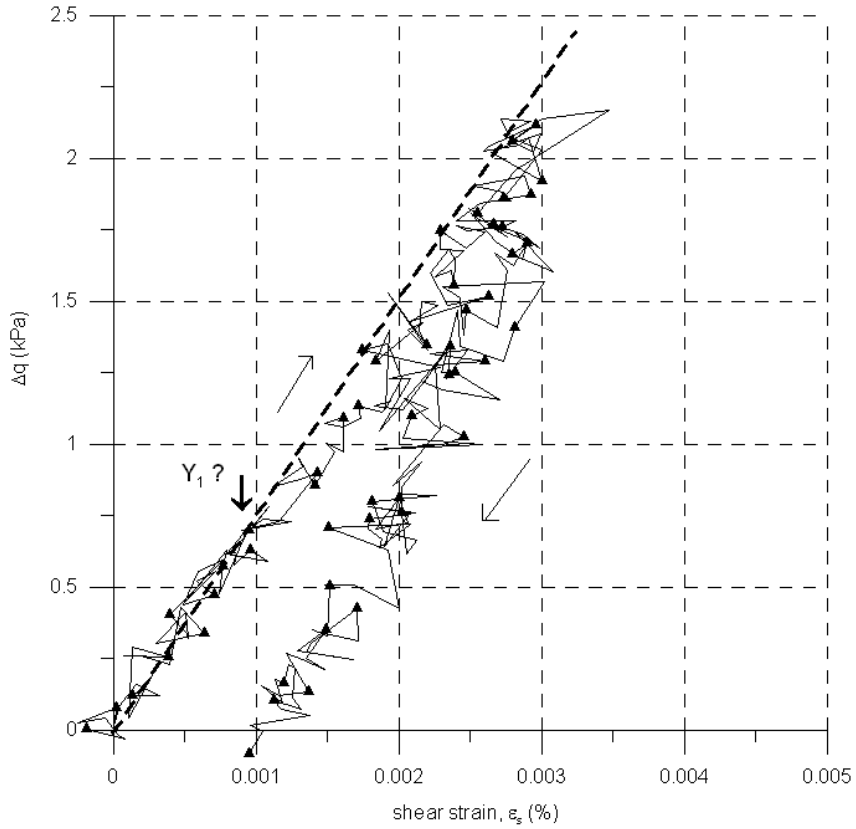


Figure 5-50: p' constant probe in compression; deviatoric stress plotted against shear strain

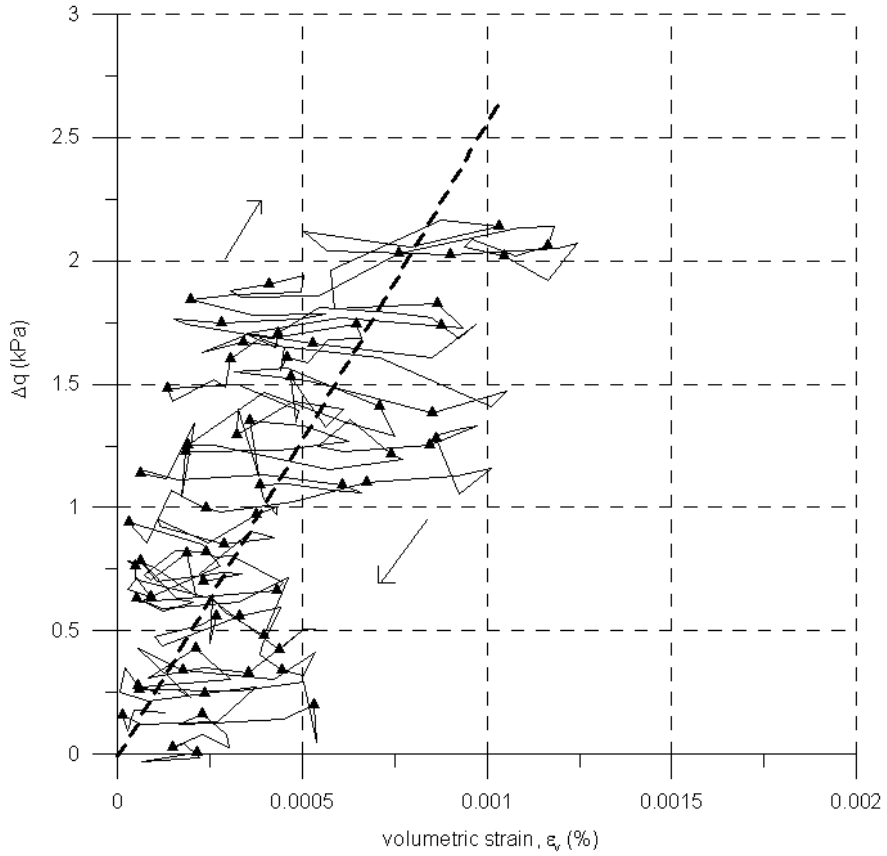


Figure 5-51: p' constant probe in compression; deviatoric stress plotted against volumetric strain

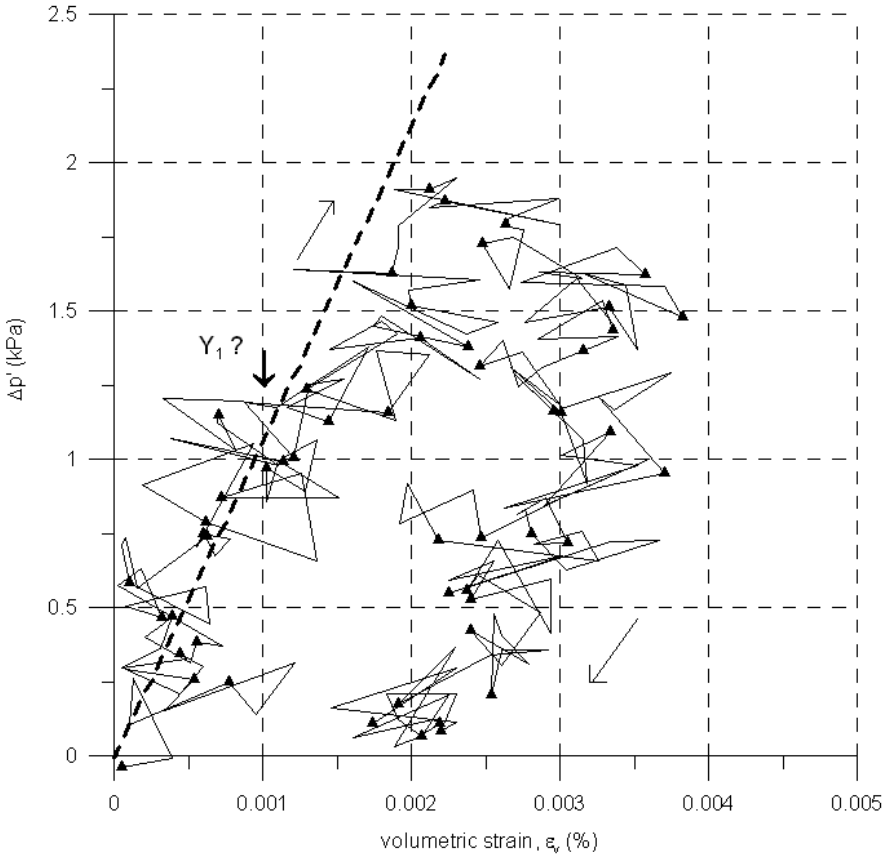


Figure 5-52: q constant probe in compression; mean effective stress plotted against volumetric strain

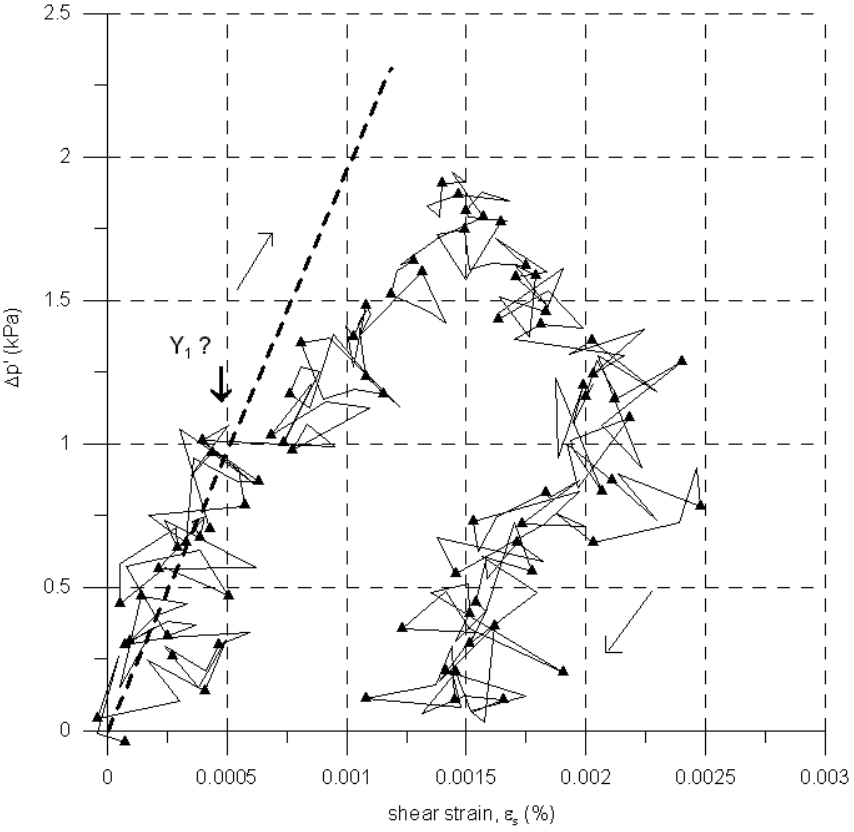


Figure 5-53: q constant probe in compression; mean effective stress plotted against shear strain

6 Kimmeridge Clay

6.1 Introduction

Kimmeridge clay was the last mudrock studied in this research, following a testing programme similar to those for Oxford and Gault clays. However, due to the time limitations a smaller number of tests were carried out on Kimmeridge clay. This chapter reviews the geotechnical behaviour of Kimmeridge clay and comparisons with other two soils will be made in Chapter 7.

6.2 Background

6.2.1 Geology and the site

Kimmeridge Clay is a marine deposit from the Upper Jurassic with volcanogenic material being present in the upper, siltier strata (Jeans et al., 2000). The thickness of the deposit varies from around 450 metres in Dorset to around 50 metres on the East Midlands Shelf (Brenchley & Rawson, 2006). It is of high importance for the oil industry as its high organic content makes it a source rock for oil fields in the North Sea. Similar to Oxford and Gault Clays, Kimmeridge Clay experienced deep burial followed by erosion and uplift resulting in the current highly overconsolidated state. The previous depth of burial has been estimated between 410 metres, based on stratigraphy, and 1080 metres, based on apatite fission track analysis (Wilkinson, 2011).

The sampling location for this project was at Willow Brook Farm, south west of Abingdon, near Steventon in Oxfordshire (Figure 6-1). This previously undeveloped site was chosen because of its proximity to the borehole investigations for the potential Upper Thames Reservoir. The site investigation data offered useful input into the current study, although, the Upper Thames Reservoir site investigation data is not yet available for public use and can not be presented in this thesis. Figures 6-2 and 6-3 show the site geotechnical profile by the author and Brosse (2012) for the sampling site. The CPT traces indicate a cemented band at around 8 metres below ground level. The main sampling horizon for testing was set to be below this band at

around 10 metres below ground level, so avoiding the clearly weathered upper material. To observe macro-structure discontinuities within Kimmeridge clay few samples were split into half. A sample from around 10m depth (the testing horizon) is shown in Figure 6-4. The spacing for the sub-horizontal fissures is about 50mm and for the ones inclined with 40°- 60° from the vertical, is between 20mm to 50mm. The particle size distribution curve from 10 metres below ground level is shown in Figure 6-5, indicating a clay fraction of around 50%. Unfortunately not much data is available for this profile and access to the data from the Upper Thames Reservoir investigation could complete this profile. A more extensive study of the site geology and profile logging has been carried out by Wilkinson (2011) as part of this project and will not be repeated here.

6.2.2 Previous studies

Most research on Kimmeridge Clay has been related to the oil industry. With few towns or cities founded on this mudrock, little geotechnical information is available for it. As mentioned in the previous section the Upper Thames Reservoir is one of the main investigations, but which can not be presented here. Nygard et al. (2004) and Nygard et al. (2006) carried out mechanical experiments on samples of Kimmeridge clay from deep horizons typical of the offshore reservoirs. They have studied the brittle-ductile behaviour of the soil in relation to shear failure and leakage through the failure planes. They concluded that the overconsolidation ratio, *OCR*, is a useful indicator of the brittleness for the mudrocks and can be used to determine the probability of the leakage through hydrocarbon seals. They also studied the compression behaviour of the soil and the effects of structure induced by mechanical loading and chemical diagenesis on the behaviour of the Kimmeridge clay. They observed that while mechanical compaction is the major factor in the predominantly horizontal particle orientation which increases the anisotropy, chemical diagenesis reduces the spacing between the particles without causing particle reorientation. All their tests were carried out on very low permeability samples of Kimmeridge clay and at very high stresses which makes the comparison with this study rather hard.

6.2.3 Evaluation of the in-situ stresses

Laboratory suction probe measurements (Ridley & Burland, 1993) were carried out by the author on rotary core samples of Kimmeridge clay; the result for a sample from 10.45 metres depth is shown in Figure 6-6. Observations during sampling showed that, unlike the Gault clay samples, which were swelled during sampling, the Kimmeridge clay samples were far less affected by the sampling process. The initial p' measured during the triaxial testing was in good agreement with the suction probe measurements. Therefore, assuming perfect sampling, the measured suction of 185 kPa was believed to represent the in-situ p'; on the path to the anisotropic state the limits on the strains (see Section 3.4.2) were reached at q= - 87 kPa, with K_0 = 1.7 and this was used in the testing programme (Table 6-1).

6.3 Intrinsic properties

Oedometer tests and a set of three triaxial tests performed on reconstituted samples of Kimmeridge clay. These were carried out primarily by Moran (2010) under the author's supervision. Details of these tests are presented in Tables 6-2 and 6-3, and the intrinsic parameters obtained from these tests are given in Table 6-4.

6.3.1 Compression behaviour

K_0 and isotropic compression curves for the reconstituted Kimmeridge clay are shown in Figures 6-7 and 6-8. Tests were carried out on four samples from between 2.5m and 11.15m. As can be seen, the two deeper samples (9.75m and 11.15m) have almost identical behaviour in compression and swelling. The two shallow more weathered samples retain higher void ratios and have flatter Cc values at higher pressures. The shallower curves tend to converge at higher pressures and their swelling curves are almost the same. There is no sign of convergence between the shallow and deep samples although their swelling lines are almost parallel. These differences can not solely be explained by specimens Atterberg Limits; as for instance, samples from 2.5m and 9.75m depths have similar plasticity index but are not convergent. However, the higher position of the specimen from 5.9m depth can partly be contributed to its higher plasticity. This could have happened because of errors involved in calculating

the initial void ratio (estimated accuracy of 0.04 for the initial void ratio) and further work is required to establish this difference in the compression lines. For consistency with the earlier testing the *ICL** curve carried forward for comparison with the natural samples was chosen based on the deep samples.

The isotropic compression curves, followed by reconstituted triaxial test samples mixed from around 10 metres depth, are presented in Figure 6-8 plotting specific volume (v) against mean effective stress (p'). All the tests started at similar specific volumes; one test was sheared from a normally consolidated state (*OCR*=1) and the other two tests were swelled back to different *OCR* values (3 and 5). As in the two previous chapters, *OCR* is used in this context in terms of mean effective stress, p', in isotropic loading and unloading. A straight line fitted to a short section of the *NCL** was used to normalise the effective stress paths of both reconstituted and natural samples.

6.3.2 Undrained shearing behaviour

Three triaxial tests were carried out on reconstituted Kimmeridge clay. The samples were prepared individually using a floating ring consolidometer as there was not enough material to prepare a 'cake' using the large consolidometer (Section 3.4.1). The first sample was isotropically consolidated to p'= 500 kPa and then sheared undrained and in compression. The second was overconsolidated with *OCR*=5 and the third sample was overconsolidated with *OCR*=3. The last test was equipped with side mounted bender elements.

Figures 6-9 to 6-11 show the samples' stress-strain behaviour of the reconstituted Kimmeridge clay. As can be seen, the overall behaviour for the normally consolidated sample and the *OCR*=3 samples was contractant with the samples developing continuum failures with bulging evident at the end of shearing reflecting effects of end restraint. The overconsolidated sample with *OCR*=5 showed a dilative behaviour while there was no visible strain localisation. The normalised stresses, q/p', are shown in Figure 6-11, plotted against axial strain. The stress ratio, M = q/p', at critical state was estimated to be 0.85 corresponding to an internal angle of shearing resistance $\phi'_{cs} = 21.8°$. In the normalisation based on p' (stress level), the two

overconsolidated tests show stiffer behaviour induced by unloading. The effective stress paths for these tests are shown in Figure 6-12. A Critical State Line, *CSL**, is plotted along with the isotropic Normal Compression Line, *NCL**, in Figure 6-13. The last point of shearing and its corresponding specific volume was used to construct the Critical State Line.

As with the Oxford and Gault clays, the effective stress paths were normalised using the equivalent pressure, p'^*_e, on the intrinsic Normal Compression Line. The same normalisation is carried out on the natural material to remove the effects of volume changes on shear strength. As mentioned earlier in Chapters 4 and 5, the Boundary Surface plotted in Figure 6-14 is based on the undrained tests which represents the Local Boundary Surface, *LBS**, other drained tests are required to identify the outer *SBS**. Similar to Gault clay, two overconsolidated tests were used to draw the Hvorslev surface. There is considerable uncertainty near the origin and tests with higher *OCR* values are required to define the Hvorslev surface fully.

6.4 Natural properties

6.4.1 Compression behaviour

Four oedometer tests have been carried out on samples of natural Kimmeridge clay at similar depths to the earlier reconstituted tests, giving the compression curves shown in Figures 6-15 to 6-17. All tests were carried out on rotary core samples, whose initial void ratios decreasing with depth. The two deeper samples (9.75m and 11.15m) show closely similar compression and swelling curves, with the deeper sample showing slightly lower compressibility. This might indicate that the deeper sample has slightly more structure to other sample. The shallower samples are slightly more compressible, probably due to greater weathering effects at shallow depths. No clear Y_3 yield point is shown by any of the four tests and in all cases the slopes of the swelling curves are relatively close to those developed in compression.

Figure 6-16 compares the natural and reconstituted Kimmeridge clay for deep and shallow samples. The natural samples surpass the *ICL** line, highlighting the presence of an aged and persistent micro-structure in the natural samples. The swelling of natural samples is less than the swelling of the reconstituted ones, again indicating the

presence of structure in the natural soil. These tests were also normalised for volume using the void index, I_v (Figure 6-17). Burland (1990) presented the *ICL** in a curved form, however a straight line passing through the reconstituted compression tests were used for the consistency with the normalisation made earlier applying a log-linear *NCL**. The combined I_v plot expresses the same key features with less significant difference being seen in the slopes of the swelling lines of the shallow and deep samples. However, compression curves of Kimmeridge clay are reaching the Sedimentation Compression Line at high pressures.

6.4.2 Shearing behaviour

a) Large strain behaviour

As summarised in Table 6-3, eight successful triaxial undrained compression and extension tests were carried out on the Kimmeridge clay; six involved 100mm in diameter samples while two were on 38mm in diameter specimens. To aid comparison with the other two mudrocks, all the Kimmeridge tests were conducted on samples from a depth of around 10 metres below ground level. Similar to the other mudrocks, additional ring shear tests were carried out by Narayana (2010) and Cunliffe (2010) under the author's direction on remoulded and natural samples respectively to investigate the markedly brittle behaviour of the soil.

Figure 6-18 shows the effective stress paths for the Kimmeridge clay. All the samples developed strain localisations which in some cases it was a single shear plane and in others it was a more complex failure with two or more shear planes. Tests in which the behaviour was not as brittle developed multiple shear planes with angles varying between 30 and 40 degrees. Other tests developed shear planes with angles between 50 and 60 degrees. As mentioned earlier fissure spacing in Kimmeridge clay is between 20mm and 50mm and most probably these affected the mode of failure. All of the tests except one, were carried out on samples with 100 mm in diameter and therefore the effect of sample size on the strength is not clear (Figure 6-19). Figures 6-20 and 6-21 show the stress-strain behaviour of all these tests. The behaviour is not as brittle as Oxford or Gault clays especially for the tests at their in-situ stress state.

Figure 6-22 shows the normalised graph of the stress ratio against axial strain. As expected the q/p' value at peak tends to be higher for tests performed at lower stresses. The stress ratio for different tests does not tend to converge to a unique value at these strain levels.

A Mohr's circle construction was carried out to obtain the failure envelopes (Section 3.5.5). The peak strength and post-rupture strength envelopes for the Kimmeridge clay are shown, with the critical state envelope, from the reconstituted tests, in Figure 6-23. Because of the ductile behaviour of Kimmeridge clay at lower stress levels no post-rupture strength data is available and only two points for the higher pressure tests, with single shear plane, are available. As can be seen, the post-rupture envelope appears to be lower than the Critical State Line. This needs to be investigated further with more tests at higher pressures as well as at very low pressures.

The significant brittleness of Kimmeridge clay was explained further in ring shear tests on the natural and remoulded samples conducted by Narayana (2010) and Cunliffe (2010) shown in Figures 6-24 and 6-25, on samples from around 10 metres depth. The first figure shows the mobilised residual angle of shearing resistance, ϕ'_r, plotted against shear displacement, d, divided by the sample height, h, for the small range of displacements. The applied displacement rates were similar to those for the other soils; 0.01mm/min for the 20mm thick remoulded sample tested in the Bishop apparatus and 0.024mm/min for the 5mm thick natural sample tested in the Bromhead cell. These tests were carried out under 400 kPa normal stress. The apparent peak strengths $\phi'_p = 17°$ and $\phi'_p = 13°$ for the natural and remoulded respectively are well below the triaxial peaks. However, at large displacements the residual strength should be similar for both natural and remoulded materials with particle re-alignment in the shearing zone removing the natural structure. As can be seen in Figure 6-25, the residual angle of shearing resistance appears slightly lower for the remoulded material, $\phi'_r = 6.2°$, compared to the $\phi'_r = 8°$ for the natural sample. It is difficult to measure such low angles precisely, especially with the simpler Bromhead apparatus used for the natural testing.

b) Effects of structure at large strains

A comparison between natural and reconstituted samples was made to investigate the effects of structure on the strength and stiffness of the Kimmeridge clay. Figure 6-26 shows the stress ratio, q/p', plotted against axial strain for the natural and the reconstituted samples. Although the natural samples sheared at their in-situ stress state show higher peak strengths compared to the reconstituted ones, the peak strengths of the natural tests at higher pressures are almost the same as the reconstituted ones.

The effective stress paths for both natural and reconstituted samples can be seen in Figure 6-27. Similar to Gault clay, the failure envelope for the natural samples is just above the reconstituted one. The effective stress paths were normalised to take the effects of volume into account by the equivalent pressure, p'^*_e, on the isotropic Normal Compression Line, Figure 6-28. As can be seen, the natural *SBS* lies close to reconstituted one, showing no clear sign of enhancement by structure.

c) Pre-failure behaviour

The pre-failure behaviour of Kimmeridge clay is discussed in this section. The undrained secant stiffness degradation curves are shown in Figure 6-29. Tests from different stress levels were chosen to highlight the effects of stress level. As anticipated the behaviour is highly non-linear with a limited region of possibly linear response. A linear plateau at small strains can be identified with a relatively high limit of around 0.007 % axial strain. Secant stiffness values for equal strain values are plotted against current mean effective stress in Figure 6-30. As can be seen, there is a significant drop in the stress exponent 'n' with increasing strain level. This is again in contrast with the widely believed trend for 'n' to rise towards unity with increasing strain level (e.g. Jardine, 1995; Viggiani & Atkinson, 1995).

Typical bender element signals are shown in Figures 6-31 and 6-32 for V_{hv} and V_{hh} respectively. As with Gault clay, no measurements of V_{vh} were made to compare G_{vh} and G_{hv}. The input signals with frequencies between 6 and 10 kHz were chosen and are plotted with their output signals in the same graph. The Y axis shows a voltage

amplitude, both input and the output signals normalised to comparable scales and the X axis is time. The point at which the output signals start to ascend was chosen as the first arrival time. After choosing the first arrival time a frequency analysis was carried out using the code developed by Alvarado (2007). The arrival time calculated from this method was in close agreement with the time domain estimate.

The bender element results are shown in Figure 6-33, plotting the logarithm of shear modulus at very small strain, G_0, against logarithm of mean effective stress, p'. The anisotropy is evident with G_{hh} values significantly higher than G_{hv} values. The G_{hh} (as will be discussed below = G_{hv}) data from the reconstituted test is also shown in this graph having lower values compared to the natural samples. However, when these data are normalised by their void ratios (Figure 6-34) a significant difference is observed between the shear modulus G_{hv} for the natural and reconstituted samples with the values being higher for the reconstituted sample (G_{hv} and G_{hh} are identical for the reconstituted samples). Similar to Oxford and Gault clays, shear modulus G_{hh} is higher for the natural samples as a result of 1*D* load/unload cycles during the geological history. This is in contrast with some previous studies in which either the shear moduli was higher for the natural material, due to the effects of structure, (Pennington et al., 1997) or both natural and reconstituted had similar values (Viggiani and Atkinson, 1995). However, Gasparre et al. (2007) observed a similar trend for most of the units of the London clay with the exception of unit C, which showed similar stiffness values for both the natural and reconstituted samples. Similar to Oxford and Gault clays, the stress level exponent 'n' is lower for the bender element result compared to that obtained from the undrained shearing at small strain levels. The reason for this difference is not clear and further investigation is needed, however the dynamic nature of the bender element tests and strain rate dependency of stiffness may possibly contribute to this discrepancy.

As mentioned earlier, the test on the reconstituted sample with *OCR* = 3 was equipped with side mounted bender elements allowing the measurement of V_{hh} and V_{hv} and Figure 6-35 shows these values during isotropic loading normalised by void ratio. There is no significant difference between the two measurements. There is also little variance between the two moduli during the isotropic unloading (Figure 6-36). These findings are in agreement with measurements on the reconstituted Gault clay (Section

5.4.2). However, the effect of overconsolidation is evident with an increase of normalised stiffness with *OCR*. When using the void ratio in the normalisation the stiffness at *OCR*=2 is about 20% more than that of normally consolidated soil, and at *OCR*=3 the difference is about 25%. These changes are larger than those for the reconstituted Gault clay (10% for *OCR*=2 and 20% for *OCR*=3).

Small strain drained probing tests were carried out on Kimmeridge clay sample KIMCL-NT-8, and the drained elastic parameters obtained are presented in Table 6-5.

Axial probes, with constant radial stress, in compression and extension are shown in Figures 6-37 and 6-38. The load-unload probes in compression and extension resulted in some irrecoverable plastic straining. However, by considering the initial linear part of the loading curve the limit to Y_1 was anticipated to be around 0.001% axial strain. The changes in the radial strains are shown plotted against axial strains in Figure 6-38 with Poisson's ratios, υ'_{vh}, equal to 0.22 for both the compression and extension tests.

Figures 6-39 and 6-39 show the radial probing tests, with constant axial stress, in compression and extension. The behaviour is practically linear under changes in the radial stress of about 3 kPa. The behaviour appears to be stiffer in radial loading than unloading. As mentioned earlier for an elastic material these two values should be the same and in this case it is not clear if the soil behaviour is not fully elastic or if there is any error in the data. Values of υ'_{hv} were calculated based on these radial probes and using Equation 3-18 and also from Equation 2-6. Constant p' and q probes were also carried out to evaluate the shear modulus, G', bulk modulus, K', and coupling moduli J_{qp} and J_{pq}. The constant q probe was not successful and therefore no direct measurements of K and J_{pq} were made. The constant p' probe (Figures 6-41 and 6-42) was carried out resulting in $G' = 42$ MPa which is in good agreement with calculated G_{eq} (= 38 MPa) based on the drained elastic parameters. However, the measured J_{qp} (= 150 MPa) and the calculated J (= 292 MPa) are not in good agreement.

6.5 Summary

The author's study of Kimmeridge clay has been presented in this chapter. Most previous research studies on Kimmeridge Clay were conducted from petroleum engineering perspective and did not provide much geotechnical information. Rotary core sampling up to 14 metres below ground level enabled the investigation of weathering effects on the shallow samples. The compressibility in the oedometer tests increased slightly with decreasing depth of samples, with the highest compressibility for the sample from 2.5m depth. This could have been caused by weathering effects at shallow depths. There was no noticeable Y_3 yield point for any of the tests and in all cases there was significant swelling. Swelling of natural samples was less than swelling of the reconstituted ones, indicating the presence of structure in the natural soil.

Triaxial tests on the natural samples of Kimmeridge clay showed that the behaviour is not as brittle as Oxford or Gault clays. Tests in which the behaviour was not as brittle developed multiple shear planes with angles varying between 30 and 40 degrees. Other tests developed shear planes with angles between 50 and 60 degrees. In general, significant fissuring was observed for the Kimmeridge clay, it is therefore it is anticipated that mode of failure was related to pre-existing fissures. Similar to Gault clay, the strength envelope of the natural *SBS* is below the reconstituted one when normalised for volume, showing that the effects of structure on shear strength of Kimmeridge clay are negative.

The stiffness of the soil was measured at small strain levels. There was a significant drop in the stress exponent 'n' with increasing strain level. This is in contrast with the widely believed trend for 'n' in which the stress level exponent of the stiffness increases towards unity with increase in strain level (e.g. Viggiani and Atkinson, 1995). The bender element results showed a significant anisotropy for the natural samples which was robust and remained at different stress levels. A significant difference was observed between the shear moduli for the natural and reconstituted samples with higher values for the reconstituted sample. It should also be noticed that for the reconstituted sample the change in shear modulus with mean effective stress is

almost double the natural sample. As for the other two soils, the drained elastic parameters were obtained for Kimmeridge clay.

Bulk unit weight, γ	21.5 (kN/m^3)
Water table below ground level	1 (m)
Sample depth	10 (m)
Estimated in-situ σ'_v	127 (kPa)
K_0	1.7
p’	185 (kPa)
q	-87 (kPa)

Table 6-1: Estimation of the in-situ stress state

Sample name	**Sample type**	**Sample depth (m)**	**Initial water content w_c (%)**	**Maximum stress reached in compression σ_v' (kPa)**	**Researcher**
KIMCL-RO-1	Reconstituted	2.5	63.5	8000	Moran (2010)
KIMCL-RO-2	Reconstituted	5.9	66.3	8000	
KIMCL-RO-3	Reconstituted	9.75	69.7	4500	
KIMCL-RO-4	Reconstituted	11.15	67.3	8000	
KIMCL-NO-1	Natural	6.1	24.0	14800	
KIMCL-NO-2	Natural	9.2	23.2	13900	
KIMCL-NO-3	Natural	3.5	22.1	27700	
KIMCL-NO-4	Natural	3.5	18.5	14000	

Table 6-2: Summary of oedometer tests on natural and reconstituted samples of Kimmeridge clay

Sample name	Sample type	Sample depth (m)	D (mm)	State before shearing		Bender elements	Shear	Researcher (if not the author)
				p' (kPa)	q (kPa)			
KIMCL-RT-1	Reconstituted	11.15	38	500	0		UC	Moran (2010)
KIMCL-RT-2	Reconstituted	11.15	38	100	0		UC (OCR=5)	Moran (2010)
KIMCL-RT-3	Reconstituted	11.15	38	167	0	●	UC (OCR=3)	
KIMCL-NT-1	Natural-Rotary	11.20	100	200	-100	●	UC	
KIMCL-NT-2	Natural-Rotary	10.00	100	215	-170	●	UC	
KIMCL-NT-3	Natural-Rotary	9.60	100	185	-90	●	UC	
KIMCL-NT-4	Natural-Rotary	9.75	100	180	-85	●	UE	
KIMCL-NT-5	Natural-Rotary	9.85	100	350	0	●	UE	
KIMCL-NT-6	Natural-Rotary	10.30	100	500	0	●	UC	
KIMCL-NT-7	Natural-Rotary	10.60	38	1000	0		UC	
KIMCL-NT-8	Natural-Rotary	9.45	38	185	-87	●	UC	

Table 6-3: Summary of triaxial tests on natural and reconstituted samples of Kimmeridge clay

φ'_{cs}	N*	Γ*	λ	κ	C_c^*	C_s^*
21.8 °	2.8	2.51	0.164	0.047	0.377	0.128

Table 6-4: Parameters measured for one-dimensionally and isotopically compressed reconstituted samples of Kimmeridge clay

	Drained															Undrained		
Probe	**G_{hh}**	**G_{hv}**	**E'_v**	**E'_h**	**υ'_{vh}**	**υ'_{hv}**	**υ'_{hv}**	**υ'_{hh}**	**G'**	**G_{eq}**	**K'**	**K'**	**J_{qp}**	**J_{pq}**	**J**	**E^u_v**		**E^u_h**
	MPa	**MPa**	**MPa**	**MPa**		**Eq 2-6**	**Eq 3-18**		**MPa**	**Eq 3-26 MPa**	**MPa**	**Eq 3-27 MPa**	**MPa**	**MPa**	**Eq 3-28 MPa**	**MPa**	**Eq 3-29 MPa**	**Eq 3-30 MPa**
Bender elements	121	70																
axial probe compression			82		0.22													
axial probe extension			78		0.22													
radial probe compression				234		0.63	0.74	0.02										
radial probe extension				202		0.54	0.85	0.15										
p'cnst probe									42	38			150		292			
q cnst probe											-	98		-				
UC																125	131	250

Table 6-5: Elastic parameters derived from static probes under in-situ stresses

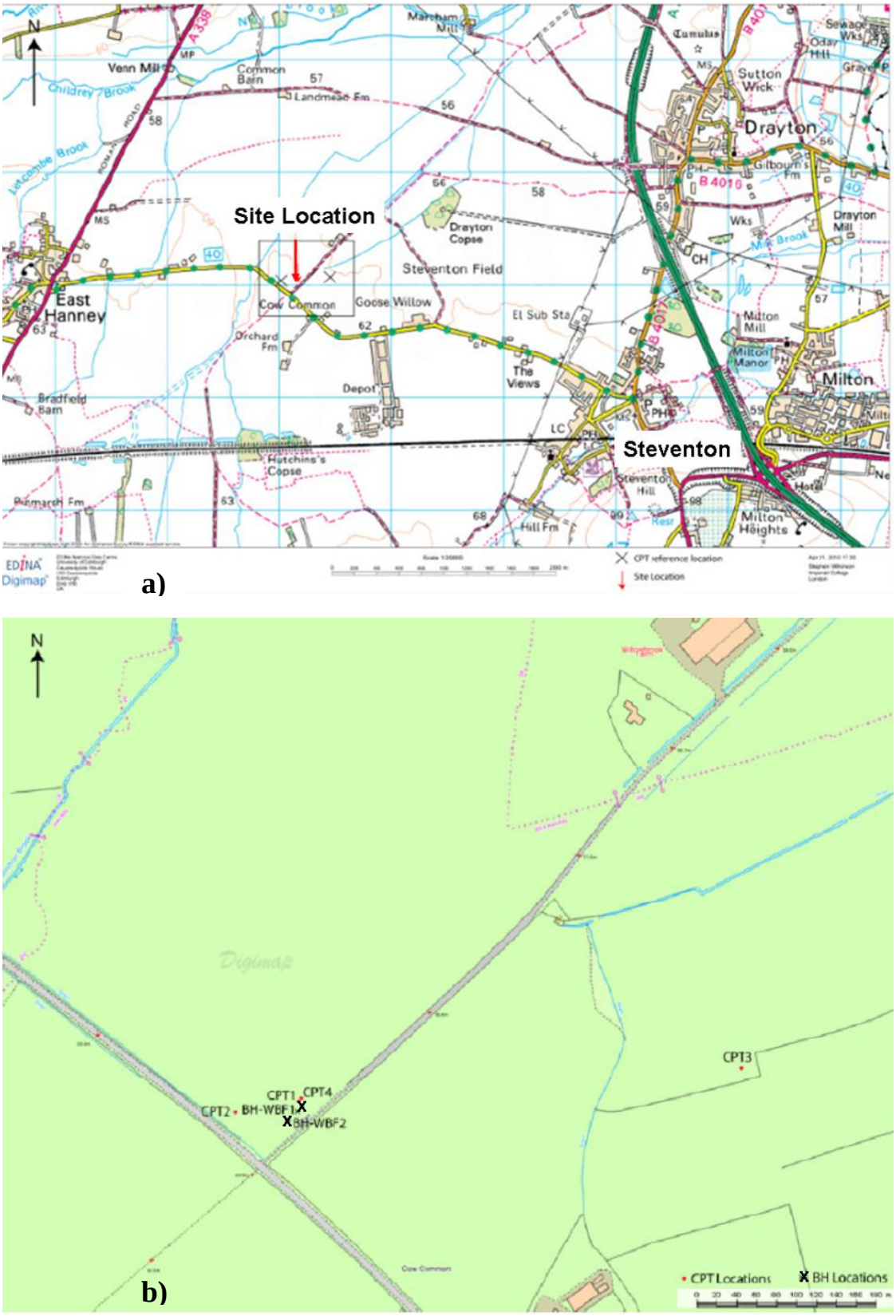
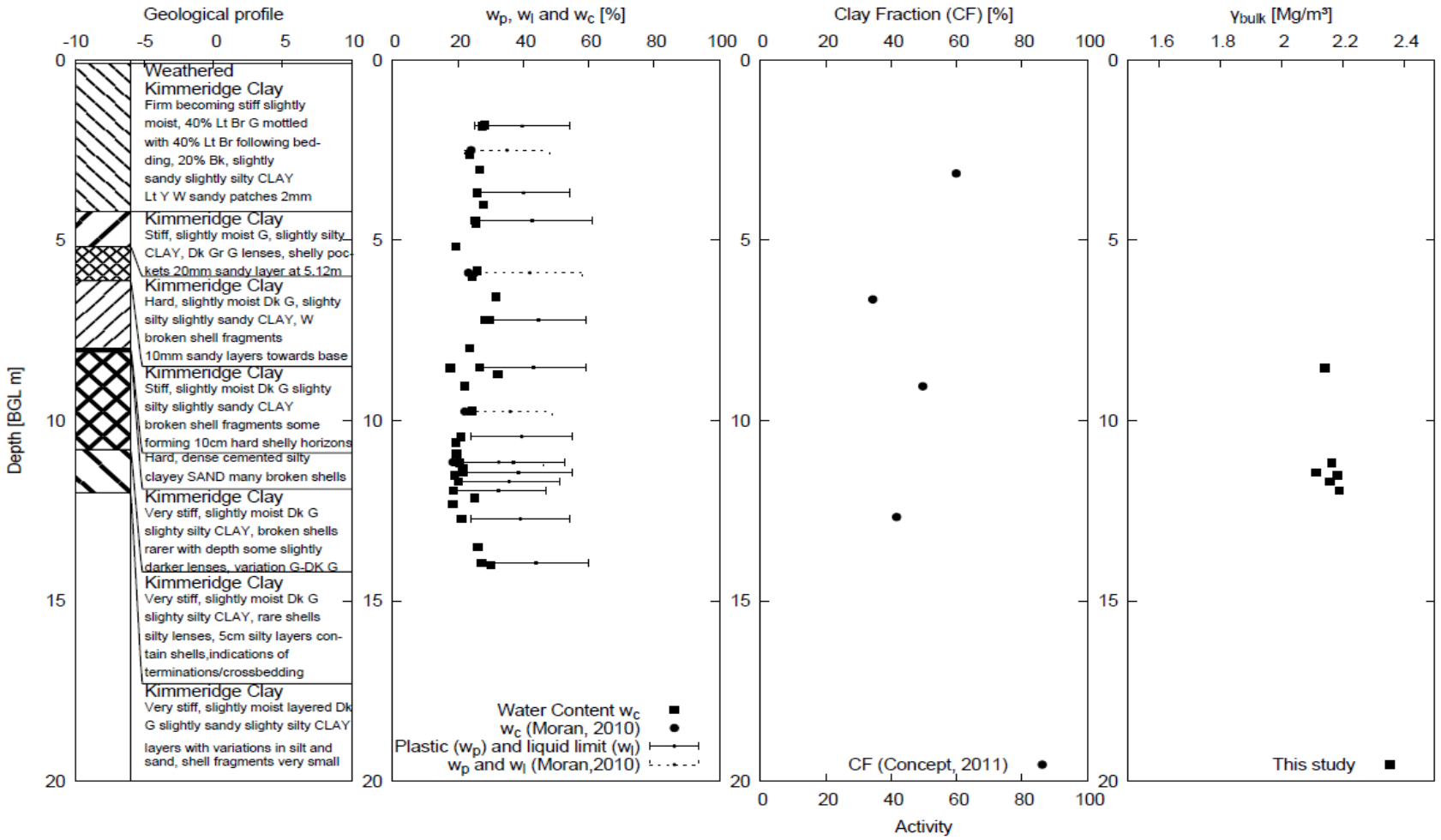


Figure 6-1: Sampling site for Kimmeridge clay; a) map of Steventon and the site location, Willow Brook Farm (Ordnance Survey, 2009b), b) field map of the sampling locations (after Wilkinson, 2011)



***Lt Y W: Light Yellowish White, G: Grey, W: White, Lt G: Light Grey, Lt Br G: Light Brownish Grey, Lt Br: Light Brown, Dk Gr G: Dark Greenish Grey, Dk G: Dark Grey**

Figure 6-2: Soil profile at Willow Brook Farm

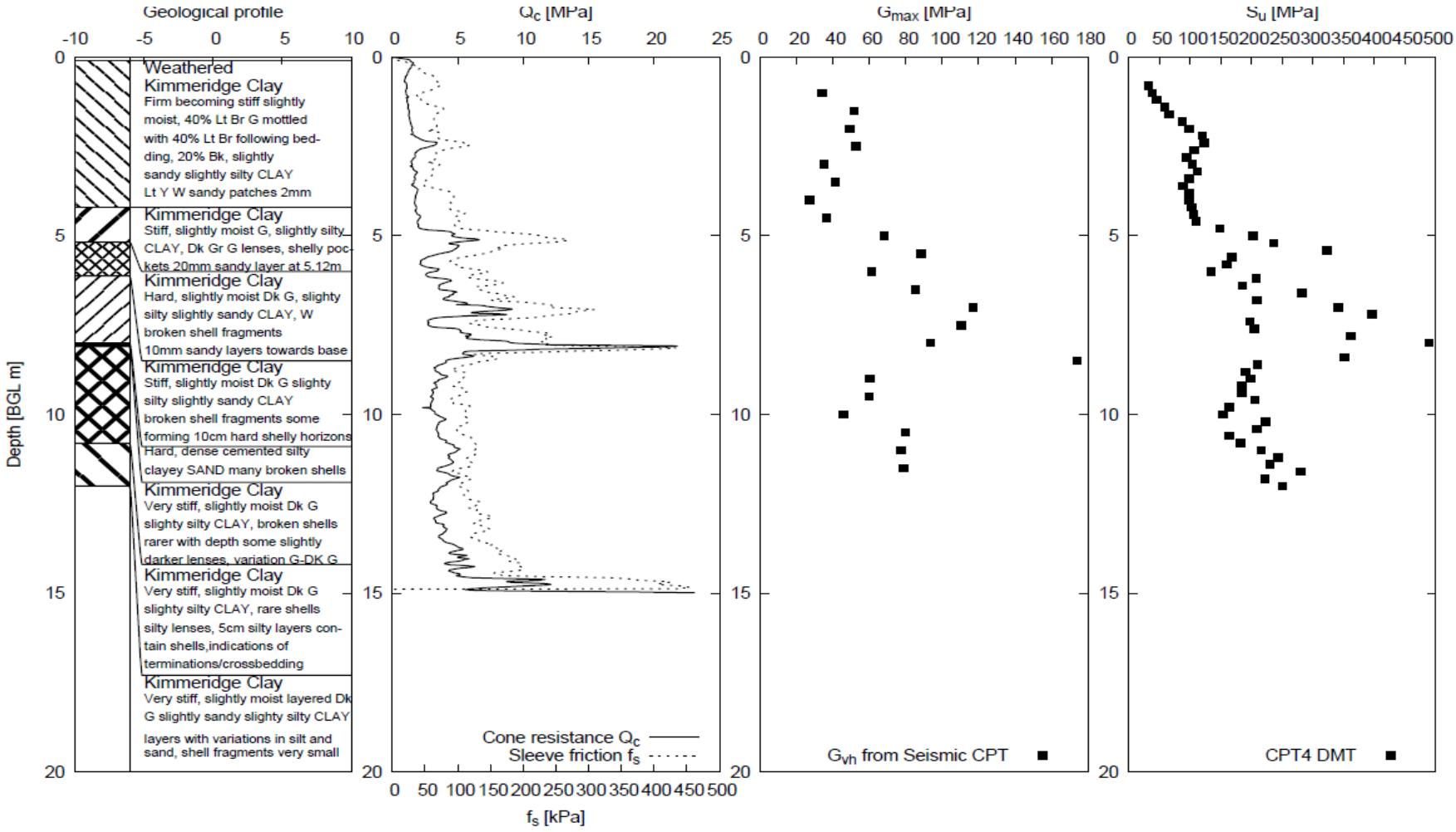


Figure 6-3: Soil profile at Willow Brook Farm (CPT data provided by In-situ SI)



Figure 6-4: Macro-structure of rotary core sample of Kimmeridge clay from 10m depth, natural discontinuities are outlined with dotted line (produced with Brosse, 2012)

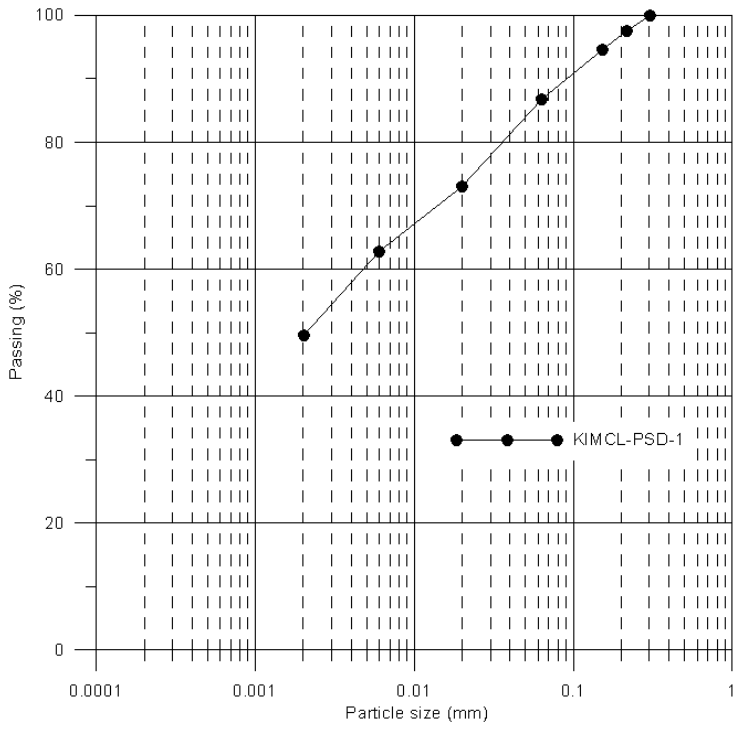


Figure 6-5: Particle size distribution of sample from 10m depth

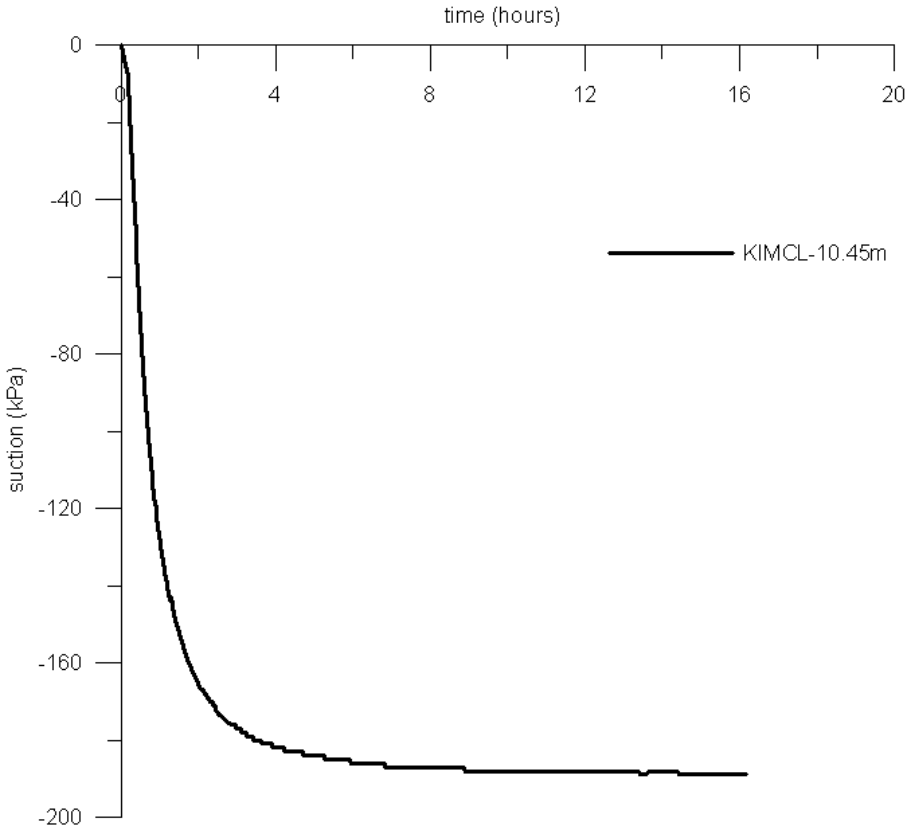


Figure 6-6: Suction probe measurment on a sample of Kimmeridge clay

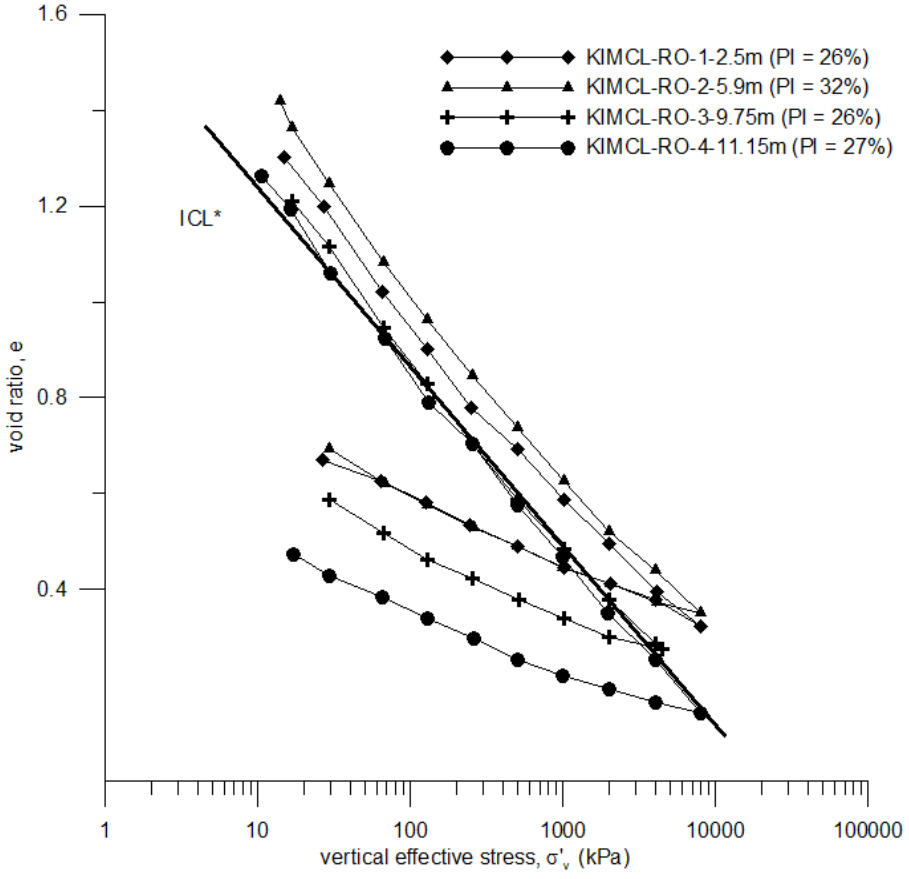


Figure 6-7: One-dimensional compression of reconstituted Kimmeridge clay

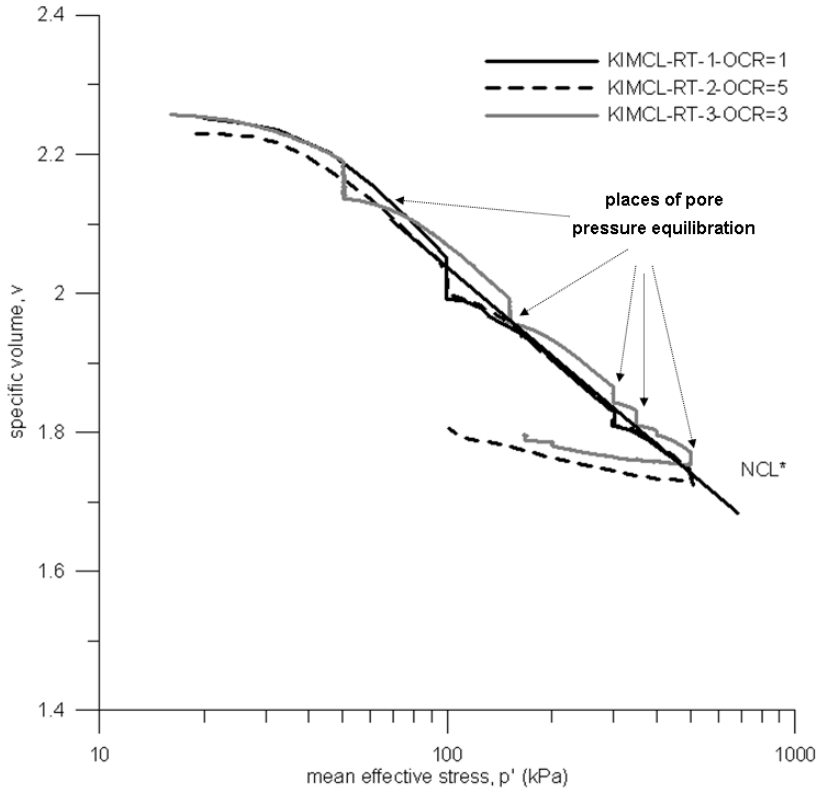


Figure 6-8: Isotropic compression of reconstituted Kimmeridge clay

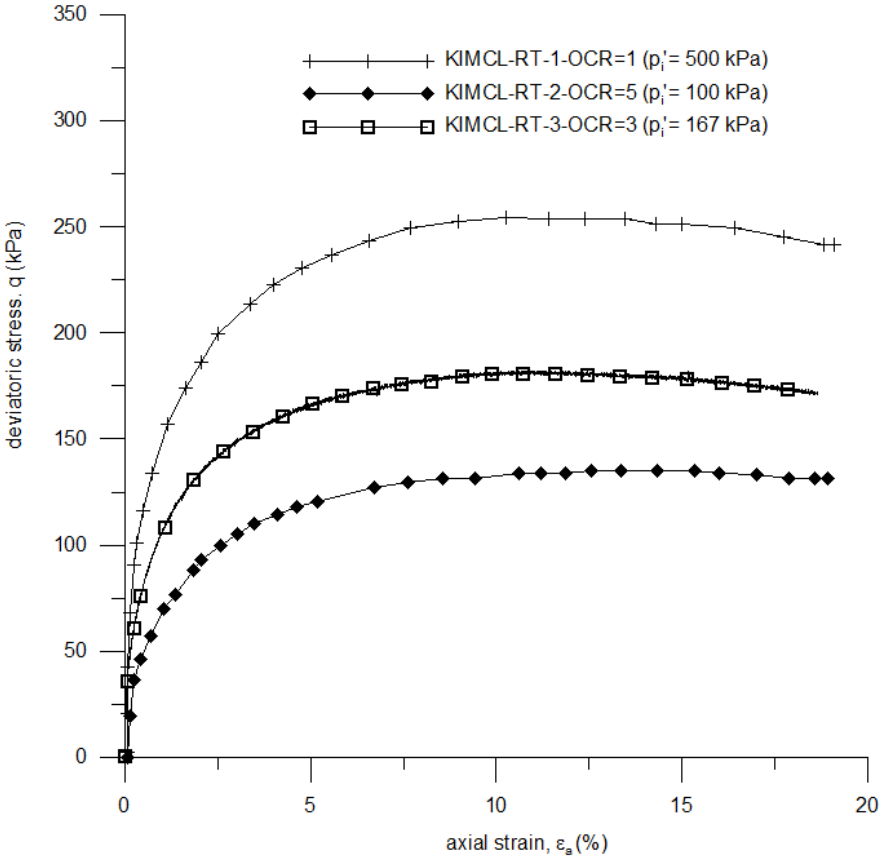


Figure 6-9: Undrained triaxial stress-strain behaviour of isotropically compressed reconstituted Kimmeridge clay

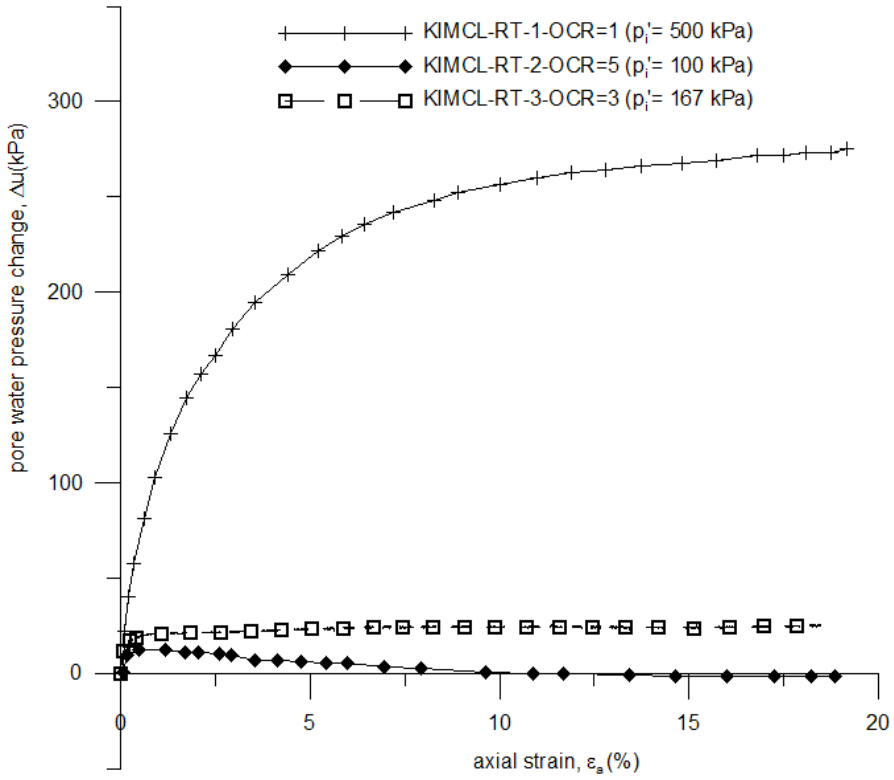


Figure 6-10: Pore water pressure change during the shearing of reconstituted Kimmeridge clay

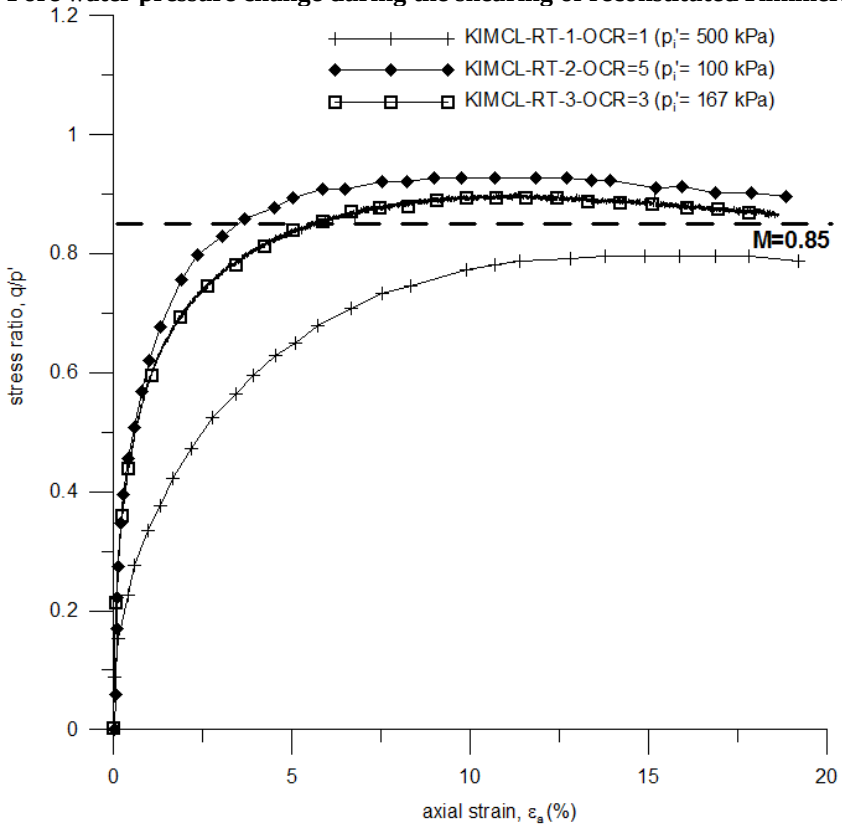


Figure 6-11: Normalised stress-strain behaviour of reconstituted Kimmeridge clay

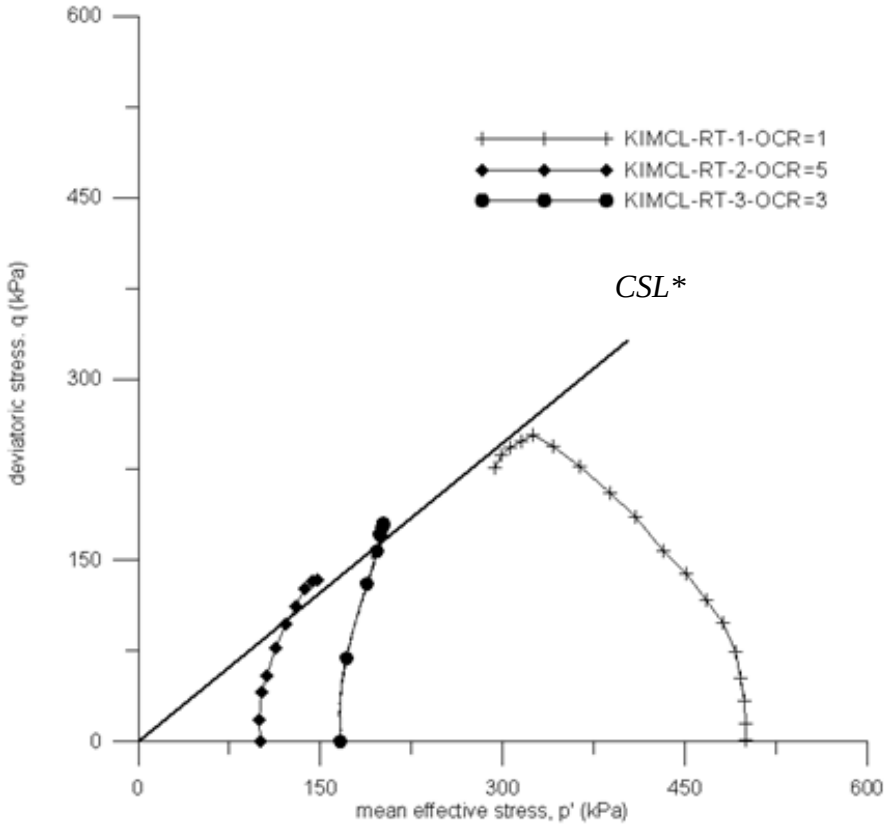


Figure 6-12: Effective stress paths for reconstituted isotropically consolidated Kimmeridge clay

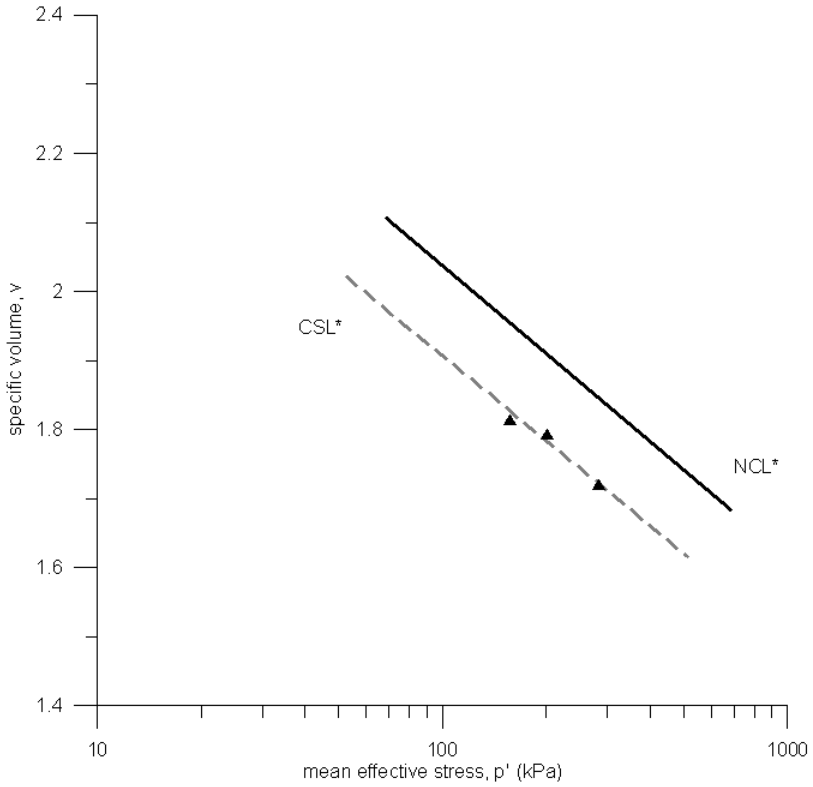


Figure 6-13: Normal Compression and Critical State Lines for reconstituted isotropically consolidated Kimmeridge clay

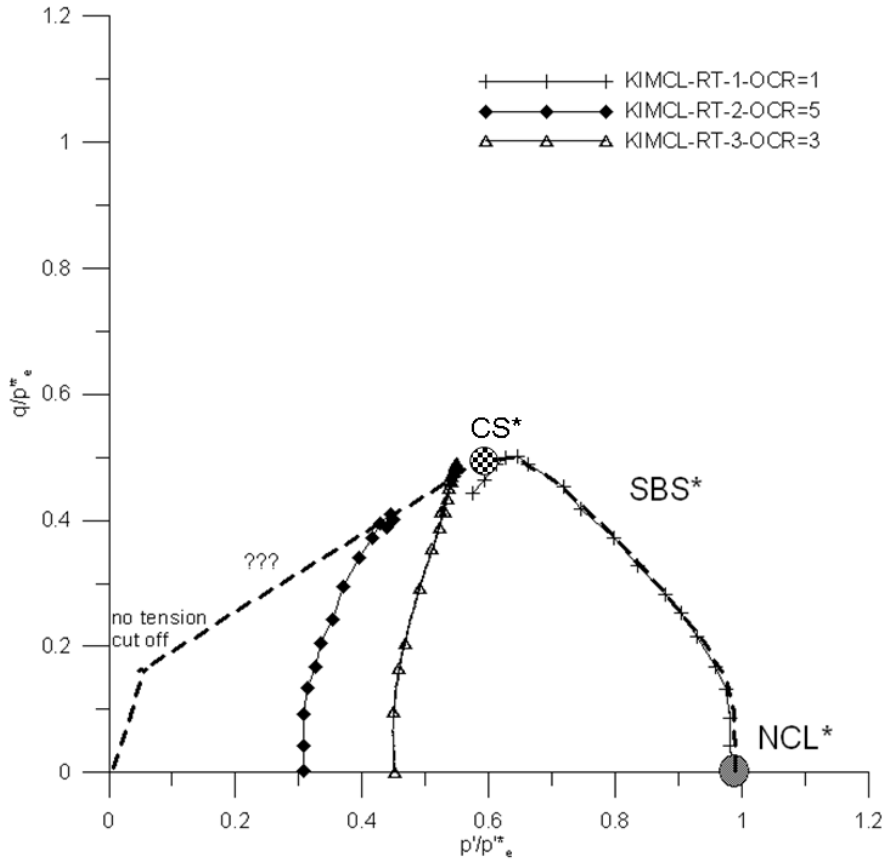


Figure 6-14: Normalised effective stress paths of reconstituted Kimmeridge clay

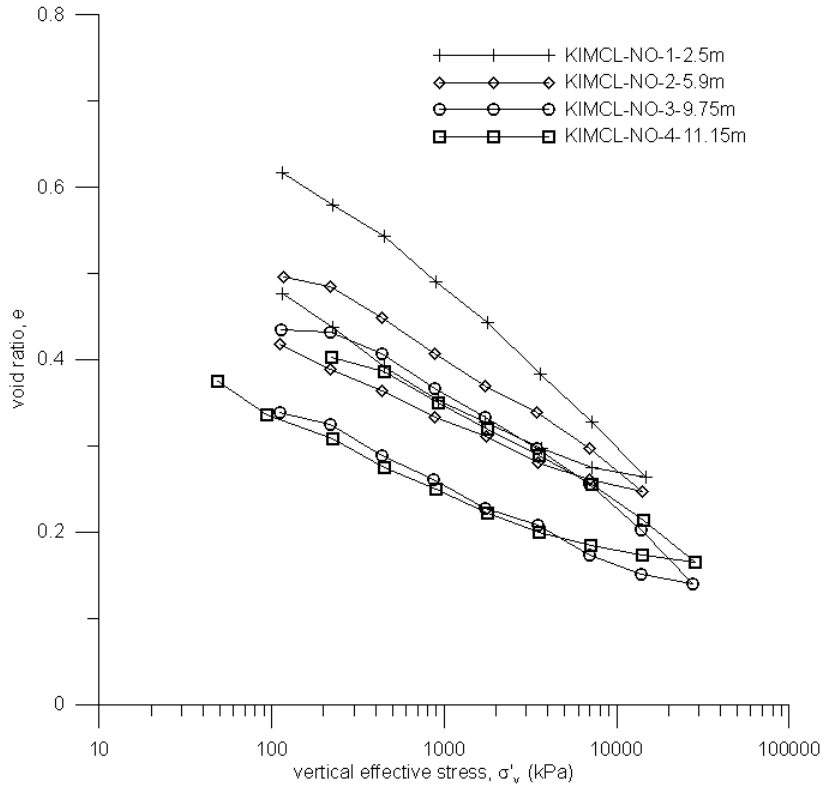


Figure 6-15: Oedometer compression curves for natural Kimmeridge clay

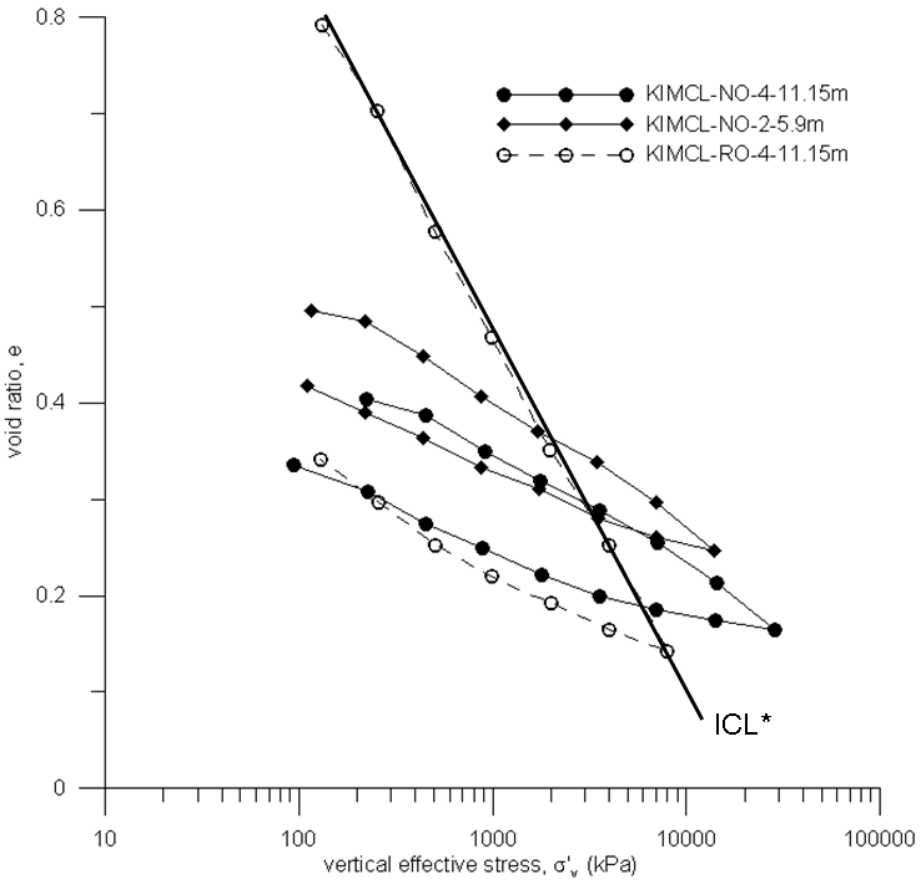


Figure 6-16: Oedometer compression lines for natural and reconstituted Kimmeridge clay

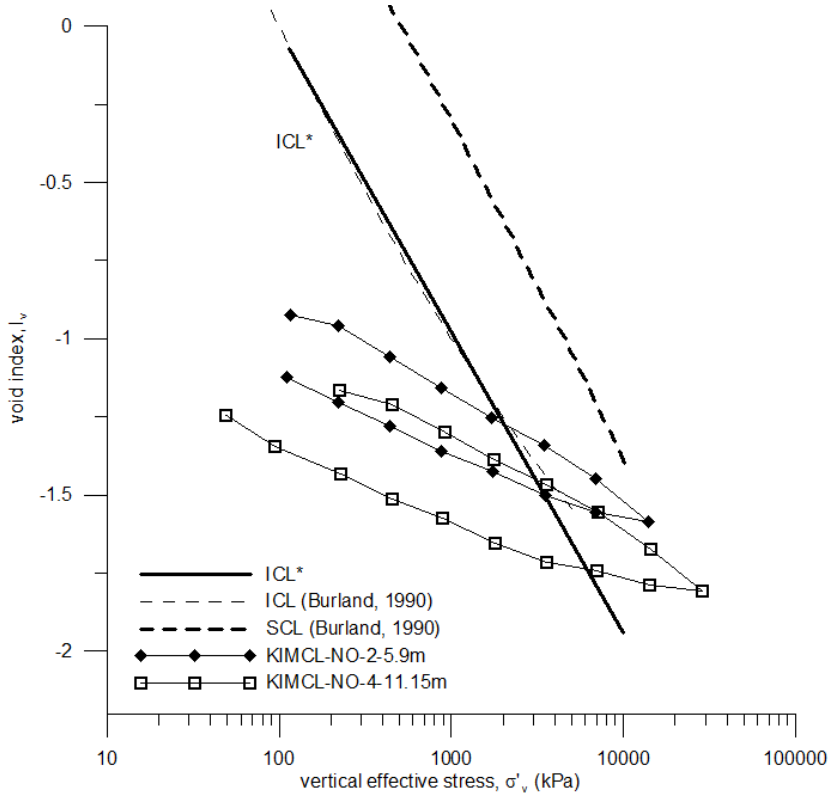


Figure 6-17: Normalised one-dimensional compression curves

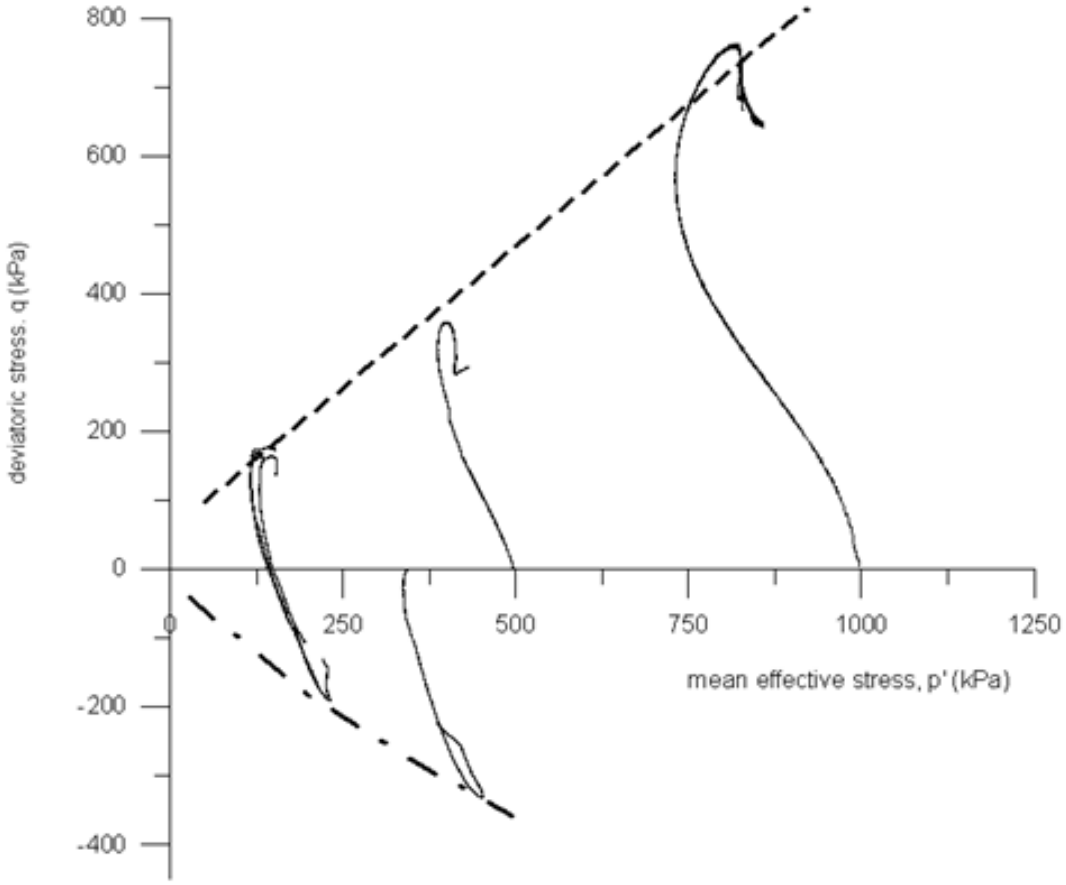


Figure 6-18: Effective stress paths for natural Kimmeridge clay

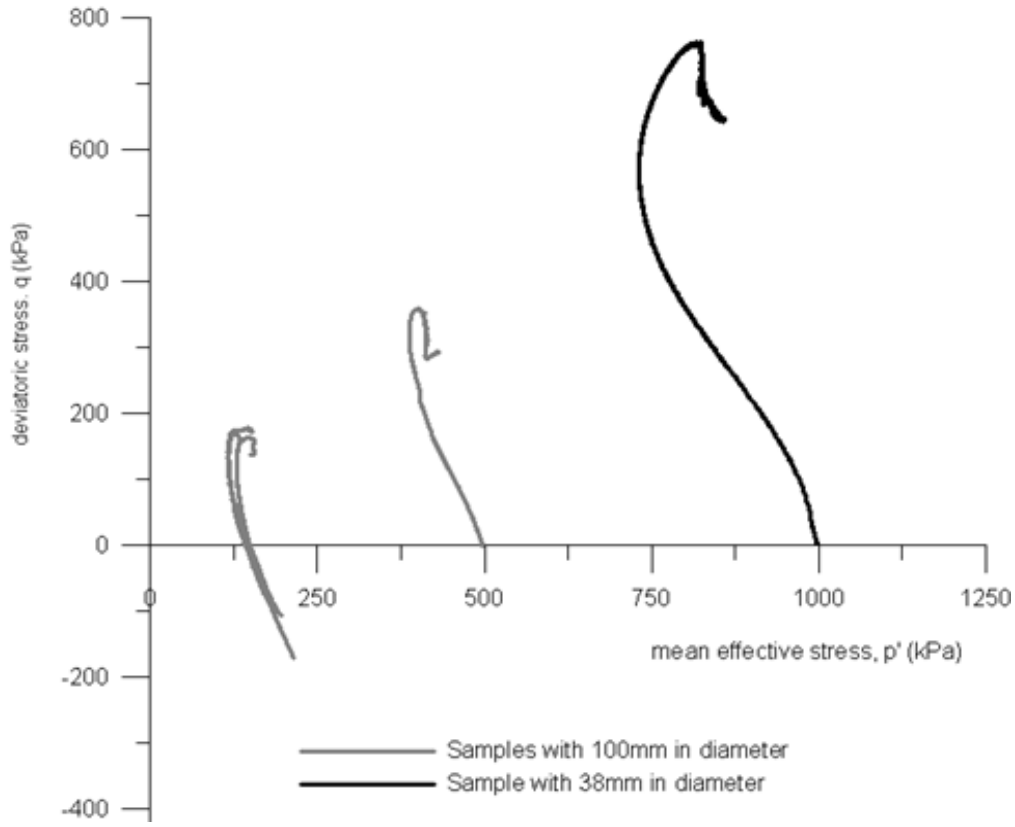


Figure 6-19: Effect of sample size on the strength of Kimmeridge clay

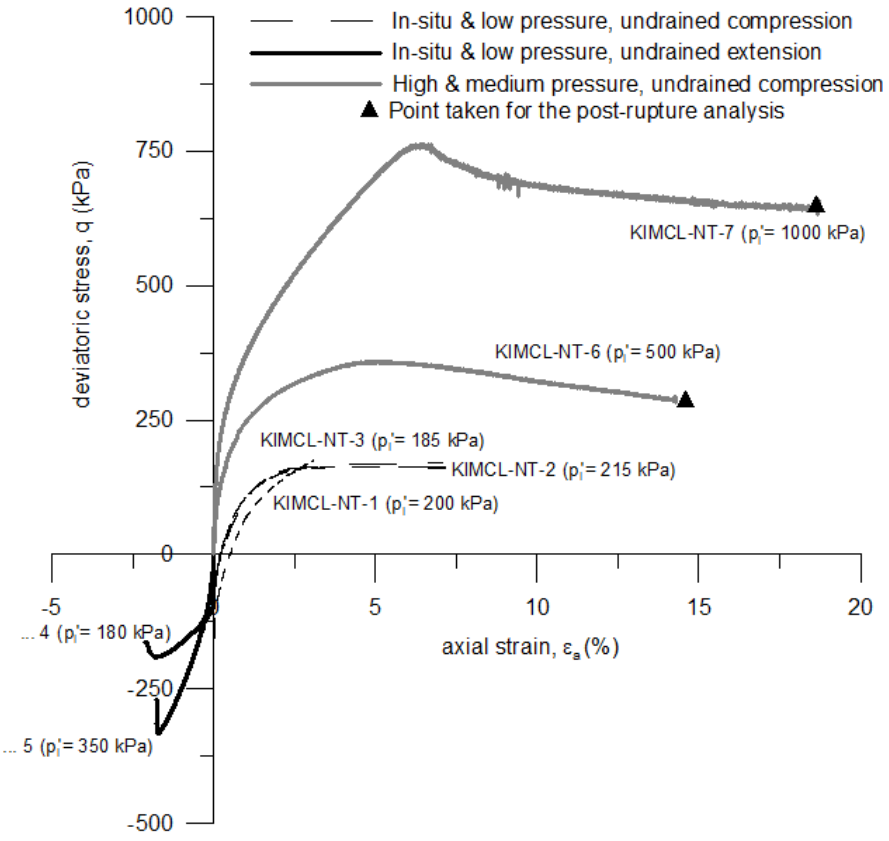


Figure 6-20: Stress-strain behaviour of natural Kimmeridge clay

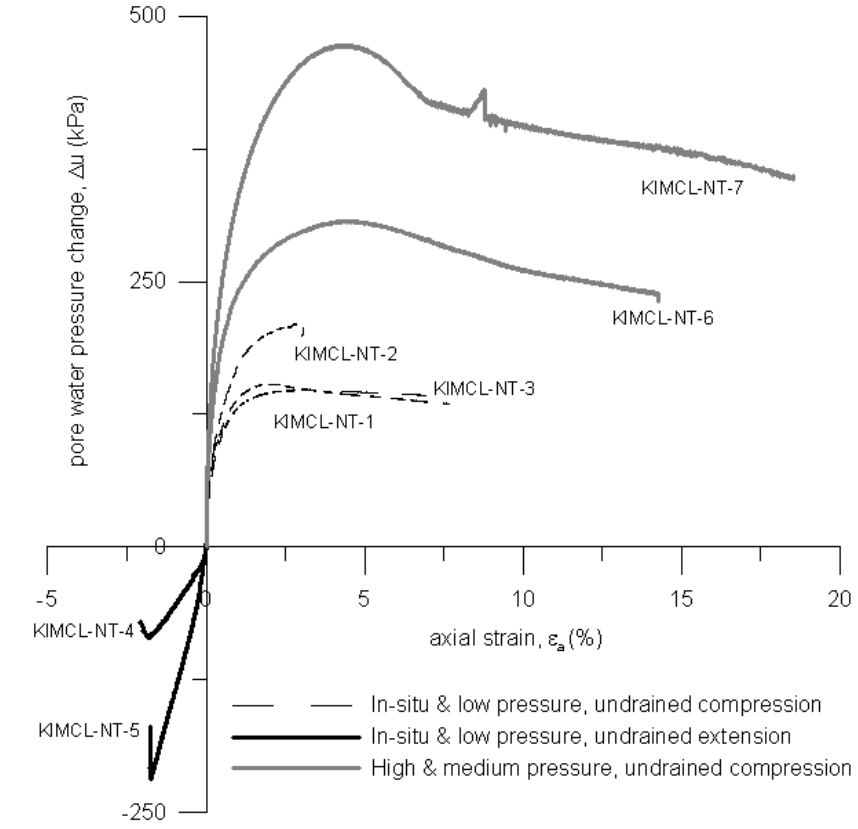


Figure 6-21: Pore water pressure change during the shearing of natural Kimmeridge clay

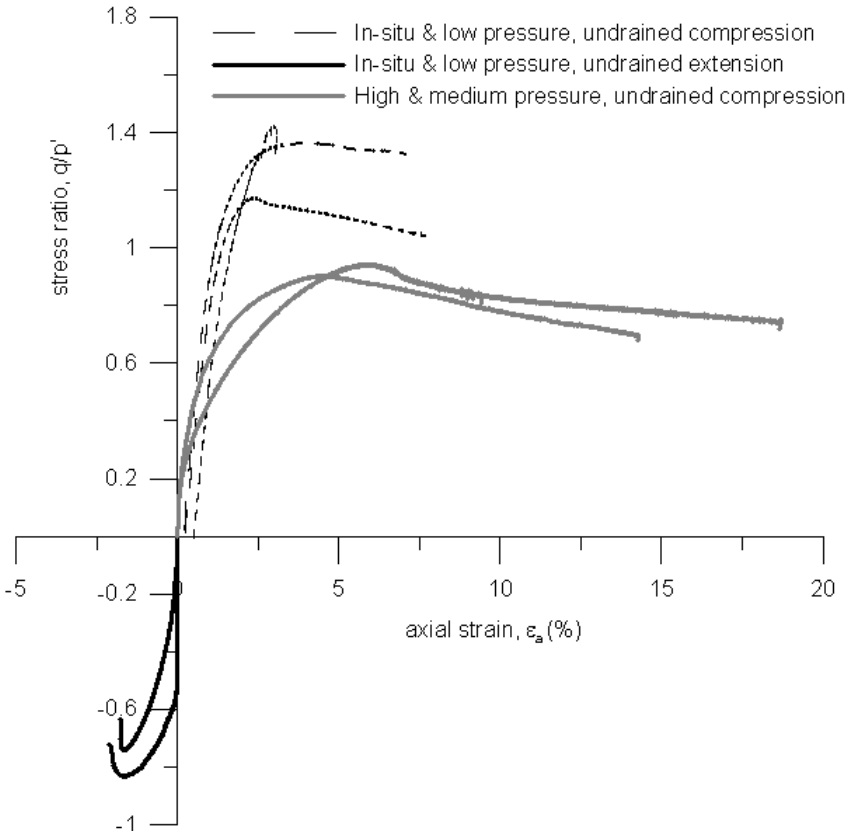


Figure 6-22: Normalised stress-strain behaviour of natural Kimmeridge clay

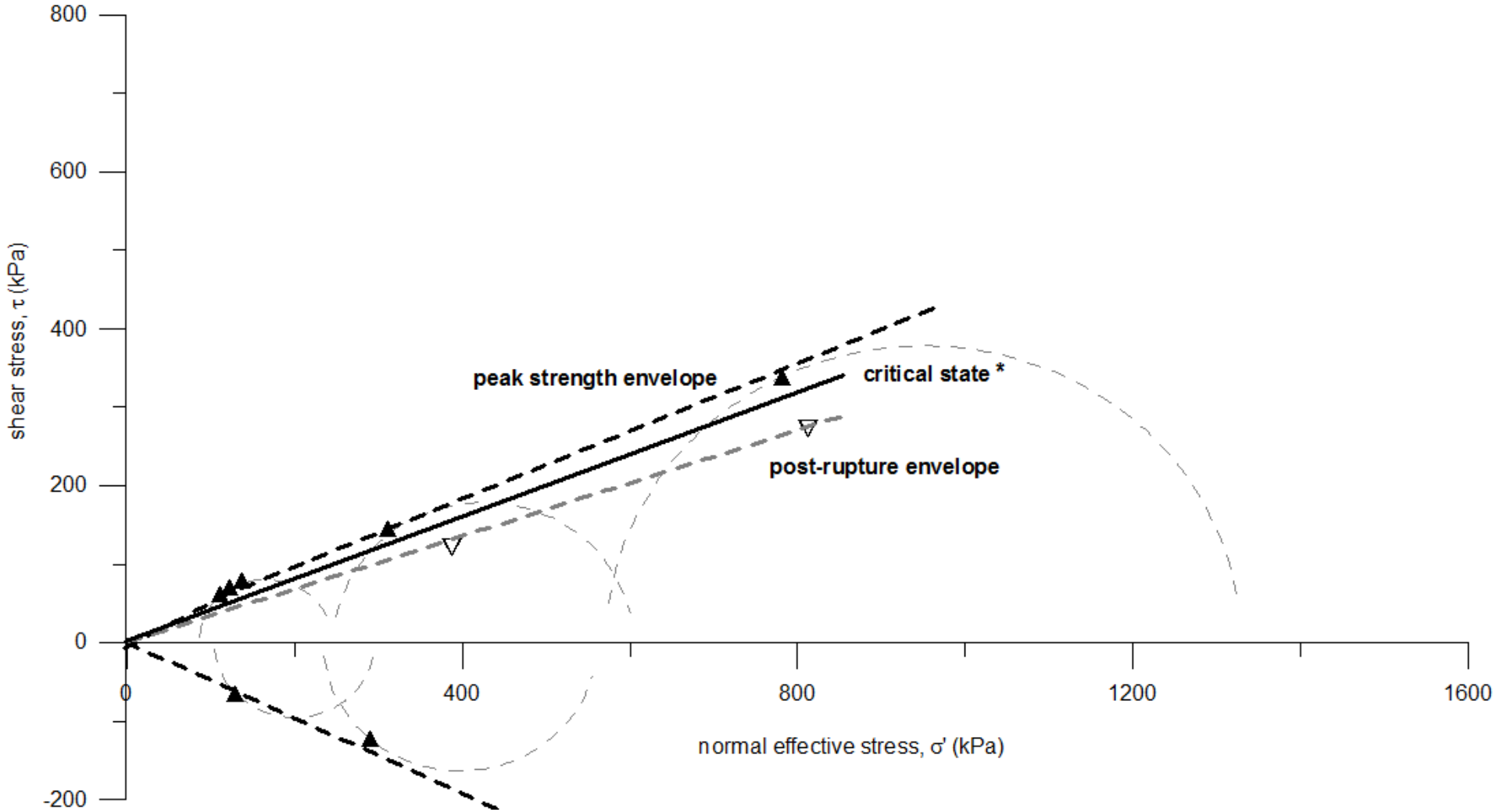


Figure 6-23: Peak and post-rupture strength envelope for natural Kimmeridge clay

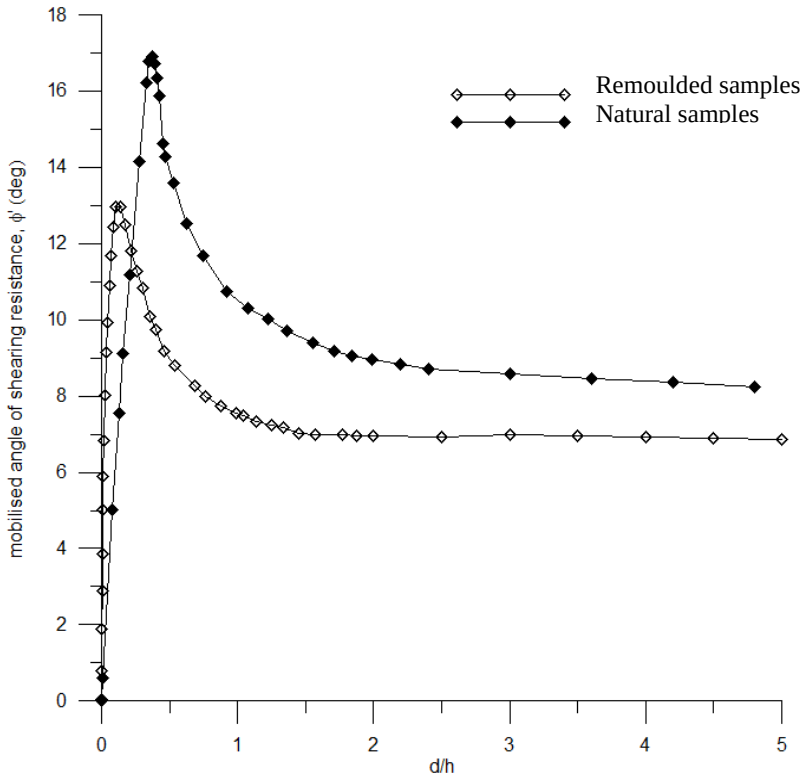


Figure 6-24: Stress-strain behaviour of natural and remoulded Kimmeridge clay at small displacements in ring shear apparatus under 400 kPa normal stress (d = shear displacement, h = sample height)

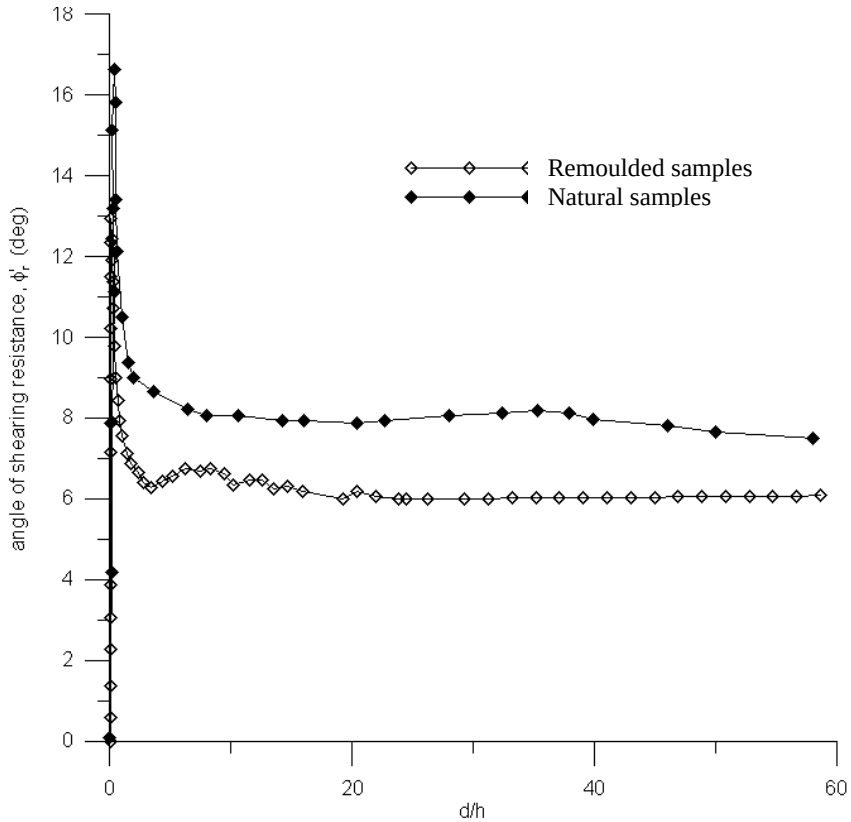


Figure 6-25: Stress-strain behaviour of natural and remoulded Kimmeridge clay at large displacements in a ring shear apparatus under 400 kPa normal stress (d = shear displacement, h = sample height)

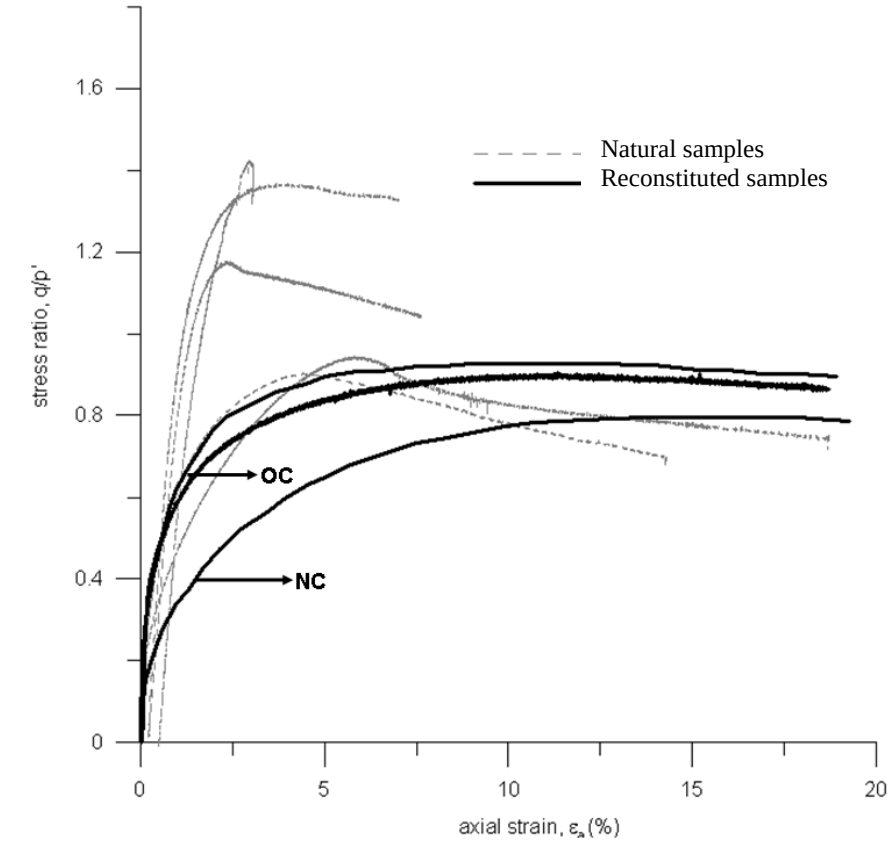


Figure 6-26: Normalised stress-strain behaviour for the natural and reconstituted (Normally consolidated & Overconsolidated) Kimmeridge clay

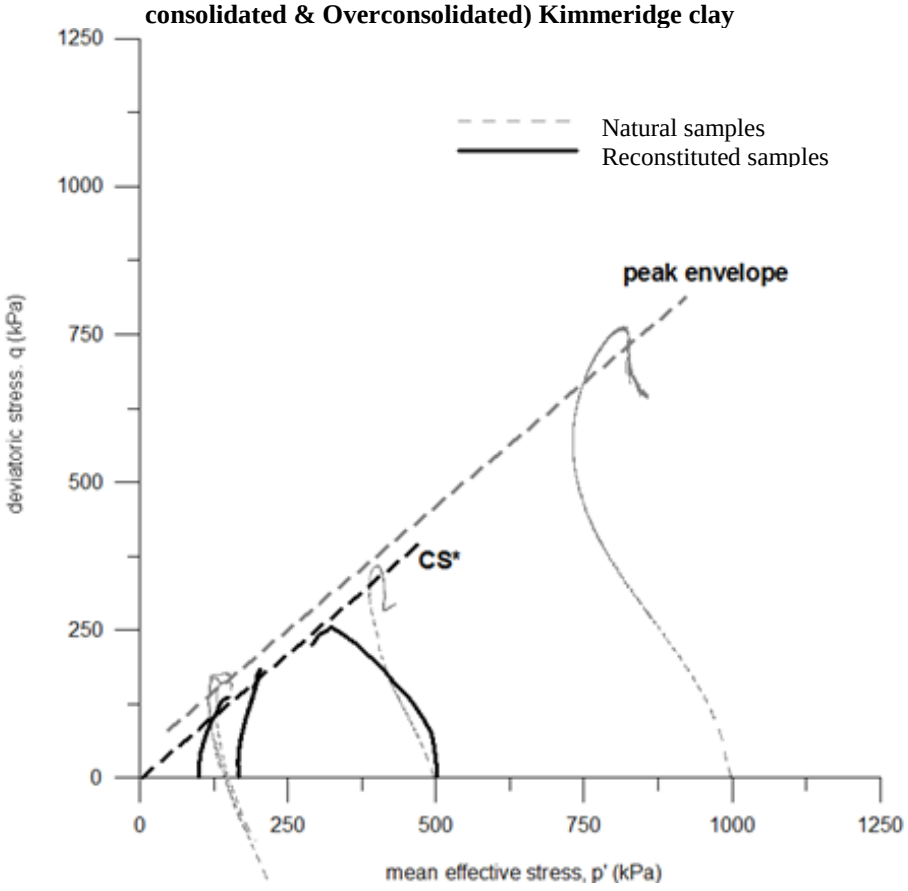


Figure 6-27: Effective stress paths for the natural and reconstituted Kimmeridge clay

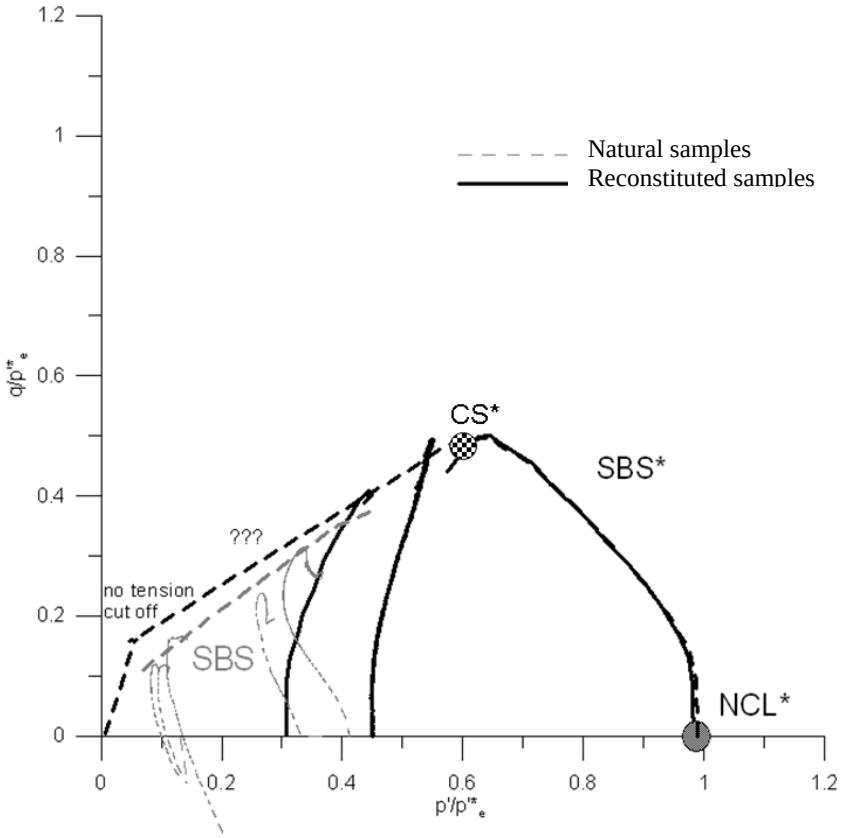


Figure 6-28: Normalised effective stress paths for the natural and reconstituted Kimmeridge clay

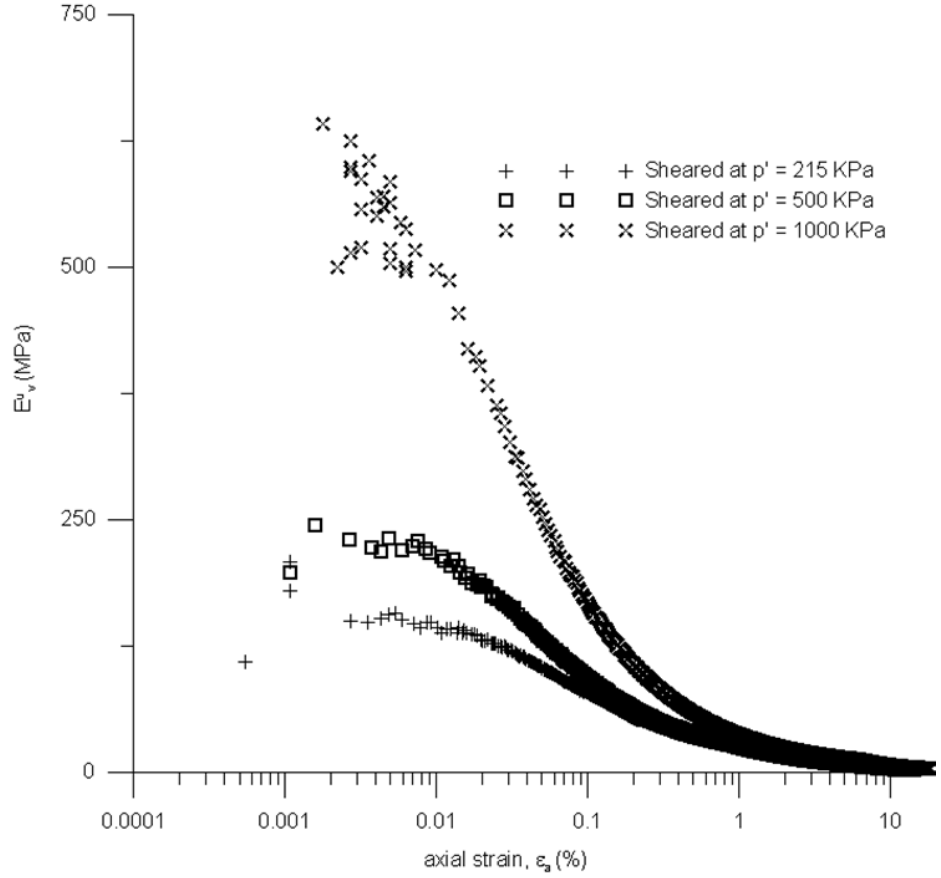


Figure 6-29: Stiffness degradation curves from the undrained compression tests on Kimmeridge clay at different consolidation effective stress levels

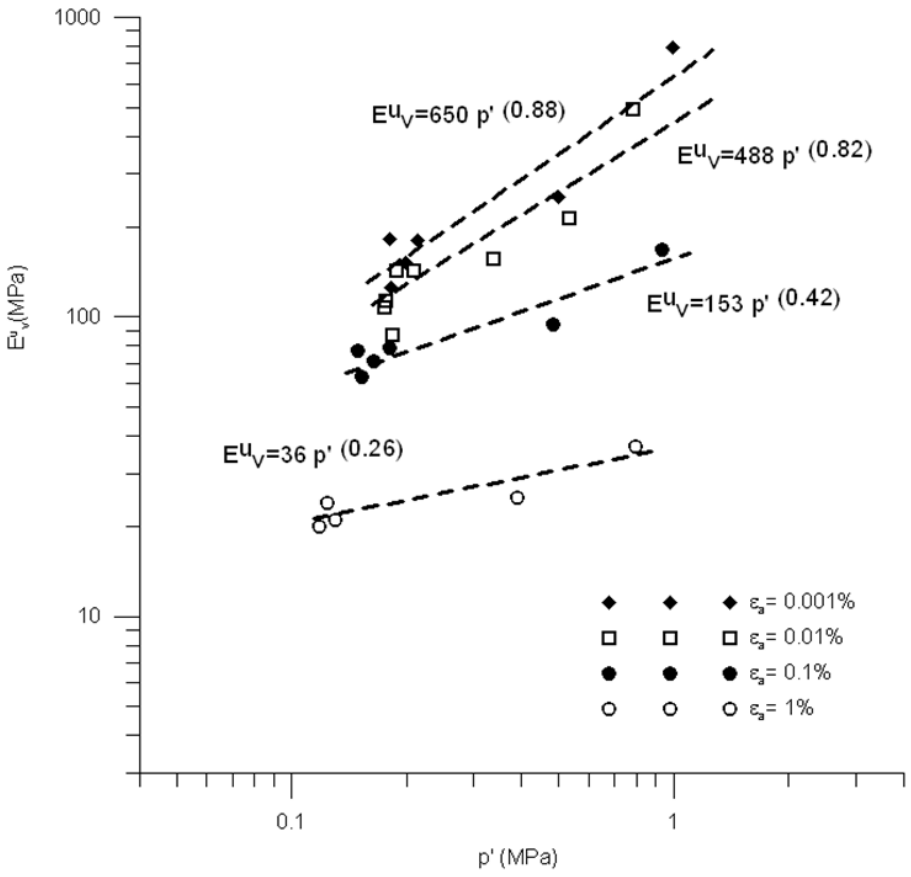


Figure 6-30: Undrained secant stiffness variation with stress level at different strain levels for the natural Kimmeridge clay

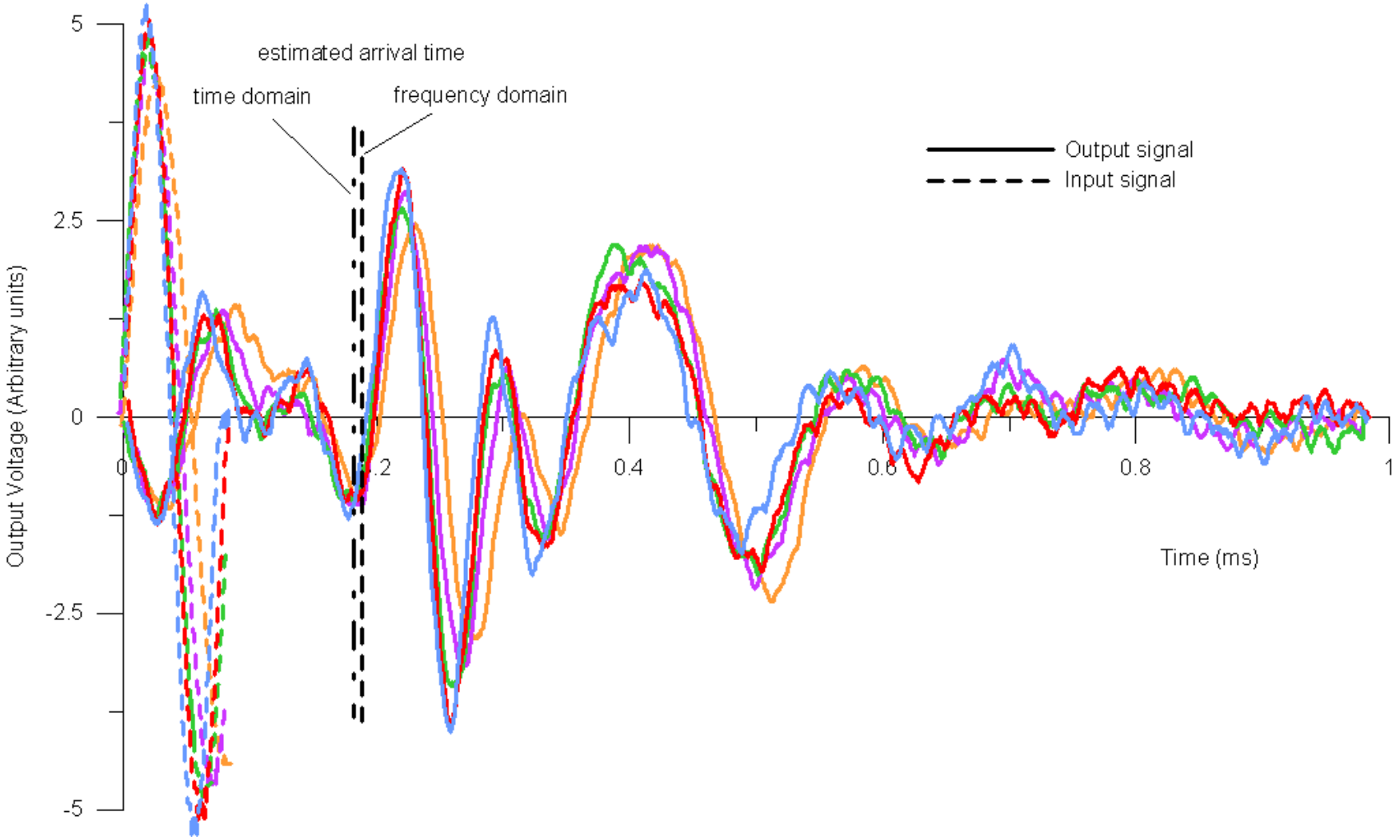


Figure 6-31: Typical bender element signals to obtain V_{hv} and G_{hv} values for the natural Kimmeridge clay (KIMCL-NT-8 at isotropic p'=220 kPa)

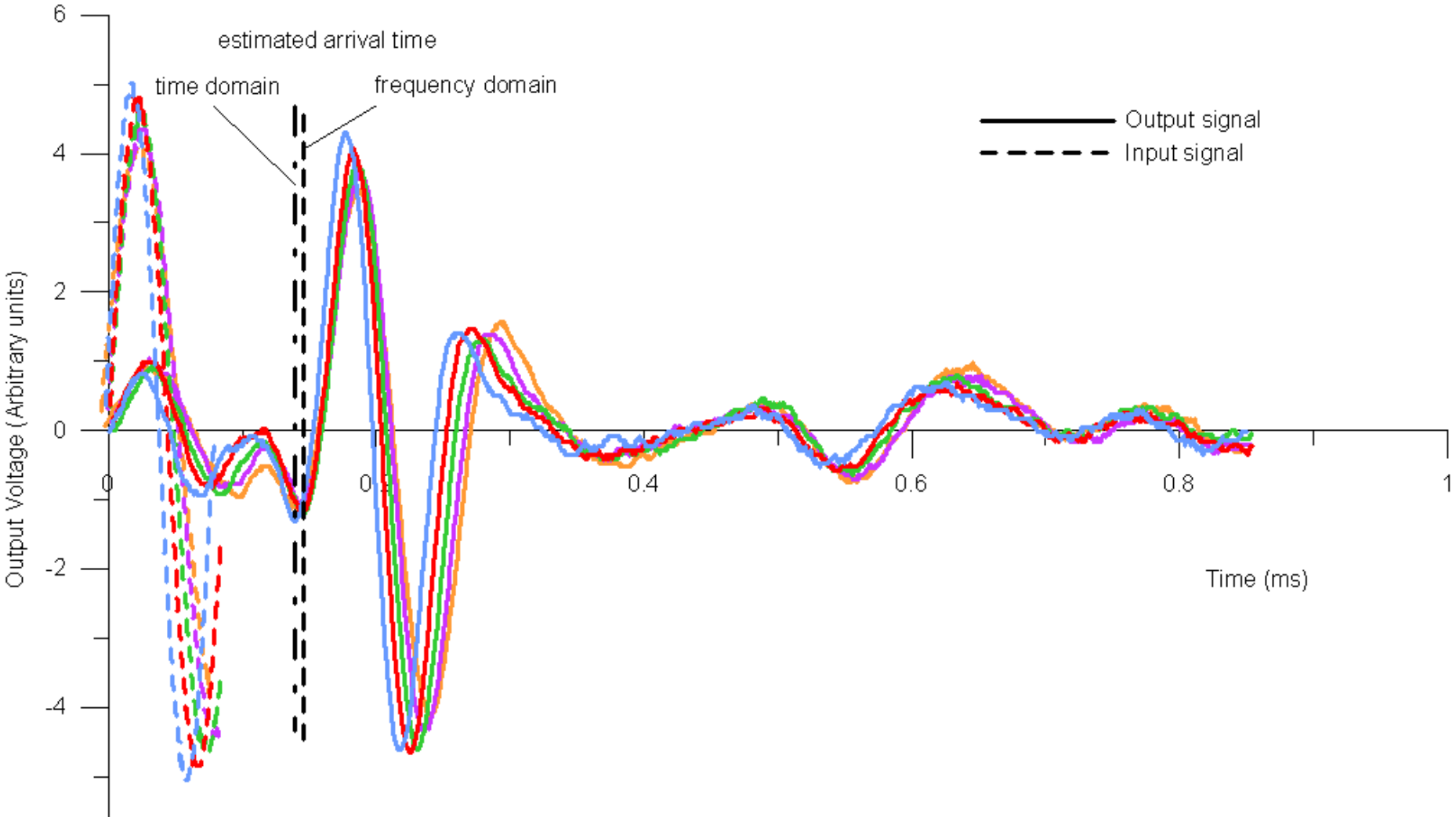


Figure 6-32: Typical bender element signals to obtain V_{hh} and G_{hh} values for the natural Kimmeridge clay (KIMCL-NT-8 at isotropic p'=220 kPa)

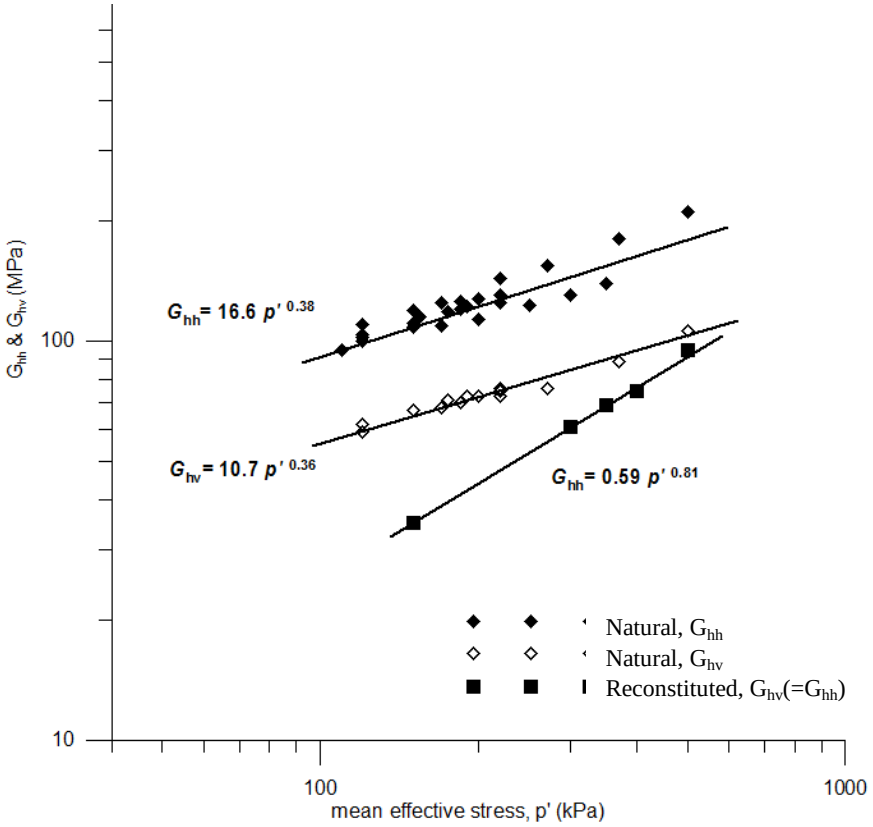


Figure 6-33: BE stiffness of the natural and reconstituted samples of Kimmeridge clay in different directions

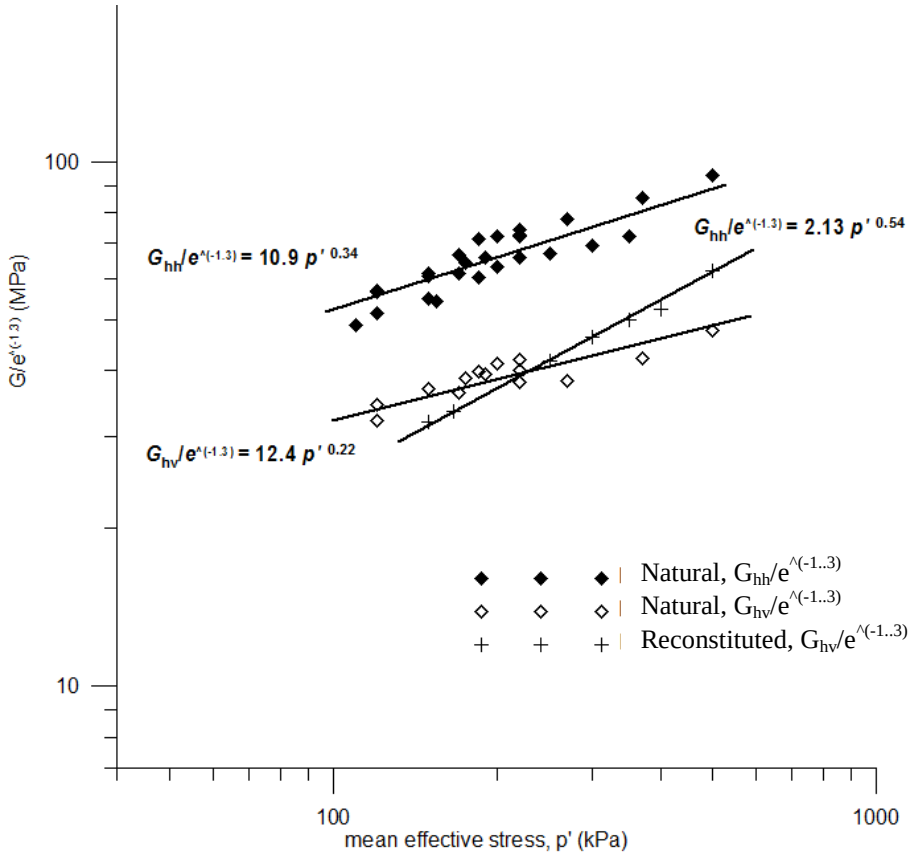


Figure 6-34: BE stiffness of the natural and reconstituted samples of Kimmeridge clay normalised for the void ratio

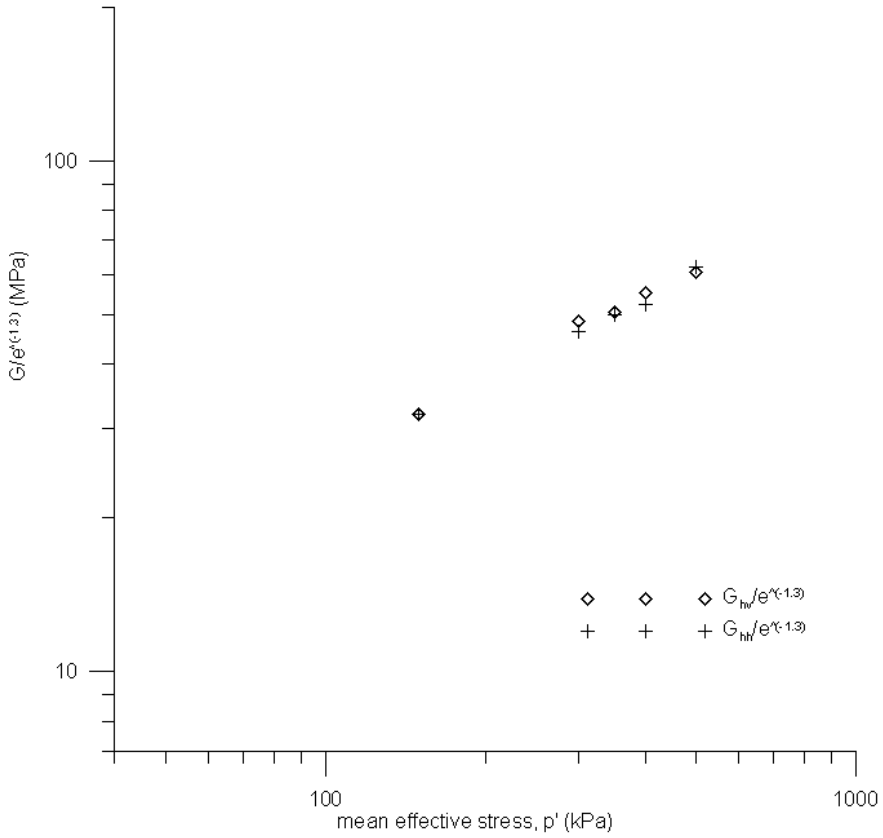


Figure 6-35: Normalised bender element shear moduli for reconstituted samples of Kimmeridge clay under isotropic loading

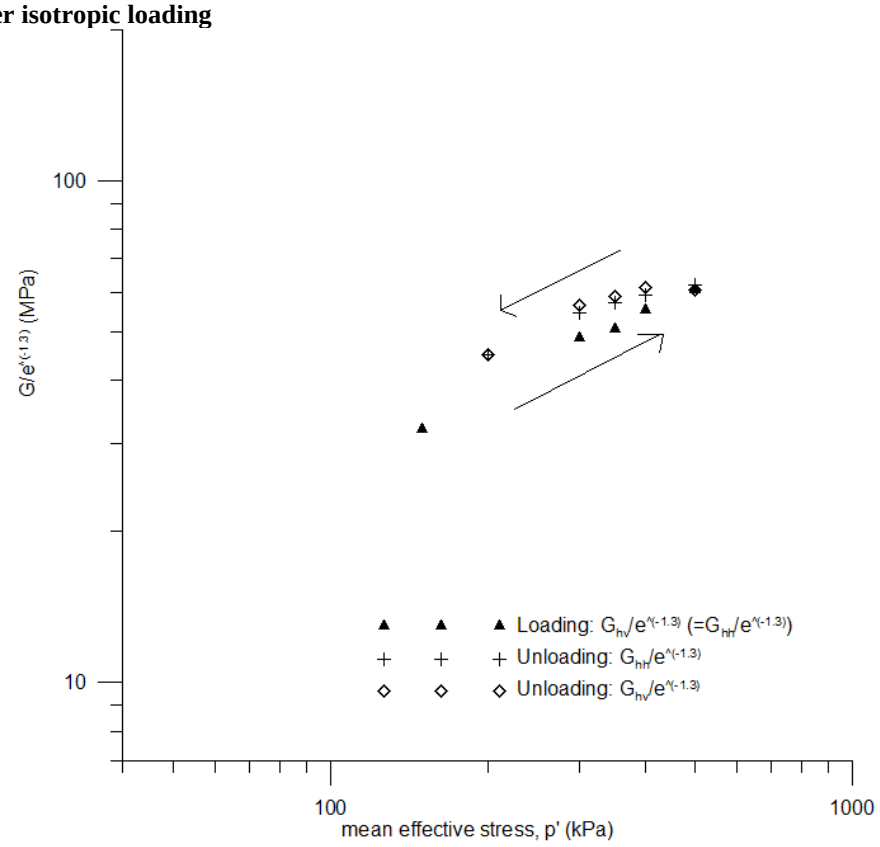


Figure 6-36: Normalised bender element shear moduli for reconstituted samples of Kimmeridge clay following isotropic loading and unloading

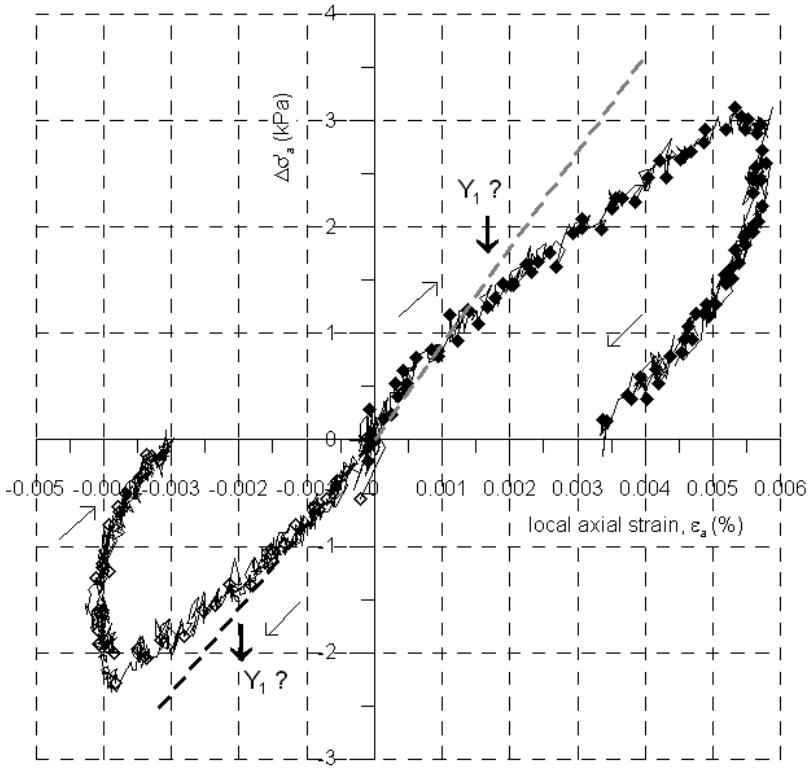


Figure 6-37: Axial probe in compression and extension; axial effective stress and strain increments

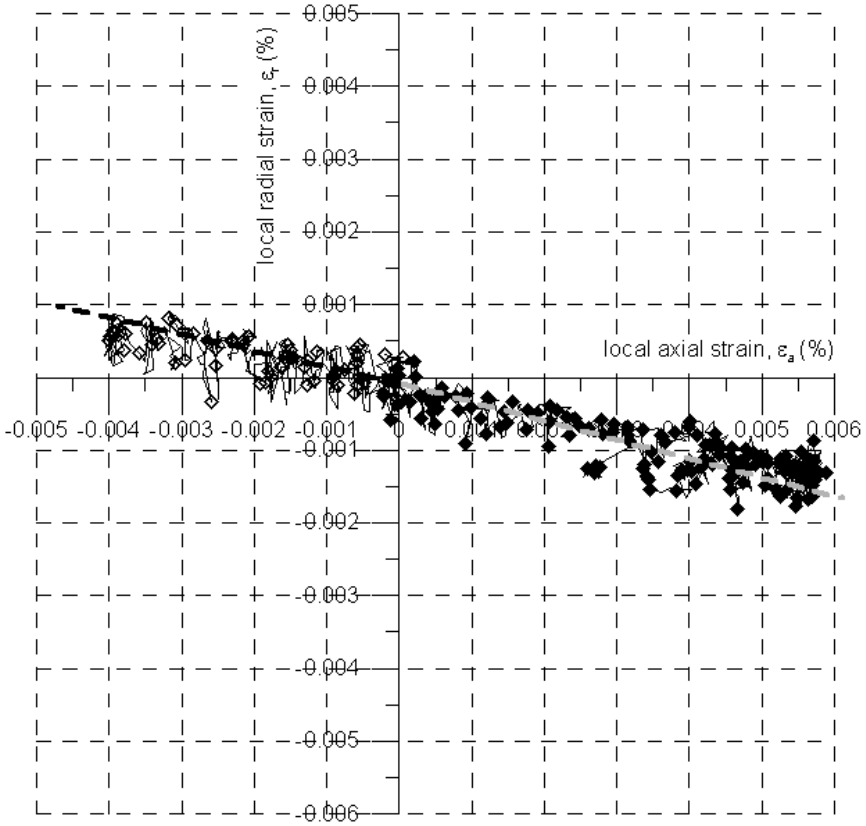


Figure 6-38: Axial probe in compression and extension; radial strain plotted against axial strain

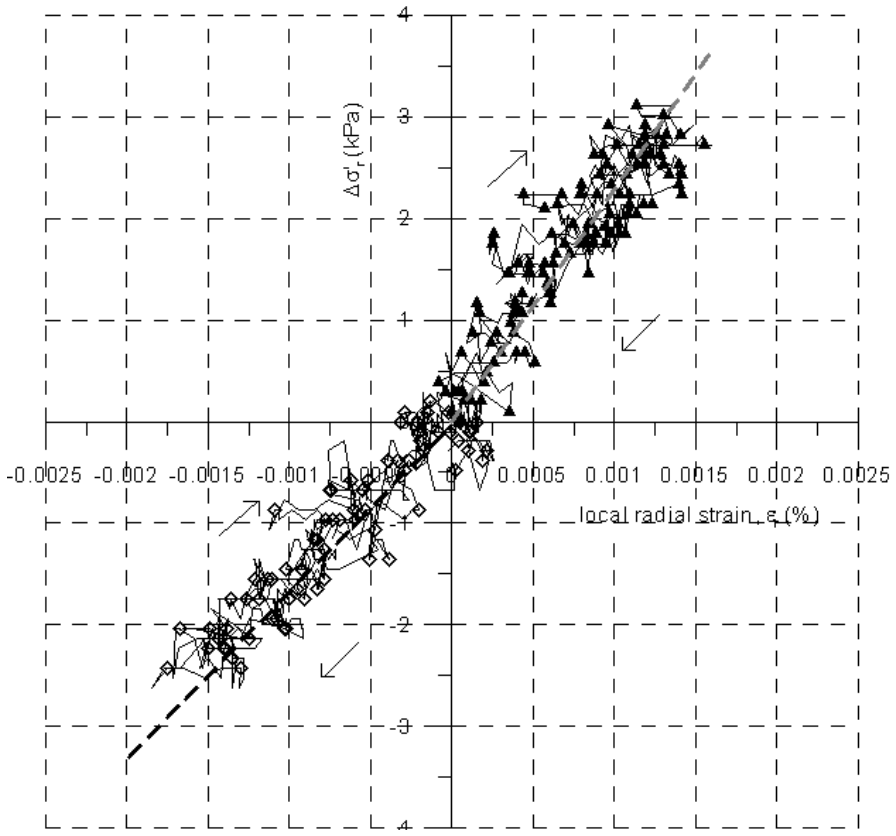


Figure 6-39: Radial probe in compression and extension; radial effective stress and strain increments

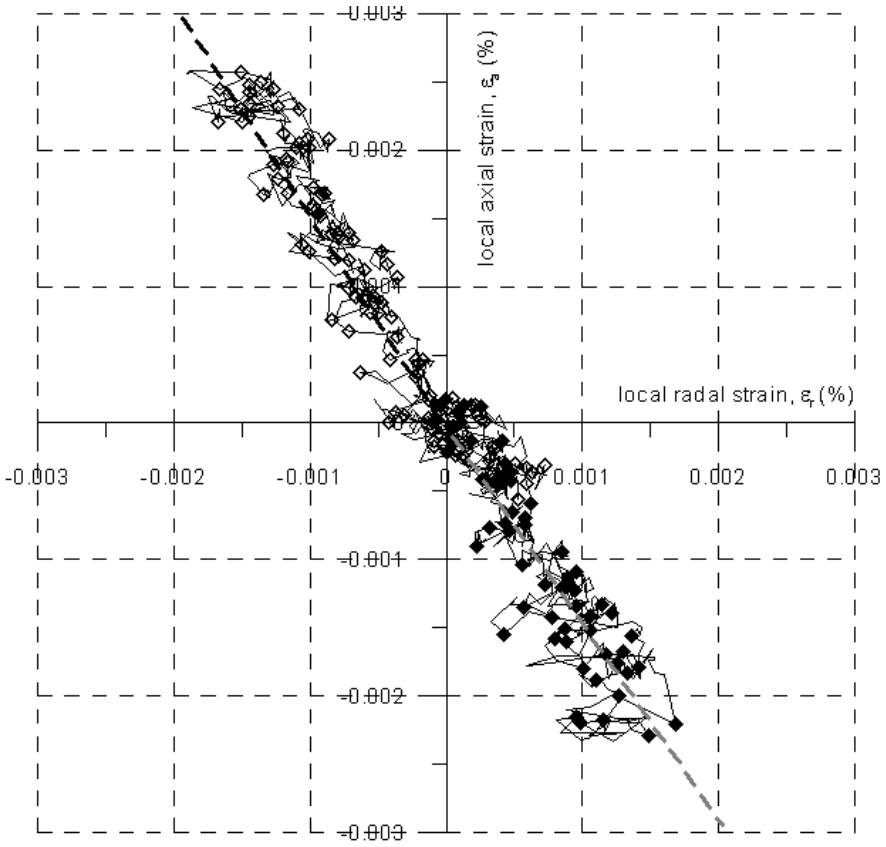


Figure 6-40: Radial probe in compression and extension; axial strain plotted against radial strain

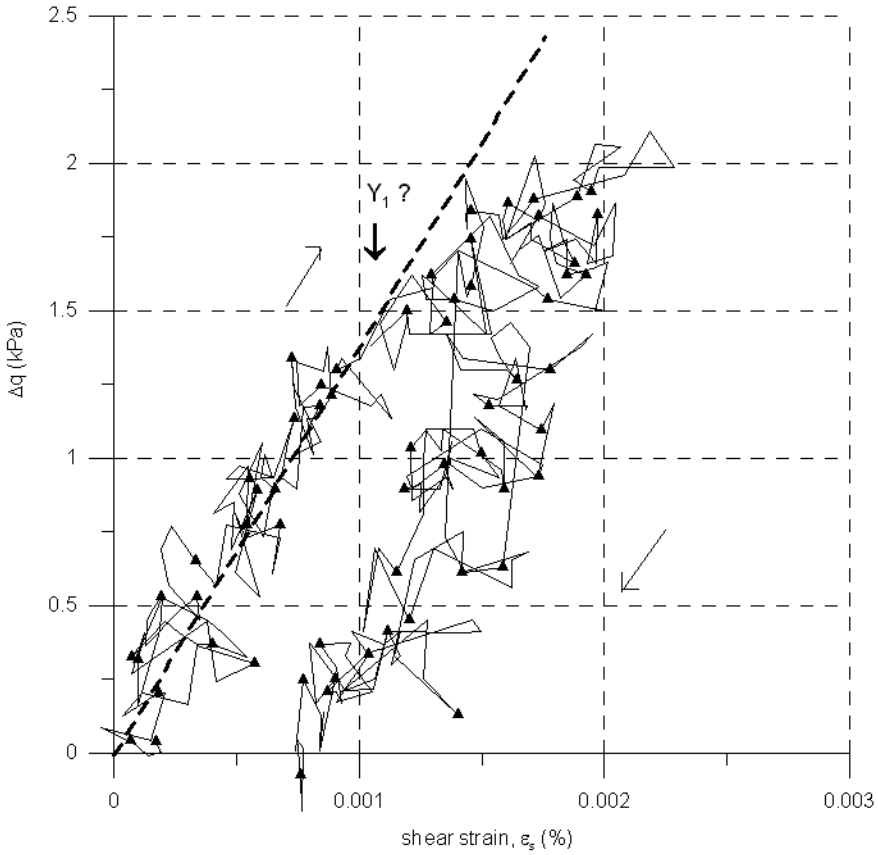


Figure 6-41: p' constant probe in compression; deviatoric stress plotted against shear strain

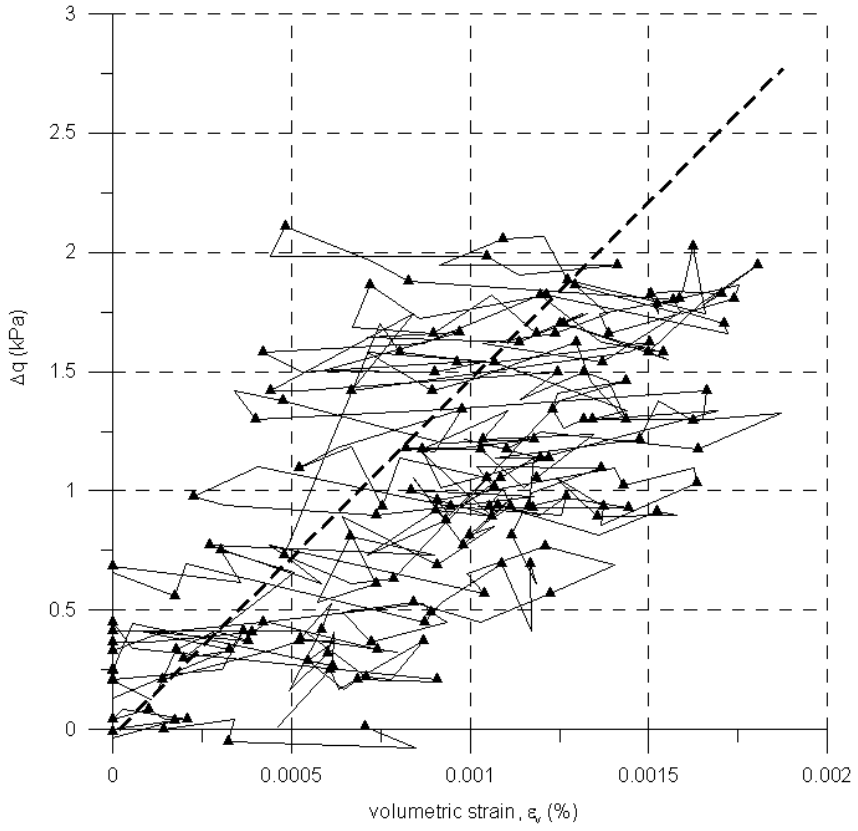


Figure 6-42: p' constant probe in compression; deviatoric stress plotted against volumetric strain

7 Discussion

7.1 Introduction

The main objective in the current project was to investigate the effects of geological age on the structure and engineering properties of UK mudrocks as well as acquiring more detailed information than was available before on geotechnical properties of these soils. The author has studied mudrocks which were deposited in different times, including upper Jurassic Oxford Clay (161 to 156 Mya), upper Jurassic Kimmeridge Clay (156 to 151 Mya), upper and middle Albian (Cretaceous) Gault Clay (112 to 99 Mya), these new data could then be compared with the previously studied lower Eocene London Clay (56 to 49 Mya). Initially it was planned to study Lias Clay (lower Jurassic 200 to 176 Mya), but the samples obtained for this deposit were not of the required quality and therefore it was not included in the laboratory testing. However, some samples of Lias clay were studied by Wilkinson (2011) for their micro-structure.

Tables 7-1 and 7-2 summarise the age, depth of burial, index properties, in-situ void ratio and mineralogy of the four soils studied in the current project. From an early stage in the research it was clear that studying mudrocks is very complex as there are many factors affecting the geotechnical properties of these deposits. The materials encountered have different particle size distributions and mineralogies, void ratios, inter-particle forces and arrangements of particles due to their particular depositional and burial environments. Geological age is only one factor that may affect their properties. It should also be kept in mind that the formations studied in the current research were taken from specific locations and depth ranges and are not necessarily representative of the whole stratum.

Noting these limitations the current chapter tries to compare the different structures and engineering properties of the four UK mudrocks. As mentioned earlier in Chapter 1, the mudrocks project was a combined effort to study the geology and micro-

structure as well as engineering properties. The former was carried out by Wilkinson (2011) and the latter by the author and Brosse (2012).

The following two sections of this chapter summarise aspects of the work completed by Wilkinson (2011). Aspects which are particular to individual soils (such as the weathering of the Gault clay) are not repeated here.

7.2 Geological history of UK mudrocks

7.2.1 General background

During the Jurassic the UK was series of islands and open seaways; the mudrocks studied here were deposited between these seaways and the UK also experienced a much warmer climate than present. The mineralogy of the materials deposited during this time depends on the nature of the original eroded material, for instance kaolinite was deposited more towards the north of the UK while illite was more common in the south. The depositional environment during the Jurassic is believed to be mainly of low energy with calm seas in a continental shelf environment. This would have been interrupted by periods of heavy storms which resulted in different particle sizes being deposited in different arrangements. The sea level was rising during this period making the deposits' structure condensed, with small inter-particle voids (Hallam, 1999). It is believed that a sea level rise had also occurred during the deposition of the Gault Clay (Cretaceous). During the deposition of London Clay in the Eocene, the open seaways were closing up due to the tectonic forces acting on the UK from the south. This caused a more enclosed and isolated depositional environment.

After deposition and during burial, high vertical effective stresses tended to rotate the platy particles into an alignment of least resistance. The particles rotated and came into contact with each other along their length and perpendicular to the applied stress, maximising their contact areas (Wilkinson, 2011). However, there is a limit to this rearrangement of platy particles and therefore the compaction (compression) of the material due to the vertical effective stresses is restricted to a certain level. When these particles are perfectly aligned they become 'locked up' and prevent further movements, however the compaction, further reduction in the porosity, may continue

due to diagenetic processes such as the conversion of clay minerals and cementation (Oertel, 1983). These processes are related to the time and depth of burial, temperature and the pore fluid chemistry. A decrease in the void ratio and the 'locking up' of preferred particle orientations are the two most important aspects of the diagenesis of mudrocks. The major mineralogical change which results in a preferred particle orientation is the transformation of smectite to illite. Also the formation of pyrite and carbonate cements can occur after the burial.

The depth of burial is an important factor that can alter the depositional structure. The depth of burial can be estimated based on the estimation of the material which could have been eroded from above a certain stratum (Jackson, 1972; Jackson & Fookes, 1974; Cox et al., 1999; Brenchley & Rawson, 2006) or by using techniques related to the changes of the temperature with depth (Green et al., 2001). In this study the ranges given by both techniques will be presented. Another factor affecting the mudrocks is tectonic activity which can alter the structure. To minimise this element in this research, the samples were taken from locations which were least affected by tectonic activity (Wilkinson, 2011).

The presence of fossils and their concentration in the mudrocks can result from different depositional environment to those of the platy particles. In some cases a layer of fossils can been created with a low concentration of platy particles present. These shell beds often indicate the extinction of a particular species over a period when little deposition took place (Wilkinson, 2011). Mineral filled macro-fossils are generally coarser than their surrounding particles and have different stiffnesses and compressibilities. These features can cause weak discontinuities to form between such bedding layers. Periods when no deposition took place can lead to a hard ground forming (Zorina et al., 2008).

7.2.2 Oxford Clay

The Oxford Clay, the oldest mudrock in the project, has high illite and quartz contents. Our Elstow samples also had the highest organic content of the soils studied at 10%. Areas of shell beds and pyrite bands were also present in the profile of the material. The different mechanical behaviour of these shell beds and the surrounding

platy particles leads to bedding features that can be weak when sheared in the horizontal plane. However, the same shells act as reinforcement in the horizontal plane under vertical loads. The depth of burial for Oxford Clay was estimated to be around 500m based on stratigraphy (Jackson, 1972; Jackson & Fookes, 1974) and around 1130m based on the changes of the temperature with depth (Green et al., 2001). There were few joints and fissures in the Oxford clay in comparison to the other younger soils (e.g. London clay). The main feature of the soil is its horizontal lamination and bedding (Parry, 1972; Burland et al., 1977; Peirpoint, 1996).

7.2.3 Kimmeridge Clay

The depositional environment of the Kimmeridge clay included some high energy periods which resulted in the clay particles aggregating to form larger grain assemblies (Wignall, 1989). Also volcanic ash is believed to have been deposited at the sampling site. The material sampled was from a highly condensed section of the stratum that has very low void ratio. Very few shell fragments were found within the material at the principal sampling depth. Some silt particles and coarse particles in the material might result from a shallow depositional environment or a high energy environment during deposition (Wilkinson, 2011). Kimmeridge Clay also contains a high organic content of around 6%. The depth of burial for this mudrock was between 410m and 1080m based on stratigraphy and the thermal methods respectively (Section 7.2.1). All of the samples were high in quartz content as the depositional material originated from volcanic ash. At the testing horizon, the Kimmeridge clay has only 14% clay minerals. The lack of platy particles is an important factor in the formation of the micro-structure of this soil with no preferred orientation of particles. The soil had a very low quantity of smectite and other platy minerals which are important factors that influence the anisotropic nature of the structure. No significant joints or fissures were observed in this material (Wilkinson, 2011).

7.2.4 Gault Clay

The main features of the Gault clay are: its high density of pre-existing fissures, its nodules and its high quantities of smectite (Wilkinson, 2011). The fissures were observable and opened in the block samples if they were allowed to dry. It was not as

easy to see these joints in the rotary core samples but it is believed that they increased in density with depth (Butcher & Powell, 1995). The material was much more fissured, fissure spacing of 60mm to 100mm at shallow depths, than the Oxford or Kimmeridge clays. The nodules are harder than the surrounding material and can cause local stress concentrations which can affect the overall behaviour of the material. Gault Clay is rich in smectite especially in the south of the UK, probably due to the presence of volcanic material in the depositional environment (Jeans et al., 1982). A high smectite content increases the swelling behaviour of the material (Jones et al., 1996). The organic content of the soil is low at less than 1%. The depth of burial for the Gault Clay is between 300m and 870m based on stratigraphy and the thermal methods respectively (Section 7.2.1).

7.2.5 London Clay

The London Clay has been studied in several projects conducted by Imperial College over the last few decades. The most recent research involved three coordinated PhD studies by Gasparre (2005), Nishimura (2006) and Minh (2007). Hight et al. (2007) summarise the outcomes and place the research into the practical context of the Heathrow T5 project. London Clay was deposited in a marine environment and experienced periodic rises and falls in sea level. The cycles of sea level change gave different sequences of the deposition by coarsening the material when the soil was deposited at shallower depths. These transgressions resulted in the series of lithological units proposed by King (1981). For comparison reasons with the other three mudrocks, London clay properties from depth of around 10 metres below ground level was required. This depth was within unit B2(c) in the London clay, and whenever no data for this sub-unit could have been found the parameters from adjacent sub-units were adopted. Based on geological evidence, Chandler (2000) estimated the depth of burial for London Clay to be around 200m. At the site where the samples were taken from, there was 6m of terrace gravel. The gravels were believed to have protected the London clay from recent weathering (Hight et al., 2007). London clay is heavily fissured with most fissures having sub-horizontal or sub-vertical orientations. The organic content of the London clay samples taken at 10m below ground level was 1.5%.

7.3 Micro-structure and macro-structure

The four mudrocks considered have important features of micro and macro-structure. The micro-structure is illustrated below by reproducing the micro-images analysed by Wilkinson (2011). These give an insight into some aspects of the structure but the observations made can not be generalised reliably to the whole stratum or even a laboratory sample as the sizes of the samples used in the imaging process were very small at around 10x10x10 mm. Table 7-3 summarises the major structural element of each soil in relation to its age and depth of burial.

7.3.1 Oxford Clay

Wilkinson's SEM images showed that his Oxford clay specimens had very strongly horizontally preferred particle orientations, an example of which is shown in Figure 7-1. Shells existing in the material are aligned horizontally and function as reinforcement under vertical loads. Normally there is a gap between these shells and the surrounding material (Wilkinson, 2011). When multiple shells are aligned on the same plane, horizontal slip can occur on this weak layer if high horizontal shear stresses are applied (Burland et al., 1977).

7.3.2 Kimmeridge Clay

Wilkinson's SEM images of different samples of Kimmeridge clay from various depths revealed no clearly preferred particle orientation and the fabric was disturbed by the presence of silt particles. The silt content of the soil increased with depth and these particles are covered with finer particles which form bridges with neighbouring particles. Very few platy particles were observed in these samples, limiting the scope for any clearly preferred particle orientation. Figure 7-2 shows SEM images of Kimmeridge clay from 12.71m and 8.54m respectively below ground level. The variation in structure is evident, with the deeper sample having larger silt particles and larger voids in contrast to smaller voids and more platy particles in the shallower sample. However, no preferred particle alignment can be seen in either of the two images.

7.3.3 Gault Clay

A large variability with depth in the structure of the Gault clay was observed. Similar structures to Oxford clay were observed in the Gault clay from 6.82m below ground level. However, the degree of preferred particle orientation was less clear at shallow depths due to the weathering (Figure 7-3) and also at the depths of the testing horizon (10m below ground level). Small rounded micro-fossils, similar in size to clay particles, were present. Also nodules were present both at micro- and macro-level. The SEM images showed that the clay particles were covered with small fragments of shells, granular crystals and micro-fossils laying on their horizontal surfaces (Wilkinson, 2011). These small shell fragments play a different role to those in the Oxford clay. While the horizontally aligned shells functioned as reinforcement, under vertical loads, in the Oxford clay, the rounded micro-fossils in the Gault clay interrupt the preferred particle orientation (Wilkinson, 2011). The clay mineral content of Gault clay reduces with depth which can be one reason for the apparently reduced horizontal particle orientation at greater depths. However this can not be the main reason and the large number of micro-fossils might also be important. Probably the macro-structure, with its close spaced fissuring, was a more dominant factor in the material behaviour compared to variable micro-structure.

7.3.4 London Clay

Moderate preferred particle alignment was observed in most of the London clay samples, an example of which is shown for a sample from around 8m below ground level in Figure 7-4. Although London clay is rich in clay mineral content, an orientation as strong as that seen in the Oxford clay could not be observed, which may be related to its relatively shallow depth of burial compared to the other soils. Gasparre et al. (2007) observed that the degree of preferred particle orientation increased with depth perhaps as a result of the higher stresses which were applied to the deeper samples. They suggested that the higher degree of anisotropy exhibited by samples from deeper units resulted from their more compacted and orientated micro-structures.

7.3.5 Analysis of particle orientation

Wilkinson (2011) carried out quantitative analysis of SEM images for each of the mudrocks in order to study the degree of preferred particle orientation. Figures 7-5 and 7-6 show his rose diagrams of the summation for particle long axes. On the left hand side of the figures the particle orientation in the vertical plane is presented and on the right hand side the particle orientation in the horizontal plane. A grey threshold is required to create binary images and Wilkinson (2011) showed that the lower quartile and the upper quartile of grey levels can be a good representation of the particle orientation. As can be seen from these diagrams, a preferred particle alignment in the horizontal orientation is evident for most of the samples, but with different intensities. To analyse these rose diagrams further, Wilkinson (2011) separated two vectors V_{max} and V_{min}, perpendicular to each other, as shown in Figure 7-7. These two vectors represent the intensity of the preferred particle orientation in the horizontal and the vertical orientations. Figure 7-8 shows examples of different structures and rose diagrams corresponding to the different soils studied. The strongest preferred particle alignment for these samples places them towards the bottom right of the figure.

Oxford clay, Gault clay from 6.82m below ground level and the Lias clay from 11.6m below ground level showed the strongest particle orientation in the horizontal direction. The Kimmeridge clay and other samples of Gault clay did not show a very strong preferred particle alignment. The depth of burial can not therefore be the only factor in aligning the particles. Although the samples of Gault clay showed this structure no alignment was observed for the Kimmeridge clay which was buried deeper than the Gault clay. Figure 7-9 shows the difference between V_{max} and V_{min} (δV), as a measure of preferred particle alignment, plotted against the clay content of each mudrock. Although there is a direct relationship between the clay content and particle orientation for most of the samples, a high clay content can not be the only factor in forming an aligned fabric because in the weathered material with a high clay mineral content there is no preferred particle orientation. The bulk mineralogy of London clay at the horizon studied here was not available and it would be valuable data to check the validity of the relation between the clay mineral content and the preferred particle orientation.

Differences in the micro-fossils present in each mudrock and their effects on the mudrock structures were also observed by Wilkinson (2011). The elongated and horizontally oriented shells in Oxford clay might have a reinforcing function while the rounded micro-fossils in the Gault clay disturbed the structure. The presence of fossils also affects the void ratio values of all these mudrocks. Both voids between fossils and other particles and voids within these fossils could increase the void ratios.

The particle size distributions of all four mudrocks are shown in Figure 7-10. As mentioned earlier the Gault clay has the highest proportion of clay particles. The Kimmeridge clay has a better graded particle size distribution which will result in smaller particles filling the voids more effectively and therefore it possesses the lowest void ratio of all four mudrocks. Changes in the in-situ void ratio with previous depth of burial (based on stratigraphy) for all four soils are shown in Figure 7-11. As expected, the general trend is decrease in the void ratio with increase in depth of burial, however as was mentioned above depositional elements such as particle size distribution and presence of fossils can alter this trend as was seen for the Kimmeridge clay.

In-situ void ratio for each soil and slope of their 1-D swelling lines were used to trace their void ratios back to the before erosion. The lower bound of previous overburden pressure was assumed to anticipate the in-situ stress state after normally consolidated stage of the deposition. The results are shown in Figure 7-12 with sedimentation compression curves produced by Skempton (1969) for different liquid limits. Although there are major uncertainties about the stress history of four mudrocks and their position on this graph is not accurate, a general agreement can be seen between these soils and Skempton's normally consolidated ones, with mudrock specimens placing slightly lower than Liquid Limit contours.

7.4 Behaviour in 1-D compression

Compression curves for oedometer tests carried out on both natural and reconstituted samples of the three mudrocks studied in this project were presented in Chapters 4 to 6 and for London clay these data are available from the previous study carried out by

Gasparre (2005). To allow comparison, test results on samples taken from a depth of around 10m below ground level were chosen to represent each soil. All the parameters obtained from these tests are presented in Table 7-4.

The compression and swelling lines of the natural mudrocks can be seen in Figures 7-13. No definite yield point can be identified for any of the tests, but gradual yielding is clearly taking place from around 10 MPa for all four samples. The maximum compressibility from this final section was used to calculate the C_c values. The compression index, C_c, is quite similar for all four soils, with Kimmeridge clay having the lowest compressibility. This lower compressibility in Kimmeridge clay probably is due to its more compacted structure and low void ratio. It should also be recalled that Kimmeridge clay has the lowest fossil content, which again decreases its compressibility. The initial void ratio depends on the particle size, grading, the abundance of fossils and also the depth/age of the mudrock. However, Kimmeridge clay, which has similar burial depth and age to Oxford clay, has the lowest void ratio. As discussed earlier this may be due to filling of the voids by smaller particles and lack of fossils.

The variance in the swelling index, C_s, is small. It should be noticed that due to high presence of smectite in Gault and London clays it was expected to see a more significant swelling for these soils, but perhaps the structure of the materials does not allow any more swelling than the other two soils. There is insufficient evidence to evaluate the degree of destructuration caused by compression of Gault clay as tests to different stress levels were not available. However, as was shown in Chapter 4, compression to different stress levels did not alter the swelling behaviour of the Oxford clay. Probably the structure is incompletely removed under the compression. The effects of mineralogy on the swelling behaviour can be best seen when comparing the swelling index, C_s, of the Kimmeridge and Gault clays. Although Kimmeridge clay has little content of swelling minerals, its swelling index is almost equal to that of Gault clay. It is not clear if the high organic content of Oxford and Kimmeridge clays is playing a similar role to the swelling minerals in the two younger mudrocks.

The results from the oedometer tests on the reconstituted samples of mudrocks are plotted in Figure 7-14. The main observation in this plot is the generally elevated position of the compression/swelling lines of Gault clay regardless of the high pressures applied. As mentioned earlier, the high percentage of swelling minerals like smectite should give this mudrock greater capacity of swelling. The reason that there is slightly higher swelling for the reconstituted soil but not for the natural material may be the effects of structure on swelling in the former case which was not completely removed under the compression. The reconstituted Gault and London clays have the highest compression and swelling indices compared to the other two soils. As effects of natural structure have been removed for all these soils, the difference in compression and swelling behaviour perhaps have been caused by the differences in their mineralogy and composition of each soil. High presence of smectite resultes in higher compression and swelling of the two younger soils. The values of the swell sensitivity for all four mudrocks, presented in Table 7-4, are around unity, which based on a conventional definition of structure shows not very strong structure for the natural materials after destructuration under compression to large stresses.

Normalised compression curves for the natural samples are plotted with the *ICL** in Figure 7-15; each test was normalised using its own reconstituted compression line. As mentioned earlier, Burland (1990) presented the *ICL** in a curved form, however a straight line passing through the reconstituted compression tests were used to keep consistency with the normalisation when using a linear isotropic *NCL**. With the exception of Gault clay, it can be said that the deeper burial and longer diagenesis results in a more compacted structure with lower void ratios, causing the natural curves to hardly pass the *ICL** at high pressures and at low void ratios. The reason for the lower position of the natural Gault clay is perhaps the substantial swelling that occurred during the reconstitution which widened the difference between the natural and reconstituted compression lines. Compression curves for different natural clays are shown in comparison with the mudrocks studied in this project in Figure 7-16. With the exception of normally consolidated Bothkennar clay and overconsolidated Pappadai clay which are yielding at or very close to SCL, other soils are either not showing a significant yielding at these stress levels, or they yield before reaching

SCL. In general at high stress levels, these old overconsolidated clays are placed in between *ICL** and SCL.

In general, the effects of structure on the behaviour of the stiff clays studied here can not be well observed only by observing the compression/swelling behaviour of the samples tested in the oedometer. Although lower compressibility (lower values of compression index) for the natural samples is a sign of structure which is being removed for the reconstituted materials, no clear yielding point and almost parallel swelling lines make it difficult to quantify structure within the sensitivity framework. The alternative method of normalisation proposed by Gasparre & Coop (2008), which takes the swelling lines into account, can not be applied here as tests on samples compressed to different stress levels are not available for the Kimmeridge and Gault clays. As mentioned in Chapter 4, this normalisation is not valid for Oxford clay either as the swelling lines of the natural material stayed parallel regardless of the stresses the samples were compressed to.

7.5 Behaviour in shear

The shear behaviour of the mudrocks was studied by the author using triaxial stress path cells and also by Brosse (2012) using Hollow Cylinder Apparatus (HCA). Detailed results obtained from triaxial testing of the three UK mudrocks have been presented in Chapters 4 to 6, and details of tests carried out on London clay are available in Gasparre (2005) and Nishimura (2006). The HCA study is being written-up in parallel with this study and a comprehensive summary is not available to incorporate here. This section is divided to two sub-sections, one focusing on the triaxial strength and the other on the stiffness characteristics of the UK mudrocks.

7.5.1 Strength of the mudrocks

The intrinsic State Boundary Surfaces, *SBS**, obtained from the triaxial compression tests on the reconstituted samples of the mudrocks are presented in Figure 7-17. These surfaces are all normalised using the equivalent pressure, p'^*_e, on the intrinsic Normal Compression Line. The Hvorslev surfaces obtained for the Gault and

Kimmeridge clays are not reliable as tests on samples with higher OCR values would have been required to locate them accurately. Reconstituted Gault clay exhibits higher intrinsic strength compared to the other mudrocks, as indicated by the critical state angles of shearing resistance, φ'_{cs}, presented in Table 7-5. As natural structure had been removed for the reconstituted tests, the differences between these strength values can only be a result of the particle size distribution, shape and mineralogy of the soils. The particle size distributions of Kimmeridge and London clays are similar, with higher presence of coarse particles (45% for London and 41% for Kimmeridge clay being retained on the 63μm sieve in comparison with 30% and 35% for the Gault and Oxford clays respectively). Also these two soils showed a well-graded particle size distribution. However, it is the Gault clay which has the highest clay content which actually shows the highest strength. As mineralogy and particle size distribution both affect the intrinsic properties of the soil, a further normalisation based on M_{cs} was carried out and is shown in Figure 7-18. From these observations it can be said that although some minor differences exist between different soils, all the intrinsic State Boundary Surfaces are essentially similar.

As mentioned earlier in Chapters 4 to 6, ring shear tests were carried out on the natural and remoulded samples of the soils studied in this research by Narayana (2010) and Cunliffe (2010) to obtain the residual angle of shearing resistance. The importance of this parameter has been highlighted as all of these soils showed a very brittle behaviour under shearing which can be a vital factor in any geotechnical design. The average values of φ'_r for the natural and remoulded samples of all four soils are shown in Table 7-5. The difference between the tests on the natural and remoulded samples were insignificant for the Oxford and Gault clays, however there was a more significant difference for the tests carried out on Kimmeridge clay (Chapter 6). The average values are considered in this chapter.

As mentioned in Chapter 2, Lupini et al. (1981) proposed that the residual shear behaviour can have three modes; a turbulent mode, a transitional mode and a sliding mode. They concluded that these different modes are dependent on the particle size and coefficient of particle friction. When dealing with soils with high platy particle contents residual behaviour develops with a final sliding mode. Therefore, the authors suggested that residual strength in the sliding mode could correlate with the clay

fraction or with plasticity index. Figures 7-19 and 7-20 show the changes of the residual angle of shearing resistance with the clay fraction and the plasticity index for various soils respectively. Although there is a wide scatter for the lower values of φ'_r in both graphs, the data points for all four soils studied in this research are in good agreement with the mean trends. The low plasticity and φ'_r value of the Kimmeridge clay place it in the limits of the data set. There is no obvious reason why there is slight difference between the φ'_r values for all four soils. A more recent correlation suggested by Wesley (2003) related the residual angle of shearing resistance to the distance of each soil's position on an I_p-LL plot. Figures 7-21 and 7-22 show this construction; the first figure shows different soils and their relative location to the A-line and the second figure shows the relationship between φ'_r and distance from the A-line. As can be seen the data points from this research are in good agreement with Wesley (2003).

The effects of natural structure on the peak strength of the UK mudrocks are considered further in Figure 7-23. It was expected that the State Boundary Surfaces of the natural materials would be located above those of the reconstituted ones. However, this is only the case for the Oxford clay and to a lower extent London clay. The significant difference between the natural and the reconstituted SBSs of these two clays may have their origins in their micro-structures. The Oxford clay showed a high degree of preferred particle alignment in the horizontal plane, inter-locking of particles due to high compaction, the existence of elongated horizontally reinforcing shells. These features, combined with the absence of any major fissuring allowed the natural soil to sustain higher effective stresses than the reconstituted soils. Micro-structure was also believed to be the reason for the more extensive SBS shown by the natural London clay compared to the soil when reconstituted (Gasparre et al., 2007). A higher degree of preferred particle orientation and hence a stronger structure, caused by deeper burial, was believed by Gasparre et al. (2007) to result in higher strengths for London clay from unit A compared to shallower units B and C. The authors also noted that strengths of the natural samples which failed on their pre-existing fissures were significantly lower than those of the reconstituted samples. The failure envelope of samples that failed on pre-existing fissures fall close to the post-rupture and critical state envelopes. This finding implies that the fissures in London

clay have not undergone in-situ shear displacements that might have taken them towards their residual strengths.

A less clear behaviour was observed for the natural State Boundary Surfaces of Kimmeridge and Gault clays, which both showed SBSs that appeared to fall within those of the reconstituted samples (Figure 7-23). However, the locations of the reconstituted Hvorslev surfaces for these two soils were not assessed accurately and additional higher OCR tests are required. These lower strengths are comparable with the strength of London clay samples which failed on their pre-existing fissures. As mentioned earlier in Chapters 5 and 6, failure on these soils was provoked by presence of fissures. Both of these soils showed very little degree of preferred particle orientation at their micro-level.

In the case of the Gault and Kimmeridge clays, the presence of abundant closely spaced fissures is a factor that led to lower shear strengths (and smaller SBSs) in the natural material. The mechanism is not completely similar to that of those London clay samples that failed on favourably oriented (and relatively widely spaced) fissure surfaces. There was no evidence of this type of failure in Gault and Kimmerideg clays, but the system of closely spaced fissures undoubtedly reduced the bulk strengths of the specimens even if the failure mechanism did not reveal a single strain localisation concentrated on an existing fissure. The Representative Element Volume (REV) was an issue for the London clay as fissure spacing was similar to the sample size and therefore presence of fissures could have changed the failure mechanism. However, the REV for the Gault and Kimmeridge clays is smaller than the sample size and therefore all of the tests on this soil resulted in similar strength regardless of the samples size. Similar behaviour was observed by Fearon & Coop (2000) for structurally complex clays and by Vitone et al. (2009) for highly fissured Santa Croce di Magliano clay (SCM). Vitone et al. (2009) concluded that intense fissuring of the SCM scaly clay resulted in significantly lower strength for samples having sizes exceeding the REV as shown schematically in Figure 7-24.

Figure 7-25 shows the natural State Boundary Surfaces on the dry side of critical state of all four mudrocks. To take the mineralogy and particle size distribution of all these soils into account when comparing their structure normalisation based on M was

carried out and is shown in Figure 7-26. Although the micro-structure and macro-structure of Kimmeridge clay, Gault clay and London clay were different (Section 7-3), their strengths are not significantly different. Figure 7-27 shows the comparison between the post-rupture strength envelops of different stiff clays. Soils which have dominant fissuring in their macro-structure –London, Gault and Kimmeridge clays- have similar post-rupture strengths, most probably strength on their pre-existing fissures. The other soils show similar values at their post-rupture strength.

A summary of the tests from the Hollow Cylinder Apparatus research carried out by Brosse (2012) on the undrained shear strength anisotropy of the natural UK mudrocks is presented in Figure 7-28. Values of peak q/p' are plotted against the angle of principal stress rotation, α. All of these tests were carried out on samples from the 10m depth range and at their estimated in-situ stress state. The HCA tests were carried out at an intermediate stress factor of b=0.5 and are not directly comparable with triaxial tests, however, the trend in Brosse's results are consistent with the current study; the Oxford clay shows higher peak shear strength and much stronger anisotropy than the Kimmeridge, Gault and London clays.

The data from the author's triaxial extension tests are presented in Figure 7-29. Similar strength values for the Kimmeridge and Gault clays are in agreement with findings of Brosse (2012), however the difference between the failure envelope of the London clay and the Oxford clay with other two soils are significant. The reason for the lower strength of the London clay is that all the samples tested in triaxial extension were affected by the presence of pre-existing fissures which as mentioned above had a significant effect on the overall strength of the soil (Gasparre, 2005). These pre-existing fissures probably did not affect the extension strength of the soil in the mechanism involved during the Hollow Cylinder testing. Although the strength of the Oxford clay in extension is higher than other soils but in comparison with the compression strength is lower. This is probably governed by weak horizontal layers, the Achilles' heel of highly bedded Oxford clay. These results show that strength of the UK mudrocks is governed by both micro- and macro-structures which in turn are not affected by the geological age alone.

7.5.2 Stiffness of the mudrocks

The small strain 'elastic' stiffnesses of the mudrocks were measured in the author's tests by dynamic bender elements and locally instrumented static testing techniques. Stiffness values were also obtained by Brosse (2012) using a Resonant Column Hollow Cylinder Apparatus (RCHCA), and these will be integrated with the author's results at a later stage.

The changes of the vertical undrained Young's modulus with stress level, p', for the strain level of 0.001% is shown in Figure 7-30 (based on the interpretation of data from Chapters 4 to 6). Contours of stiffness at different strain levels were not available for the London clay. As can be seen, the stiffnesses of Gault and Kimmeridge clays appear practically identical at this strain level over a broad range of effective stresses. However, the Oxford clay shows much higher stiffness, especially at lower p'. This difference can be attributed to the strong structure of the Oxford clay. As mentioned earlier in Chapters 4 to 6, the stress level exponent of the stiffness, n, did not increase towards unity with the increase in strain level. This can be seen in Figure 7-31, with 'n' values falling with strain level. The variation is less significant for Oxford clay, which is similar to the finding of Hird & Pierpoint (1997) that the 'n' value for the Oxford clay was constant at different strain levels and was 0.67.

Shear moduli, obtained from bender element testing, normalised for void ratio are presented in Figures 7-32 to 7-33. The data from reconstituted mudrock samples are shown in Figure 7-32 normalised by their void ratios. Data from three different units of London clay are also shown on this graph. As can be seen the data fall within a relatively narrow spread with London clay units B and C providing the upper and lower limits. Considering the difficulties of bender element interpretation these differences may not be significant.

The average value of G_{hv} for these reconstituted data is plotted with the average values of the natural samples in Figure 7-33. Oxford clay shows slightly higher natural stiffness but the other three mudrocks showing similar or slightly lower G_{hv} to the mean reconstituted trend. From these two graphs it can be proposed that structure affects the stiffness more than the mineralogy and particle size distribution. Figure 7-

34 shows the G_{hv} and G_{hh} values obtained from BE tests on the natural samples. The Kimmeridge, Gault and London clays display broadly comparable trends, particularly for G_{hv}. While Oxford clay showed much higher stiffness due to its strong structure, with wider differences in G_{hh} values as expected from its micro-structure. The degree of anisotropy is robust and does not change significantly with increasing stress level for all four mudrocks. Figure 7-35 shows the difference between the in-situ and laboratory measurements of the shear moduli G_{vh} and G_{hv} and their changes with the previous depth of burial for each soil. The difference between the two methods of measurement is most significant in case of Oxford clay and reasonably good agreement can be seen for the other soils. Also there is no clear trend in changes of the stiffness values with depth of burial.

Drained elastic parameters for all of these soils are summarised in Table 7-6. These values are not directly comparable as each test had been carried out at different stress levels. What can be observed in Figures 7-36 and 7-37, is the degree of anisotropy based on both shear moduli and Young's moduli in horizontal and vertical orientations and their relation to the preferred particle orientation. There is some inconsistency between the anisotropy factor, α, calculated based on shear modulus, G, and Young's modulus, E, with maximum difference for Oxford and London clays. Similar inconsistency was reported for the London clay by Gasparre (2005) and for the Gault clay by Lings et al. (2000). It can be seen that Oxford clay with maximum preferred particle alignment has the highest degree of anisotropy. Kimmeridge clay on the other hand has the lowest degree of anisotropy based on its non-orientated micro-structure.

7.6 Summary

This chapter summarised the study carried out on three different UK mudrocks and the previously studied London clay. Comparisons were made to investigate the effects of geological age and in general the geological background of each soil on its engineering behaviour. The study of the micro-fabric carried out by Wilkinson (2011) showed that the Oxford clay has the highest degree of preferred particle alignment with reinforcing shells on similar planes as the platy clay particles. The effects of this

strongly orientated structure were observed both in terms of strength and stiffness of the soil. Oxford clay had the highest degree of strength and stiffness anisotropy, the highest shear strength for the natural material and highest stiffness for the natural samples.

It was shown that although Kimmeridge clay was deposited not long after Oxford clay, and which was buried to depths that were not much shallower than the Oxford clay, it posses a completely different micro-structure with the least preferred particle orientation. This was probably not affected by the geological age, but by the depositional environment. As a consequence, this material had lowest degree of anisotropy as well as low strength and stiffness for the natural material. The significance of macro-structure was highlighted based on the shear behaviour of the closely fissured Gault and Kimmeridge clays. The matrix of fissures within this soil probably had an effect on the bulk strength of the soil without samples failing necessarily on the fissure surfaces. This fissuring did not alter the small strain stiffness and anisotropy of the material.

As mentioned earlier in Chapters 4 to 6, in-situ tests were carried out at each site. This can provide a comparison between the mudrocks. Figure 7-38 shows a combined profile of these four mudrocks studied in this chapter. The Qc profile obtained from CPT tests are in agreement with the strength trend which was obtained in laboratory. London, Gault and Kimmeridge clays practically had similar strengths, except the high values at hard bands in Kimmeridge clay. As expected the strength of Oxford clay is much higher than the other three mudrocks. This trend is definitely evident at the testing horizon of 10m below ground level. In terms of stiffness, the G_{vh} values, measured via downhole seismic CPT, show some scatter for the Oxford and Kimmeridge clays. However, the stiffnesses are essentially very close for all of the four mudrocks. Atterberg limits are also shown in this figure with equal Plastic Limits for all mudrocks and higher Liquid Limits for the Gault and London clay as was expected from their high clay mineral content.

Mudrock	Age (Mya)	Depth of burial* (m)	Gs	In-situ void ratio (e)	LL (%)	PL (%)	PI (%)	Clay fraction (%)	Activity	Organic content (%)
Oxford clay	161-156	500-1130	2.46	0.60	66	34	32	45	0.71	10
Kimmeridge clay	156-151	410-1080	2.50	0.46	49	23	26	50	0.52	6
Gault clay	112-99	300-870	2.59	0.67	74	28	46	57	0.81	1
London clay (unit $B_{2(c)}$)	56-49	200-	2.65	0.82	66	29	37	47	0.79	1.5

* The lower limit is based on the stratigraphy and the higher limit is based on the methods considering geo-thermal variation with depth (see Section 7.2.1 and Wilkinson (2011))

Table 7-1: Estimate of the variation in age and depth of burial with index properties and in-situ void ratio obtained for the UK mudrocks (London clay parameters from Gasparre, 2005)

Mudrock	Quartz* (%)	Illite (%)	Illite-rich illite-smectite (%)	Smectite-rich illite-smectite (%)	Chlorite (%)	Kaolinite (%)
Oxford clay	25	76	2	4	2	16
Kimmeridge clay	65	47	34	0	5	15
Gault clay	26	28	0	61	2	10
London clay (unit B_2)	-	21	3	63	3	11

* Percentage from the bulk mineralogy of the UK mudrocks (Wilkinson, 2011)

Table 7-2: Percentage of the minerals contained within the clay grading part of the UK mudrocks (Wilkinson, 2011; London clay parameters from Gasparre, 2005)

Mudrock	Age (Mya)	Depth of burial* (m)	Micro-structure	Macro-structure	Preferred particle orientation**: V_{max} / V_{min}
Oxford clay	161-156	500-1130	Strong preferred particle orientation in the horizontal plane-Presence of elongated shells in the horizontal plane	No significant fissuring-Weak horizontal shell beds	2.5
Kimmeridge clay	156-151	410-1080	No significant preferred particle orientation due to presence of larger silt particles	Close spaced fissuring-High silt content	1.3
Gault clay	112-99	300-870	Variable structure with depth- No significant preferred particle orientation due to presence of round micro-fossils	Close spaced fissuring (of the order of a few centimetres)- Presence of nodules	1.5
London clay (unit $B_{2(c)}$)	56-49	200-	Moderate preferred particle orientation	Highly fissured (spacing of 10 to 20 cm) in the sub-vertical and sub-horizontal orientations	1.7

* The lower limit is based on the stratigraphy and the higher limit is based on the methods considering geo-thermal variation with depth (see Section 7.2.1 and Wilkinson (2011))
** (see Section 7.3.5)

Table 7-3: Variation in age and depth of burial with micro- and macro-structure of the UK mudrocks (after Wilkinson, 2011)

Mudrock	N*	Γ*	λ	κ	C_c^*	C_s^*	C_c	C_s	C_s^*/C_s
Oxford clay	2.85	2.77	0.169	0.036	0.390	0.104	0.216	0.076	1.37
Kimmeridge clay	2.8	2.51	0.164	0.047	0.377	0.128	0.160	0.091	1.40
Gault clay	2.99	2.85	0.215	0.040	0.496	0.168	0.221	0.095	1.77
London clay (unit $B_{2(c)}$)	2.95	2.85	0.168	0.069	0.522	0.144	0.254	0.106	1.36

Table 7-4: Parameters measured for one-dimensionally and isotopically compressed reconstituted and natural samples of the UK mudrocks (London clay parameters from Gasparre, 2005)

Mudrock	φ'_{cs}	φ'_r
Oxford clay	24.9 °	10 °
Kimmeridge clay	21.8 °	7 °
Gault clay	24.8 °	10 °
London clay (unit $B_{2(c)}$)	21.3°	12 °

Table 7-5: Angle of shearing resistance at Critical State and at residual state for the reconstituted UK mudrocks (London clay CS parameter from Gasparre, 2005)

Mudrock	Stress state p' (kPa)	G_{hh} (MPa)	G_{hv} (MPa)	$\alpha = G_{hh} / G_{hv}$	E'_v (MPa)	E'_h (MPa)	$\alpha = \sqrt{E'_h / E'_v}$	υ'_{vh}	υ'_{hv}	υ'_{hh}	Preferred particle orientation: V_{max} / V_{min}	E^u_v (MPa)
Oxford Clay	250	244	105	**2.3**	100	321	**1.8**	0.21	0.77	-0.34	**2.5**	200
Kimmeridge Clay	185	121	70	**1.7**	80	218	**1.6**	0.22	0.79	0.08	**1.3**	125
Gault Clay	160	110	57	**1.9**	71	239	**1.8**	0.20	0.93	0.06	**1.5**	137
London Clay (unit $B_{2(c)}$)	260	128	70	**1.8**	125	240	**1.4**	0.14	0.87	-0.03	**1.7**	193

Table 7-6: Drained elastic parameters of the natural UK mudrocks (London clay parameters from Gasparre, 2005; preferred particle orientation calculated based on Wilkinson, 2011)

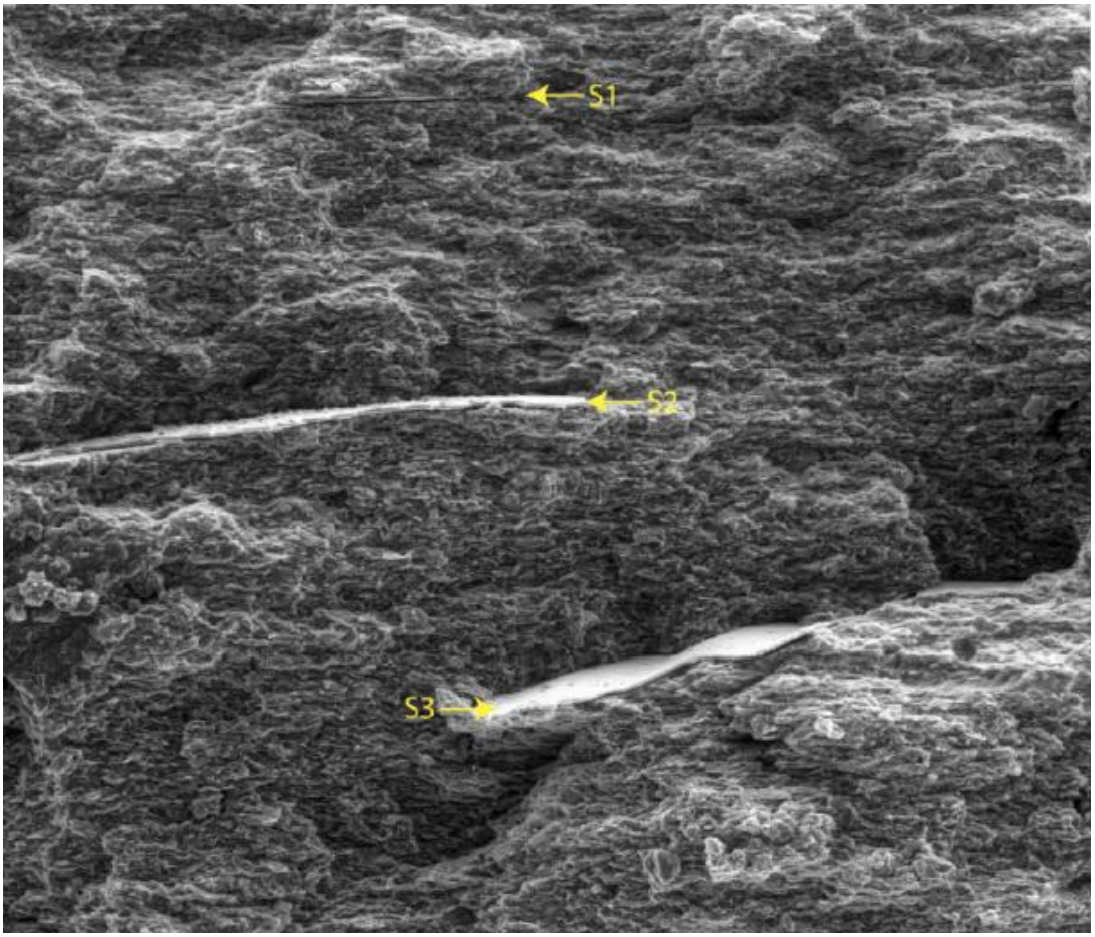


Figure 7-1: Montage of 16 SEM images taken of the surface of the Oxford clay 10m below ground level. S1, S2 and S3 are shells. Scale: 1.2mm across image (Wilkinson, 2011)

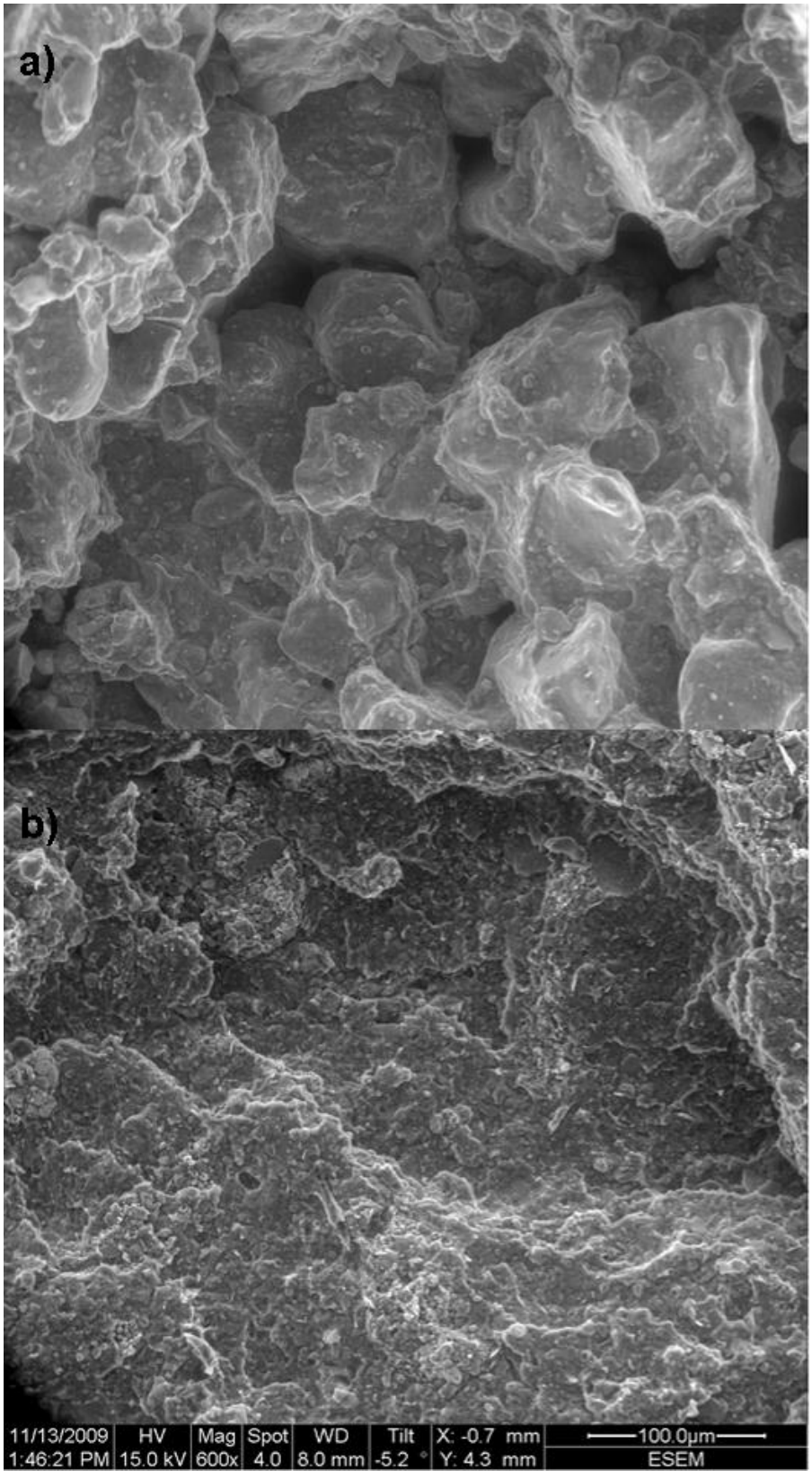


Figure 7-2: SEM images of Kimmeridge clay; a) 12.71m below ground level, b) 8.54m below ground level (Wilkinson, 2011)

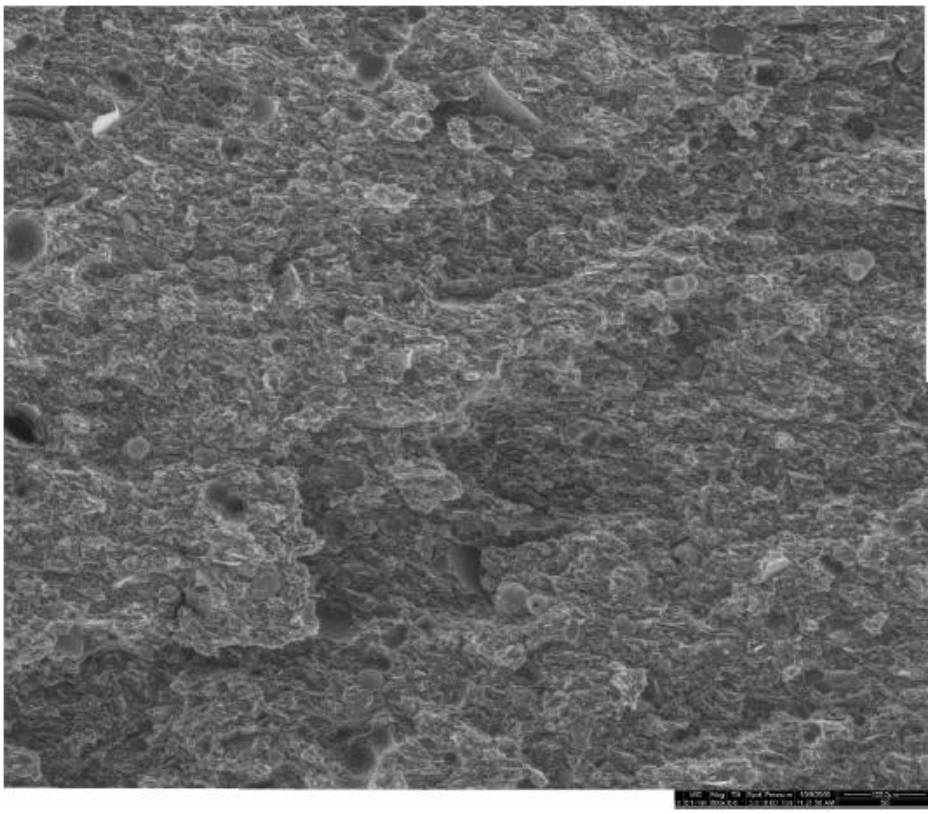


Figure 7-3: Montage of 16 SEM images of a vertical broken surface taken from a block sample of Gault clay, 3.5m below ground level. Scale: 1.2mm across image (Wilkinson, 2011)

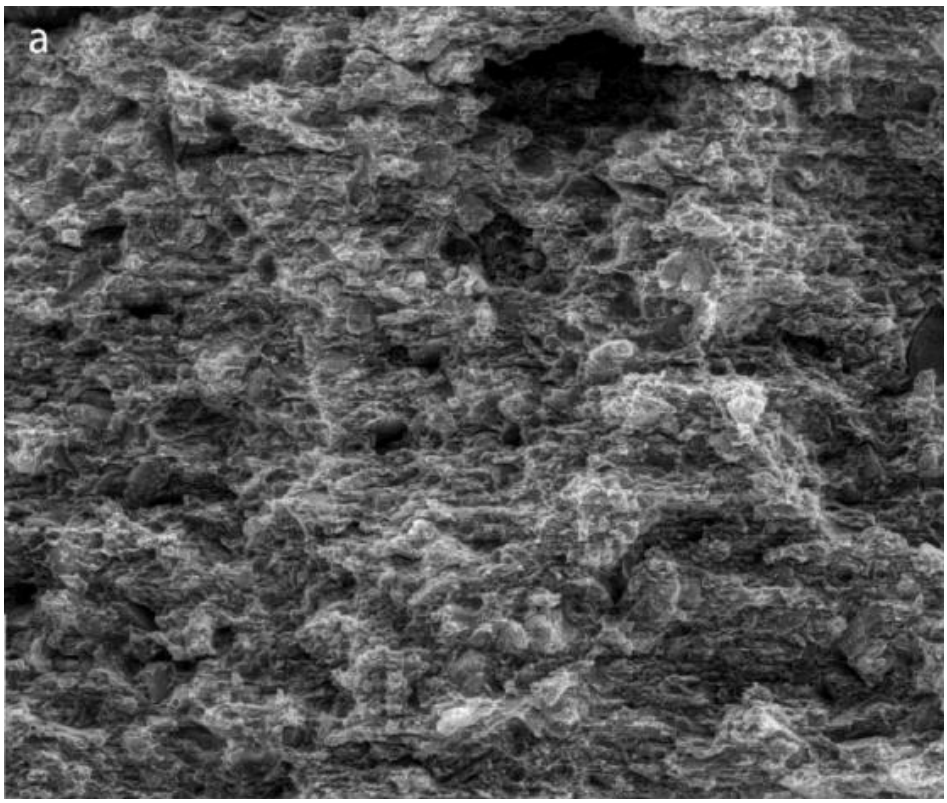


Figure 7-4: Montage of 16 SEM images of a vertical broken surface of London clay from 7.9 - 9.4m below ground level (Wilkinson, 2011)

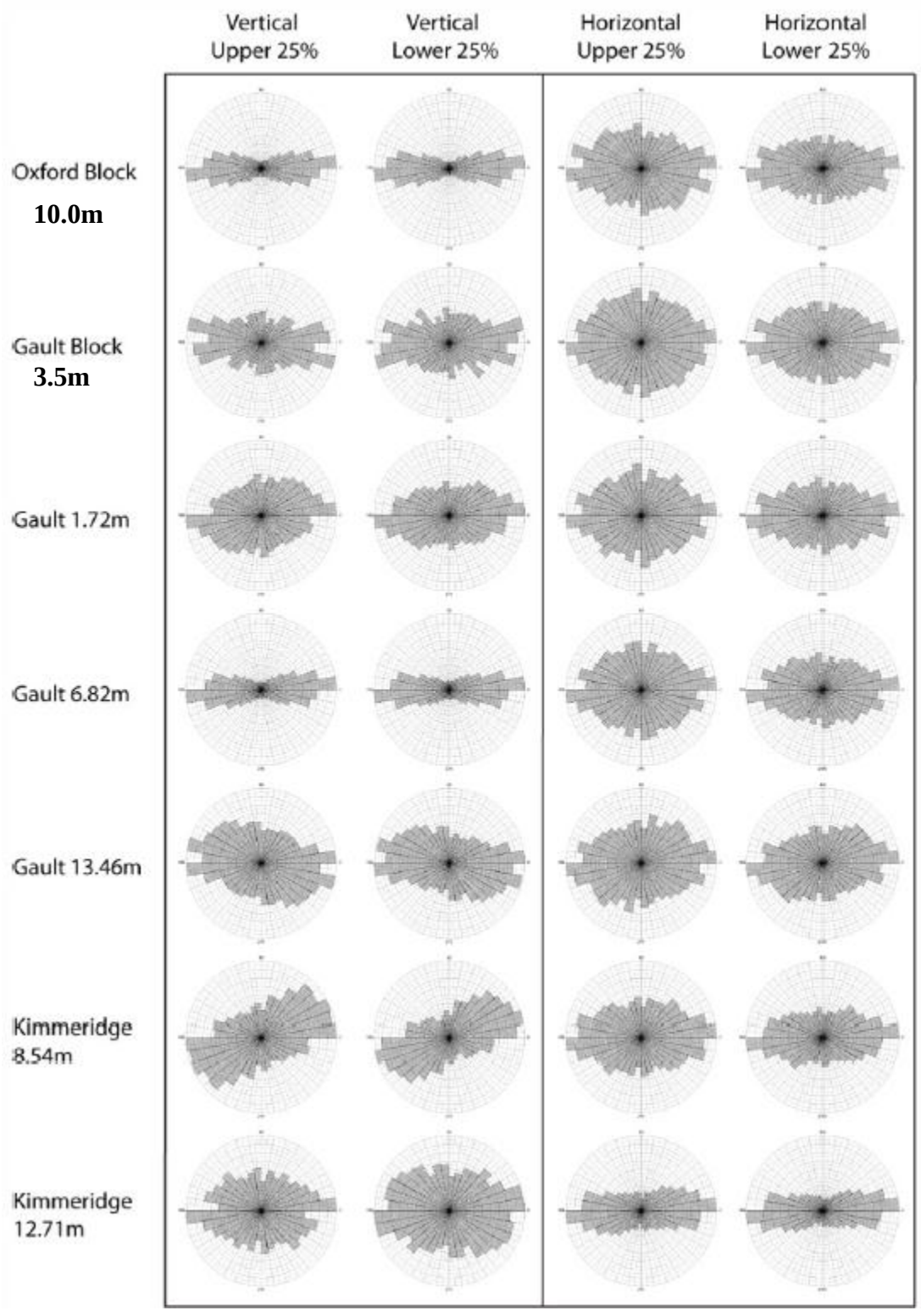


Figure 7-5: Rose diagrams of the summation of particle long axis orientations (Wilkinson, 2011)

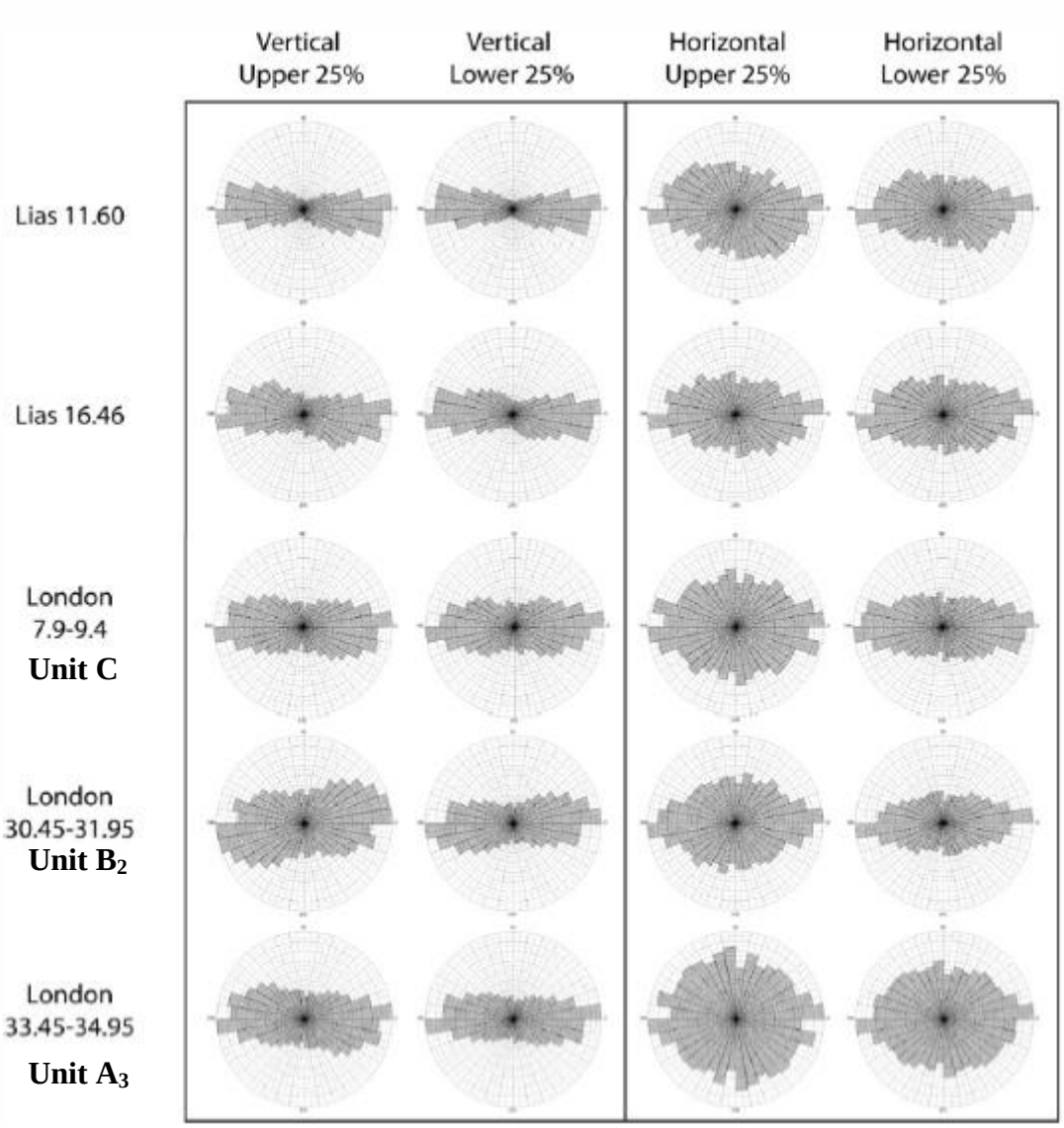


Figure 7-6: Rose diagrams of the summation of particle long axis orientations (Wilkinson, 2011)

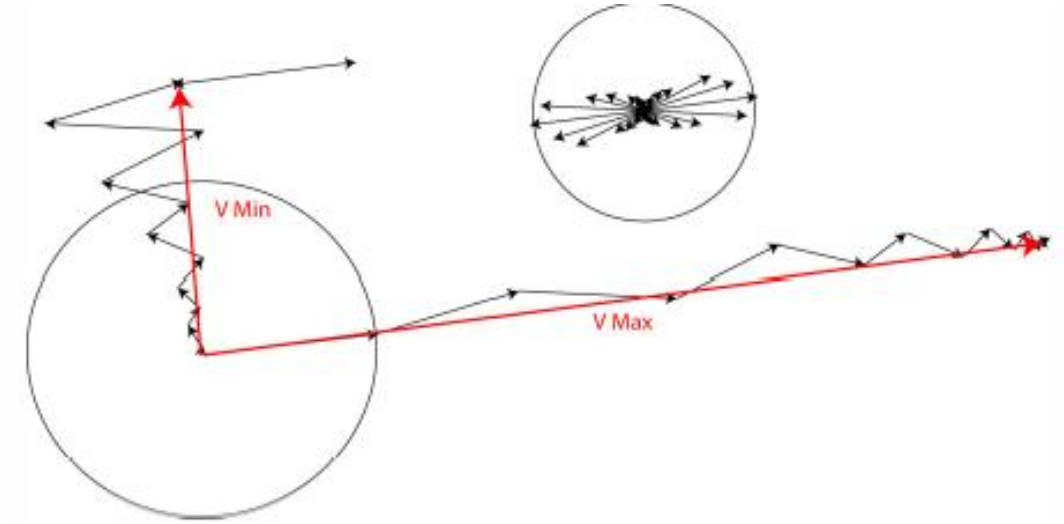


Figure 7-7: Vectors V_{max} and V_{min} (Wilkinson, 2011)

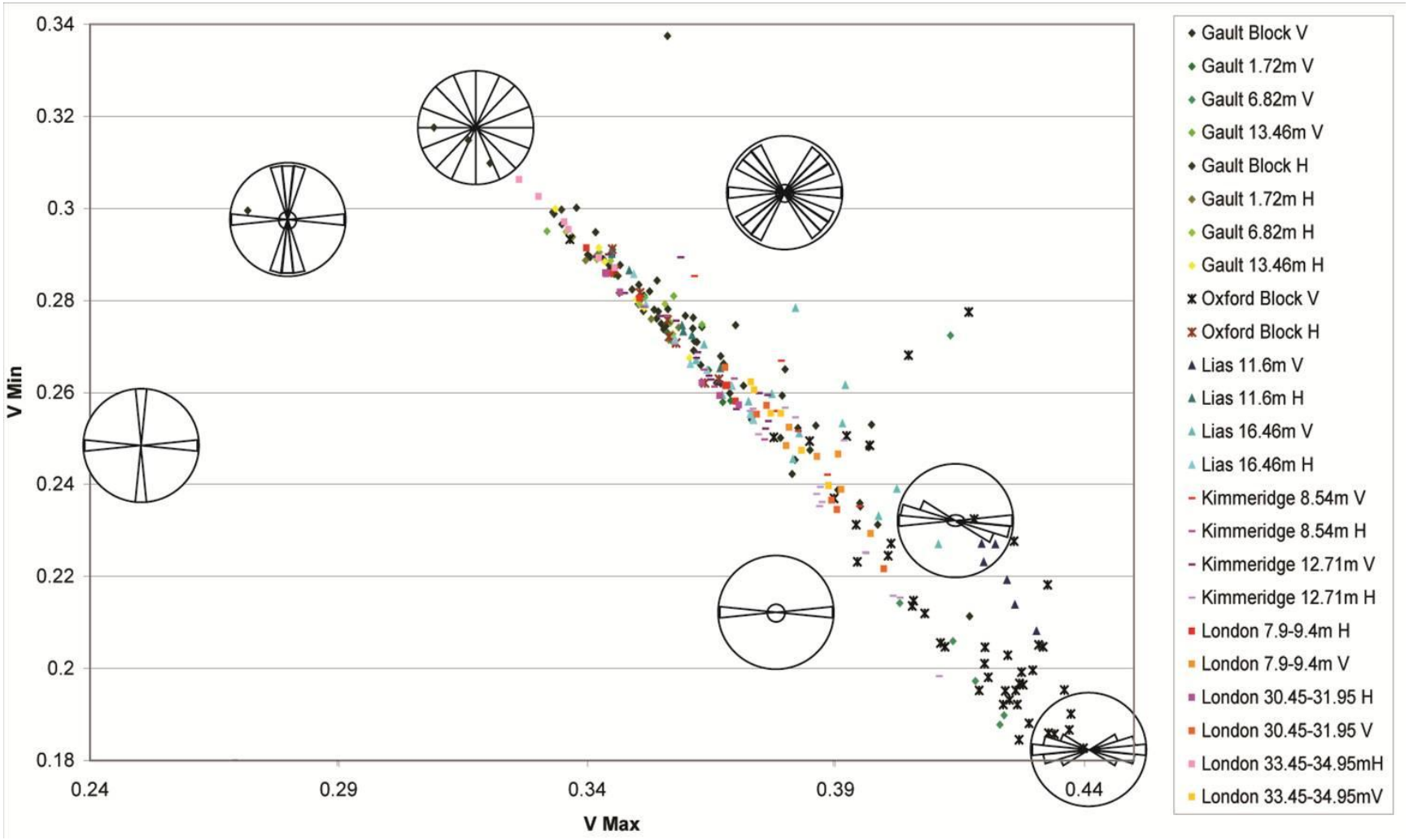


Figure 7-8: Examples of where rose diagrams of different shapes plot on the Vmax-Vmin graph (Wilkinson, 2011)

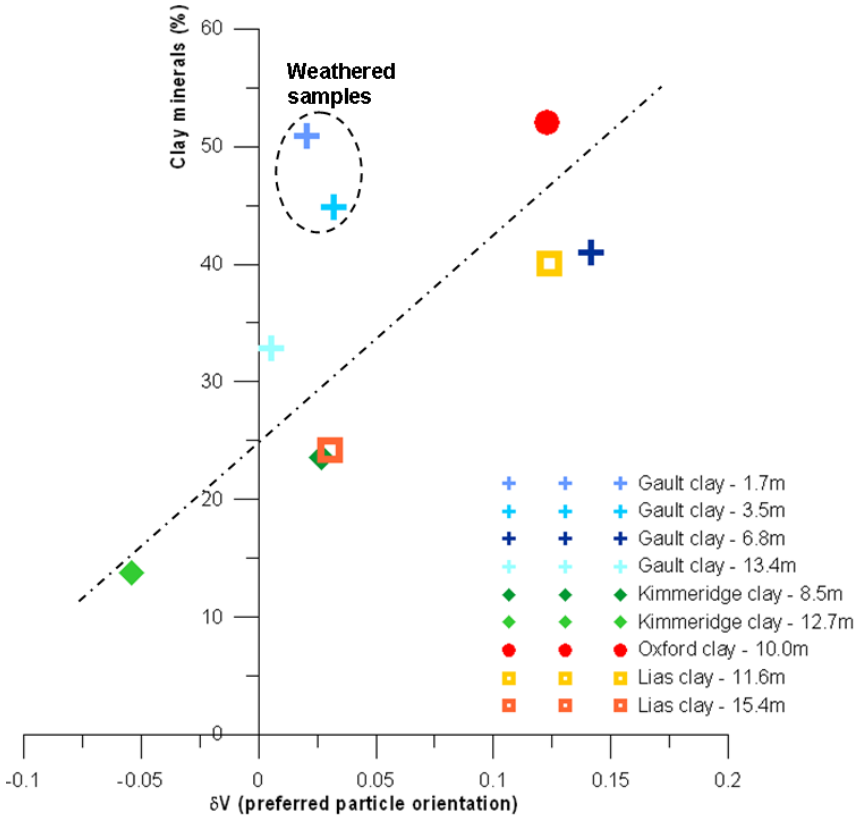


Figure 7-9: Plot of preferred particle orientation δV plotted against percentage of clay minerals (redrawn from Wilkinson, 2011)

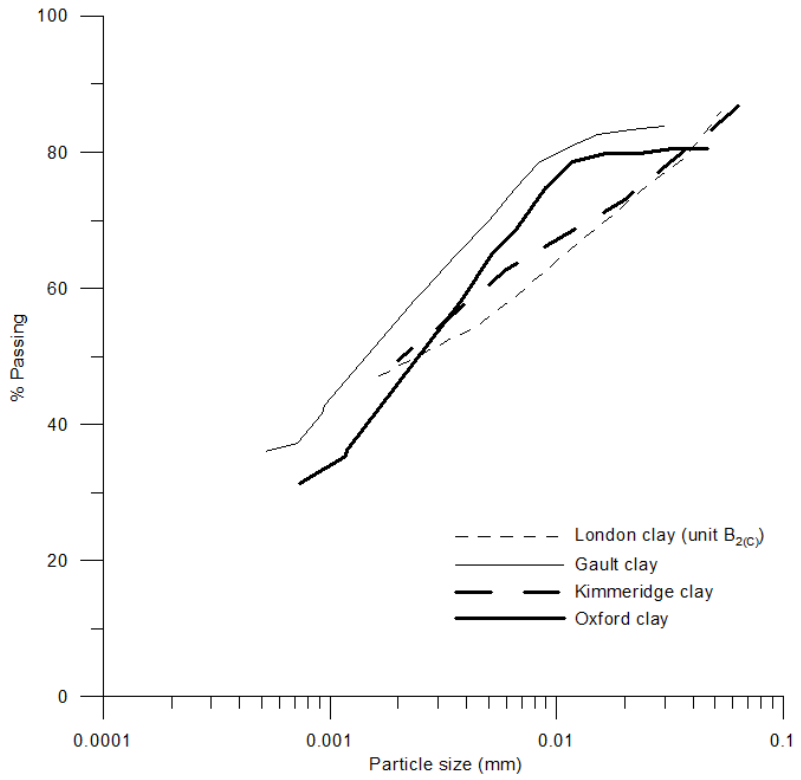


Figure 7-10: Particle size distributions of four UK mudrocks sampled at around 10m depth (London clay curve re-plotted from Gasparre, 2005)

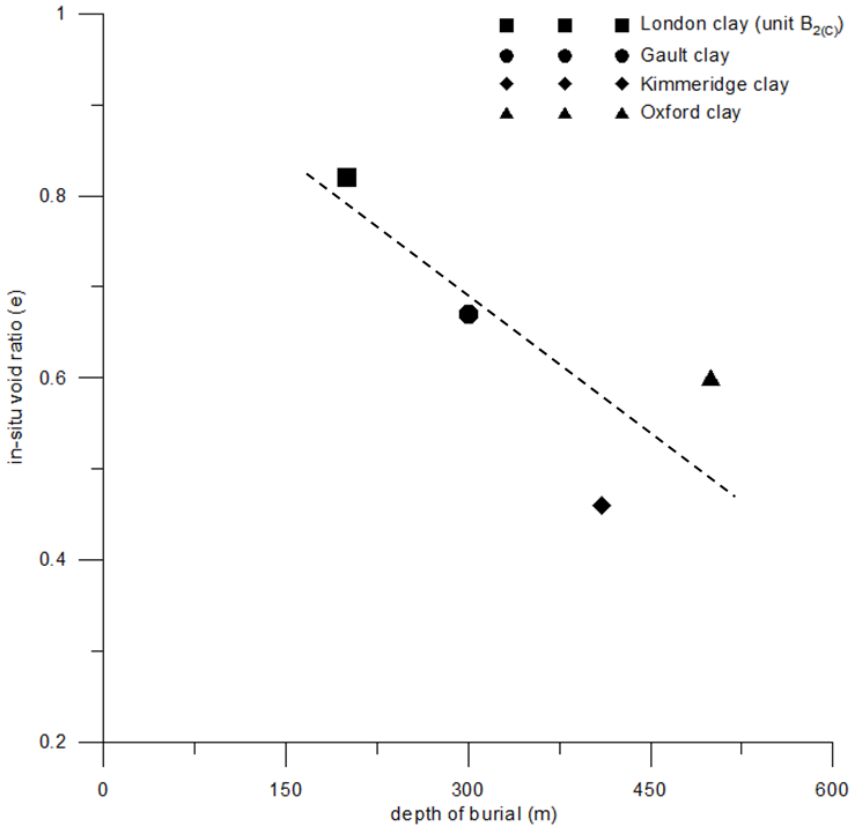


Figure 7-11: Changes in the in-situ void ratio with previous depth of burial (London clay data from Gasparre, 2005)

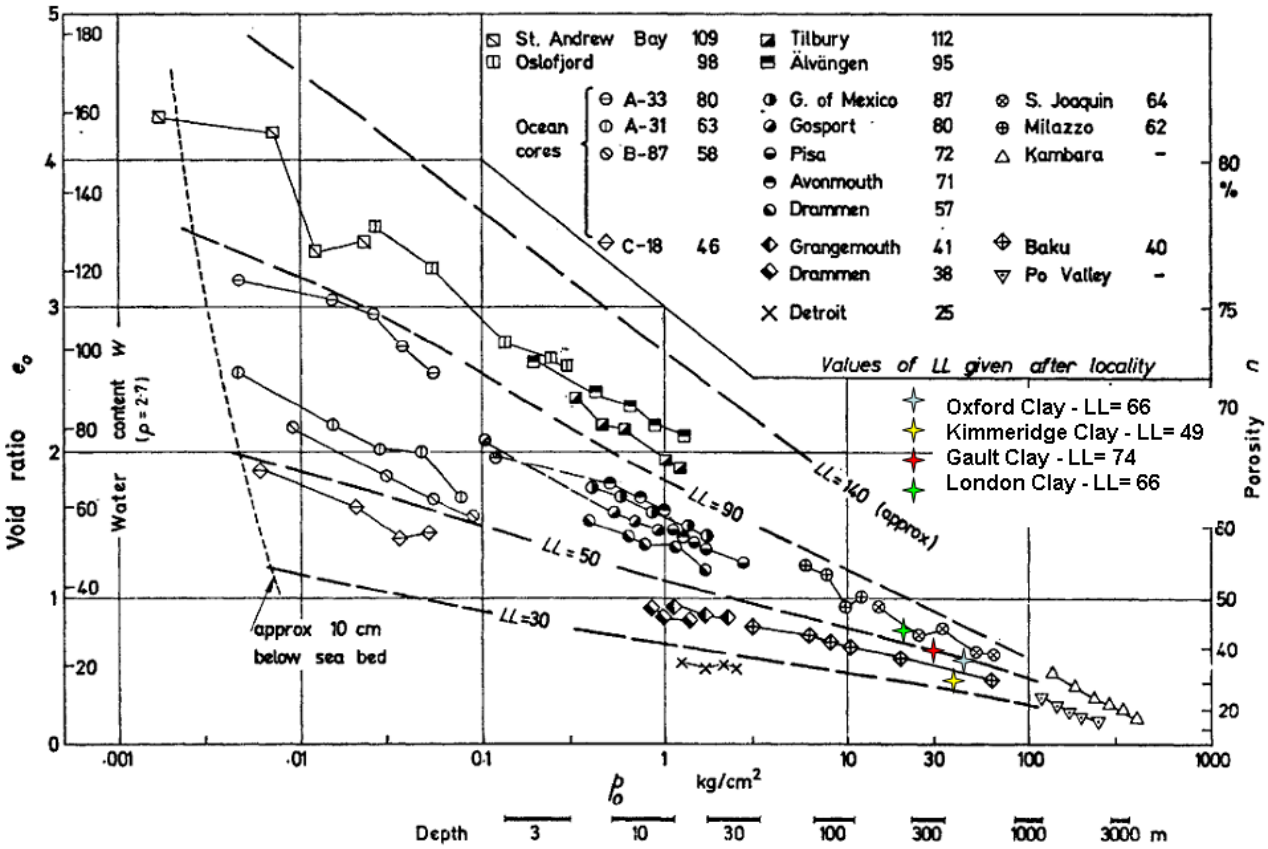


Figure 7-12: Estimated in-situ void ratio and effective stresses of four mudrocks in comparison with normally consolidated soils studied by Skempton (1969)

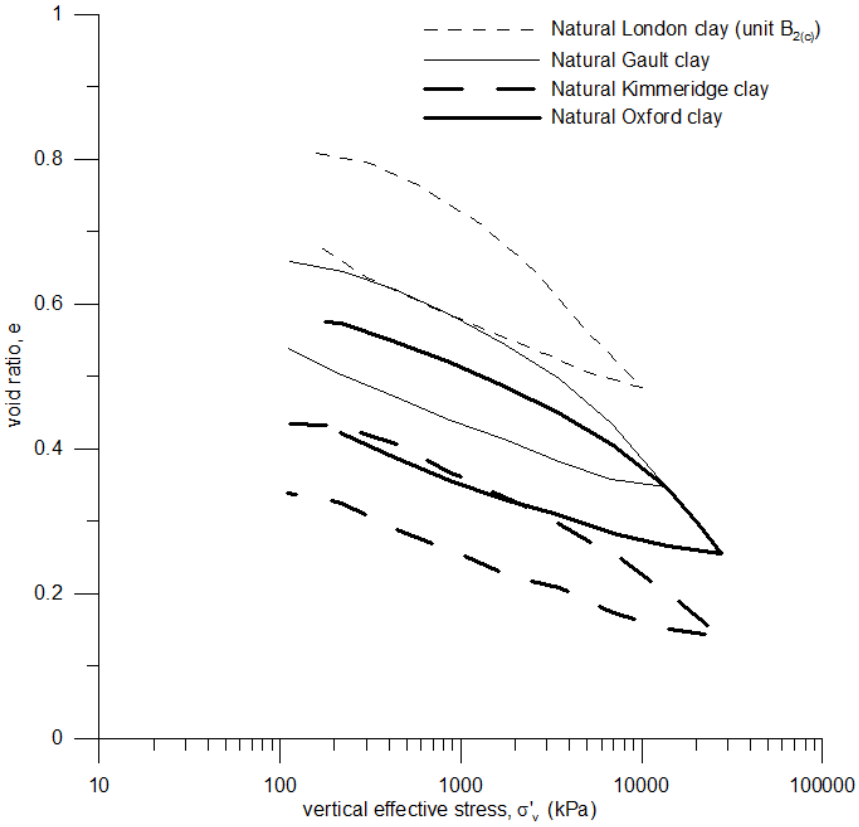


Figure 7-13: 1-D compression and swelling curves of natural UK mudrocks (London clay curve re-plotted from Gasparre, 2005)

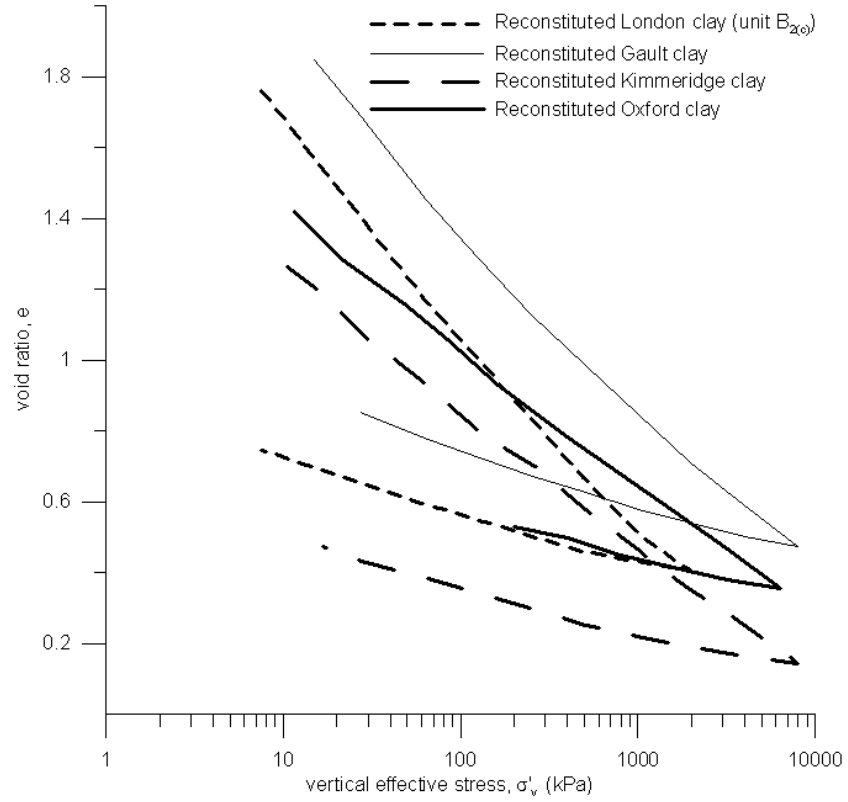


Figure 7-14: Compression and swelling curves of reconstituted UK mudrocks (London clay curve re-plotted from Gasparre, 2005)

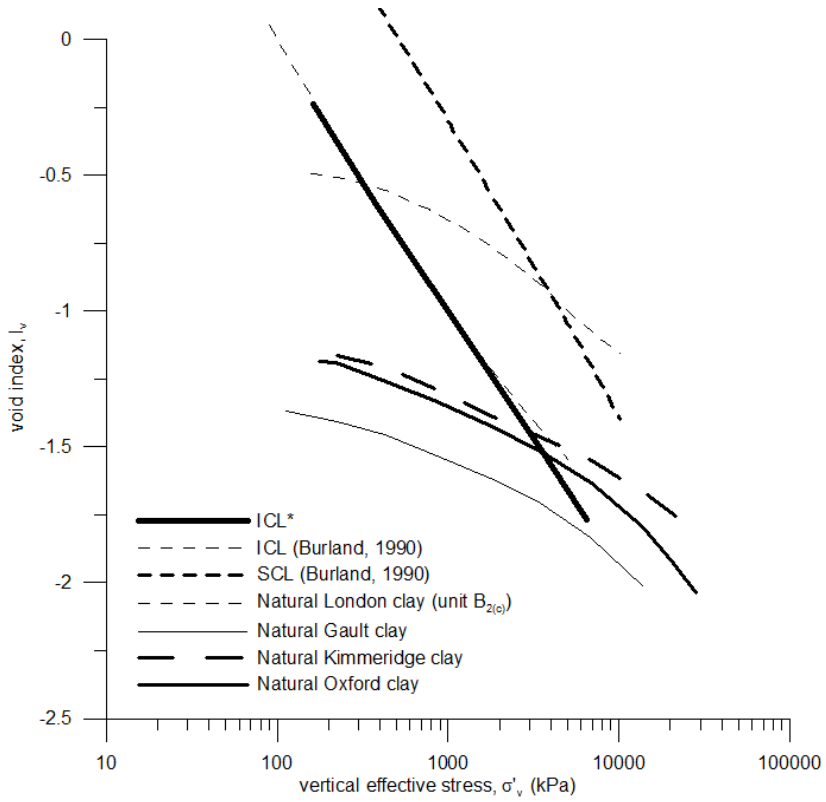


Figure 7-15: Normalised compression curves of natural UK mudrocks and the *ICL (London clay curve re-plotted from Gasparre, 2005)**

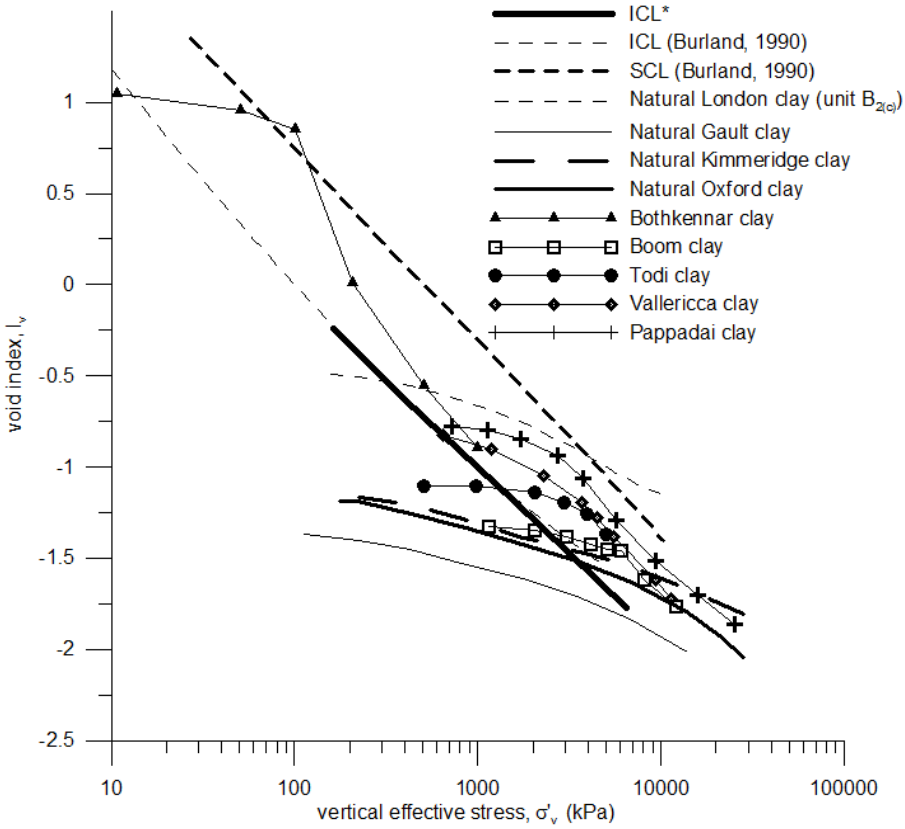


Figure 7-16: 1-D compression of natural and reconstituted clays (data from Burland, 1990; Smith, 1992; Coop et al., 1995; Burland et al., 1996; Cotecchia, 1996; Gasparre, 2005)

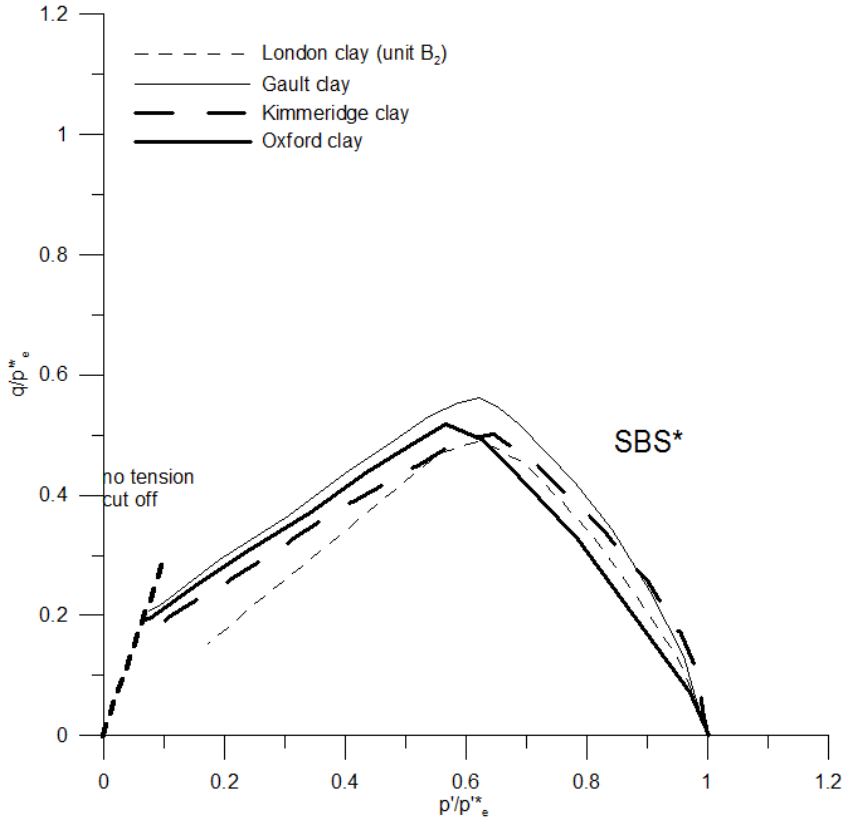


Figure 7-17: State Boundary Surfaces of reconstituted UK mudrocks (London clay curve re-plotted from Gasparre, 2005)

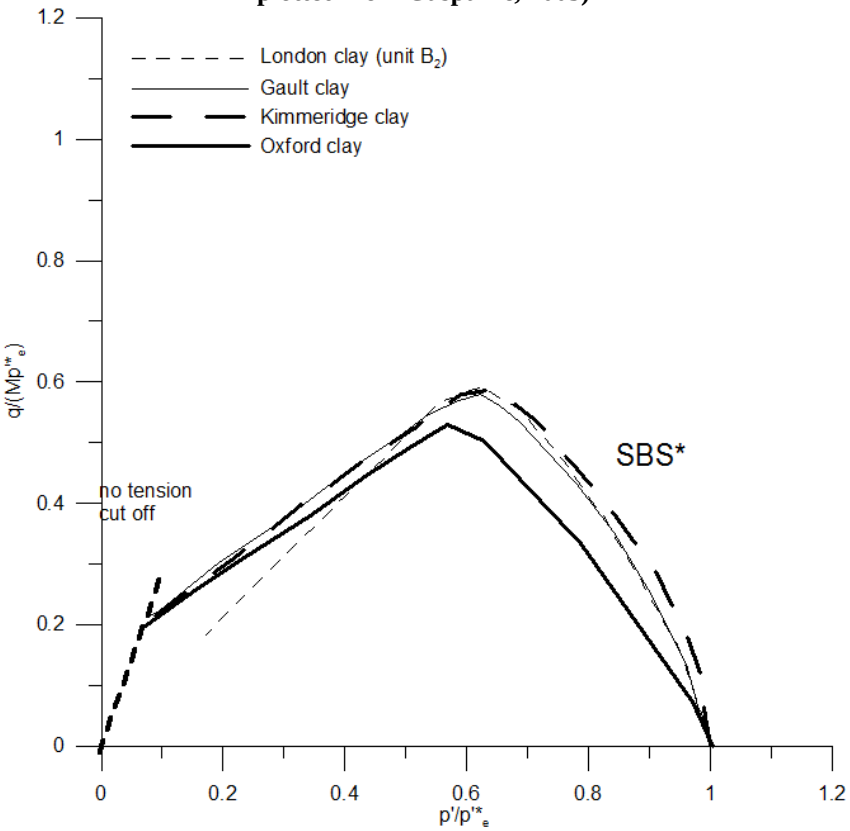


Figure 7-18: State Boundary Surfaces of reconstituted UK mudrocks normalised based on p'^{*}_{e} and M (London clay curve re-plotted from Gasparre, 2005)

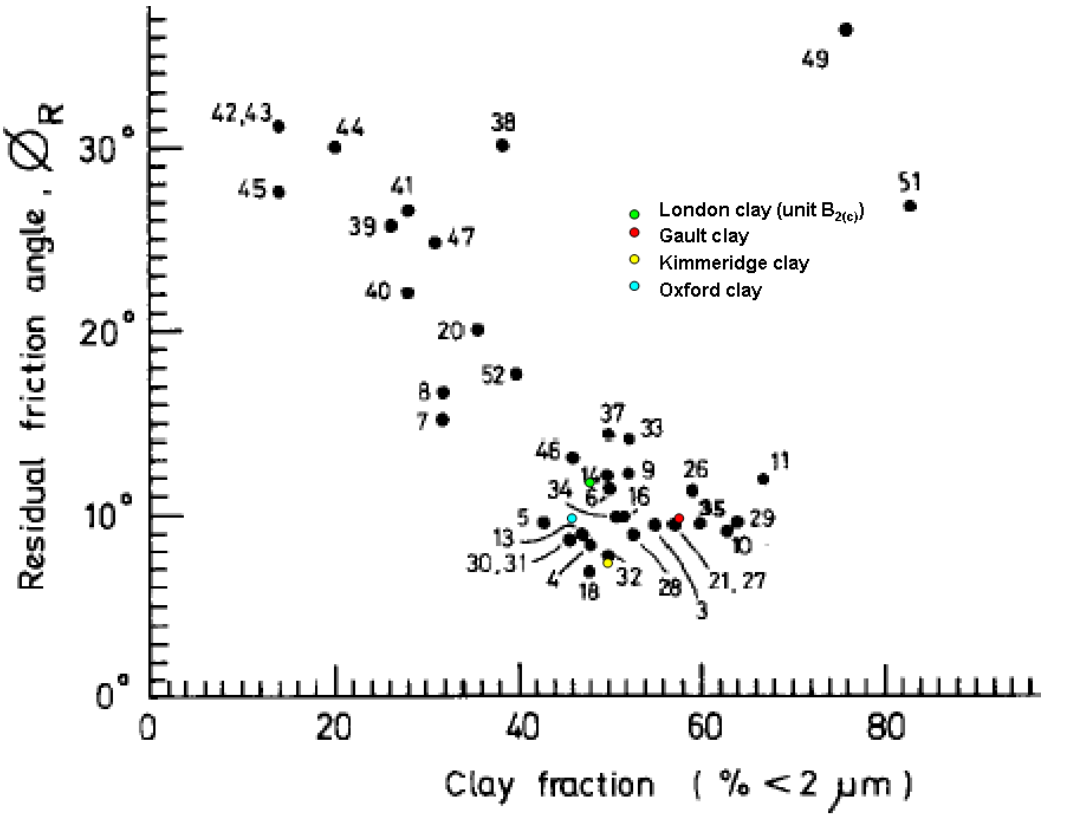


Figure 7-19: Changes in the residual angle of shearing resistance with the clay fraction (Lupini et al., 1981)

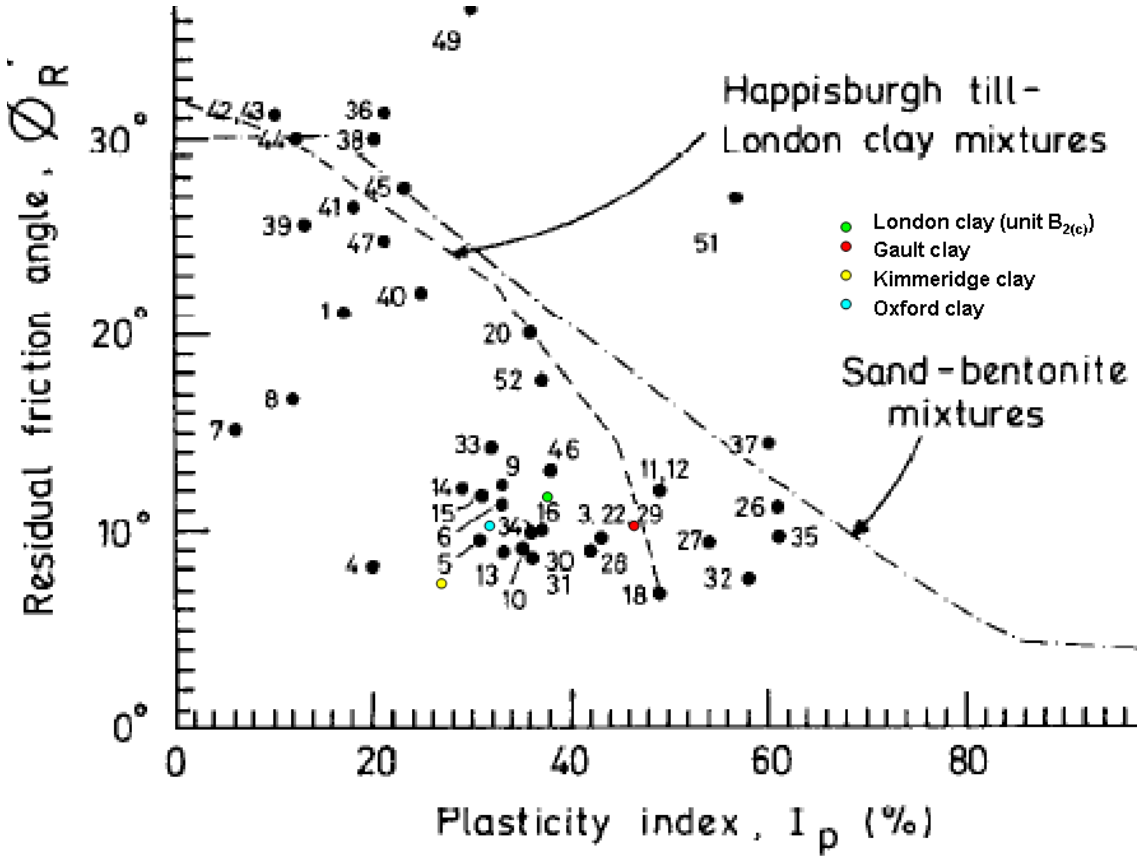


Figure 7-20: Changes in the residual angle of shearing resistance with the plasticity index (Lupini et al., 1981)

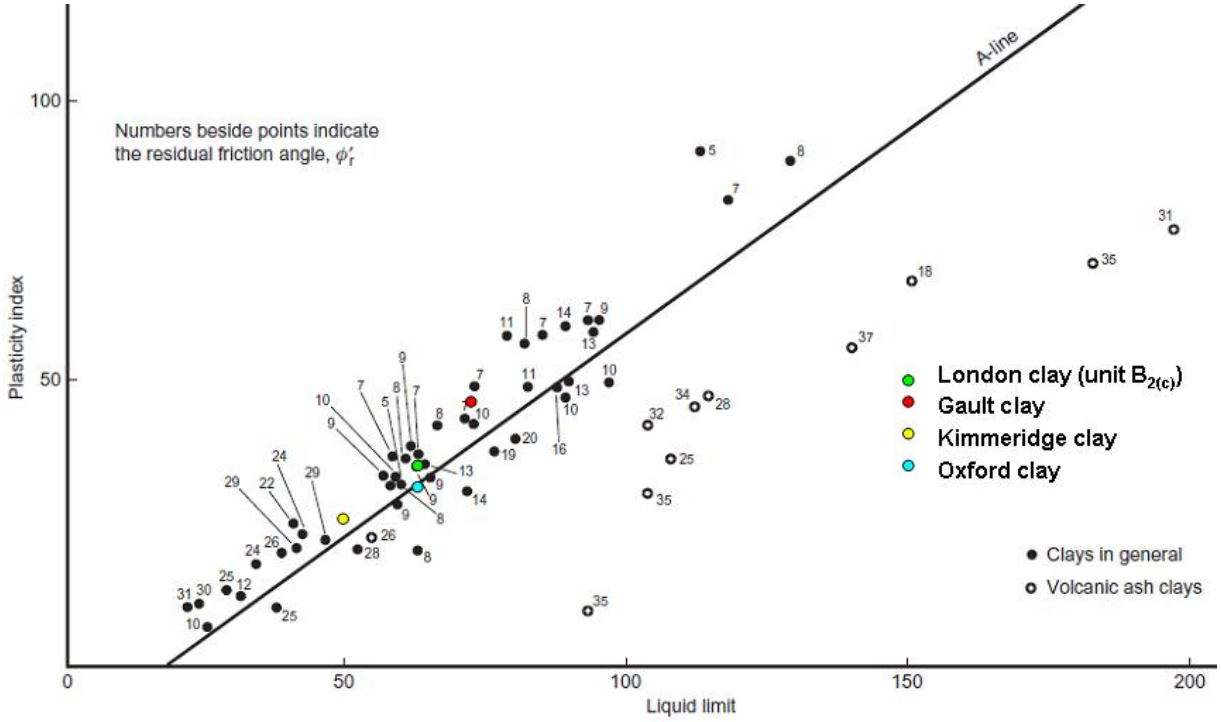


Figure 7-21: Plasticity chart for a wide range of soil types (Wesley, 2003)

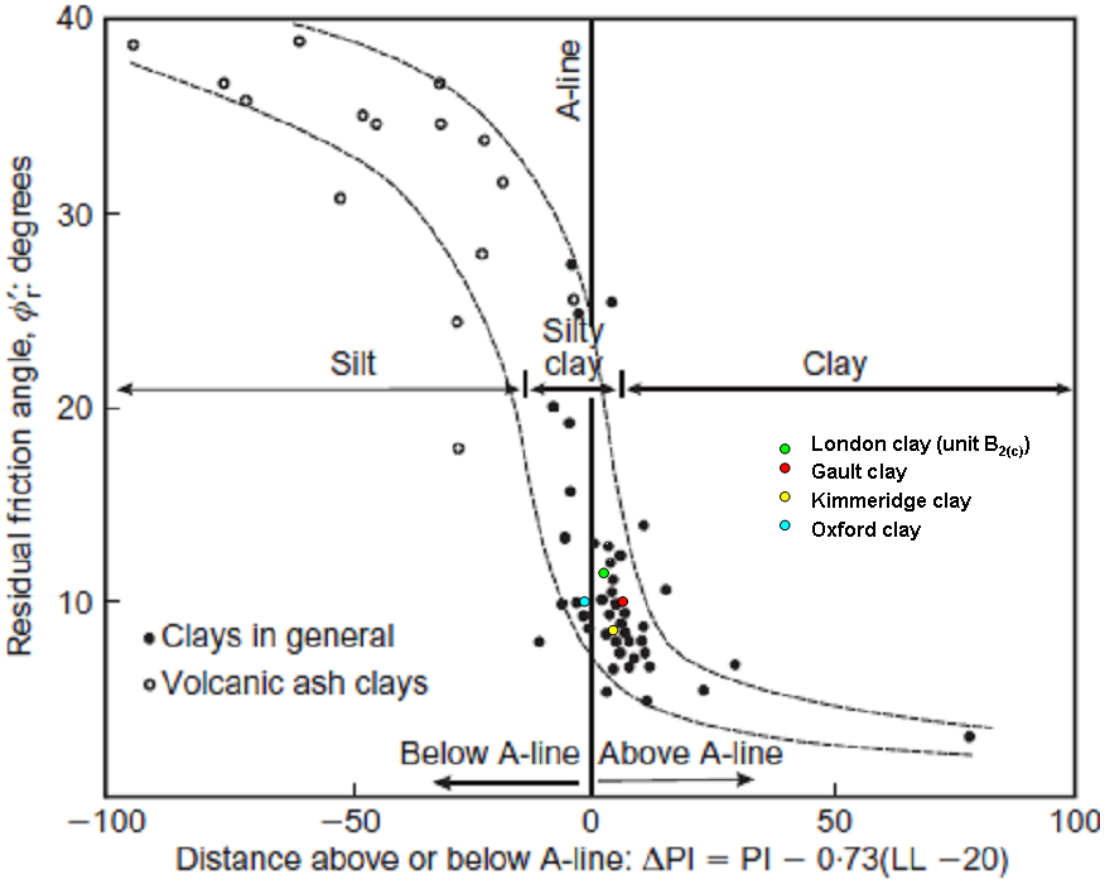


Figure 7-22: Residual angle of shearing resistance plotted against distance above or below the A-line (Wesley, 2003)

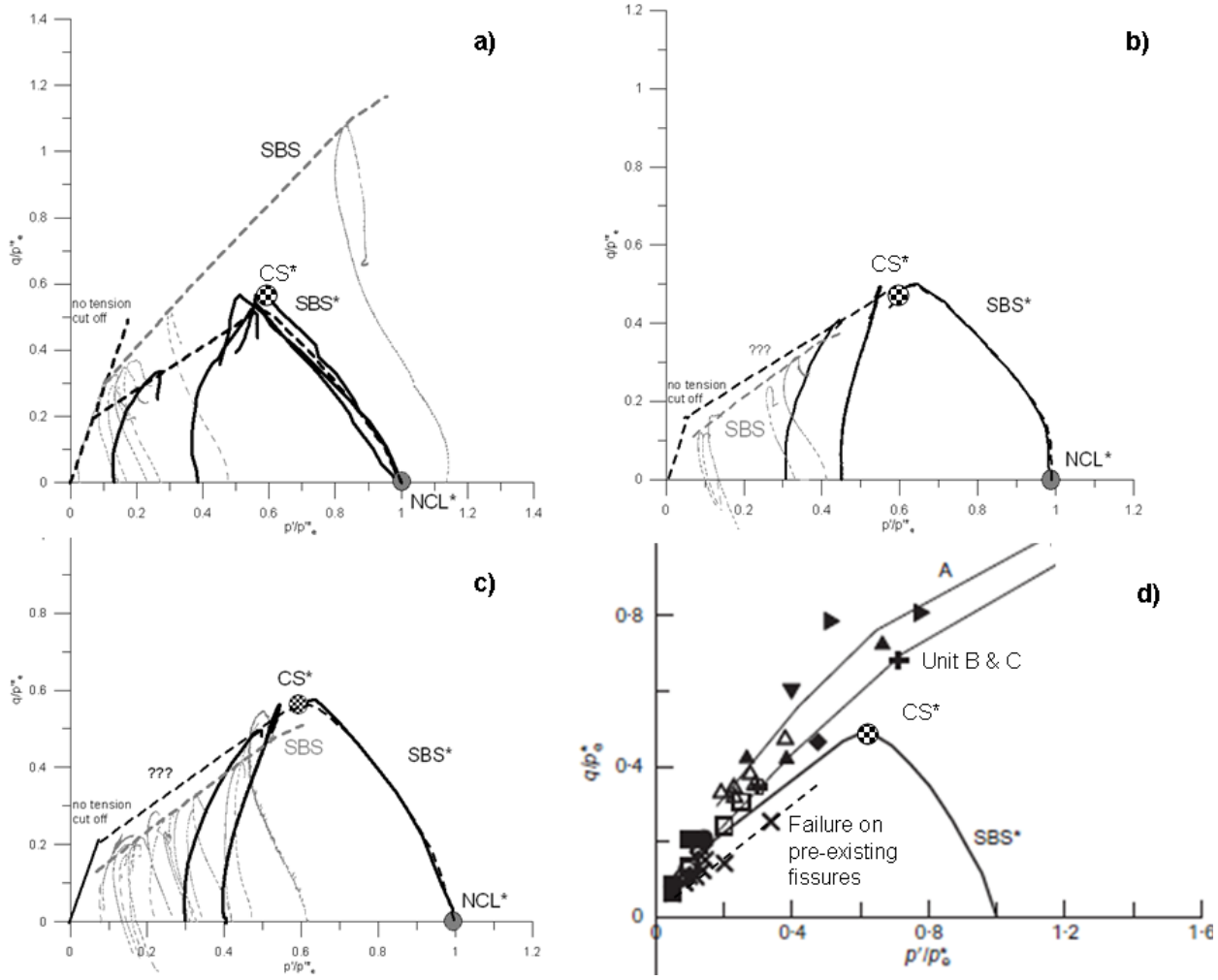


Figure 7-23: State Boundary Surfaces of reconstituted and natural UK mudrocks; a) Oxford clay, b) Kimmeridge clay, c) Gault clay, d) London clay (from Gasparre, 2005)

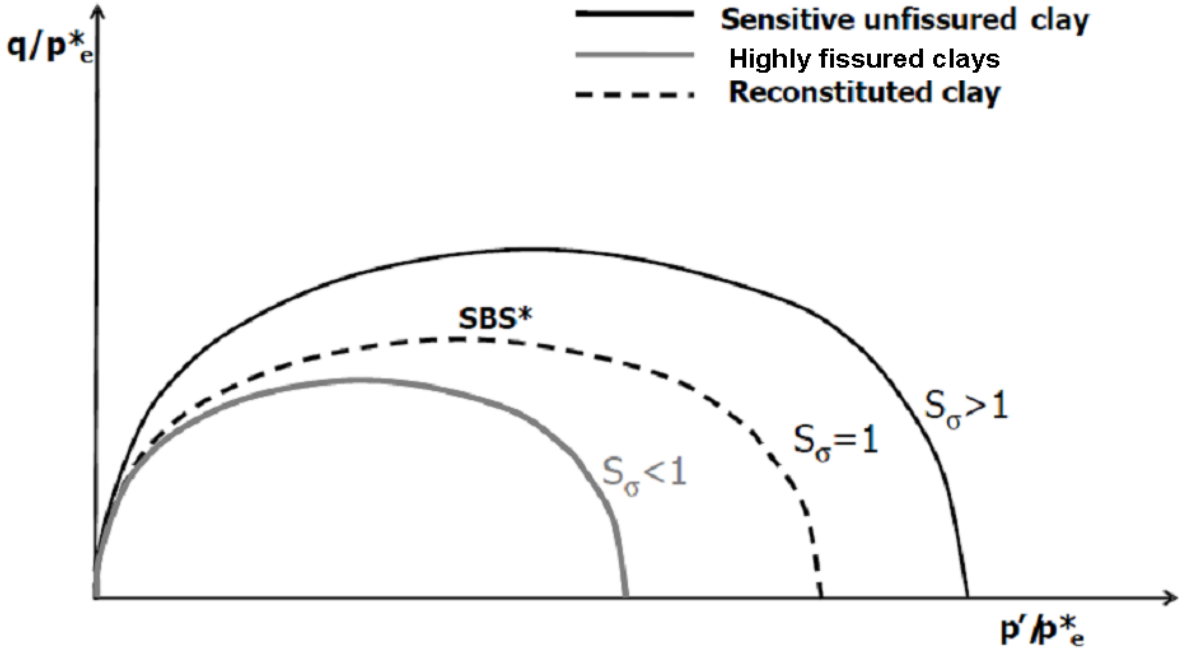


Figure 7-24: Framework of shearing behaviour of natural and reconstituted clays (Vitone et al., 2009)

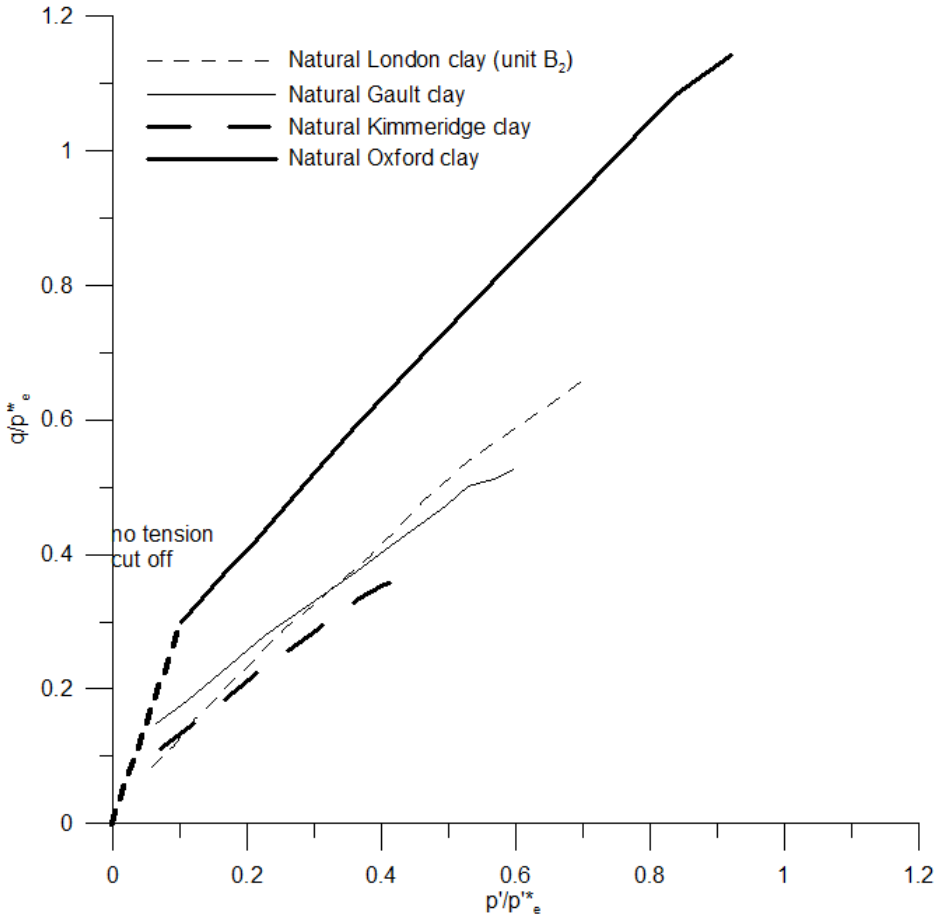


Figure 7-25: State Boundary Surfaces of natural UK mudrocks (London clay curve re-plotted from Gasparre, 2005)

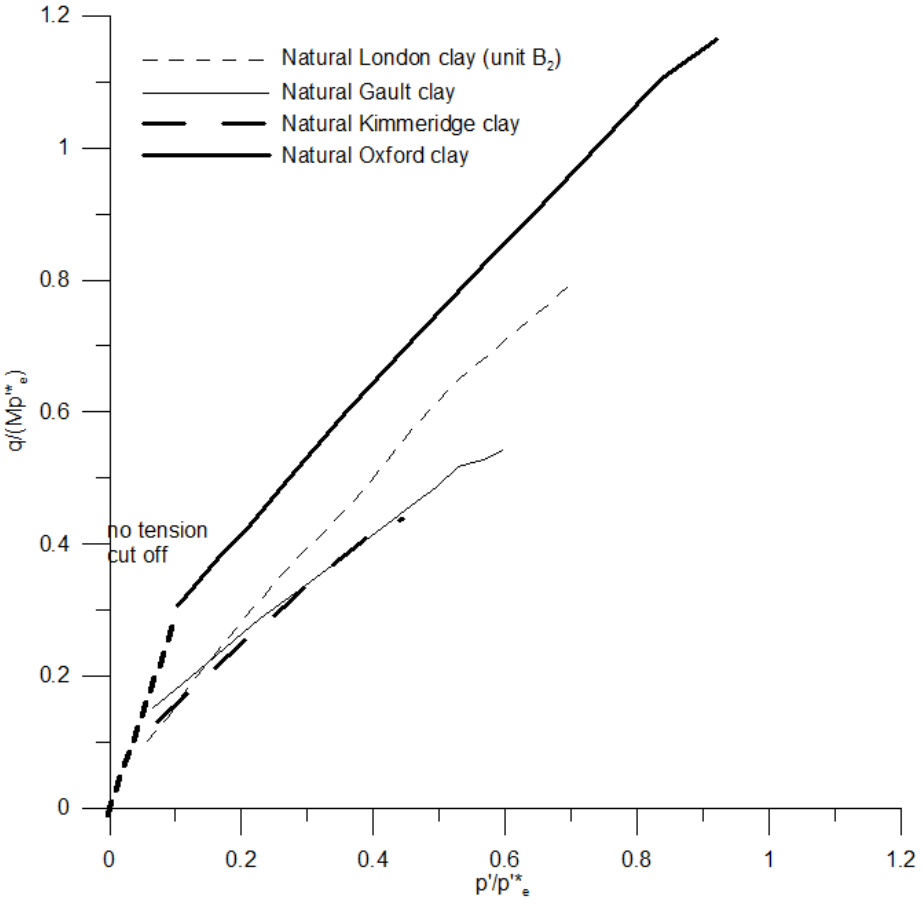


Figure 7-26: State Boundary Surfaces of natural UK mudrocks normalised based on P'^{*}_{e} and M (London clay curve re-plotted from Gasparre, 2005)

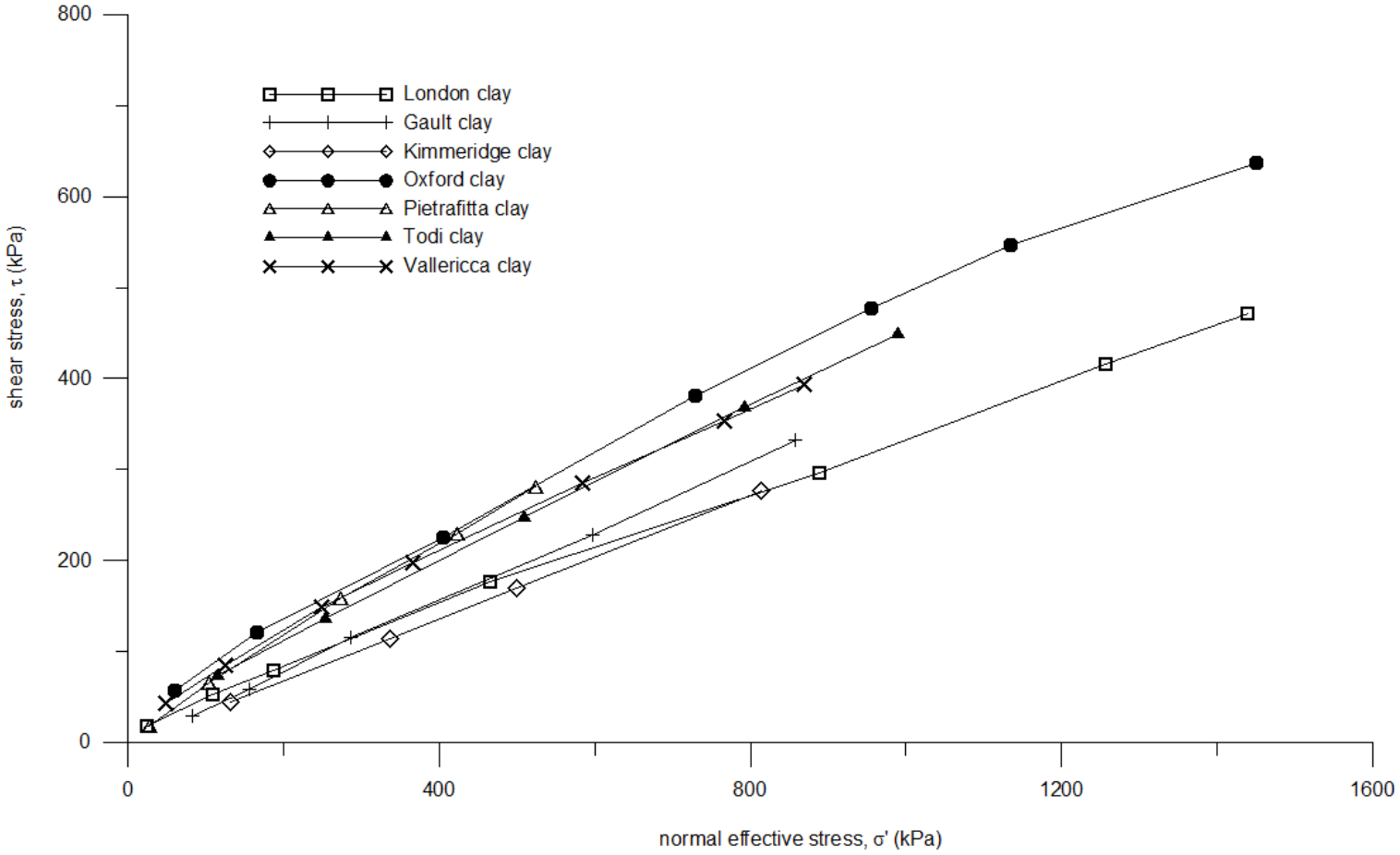


Figure 7-27: Post-rupture strength envelope for different overconsolidated clays (data from Burland, 1990; Burland et al., 1996)

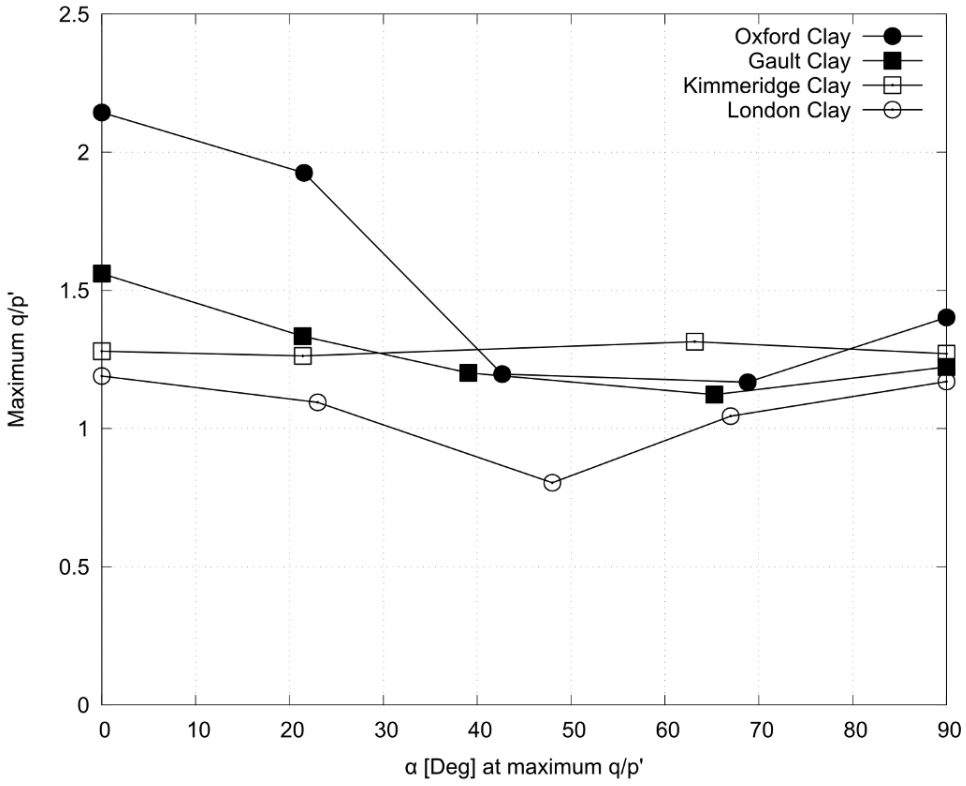


Figure 7-28: Anisotropy of peak shear strength of UK mudrocks (Brosse, 2012)

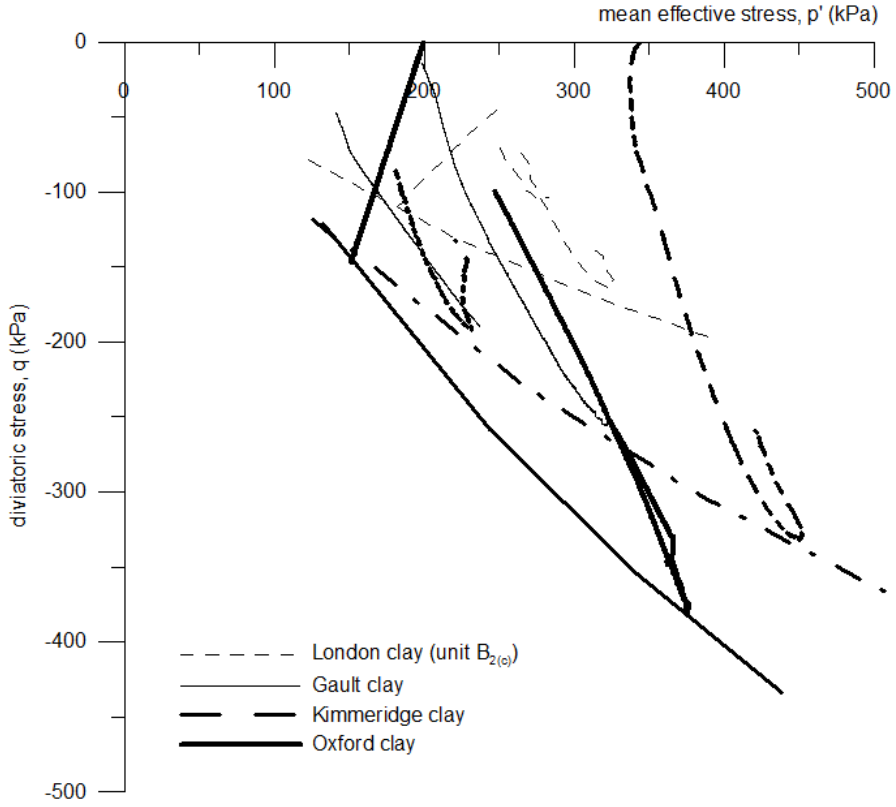


Figure 7-29: Shear strength of UK mudrocks in extension (London clay curve re-plotted from Gasparre, 2005)

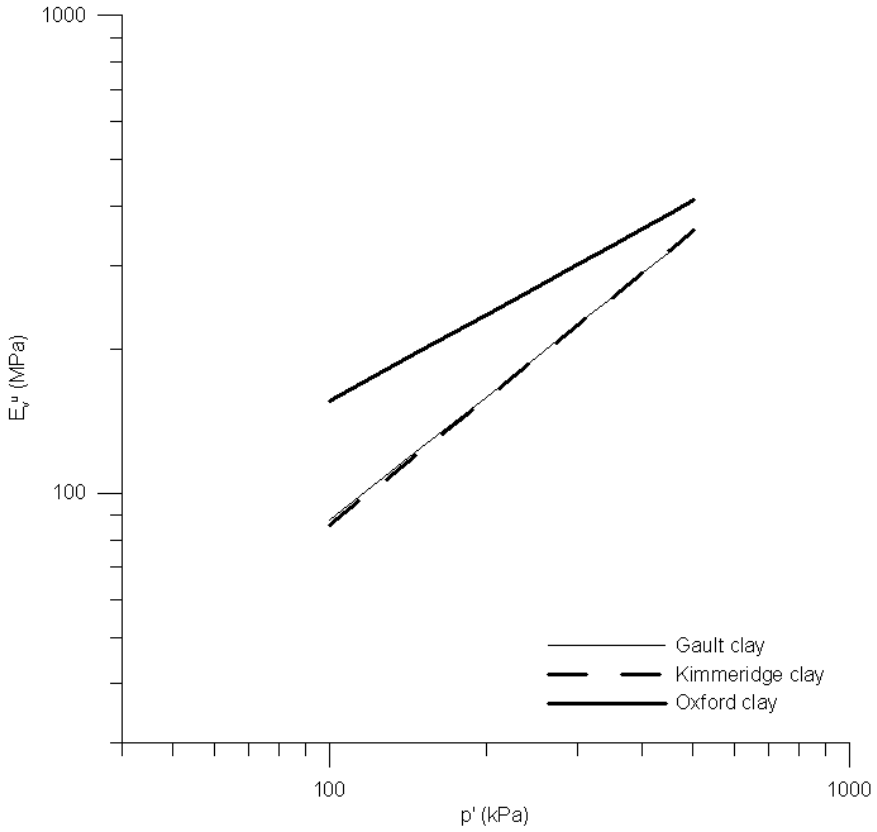


Figure 7-30: Stiffness variation with stress level at 0.001% strain level for natural soil

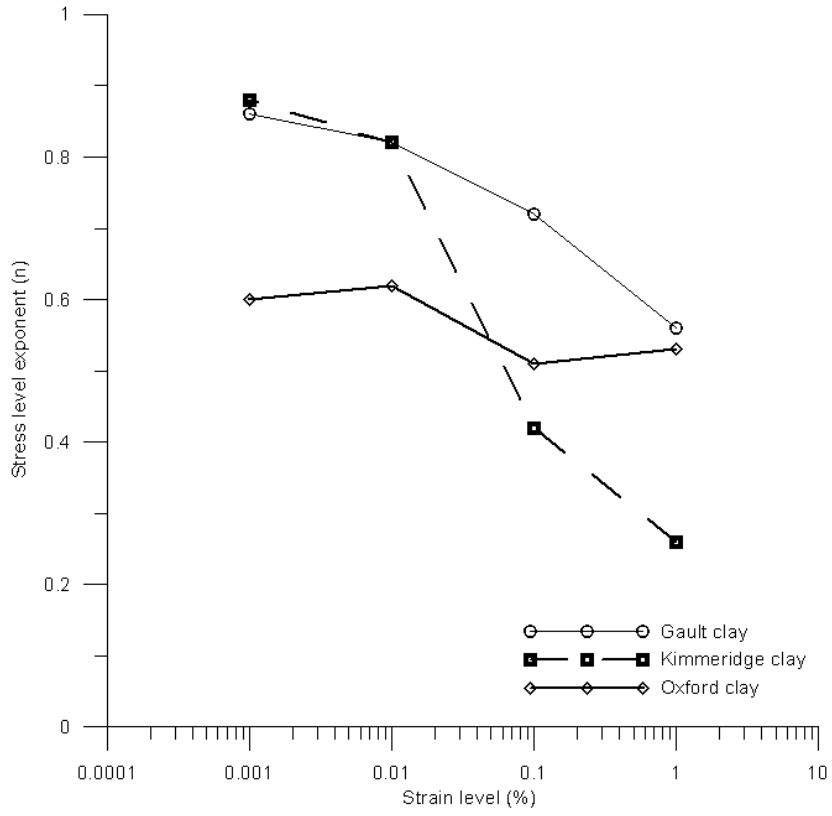


Figure 7-31: Variation of the mean effective stress level exponent, n, of stiffness (E^u_v) with strain level for natural soil

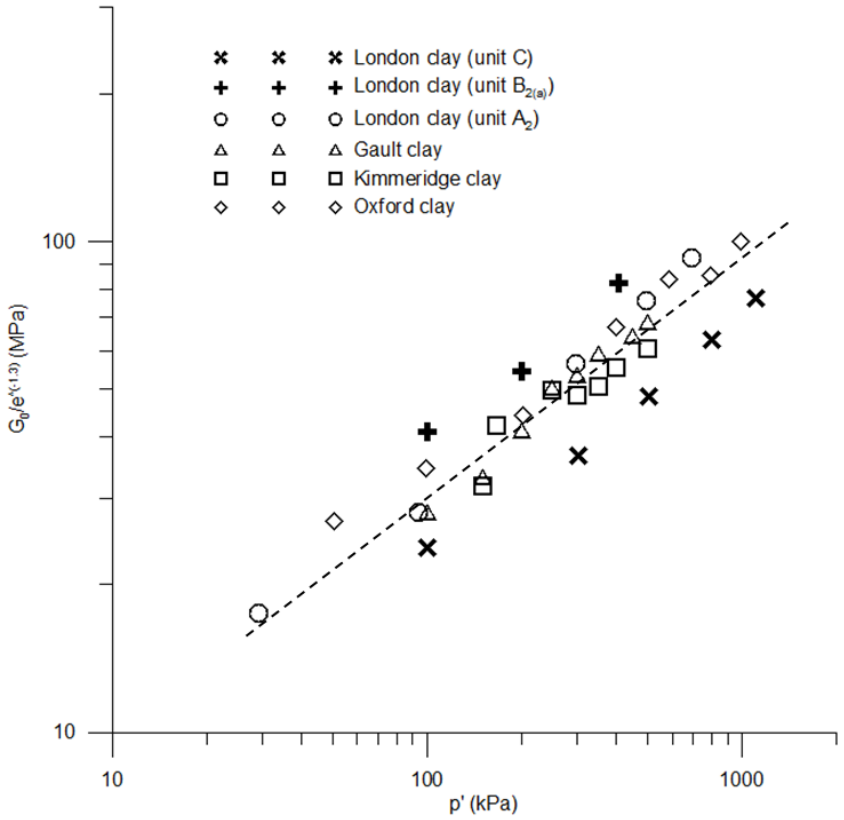


Figure 7-32: Variation of the normalised stiffness with stress level for the reconstituted samples of mudrocks (London clay data re-plotted from Gasparre et al., 2007)

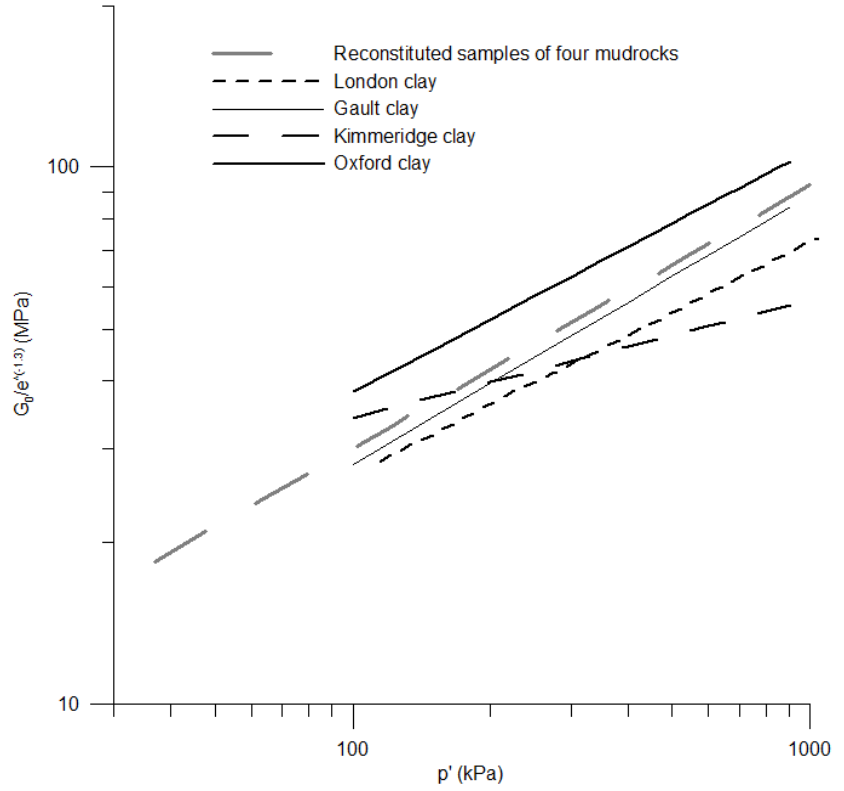


Figure 7-33: Variation of the normalised stiffness (G_{hv}) with stress level for the reconstituted and natural samples of mudrocks (London clay unit B_2 data re-plotted from Gasparre et al., 2007)

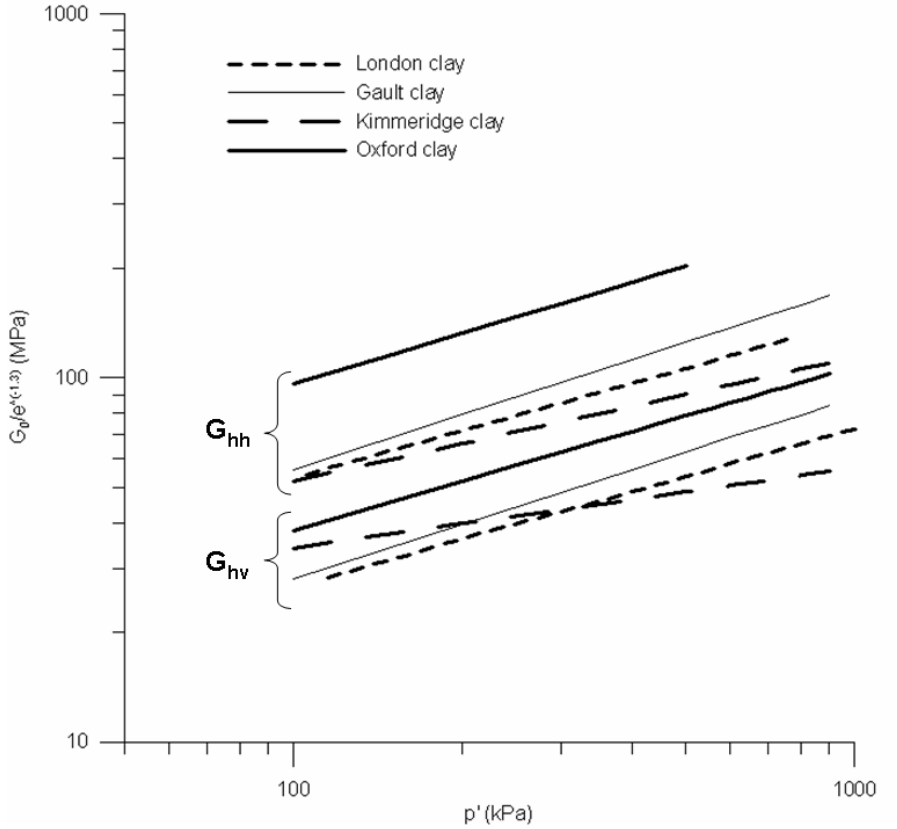


Figure 7-34: Variation of the normalised stiffness with stress level for the natural samples of mudrocks (London clay unit B_2 data re-plotted from Gasparre et al., 2007)

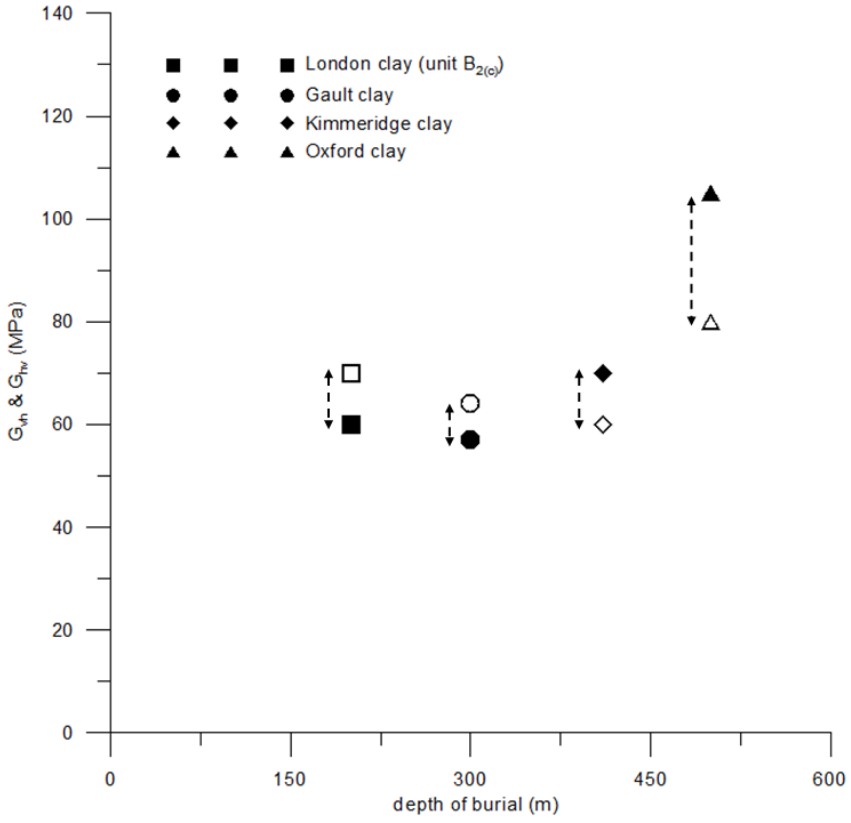


Figure 7-35: Shear moduli G_{vh} and G_{hv} measured in-situ, empty symbols, and in the laboratory, filled symbols (London clay data re-plotted from Gasparre et al., 2007)

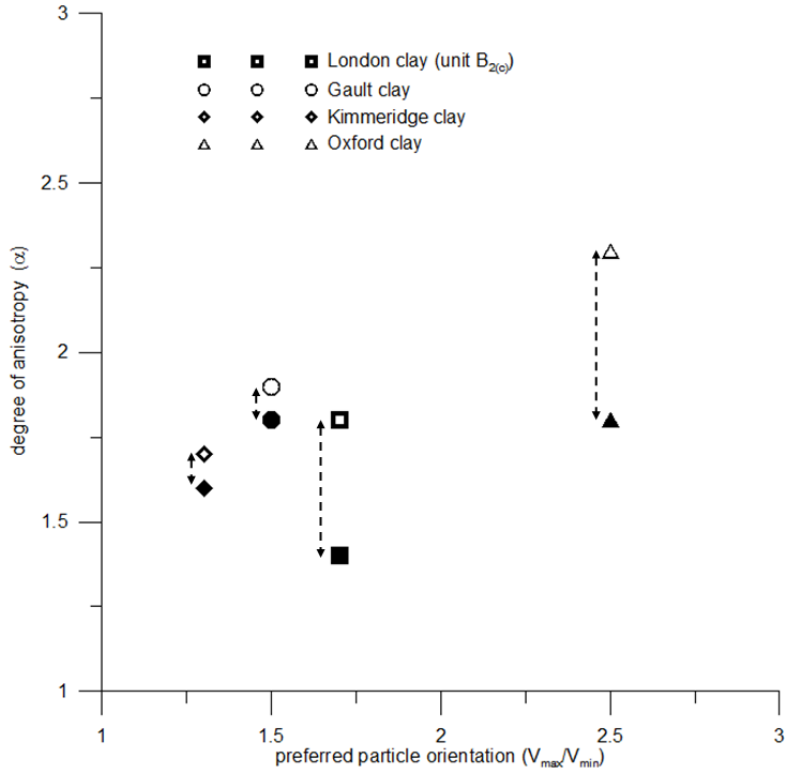


Figure 7-36: Effect of preferred particle orientation on the degree of anisotropy calculated based on G, empty symbols, and E, filled symbols (London clay data re-plotted from Gasparre et al., 2007)

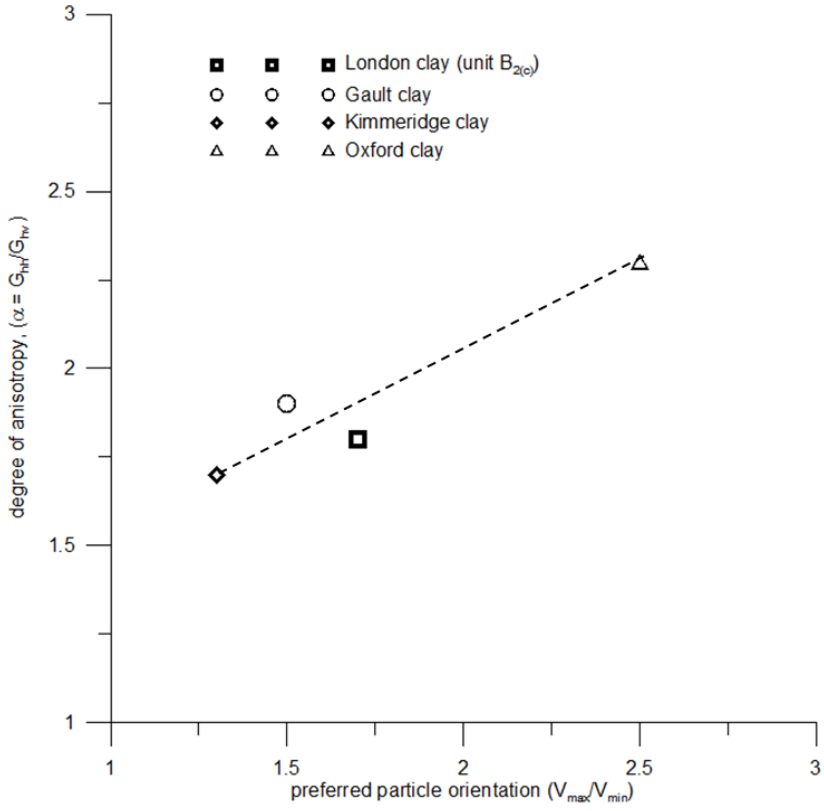


Figure 7-37: Effect of preferred particle orientation on the degree of anisotropy calculated based on G (London clay data re-plotted from Gasparre et al., 2007)

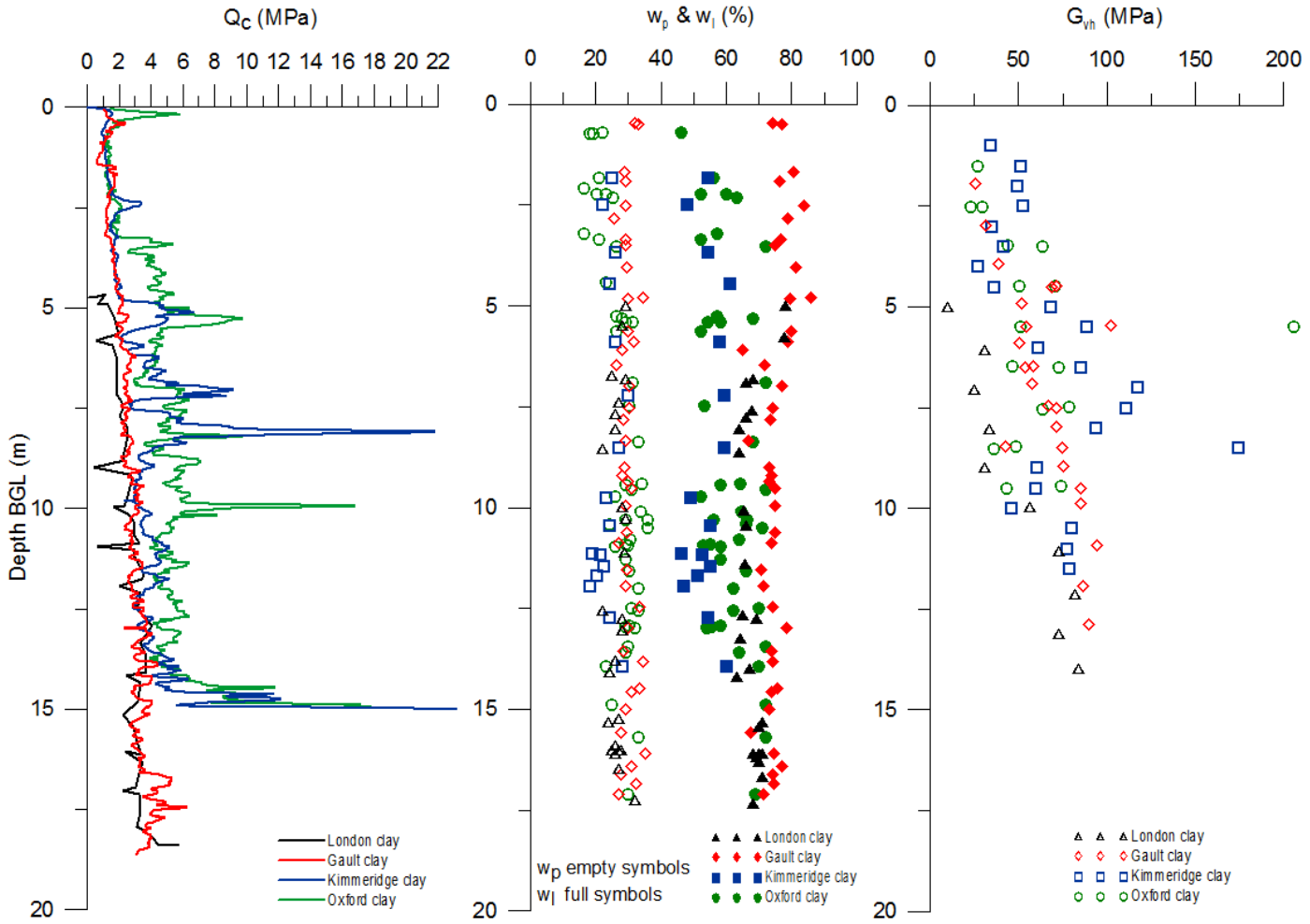


Figure 7-38: Profiles of the four UK mudrocks (some of the Atterberg limits for Oxford clay re-plotted from Hird & Pierpoint 1997; some of the Atterberg limits for Gault clay re-plotted from Butcher & Lord 1993; Gmax for Gault clay re-plotted from Butcher & Powell; 1993; London clay data re-plotted from Hight et al., 2007, CPT data provided by In-situ SI)

8 Conclusions

8.1 Current study

This thesis summarised the research which has been carried out on three different UK mudrocks. This project was continuation of the research which was completed on London Clay at Imperial College (Hight et al., 2007; Gasparre, 2005; Nishimura, 2006; Minh, 2007). The main objective of the research was to expand the knowledge surrounding these stiff clays by investigating geologically older clays than London Clay. Oxford Clay, Kimmeridge Clay and Gault Clay were chosen each with different geological age from upper Jurassic to lower Craterous. Very soon into the research it was realised that the complex depositional and post-depositional environments resulted in different structures for each of the mudrocks and geological age could not be the only comparative factor. The thesis started with overviewing the existing literature related to the stiff clays, particularly the effects of structure on their behaviour. Sampling and site locations, as well as the equipment and procedures were explained in Chapter 3. The difficulties of carrying out the stress probes mainly due to problems with the displacement measurements and full drainage of the sample were discussed and a new set-up for radial displacement measurement was introduced.

The current PhD project started in October 2007 with block sampling of Oxford clay from the base of a 10 metre deep excavation at Elstow. Block samples of Gault clay were retrieved a year after, from High Cross, Cambridge, and from 3.5 metres below ground level. High initial p' measurements in the triaxial apparatus and also the CPT profile at the site indicated high suction values for these block samples. Further investigations revealed that these samples were both weathered and affected by tree roots. To avoid both of these effects and have a comparable depth of sampling to that of Oxford clay, rotary core sampling was carried out in summer 2009 on the same site at High Cross. The same approach was used at the same time, in sampling of the Kimmeridge clay at Willow Brook Farm, south west of Abingdon.

Although it was not initially part of the project the rotary core samples allowed the study of weathering on the mudrock structures. A more disturbed structure with

higher clay content was observed by Wilkinson (2011) for the weathered Gault clay. The effects of weathering on the structure of the Gault and Kimmeridge clays were evident in the oedometer tests carried out on their natural samples. However, triaxial tests carried out on the natural samples of Gault clay did not show any significant difference between the strength and stiffness of the weathered and unweathered materials. The reason for this could have been caused by the close spaced fissuring at depths below the weathered zone which could have had a similar effect on the strength as that of the weathering.

Oxford clay, the oldest mudrock tested in the project, was deposited in a rising sea and in a low energy environment. It was buried deeper than other soils in this study, to about 500 to 1450 metres (depending on the method of estimation) below deposits which were in turn eroded with time. This resulted in a high overconsolidation of Oxford clay with very high horizontal stresses. The micro-structure of the soil was the strongest in this study with high degree of preferred particle alignment in the horizontal plane. This structure was reinforced with existence of horizontally bedded elongated fossils. This micro-structure was not accompanied with any significant fissuring at the macro-level resulting in a higher strength, stiffness and anisotropy of this soil compared to the others. However, it was observed that when the intensity of the horizontally bedded fossils was high, due to pauses during the deposition or during the extinction of species, the planes consisting of these fossils were very weak and prone to horizontal slip.

The mudrock which was closest in age and depth of burial to Oxford clay was Kimmeridge clay. There are few studies relevant to the conventional geotechnical properties of this clay and most studies are concentrated on the deep samples of Kimmeridge clay which form the reservoir rocks of several oil fields in the North Sea. A very different structure was observed for the Kimmeridge clay, with a high presence of silt particles and low clay content resulting in a structure with little preferred particle orientation. This structure was probably formed under a high energy environment which was different to that of Oxford clay. There was also a smaller amount of fossils in this soil and no major fissuring was observed at the macro-level. This structure affected all aspects of the soil behaviour with lower strength, stiffness and anisotropy.

Gault clay had the highest clay content and a particularly high amount of swelling minerals like smectite. However, the structure of the soil, except in one horizon, was not influenced by the amount of platy particles and the degree of preferred particle alignment was relatively low. The low strength of the soil in comparison with its reconstituted equivalent was probably caused not only by its micro-structure but by its close space fissuring at the macro-level. Unlike the reinforcing fossils in the Oxford clay, round fossils and nodules in the Gault clay had a disturbing effect on the structure and preferred particle orientation.

The comparisons were made between the three mudrocks mentioned above with the younger London clay. A more open structure was observed for this soil as it was not compressed as much as other older soils under deeper deposits. This study showed that both micro- and macro-structures are formed in various ways during different depositional and post-depositional environments which can result in different geotechnical behaviours regardless of the geological age. The research also provided a database of geotechnical parameters for these three UK mudrocks.

8.2 Future work

One of the observations made during this research was the changes in the stress exponent of the stiffness 'n' with strain level. Unlike the more common belief that expects 'n' to increase towards unity with increasing strain level (e.g. Viggiani and Atkinson, 1995), the 'n' value decreased with strain level for both the Kimmeridge and Gault clays while being almost constant for the Oxford clay. This needs to be further investigated by carrying out tests on normally consolidated and overconsolidated samples of these clays as well as studying other materials in their natural state.

In the case of the Kimmeridge and Gault clays the intrinsic State Boundary Surface, *SBS**, was constructed based on three tests at different *OCR* values with highest value of five. The Hvorlsev surface was not clearly defined based on these tests and higher *OCR* tests are required for this purpose.

Some high pressure tests were carried out on Oxford clay but still not high enough to capture the wet side of the natural State Boundary Surface. There were fewer high pressure tests for the other two soils. It would be useful to perform high pressure tests on all of these soils.

Bender elements were used to measure the shear moduli G_{hh}, G_{hv} and G_{vh}. The first pair could be obtained using the T shape bender elements and the last using top and bottom elements. The comparison between G_{hv} and G_{vh} was made for the Oxford clay and there was good agreement between the two although the values were measured on different samples. Measurements of G_{vh} were not carried out for the other two soils and it would be valuable to perform tests equipped with bender elements in different directions on a same sample so a comparison could be made between G_{hv} and G_{vh}.

As mentioned earlier, the effects of weathering were studied only for the Gault clay. Given the very strong structure of the Oxford clay, it would be interesting to see how weathering influenced this soil as well as Kimmeridge clay.

Micro-analysis was not part of the current PhD, but it helped with the understanding of the structures of the different materials. Further micro-analysis could be made on the reconstituted samples of these mudrocks to highlight the effects of reconstitution on the micro-structure and correspondingly on the mechanical behaviour.

References

Al-Tabbaa, A. and D. M. Muir Wood (1989). An experimentally based bubble model for clay. *Numerical methods in Geomechanics NUMOG III, Elsevier Applied Science*, 91–99.

Alvarado, G. (2007). *Influence of late cementation on the behaviour of reservoir sands*. Ph. D. thesis, Imperial College of Science, Technology and Medicine, University of London.

Alvarado, G. and M. R. Coop (2011). On the performance of bender elements in triaxial tests. *Submitted to Geotechnique*.

Amorosi, A. and S. Rampello (2007). An experimental investigation into the mechanical behaviour of a structured stiff clay. *Geotechnique 57*(2), 153–166.

Andersland, O. B. and A. G. Douglas (1970). Soil deformation rates and activation energies. *Geotechnique 20*(1), 1–16.

Arulnathan, R., Boulanger, R.S., and M. Riemer (1998). Analysis of bender element tests. *Geotechnical Testing Journal 21*(2), 120–131.

Atkinson, J. H. (2000). Non-linear soil stiffness in routine design. *Geotechnique 50*(5), 487–508.

Atkinson, J. H. (2007). Peak strength of overconsolidated clays. *Geotechnique 57*(2), 127–135.

Atkinson, J. H. and D. Richardson (1987). The effect of local drainage in shear zones on the undrained strength of overconsolidated clay. *Geotechnique 37*(3), 393–403.

Atkinson, J. H., D. Richardson, and S. E. Stallebrass (1990). Effect of stress history on the stiffness of overconsolidated soil. *Geotechnique 40*(4), 531–540.

Baudet, B. and S. E. Stallebrass (2004). A constitutive model for structured clays. *Geotechnique 54*(4), 269–278.

Biddle, P. G. (1983). Patterns of soil drying and moister deficit in the vicinity of trees on clay soils. *Geotechnique 33*(2), 107–126.

Bishop, A. and D. Henkel (1957). *The measurement of soil properties in the triaxial tests*. Edward Arnold LTD, London.

Bishop, A. W. (1967). Progressive failure-with special reference to the mechanism causing it. Proceedings of the Geotechnical Conference, Oslo, Norway.

Bishop, A. W. and L. D. Wesley (1975). A hydraulic triaxial apparatus for controlled stress path testing. *Geotechnique 25*(4), 657–670.

Blewett, J., I. Blewett, and P. Woodward (2000). Phase amplitude responses associated with the measurement of shear-wave velocity in sand by bender elements. *Canadian Geotechnical Journal 37*, 1348–1357.

Blight, G. E. (2005). Desiccation of a clay by grass, bushes and trees. *Geotechnical and Geological Engineering 23*, 697–720.

Bozozuk, M. and K. N. Burn (1960). Vertical ground movement near Elm trees. *Geotechnique 10*(1), 19–32.

Brenchley, P. J. and P. Rawson (2006). The Geology of England and Wales. *The Geological Society London*, 559.

Brosse, A. (2008). Study of the anisotropy of British mudrocks and stiff clays. M.Phil. Transfer report, Imperial College London.

Brosse, A. (2012). *Study on the anisotropy of British mudrocks using a Hollow Cylinder Apparatus*. Ph. D. thesis, Imperial College London.

Burland, J. B. (1990). On the compressibility and shear strength of natural soils. *Geotechnique 40*(3), 329–378.

Burland, J. B. (2006). Soil Strength and Deformation. MSc. Soil mechanics lecture notes.

Burland, J. B., T. I. Longworth, and J. F. A. Moore (1977). A study of ground movement and progressive failure caused by a deep excavation in Oxford Clay. *Geotechnique 27*(4), 557–591.

Burland, J. B., S. RAMPELLO, V. N. GEORGIANNOU, and G. CALABRESI (1996). A laboratory study of the strength of four stiff clays. *Geotechnique 46*(3), 491–514.

Butcher, A. and J. Lord (1993). Engineering properties of the Gault Clay in and around Cambridge, UK. Proceedings of the International Symposium on Geotechnical Engineering of Hard Soils–Soft Rocks, Athens, Greece, pp. 405–416.

Butcher, A. P. and J. M. M. Powell (1995). The effects of geological history on the dynamic stiffness in soils. Volume 1 of *Proc. 11th European Conf. on Soil Mechanics*, Copenhagen, Denmark, pp. 1.27–1.36.

Cafaro, F. and F. Cotecchia (2001). Structure degradation and changes in the mechanical behaviour of a stiff clay due to weathering. *Geotechnique 51*(5), 441–453.

Cameron, D. A. (2001). The extent of soil desiccation near trees in a semi-arid environment. *Geotechnical and Geological Engineering 19*, 357–370.

Casagrande, A. and S. D. Wilson (1951). Effect of rate of loading on the strength of clays and shales at constant water content. *Geotechnique 2*(3), 251–263.

Chandler, R. J. (1966). The measurement of residual strength in triaxial compression. *Geotechnique 16*(3), 181–186.

Chandler, R. J. (1969). The effect of weathering on the shear strength properties of Keuper Marl. *Geotechnique 19*(3), 321–334.

Chandler, R. J. (1972). Lias clay: weathering processes and their effect on shear strength. *Geotechnique 22*(3), 403–431.

Chandler, R. J. (2000). Clay sediments in depositional basins: the geotechnical cycle. *The Third Glossop Lecture. Q. J. Engng Geol. And Hydrogeol 33*, 7–39.

Chandler, R. J. and J. P. Apted (1988). The effect of weathering on the strength of london clay. *Quart. Journal of Engineering Geology 21*, 59–68.

Clayton, C. R. I. (2011). Stiffness at small strain: research and practice. *Geotechnique 61*(1), 5–37.

Clayton, C. R. I. and G. Heymann (2001). Stiffness of geometerials at very small strains. *Geotechnique 51*(3), 245–255.

Coop, M. R., J. H. Atkinson, and R. N. Taylor (1995). Strength, yielding and stiffness of structured and unstructured soils. Number 1 in Proc. 11th ECSMFE, Copenhagen, pp. 55–62.

Cooper, M., E. Bromhead, D. Petley, and D. Grant (1998). The Selborne cutting stability experiment. *Geotechnique 48*, 83–101.

Cotecchia, F. (1996). *The effects of structure on the properties of an Italian Pleistogene clay.* Ph. D. thesis, University of London.

Cotecchia, F. (2007). Personal communication.

Cotecchia, F. and R. J. Chandler (1997). The influence of structure on the prefailure behaviour of a natural clay. *Geotechnique 47*(3), 523–544.

Cotecchia, F. and R. J. Chandler (2000). A general framework for the mechanical behaviour of clay. *Geotechnique 50*(4), 431–447.

Cox, B., M. Sumbler, and H. Ivimey-Cook (1999). A formational framework for the lower jurassic of england and wales (onshore area).

Crabb, G. I. and J. H. Atkinson (1991). *Determination of soil strength parameters for the analysis of highway slope failures. In: Slope stability engineering: Developments and applications (ed. R. Chandler).* Thomas Telford, London.

Crilly, M. S. and R. Driscoll (2000). The behaviour of lightly loaded piles in swelling ground and implications for their design. Volume 143 of *Proc. Instn Civ. Engrs, Geotech. Engng*, pp. 3–16.

Cuccovillo, T. and M. R. Coop (1997). The measurements of local axial strains in triaxial tests using LVDTs. *Geotechnique 47*(1), 167–171.

Cunliffe, D. (2010). A study of the brittle behaviour of intact UK mudrocks in shear. Master's thesis, Imperial College London.

Dasari, G. R. and M. D. Bolton (1998). Comparison of field and laboratory stiffness of Gault Clay. Symposium on Pre-failure Deformation behaviour of geomaterials, Thomas Telford, pp. 345–352.

Driscoll, R. (1983). The influence of vegetation on the swelling and shrinking of clay soils in Britain. *Geotechnique 33*(2), 93–105.

Dyvik, R. and C. Madshus (1985). Labarotry measurement of Gmax using bender elements. Proc. ASCE Annual Convention: Advances in the art of testing soils under cyclic conditions, Detroit, USA.

Fearon, R. E. and M. R. Coop (2000). Reconstitution-what makes an appropriate reference material? *Geotechnique 50*(4), 471–477.

Fearon, R. E. and M. R. Coop (2002). The influence of landsliding on the behaviour of a structurally complex clay. *Q J ENG GEOL HYDROGE 35*, 25–32.

Feda, J. (1989). Interpretation of creep of soils by rate process theory. *Geotechnique 39*(4), 667–677.

Gao, Y. (2009). Investigation of the transitional behaviour of clays. Master's thesis, Imperial College London.

Garrett, C. and S. J. Barnes (1984). A laboratory study of post-rupture strength. *Geotechnique 34*, 533–548.

Gasparre, A. (2005). *Advanced laborotay characterization of London clay*. Ph. D. thesis, Imperial College of Science, Technology and Medicine, University of London.

Gasparre, A. and M. R. Coop (2008). The quantification of the effects of structure on the compression of a stiff clay. *Canadian Geotechnical Journal 45*, 1324–1334.

Gasparre, A., S. Nishimura, M. R. Coop, and R. J. Jardine (2007). The influence of structure on the behaviour of London Clay. *Geotechnique 57*(1), 19–31.

Gasparre, A., S. Nishimura, N. A. Minh, M. R. Coop, and R. J. Jardine (2007). The stiffness of natural London Clay. *Geotechnique 57*(1), 33–47.

Gens, A. (1982). *Stress-strain and strength of a low plasticity clay*. Ph. D. thesis, Imperial College of Science, Technology and Medicine, University of London.

Georgiannou, V. N. and J. B. Burland (2001). A laboratory study of post-rupture strength. *Geotechnique 51*(8), 665–675.

Graham, G. and G. T. Houlsby (1983). Anisotropic elasticity of a natural clay. *Geotechnique 33*(2), 165–180.

Green, P., K. Thompson, and J. Hudson (2001). Recognition of tectonic events in undeformed regions: contrasting results from the Midland Platform and East Midland Shelf, Central England. *Journal of the Geological Society London 158*, 59–73.

Green, P. F. (1989). Thermal and tectonic history of the East Midlands shelf (onshore UK) and surrounding regions assessed by apatite fission track analysis. *Journal of the Geological Society 146*, 775–773.

Greening, P. D. and F. T. Nash (2004). Frequency domain determination of $G_0 using bender elements. Geotechnical Testing Journal$ $27(3), 288 - -294$.

Hallam, A. (1975). *Jurassic environments*. Cambridge University Press.

Hallam, A. (1999). Evidence of sea-level fall in sequence stratigraphy Examples from the Jurassic. *Geology 27*, 343–346.

Hawkins, A. B., M. S. Lawrence, and K. D. Privett (1988). Implications of weathering on the engineering properties of the Fuller's earth formation. *Geotechnique 38*(4), 517–532.

Hight, D. W. (1982). A simple piezometer probe for the routine measurements of pore water pressure in triaxial tests on saturated specimens. *Geotechnique 32*(4), 396–401.

Hight, D. W., A. J. Bond, and J. D. Legge (1992). Characterization of the Bothkennar clay: an overview. *Geotechnique 42*, 303–347.

Hight, D. W., A. Gasparre, S. Nishimura, N. A. Minh, R. J. Jardine, and M. R. Coop (2007). The influence of structure on the behaviour of London Clay. *Geotechnique 57*(1), 3–18.

Hird, C. C. and N. D. Pierpoint (1997). Stiffness determination and deformation analysis for a trial excavation in Oxford Clay. *Geotechnique 47*(3), 665–691.

Hvorslev, M. (1937). Uber die Festigkeitseirgenschaften Gestorter Bindiger Boden. Danmarks Naturvidenskabelige Samfund. *Ingeniorvidenskabelige Skrifter A*(45).

Indraratna, B., B. Fatahi, and H. Khabbaz (2006). Numerical analysis of matric suction effects of tree roots. Proceedings of the institution of Civil engineers Geotechnical Engineering 159. April 2006, Issue GE2.

Jackson, J. (1972). *Geotechnical properties of the Lower Oxford Clay related to deep burial*. Ph. D. thesis, Imperial College of Science, Technology and Medicine, University of London.

Jackson, J. O. and P. G. Fookes (1974). Relationship of the estimated former burial depth of Lower Oxford Clay to some soil properties. *Quart. J. Eng. Geol 7*, 137–179.

Jamiolkowski, M., S. Leroeuil, and D. C. F. Lo Presti (1991). Design parameters from theory to practice. Volume 2 of *Geo-coast '91 Int. Conf., Yokohama, Port and Harbour research Institute*, Yokosuka, pp. 877–917.

Jardine, R. J. (1992). Some observations on the kinematic nature of soil stiffness. *Soils and foundations 32*(2), 111–124.

Jardine, R. J. (1994). One perspective of the pre-failure deformation characteristics of some geomaterials. Proc. International Symposium on Pre-failure Deformation Characteristics of Geomaterials IS, Hokkaido, Sapporon.

Jardine, R. J. (1995). One perspective of the pre-failure deformation characteristics of some geomaterials. Volume 2 of *Proc. of the Int. conference on the prefailure deformation characteristics of geomaterials*, Hokkaido, Japan, pp. 855–885.

Jardine, R. J., A. Gens, D. W. Hight, and M. R. Coop (2004). Development in understanding soil behaviour. *Advances in Geotechnical Engineering: The Skempton Conference. Jardine, R.J., Potts, D.M. & Higgins, K.G. eds., Thomas Telford, London*, 103–206.

Jardine, R. J., D. M. Potts, A. B. Fourie, and J. B. Burland (1986). Studies of the influence of non-linear characteristics in soil-structure interaction. *Geotechnique 36*(3), 377–396.

Jeans, C., R. Merriman, J. Mitchell, and D. Bland (1982). Volcanic clays in the Cretaceous of Southern England and Northern Ireland. *Clay Minerals 17*, 105–156.

Jeans, C., D. Wray, R. Merriman, and M. Fisher (2000). Volcanogenic clays in Jurassic and Cretaceous strata of England and the North Sea Basin. *Clay Minerals 35*, 25–55.

Jones, L., P. Hobbs, and A. Cripps (1996). Report on visit to Arlesey brick pit and Leighton Buzzard sand pit for the swelling and shrinkage of soils project (77BH), Project No. PN/96/17, BGS, p. 12.

Jovicic, V, C., M. R., and M. Simic (1996). Objective criteria for determining gmax from bender element tests. *Geotechnique 46*(2), 357–362.

Jovicic, V. and M. R. Coop (1998). The measurement of stiffness anisotropy in clays with bender element tests in the triaxial apparatus. *Geotechnical testing journal, GTJODJ 21*(1), 3–10.

Jovicic, V. and G. Vilhar (2009). Measurment and interpretation of the small strain stiffness of Bostanj silty sand. *ACTA GEOTECHNICA SLOVENICA 2*.

Kavvadas, M. and A. Amorosi (2000). A constitutive model for structured soils. *Geotechnique 50*(3), 263–273.

King, C. (1981). The stratigraphy of the London Basin and associated deposits. Volume 6 of *Tertiary Research Special Paper*, Backhuys, Rotterdam.

Krizek, R. J., K. S. Chawla, and T. B. Edil (1977). Directional creep response of anisotropic clays. *Geotechnique 27*(1), 37–51.

Kutter, B. L. and N. Sathialingam (1992). Elastic-viscoplastic modelling of the rate-dependent behaviour of clays. *Geotechnique 42*(3), 427–441.

Kuwano, R. (1999). *The stiffness and anisotropy of sand*. Ph. D. thesis, Imperial College of Science, Technology and Medicine, University of London.

Kuwano, R. and R. J. Jardine (1998). Stiffness measurements in a stress-path cell. In Pre-failure Deformation Behaviour of Geomaterials, eds R. J. Jardine et al., London: Thomas Telford, pp. 391–394.

Kuwano, R. and R. J. Jardine (2002). On the applicability of cross-anisotropy elasticity to granular materials at very small strains. *Geotechnique 52*(10), 727–749.

Lambe, T. W. and R. V. Whitman (1969). *Soil Mechanics*. John Wiley & Sons Inc., New York.

Lee, J. S. and J. Santamarina (2005). Bender elements: performance and signal interpretation. *Journal of Geotechnical and Geoenvironmental Engineering 131*(9), 1063–1070.

Leong, E., J. Cahyadi, and H. Rahardjo (2009). Measuring shear and compression wave velocities of soil using bender-extender elements. *Canadian Geotechnical Journal 46*, 792–812.

Lings, M., D. Nash, C. NG, and M. Boyce (1991). Observed behaviour of a deep excavation in Gault Clay: a preliminary appraisal. Volume 2 of *Proceedings of the 10th European Conference on Soil Mechanics and Foundation Engineering*, Florence, Italy, pp. 467–470.

Lings, M. L. (2001). Drained and undrained anisotropic elastic stiffness parameters. *Geotechnique 51*(6), 555–565.

Lings, M. L., D. S. Pennington, and D. F. Nash (2000). Anisotropic stiffness parameters and their measurement in a stiff natural clay. *Geotechnique 50*(2), 109–125.

Love, A. E. H. (1927). *A treatise on the mathematical theory of elasticity*. Dover publications, New York.

Lupini, J. F., A. E. Skinner, and P. R. Vaughan (1981). The drained residual strength of cohesive soils. *Geotechnique 31*(2), 181–213.

Marsh, A. and N. Greenwood (1995). Foundations in Gault Clay. Volume 10 of *EDDLESTON, M., Walthall, S., Cripps, J.C., and Culshaw, M.G., eds., Engineering Geology of Construction, Geological Society Engineering Geology Special Publication*, pp. 143–160.

Mayne, P. W. and F. H. Kulhawy (1982). Ko-OCR relationship in soil. *ASCE, GT6 108*, 851–872.

Mesri, G., E. Febres Cordero, D. R. Shields, and A. Castro (1981). Shear stress-strain-time behaviour of clays. *Geotechnique 31*(4), 537–552.

Minh, N. A. (2007). *An investigation of the stress-strain-strength characteristics of an Eocence clay.* Ph. D. thesis, Imperial College of Science, Technology and Medicine, University of London.

Mitchell, J. K. (1960). Fundamental aspects of thixotropy in soils. *Journal of SMFE Div., Proc of ASCE 83*(3), 19–52.

Mitchell, J. K. (1964). Shearing resistance of soils as a rate process. J.Soil Mech. Fdns Div. Am. Soc. Civ. Engrs, 90, SM1, pp. 231–253.

Mitchell, J. K. and K. Soga (2005). *Fundamentals of Soil Behavior.* John Wiley & Sons Inc., New York.

Moore, R. (1991). The chemical and mineralogical controls upon the residual strength of pure and natural clays. *Geotechnique 41*(1), 35–47.

Moran, P. (2010). Obtaining the intrinsic parameters of stiff clays to evaluate the effects of structure. Master's thesis, Imperial College London.

Narayana, M. (2010). A study of the residual shear strength characteristics of remoulded UK mudrocks. Master's thesis, Imperial College London.

Ng, C. W. W. (1998). Observed performance of multipropped excavation in stiff clay. *Journal of Geotechnical and Geoenvironmental Engineering*, 889–905.

Nishimura, S. (2005). *Laboratory study on anisotropy of natural London clay.* Ph. D. thesis, Imperial College of Science, Technology and Medicine, University of London.

Nygard, R., M. Gutierrez, R. K. Bratli, and K. Hoeg (2006). Brittle-ductile transition, shear failure and leakage in shales and mudrocks. *Marine and Petroleum Geology 23*, 201–212.

Nygard, R., M. Gutierrez, R. Gautam, and K. Hoeg (2004). Compaction behaviour of argillaceous sediments as function of diagenesis. *Marine and Petroleum Geology 21*, 349–362.

Oertel, G. (1983). The relationship of strain and preferred orientation phyllosilicate grains in rocks, a review. *Tectonophysics 100*, 413–447.

Parry, R. H. G. (1972). Some properties of heavily overconsolidated Oxford Clay at a site near bedford. *Geotechnique 22*(3), 485–507.

Pennington, D. S., D. Nash, and M. Lings (2001). Horizontally mounted bender elements for measuring anisotropic shear moduli in triaxial clay specimens. *Geotechnical Testing Journal 24*(2), 133–144.

Pennington, D. S., D. F. T. Nash, and M. L. Lings (1997). Anisotropy of G0 shear stiffness in Gault clay. *Geotechnique 47*(3), 391–398.

Pickering, D. J. (1970). Anisotropic elastic parameters for soils. *Geotechnique 20*(3), 271–276.

Pierpoint, N. D. (1996). *The prediction and back analysis of excavation behaviour in Oxford Clay.* Ph. D. thesis, University of Sheffield.

Puzrin, A. M. and J. B. Burland (1998). Non-linear model of small-strain behaviour of soils. *Geotechnique 20*(48), 217–233.

Richards, B. G., P. Peter, and W. W. Emerson (1983). The effects of vegetation on the swelling and shrinking of soils in Australia. *Geotechnique 33*(2), 127–139.

Ridley, A. and J. Burland (1993). A new instrumentation for the measurement of soil moisture suction. *Geotechnique 43*(2), 321–324.

Rolo, R. (2003). *The anisotropic stress-strain-strength behaviour of brittle sediments*. Ph. D. thesis, Imperial College of Science, Technology and Medicine, University of London.

Rudrum, D. M. (1990). The short term behaviour of a trial excavation in Oxford Clay. Master's thesis, Imperial College London.

Samuels, S. G. (1975). Some properties of the gault clay from the ely-ouse essex water tunnel. *Geotechnique 25*(2), 239–264.

Sandroni, S. (1977). *The strength of London Clay in total and effective stress terms*. Ph. D. thesis, University of London.

Schmertmann, J. H. (1969). Swell Sensitivity. *Geotechnique 19*(41), 530–533.

Shipton, B. (2010). *The Mechanics of Transitional Soils*. Ph. D. thesis, Imperial College of Science, Technology and Medicine, University of London.

Sides, G. and L. Barden (1970). The microstructure of dispersed and flocculated samples of kaolinite, illite and montmorillonite. *Canadian Geotechnical Journal 8*, 391–399.

Simpson, B., J. H. Atkinson, and V. Jovicic (1996). The influence of anisotropy on calculations of ground settlements above tunnels. Proceedings, Geothecnical Aspects of underground construction in soft ground, Balkema, Rotterdam, pp. 591–595.

Skempton, A. W. (1964). Long-term stability of clay slopes. *Geotechnique 14*, 77–101.

Skempton, A. W. (1969). The consolidation of clays by gravitational compaction. *Quarterly Journal of the Geological Society 125*, 373–411.

Smith, P., R. J. Jardine, and D. W. Hight (1992). The yielding of Bothkennar clay. *Geotechnique 42*(2), 257–274.

Snchez Salinero, I., J. M. Roesset, and K. H. Stokoe (1986). Analytical studies of body wave propagation and attenuation. Geotechnical Engineering Report No. GR86-15. Civil Engineering Department, University of Texas at Austin.

Sorensen, K. K., B. A. Baudet, and B. Simpson (2007). Influence of structure on the time-dependent behaviour of a stiff sedimentary clay. *Geotechnique 57*(1), 113–124.

Stallebrass, S. E. and R. N. Taylor (1997). The development and evaluation of a constitutive model for the prediction of ground movements in overconsolidated clay. *Geotechnique 47*(2), 235–353.

Tatsuoka, F. (2006). Keynote lecture: Inelastic deformation characteristics of geomaterials and their simulations. Soil Stress-Strain Behaviour: Measurement, Modelling and Analysis. Proceeding of the Geotechnical Symposium, Roma, Italy, pp. 1–108.

Tatsuoka, F., M. Ishihara, H. Di Benedetto, and R. Kuwano (2002). Time-dependent shear deformation characteristics of geomaterials and their simulation. *Soils Found 42*(2), 103–129.

Tatsuoka, F., F. Santucci de Magistris, K. Hayano, Y. Momoya, and J. Koseki (1998). Some new aspects of time effects on the stress-strain behaviour of stiff geomaterials. *2HSSR, Napoli*.

Teachavorasinskun, S., P. Thongchim, and P. Lukkunaprasit (2002). Stress rate effect on the stiffness of a soft clay from cyclic, compression and extension triaxial tests. *Geotechnique 52*(1), 51–54.

Terzaghi, K. (1944). Ends and means in Soil Mechanics. *Engng J. Canada 27*, 608.

Vaughan, P. R. (1997). Engineering behaviour of weak rock: Some answers and some questions. Volume 3 of *Proc. Of the First Int. Conf. On Hard Soils and Soft Rocks*, Balkema, Rotterdam, pp. 1741–1765.

Vaughan, P. R. and C. W. Kwan (1984). Weathering structure and in situ stress in residual soils. *Geotechnique 22*(3), 403–431.

Viggiani, G. and J. H. Atkinson (1995a). The interpretation of the bender element tests. *Geotechnique 45*(1), 149–155.

Viggiani, G. and J. H. Atkinson (1995b). Stiffness of fine-grained soil at very small strains. *Geotechnique 45*(2), 249–265.

Vitone, C., F. Cotecchia, J. Desrues, and G. Viggiani (2009). An approach to the interpretation of the mechanical behaviour of intensely fissured clays. *Soils and foundations 49*(3), 355–368.

Wesley, L. D. (2003). Residual strength of clays and correlations using Atterberg limits. *Geotechnique 53*(7), 669–672.

Wignall, P. (1989). Sedimentary dynamics of the Kimmeridge Clay: tempests and earthquakes. *Journal of the Geological Society London 146*, 273–284.

Wilkinson, S. (2008). The Engineering Behaviour and Microstructure of UK Mudrocks. M.Phil. Transfer report, Imperial College London.

Wilkinson, S. (2011). *The microstructure of UK mudrocks*. Ph. D. thesis, Imperial College London.

Wroth, C. P. and G. T. Houlsby (1985). Soil mechanics property characterisation and analysis procedures. Proc. 11th Conf. Soil Mech., San Francisco , USA, pp. 1–55.

Wu, T. H. and A. Watson (1998). In situ shear tests of soil blocks with roots. *Canadian Geotechnical Journal 35*, 579–590.

Zhang, G., J. T. Germaine, A. J. Whittle, and C. C. Ladd (2004). Soil structure of a highly weathered old alluvium. *Geotechnique 54*(7), 453–466.

Zorina, S., O. Dzyuba, B. Shurygin, and D. Ruban (2008). How global are the Jurassic-Cretaceous unconformities? *Terra Nova 20*, 341–346.